

**VIBRATION-BASED DAMAGE IDENTIFICATION
METHODS FOR CIVIL ENGINEERING STRUCTURES
USING ARTIFICIAL NEURAL NETWORKS**

By
Ulrike Dackermann

A thesis submitted in fulfilment
of the requirements for the degree of
Doctor of Philosophy

Faculty of Engineering and Information Technology
University of Technology Sydney

May 2010

CERTIFICATE OF AUTHORSHIP/ORIGINALITY

I certify that the work in this thesis has not previously been submitted for a degree nor has it been submitted as part of requirements for a degree except as fully acknowledged within the text.

I also certify that the thesis has been written by me. Any help that I have received in my research work and the preparation of the thesis itself has been acknowledged. In addition, I certify that all information sources and literature used are indicated in the thesis.

Ulrike Dackermann

May 2010

ABSTRACT

This thesis investigates the viability of using dynamic-based ‘damage fingerprints’ in combination with artificial neural network (ANN) techniques and principal component analysis (PCA) to identify defects in civil engineering structures. Vibration-based damage detection techniques are global methods and are based on the principle that damage alters both the physical properties, such as mass, stiffness and damping, as well as the dynamic properties of a structure. It is therefore feasible to utilise measured dynamic quantities, such as time histories, frequency response functions (FRFs) and modal parameters, from structural vibration to detect damage. Damage identification based on vibrational characteristics is essentially a form of pattern recognition problem, which looks for the discrimination between two or more signal categories, e.g., before and after a structure is damaged, or differences in damage levels or locations. Artificial neural networks are capable of pattern recognition, classification, signal processing and system identification, and are therefore an ideal tool in complementing dynamic-based damage detection techniques. Likewise, PCA has pattern recognition abilities and is capable of data reduction and noise filtering. With these characteristics, both techniques can help overcome limitations associated with previously developed vibration-based methods and assist in delivering more accurate and robust damage identification results.

In this study, two types of dynamic-based damage identification methods are proposed. The first is based on the damage index (DI) method (initially proposed by Stubbs et al.), while the second approach uses changes in FRF data as damage fingerprints. The advantage of using damage patterns from the DI method, which is based on changes in modal strain energies, is that only measured mode shapes are required in the damage identification, without having to know the complete stiffness and mass matrices of the structure. The use of directly measured FRF data, which provide an abundance of information, is further beneficial as the execution of experimental modal analysis is not required, thus greatly reducing human induced errors. Both proposed methods utilise PCA and neural network techniques for damage feature extraction, data reduction and noise filtering. A hierarchical network training scheme based on network ensembles is proposed to take advantage of individual characteristics of damage patterns obtained from different sources (different vibrational modes for the DI-based method and

different sensor locations for the FRF-based method). In the ensemble, a number of individual networks are trained in parallel, which optimises the network training and delivers improved damage identification outcomes. Both methods are first tested on a simple beam structure to assess their feasibility and performance. Then, the FRF-based method is applied to a more complicated structure, a two-storey framed structure, for validation purposes. The two methods are verified by numerical simulations and laboratory testing for both structures. As defects, notch type damage of different severities and locations are investigated for the beam structure. For the two-storey framed structure, three different types of structural change are studied, i.e. boundary damage, added mass changes and section reduction damage. To simulate field-testing conditions, the issue of limited sensor availability is incorporated into the analysis. For the DI-based method, sensor network limitations are compensated for by refining coarse mode shape vectors using cubic spline interpolation techniques. To simulate noise disturbances experienced during experimental testing, for the numerical simulations, measurement data are polluted with different levels of white Gaussian noise.

The damage identifications of both methods are found to be accurate and reliable for all types of damage. For the DI-based method, the results show that the proposed method is capable of overcoming limitations of the original DI method associated with node point singularities and sensitivities to limited number of sensors. For the FRF-based method, excellent results are obtained for damage identification of the beam structure as well as of the two-storey framed structure. A major contribution is the training of the neural networks in a network ensemble scheme, which operates as a filtering mechanism against individual networks with poor performance. The ensemble network, which fuses results of individual networks, gives results that are in general better than the outcomes of any of the individual networks. Further, the noise filtering capabilities of PCA and neural networks demonstrate great performance in the proposed methods, especially for the FRF-based identification scheme.

Für Mutti und Papa

ACKNOWLEDGEMENTS

This PhD project could not have been possible without the support provided by numerous people. In particular, I would like to express my deepest appreciation and gratitude to:

- My supervisor, Professor Bijan Samali, for his outstanding guidance, encouragement, wisdom and caring support provided throughout this project. It was an honour and a pleasure to be one of his students. Bijan's professional and far-thinking leadership ensured the steady progress, timely completion and high standard of this thesis. Over the years, Bijan's exceptional personality became a source of inspiration and a role model for my professional and personal development, which will be of guidance throughout my life. I thank him from the bottom of my heart for his invaluable advice and support given throughout the years.
- My co-supervisor, Associate Professor Jianchun Li, for his first-class and unfailing assistance, guidance and support over the past few years. His brilliant and sharp mind combined with his extensive technical knowledge, experience and dedication contributed largely to the success of this project. In Jianchun, I found an exceedingly competent, enthusiastic and supportive supervisor on whom I could always rely. And as Peter Brown always says, "he is right 99.9% of the time". I sincerely thank him for his extraordinary help.
- My mentor and dear friend, Dr Fook Choon Choi, who went to tremendous lengths to assist and guide me throughout my research. He was always available to discuss with me any of my concerns and worries, ranging from the technical to the purely philosophical. I benefitted enormously from our many (often long) conversations, which somehow always delivered the answers I was looking for. For the future, I wish him happiness, love, peace of mind and good health, whatever path he chooses in life (whether as a Buddhist monk or a 'layperson'). No doubt wherever he goes, he will delight those around him with his wisdom and 'loving kindness'.
- The UTS Structures Laboratory staff, Peter Brown, Rami Haddad, David Dicker, Warwick Howse, Wolfgang Stengl, David Hooper, Laurence Stonard and Richard Turnell, for their extensive assistance in conducting the experimental works. Special thanks go to Peter Brown, for his remarkable help in all technical matters concerning experimental modal analysis & testing (you are a champ!), and to David Dicker, who was always there to give a helping hand and to find that special screw I was just looking for.

- The administrative and support staff at the UTS Faculty of Engineering and IT, Phyllis Agius, Anya Van Eeuwen, Craig Shuard, Matt Gaston and the IT support team, for doing an excellent job in keeping the show running.
- Professor Keith Crews, for providing my first contact with UTS and for initiating and supporting a number of conference trips.
- My friends from UTS, for walking the winding path to a PhD together. Special thanks go out to Debborah Marsh, Janitha Wijesinghe, Peter Brady, Greg Gibbes, Brad Skinner, Dominic Dowling, Christoph Gerber, Nassif Nassif, Zhinous Zabihi, Tuyen Hoang Trieu, Thuyen Ngo Van, Laszlo Erdei, Fabio Cumbe, Reza Fathollahzadeh, Thorsten Kostulski, Yujue Wang, Amir Zad, Benjamin Kus and Javeed Abdul.
- My personal friends, for providing indispensable diversions and distractions from my studies. In particular, my housemates from 5 St John Street, Evie Matkowska, Ryan Wildman, Peter Fenwick, Mikey Scanu, Rodney Boyd and Maggie Gorecki, for their remarkable friendship, inspiring conversations and the Rock'n'Roll. My housemate from Little Eveleigh Street, Ross West, for countless hours of talking (up in the attic) with a good glass of wine and the occasional Cuban cigar. My Sydney friends, Bora Wiemann, Christiane Alber, Martin Kehrt, Christine Schneyer, Vanessa Walker, Susanne Klar, H el ene Chanvrier, Winnie Yong and Max Gordin, for unforgettable weekend getaways and night time gatherings. My friends from overseas, Stefanie Schaberreiter, Christoph Piezonka, Steve Marchand, Wolfgang Pech, Alexander Hartl, Dorothea J akel, Britta Ga bling and Tyron Leitso, for providing remote support with long emails and phone calls.
- My family, including my mum, Brigitte Dackermann (n ee Guskowsky), my dad, Wolfgang Dackermann, my brother, Uwe Dackermann, as well as my grandparents, Dora and Karl-Heinz Dackermann, and Anni and Walter Guskowsky, for their love and understanding, and for instilling in me the values, perseverance and wisdom needed to complete this PhD project.
- Wade, for his enduring love, endless patience, constant words of encouragement and limitless support. I thank him wholeheartedly for his phenomenal proofreading work and for keeping up with my odd working hours and my limited availability, especially during the writing of this thesis.

Ulrike Dackermann

Sydney, May 2010

LIST OF PUBLICATIONS BASED ON THIS RESEARCH

Book Chapters

1. Samali, B., Li, J., Dackermann, U. & Choi, F.C. (2010), 'Vibration-based damage detection for timber structure in Australia', in, *Structural Health Monitoring and its Application*, World Scientific, Singapore, In press.*

Journal Articles

2. Dackermann, U., Li, J. & Samali, B. (2009), 'Vibration-based damage identification in timber structures utilising the damage index method and neural network ensembles', *Australian Journal of Structural Engineering*, vol. 9, no. 3.*
3. Dackermann, U., Li, J. & Samali, B. (2010), 'Vibration-based damage identification based on damage index method using neural network ensembles', *Advances in Structural Engineering*, In press.*
4. Li, J., Dackermann, U., Xu, Y.-L. & Samali, B. (2010), 'Damage identification in civil engineering structures utilising PCA-compressed residual frequency response functions and neural network ensembles', *Structural Control & Health Monitoring*, In press. (published online 1 Dec 2009)*
5. Samali, B., Dackermann, U. & Li, J. (2010), 'Location and severity identification of notch-type damage in a two-storey framed structure utilising frequency response functions and artificial neural networks', In preparation.*
6. Dackermann, U., Li, J. & Samali, B. (2010), 'Identification of boundary damage and mass changes on a two-storey framed structure using residual frequency response functions and artificial neural networks', In preparation.*

Conference Papers

7. Dackermann, U., Li, J., Samali, B., Choi, F.C. & Crews, K. (2008), 'Vibration-based damage identification in civil engineering structures utilising artificial neural networks', *Proceedings of the 12th International Conference on Structural Faults + Repair*, 10-12 June 2008, Edinburgh, Scotland, Paper #NDTM-DACKER, (published on CD).
8. Dackermann, U., Li, J. & Samali, B. (2008), 'Damage identification based on modal strain energy utilising neural network ensembles', *Proceedings of the Australasian Structural Engineering Conference (ASEC 2008)*, 26-27 June 2008, Melbourne, Australia, Paper #10, (published on CD).*
9. Dackermann, U., Li, J., Samali, B., Choi, F.C. & Crews, K. (2008), 'Experimental verification of a vibration-based damage identification method in a timber structure utilising neural network ensembles', *Proceedings of the International RILEM Conference - On site Assessment of Concrete, Masonry and Timber Structures (SACoMaTiS 2008)*, 1-2 September 2008, Politecnico Di Milano, Varenna, Italy, pp. 1049-1058.*
10. Dackermann, U., Li, J. & Samali, B. (2008) 'Damage index method for damage identification utilising artificial neural networks', *Proceedings of the 9th International Conference on Motion and Vibration Control (MOVIC 2008)*, 15-18 September 2008, Technische Universität München, Munich, Germany, Paper #1111, (published on CD).*
11. Dackermann, U., Li, J. & Samali, B. (2008) 'Structural damage identification utilising PCA-compressed frequency response functions and neural network ensembles', *Proceedings of the 20th Australasian Conference on the Mechanics of Structures and Materials (ACMSM 20)*, 2-5 December 2008, Toowoomba, Australia, pp. 803-809.*
12. Dackermann, U., Li, J., Samali, B. (2010), 'Quantification of notch-type damage in a two-storey framed structure utilising frequency response functions and artificial neural networks', *Proceedings of the 5th World Conference on Structural Control and Monitoring (5WCSCM)*, 12-14 July 2010, Tokyo, Japan, In press.

13. Dackermann, U., Li, J., Samali, B. (2010), 'Boundary damage identification of a two-storey framed structure utilising frequency response functions and artificial neural networks ', *Proceedings of the 10th International Conference on Motion and Vibration Control (MOVIC 2010)*, 17-20 August 2010, Tokyo, Japan, In press.*
14. Dackermann, U., Li, J., Samali, B. (2010), 'Identification of added mass on a two-storey framed structure utilising frequency response functions and artificial neural networks', *Proceedings of the 21st Australasian Conference on the Mechanics of Structures and Materials (ACMSM 21)*, 7-10 Decenber 2010, Melbourne, Australia, In press.*
15. Dackermann, U., Li, J., Samali, B., Choi, F.C. & Crews, K. (2011), 'Damage severity assessment of timber bridges using frequency response functions and artificial neural networks', *Proceedings of the International Conference on Structural Health Assessment of Timber Structures (SHATIS 11)*, 16-17 June 2011, Lisbon, Portugal, In preparation.

(* indicated peer-reviewed publications)

TABLE OF CONTENTS

CERTIFICATE OF AUTHORSHIP/ORIGINALITY	i
ABSTRACT	ii
ACKNOWLEDGEMENTS	v
LIST OF PUBLICATIONS BASED ON THIS RESEARCH	vii
TABLE OF CONTENTS	x
LIST OF FIGURES	xv
LIST OF TABLES	xxxii
CHAPTER 1 INTRODUCTION.....	1
1.1 Background.....	1
1.2 Research Objectives.....	4
1.3 Research Scope.....	5
1.4 Summary of Contributions.....	5
1.5 Outline of Thesis.....	7
CHAPTER 2 LITERATURE REVIEW ON VIBRATION-BASED DAMAGE IDENTIFICATION METHODS	8
2.1 Introduction.....	8
2.2 General Remarks.....	8
2.3 An Overview of Damage Identification.....	9
2.4 Previous Literature Reviews and Surveys	10
2.5 Natural-Frequency-Based Methods	12
2.6 Damping-Based Methods.....	15
2.7 Mode-Shape-Based Methods	16
2.7.1 Direct Mode-Shape-Based Methods	16
2.7.2 Mode-Shape-Curvature-Based Methods.....	20
2.7.3 Flexibility-Based Methods.....	21
2.7.4 Modal-Strain-Energy-Based Methods	24
2.8 Frequency-Response-Function-Based Methods.....	26

2.9	Time-Domain-Based Methods	29
2.10	Artificial-Neural-Network-Based Methods	32
2.10.1	Neural Networks Trained with Modal Parameters and Their Derivatives	34
2.10.2	Neural Networks Trained with Frequency Response Functions	39
2.10.3	Neural Networks Trained with Time Domain Data	43
2.11	Summary	45

CHAPTER 3 INTRODUCTION TO ARTIFICIAL NEURAL NETWORKS AND PRINCIPAL COMPONENT ANALYSIS 48

3.1	Introduction.....	48
3.2	The Biological Neural Network.....	48
3.3	The Artificial Neural Network.....	50
3.3.1	The Single Neuron	50
3.3.2	Multi-Layer Perceptron Networks	52
3.3.3	Artificial Neural Network Design.....	54
3.3.4	Neural Network Ensemble	58
3.4	Principal Component Analysis	63
3.5	Summary	65

CHAPTER 4 MODAL TESTING AND EXPERIMENTAL MODAL ANALYSIS 66

4.1	Introduction.....	66
4.2	Fundamentals of Modal Testing and Experimental Modal Analysis.....	66
4.2.1	Signal Processing	67
4.2.2	Frequency Response Function	71
4.2.3	Modal Parameter Estimation.....	73
4.3	Experimental Set Up and Testing of Laboratory Beams	76
4.3.1	The Test Beams.....	76
4.3.2	Modal Test Set Up	77
4.3.3	Modal Testing and Experimental Modal Analysis Results of Beams.....	80
4.4	Experimental Set Up and Testing of Laboratory Two-Storey Framed Structure	91
4.4.1	The Two-Storey Framed Structure.....	91

4.4.2	Damage/Added Mass Scenarios in Two-Storey Framed Structure.....	93
4.4.3	Modal Test Set Up	97
4.4.4	Impact Point Determination	100
4.4.5	Experimental Modal Testing and Analysis Results of Laboratory Two-Storey Framed Structure.....	102
4.5	Summary	114

CHAPTER 5 FINITE ELEMENT MODELLING 116

5.1	Introduction.....	116
5.2	Numerical Modelling of Beam Structure.....	116
5.2.1	Finite Element Modelling of Intact Beam.....	116
5.2.2	Simulation of Damage in Beam Model.....	118
5.2.3	Transient Analysis and Noise Pollution.....	119
5.2.4	Dynamic Characteristics of the Numerical Beam Structure	123
5.3	Numerical Modelling of Two-Storey Framed Structure	133
5.3.1	Finite Element Modelling of Two-Storey Framed Structure	133
5.3.2	Simulation of Damage/Added Mass Scenarios.....	137
5.3.3	Transient Analysis and Noise Pollution.....	139
5.3.4	Dynamic Characteristics of the Two-Storey Framed Structure	141
5.4	Summary	154

CHAPTER 6 METHODOLOGY OF DAMAGE IDENTIFICATION METHODS 155

6.1	Introduction.....	155
6.2	Proposed Method 1: Damage Identification Based on Damage Index Method.....	156
6.2.1	Theory of Damage Identification using Damage Index Method.....	157
6.2.2	Reconstruction of Mode Shapes.....	160
6.2.3	Limitations of Damage Index Method	165
6.2.4	Principal Component Analysis for Damage Index Values.....	169
6.2.5	Methodology of Neural-Network-Based Damage Identification using Damage Index Method.....	176
6.3	Proposed Method 2: Damage Identification Method Based on Frequency Response Functions.....	180

6.3.1	Damage Fingerprints in Frequency Response Functions	182
6.3.2	Principal Component Analysis for Frequency-Response-Function-Based Damage Identification	186
6.3.3	Methodology of Neural-Network-Based Damage Identification using Frequency Response Function Data.....	193
6.3.4	Summary	196

CHAPTER 7 DAMAGE IDENTIFICATION OF BEAM STRUCTURE..... 198

7.1	Introduction.....	198
7.2	Artificial Neural Network Design.....	198
7.3	Damage Identification Based on Damage Index Method	204
7.3.1	Results of Damage-Index-Based Damage Identification Method Applied to Numerically Simulated Beam	204
7.3.2	Results of Damage-Index-Based Damage Identification Method Applied to Laboratory Test Beams	217
7.4	Damage Identification Based on Frequency Response Functions	223
7.4.1	Results of Frequency-Response-Function-Based Damage Identification Method Applied to Numerically Simulated Beam	224
7.4.2	Results of Frequency-Response-Function-Based Damage Identification Method Applied to Laboratory Test Beams	229
7.5	Summary	232

CHAPTER 8 DAMAGE IDENTIFICATION OF TWO-STOREY FRAMED STRUCTURE BASED ON FREQUENCY RESPONSE FUNCTIONS 236

8.1	Introduction.....	236
8.2	Artificial Neural Network Design.....	237
8.3	Damage Identification Results Using Data from Numerical Simulations of the Two-Storey Framed Structure	242
8.3.1	Boundary Condition Identification	242
8.3.2	Added Mass Identification	244
8.3.3	Section Reduction Damage Identification	246
8.4	Damage Identification Results Using Experimental Data From the Laboratory Two-Storey Framed Structure	255

8.4.1	Boundary Condition and Added Mass Identification.....	255
8.4.2	Section Reduction Damage Identification	256
8.5	Summary	261
CHAPTER 9 CONCLUSIONS AND RECOMMENDATIONS.....		264
9.1	Summary and Conclusions	264
9.2	Contribution to Knowledge.....	271
9.3	Recommendations and Future Work.....	273
REFERENCES		276
APPENDICES		288

LIST OF FIGURES

Figure 3.1 Two biological interconnected neurons	49
Figure 3.2 Model of a single multiple-input neuron	50
Figure 3.3 Model of a three-layer network (Hagan, Demuth & Beale 1996).....	52
Figure 3.4 Transfer functions: (a) hard limit transfer function, (b) linear transfer function, (c) logistic sigmoid transfer function and (d) hyperbolic tangent sigmoid function (Hagan, Demuth & Beale 1996)	56
Figure 3.5 A two-stage neural network ensemble.....	59
Figure 3.6 Geometrical description of principal components.....	64
Figure 4.1 Digital signal processing (Abdul Rahman 1999).....	67
Figure 4.2 Aliasing phenomenon (Allemang 1999).....	68
Figure 4.3 Discrete Fourier transform concept (Allemang 1999).....	70
Figure 4.4 Windowing functions (a) force window and (b) exponential window.	70
Figure 4.5 Transfer function method (AgilentTechnologies 2000).....	71
Figure 4.6 FRF graphs in (a) rectangular and (b) polar coordinates for a single-degree-of-freedom system.	72
Figure 4.7 Modal parameter estimation methods (Schwarz & Richardson 1999).....	73
Figure 4.8 MDOF – SDOF Superposition (Allemang 1999).....	74
Figure 4.9 Experimental test set up.....	76
Figure 4.10 Experimental damage (a) 1 mm, (b) 4 mm, (c) 8 mm and (d) 12 mm cut.	77
Figure 4.11 Schematic diagram of MT&EMA.	78
Figure 4.12 The first seven flexural mode shapes and their node points.	78
Figure 4.13 Test equipment (a) Modal hammer, (b) accelerometer model PCB 356A08, (c) accelerometer model PCB 337A26 (d) battery powered signal conditioner (e) multi-channel signal conditioner and (f) data acquisition system E1432A.....	79
Figure 4.14 FRF summation function of undamaged beam 1.....	81
Figure 4.15 First seven flexural mode shapes of beam 1.	83

Figure 4.16 Comparison of reduction in natural frequencies [Hz] of different severities of damage at location '4' (beam 1).....	85
Figure 4.17 Comparison of increase in damping ratios [%] of different severities of damage at location '4' (beam 1).....	86
Figure 4.18 Mode shapes ((a) and (c)) and absolute mode shape differences ((b) and (d)) of various damage severities. (a) and (b) display mode 1 of beam 2 damaged at location '5' and (c) and (d) illustrate mode 2 of beam 3 damaged at location '6'.....	87
Figure 4.19 Effects of different damage severities on FRF data. Displayed are FRF summation functions from beam 3 in the undamaged state and damaged states with defects at location '6' of severities extra-light (6XL), light (6L), medium (6M) and severe (6S) with subfigure (a) displaying a frequency range from 0 Hz to 700 Hz and subfigure (b) illustrating a close-up of the frequency peak of mode 7.	89
Figure 4.20 Effects of different damage locations on FRF data. Displayed are FRF summation functions of undamaged beam and damaged beams 1 to 4 with defects of severe extent at locations '4' to '7' (4S to 7S) with subfigure (a) displaying a frequency range from 0 Hz to 700 Hz and subfigure (b) illustrating a close-up of the frequency peak of mode 7.	90
Figure 4.21 Laboratory two-storey framed structure.	91
Figure 4.22 Connection details (a) steel base - column connection (b) column - joint - crossbeam connection.	92
Figure 4.23 Modified elements of the two-storey framed structure.....	93
Figure 4.24 (a) Fixed joint (b) pinned joint.....	94
Figure 4.25 Added mass at location M1.....	95
Figure 4.26 Cutting of damage using a disk grinder.	96
Figure 4.27 Section loss of (a) 16.25 mm, (b) 21.7 mm and (c) 32.5 mm width and 4 mm height.....	96
Figure 4.28 (a) Accelerometer locations and (b) hammer impact points of the two-storey framed structure.	98
Figure 4.29 (a) Accelerometer chip ADXL320 (b) accelerometer with housing and (c) data acquisition system Iotech Daqbook 260.....	99
Figure 4.30 FRF summation functions of impact points (a) H1, (b) H2, (c) H3 ,(d) H4 and (e) H5.	101

Figure 4.31 Horizontal FRF summation function of baseline structure.	102
Figure 4.32 First seven flexural mode shapes of laboratory and numerical baseline two-storey framed structure.	104
Figure 4.33 Horizontal FRF summation functions of baseline structure (FFFF) and different multiple boundary condition scenarios.	105
Figure 4.34 Horizontal FRF summation functions of baseline structure (FFFF) and different single boundary condition scenarios.	106
Figure 4.35 Horizontal FRF summation functions of baseline structure (FFFF) and structure with boundary configuration PFFF.	107
Figure 4.36 Mode shapes of two-storey framed structure with boundary configuration PFFF and baseline structure (FFFF).	108
Figure 4.37 Drop in natural frequencies of all boundary condition scenarios.	109
Figure 4.38 Horizontal FRF summation functions of baseline structure and structure with mass added to the lower crossbeam at locations M1, M2 or M3.	110
Figure 4.39 Horizontal FRF summation functions of baseline structure and structure with mass added to the upper crossbeam at locations M4, M5 or M6.	111
Figure 4.40 New mode (mode 2a) of the two-storey framed structure when mass is added to the upper crossbeam, (a) experimental and (b) numerical mode shape.	111
Figure 4.41 Drop in natural frequencies of all added mass scenarios.	112
Figure 4.42 Horizontal FRF summation functions of baseline structure (intact) and structure with light, medium and severe cross-section reductions at location C1.	113
Figure 4.43 Horizontal FRF summation functions of baseline structure (intact) and structure with light, medium and severe cross-section reductions at location C3.	113
Figure 4.44 Drop in natural frequencies of all section reduction scenarios.	114
Figure 5.1 Geometric properties of SOLID45 (ANSYS Inc 2007c).	117
Figure 5.2 Finite element modelling of a pin-pin supported steel beam.	118
Figure 5.3 Damage locations of numerical beam model.	118
Figure 5.4 Finite element modelling of damage with a width of 1 mm and varying heights of (a) 1 mm, (b) 4 mm, (c) 8 mm and (d) 12 mm.	119

Figure 5.5	Generation of noise-polluted numerical data with subsequent determination of the modal parameters.	120
Figure 5.6	(a) Hammer impact force and (b) displacement response time history of location ‘5’ of the beam structure.	122
Figure 5.7	First seven flexural mode shapes of numerical beam model derived from the eigenvalue solution.	125
Figure 5.8	FRF summation function of undamaged numerical beam of (a) 1% noise-polluted data and (b) 10% noise-polluted data.	127
Figure 5.9	Comparison of reduction in natural frequencies of the numerical beam model of different severities of damage at location ‘4’.	129
Figure 5.10	(a) Mode shapes and (b) absolute mode shape differences of mode 3 of a numerical beam damaged at location ‘4’ with various damage severities.	130
Figure 5.11	Effects of different damage severities on FRF data. Displayed are FRF summation functions from the numerical beam in the undamaged state and different damaged states with defects at location ‘5’ of severities extra-light (5XL), light (5L), medium (5M) and severe (5S), with subfigure (a) displaying a frequency range from 0 Hz to 700 Hz and subfigure (b) illustrating a close-up of the frequency peak of mode 7.	131
Figure 5.12	Effects of different damage locations on FRF data. Displayed are FRF summation functions from the numerical beam in the undamaged state and different damaged states with defects of severe extent at locations ‘4’ to ‘7’ (4S to 7S), with subfigure (a) displaying a frequency range from 0 Hz to 700 Hz and subfigure (b) illustrating a close-up of the frequency peak of mode 7.	132
Figure 5.13	Geometric model of numerical two-storey framed structure.	134
Figure 5.14	Contact regions (red) and support faces (blue) of the two-storey framed structure.	135
Figure 5.15	Geometric properties of SOLID187 (ANSYS Inc 2007c).	135
Figure 5.16	Meshed two-storey framed structure.	136
Figure 5.17	Pinned joint modelled as revolute connection.	137
Figure 5.18	Modelling of added mass.	138
Figure 5.19	Finite element modelling of section reduction damage of a column with (a) 16.25 mm, (b) 21.7 mm and (c) 32.5 mm notch depth and 4 mm notch width. Figure (d) depicts	

the locations of the damage, i.e. locations ‘1a’ to ‘1c’ of the lower column half and locations ‘3a’ to ‘3c’ of the upper column half.	139
Figure 5.20 (a) Hammer impact force and (b) displacement response time history of location ‘4’ of the two-storey framed structure.	140
Figure 5.21 First seven flexural mode shapes of laboratory and numerical baseline two-storey framed structure.	143
Figure 5.22 Horizontal FRF summation function of baseline structure of numerical two-storey framed structure.	144
Figure 5.23 FRFs of (a) location ‘2’, (b) location ‘3’, (c) location ‘4’ and (d) location ‘9’.....	145
Figure 5.24 Horizontal FRF summation functions of baseline structure (FFFF) and different multiple boundary condition scenarios of numerical two-storey framed structure.....	146
Figure 5.25 Horizontal FRF summation functions of baseline structure (FFFF) and different single boundary condition scenarios of numerical two-storey framed structure.....	147
Figure 5.26 New mode shapes of (a) boundary scenario PPF and (b) boundary scenario FFPP of numerical two-storey framed structure.	147
Figure 5.27 Changes in natural frequencies of all boundary condition scenarios of the numerical two-storey framed structure.	148
Figure 5.28 Horizontal FRF summation functions of baseline structure and structure with mass added to the lower crossbeam at locations M1, M2 or M3 of numerical two-storey framed structure.....	149
Figure 5.29 Horizontal FRF summation functions of baseline structure and structure with mass added to the upper crossbeam at locations M4, M5 or M6 of numerical two-storey framed structure.....	150
Figure 5.30 New mode (mode 2a) of numerical two-storey framed structure that emerges when mass is added to the upper crossbeam.....	150
Figure 5.31 Changes in natural frequencies of all added mass scenarios of the numerical two-storey framed structure.....	151
Figure 5.32 Horizontal FRF summation functions of baseline structure (intact) and structure with light, medium and severe section reduction damage at (a) location 1a and (b) location 3a.	152
Figure 5.33 Reduction in natural frequencies of section reduction scenarios at locations ‘1a’ and ‘3a’ of the numerical two-storey framed structure.	153

Figure 6.1	Damage indicator Z_j derived from mode 1 of noise-free numerical simulations. Damage is situated at (a) location ‘4’, (b) location ‘5’ and (c) location ‘6’	159
Figure 6.2	Severity estimator α_j derived from mode 1 of noise-free numerical simulations. Damage is situated at location ‘4’ with severity (a) light, (b) medium and (c) severe.....	160
Figure 6.3	Z_j values derived from mode shapes with 9 and 41 data points, respectively. The DI values are derived from modes 2 to 4 of an experimental beam with medium damage at location ‘5’	162
Figure 6.4	Z_j values derived from mode shapes with 9, 41b and 41a data points, respectively. The DI values are based on modes 2, 3 and 4 from noise-free numerical simulations of a beam with medium damage at location ‘5’	164
Figure 6.5	Z_j values from noise-free numerical simulations of a beam with medium damage at location ‘6’ derived from (a) to (c) fine mode shapes of 41a data points, and (d) to (f) reconstructed mode shapes of 41b data points. DI values are calculated from (a) and (d) mode 3, (b) and (e) mode 6, and (c) and (f) mode 7.	166
Figure 6.6	Z_j values from reconstructed mode shapes of noise-free numerical simulations of a beam with medium damage at location ‘4’ derived from (a) mode 2, (b) mode 4 and (c) mode 6.	167
Figure 6.7	Z_j values from reconstructed mode shapes of noise-free numerical simulations of beams with medium damage at (a) location ‘5’ (data derived from mode 6), (b) location ‘6’ (mode 1) and (c) location ‘7’ (mode 3).....	167
Figure 6.8	Z_j values from numerical simulations of a beam with light damage at location ‘4’. Data polluted with three different signals of 2% white Gaussian noise derived from (a) to (c) mode 1, and (d) to (f) mode 5.....	168
Figure 6.9	Individual and cumulative contribution of the 41 PCs of Z_j values derived from mode 5 of noise-polluted numerical beam simulations.....	170
Figure 6.10	The first ten PCs derived from Z_j and α_j of (a) and (b) mode 5 and (c) and (d) mode 7 from numerical beam simulations polluted with 1% white Gaussian noise of (a) and (c) different damage locations and (b) and (d) different damage severities.	173
Figure 6.11	The first ten PCs derived from (a) Z_j and (b) α_j of mode 3 from laboratory beams of (a) different damage locations and (b) different damage severities.	174
Figure 6.12	The first ten PCs derived from Z_j of mode 3 from numerical beam simulations polluted with (a) 1%, (b) 2%, (c) 5% and (d) 10% white Gaussian noise of a beam with medium size damage at location ‘5’	175

Figure 6.13 Concept of utilising neural network ensembles for damage identification. Input features of individual neural networks are separated by mode shapes in order to take advantage of the unique features of PCA-compressed DI values.	177
Figure 6.14 Procedure of damage identification based on DI method.	179
Figure 6.15 Effects of (a) different damage locations and (b) different damage severities to residual FRFs of numerical beam simulations polluted with 1% white Gaussian noise.	183
Figure 6.16 Effects of (a) different damage severities and (b) different damage locations to CNR-FRFs from numerical beam simulations polluted with 1% white Gaussian noise.	185
Figure 6.17 The first ten PCs of residual FRFs (from the FRF summation function) of numerical beam data polluted with 1% white Gaussian noise of (a) different damage locations and (b) different damage severities.	190
Figure 6.18 The first ten PCs derived from residual FRFs (from the FRF summation function) from laboratory beams of (a) different damage locations and (b) different damage severities.	191
Figure 6.19 First ten PCs obtained from residual FRFs of numerical beam simulations polluted with (a) 1%, (b) 2%, (c) 5% and (d) 10% white Gaussian noise of a medium size damage at location '5'.	193
Figure 6.20 Procedure of damage identification based on FRFs.	195
Figure 7.1 AE performance graph.	203
Figure 7.2 Outcomes of ensemble network trained with PCA-compressed Z_j values of noise-free numerical beams to identify damage locations.	206
Figure 7.3 Neural network testing set performance (in AMNE) subdivided by damage severities trained with PCA-compressed Z_j values from noise-polluted numerical beams to localise damage.	208
Figure 7.4 Neural network testing set outcomes of networks from (a) mode 1, (b) mode 4, (c) mode 5 and (d) the ensemble network trained with PCA-compressed Z_j values to locate damage of numerical data polluted with 1% noise.	210
Figure 7.5 Comparison of testing set outcomes of networks trained with PCA-compressed Z_j values to identify damage locations of noise-polluted numerical beams subdivided by damage severity and noise pollution level.	212
Figure 7.6 Neural network testing set performance (in AMNE) subdivided by damage severity trained with PCA-compressed α_j values from noise-free numerical beams to identify damage severities.	214

Figure 7.7 Neural network testing set performance (in AMNE) subdivided by damage severity trained with PCA-compressed α_j values from noise-polluted numerical beams to identify damage severity.....	216
Figure 7.8 Comparison of testing set outcomes of networks trained with PCA-compressed α_j values to identify damage severities of noise-polluted numerical beams subdivided by damage severity and noise pollution level.....	217
Figure 7.9 Neural network testing set performance (in AMNE) subdivided by damage severity trained with PCA-compressed Z_j values from laboratory beams to identify damage locations.....	219
Figure 7.10 Neural networks testing set outcomes of network trained with PCA-compressed Z_j values of mode 7 to identify damage locations of laboratory beams.	220
Figure 7.11 Neural network testing set performance (in AMNE) subdivided by damage severity trained with PCA-compressed α_j values from laboratory beams to identify damage severity..	221
Figure 7.12 Neural network testing set outcomes for the network of mode 7 trained with PCA-compressed α_j values to identify damage severities of laboratory beams.	222
Figure 7.13 Neural network testing set performance (in AMNE) subdivided by damage severity trained with PCA-compressed residual FRFs from noise-polluted numerical beams to identify damage locations.....	225
Figure 7.14 Comparison of testing set outcomes of networks trained with PCA-compressed residual FRFs to identify damage locations of noise-polluted numerical beams subdivided by damage severity and noise pollution levels.....	227
Figure 7.15 Neural network testing set performance (in AMNE) subdivided in damage severities trained with PCA-compressed residual FRFs from noise-polluted numerical beams to identify damage severities.....	229
Figure 7.16 Neural network testing set performance (in AMNE) subdivided in damage severities trained with PCA-compressed residual FRFs from laboratory beams to identify damage locations.....	231
Figure 7.17 Neural network testing set performance (in AMNE) subdivided in damage severities trained with PCA-compressed residual FRFs from laboratory beams to identify damage severities.	232
Figure 8.1 (a) Measurement sensor locations ‘1’ to ‘14’ and hammer impact point H5, and (b) damage/added mass scenarios of the two-storey framed structure.	237
Figure 8.2 CCR performance graph.....	241

Figure 8.3 Neural network testing set performance (in AMNE) subdivided by damage severities trained with data from noise-polluted numerical simulations to locate section reduction damage.	249
Figure 8.4 Comparison of testing set outcomes of networks trained with PCA-compressed residual FRFs to identify damage locations of noise-polluted numerical beams subdivided by damage severity and noise pollution level.	250
Figure 8.5 Neural network testing set performance (in AMNE) subdivided by damage severities trained with data from noise-polluted numerical simulations to estimate severities of section reduction damage.	253
Figure 8.6 Comparison of testing set outcomes of networks trained with PCA-compressed residual FRFs to identify damage locations of noise-polluted numerical beams subdivided by damage severity and noise pollution level.	254
Figure 8.7 Neural network testing set performance (in AMNE) trained with data from the laboratory two-storey framed structure subdivided by damage severities to identify locations of section reduction damage.	258
Figure 8.8 Neural network testing set performance (in AMNE) trained with data from the laboratory two-storey framed structure subdivided by damage severities to identify severities of section reduction damage.	260
Figure A.1 Comparison of reduction in natural frequencies [%] of various damage cases of (a) beam 1, (b) beam 2, (c) beam 3 and (d) beam 4.	291
Figure A.2 Comparison of increase in damping ratios of various damage cases of (a) beam 1, (b) beam 2, (c) beam 3 and (d) beam 4.	293
Figure B.1 Dynamic characteristics of laboratory baseline structure (FFFF).	295
Figure B.2 Dynamic characteristics of laboratory structure PFFF.	296
Figure B.3 Dynamic characteristics of laboratory structure FFFF.	297
Figure B.4 Dynamic characteristics of laboratory structure FFFF.	298
Figure B.5 Dynamic characteristics of laboratory structure FFFF.	299
Figure B.6 Dynamic characteristics of laboratory structure PFFF.	300
Figure B.7 Dynamic characteristics of laboratory structure FFFF.	301
Figure B.8 Dynamic characteristics of laboratory structure FFFF.	302
Figure B.9 Dynamic characteristics of laboratory structure PFFF.	303

Figure B.10 Dynamic characteristics of laboratory structure FPPF.....	304
Figure B.11 Dynamic characteristics of laboratory structure PFFP.....	305
Figure B.12 Dynamic characteristics of laboratory structure with added mass at M1.....	306
Figure B.13 Dynamic characteristics of laboratory structure with added mass at M2.....	307
Figure B.14 Dynamic characteristics of laboratory structure with added mass at M3.....	308
Figure B.15 Dynamic characteristics of laboratory structure with added mass at M4.....	309
Figure B.16 Dynamic characteristics of laboratory structure with added mass at M5.....	310
Figure B.17 Dynamic characteristics of laboratory structure with added mass at M6.....	311
Figure C.1 Comparison of reduction in natural frequencies [%] of various damage cases of the numerical beam damaged at (a) location '4' (b) location '5', (c) location '6' and (d) location '7'.	315
Figure D.1 Dynamic characteristics of numerical baseline structure (FFFF).	317
Figure D.2 Dynamic characteristics of numerical structure PFFF.....	318
Figure D.3 Dynamic characteristics of numerical structure FFFF.....	319
Figure D.4 Dynamic characteristics of numerical structure FFFP.....	320
Figure D.5 Dynamic characteristics of numerical structure FFFP.....	321
Figure D.6 Dynamic characteristics of laboratory structure PFFF.....	322
Figure D.7 Dynamic characteristics of laboratory structure FFPP.....	323
Figure D.8 Dynamic characteristics of numerical structure FFFP.....	324
Figure D.9 Dynamic characteristics of numerical structure PFFF.....	325
Figure D.10 Dynamic characteristics of numerical structure FFFF.....	326
Figure D.11 Dynamic characteristics of numerical structure PFFP.....	327
Figure D.12 Dynamic characteristics of numerical structure with added mass at M1.....	328
Figure D.13 Dynamic characteristics of numerical structure with added mass at M2.....	329
Figure D.14 Dynamic characteristics of numerical structure with added mass at M3.....	330
Figure D.15 Dynamic characteristics of numerical structure with added mass at M4.....	331
Figure D.16 Dynamic characteristics of numerical structure with added mass at M5.....	332
Figure D.17 Dynamic characteristics of numerical structure with added mass at M6.....	333

Figure E.1 Z_j values derived from modes 1 to 7 of numerical noise-free simulations of a beam with medium size damage at location ‘4’	335
Figure E.2 Z_j values derived from modes 1 to 7 of numerical noise-free simulations of a beam with medium size damage at location ‘5’	336
Figure E.3 Z_j values derived from modes 1 to 7 of numerical noise-free simulations of a beam with medium size damage at location ‘6’	337
Figure E.4 Z_j values derived from modes 1 to 7 of numerical noise-free simulations of a beam with medium size damage at location ‘7’	338
Figure E.5 α_j values of numerical noise-free simulations of a beam damaged at location ‘4’ of light, medium and severe size, respectively. α_j values are derived from (a) to (c) mode 1, (d) to (f) mode 2, (g) to (i) mode 3, and (j) to (l) mode 4.	339
Figure E.6 α_j values of numerical noise-free simulations of a beam damaged at location ‘4’ of light, medium and severe size, respectively. α_j values are derived from (a) to (c) mode 5, (d) to (f) mode 6, and (g) to (i) mode 7.....	340
Figure E.7 α_j values of numerical noise-free simulations of a beam damaged at location ‘5’ of light, medium and severe size, respectively. α_j values are derived from (a) to (c) mode 1, (d) to (f) mode 2, (g) to (i) mode 3, and (j) to (l) mode 4.	341
Figure E.8 α_j values of numerical noise-free simulations of a beam damaged at location ‘5’ of light, medium and severe size, respectively. α_j values are derived from (a) to (c) mode 5, (d) to (f) mode 6, and (g) to (i) mode 7.....	342
Figure E.9 α_j values of numerical noise-free simulations of a beam damaged at location ‘6’ of light, medium and severe size, respectively. α_j values are derived from (a) to (c) mode 1, (d) to (f) mode 2, (g) to (i) mode 3, and (j) to (l) mode 4.	343
Figure E.10 α_j values of numerical noise-free simulations of a beam damaged at location ‘6’ of light, medium and severe size, respectively. α_j values are derived from (a) to (c) mode 5, (d) to (f) mode 6, and (g) to (i) mode 7.....	344
Figure E.11 α_j values of numerical noise-free simulations of a beam damaged at location ‘6’ of light, medium and severe size, respectively. α_j values are derived from (a) to (c) mode 1, (d) to (f) mode 2, (g) to (i) mode 3, and (j) to (l) mode 4.	345
Figure E.12 α_j values of numerical noise-free simulations of a beam damaged at location ‘7’ of light, medium and severe size, respectively. α_j values are derived from (a) to (c) mode 5, (d) to (f) mode 6, and (g) to (i) mode 7.....	346

Figure F.1 The first 30 PCs of residual FRFs of numerical simulations of the two-storey framed structure polluted with 1% white Gaussian noise of (a) different boundary condition scenarios with one altered joint and (b) boundary condition scenarios with two joints altered.....	354
Figure F.2 The first 30 PCs of residual FRFs of numerical simulations of the two-storey framed structure polluted with 1% white Gaussian noise of (a) added mass scenarios and (b) different section reduction cases.....	355
Figure F.3 The first 30 PCs of residual FRFs of laboratory two-storey framed structure of (a) different boundary condition scenarios with one altered joint and (b) boundary condition scenarios with two joints altered.	356
Figure F.4 The first 30 PCs of residual FRFs of laboratory two-storey framed structure of (a) added mass scenarios and (b) different section reduction cases.....	357
Figure G.1 Neural network testing set outcomes trained with PCA-compressed Z_j values of noise-free numerical beams to identify damage locations.	359
Figure G.2 Neural network testing set outcomes of networks trained with PCA-compressed Z_j values to identify damage locations of numerical beams polluted with 1% noise.	360
Figure G.3 Neural network testing set outcomes of networks trained with PCA-compressed Z_j values to identify damage locations of numerical beams polluted with 2% noise.....	361
Figure G.4 Neural network testing set outcomes of networks trained with PCA-compressed Z_j values to identify damage locations of numerical beams polluted with 5% noise.....	362
Figure G.5 Neural network testing set outcomes of networks trained with PCA-compressed Z_j values to identify damage locations of numerical beams polluted with 10% noise.....	363
Figure G.6 Comparison of testing set outcomes of networks trained with PCA-compressed Z_j values to identify damage locations of noise-polluted numerical beams subdivided by damage severity and noise pollution level.....	364
Figure G.7 Neural network testing set outcomes of networks trained with PCA-compressed α_j values of noise-free numerical beams to identify damage severities.	365
Figure G.8 Neural networks testing set outcomes of networks trained with PCA-compressed α_j values to identify damage severities of numerical beams polluted with 1% noise.	366
Figure G.9 Neural networks testing set outcomes of networks trained with PCA-compressed α_j values to identify damage severities of numerical beams polluted with 2% noise.	367
Figure G.10 Neural networks testing set outcomes of networks trained with PCA-compressed α_j values to identify damage severities of numerical beams polluted with 5% noise.	368

Figure G.11 Neural networks testing set outcomes of networks trained with PCA-compressed α_j values to identify damage severities of numerical beams polluted with 10% noise.	369
Figure G.12 Comparison of testing set outcomes of networks trained with PCA-compressed α_j values to identify damage severities of noise-polluted numerical beams subdivided by damage severity and noise pollution level.	370
Figure G.13 Neural networks testing set outcomes of networks trained with PCA-compressed Z_j values to identify damage locations of laboratory beams.	371
Figure G.14 Neural networks testing set outcomes of networks trained with PCA-compressed α_j values to identify damage severities of laboratory beams.	372
Figure H.1 Neural networks testing set outcomes of networks trained with PCA-compressed residual FRFs to identify damage locations of numerical beams polluted with 1% noise.	374
Figure H.2 Neural networks testing set outcomes of networks trained with PCA-compressed residual FRFs to identify damage locations of numerical beams polluted with 2% noise.	375
Figure H.3 Neural networks testing set outcomes of networks trained with PCA-compressed residual FRFs to identify damage locations of numerical beams polluted with 5% noise.	376
Figure H.4 Neural networks testing set outcomes of networks trained with PCA-compressed residual FRFs to identify damage locations of numerical beams polluted with 10% noise.	377
Figure H.5 Comparison of testing set outcomes of networks trained with PCA-compressed residual FRFs to identify damage locations of noise-polluted numerical beams subdivided by damage severity and noise pollution level.	378
Figure H.6 Neural networks testing set outcomes of networks trained with PCA-compressed residual FRFs to identify damage severities of numerical beams polluted with 1% noise.	379
Figure H.7 Neural networks testing set outcomes of networks trained with PCA-compressed residual FRFs to identify damage severities of numerical beams polluted with 2% noise.	380
Figure H.8 Neural networks testing set outcomes of networks trained with PCA-compressed residual FRFs to identify damage severities of numerical beams polluted with 5% noise.	381
Figure H.9 Neural networks testing set outcomes of networks trained with PCA-compressed residual FRFs to identify damage severities of numerical beams polluted with 10% noise.	382
Figure H.10 Comparison of testing set outcomes of networks trained with PCA-compressed residual FRFs to identify damage severities of noise-polluted numerical beams subdivided by damage severity and noise pollution level.	383

Figure H.11 Neural networks testing set outcomes of networks trained with PCA-compressed residual FRFs to identify damage locations of laboratory beams.	384
Figure H.12 Neural networks testing set outcomes of networks trained with PCA-compressed residual FRFs to identify damage severities of laboratory beams.....	385
Figure I.1 Neural network testing set performance (in AMNE) subdivided by damage severity trained with PCA-compressed CNR-FRFs from noise-polluted numerical beams to identify damage locations.	387
Figure I.2 Comparison of testing set outcomes of networks trained with PCA-compressed CNR-FRFs to identify damage locations of noise-polluted numerical beams subdivided by damage severity and noise pollution level.	388
Figure I.3 Neural networks testing set outcomes of networks trained with PCA-compressed CNR-FRFs to identify damage locations of numerical beams polluted with 1% noise.	389
Figure I.4 Neural networks testing set outcomes of networks trained with PCA-compressed CNR-FRFs to identify damage locations of numerical beams polluted with 2% noise.	390
Figure I.5 Neural networks testing set outcomes of networks trained with PCA-compressed CNR-FRFs to identify damage locations of numerical beams polluted with 5% noise.	391
Figure I.6 Neural networks testing set outcomes of networks trained with PCA-compressed CNR-FRFs to identify damage locations of numerical beams polluted with 10% noise.	392
Figure I.7 Neural network testing set performance (in AMNE) subdivided by damage severity trained with PCA-compressed CNR-FRFs from noise-polluted numerical beams to identify damage severities.	393
Figure I.8 Comparison of testing set outcomes of networks trained with PCA-compressed CNR-FRFs to identify damage severities of noise-polluted numerical beams subdivided by damage severity and noise pollution level.	394
Figure I.9 Neural networks testing set outcomes of networks trained with PCA-compressed CNR-FRFs to identify damage severities of numerical beams polluted with 1% noise.	395
Figure I.10 Neural networks testing set outcomes of networks trained with PCA-compressed CNR-FRFs to identify damage severities of numerical beams polluted with 2% noise.	396
Figure I.11 Neural networks testing set outcomes of networks trained with PCA-compressed CNR-FRFs to identify damage severities of numerical beams polluted with 5% noise.	397
Figure I.12 Neural networks testing set outcomes of networks trained with PCA-compressed CNR-FRFs to identify damage severities of numerical beams polluted with 10% noise.	398

Figure I.13 Neural network testing set performance (in AMNE) subdivided by damage severity trained with PCA-compressed CNR-FRFs from laboratory beams to identify damage locations.	399
Figure I.14 Neural networks testing set outcomes of networks trained with PCA-compressed CNR-FRFs to identify damage locations of laboratory beams.	400
Figure I.15 Neural network testing set performance (in AMNE) subdivided by damage severity trained with PCA-compressed CNR-FRFs from laboratory beams to identify damage severities.	401
Figure I.16 Neural networks testing set outcomes of networks trained with PCA-compressed CNR-FRFs to identify damage severities of laboratory beams.	402
Figure J.1 Comparison of testing set outcomes of networks trained with PCA-compressed residual FRFs to identify damage locations of noise-polluted numerical two-storey framed structures subdivided by damage severity and noise pollution levels. Outcomes of networks trained with data from locations ‘1’ to ‘8’ are shown.	404
Figure J.2 Comparison of testing set outcomes of networks trained with noise-polluted numerical data to locate damage subdivided by damage severity and noise pollution level. Outcomes of networks trained with data from locations ‘9’ to ‘14’ and data from horizontal/vertical summation FRFs, and of the network ensemble are shown.	405
Figure J.3 Neural network testing set outcomes of networks trained with data of 1% noise pollution to locate damage of numerical two-storey framed structure. Outcomes of networks trained with data from locations ‘1’ to ‘8’ are shown.	406
Figure J.4 Neural network testing set outcomes of networks trained with data of 1% noise pollution to locate damage of numerical two-storey framed structure. Outcomes of individual networks trained with data from locations ‘9’ to ‘14’ and data from horizontal/vertical summation FRFs, and of the network ensemble are shown.	407
Figure J.5 Neural network testing set outcomes of networks trained with data of 2% noise pollution to locate damage of numerical two-storey framed structure. Outcomes of networks trained with data from locations ‘1’ to ‘8’ are shown.	408
Figure J.6 Neural network testing set outcomes of networks trained with data of 2% noise pollution to locate damage of numerical two-storey framed structure. Outcomes of individual networks trained with data from locations ‘9’ to ‘14’ and data from horizontal/vertical summation FRFs, and of the network ensemble are shown.	409

Figure J.7 Neural network testing set outcomes of networks trained with data of 5% noise pollution to locate damage of numerical two-storey framed structure. Outcomes of networks trained with data from locations ‘1’ to ‘8’ are shown. 410

Figure J.8 Neural network testing set outcomes of networks trained with data of 5% noise pollution to locate damage of numerical two-storey framed structure. Outcomes of individual networks trained with data from locations ‘9’ to ‘14’ and data from horizontal/vertical summation FRFs, and of the network ensemble are shown. 411

Figure J.9 Neural network testing set outcomes of networks trained with data of 10% noise pollution to locate damage of numerical two-storey framed structure. Outcomes of networks trained with data from locations ‘1’ to ‘8’ are shown. 412

Figure J.10 Neural network testing set outcomes of networks trained with data of 10% noise pollution to locate damage of numerical two-storey framed structure. Outcomes of individual networks trained with data from locations ‘9’ to ‘14’ and data from horizontal/vertical summation FRFs, and of the network ensemble are shown. 413

Figure J.11 Comparison of testing set outcomes of networks trained with PCA-compressed residual FRFs to identify damage severities of noise-polluted numerical two-storey framed structures subdivided by damage severity and noise pollution level. Outcomes of networks trained with data from locations ‘1’ to ‘8’ are shown. 414

Figure J.12 Comparison of testing set outcomes of networks trained with noise-polluted numerical data to identify severities subdivided by damage severity and noise pollution level. Outcomes of networks trained with data from locations ‘9’ to ‘14’, data from horizontal/vertical summation FRFs and of the network ensemble are shown. 415

Figure J.13 Neural network testing set outcomes of networks trained with data of 1% noise pollution to estimate the severity of damage of numerical two-storey framed structure. Outcomes of networks trained with data from locations ‘1’ to ‘8’ are shown. 416

Figure J.14 Neural network testing set outcomes of networks trained with data of 1% noise pollution to estimate damage severity of numerical two-storey framed structure. Outcomes of individual networks trained with data from locations ‘9’ to ‘14’ and data from horizontal/vertical summation FRFs, and of the network ensemble are shown. 417

Figure J.15 Neural network testing set outcomes of networks trained with data of 2% noise pollution to estimate the severity of damage of numerical two-storey framed structure. Outcomes of networks trained with data from locations ‘1’ to ‘8’ are shown. 418

Figure J.16 Neural network testing set outcomes of networks trained with data of 2% noise pollution to estimate damage severity of numerical two-storey framed structure. Outcomes of individual networks trained with data from locations ‘9’ to ‘14’ and data from horizontal/vertical summation FRFs, and of the network ensemble are shown..... 419

Figure J.17 Neural network testing set outcomes of networks trained with data of 5% noise pollution to estimate the severity of damage of numerical two-storey framed structure. Outcomes of networks trained with data from locations ‘1’ to ‘8’ are shown..... 420

Figure J.18 Neural network testing set outcomes of networks trained with data of 5% noise pollution to estimate damage severity of numerical two-storey framed structure. Outcomes of individual networks trained with data from locations ‘9’ to ‘14’ and data from horizontal/vertical summation FRFs, and of the network ensemble are shown..... 421

Figure J.19 Neural network testing set outcomes of networks trained with data of 10% noise pollution to estimate the severity of damage of numerical two-storey framed structure. Outcomes of networks trained with data from locations ‘1’ to ‘8’ are shown..... 422

Figure J.20 Neural network testing set outcomes of networks trained with data of 10% noise pollution to estimate damage severity of numerical two-storey framed structure. Outcomes of individual networks trained with data from locations ‘9’ to ‘14’ and data from horizontal/vertical summation FRFs, and of the network ensemble are shown..... 423

Figure J.21 Neural network testing set outcomes of networks trained to locate damage of laboratory two-storey framed structure. Outcomes of networks trained with data from locations ‘1’ to ‘8’ are shown..... 424

Figure J.22 Neural network testing set outcomes of networks trained to locate damage of laboratory two-storey framed structure. Outcomes of networks trained with data from locations ‘9’ to ‘14’, and data from horizontal/vertical summation FRFs, and of the network ensemble are shown..... 425

Figure J.23 Neural network testing set outcomes of networks trained to quantify damage of laboratory two-storey framed structure. Outcomes of networks trained with data from locations ‘1’ to ‘8’ are shown..... 426

Figure J.24 Neural network testing set outcomes of networks trained to quantify damage of laboratory two-storey framed structure. Outcomes of networks trained with data from locations ‘9’ to ‘14’ and data from horizontal/vertical summation FRFs, and of the network ensemble are shown..... 427

LIST OF TABLES

Table 4.1	Experimental damage cases.	77
Table 4.2	Natural frequencies of the first seven flexural modes of beams 1 to 4.	82
Table 4.3	Damping ratios of the first seven flexural modes of beam 1 to 4.	82
Table 4.4	Natural frequencies [Hz] of the first seven flexural modes of the intact state and all damaged states of beam 1.....	84
Table 4.5	Damping ratios [%] of the first seven flexural modes of the intact state and all damaged states of beam 1.....	85
Table 4.6	Boundary change scenarios.....	94
Table 4.7	Section reduction scenarios.....	97
Table 4.8	Frequencies of the first seven flexural modes.....	103
Table 4.9	Natural frequencies of the first seven flexural modes of the baseline structure and all boundary condition scenarios.....	109
Table 4.10	Natural frequencies of the first seven flexural modes of the baseline structure and all added mass scenarios.	112
Table 4.11	Natural frequencies of the first seven flexural modes of the baseline structures and all section reduction scenarios.....	114
Table 5.1	Comparison of natural frequencies between numerical and laboratory beam.	124
Table 5.2	Mode shape correlation between numerical and laboratory beams.....	125
Table 5.3	Comparison of natural frequencies [Hz] of numerical beams.....	126
Table 5.4	Natural frequencies [Hz] of the first seven flexural modes of the intact state and all damaged states of a beam damaged at location ‘4’.....	128
Table 5.5	Comparison of natural frequencies between numerical and laboratory two-storey framed structure.	141
Table 5.6	Mode shape correlation between numerical and laboratory two-storey framed structure.....	142
Table 5.7	Natural frequencies of the first seven flexural modes of the baseline structure and all boundary condition scenarios.....	148

Table 5.8 Natural frequencies of the first seven modes of the baseline structure and all added mass scenarios.....	151
Table 5.9 Natural frequencies of the first seven modes of the baseline structure and all section reduction scenarios.....	153
Table 6.1 Specifications for PCA transformation of DI data from numerical and laboratory beam structure.....	170
Table 6.2 Individual contributions of PCs of noise-polluted numerical beam simulations.	171
Table 6.3 Individual contributions of PCs of laboratory beams.....	172
Table 6.4 Specifications for PCA transformation of FRF-based data from numerical and laboratory beam structure. FRF data points refer to residual FRF spectral lines and CNR-FRF data points (in brackets), respectively.....	187
Table 6.5 Specifications for PCA transformation of FRF-based data from numerical and laboratory two-storey framed structure.....	188
Table 6.6 Individual contributions of PCs from residual FRFs of numerical beams for measurement locations ‘1’ to ‘7’ and the FRF summation function (‘Sum’).	189
Table 6.7 Individual contributions of PCs from residual FRFs of laboratory beams for measurement locations ‘1’ to ‘7’ and the FRF summation function (‘Sum’).	189
Table 7.1 Chessboard selection for laboratory beam data.....	200
Table 7.2 Chessboard selection for noise-free numerical beam data.....	200
Table 7.3 Training, validation and testing partitioning of numerical and laboratory beam structure.....	201
Table 7.4 Neural network target output values.	201
Table 7.5 Neural network specifications and performance (in AMNE) trained with PCA-compressed Z_j values from noise-free numerical beam simulations to identify damage locations.	205
Table 7.6 Neural network specifications and performance (in AMNE) trained with PCA-compressed Z_j values from noise-polluted numerical beam simulations to identify damage locations.	207
Table 7.7 Neural network specifications and performance (in AMNE) trained with PCA-compressed α_j values from noise-free numerical beam simulations to identify damage severities.	213

Table 7.8 Neural network specifications and performance (in AMNE) trained with PCA-compressed α_j values from noise-polluted numerical beam simulations to identify damage locations.	215
Table 7.9 Neural network specifications and performance (in AMNE) trained with PCA-compressed Z_j values from laboratory beams to identify damage locations.	218
Table 7.10 Neural network specifications and performance (in AMNE) trained with PCA-compressed α_j values from laboratory beams to identify damage severities.	220
Table 7.11 Neural network specifications and performance (in AMNE) trained with PCA-compressed residual FRFs from noise-polluted numerical beams to identify damage locations.	224
Table 7.12 Neural network specifications and performance (in AMNE) trained with PCA-compressed residual FRFs from noise-polluted numerical beams to identify damage severities.	229
Table 7.13 Neural network specifications and performance (in AMNE) trained with PCA-compressed residual FRFs from laboratory beams to identify damage locations.	230
Table 7.14 Neural network specifications and performance (in AMNE) trained with PCA-compressed residual FRFs from laboratory beams to identify damage severities.	232
Table 8.1 Training, validation and testing partitioning of damage/added mass scenarios for the numerical two-storey framed structure.	238
Table 8.2 Training, validation and testing partitioning of damage/added mass scenarios for the laboratory two-storey framed structure.	239
Table 8.3 Neural network output encoding of boundary condition scenarios.	239
Table 8.4 Neural network output encoding of added mass scenarios.	239
Table 8.5 Neural network target output of section reduction cases.	240
Table 8.6 Neural network specifications and performance (in MCCR) trained with data from the numerical two-storey framed structure with different boundary conditions.	243
Table 8.7 MCCRs [%] of boundary condition predictions of networks trained with data from the numerical structure of locations (a) '2', (b) '4', (c) '6' and (d) '8'. Tables present testing data of noise intensities from 1% to 10% (N 1% to N 10%).	244
Table 8.8 Neural network specifications and performance (in MCCR) trained with data from the numerical two-storey framed structure with different added mass scenarios.	245

Table 8.9 MCCRs [%] of added mass localisations of networks trained with data from the numerical two-storey framed structure of locations ‘1’ to ‘8’. Tables present testing data of noise intensities from 1% to 10% (N 1% to N 10%).....	246
Table 8.10 Neural network specifications and performance (in AMNE) trained with data from the numerical two-storey framed structure of different cross-section reductions to identify damage locations.....	248
Table 8.11 Neural network specifications and performance (in AMNE) trained with data from the numerical two-storey framed structure of different cross-section reductions to identify damage severities.	252
Table 8.12 Neural network specifications and performance (in MCCR) trained with data from the laboratory two-storey framed structure of different boundary condition changes.	255
Table 8.13 Neural network specifications and performance (in MCCR) trained with data from the laboratory two-storey framed structure of different added mass changes.....	256
Table 8.14 Neural network specifications and performance (in AMNE) trained with data from the laboratory two-storey framed structure of different section reduction damage cases to identify damage locations.....	257
Table 8.15 Neural network specifications and performance (in AMNE) trained with data from the laboratory two-storey framed structure of different section reduction damage cases to identify damage severities.....	259
Table A.1 Natural frequencies of the first seven flexural modes of the intact state and all damaged states of beams 1 to 4.....	290
Table A.2 Damping ratios of the first seven flexural modes of the intact state and all damaged states of beams 1 to 4.	292
Table C.1 Natural frequencies of the first seven flexural modes of the intact state and all damaged states of the numerical beams.	314
Table F.1 Individual contributions of first 30 PCs from residual FRFs of numerical two-storey framed structure of different boundary conditions for measurement locations ‘1’ to ‘14’ and horizontal and vertical summation FRFs (SumH and SumV).....	348
Table F.2 Individual contributions of first 30 PCs from residual FRFs of numerical two-storey framed structure of different added mass scenarios for measurement locations ‘1’ to ‘14’ and horizontal and vertical summation FRFs (SumH and SumV).....	349

Table F.3 Individual contributions of first 30 PCs from residual FRFs of numerical two-storey framed structure of different section reduction cases for measurement locations ‘1’ to ‘14’ and horizontal and vertical summation FRFs (SumH and SumV).....	350
Table F.4 Individual contributions of first 30 PCs from residual FRFs of laboratory two-storey framed structure of different boundary conditions for measurement locations ‘1’ to ‘14’ and horizontal and vertical summation FRFs (SumH and SumV).....	351
Table F.5 Individual contributions of first 30 PCs from residual FRFs of laboratory two-storey framed structure of different added mass scenarios for measurement locations ‘1’ to ‘14’ and horizontal and vertical summation FRFs (SumH and SumV).....	352
Table F.6 Individual contributions of first 30 PCs from residual FRFs of laboratory two-storey framed structure of different section reduction cases for measurement locations ‘1’ to ‘14’ and horizontal and vertical summation FRFs (SumH and SumV).....	353
Table I.1 Neural network specifications and performance (in AMNE) trained with PCA-compressed CNR-FRFs from noise-polluted numerical beams to identify damage locations..	387
Table I.2 Neural network specifications and performance (in AMNE) trained with PCA-compressed CNR-FRFs from noise-polluted numerical beams to identify damage severities.	393
Table I.3 Neural network specifications and performance (in AMNE) trained with PCA-compressed CNR-FRFs from laboratory beams to identify damage locations.	399
Table I.4 Neural network specifications and performance (in AMNE) trained with PCA-compressed CNR-FRFs from laboratory beams to identify damage severities.....	401

CHAPTER 1

INTRODUCTION

1.1 BACKGROUND

During the years following World War II, the building industry boomed worldwide. As a result, many civil engineering structures are now, or will soon be, approaching the end of their design lives. Since it is economically not possible to replace all of these aged structures, health monitoring and integrity assessment are necessary to ensure the reliability of the structures and the safety of the public. In civil engineering practice, current non-destructive damage detection methods are based, for instance, on visual inspection, stress waves, ultrasonic waves, X-ray, acoustics or radiography. Most of these methods, however, are restricted to local examinations in limited areas and rely on a presumption of likelihood of damage in the inspected areas. When applied to large structures, these methods are very time-consuming and costly.

Vibration-based damage identification techniques are, on the other hand, global methods that are able to assess the condition of the entire structure at once. These techniques are based on the principle that damage alters both the physical properties of a structure (e.g. mass, stiffness and damping) as well as its dynamic characteristics (e.g. frequency response functions (FRFs), natural frequencies, damping ratios and mode shapes). Therefore, by analysing a structure's dynamic properties from structural vibration, any damage, including its location and severity, can be identified.

Over the past three decades, intensive research has been undertaken in the field of vibration-based damage identification, and many algorithms have been developed. Most of the work carried out so far use modal data (that are extracted from FRF data) such as natural frequencies and mode shapes. In the early years of dynamic-based damage detection, resonant frequencies were especially popular as damage indicators as they are easy to obtain (Adams et al. 1978; Lifshitz & Rotem 1969). Unfortunately, in many cases natural frequencies turned out to be insensitive to structural damage, especially for damage of lower severity (Chen, Spyrakos & Venkatesh 1995; Trendafilova 2005). For

field applications, another critical problem is that resonant frequencies are heavily affected by environmental changes, such as temperature or humidity fluctuations (Kim, Park & Lee 2007). Mode shapes and related functions or parameters are also frequently used as damage indicators for structural damage detection. Changes in mode shape measurements before and after damage are used either directly (Salawu & Williams 1995a) or indirectly as measures of mode shape curvatures (Pandey, Biswas & Samman 1991), modal strain energy changes (Stubbs & Osegueda 1990a; Stubbs & Osegueda 1990b) or dynamic flexibility (Pandey & Biswas 1994).

Particularly promising in the field of mode shape-based damage identification is the damage index (DI) method (Stubbs, Kim & Topole 1992), which is based on changes in modal strain energy. This method is capable of locating and quantifying damage and has been applied by many researchers in various fields and applications with a certain degree of success. Several modifications of the algorithm have been developed and verified by analytical and experimental studies (Choi et al. 2008; Kim & Stubbs 2002; Stubbs, Kim & Farrar 1995; Stubbs & Park 1996). Despite the reported successful applications of the algorithm, the method still has some inherent problems, especially when errors due to measurement noise interferences, limited number of sensors or experimental modal analysis uncertainties are considered. When the method is applied to real structures under real testing environment, those issues are inevitable. The presence of measurement noise amplifies the error and uncertainties from modal analysis and limited sensors especially affect the quantification of damage. Also, the identification of light damage still remains problematic and challenging (Barroso and Rodriguez, 2004; Pereyra et al., 1999).

In recent years, an approach has been proposed to use measured FRF data directly to detect structural damage (Huynh, He & Tran 2005). Utilising FRFs to form a damage indicator may have several advantages. FRFs are closer to directly measured data and one of the easiest to obtain in real-time as they require only a small number of sensors and very little human involved processing (Fang & Tang 2005). Measured FRF data are usually the most compact form of data obtained from vibrational testing, and hence, they provide an abundance of information on a structure's dynamic behaviour. Unlike modal parameter methods, FRF-based damage detection techniques do not require experimental modal analysis, which involves intensive labour and is very susceptible to

human error. Due to the high sensitivity of FRF data to structural changes, they are a much better dynamic quantity to form damage signatures. Researchers have been developing damage detection algorithms that use either direct FRF measurements (Choudhury 1996) or their derivatives such as FRF curvatures (Sampaio, Maia & Silva 1999), FRF differences (Trendafilova & Heylen 2003) or compressed FRFs (Ni, Zhou & Ko 2006). However, a major obstacle for the use of FRF data is its large size and complexity. Further, besides being sensitive to structural changes, FRFs are also responsive to uncertainties such as measurement noise and environmental fluctuations, which can lead to incorrect damage detection.

Most of vibration-based damage identification methods developed can be considered as some form of pattern recognition approach since they seek for the discrimination between two or more signal categories, e.g. before and after a structure is damaged or differences in damage levels or locations. Artificial neural networks (ANNs) – a form of artificial intelligence – simulate the operation of the human brain and thereby learn by example and not by following programming rules. Once trained, they are capable of pattern recognition and classification, and are robust in the presence of noise. These characteristics make ANNs powerful tools for vibrational damage identification. With incorporating ANNs, some critical issues of traditional damage detection methods can be overcome, and accuracy and reliability of damage detection can be greatly improved.

In this study, numerical and experimental investigations are employed to study the potential of using ANNs in combination with selected dynamic quantities for improved damage identification. Two different vibration-based damage identification methods are proposed. The first one is based on the DI method, while the second approach uses changes in FRF data as a damage indicator. Both methods utilise principal component analysis (PCA) and neural network techniques for damage feature extraction, data reduction and noise filtering.

1.2 RESEARCH OBJECTIVES

The main aim of this research is to develop novel ANN-based damage detection methods for localisation and severity estimation in civil engineering structures. The capabilities and limitations of employing ANNs in vibration-based damage identification are investigated using numerical and experimental studies. The specific objectives of this research work are:

1. To develop ANN-based damage identification methods suitable for civil engineering applications.
 - To determine suitable dynamic-based damage fingerprints to be used as input patterns for ANNs.
 - To study selected vibration-based damage patterns and to generate optimised input parameters for efficient ANN training.
 - To investigate different tools for use in feature extraction and noise reduction, such as PCA, and to study their limitations and capabilities.
 - To design superior ANN systems, such as hierarchical networks in network ensembles, for optimised network training.
2. To develop finite element models to verify numerically the proposed damage identification methods.
 - To apply the proposed damage detection techniques to a simple and a more complicated numerical structure.
 - To consider real testing limitations such as measurement noise and limited number of sensors.
 - To investigate various types of damage scenarios.
3. To conduct laboratory investigations to validate experimentally the proposed damage identification methods.
 - To investigate the applicability of the developed damage detection procedures on laboratory structures with real life testing conditions.

1.3 RESEARCH SCOPE

This research is concerned with the use of ANNs in vibration-based damage detection for improved damage identification in civil engineering structures. The scope of this study is limited to the following areas:

1. The investigation of existing vibration-based damage detection methods used in civil engineering applications.
2. The development of novel ANN-based damage identification methods suitable for civil engineering structures.
3. The investigation of factors that influence the performance of damage identification, especially those associated with field applications.
4. The investigation of techniques and procedures for improvement of reliability and accuracy of damage detection.
5. The numerical verification of proposed damage identification methods with finite element models.
6. The experimental validation of developed damage detection procedures with laboratory structures.

1.4 SUMMARY OF CONTRIBUTIONS

The principal contribution of this study is the development and verification of novel vibration-based damage identification methods with integration of ANN techniques. The original contributions of this research work include:

1. A new ANN-based damage identification algorithm is developed with modal parameters as input parameters. The proposed procedure integrates ANNs (in the form of network ensembles) and PCA to improve the original DI method for damage localisation and severity estimation. Through the separation of the damage indices based on their mode shape origins, individual characteristics of the indices are preserved for enhanced damage patterns and efficient network training. Through the employment of network ensemble techniques, an intelligent means is adopted to analyse prediction outcomes from individual networks and to give final superior damage identification results. The new algorithm is capable of reliably and accurately determining locations and severities of damage while overcoming

limitations of the original DI method associated with node point singularities and sensitivities to limited number of sensors.

2. Another novel ANN-based damage detection algorithm is developed using FRFs as input features for neural networks. Extensive studies on the characteristics of FRF data from different measurement locations as well as FRF summation functions (obtained by summing FRF data from multiple measurement locations) provide an understanding of the effects of damage on individual FRFs. This understanding led to the development of the FRF-based damage identification method, in which FRF data from different measurement locations are analysed separately to take advantage of their unique characteristics. Residual FRFs, which are differences in FRF data from the undamaged structure and the damaged structures, rather than direct FRF measurements are utilised as damage indices in order to enhance damage features and reduce excessive information. PCA techniques are employed to reduce the size of input data for effective network training and to filter noise features. Individual neural networks are trained separately with PCA-compressed FRF data from different measurement locations to produce optimal network outcomes. The fusion of the outcomes from individual networks using network ensemble techniques provides a superior means to give surpassing damage identification results.
3. The introduction of PCA and ANNs enhances damage patterns and reduces uncertainties from sources such as experimental modal analysis, measurement noise, experimental imperfections and environmental effects. PCA and ANNs have strong noise filtering capabilities and are able to separate dominant data set characteristics from unwanted irregularities. For both developed damage identification techniques (one based on the DI method and the other based on FRF data) noise sensitivity studies showed that PCA and ANNs are effective in reducing the effects of noise and thereby providing more reliable damage identification results.
4. Both developed methods are validated on numerical and experimental models. Two such models are used: a simple beam structure and a two-storey framed structure. In numerical modelling, real testing limitations, such as measurement noise and limited number of sensors, are incorporated to simulate real life conditions as closely as possible. In an extensive experimental program, four steel beams and a two-storey framed structure are dynamically tested and analysed. Structural changes of various

types (i.e. section reduction damage (of different severities and locations), boundary condition damage and added mass changes) are introduced to the structures and successfully evaluated by the developed damage identification methods.

1.5 OUTLINE OF THESIS

This thesis consists of nine chapters, organised as follows.

Chapter 1 gives an introduction to the work, the objectives of the study, the scope of the work and the contribution to knowledge.

Chapter 2 provides a literature search and an overview of existing vibration-based damage identification methods, with emphasis on algorithms using ANNs.

Chapter 3 gives some theoretical background on ANNs and PCA.

Chapter 4 presents modal testing and experimental modal analysis (MT&EMA) of two test structures: the simple beam structure and the two-storey framed structure. It describes the fundamentals of MT&EMA, introduces the test structures, explains the damage scenarios and presents the dynamic characteristics obtained from MT&EMA.

Chapter 5 describes the finite element modelling of the two test structures and presents their dynamic properties obtained from transient analysis.

Chapter 6 gives the theory, background and methodology of two proposed damage identification methods: the DI-based method and the FRF-based method. Both techniques are complemented by ANN and PCA techniques for pattern recognition and noise reduction.

Chapter 7 presents the damage detection results of the two proposed methods applied to the beam structure. Both methods identify locations and severities of section reduction damage from data obtained from numerical simulations and laboratory testing.

Chapter 8 discusses the results of the proposed FRF-based damage identification method applied to numerical and experimental data of the two-storey framed structure. Three types of structural changes are investigated: boundary damage (i.e. change of joint connections from fixed to pinned), added mass changes and section reduction damage.

Chapter 9 summarises the work of this thesis, draws conclusions and gives recommendations for future work.

CHAPTER 2

LITERATURE REVIEW ON VIBRATION-BASED DAMAGE IDENTIFICATION METHODS

2.1 INTRODUCTION

This chapter details some of the most significant work regarding the development of damage identification methods in various engineering applications. The findings from the previous work, by other researchers, serve as the motivation and the base on which the original research offered in this study is founded.

The chapter opens with general remarks pertaining to the ever increasing need to strengthen, repair or replace all ageing infrastructure due to different kinds of damage or defects commonly found in civil engineering structures. Before reviewing methods of damage identification, four levels of damage identification are introduced. Then, an overview is given on methods that were developed over the past three decades to characterise structural damage by examining changes in measured dynamic response. It follows with specific literatures of artificial neural networks (ANNs) in the field of vibration-based damage identification. And finally, it identifies research and development needs that are addressed in this thesis.

2.2 GENERAL REMARKS

Nowadays, many existing civil engineering structures are aged and decayed due to harsh climatic conditions, ageing materials, overloading or inadequate maintenance (Chong, Carino & Washer 2003). To ensure the reliability of these structures and the safety of the public, health monitoring, condition assessment and safety evaluation have become necessary. According to the U.S. Department of Transportation (2006), about 25% of the almost 600,000 bridges in the United States are structurally deficient. It is estimated that these bridges would need more than AUD \$72 billion (US \$65 billion) of investment for replacement or otherwise addressing the existing deficiencies. In Australia, there are about 50,000 public bridges, most of which are considered old and

functionally obsolete (Connor 2007 quoted in Sumitomo 2009). Many of them do not meet the current requirements given in the Australian Standards. Combining all these factors, there clearly exists a major challenge to the civil/structural engineering community with the higher risk of bridges collapsing if their structural deficiencies are not identified early enough to undertake any strengthening or remedial action. The collapse of the I-35W Bridge in Minneapolis, Minnesota, U.S. in 2007 provided a reminder, for the governments and the civil/structural engineering community alike, about the importance of structural health diagnostics. According to the Australian public road departments (Engineering 2008 quoted in Sumitomo 2009), it is estimated that on average more than AUD \$220 million per annum is allocated solely to bridge maintenance. A recent survey by the Roads and Traffic Authority (RTA) of New South Wales (NSW) found that about 63% of their bridges were deemed to be unsatisfactory and requiring repairs and remedial work. It is apparent that techniques of damage identification and structural health monitoring are necessary for better routine maintenance of the current ‘distressed’ civil infrastructure in Australia and other parts of the world.

2.3 AN OVERVIEW OF DAMAGE IDENTIFICATION

The fundamental concept of damage identification can be defined as ways or methods that are able to capture the changes in structural characteristics due to damage or degradation. Damage can be broadly defined as changes occurring within a structural system that negatively impact on the current or future performance of that system. In general, damage identification methods can be categorised as global or local techniques. Traditional local damage identification methods usually require that the vicinity of any damage is known before damage identification, and that the location of damage being inspected is easily accessible. Subject to such limitations, these local methods can detect damage on or near the surface of a structure. However, in the case of health monitoring for civil structures, information regarding damage is usually not available before damage identification, and the location of damage may be inaccessible. This fact accounts for the development of an altogether different paradigm of methodology: global damage identification methods. These methods were developed in order to facilitate the analysis of complex structures (Sohn et al. 2003). Hence, this chapter

presents an extensive review of vibration-based damage identification methods of a mainly global nature.

In general, the main objectives of non-destructive damage identification schemes are to identify structural damage at a very early stage, to locate the damage within the sensor resolution being used, to provide some estimate of the severity of the damage and to predict the remaining lifetime of the structure without causing harm to the structural integrity. These objectives led to the four level classification system presented by Rytter (1993):

Level 1: Determination of the presence of damage.

Level 2: Determination of the geometric location of the damage.

Level 3: Quantification of the severity of the damage.

Level 4: Prediction of the remaining service life of the structure.

To date, vibration-based damage identification methods that do not use any structural model primarily provide Level 1 and Level 2 damage identification. When vibration-based methods are coupled with a structural model, Level 3 damage identification can be obtained. Level 4 prediction is generally associated with the fields of fracture mechanics, fatigue-life analysis, or structural design assessment (Doebling, Farrar & Prime 1998). The scope of this research is to provide Level 2 and Level 3 identification.

2.4 PREVIOUS LITERATURE REVIEWS AND SURVEYS

A comprehensive literature review on vibration-based damage identification methods covering the period 1968 to 1996 was carried out by Doebling et al. (1996). This review covered a wide range of damage identification methods using various vibration-based damage identification techniques. The focus of the review was on damage-induced parameter changes, such as resonant frequencies, flexibility, and mode shapes and their derivatives. It is important to note that methods using mode shapes, mode shape curvatures, modal strain energy and their derivatives have been widely researched and applied to real life civil engineering structures such as bridges. Doebling et al. also discussed some important areas such as intelligent-system-based methods and methods that are widely used in other engineering practice, which have recently found application in civil engineering structures (Choi 2007).

Some review papers addressing damage identification and related issues, such as Farrar and Doebling (1997) and Doebling, Farrar and Prime (1998), reported an overview of modal-based damage identification methods. An extensive review on using natural frequency data to identify structural damage was provided by Salawu (Salawu 1997). The advantages of using natural frequencies are that they are easy to implement and the cost involved is relatively low. Bishop (1994) reviewed several applications of neural networks in vibration-based damage detection and a guide to the neural literature was also appended. Expanding on Bishop's (1994) literature list, a thorough review of the most recently published ANN-based studies is provided in section 2.10 of this thesis. Housener et al. (1997) published a comprehensive overview on the state-of-the-art in structural health monitoring for the past two decades, wherein they indicated the importance of damage identification in civil engineering structures. Online damage identification and health monitoring techniques for delaminated composite structures were reviewed by Zou, Tong and Steven (2000). Avitabile (2002) provided an extensive review of the developments, during the 1980s and 1990s, in structural dynamic modification techniques, related to damage identification. An extensive review of the use of new techniques in structural health monitoring was undertaken by Sohn et al. (2003). This review identified the need to improve structural health monitoring applications in real engineering structures. Carden and Fanning (2004) also presented a review on vibration-based condition monitoring, as a follow-up work to the broad and extensive review done by Doebling et al. (1996). An overview of fault identification using intelligent systems was presented by Worden and Dulieu-Barton (2004). This work encompassed the taxonomy of the relevant concepts in damage identification, operational evaluation of a hierarchical damage identification scheme, sensor optimisation and data processing methodology based on data fusion methods.

In an effort to focus on relevant research work, this literature review is presented in the following categories.

- Natural-frequency-based methods
- Damping-based methods
- Mode-shape-based methods
 - Direct mode-shape-based methods
 - Mode-shape-curvature-based methods

- Flexibility-based methods
- Modal-strain-energy-based methods
- Frequency-response-function-based methods
- Time-domain-based methods
- Artificial-neural-network-based methods

This review focuses mainly on papers and articles published after the year 2000, though any articles and papers published prior to 2000 and considered pertinent are also included. Readers interested in the finer details of damage identification developments are referred to the reviews and surveys mentioned above.

2.5 NATURAL-FREQUENCY-BASED METHODS

In the late 1970s, the consideration of the physical, tangible relationship between stiffness, mass and natural frequency changes was the impetus for using modal methods in the identification of damage. In theory, when damage occurs, the natural frequencies of a structure decrease. Since the early work, an extensive amount of research has been undertaken that utilises changes of natural frequencies as damage indicators. It is not only the most researched subject in vibration-based damage identification but also the most widely applied approach. The main reason for its great popularity is that natural frequencies are rather easy to determine with a relatively high level of confidence and in many applications only a single sensor is required (Choi 2007). Also, natural frequencies have much less statistical variation from random error sources than other modal parameters, which makes them a more robust means in the assessment of damage (Doebbling, Farrar & Prime 1998).

Natural frequencies, however, are in general a global property of a structure and cannot provide spatial information about structural changes. Thus, the identification of damage at Level 2 and Level 3 is considered challenging. Only higher modes, which due to the nature of their mode shapes, can be associated with local responses, are feasible for Level 2 and Level 3 damage identification. Higher frequency modes, however, require more energy to excite than lower frequency modes and are thereby impractical for many structural applications. Multiple frequency shifts can also provide spatial information about structural damage. This is based on the fact that changes at different locations of a structure will cause different combinations of natural frequencies to change. In practical

applications, however, often only a few natural frequencies with significant enough changes are available, which in general is not sufficient for the localisation of the damage (Doebbling, Farrar & Prime 1998).

Another drawback of the utilisation of natural frequencies is that the somewhat low sensitivity of the frequency shifts to damage requires either very precise measurements or large levels of damage (Doebbling, Farrar & Prime 1998). Also, these methods cannot distinguish damage at symmetrical locations in a symmetric structure, and the number of measured natural frequencies is generally lower than the number of unknown parameters, resulting in a non-unique solution (Maeck 2003). A major handicap for the application in real structures is that natural frequencies are easily affected by environmental changes such as temperature or humidity fluctuations. All these obstacles have led at times to unrealistic damage predictions when only natural frequencies were used (Maeck 2003).

Amidst some drawbacks in using natural-frequency-based methods for damage identification, Friswell and Motterhead (2001) presented some very useful observations on selecting an appropriate range of natural frequencies to identify damage. The range of frequencies employed in locating damage was reported to greatly influence the resolution of the results. For the lower frequency range, which usually corresponds to global modes, the vibration sensors may be mounted away from the damage site and thus fewer sensors may be used to successfully identify damage. Nevertheless, the problem with low frequency modes is that the spatial wavelength of the modes is large, and therefore a significant change between two adjacent potential damage sites may be necessary in order to identify the damage. That is, for low frequency modes, the spatial wavelength of the mode can lead to poor damage identification results.

Although using natural frequencies to identify damage can be difficult in practice, some researchers have made great progress in this area. Kim and Stubbs (2003) developed a crack-location model to locate cracks and estimate their size in beams using any available natural frequencies. The method can identify crack size and location with small marginal errors. However, the method is confined to identifying only cracks in beams, and it is not clear whether the method will perform well on different types of damage or on different structures.

Ndambi, Vantomme and Harri (2002) performed experimental tests in order to evaluate the correlation between the progressive cracking process in reinforced concrete (RC) beams and the changes in their dynamic characteristics. In their tests, cracks were progressively induced in the RC beams using a static loading method. Each static test was followed by a dynamic test on the same beam with a simulated free-free boundary condition. The results demonstrated that the acquired natural frequencies were affected by the accumulation of cracks in the RC beams, but these changes were not influenced by the crack damage locations. It was also noted that the decrease in natural frequencies remained steady throughout the cracking process, which allowed the severity of the damage to be estimated.

Garesci, Catalano and Petrone (2006) reported a methodology for identifying the location of damage. In the method, damage locations were determined through analysis of the mode shapes corresponding to those natural frequencies which presented the highest percentage differences compared to the undamaged system. The method was applied first on rectangular plates that had a milled slot in different positions, and afterwards on mechanical components. The results showed that it was possible to identify the damaged zone using the developed method. However, to obtain clear evidence of damage, an appropriate choice of chromatic scale for the graphic output was required.

Kim et al. (2003) developed a frequency-based damage detection (FBDD) method to identify the location and size of damage. The FBDD method is based on two ratios: the fractional change in natural frequencies due to damage and the fractional change of modal energy (sensitivity). The two ratios were used to form a single damage indicator that would locate the damage using a localisation error norm. Damage is located when the single damage indicator approaches its peak. To determine the size of damage, an algorithm based on Euler-Bernoulli beam theory was developed using the relationship between fractional changes in modal strain energy and fractional changes in natural frequency. The change in the modal strain energy due to damage could then be correlated with the energy loss rate. Eventually, this led to a relationship between crack depth and fractional change in natural frequencies. The FBDD method was found to be capable of predicting a rough range for single damage location. It also displayed a symmetrical false positive (prediction of locations that were not damaged) for damage

at $\frac{1}{4}$ span. For estimating the size of damage, the method produced errors ranging from 2% to 57%. The method was reported to work considerably well for single damage scenarios but multiple damage scenarios were not addressed. The attempt to quantify the damage size using changes in frequency was also encouraging but more work is required to make the method viable.

An extension of the work of Kim et al. (2003) was done by Kim, Park and Lee (2007). The authors performed experimental tests using natural frequencies to predict the severity of damage. In addition, the authors also tried to filter the effects from environmental factors such as temperature fluctuations. A statistically based control technique was used to monitor the damage in the test specimen subjected to different temperatures. As the structure experienced changes in temperature, the mean and variance of the acquired natural frequencies also changed. A control chart consisting of natural frequencies versus temperatures was then obtained. The existence of damage was predicted if any obtained natural frequencies fell outside the determined control limits.

2.6 DAMPING-BASED METHODS

Damping, being one of the modal parameters of a structure, has also been used in a few applications as an indicator for damage. Theoretically, when damage occurs in a structure the damping ratio increases. One major obstacle, however, is that at present the determination of the damping ratio in real structures is still very unreliable. This explains why damage identification based on damping factors is still not widely developed. Though some attempts have been made to use damping as a damage indicator, most studies have failed to observe a clear relation between the damping values and the damage.

Salane and Baldwin (1990) performed a dynamic test on a steel girder bridge with concrete decking to measure the steady-state response and the natural frequencies. The results of the test showed that damping ratios were affected by deterioration but they were unreliable as a damage indicator, because the trend was inconsistent with the severity of inflicted damage. This finding was confirmed by an experimental study by Farrar and Jauregui (1998), wherein the damping of a steel plate girder bridge did not consistently increase or decrease as damage severity increased.

Salawu and Williams (1995a) performed dynamic tests on concrete highway bridges to investigate any correlation that may exist between the repair works and changes in the dynamic characteristics of the bridges. The results showed that there was no identifiable pattern to the changes in damping ratios caused by the repairs. Four pairs of reinforced concrete beams were used by Casas and Aparicio (1994) for damage identification tests. The results of the tests revealed no obvious direct relationship between damage and damping ratios.

Even though inconsistency in changes of damping ratios have been noted previously and many researchers believe that damping is an unreliable indicator for damage identification, Abdul Razak and Choi (2001) drew a different conclusion. In their study, three reinforced concrete beams, one undamaged and the remaining two subjected to different states of reinforcement corrosion, were dynamically tested. The results showed that with increased damage severity, the damping ratios for modes 2 and 3 increased considerably. The authors concluded that the damping ratios of the second and third modes reflected a pattern consistent with the severity of the corrosion damage.

2.7 MODE-SHAPE-BASED METHODS

The mode shape is a unique characteristic of a structural system. Many researchers suggest that mode shapes be a far more consistent and satisfactory damage indicator than natural frequencies and damping ratios. A large number of damage identification methods have been developed based on directly measured mode shapes or their derivatives. The direct comparison of mode shapes and other modal-based damage identification methods are also used for structural health monitoring (Mufti 2001).

2.7.1 Direct Mode-Shape-Based Methods

A mode shape is a deflection-pattern associated with a particular natural frequency. It represents the relative displacement of all parts of a structure for that particular mode and can thereby provide spatial information. Normal mode shapes (for structures with low damping) are characterised by the fact that all parts of the structure are moving either in-phase or 180° out-of-phase with each other. They can thus be thought of as standing waves with fixed node lines (Døssing 1988). If a structure is locally damaged, mode shape changes will occur in the vicinity of that damage. Therefore, a comparison

between two sets of mode shape data (either direct mode shape measurements or their derivatives) can be used to identify damage.

Two commonly used methods to compare two sets of mode shapes are the Modal Assurance Criterion (MAC) and the Coordinate Modal Assurance Criterion (COMAC).

The MAC value can be considered as a measure of the similarity of two modes. For the mode shape vectors ϕ^A and ϕ^B (e.g. mode shapes in the undamaged and damaged state) the MAC is defined as

$$MAC_{A,B} = \frac{\left| \sum_{j=1}^n \phi_j^A \phi_j^B \right|^2}{\sum_{j=1}^n (\phi_j^A)^2 \cdot \sum_{j=1}^n (\phi_j^B)^2} \quad (2.1)$$

with n being the modal degrees of freedom. A MAC value of 1 is a perfect match and a value of 0 means they are completely dissimilar. Thus, a reduction of the MAC value may be an indication of damage.

The COMAC differs from the MAC definition in the way that it gives a pointwise measure of the difference between two sets of mode shapes. The COMAC value at modal co-ordinate i for n modes is defined as

$$COMAC_{i,A,B} = \frac{\left| \sum_{j=1}^n \phi_{i,j}^A \phi_{i,j}^B \right|^2}{\sum_{j=1}^n (\phi_{i,j}^A)^2 \cdot \sum_{j=1}^n (\phi_{i,j}^B)^2} \quad (2.2)$$

A low COMAC value would indicate discordance at point i and thus is also a possible damage location indicator.

Research that utilised these two techniques gave somewhat good results in the identification of damage. The techniques were, however, mainly applied to numerical models, and superseded in recent times by methods that are more sensitive to damage. The MAC and COMAC approaches are still being used in the field of damage assessment for model updating or calibration of finite element modelling with experimental data (Choi 2007).

Abdul Razak et al. (2001) developed a simplified version of the Laplacian Operator suggested by Ratcliffe (1997) to identify sawcut damage for a reinforced concrete beam. The simplified Laplacian Operator utilises the difference in discrete functions of the mode shape displacements to detect single localised damage. The results showed that the method performed better than its original form. With the use of higher modes, crack locations could be identified for less severe cases. The advantage of the method is that it does not require a comparative data set to determine the damage locations for single damage scenarios. However, the spacing of the sensors used in the study was relatively small (only 40 mm, covering a span length of 2,200 mm) and it is uncertain how well the method would work if fewer sensors were employed. Further, the work was done for a simple beam and multiple damage cases were not discussed.

Ching and Beck (2004) studied damage identification and assessment of a test structure using pre and post damage mode shape data, which were collected in hammer impact and ambient vibration dynamic tests. The experimental tests were performed on nine configurations. Configurations one to six were braced cases, with configuration one being the undamaged case; configurations seven to nine were unbraced cases, with configuration seven being the undamaged case. For the braced cases, damage was simulated by removing braces, and for the unbraced cases, the damage was simulated by decreasing the rotational stiffness of some beam column connections. In the results, the brace damage was detected and assessed, either from hammer or ambient vibration data. However, the connection damage was much more difficult to reliably detect and assess, because the identified modal parameters were less sensitive to connection damage, allowing modelling errors to influence the results more strongly.

Choi, Park and Stubbs (2005) presented a methodology to identify the location and size of damage in a structure using a compliance index, which represents the change in the distribution of the compliance of a structure due to damage. The change in the compliance distribution was obtained using the changes in the mode shapes of a structure. A simply supported beam and a continuous two span beam were tested numerically. A free-free beam was also tested experimentally to verify the proposed method. The results revealed that the compliance index could identify single and multiple damage locations, and the method yielded less damage identification error than the other existing modal energy methods. The researchers also suggested that the

performance of both damage localisation and severity estimation might be improved when composite damage indices, obtained from multiple mode shapes, were used simultaneously.

Ismail, Abdul Razak and Abdul Rahman (2006) formulated a method to determine, experimentally, the damage locations of a single crack and honeycombs in reinforced concrete beams. This indicator – a local stiffness indicator using $|\lambda^4|$ derived from the Euler beam – was obtained by rearranging the equation for free transverse vibration of a uniform beam and applying the fourth order centred finite-difference formula to the regressed mode shape data. Five reinforced concrete beams were used to investigate the method. The results showed that the indicator was able to identify the damage location and estimate the damage severity within reasonable error limits, although it was found to produce a poor indication of damage near the supports. Furthermore, the method was applied to single damage scenarios only, which were mode dependent.

Kim, Park and Voyiadjis (2006) proposed a vibration-based damage evaluation method using the lower frequency ranged mode shapes. The work attempted to develop a damage identification method that is less mode dependent. Further, the study intended to resolve the mode selection problem, the singularity problem, the axial force problem and the absolute severity estimation problem, all of which remained unsolved in earlier research. The proposed method was successful only in estimating the relative severity of damage but did not succeed in locating all levels of damage in a real structure.

Hu and Afzal (2006) used a damage indicator for the identification of single and double damage scenarios on timber beams. The damage indicator was expressed using a statistically normalised discrete Laplace transform, derived from the difference of the mode shapes before and after damage. Using either the first or second mode, the method successfully identified single inflicted damage at different locations and a two damage case with equal spacing and a similar level of damage severity. However, the method was not able to evaluate quantitatively the damage severity, and it struggled to generate good results when combining the first and second modes. Furthermore, the results of the study were based on a dense sensor acquisition system, which is costly and time consuming.

2.7.2 Mode-Shape-Curvature-Based Methods

Mode shape curvatures have been used in damage identification due to the fact that curvature changes are highly localised to the region of damage. They are more pronounced than changes in the displacement of mode shapes themselves and are therefore more sensitive to damage. Mode shape curvature changes are listed in ‘Guidelines for Structural Health Monitoring’ published by ISIS Canada (Mufti 2001) as one of the structural health monitoring techniques for civil engineering structures.

Curvatures are often calculated from the measured displacements of mode shapes of the intact and the damaged state using the central difference approximation:

$$\phi_{ji}'' = \frac{\phi_{(j+1)i} - 2\phi_{ji} + \phi_{(j-1)i}}{l^2} \quad (2.3)$$

with i being the mode shape number, j the node number and l the distance between the nodes.

The use of mode shape curvatures to predict the location of damage has shown reasonably good results. A comparative research study confirmed that the mode shape curvature is a far more sensitive indicator than the MAC or COMAC values of the mode shapes themselves (Pandey, Biswas & Samman 1991). However, most successful results were obtained from numerical data, and a big challenge is still to determine, in an accurate way, mode shape curvature from experimental data (Ratcliffe 1997).

Yoon et al. (2001) utilised a global mathematical fitting method, namely, the ‘gapped smoothing method’ (Ratcliffe 2000; Ratcliffe & Bagaria 1998), to identify damage locations in a beam. The approach used a ‘global optimised smooth shape method’ on mode shape curvatures by subtracting values of the damaged structure from those of the undamaged structure (Pandey, Biswas & Samman 1991; Wahab & De Roeck 1999). First, the mode shape curvature of the damaged beam was obtained by twice differentiating its mode shape (step A). The smoothing of the damaged beam mode shape by a global curve-fitting method (third order polynomial curve-fitting) was also carried out. The smoothed mode shape, assumed to be from the undamaged state, was subsequently differentiated twice to obtain the mode shape curvature (step B). A damage index was then formed by subtracting the mode shape curvature of step A from

the one of step B. To increase the damage detection capability, the damage index was summed up by normalising the curvature change peak values. Using a finite element model and an experimental test, the method was able to identify single damage scenarios of very low damage severity (depth of damage to thickness ratios less than 1%) using the finite element approach, and more severe damage (depth of damage to thickness ratio of at least 20%) using the experimental approach. This method showed that an input from the undamaged state is not required to detect the location of damage. The method was performed successfully on single damage scenarios but no tests were conducted on multiple damage scenarios or more complex structures such as a bridge.

Maeck and De Roeck (2002), Maeck (2003), and Unger, Teughels and De Roeck (2005) developed a technique utilising the calculated modal bending moments and mode shape curvatures to derive the bending stiffness at each location. The direct stiffness calculation technique was developed to calculate the mode shape curvatures and torsion rates without direct numerical derivation using mode shapes. Combining the modal internal forces, this led to a direct estimation of the reduction in stiffness due to damage in a structure. The technique was tested on a reinforced concrete beam that was loaded in six steps by a four point bending static test. Bending and torsional stiffness decreased significantly as the damage became more severe. The method provided a good qualitative damage identification, but was less accurate in quantifying the damage.

Hamey et al. (2004) made use of mode shape curvatures to identify damage in carbon/epoxy composite beams experimentally. Smart piezoelectric materials were used simultaneously as sensors and as actuators to acquire the curvature of the modes of structures. These materials were bonded to the surface of the beams. A single location delamination damage was created on the cantilever test beams. The experimental results indicated that the curvature modes and piezoelectric materials can be effectively used in damage detection and health monitoring for composite simple beam structures with single damage scenarios.

2.7.3 Flexibility-Based Methods

Another class of damage identification methods uses the dynamically measured flexibility matrix to estimate changes in the static behaviour of a structure. Since the flexibility matrix is defined as the inverse of the static stiffness matrix, it relates the

applied static force to the resulting structural displacement. Therefore, each column of the flexibility matrix represents a set of nodal displacements of a structure due to a unit force applied at one of the degrees of freedom (DOF). The measured flexibility matrix F is estimated from the mass-normalised measured mode shapes ϕ_i and frequencies ω_i as:

$$F = \phi \Lambda^{-1} \phi^T = \sum_{i=1}^n \frac{1}{\omega_i^2} \phi_i \phi_i^T \quad (2.4)$$

with $\Lambda = \text{diag}(\omega_i^2)$ being the matrix of eigenvalues. The formulation of the flexibility matrix is approximate due to the fact that usually (for practical applications) only the first few modes of a structure are available. The synthesis of the complete static flexibility matrix would require the measurement of all of the mode shapes and frequencies of the system being analysed. Typically, damage is detected by comparing the flexibility matrix synthesised using the modes of the damaged structure to either the flexibility matrix synthesised using the modes of the undamaged structure or the flexibility matrix from a finite element model. Because of the inverse relationship with the square of the natural frequencies, the measured flexibility matrix converges rapidly with increasing values of frequency. Hence, a good estimation for the flexibility matrix can be obtained from only a few of the lower frequency modes (Pandey & Biswas 1994). Thereby, damage identification using flexibility is most sensitive to changes of modes in the lower frequency range (Maeck 2003).

Research utilising the flexibility matrix as a damage indicator has demonstrated good results to date. Besides locating the damage, the method is also capable of evaluating the extent of the damage. This, however, has been mainly demonstrated in numerical applications with single damage cases. One study, comparing natural frequencies, mode shapes and modal flexibility applied to a numerical five degree of freedom spring-mass-system, found that modal flexibility was the most sensitive to damage (Zhao & DeWolf 1999).

Bernal (2002) presented a ‘damage locating vector’ (DLV) method to locate damage in structures that could be treated as linear in regard to pre- and post-damage. The method was developed based on the lack of deterministic information on the input data, which can partially be compensated for by knowledge of the structure of the mass matrix. The

method could be used to identify damage location by inspecting stress fields created by vectors that were contained in the null space of the change in flexibility. The method was applied to a planar steel truss, consisting of 44 bars and a total of 39 DOF. The numerical results showed that the DLV method only identified certain damaged elements.

Gao et al. (2006) extended the damage locating vector (DLV) method for continuous structural health monitoring. The essence of the proposed method was to construct an approximate flexibility matrix for the damaged structure using the modal normalisation constants from the undamaged structure. In a numerical simulation, a planar truss structure consisting of 53 steel bars was adopted to verify the method. Damage was simulated by reducing the stiffness in one element of the truss. The numerical results showed that the proposed method was able to identify the damage location by showing that the normalised cumulative stress value of the damaged element was smaller than that of the undamaged elements. However, false positive errors were generated in the results, which is not desirable in damage identification.

Patjawit and Kanok-Nukulchai (2005) proposed a global flexibility index (GFI) for health monitoring of highway bridges. The index was formulated using the spectral norm of the modal flexibility matrix, obtained from selected reference points that were sensitive to the deformation of the bridge structure. In the laboratory investigation, a simple steel beam and a reinforced concrete beam were selected to test the method. Different degrees of damage severity were introduced by cuts in the bottom flanges at the mid span of the beam. The results indicated that the GFI value decreased as the single cut size increased. The GFI method was implemented on a bridge and the authors concluded that regular monitoring of the structure's GFI value would provide an advanced warning for any global weakening of the bridge.

Choi et al. (2008) developed a new damage indicator combining DI and flexibility methods. The newly developed method was tested numerically and experimentally on timber beams using single and multiple damage scenarios. The results showed that the method was capable of simultaneously identifying damage location for up to four locations for a simple beam structure. The method was quite accurate in estimating damage severity for single damage cases but became less effective as the number of damage locations increased.

2.7.4 Modal-Strain-Energy-Based Methods

Modal-strain-energy-based damage identification algorithms utilise the relative differences in modal strain energy before and after damage. A mode shape stores an enormous amount of strain energy in a particular structural load path. When damage occurs, the modal strain energy in that load path alters due to the high sensitivity of the frequency and shape of that mode. By using changes in modal strain energy as a damage indicator, not only the damage location but also the magnitude of the damage can be determined. Modal strain energy has been widely investigated as an indicator in various fields of damage identification. Several modifications of the algorithm, originally developed by Stubbs, Kim and Topole (1992), have been developed and verified by analytical and experimental studies. Some formulations of modal-strain-energy-based damage identification algorithms are given in section 6.2.1. Two studies, both comparing the MAC, COMAC, flexibility and modal strain energy approaches, concluded that the modal strain energy method was the most precise of the four and also the most stable when different levels of noise were present. Many obstacles, however, remain to be resolved. The identification of light damage, for instance, is still problematic (Barroso & Rodriguez 2004; Pereyra et al. 1999). Also, the phenomenon of false positive damage identifications has been widely reported (Barroso & Rodriguez 2004). Another challenge is the sensitivity to noise, especially in the quantification of defects (Lee & Yun 2006; Shi, Law & Zhang 1998, 2000).

In 1995, Kim and Stubbs (1995) presented an experimental verification using modal strain energy to locate and estimate damage from a few mode shapes of a structure. The proposed damage detection method was verified by a two-span aluminium model plate girder of 4.5 m each in span length. The test structure was supported with a pin on the left edge, a roller support in the middle, and another roller support on the right edge. Crack damage was inflicted in the structure. Eleven accelerometers were placed along the deck of the structure and excited by ambient forces from lightweight traffic in order to extract its dynamic characteristics. The experimental results showed that the method was able to identify the damage location, though both false negative errors (missing detection of true damage location) and false positive errors were present. For damage severity estimation, the method generated relatively high errors.

In 2002, the same researchers (Kim & Stubbs 2002) expanded their method. New damage identification techniques, namely Damage Index A, Damage Index B and Damage Index C, were formulated. This was done in order to improve the accuracy of both damage localisation and severity estimation, by eliminating some assumptions and limitations of the previous method. A numerical two span continuous beam was created and inflicted with ten different damage scenarios. Modal parameters of the first three modes for the undamaged and damaged states were obtained. The results showed that the newly formulated method was able to locate damage and estimate its severity with reasonable accuracy. However, the entire research was performed with purely numerical data. In the paper, the authors discussed neither the influence of noise nor any experimental results.

Choi et al. (2007) further developed a modified damage index (MDI) method, based on modal strain energy, to identify damage in a timber beam. A cubic spline data interpolation function was adopted to perform mode shape reconstructions of the obtained experimental mode shape data. The reconstructed mode shapes were then twice differentiated to obtain mode shape curvatures, which were then normalised for DI calculations. The proposed MDI method was capable of detecting the damage locations from experimental data (some damage cases, however, with false positive errors). Using higher modes proved to be more favourable for identifying multiple damage locations. Regarding the estimation of damage severity, the authors claimed that it would be possible if the method was further investigated.

Shi, Law and Zhang (1998, 2000) proposed a damage indicator using the ratio of changes in modal strain energy in each element. The method required only the elemental stiffness matrix, the analytical mode shapes and incomplete measured mode shapes. The contribution of analytical mode truncation, incomplete measured mode shapes and measurement noise in the damage identification results were discussed. It was shown from the results that the presented method is effective in locating damage. However, it was sensitive to noise in quantifying the extent of damage. Shi et al. (2002) expanded the previous work and improved the quantification of stiffness changes by minimising the modal truncation error in the process of damage identification. However, the method's convergence property prevented it from delivering satisfactory performance.

Li, Yang and Hu (2006) presented a modal strain energy decomposition method for damage localisation. The method was based on decomposing the modal strain energy of each structural element into axial and transverse coordinates. Hence, two damage indicators (axial damage indicator and transverse damage indicator) were formulated for each element in the structure. The numerical and experimental results showed that the axial damage indicator was able to locate damage occurring in horizontal elements, and that the transverse damage indicator was able to locate damage occurring in vertical elements. However, false positive errors were generated in the results, and the method did not perform well in estimating damage severity.

Hu, Wang and Li (2006) presented a cross-modal strain energy (CMSE) method for estimating the severity of damage. In this research, the authors used the structural cross-modal strain energy between the i^{th} mode of the undamaged structure and the j^{th} mode of the damaged structure. The corresponding elemental cross-modal strain energy for the stiffness matrix was also mathematically established. After many steps in the derivation, a parameter α_n was formulated and then used to estimate the severity of damage. A three-dimensional five-storey frame structure was numerically developed to test the proposed method. Damage was simulated by the decrease of elemental stiffnesses. The numerical results indicated that the CMSE method is capable of estimating the severity of damage under noise-free measurement conditions and without any numerical singularity problems. The method was found to be incapable of identifying the damage location.

2.8 FREQUENCY-RESPONSE-FUNCTION-BASED METHODS

Using frequency response function (FRF) measurements directly instead of modal analysis data for damage identification may have certain advantages. Firstly, numerical errors inherent in modal analysis due to inaccurate curve fitting or unavailable residual terms are avoided. Secondly, no effort is required to process measured FRFs in order to obtain modal analysis data. Finally, the most significant advantage lies in the fact that the FRF provides abundant information on the dynamic behaviour of a structure, whereas with modal analysis data much of that information is lost in the course of the numerical extraction process (Sánchez 2005).

One of the FRF-based damage identification approaches is the FRF-curvature-based method. It encompasses damage identification levels 1 to 3 (existence, location and severity) and is based on directly measured FRF data, which includes all frequencies in the measured range and not just the modal frequencies. The absolute difference between the FRF curvatures of the damaged ($*$) and undamaged structure is obtained by

$$\Delta H_{ij}'' = \sum_{\omega} \left| H_{ij}''^* (\omega) - H_{ij}'' (\omega) \right| \quad (2.5)$$

with H_{ij}'' being the receptance FRF measured at location i due to an impact force at point j . The absolute FRF differences for several force locations are then added together.

To date, different FRF-based algorithms to identify damage have been developed and evaluated. Good results have been obtained in the damage identification of numerically modelled structures (Wang, Lin & Lim 1997). The damage assessment for real applications, however, is still problematic and needs further development (Kessler et al. 2002). A ‘bottleneck’ limiting the use of FRFs is the huge size of the required data set. Researchers tried to circumvent this problem by only using a partial set of FRF data. An improper selection of the frequency windows from which the data are drawn, however, results in the loss of important information and thereby introduces errors to the damage identification scheme. This again may result in improper or faulty damage identification (Ni, Zhou & Ko 2006). Thus, one of the main challenges in FRF-based damage identification is the development of algorithms that assist in the processing of the enormous amounts of FRF data.

Wang, Lin and Lim (1997) developed a new damage identification method using measured FRF data. The method was tested experimentally on a 3-bay plane frame mild steel structure. The structure was designed to have two replaceable joints located in the middle of two horizontal bars in order to then introduce different kinds of damage. Numerical results indicated that the method was able to identify the locations and severities of damage within reasonable error limits. The experimental results, however, were less satisfactory. The authors drew the conclusion that the proposed damage identification method may not be effective in identifying small scale damage (such as

surface or internal cracks, flaws, voids and thin spots) because the changes in vibration data caused by minor damage might not be detectable in the presence of noise.

Sampaio, Maia and Silva (1999) formulated a damage identification method using FRF curvature data. This method was based on the absolute difference of FRF curvatures when comparing the undamaged and damaged states of a structure. In the numerical studies using a free-free beam, the method was found to be capable of locating damage, even in the presence of noise. In comparison with other methods (e.g. the DI method), the results showed better performance on the part of the FRF method. From the experimental studies, it was reiterated that the method was able to identify damage but required further development for better characterisation.

Maia et al. (2003) investigated the effectiveness of mode-shape-based and FRF-based damage identification methods. In their research work, a numerical free-free beam was modelled with 99 elements and 100 nodes simulating an undamaged structure. To simulate damaged structures, three other models were constructed with reductions of 25%, 50% and 75% of the Young's modulus at element 70. The numerical results showed that all methods, with the exception of the direct mode shape method, were capable of identifying the actual inflicted damage location. However, some false damage was indicated at the boundaries, which might have been due to the interpolation method used to calculate the derivatives. In the experimental work, a steel beam with constant rectangular cross section was used. The results showed that only the FRF-based mode shape curvature method, the FRF-based mode shape curvature square method and the FRF-based damage index method were successful in locating the damage (a sawcut in the beam), albeit with some false damage identifications. It was suggested that improvements to the methods could be made to the interpolation technique on processing the data, by imposing some noise in the numerical simulations, by applying statistical analysis to enhance the results and by improving the experimental set-up.

Kessler et al. (2002) presented an experimental and analytical application of an FRF method to detect damage in graphite/epoxy specimens. The FRF method was found to be successful in detecting even small amounts of damage in a simple composite structure (i.e. level 1 detection). However, the method was not able to provide

information about the damage type, size, location and orientation of damage since combinations of different variables could yield identical response signatures.

Owolabi, Swamidas and Seshadri (2003) used measured changes in the first three natural frequencies and the corresponding amplitudes of the measured acceleration FRFs for damage identification. In their research, two sets of aluminium beams were used for experimental investigation. Each set consisted of seven aluminium beam models with different boundary conditions, i.e. fixed ends and simply supported ends. A sawcut on the beam was created to simulate the desired level of damage. Crack depth varied from $0.1d$ to $0.7d$ (d was the depth of the beam), with an increment of $0.1d$ at each crack location. From the experimental results, it was noticed that the fundamental frequency showed a clear downward trend as the crack depth ratio increased. The amplitudes of the FRFs also showed a decreasing trend as the crack became larger. The amplitude of the FRFs of the second mode reduced in a similar pattern to the first mode. However, the third mode did not follow the trend. A contour line map was plotted based on the changes of amplitudes of the FRFs resulting from a combination of different crack locations and crack depths. The contour was able to identify the cracks but with some errors. To improve it, the method still requires further development.

Another method using FRF data to detect damage was presented by Furukawa and Otsuka (2006). The research utilised hypothesis testing based on the bootstrap method to minimise errors from noise. The method was tested numerically on a small aluminium beam modelled with 11 nodes and 10 elements. The damage was introduced on different elements by changing the stiffness of the corresponding elements. The authors claimed that the proposed method provided accurate damage identification even in the presence of relatively large noise levels.

2.9 TIME-DOMAIN-BASED METHODS

In recent years, time-domain-based methods have gained much attention in developing damage identification and continuous structural health monitoring schemes. One of the reasons for this popularity is that in their approaches, system parameters are determined directly from the structure's time history response. It is thereby independent of the modal domain, and time data can easily be obtained using simple tools.

Two of the most employed time domain methods are wavelet analysis and Hilbert-Huang transform (HHT). These approaches first decompose the signals in the time domain and then determine the time instant of the occurrence of the damage (damage spike) by detecting discontinuities in the recorded acceleration data. Some methods then locate the damage by analysing the spatial distribution of the damage spike along the structure. Others extract the structural properties (e.g. natural frequencies, damping ratios or mode shapes) before and after inflicting damage and subsequently determine the location and extent of the defect.

Reasonably good results have been obtained with the use of directly measured time data on numerical models. Some experimental studies have been able to determine the location of damage, although damage quantification remains very problematic (Xu & Chen 2004; Yang et al. 2004). A major drawback for real applications is the lack of information on the actual dynamic excitation. Some methods were developed that rely only on structural responses. They, however, can only detect the location and not the extent of damage. Another shortcoming of the response-only techniques is that measured structural responses are highly variable in a changing environment, which has caused many of the methods to fail when applied to real structures (Savov & Wenzel 2005). Also, noise polluted data is a major obstacle (Yang et al. 2004).

Xu et al. (2003) first applied a method based on Hilbert-Huang-transform (HHT) to analyse the dynamic characteristics of a sixty-nine-storey building, and then compared the results with those obtained from a method based on fast Fourier transform (FFT). The sixty-nine-storey Di Wang building is located in the city of Shengzhen, China. The measured data were recorded from the wind velocity and structural dynamic response of the building during Typhoon York in September 1999. The HHT and FFT methods were applied to the measured data to obtain the dynamic characteristics of the building. The analysis results showed that the natural frequencies identified by the HHT method were almost the same as those obtained with the FFT method. The damping ratios of the first two modes predicted by the HHT method were generally lower than those by the FFT method. Chen, Xu and Zhang (2004) performed similar work on the Tsing Ma suspension bridge during Typhoon Victor, and they arrived at a similar conclusion.

Expanding their previous research on the use of the HHT method, Xu and Chen (2004) further investigated the use of the method for identification of structural damage caused

by a sudden change of structural stiffness. The experimental research was performed on a three-storey steel plate building model. Damage was simulated by pulling out a pin connecting the floor plate and the spring, thereby releasing the spring during the vibration of the building. The results showed that the method was able to identify the damage time instant by observing the occurrence time of damage spikes appearing in the first intrinsic mode function component of the acceleration response. However, the method was not robust in locating damage, and no quantitative relationship between the spike amplitude and the damage severity was established by the experimental work. The authors suggested that further investigation was therefore required.

Yang et al. (2004) proposed two methods to extract damage information from measured time history data obtained from a structure. The first method was based on the Empirical Mode Decomposition (EMD), which was designed to extract damage spikes of a sudden change in structural stiffness, and thereby to identify the damage time instants. The second method was based on a combination of EMD and HHT, and was designed to detect the damage time instants as well as the natural frequencies and damping ratios of the structure before and after damage. The four-storey ASCE benchmark building, established by the ASCE Task Group on Structural Health Monitoring, was used in the numerical study to verify the two methods. The first method was found to be able to identify the damage time instants only if the noise pollution level was very small and the changes in the structure were not abrupt. The second method was able to determine the time instant of damage occurrence and was also capable of identifying the natural frequencies and damping ratios of the structure, both before and after damage was inflicted. However, with only a single record, the location and the severity of damage in the structure were not identified. Similar work was performed experimentally by Xu and Chen (2004), who used EMD to detect sudden change of structural stiffness for a three-storey shear building model.

Zhu and Law (2006) developed a new method for crack identification on a beam in bridge structures using wavelet analysis of the operational deflection time history with a moving load. Numerical and experimental examples were used to demonstrate the response at a single measuring point, employing a continuous wavelet transform to detect the damage location. A damage index system was proposed to estimate the relative depth of the cracks. The method was found to be capable of identifying damage

location for single and multiple cracks for the numerical cases, but not for the experimental cases.

An application of time series analysis to bridge structural health monitoring was performed by Omenzetter and Brownjohn (2006). The work intended to address long term SHM problems through the analysis of static strain time history data obtained for the Singapore-Malaysia Second Link (the Tuas Link) and operating continuously over a long period. A vector seasonal 'autoregressive integrated moving average' (ARIMA) model was formulated for recording the strain signals. The coefficient of the ARIMA model varied with time and was identified using an adaptive extended Kalman filter (Harvey 1989). By observing various changes in the ARIMA model coefficients, unusual events such as structural changes or inflicted damage could be identified.

2.10 ARTIFICIAL-NEURAL-NETWORK-BASED METHODS

Most of the damage identification methods presented above make use of mathematical models to represent relationships between damage characteristics and dynamic changes in structures. Vibration-based damage detection is an inverse problem where causes must be determined from its effects. Often a unique solution does not exist for an inverse problem, especially when the relationships are very complex and only limited data are available. In general, dynamic-based damage identification is a pattern recognition problem, where changes in the vibrational properties of a structure are attributed to certain characteristics of damage. ANNs are capable of pattern recognition and classification. They can model complex non-linear relationships and are robust in the presence of noise. These characteristics make ANNs powerful complementary tools in vibration-based damage identification. With the use of ANNs, some critical issues of traditional damage detection methods can be overcome and damage detection accuracy and reliability greatly improved. The advantages of ANN-based approaches over traditional mathematical damage detection methods include the following (Bakhary 2008):

- ANN-based methods are capable of reliable damage identification, even when trained with incomplete data, without using data expansion or finite element reduction methods.
- Once ANNs are properly trained, damage identification is relatively fast and mathematical models do not need to be constructed.
- There are no limitations on the type of vibration parameters to be used as inputs for ANNs. The input and output parameters can be selected with much flexibility without increasing the complexity of network training.
- Noise filtering capabilities of ANNs make them more robust in the presence of measurement noise and other uncertainties.

The first researchers to introduce ANNs in vibration-based damage detection in civil structures were Wu, Ghaboussi and Garrett (1992). Their paper published in 1992 concluded that ‘the use of neural networks for structural damage assessment is a promising line of research’. The basic strategy for the use of ANNs in dynamic-based damage detection is to train a network to recognise changes in structural properties based on measured vibrational response. Through the training, the network is able to extract relationships between inputs and outputs, and it stores them within the network’s connection strengths (Bakhary 2008). In the testing stage, the network is fed with as-yet unseen inputs, and through the established connection strengths, the network is able to produce generalised outcome predictions.

Over the past two decades, researchers have used different types of vibration-based parameters as inputs to ANNs. A selection of literature that has significantly contributed to this area is presented below, subdivided into the following categories.

- Neural networks trained with modal parameters and their derivatives
- Neural networks trained with frequency response functions
- Neural networks trained with time domain data

Readers who are not familiar with ANNs are referred to CHAPTER 3, which gives some theoretical background information on neural networks.

2.10.1 Neural Networks Trained with Modal Parameters and Their Derivatives

In one of the earliest research papers on ANN-based dynamic damage detection, Elkordy, Chang and Lee (1992) demonstrated that using percentage changes in vibrational signatures, rather than using their absolute values, can effectively distinguish between patterns corresponding to different damage states. In 1993, Elkordy, Chang and Lee (1993) extended their previous research and investigated the feasibility of identifying damage from experimental data with networks that were trained with analytically generated data. Three different models of a five-storey steel frame structure served as testing objects. Two of these models were finite element models; the first one being a very simplified two-dimensional frame using only beam elements, and the second model being a more detailed finite element model using beam, truss and plate elements. The third model was an experimental structure. Damage was simulated by reducing the member stiffness in the bottom two stories by between 10% and 70%. The researchers used mode shapes (obtained from numerical simulations and shake-table testing, respectively) as input patterns, and the percentage change in member stiffness formed the outputs of the networks. Two networks were created; the first was trained with data obtained from the simplified numerical model, while the second was trained with data from the more complex numerical structure. The researchers found that the network trained with data of the first model produced poor predictions, whereas the network of the more detailed model gave reasonably good damage estimations, generally with absolute prediction errors of less than 10% for damage severities.

Zapico, Worden and Molina (2001) presented a damage assessment procedure on a two-storey steel frame and steel-concrete composite floor structure. A simplified finite element model, previously updated using two natural frequencies and the stiffness and masses of the beams, was used to generate input data for neural network training. Three neural network approaches based on multi-layer perceptron networks were proposed. For the first and second approaches, the input parameters were the first natural frequency and the first mode shape, respectively; for the third approach, the first two longitudinal bending frequencies were used as inputs. The performance of each network was tested on numerical and experimental data of the 'Steelquake' benchmark structure. The first neural network approach failed completely. The authors suspected that too

many damage parameters were defined and hence, different combinations of damage led to similar modal results. The network was therefore unable to generalise from the selected input. In the second approach, the neural network showed an excellent generalisation over the analytical data; however, it failed completely with experimental data due to the poor accuracy of the extracted mode shapes. The third approach gave reasonable results. The corresponding trained network achieved a good generalisation over both the analytical and experimental data.

Ko, Sun and Ni (2002) proposed a three-stage hierarchical damage detection scheme for successively identifying occurrence, location and severity of structural damage based on changes in modal parameters. The feasibility of the proposed method was studied on a precise three-dimensional finite element model of the cable-stayed Kap Shui Mun Bridge located in Hong Kong. In the first stage of the method, auto-associated neural networks were fed with natural frequencies of the structure from both the intact and damaged states for the purpose of damage alarming. In the second stage, a combination of the modal curvature index and modal flexibility index was used to identify the damage region. In the third stage, specific damaged members and damage severities were identified by using multi-layer perceptron neural networks fed with input vectors determined from changes in the natural frequencies and mode shapes. The damage identification results of the bridge model showed some promising signs but also demonstrated some problems with the proposed method. In two of the twelve investigated cases, the method failed to give damage alarm in the first stage, which could eventually lead to an oversight of that damage. When damage was located near the support area, the modal curvature index and modal flexibility index were sometimes unable to produce accurate damage identification.

Sahin and Sheno (2003) examined the effectiveness of using natural frequencies and mode shape curvatures as inputs for ANNs. As a test structure, numerical models of fibre-reinforced plastic laminated beams were created and inflicted with various damage scenarios. Different types of networks with various input-output parameters were designed to estimate locations and severities of damage. The first type of network was trained with data obtained from the reduction of the first three natural frequencies. The input parameters of the second network were the absolute differences in mode shape curvatures. The third network inputs were the maximum absolute differences in

curvature of the mode shapes and their corresponding locations along the beam. Additional networks were trained with combinations of the aforementioned parameters. To simulate experimental uncertainties, artificial random noise was added to the normalised frequencies and the maximum differences in mode shape curvature data. The authors concluded that although reduction in natural frequency was considered an indicator for damage, it did not provide any useful information about either the location or about the severity of the defects. Maximum absolute differences in mode shape curvatures and their corresponding locations along the beam, however, provided fairly good indications of the damage location. The results from the combination of all three features were less promising than those obtained from the individual networks. Hence, the researchers concluded that separate neural networks function more efficiently than one trained network that uses all the combined inputs. This study further found that when noise-polluted data were introduced to the networks, more accurate and robust predictions were obtained in the damage localisation compared to the quantification of the damage.

Lee et al. (2005) presented an ANN-based damage detection method using three different types of mode-shape-based parameters as inputs for the networks. The employed parameters were direct mode shape measurements, mode shape differences and mode shape ratios between the pre- and post-damage states. An important task for the researchers was to develop a method that is effective in dealing with modelling errors in the baseline finite element model from which training patterns for the networks are generated. The proposed approaches were first tested on two numerical structures, a simple beam structure and a multi-girder bridge, and then applied to a laboratory bridge model and a real bridge (the Hannam Grand Bridge in Seoul, Korea). From the results of the numerical models, which were generated with modelling errors of up to 20%, the researchers found that when using direct mode shape measurements as network inputs, the accuracy of damage detection could not be guaranteed; for mode shape differences and mode shape ratios, however, fairly good damage estimations were produced. For the laboratory bridge model, from which dynamic data were extracted using ambient vibrations, similar findings as for the numerical models were obtained. For the real bridge, the damage estimation was performed on substructures using selective information excluding the mode shape data near the node points. The networks trained with mode shape differences and mode shape ratios produced good location accuracy

for all damage cases, whereas the estimated damage severities contained minor false positive errors at several locations.

In 2006, Lee and Yun (2006) extended their method and applied a two-step substructural identification approach to identify damage in the aforementioned numerical multi-girder bridge and the real Hannam Grand Bridge. In the first step, damage indicators based on modal strain energy were used to screen the entire structure to identify potential damaged regions. In the second step, ANNs were trained with mode shape differences between the pre- and post-damage states to produce predictions of damage location and severity in the potentially damaged members identified in the first step. For the real bridge, mode shape data were identified from ambient vibrations and were reconstructed using a cubic polynomial function to obtain finer mode shapes. To illustrate the effects of measurement noise, mode shape data from the numerical bridge model were polluted with three levels of noise. From the results of the numerical model, the authors found that the damaged members were reasonably well identified providing, of course, that they were selected in the first step as potentially damaged. Fairly large errors were caused by noise pollution. For the real bridge, while all damage cases were correctly selected in the first step, some false positive damage alarms were also produced.

In 2006, Xu and Humar (2006) proposed a two-step algorithm that first utilised modal strain energy damage indices to locate damage and then a neural-network-based approach to estimate the damage severity. The proposed algorithm was applied to detect simulated damage in finite element models of a girder and a model of a real bridge (the Crowchild Bridge located in Alberta, Canada). Three damage cases, two single and one double, were investigated. Measurement errors were simulated by adding different levels of random noise (up to 5%) to the mode shapes. The authors found that the modal-strain-energy-based damage indices were quite effective in predicting the location of damage in the girder model. However, when damage indices were determined from translational modes, the numerical differentiation involved in obtaining the curvatures magnified the measurement errors and introduced faults in the damage localisations. For the severity estimation, the neural-network-based approach was quite effective in predicting the damage magnitude after the damage location was determined. Errors were encountered, however, for small amplitude damage cases.

Gonzalez and Zapico (2008) developed a method for damage identification for buildings with a steel moment resisting structure. The method was based on ANNs trained with modal parameters (natural frequencies and mode shapes). A simplified finite element model of a five-storey building was used to generate data for neural network training. The inputs to the networks were the first flexural modes (natural frequencies and mode shapes) at each principal direction of the structure, and the outputs were the spatial variables (mass and stiffness). The proposed method consisted of two stages; in the first stage, the undamaged structure was calibrated, and in the second stage, damage due to a simulated earthquake was identified. In each stage, multi-layer perceptron networks were trained with the modal parameters to obtain the spatial variables. The proposed method was successful in determining which storey of the building was damaged. A statistical study on the influence of modal errors (simulated by data polluted with Gaussian noise) concluded that the method was quite sensitive to errors, especially to mode shape errors. It was found that the coefficient of variation of the modal errors should be less than 0.1% for natural frequencies and 0.02% for mode shapes in order to obtain absolute values of damage identification errors less than 0.05 with 95% confidence.

Mehrjoo et al. (2008) presented a method for estimating joint damage intensities for truss bridge structures using ANNs. To overcome issues of large structural systems associated with many unknown parameters, a substructuring technique was employed. As input parameters to ANNs, natural frequencies and mode shapes were used. To demonstrate the proposed technique, it was applied to numerical models of a simple truss (with five joints) and a more complex truss bridge (with 16 joints). For the more complex truss bridge, the model was subdivided into three substructures and the joint damage identification was achieved on one substructure at a time. From the results of the simple truss, it was found that the damage states of all five joints were accurately identified with an average error of 1.28% when the first four modes were employed. For the Louisville Bridge model, a number of ANNs were trained with different numbers of modes included in the input patterns. The identification outcomes showed that when only one mode was used, an average error of more than 8% was obtained. It was found that the optimum number of modes to be included was five, producing an average error of about 1%. However, this study only investigated data from noise-free numerical simulations - real testing uncertainties such as measurement noise were not considered.

2.10.2 Neural Networks Trained with Frequency Response Functions

Wu, Ghaboussi and Garrett (1992) were the first to introduce ANNs to vibration-based damage detection in civil structures, as mentioned earlier. As input parameter to ANNs, the researchers used Fourier spectrum recordings of relative acceleration time histories. The test structure, a simple three-storey building, modelled as two-dimensional shear structure with three degrees of freedom, was excited by earthquake base acceleration and the structure's dynamic responses were captured at the third (top) and the second floor. Damage was modelled by reducing the column member stiffness by 50% to 75%. From the fast Fourier transform, the first 200 points (0 Hz to 20 Hz) were used as inputs for neural network training. The network output consisted of three nodes, each representing the damage level for each column member in the structure. In a first attempt, only acceleration data from the third floor were used as network inputs. Here, only damage of the column member connected to the third floor was correctly identified. In a second attempt, data from the top and second floor were fed to a second network. This network was able to produce correct damage estimations to both third and first floor members, with an accuracy of about 25%, but it was still unable to identify the column member between the first and the second floor.

In 2001, Zang and Imregun (2001b) proposed another FRF-based damage identification method using ANNs. Instead of utilising a partial set of FRF data, the authors employed principal component analysis (PCA) to reduce the size of measured FRFs. The compressed FRF data, represented by their projection onto the most significant principal components (PCs), were then used as input variables to ANNs. The proposed method was applied to a numerically simulated railway wheel from which FRF data with 4,096 data points in x, y and z direction were generated. To assess the robustness of the method, a number of FRFs were polluted by adding 5% random noise. After applying PCA, the generated FRFs (noise-free and noise-polluted) were reduced to 7, 9 and 13 PCs for x, y and z direction, respectively. In total, three different networks, each corresponding to a co-ordinate direction, were trained to predict the condition of the specimen, i.e. healthy or damaged. From the results, it was found that for all investigated cases the health condition was correctly identified. In a successive paper, Zang and Imregun (2001a) applied the method to identify three different states of a numerical space antenna, i.e. healthy antenna, slight mass damage and slight stiffness

damage. The results showed that, provided an adequate number of PCs together with a suitable neural network configuration was used, it was possible to distinguish between the three states of the antenna.

In 2003, Zang, Friswell and Imregun (2003a; 2003b) presented another approach for the use of FRFs in ANN-based damage identification. In two coherent papers, the authors proposed two correlation criteria for measured FRF data, the global shape and the amplitude correlation criteria (GSC and GAC), to be used as damage indicator. To demonstrate their method, it was applied to an experimental three-storey book shelf structure. Radial basis function networks were fed with two input parameters, the averaged integration of the GSC (AIGSC) and the averaged integration of the GAC (AIGAC), to predict various structure states (including undamaged and damaged states, damage locations and severities) and the environmental variability. The network results showed that the proposed method was capable of distinguishing between various structural states; except for a few false identifications, most structure states were successfully classified. In a paper from 2007, Zang, Friswell and Imregun (2007) extended their method to allow the quantification of the change in structural response. The researchers defined two new damage indicators, the window-averaged GSC (WAIGSC) and the window-averaged GAC (WAIGAC). By introducing these two indicators, a significant reduction in the size of the data was achieved, which was beneficial for network training. The method was again applied to the three-storey book shelf to identify undamaged and damage states, single and multiple damage locations, as well as damage levels. Again, the network predictions were correct for most damage cases, although there were some small fluctuations for some outputs.

Qu, Zou and Wang (2004) investigated a damage detection method for large scale structures using a substructuring approach and FRF data. In the proposed method, damage features for ANN inputs were extracted from FRFs by applying independent component analysis. A two-span planar truss with 55 truss elements served as test structure to demonstrate the feasibility of the method. Damage scenarios were simulated by stiffness reductions of two truss members. Instead of identifying the structure as a whole, it was subdivided into three substructures and only the internal substructure was considered. FRF data from 0 Hz to 200 Hz with a frequency resolution of 0.2 Hz per data point were compressed and used as network input. The results of this study showed

that the substructuring identification improved the ability and computational efficiency to identify damage in large scale structures.

Yeung and Smith (2005) presented a damage detection approach using unsupervised neural networks and frequency spectra derived from time history data. As network inputs, the use of frequency spectra from pairs of nodes and peaks of mode shapes was proposed. Two types of unsupervised neural networks, the probabilistic resource allocating network (PRAN) and the DIGNET network, were utilised to identify damage in a clustering approach. To verify the method, it was tested analytically using a finite element model of a historic suspension bridge. To simulate real testing conditions, Gaussian noise was added to time history data and environmental effects were simulated in the form of thermal stressing. The damage detection outcomes were reasonably good, with the PRAN network generally outperforming the DIGNET network. In a sensitivity study, the effects of varying thresholds and noise levels were examined. The researchers found that the sensitivity of the network could be increased by reducing the threshold, but at the expense of greater computation and increased misclassification of undamaged signals. When compromising between sensitivity and misclassification, a damage identification rate of about 70% was obtained.

Ni, Zhou and Ko (2006) presented an experimental investigation of seismic damage identification of a 38-storey tall building model using measured FRFs and neural networks. A 1:20 scale reinforced concrete structure was tested on a shake table by exerting successively enhanced ground earthquake excitations to generate different levels of damage, i.e. trifling, moderate, serious and complete (nearly collapsed) damage. After incurring the earthquake excitations at each level, white-noise random excitation of low intensity was applied to produce ambient vibration responses from which FRFs were measured. PCA was performed on the measured FRFs to reduce the dimension of the FRF and to eliminate noise. The PCA-compressed FRF data were then used as inputs to neural networks for overall damage evaluation and localisation. The results showed that, provided a sufficient enough sensor distribution is given, a quite satisfactory evaluation and localisation of damage is obtained with the proposed method. The authors further found that compared to the direct FRF method, the PCA-compressed FRF method provided much higher identification accuracy in assessing the damage.

An extension to ANNs are neural network ensembles (also referred to as network committees or classifier ensembles), which are a hierarchy of networks that are trained independently for the same task and whose outcomes are fused at different stages by ensemble networks. These neural network committees were observed to perform better than the best network used in isolation (Perrone & Cooper 1993) and are currently used in many fields of research. The idea of a hierarchical network training was first employed in the area of vibration-based damage detection by Marwala and Hunt (1999). The researchers proposed a two-stage neural network committee (also termed neural network ensemble) to combine information from modal data and FRFs. In the network committee, first, two individual networks were trained with either mode shape vectors or frequency energies, which are integrals of the real and imaginary components of the FRFs over various frequency ranges. The outcomes of the two individual networks were then jointly fed to a third ensemble network producing final predictions on the condition of the structure. To verify the method, it was applied to numerical simulations of a cantilever beam. The beam was divided into five segments and the networks were trained to identify the damage existence in each segment. The authors found that the ensemble network gave a mean error of 7.7% compared to 9.50% and 9.75%, respectively, of the individual networks. In an extension to this work, Marwala (2000) presented a committee of neural network approach, which employed modal properties (natural frequencies and mode shapes), FRFs and wavelet transform data as inputs to individual networks. This new approach was numerically tested on data from a three-degree-of-freedom mass-spring-damper system. The experimental demonstration was conducted on cylindrical shells inflicted with four types of damage. The generated data were separately fed into three neural networks, and later combined in an ensemble network. It was again found that the ensemble identified the damage cases better than the three approaches used individually. The author further claimed that the effectiveness of the method was enhanced when experimentally measured data were used, which was in contrast to many existing methods. This was because the committee approach assumed that the errors given by the three approaches were uncorrelated, a situation that becomes more apparent when measured data rather than simulated data were used.

2.10.3 Neural Networks Trained with Time Domain Data

Masri et al. (1996) explored a methodology based on the use of ambient vibration for ANN-based damage detection. Input to ANNs were the structure's relative displacement and velocity time histories, and the output were the corresponding restoring forces obtained from the exciting force and the acceleration time histories. In the proposed approach, a network was trained with time history data of the undamaged system only. In the testing stage, data from damaged structures were fed to the network producing erroneous restoring forces. By determining the abnormality in terms of root-mean-square error between the network output and the actual restoring force, a measure on the changes of the structure was obtained. The method was verified through simulation studies with linear and nonlinear single-degree-of-freedom systems. The effect of measurement noise was also investigated. The results demonstrated the feasibility of the proposed approach. It was found that better predictions were obtained when longer vibration signatures were used as input. The authors acknowledged that due to the nonparametric nature of the mean-square deviation error, the method cannot ascertain which component of the restoring force changed and by what amount; it can only detect changes in the global measures. In 2000, Masri et al. (2000) extended their method and proposed two new time-history-based input-output sets for ANNs. In the first set, displacement, velocity and acceleration vectors were used as inputs and the system excitations were the outputs. In the second set, displacement, velocity and excitation vectors were the input parameters and the outputs were the system accelerations. Both approaches were tested on nonlinear multi-degree-of-freedom systems. The results showed fairly good detections for both sets of input-output parameters. Due to the dimensionless nature of the error measure and the lack of information about the systems nonlinear dynamic behaviour, changes could only be detected but not quantified.

Yam, Yan and Jiang (2003) presented an integrated method for damage location and severity identification of composite structures using wavelet transforms and ANNs. Structural damage feature proxy vectors were constructed and calculated based on energy variation of the structural vibration responses decomposed using wavelet transforms. ANNs were used to map the relationship between structural damage feature proxy and damage status. Numerical and experimental PVC sandwich plates were used to verify the proposed method. In the numerical study, 12 cases of crack-type damage

were investigated, and in the experimental study, 6 crack cases with different lengths were considered. The proposed method was able to correctly locate the 12 damage cases of the numerical investigation; however, some errors in the results were observed in determining the crack length in the experimental study.

Su and Ye (2004) proposed a lamb wave-based quantitative identification technique for delamination in carbon fiber/epoxy (CF/EP) composite structures using ANNs. First, the researchers developed an intelligent signal processing and pattern recognition (ISPPR) package based on wavelet transforms and ANNs. By means of ISPPR, a damage parameter database (DPD) was constructed by extracting the spectrographic characteristics of simulated lamb wave signals and digitising them as digital damage fingerprints (DDF). The DPD was then employed offline to train ANNs under the supervision of an error-backpropagation algorithm. Finally, the proposed methodology was validated online by identifying actual delaminations in CF/EP quasi-isotropic composite laminates. The delamination locations estimated by this method were close to the actual locations. However, the research did not mention either multiple damage detection cases or damage severity estimation.

Kao and Hung (2005) proposed a damage identification procedure based on the free vibration responses of a structure. The ANN-based method involved two steps. In the first step (system identification), neural system identification networks (NSINs) were trained to identify the undamaged and damages states of a structure. In the second step (structural damage detection), the trained NSINs from the first step were used to generate free vibration responses with the same initial condition or impulsive force. The extent of changes in a structural system was assessed by comparing the period and amplitude of the free vibration responses of the damaged and undamaged states. The method was experimentally tested on a five-storey steel frame structure by subjecting it to various intensities of the 1995 Kobe earthquake on a shake table. From the results, it was found that the proposed method is very promising for application to linear and nonlinear structures.

2.11 SUMMARY

This chapter presented a review of important literature published over the past three decades in the area of vibration-based damage identification. From the review, it was found that researchers have used a broad range of dynamic-based parameters to identify damage. Traditionally, the most popular damage fingerprints used were derived from natural frequencies or mode shapes, as these two quantities are easy to determine with a relatively high level of confidence. In recent years, the use of frequency response functions (FRFs) and time history data has gained more attention as signal processing techniques and computational power have improved. Further, ANNs with their pattern recognition and classification capability have proved to be an efficient tool in complementing vibration-based damage identification, and several research publications exist in this area. To verify the proposed methods, researchers have applied them to different types of numerical and experimental structures; in rare cases, some techniques have even been tested on real structures. Although a large number of publications exist, the area of vibration-based damage identification is still an active field of research and several problems still need to be resolved before applicable methods become readily available. Some major challenges include the following:

- Uncertainties from field testing conditions such as measurement noise, measurement errors and environmental fluctuations.
- Real testing limitations such as limited number of sensors and incomplete data sets.
- Complex behaviour and large number of unknown parameters in complex structures.
- Identification of existence, location and severity of different damage scenarios, i.e. various types of damage at different locations and with varying severities.
- Identification of small size damage and multiple damage scenarios.
- Modelling errors in finite element models.
- For ANN-based damage identification: optimisation of input patterns, network design and network training scheme.

Even though researchers have addressed parts of these problems, the algorithms hitherto proposed are still far from resolving them. The research presented in this thesis aims to improve currently available vibration-based damage identification methods with consideration of the unsolved challenges listed above. The key issues that were identified in the literature review and were considered in this thesis are: robustness of

damage identification algorithms to measurement noise and measurement errors; problems related to limited number of measurement sensors and incomplete data sets; accuracy and reliability in identification of damage location and severity; detection of different damage types; identification of small-size damage; and, optimisation of neural network design, including input parameters and network training schemes.

Based on the literature review, the following steps will be carried out to develop improved ANN-based damage detection algorithms. First, thorough investigations will be undertaken on a simple structure to provide an in-depth understanding on the effects of damage to vibrational characteristics. Second, currently available highly promising damage identification methods (identified from the literature review) will be applied to the simple structure and their performance will be evaluated in regard to key issues identified above. Third, the studied methods will be improved and refined while employing ANN techniques to overcome the identified problems. Finally, the improved methods will be applied to a more complicated structure to verify the methods and to study their performance under more complex conditions.

From the literature review, two methods were identified that are highly promising in the field of vibration-based damage identification. Both methods fulfil three criteria: first, they have already given successful damage identification results when applied by other researchers; second, they are suffering from shortcomings; and third, they have great potential for improvement. The first method is the DI method developed by Stubbs, Kim & Topole (1992). This method is a modal parameter method based on changes in modal strain energy, and it has been successfully applied by several researchers in various fields and applications (see section 2.7.4). Despite reported successful applications of this technique, the method has several unresolved issues. For example, if damage is located close to a node point of a given mode, the defect remains undetected unless additional modes are used for detection. Further, when multiple mode shapes are used, false positive damage identifications are often produced, especially when only limited measurements are available. The reliability and accuracy of damage identification with the DI method is greatly jeopardised when exposed to field testing conditions such as measurement noise interferences, limited number of sensors, experimental modal analysis uncertainties and environmental influences. Although a number of researchers have developed modified and extended versions of the DI

method (Choi 2007; Kim & Stubbs 2002), this technique is still in need of improvement to overcome the issues highlighted above.

The second method identified from the literature review as being highly viable is based on measured frequency response functions (FRFs). FRF data are directly measured data that provide an abundance of information on a structure's dynamic behaviour. As FRF data are very sensitive to structural change, they have been used as damage indicators in various forms. In particular, the use of residual FRFs, which are differences between FRF data of the undamaged and the damaged structure, have revealed very promising results (Trendafilova & Heylen 2003). The use of ANNs to extract damage patterns from FRF-based data has also been frequently reported (see section 2.10.2). To overcome the issues associated with the large size of FRF data and to improve the performance of ANNs, some researchers have employed PCA for data compression and noise reduction (Ni, Zhou & Ko 2006; Zang & Imregun 2001a, 2001b). The use of ANNs and PCA in FRF-based damage identification has so far only been applied to numerical structures for the determination of damage presence and severity (Zang & Imregun 2001a, 2001b), and to an experimental structure for the prediction of overall and local damage severity (Ni, Zhou & Ko 2006). For both approaches, the damage identification outcomes were highly dependent on sensor availability and distribution. Further, the investigated damage cases were of large severity and several false detections were obtained, which challenges the reliability of the proposed procedures.

In this thesis, two new damage identification procedures will be proposed based on the two methods described above. For both proposed procedures, the implementation of PCA and neural network ensemble techniques will form the basis to enable the accurate and robust identification of damage while overcoming the shortcomings of the current methods identified above. For preliminary investigations and development of the improved DI- and FRF-based damage detection methods, a simple pin-pin supported beam structure will be employed. The use of a simple rather than a complex structure will enable the fundamental study of the effects of damage to vibrational characteristics without having to deal with the complicated dynamic interactions associated with complex structures. For later verification of the developed methods, a two-storey framed structure will be used. For both structures, damage cases and damage types will be investigated to test the performance of the methods.

CHAPTER 3

INTRODUCTION TO ARTIFICIAL NEURAL NETWORKS AND PRINCIPAL COMPONENT ANALYSIS

3.1 INTRODUCTION

This chapter presents theoretical and practical background information on artificial neural networks (ANNs) and principal component analysis (PCA). Both techniques are core elements in the developed damage identification methods and their application discussed throughout this thesis. To provide an introduction to the subject, this chapter first gives an overview of the origin of ANNs, the biological neural network. Second, it describes the functionality of a single processing unit of a network (the single neuron). Third, it explains the operation of multi-layer perceptron networks and the backpropagation algorithm. Fourth, it gives practical comments on the design of neural networks. Fifth, it presents an overview on network ensembles, and finally, it gives background information on PCA.

3.2 THE BIOLOGICAL NEURAL NETWORK

The creation of neural networks was originally inspired by the human brain and the way it processes information. The human brain consists of about 10^{11} electrically active cells called neurons, which are heavily interconnected. A basic neuron is composed of a body, axons, dendrites and synapses, which are illustrated in Figure 3.1. The branching dendrites provide input information to the neuron, while the long cylindrical axons carry impulses from the neuron to neighbouring neurons and thereby act as outputs. Communication between neurons takes place at junctions called synapses. Each neuron typically makes connections to many thousands of other neurons, with as many as 10^4 synapses per neuron and a total number of synapses in the brain exceeding 10^{14} . Although each neuron is a relatively slow information processing system (with an average rate of 3 m/s), the massive parallelism of information processing at many synapses simultaneously creates an effective processing power. It also leads to a high degree of fault tolerance, with many neurons dying each day with little adverse effect on

performance (Bishop 1994). In the event of traumatic neural loss, healthy neurons can take over the functions of damaged cells (Fausett 1994).

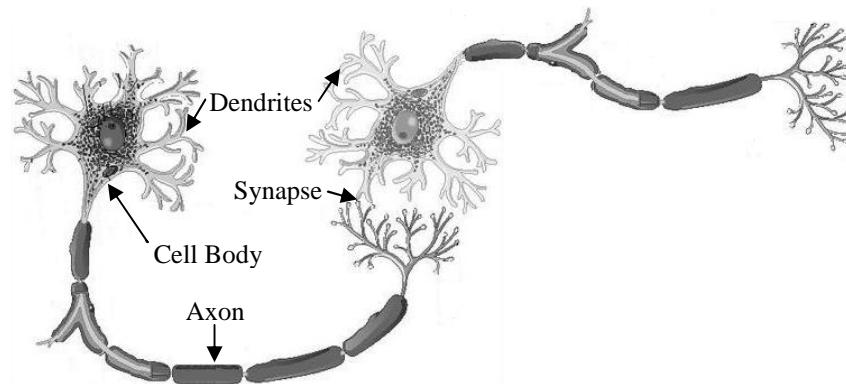


Figure 3.1 Two biological interconnected neurons

Neurons act in an ‘all-or-nothing’ manner. A response is only generated if the total impulse potential coming from the input of other neurons reaches a certain threshold level (typically about 40 mV). Incoming impulses can be excitatory if they cause the firing of a neuron, or inhibitory if they hinder the firing of a response. When a neuron fires, it sends an electrical impulse (called action potential) that propagates from the cell body along the axon. When the impulse reaches a synapse, it triggers the release of chemical neuro-transmitters that cross the synaptic junction to the next neuron. Depending on the type of synapse, the probability of the subsequent neuron firing either increases or decreases. Each synapse has an associated strength (or weight) that determines the magnitude of the effect of an impulse on the post-synaptic neuron (Bishop 1994).

A key property of the neural system is its ability to modify its responses as a result of exposure to external signals, which is called learning. These learning or memorising modifications are implemented by strengthening or weakening the synaptic junctions (Hagan, Demuth & Beale 1996).

3.3 THE ARTIFICIAL NEURAL NETWORK

The biological neural system provided the basis for a great deal of research into artificial neural network models. This research was driven by the desire to build better pattern recognition and information processing systems (Bishop 1994). By definition, ‘artificial neural systems, or neural networks, are physical cellular systems which can acquire, store, and utilize experiential knowledge’ (Zurada 1992). To model such a system requires, first, a model of the network’s basic building block, the single neuron.

3.3.1 The Single Neuron

In 1943, a simple mathematical model of a single neuron was formulated by McCulloch and Pitts (McCulloch & Pitts 1943). A single neuron, also referred to as a processing unit or simply a unit, can be regarded as a non-linear function that transforms a set of input variables p_i ($i = 1, 2, \dots, q$) into an output variable a . A single multiple-input neuron is shown in Figure 3.2.

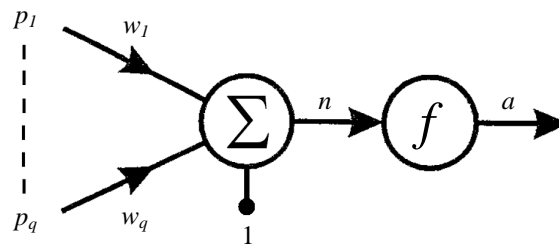


Figure 3.2 Model of a single multiple-input neuron

The signal p_i at input i is first multiplied by a parameter w_i , known as weight, and then added to all the other weighted input signals by the summation function to give a total input to the unit of the form

$$n = w_1 p_1 + w_2 p_2 + \dots + w_q p_q + b = \sum_{i=1}^q w_i p_i + b = \mathbf{w} \mathbf{p} + b \quad (3.1)$$

where the offset parameter b is called a bias. The bias can be regarded as a special case of a weight from an extra input of 1. The output a of the unit depends on a particular transfer function f and is calculated as

$$a = f(n) = f(\mathbf{w} \mathbf{p} + b) \quad (3.2)$$

The transfer function f can be a linear or nonlinear function of n .

To relate the artificial neuron back to the biological neuron, the weights w_i correspond to the strengths of the synapses, the cell body is represented by the sum function and the transfer function, and the neuron output a can be regarded as analogous to the signal (firing rate) of the axon (Bishop 1994).

Learning (or training) of the neuron is achieved by modifying the weights and bias parameters, \mathbf{w} and b , following special learning rules. Based on the McCulloch and Pitts neuron model, Rosenblatt formulated the perceptron learning rule in 1958 (Rosenblatt 1958). The neuron learns from a set of examples (the training set),

$$\{p_1, t_1\}, \{p_2, t_2\}, \dots, \{p_q, t_q\} \quad (3.3)$$

where p_q is an input to the unit and t_q is the corresponding correct output, also referred to as the target. As the inputs are applied to the network, the network outputs are compared to the targets in order to move the network outputs closer to the targets. The learning rule is used to iteratively adjust the weights and bias of the unit according to the following expressions,

$$\Delta \mathbf{w} = (\mathbf{t} - \mathbf{a}) \mathbf{p}^T = \mathbf{e} \mathbf{p}^T \quad (3.4)$$

and

$$\Delta \mathbf{b} = (\mathbf{t} - \mathbf{a}) = \mathbf{e} \quad (3.5)$$

where the perceptron error vector \mathbf{e} is the difference between the target vector \mathbf{t} and the actual output vector \mathbf{a} . The perceptron learning rule is then written as,

$$\mathbf{w}(k+1) = \mathbf{w}(k) + \mathbf{e}(k) \cdot \mathbf{p}^T \quad (3.6)$$

$$\mathbf{b}(k+1) = \mathbf{b}(k) + \mathbf{e}(k) \quad (3.7)$$

where k represents the iteration or epoch number. The process of updating the weights and bias is repeated until the errors approach a prescribed error goal.

3.3.2 Multi-Layer Perceptron Networks

While the simple model of a single neuron network has some practical significance, it is only able to solve linear problems (Bishop 1994). A much more powerful class of networks is obtained by connecting many neuron elements. A number of neurons linked together in parallel are called a layer of neurons, and when several of these neuron layers are linked in series, a multi-layer neural network is created. The schematic model of a three-layer network is illustrated in Figure 3.3.

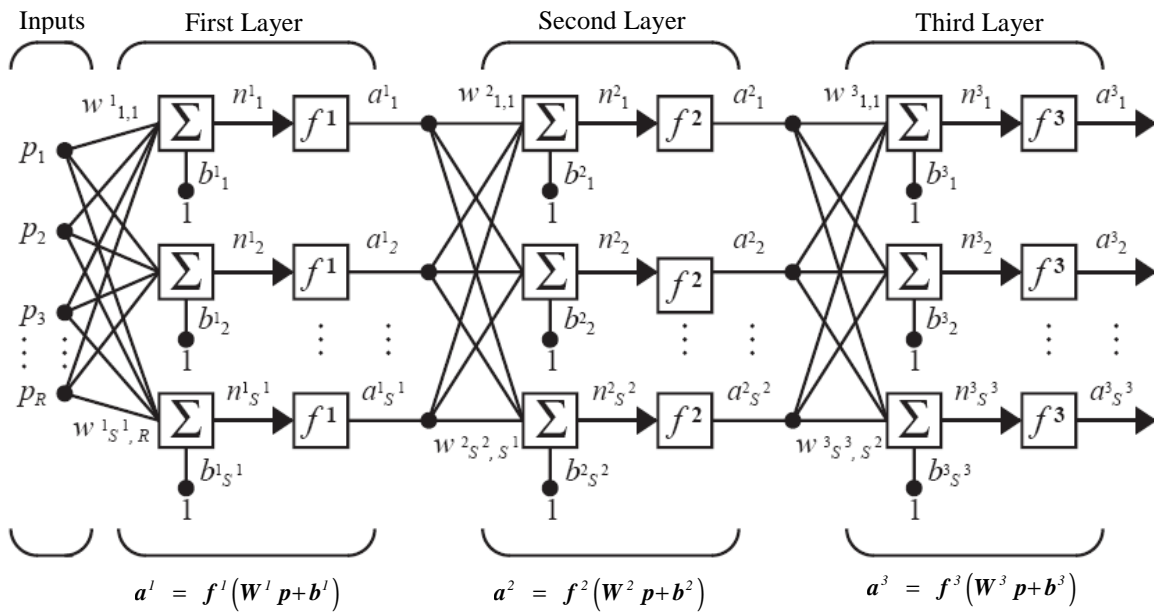


Figure 3.3 Model of a three-layer network (Hagan, Demuth & Beale 1996)

A multi-layer network typically consists of an input vector, a number of intermediate layers, termed hidden layers, and an output layer. Each neuron has a bias b_i , a summation function, a transfer function f and an output a_i . Neurons in each layer are connected to all the neurons in both the previous and the subsequent layer. The outputs of the first layer are the inputs for the second layer; the outputs of the second layer are then again the inputs for the third layer, and so on (Hagan, Demuth & Beale 1996). As the information in a multi-layer perceptron network moves in only one direction (forward) from the input nodes, through the hidden nodes to the output nodes, the type of network is called a feed-forward neural network, i.e. there are no loops in the architecture.

The Backpropagation Algorithm

The development of a powerful learning algorithm for the feed-forward multi-layer perceptron network, however, turned out to be problematic. During the 1960's and 1970's, neural computing suffered fierce criticism from proponents of the field of Artificial Intelligence, and in particular from the book 'Perceptrons' by Minsky and Papert (Minsky & Papert 1969). Their criticism focused on a class of problems called linearly non-separable, which could not be solved by any of the then-available training algorithms. In the early 1980's, however, a dramatic resurgence of interest in neural networks began with the discovery of learning algorithms based on error backpropagation, which was popularised by the book 'Parallel Distribution Processing' by Rumelhart et. al (Rumelhart, Hinton & Williams 1986). With the backpropagation algorithm the solving of linearly non-separable pattern classification problems was finally possible (Bishop 1994). The main objective of the backpropagation algorithm is to optimise the weight and bias parameters of a network in order to minimise a specified error function. This is achieved by determining the errors for the neurons of the hidden layer by back-propagating the errors of the neurons of the output layer. A brief description of the general backpropagation algorithm is presented below.

The backpropagation algorithm falls into the class of supervised learning, where a learning algorithm is trained on examples of desired behaviour. In a backpropagation multi-layer network, the outputs of one layer become the input to the subsequent layer following equation

$$\mathbf{a}^{m+1} = \mathbf{f}^{m+1}(\mathbf{W}^{m+1} \mathbf{a}^m + \mathbf{b}^{m+1}) \quad (3.8)$$

for $m = 0, 2 \dots, M-1$, with M being the number of layers. The neurons in the first layer receive external inputs ($\mathbf{a}^0 = \mathbf{p}$), and the outputs of the neurons in the last layer (the output layer) are the network outputs ($\mathbf{a} = \mathbf{a}^M$). The backpropagation algorithm is provided with a set of example data:

$$\{\mathbf{p}_1, \mathbf{t}_1\}, \{\mathbf{p}_2, \mathbf{t}_2\}, \dots, \{\mathbf{p}_Q, \mathbf{t}_Q\} \quad (3.9)$$

where \mathbf{p}_q is an input to the network and \mathbf{t}_q is the corresponding target value. As each input is applied to the network, the network output is calculated and compared to the

target. The algorithm then adjusts the network's weight and bias parameters, \mathbf{w} and \mathbf{b} , in order to minimise an error function. Here, the mean square error function is employed:

$$F(\mathbf{x}) = E \left[(\mathbf{t} - \mathbf{a})^2 \right] = E \left[(\mathbf{e})^2 \right] \quad (3.10)$$

with

$$\mathbf{x} = \begin{bmatrix} \mathbf{W} \\ \mathbf{b} \end{bmatrix} \quad (3.11)$$

where \mathbf{W} is the weight matrix and \mathbf{b} the bias vector of the network. If the network has multiple outputs, equation (3.10) can be generalised to

$$F(\mathbf{x}) = E \left[(\mathbf{t} - \mathbf{a})^T (\mathbf{t} - \mathbf{a}) \right] = E \left[\mathbf{e}^T \mathbf{e} \right] \quad (3.12)$$

The mean square error can be approximated by

$$\hat{F}(\mathbf{x}) = (\mathbf{t}(\mathbf{k}) - \mathbf{a}(\mathbf{k}))^T (\mathbf{t}(\mathbf{k}) - \mathbf{a}(\mathbf{k})) = \mathbf{e}^T(\mathbf{k}) \mathbf{e}(\mathbf{k}) \quad (3.13)$$

where the expectation of the squared error is replaced by the squared error at iteration k .

The propagation of one set of input/target vectors $\{\mathbf{p}_1, \mathbf{t}_1\}$ is called a cycle. The propagation of an entire set of training data $\{\mathbf{p}_1, \mathbf{t}_1\}, \{\mathbf{p}_2, \mathbf{t}_2\}, \dots, \{\mathbf{p}_Q, \mathbf{t}_Q\}$ is called an epoch. Training of a network may require hundreds or thousands of epochs for all of the training cases to be learned within a specified error tolerance.

3.3.3 Artificial Neural Network Design

A key issue in neural network applications is to determine the architecture of the networks. The design of a neural network comprises a series of steps. The following entities must be decided upon:

- Type of neural network (feed-forward neural network, radial basis function network, Kohonen self-organizing network, recurrent network, stochastic neural network, modular neural network, etc.)
- Learning algorithm (backpropagation, perceptron learning rule, Widrow-Hoff learning rule, etc.)
- Number of layers and neurons

- Transfer function (hard limit, linear, logistic sigmoid, tangent sigmoid, hyperbolic tangent sigmoid, etc.)
- Convergence algorithms (Levenberg-Marquardt, Quasi-Newton, conjugate gradient descent, quick propagation, online backpropagation, steepest descent algorithm, etc.)

For this study, feed-forward multi-layer neural networks based on backpropagation are used as they are the most widely and successfully applied networks in structural damage detection. Feed-forward networks are universal approximators, which are able to approximate any continuous multivariate function to any degree of accuracy (Funahashi 1989). The propagation of one set of input/target vectors $\{p_1, t_1\}$ is called a cycle. The propagation of an entire set of training data $\{p_1, t_1\}, \{p_2, t_2\}, \dots, \{p_Q, t_Q\}$ is called an epoch. Training of a network may require hundreds or thousands of epochs for all of the training cases to be learned within a specified error tolerance.

Number of Hidden Layers and Neurons

The determination of the appropriate number of hidden layers and neurons is rather problematic as no standard rules are available. An optimum number is dependent on the complexity of the problem, the number of training cases, the amount of noise in the target, and the utilisation of overfitting regularisations. Using too few hidden units results in high training error and high generalisation error due to underfitting and high statistical bias. A network with too many hidden units tends to memorise the training cases, which leads to a low training error but a high generalisation error due to overfitting and high variance. Some general rules have been proposed by a number of researchers. Masters (1993) suggests the geometric pyramid rule, which states that, for many practical networks, the number of neurons follows a pyramid shape, with the number decreasing from the input toward the output. Kalmorogov and Lippmann propose that the number of hidden neurons be calculated as $2N+1$, where N is the number of input neurons (Maren, Jones & Franklin 1990). According to Sarle (1995), if early stopping is used, it is essential to use many hidden units to avoid bad local optima. Other researchers suggest the use of the trial and error principle to obtain the best suitable number of hidden layers and neurons for a given problem. In this study, the networks are designed following the geometric pyramid rule with a large number of hidden neurons and overfitting regulations.

Transfer Function

The transfer function is another component that needs to be specified. A selection of typical transfer functions is shown in **Error! Reference source not found.**

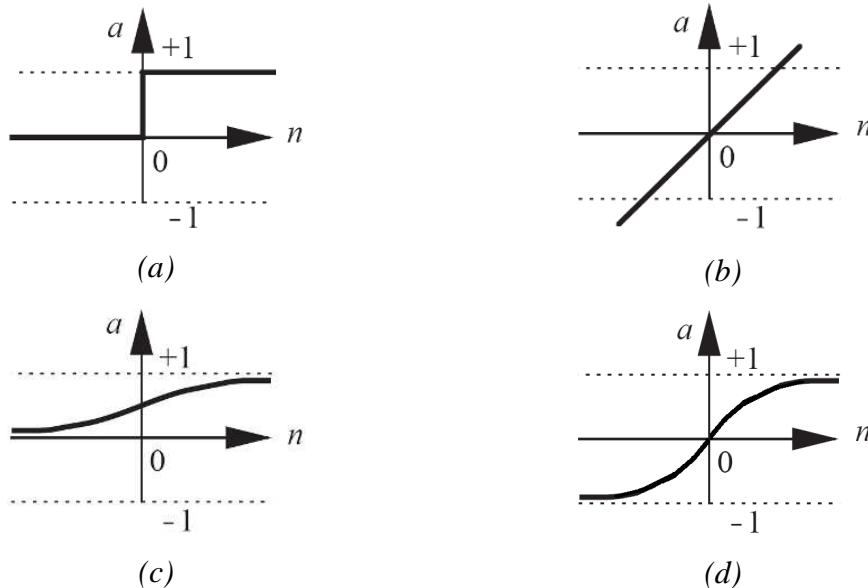


Figure 3.4 Transfer functions: (a) hard limit transfer function, (b) linear transfer function, (c) logistic sigmoid transfer function and (d) hyperbolic tangent sigmoid function (Hagan, Demuth & Beale 1996)

The hard limit transfer function (**Error! Reference source not found.** (a)) sets the output of the neuron to 0 if the function argument is less than 0, or 1 if its argument is greater than or equal to 0. This function is used to classify inputs into two distinct categories. The linear transfer function shown in **Error! Reference source not found.** (b) produces outputs identical to the inputs; in other words, it just passes the activation level directly as the output. The logistic sigmoid transfer function (**Error! Reference source not found.** (c)) converts the input, which may have any value between plus and minus infinity, into outputs ranging from 0 to 1, according to:

$$a = \frac{1}{1 + e^{-n}} \quad (3.14)$$

The hyperbolic tangent sigmoid function, which is plotted in **Error! Reference source not found.** (d), is very similar to the logistic sigmoid transfer function, with its output ranging from -1 to +1 rather than from 0 to 1. This function is defined as:

$$a = \tanh(n) = \frac{(e^n - e^{-n})}{(e^n + e^{-n})} \quad (3.15)$$

Most networks of practical interest make use of sigmoidal transfer functions (logistic sigmoid or hyperbolic tangent sigmoid). Empirically it is often found that the hyperbolic tangent sigmoid transfer function gives rise to faster convergence of training algorithms than the logistic sigmoid function (Bishop 1994). In this study, networks are designed with the hyperbolic tangent sigmoid transfer function for all hidden layers and the output layer. As the hyperbolic tangent sigmoid transfer function operates in the range of -1 to 1, all input and output data are normalised between the interval of [-1, 1] according to the equation

$$x_n = \frac{2(x - x_{min})}{x_{max} - x_{min}} - 1 \quad (3.16)$$

where x_n is the normalised input/output value, x is the actual input/output value, x_{min} is the minimum actual value of the input/output matrix and x_{max} is the maximum actual value of the input/output matrix.

Convergence Algorithm

The selection of an appropriate convergence function is similarly problematic. Again, many factors influence the choice of an adequate convergence function, such as the complexity of the problem, the size of the training set, the number of parameters in the network, the error goal, and the type of problem (function approximation or pattern recognition). Further, different convergence functions vary in terms of convergence performance, memory requirements, training efficiency and convergence speed. Many studies comparing different convergence functions have been undertaken (Demuth & Beale 2002; Fang, Luo & Tang 2005; Hagan & Menhaj 1994). Due to the high dependence of the performance of the convergence function on the actual problem, in this study, three types of convergence algorithms are employed; the quick propagation function, the conjugate gradient descent function and the online backpropagation function. Each network is trained with each of the three convergence functions, and then the best one is selected by comparing their performance.

Generalisation/Overfitting

A crucial element for neural network training is generalisation, which is the capability of a network to reproduce correct output values for the training samples while also delivering reasonable outputs for new data that have not yet been presented to the network. Overfitting is a well-known phenomenon in which a learning algorithm fits the parameters of a network too close to the training set and thereby drives the training error to a very small value. An overfitted network memorises the training examples, but it has not learnt to generalise for new situations, so that when new data is presented to the network the error is large (Xu 2005).

To avoid overfitting during training and to increase the generalisation capability of the network, several methods have been proposed by researchers, such as pruning (Hassibi & Stork 1993), regularisation methods (Krogh & Hertz 1995) and the early stopping method (Prechelt 1995). All networks in this study use the early stopping method during training. Here, the input sets of the networks are divided into three sets: a training, a validation and a testing set. While the network adjusts its weight from the training samples, its performance is supervised utilising the validation set to avoid overfitting. The network training stops when the error of the validation set increases while the error of the training set continues to decrease, which is the point at which the generalisation ability of the network is lost and overfitting occurs.

3.3.4 Neural Network Ensemble

Biological studies have shown that the human brain functions not as a single massive network, but as a collection of small networks that are dedicated to different subtasks and work together to accomplish complex nervous system tasks. This realisation gave birth to the concept of neural network ensembles (also referred to as committees, classifier ensembles or modular networks), in which several small networks cooperate or compete to solve problems. Hansen and Salamon (1990) were the first researchers to form the idea of the neural network ensemble, which is a learning paradigm wherein several ANNs are trained simultaneously and independently for the same task (Sollich

& Krogh 1996). Since 1990 this technology has become a hot topic in both the neural networks and machine learning communities (Sharkey 1996), and has already been successfully applied to areas such as face recognition, optical character recognition, scientific image analysis, medical diagnosis, seismic classification and financial trend prediction. In a neural network ensemble, each network is first trained individually, then the outputs of each of the networks a_e ($e = 1, 2 \dots n$) are fused to produce the ensemble output a . A model of a two-stage neural network ensemble is shown in Figure 3.5.

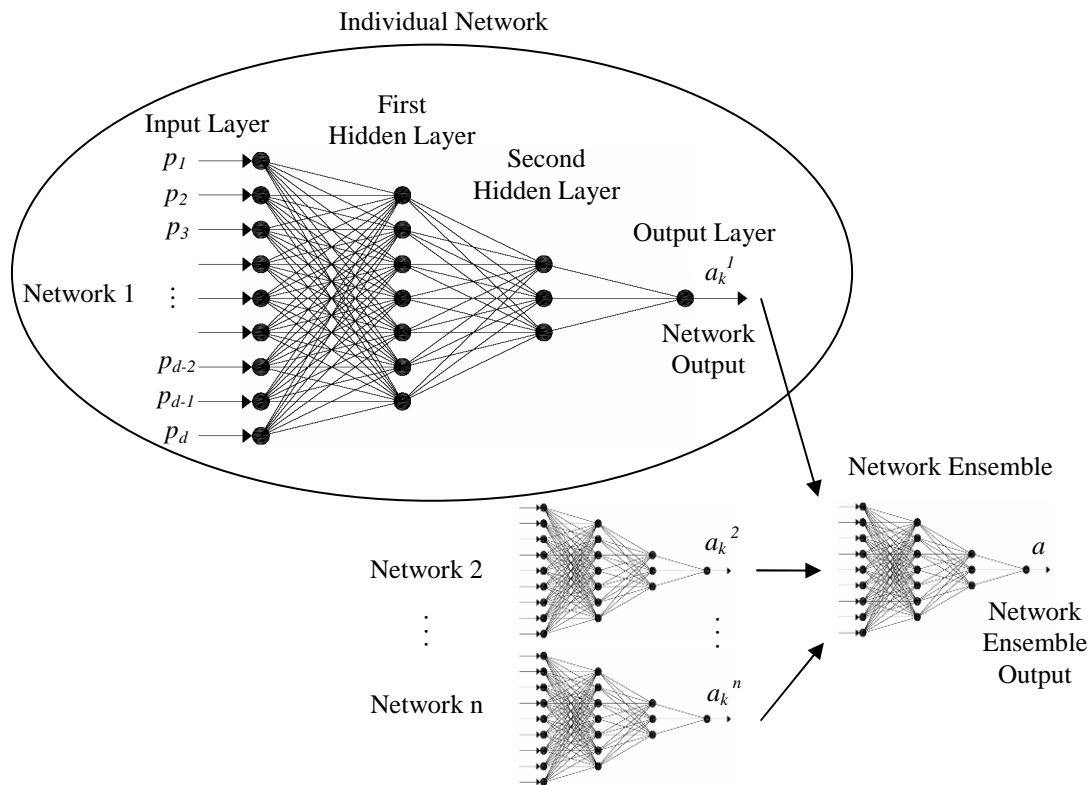


Figure 3.5 A two-stage neural network ensemble.

Hansen and Salamon showed that the generalisation ability of a neural network system can be significantly improved through ensembling a number of neural networks and then combining their predictions (Zhou, Wu & Tang 2002). As each network makes generalisation errors on different subsets of the input space, the collective decision produced by the ensemble is less likely to be faulty than the decision made by any of the individual networks (Ying, Jun & Xuezhi 2005). Further, as processing in a network ensemble is divided into separate, smaller subtasks, the computational effort is generally greatly reduced (Kosslyn 1994). A neural network ensemble can learn a set of functional mappings faster than a corresponding global monolithic neural network because each individual network only has to learn a (possibly simpler) part of the

overall functional mapping. Also, network ensembles have an inherent capability of decomposing separable tasks into a set of simpler tasks, thus enhancing the network's learning ability and reducing the learning time (Azom 2000).

In 1995, Krogh and Vedelsby (1995) derived the formulation for ensemble error in the case of regression using a linearly weighted ensemble. The researchers showed that the ensemble error can be divided into a term measuring the average generalisation error of each individual network and a term called diversity (or ambiguity) that measures the disagreement among the individual networks. For an ensemble consisting of n networks, the output of network r on input x is called $a^r(x)$. The weighted ensemble average (being the final output of the ensemble) is denoted by

$$\bar{a}(x) = \sum_r w_r a^r(x) \quad (3.17)$$

The diversity term d^r of network r on input x is then defined as

$$d^r(x) = [a^r(x) - \bar{a}(x)]^2 \quad (3.18)$$

The quadratic error of network r , ε^r , and of the ensemble, e , are, respectively

$$\varepsilon^r(x) = [a^r(x) - f(x)]^2 \quad (3.19)$$

and

$$e(x) \equiv [\bar{a}(x) - f(x)]^2 \quad (3.20)$$

where $f(x)$ is the target value for input x . Defining the averages over the input distribution of d^r , ε^r and e as D^r , E^r and E respectively, then the ensemble's generalisation error can be shown to consist of two distinct portions:

$$E = \bar{E} - \bar{D} \quad (3.21)$$

where $\bar{E} \left(= \sum_r w_r E^r \right)$ is the weighted average of the individual networks'

generalisation error and $\bar{D} \left(= \sum_r w_r D^r \right)$ is the weighted average of the diversity

among these networks, which is a nonnegative value. This equation shows that an ideal ensemble consist of highly correct networks that disagree as much as possible, and the

generalisation error of the ensemble is always smaller than the average of the individual errors, that is

$$E < \bar{E} \quad (3.22)$$

In general, the individual networks in a network ensemble exhibit the following characteristics (Azom 2000):

- The individual networks are domain specific and have specialised computational architectures to recognise and respond to certain subsets of the overall task.
- Each individual network is typically independent of other networks in its functioning and does not influence or become influenced by other modules.
- The individual networks generally have a simpler architecture as compared to the system as a whole. Thus, a single network can respond to a given input faster than can a complex monolithic system.
- The responses of the individual networks are simple and have to be combined by some integrating mechanism to generate the complex overall system response.

Design of a Neural Network Ensemble

A neural network ensemble is designed in two steps. First a number of individual networks must be created, and then the networks' predictions must be combined according to certain rules (Ying, Jun & Xuezhi 2005).

Design of the Individual Neural Networks

Combining the output of several networks is only useful if there is disagreement on some inputs. Combining several identical networks clearly produces no benefit. Theoretical and empirical work shows that an effective ensemble should consist of a set of individual networks that are not only highly correct, but also make their errors on different parts of the input space (Hansen & Salamon 1990; Krogh & Vedelsby 1995). The individual networks can be designed in three different ways.

- Networks can be designed differently by varying the network type (such as multi-layer perceptron networks or radial basis function networks), number of hidden layers and neurons, learning algorithm, transfer functions or initial random weights.

- Networks can be trained with different training sets. These can, for example, be obtained by randomly splitting the data set, or by using learning sets extracted from different data sources (e.g. sensor).
- Networks can be both, individually designed and trained with different training sets.

The last method was evaluated experimentally by Partridge (1996), who concluded that varying the network type and the training data are the two best ways for creating individual networks that make different errors.

Combination of Neural Outputs

When a network ensemble is applied to a classification problem, voting is usually used to combine the network outputs. Hansen and Salamon (1990) proved that if the average error rate for a certain problem is less than 50% and the networks in the ensemble are independent in the production of their errors, the expected error for that problem can be reduced to zero as the number of combined networks approaches infinity. However, this theory rarely holds in practice as the networks are generally not independent. When a network ensemble is applied to a regression problem, either simple or weighted averaging is used. Opitz and Shavlik (1996) found that simple averaging outperforms weighted averaging, since optimising the combining weights can easily lead to overfitting problems. Perrone and Cooper (1993) proposed that weighted averaging performs better as each network can avoid overfitting by using cross-validation. Sollich and Krogh (1996) concluded that in large network ensembles, simple averaging should be used. In this way, a global optimal generalisation error on the basis of all available data can be reached by optimising the training set sizes of the individual networks. For ensembles of a more realistic size, optimising the ensemble weights can still yield substantially better generalisation performance than an optimally chosen single network trained with all data with the same amount of training noise.

Training the network ensemble

As for training the neural network ensemble, the most common methods are bagging, boosting and cross-validation. Bagging was proposed by Breiman (1996) and is based on bootstrap sampling (Efron & Tibshirani 1993). First, several training sets are generated from the original training set, and then an ensemble neural network is trained from each of those training sets. In boosting, proposed by Schapire (1990), the training

sets of the single networks are determined by the performance of former networks. Training variables that are wrongly predicted by previous networks will play more important roles in the training of later networks (Zhou, Wu & Tang 2002). In cross-validation, only a portion of the dataset is used to train the networks, and the rest of the set is used to assess the capacity of the networks' generalisation ability.

3.4 PRINCIPAL COMPONENT ANALYSIS

Principal Component Analysis (PCA), also known as Karhunen-Loève transform, Hotelling transform or proper orthogonal decomposition, was developed by Pearson (1901) and is one of the most powerful statistical multivariate data analysis techniques for achieving dimensionality reduction. Hotelling (1933) proposed this technique for the purpose of analysing the correlation structure between random variables. In general, PCA linearly transforms an original set of k variables into a smaller set of n ($n \leq k$) uncorrelated variables, the so-called principal components (PCs). Eigenvalue decomposition of the covariance matrix forms the basis of PCA. The direction of the resulting eigenvectors represents the direction of the PCs, which are weighted according to the value of the corresponding eigenvalues. Each PC is a linear combination of the original variables. All PCs are orthogonal to each other and form an orthogonal basis for the space of the data. The full set of PCs is equal to the original set of the variables. By removing PCs of low power, a dimensional reduction is achieved with minimum loss of information (White, Tan & Hammond 2006). Besides the benefit of data reduction, PCA is also a powerful tool for minimising unwanted measurement noise. As noise exhibits in a random pattern, which is not correlated with a global characteristic of the data set, it is represented by less significant PCs. Therefore, by disregarding PCs of low power, measurement noise is filtered out. Today, PCA is used for data compression, feature extraction, noise reduction and data pre-processing in a variety of fields, such as image processing, flow visualisation, pattern recognition, time-series prediction and structural dynamics.

Geometrically, PCA can be considered as a rotation of the axes of the original variable coordinate system to new orthogonal axes, called 'principal axes', such that the new axes coincide with the directions of maximum variation of the original observations. An example is depicted in Figure 3.6.

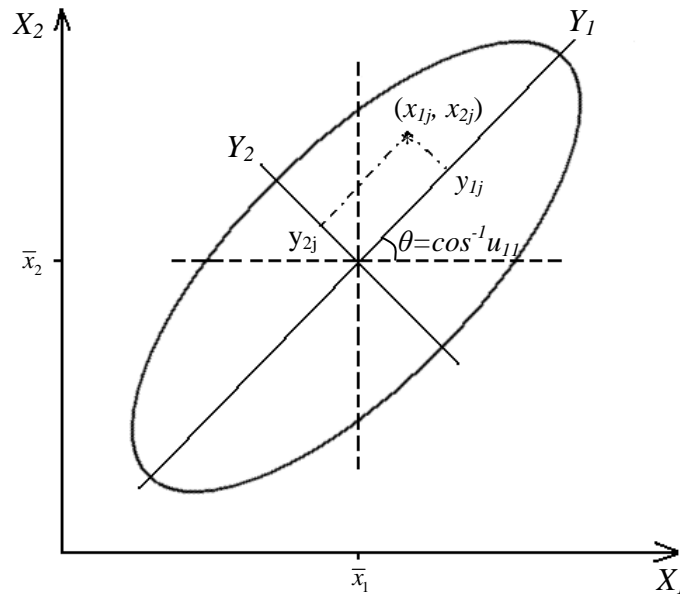


Figure 3.6 Geometrical description of principal components.

In the example, Y_1 and Y_2 are the principal axes; the points y_{1j} and y_{2j} give the PC scores for the observation $x_{1j} = (x_{1j}, x_{2j})$; the cosine of the angle θ between Y_1 and X_1 gives the first component of the eigenvector corresponding to Y_1 . The point y_{1j} is the projection of the point $x = (x_{1j}, x_{2j})$ onto the axis defined by the direction Y_1 . This axis has the property that the variance of the projected points y_{1j} , with $j = 1, 2, \dots, k$ is greater than the variance of the points when projected onto any other line or axis passing through (\bar{x}_1, \bar{x}_2) . The point y_{2j} is the projection of the point $x = (x_{1j}, x_{2j})$ onto the axis defined by the direction Y_2 , orthogonal to Y_1 .

Following is a description of the derivation of PCA. Given is the data set \mathbf{X}_{ij} with $(i = 1, 2, \dots, m)$ and $(j = 1, 2, \dots, k)$, where m is the total number of observations and k the dimension (variables) of the observations (i.e. the number of observed variables). First, the mean \bar{x}_j and the standard derivation s_j of the j^{th} column is obtained from

$$\bar{x}_j = \frac{1}{m} \sum_{i=1}^m x_{ij} \quad (3.23)$$

and

$$s_j = \sqrt{\frac{\sum_{i=1}^m (x_{ij} - \bar{x}_j)^2}{m}} \quad (3.24)$$

Then, the data set \mathbf{X} is transformed into the standard normal space, yielding the variation matrix $\tilde{\mathbf{X}}$. A normalised element \tilde{x}_{ij} is given by

$$\tilde{x}_{ij} = \frac{x_{ij} - \tilde{x}_j}{s_j} \quad (3.25)$$

The covariance matrix \mathbf{C} is expressed as

$$\mathbf{C} = \frac{\tilde{\mathbf{X}}^T \tilde{\mathbf{X}}}{m-1} \quad (3.26)$$

Finally, the PCs are obtained from

$$\mathbf{C} \mathbf{p}_i = \lambda_i \mathbf{p}_i \quad (3.27)$$

which is the eigenvalue decomposition of the covariance matrix \mathbf{C} , with λ_i being the i^{th} eigenvalue and \mathbf{p}_i the corresponding eigenvector. If the eigenvalues are sorted in descending order ($\lambda_1 \geq \lambda_2 \geq \dots \geq \lambda_n$), their corresponding eigenvectors, $(\mathbf{p}_1, \mathbf{p}_2, \dots, \mathbf{p}_n)$, are the PCs. In general, $\lambda_i / \sum \lambda_i$ gives the relative amount of variance that the i^{th} PC captures. The first PC, which is the largest eigenvalue and its associated eigenvector, represents the direction and amount of maximum variability in the original data set. The second PC, which is orthogonal to the first PC, represents the second most significant contribution from the data set, and so on. The most significant PCs represent the features that are most dominant in the data set. So by discarding components that contribute least to the overall variance, the dimension of the original data set can be reduced significantly (Zang & Imregun 2001b).

3.5 SUMMARY

This chapter presented fundamental information on ANNs and PCA. An overview was given on the biological neural network and the information processing in a single artificial neuron. The operation of multiple neurons of a multi-layer perceptron network was described and the backpropagation algorithm explained. Further, practical comments were given on the creation of efficient neural network designs. Lastly, basic information relating to PCA was presented.

CHAPTER 4

MODAL TESTING AND EXPERIMENTAL MODAL ANALYSIS

4.1 INTRODUCTION

Modal testing and experimental modal analysis (MT&EMA) is the process of characterising the dynamic properties of a test structure by exciting the structure artificially and identifying its modes of vibration (Ramsey 1982). When a structure is damaged, e.g. its geometrical properties change, its boundary conditions modify or its material properties alter, the dynamic characteristics of the structure change. These changes are the basis for the presented damage identification methods, and MT&EMA serves as a means to extract the dynamic properties for the given structures.

This chapter, firstly, describes the fundamentals of MT&EMA; secondly, introduces the two test structures (the simply supported steel beam and the two-storey framed structure) and describes the different damage/added mass scenarios; thirdly, explains the experimental set-up and testing; and finally, presents the extracted dynamic characteristics of the two baseline structures and their modifications.

4.2 FUNDAMENTALS OF MODAL TESTING AND EXPERIMENTAL MODAL ANALYSIS

In MT&EMA the dynamic characteristics of a structure are identified from its vibrational responses. While modal testing describes the performance of the testing and the acquisition of the modal data from the test structure, experimental modal analysis is the process of determining the modal parameters (natural frequencies, damping ratios and mode shapes) from the acquired data. Generally, MT&EMA can be divided into three major steps: signal processing, frequency response function (FRF) and modal parameter estimation.

4.2.1 Signal Processing

Signal processing deals with the analysis of electrical signals. One concern is the conversion of analogue signals into a corresponding sequence of digital values. The other concern is the transformation of the digital data from the time domain to the frequency domain by using the discrete Fourier transform algorithm. As the Fourier transform algorithm involves discrete data over a limited time period, digital signal processing errors such as leakage and aliasing may be introduced. Further, noise interferences due to electrical noise on the transducer signals (e.g. power supply noise, cabling motion, rattles) may also create errors. In signal processing, these errors are reduced as much as possible by using different techniques to obtain a better spectrum of results (Allemang 1999). The process of acquiring and converting physical quantities from analogue to digital electrical signals and from time to frequency domain is shown in Figure 4.1.

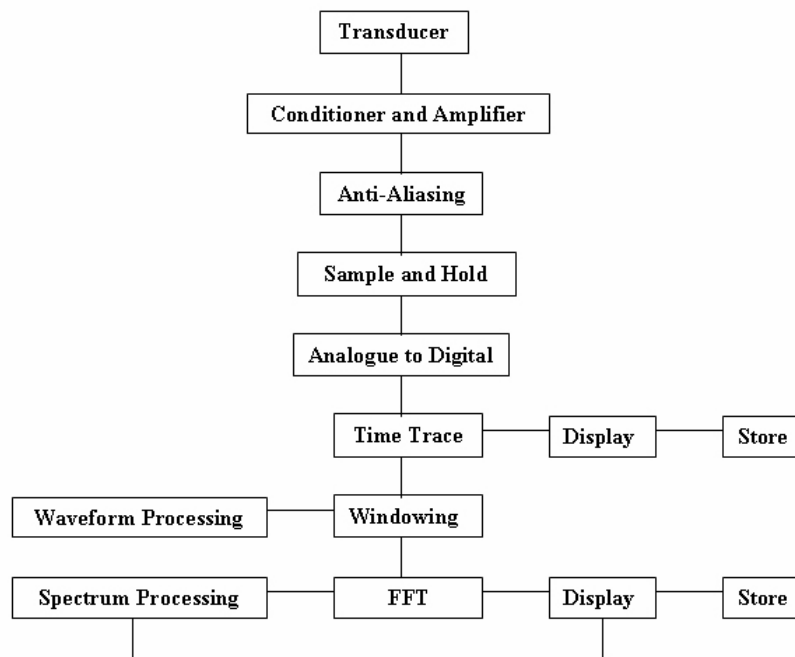


Figure 4.1 Digital signal processing (Abdul Rahman 1999).

When a structure is excited, its physical motion is captured by transducers. Transducers convert the physical motion to electrical signals. Common transducers for vibration measurement include piezoelectric accelerometers (or piezoresistive accelerometers) and force transducers in mechanical and structural applications. Piezoelectric sensors

are commonly comprised of materials such as quartz or ceramic. When a piezoelectric sensor experiences a change in load, such as compressive force, an electrical charge is generated, which is usually a function of frequency. Piezoelectric sensors can measure the generated charge by preloading the internal frictional forces. These types of sensors usually operate within a wide range of frequency. The electrical signals acquired by the transducers are analogue signals, which require conditioning and amplifying. A signal conditioner is used to condition the analogue signals from the transducer into voltage proportional to the measured physical quantities. Signal amplification increases the resolution of the input signal and increases its signal-to-noise ratio.

In signal processing, there are some pitfalls that might result in a loss of accuracy of the signal, such as aliasing and spectral leakage. Aliasing is a phenomenon that occurs when the sampling rate is less than twice the highest frequency in the data. It is a result of the inability of the Fourier transform to decide which frequencies are within and which ones are outside the analysis band (Allemang 1999). Aliasing produces a distorted representation of data, which could result in significant erroneous frequency interpretation in the vibration analysis. Aliasing also occurs when converting analogue (continuous) data to digital (discrete) data. Figure 4.2 gives an illustration of the aliasing phenomenon.

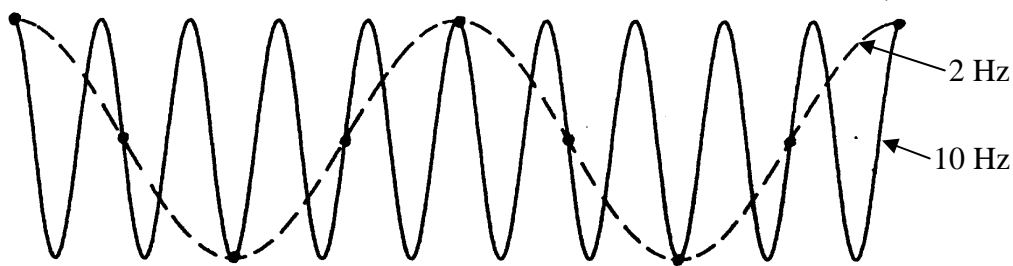


Figure 4.2 Aliasing phenomenon (Allemang 1999).

Aliasing can be minimised by using a sampling rate of at least twice the highest frequency present in the data, which is formulated by Shannon's Sampling Theorem:

$$F_{\text{Samp}} = \frac{1}{\Delta t} = F_{\text{Nyq}} \times 2 \quad (4.1)$$

$$F_{\text{Nyq}} \geq F_{\text{Max}} \quad (4.2)$$

The Nyquist frequency, F_{Nyq} , is the theoretical limit for the maximum frequency F_{Max} . Signals above F_{Nyq} will appear after being digitised as a frequency below F_{Nyq} . This serious error is controlled by using anti-aliasing or analogue filters, which are low-pass filters that automatically cut-off frequencies at or above half of the sampling frequency, F_{Samp} , (Allemang 1999).

An analogue-to-digital converter (ADC) converts the analogue input signal into a digital form. The acquired continuous signal is first sampled and then converted into a discrete-time series digital signal. The time interval between two samples is equal to the inverse of the sampling frequency. The resolution of digital signal samples is equal to 2^B , where B is the number of bits used in the ADC. For example, a 16-bit ADC will discretise the amplitude range of the signal to a resolution of 65536 grids.

After the digitising process, the continuous time signals are discretised into a sequence of values commonly known as discrete time series. A discrete time series has values that are defined only at discrete values of time. Discrete time signals, also known as signals in the time domain, usually consist of many frequency components that are superimposed. The conversion of a time signal into its various frequency components is, for example, performed by the fast Fourier transform (FFT). The FFT algorithm is given as:

$$x(k) = \sum_{j=0}^{N-1} X(j) W_N^{-jk} \quad (4.3)$$

which represents the discrete series $x(k)$ at the time instant k of a sampled data N , with $k = 0, 1, 2, \dots, N-1$ and $j = 0, 1, 2, \dots, N-1$ where $W_N = e^{-i2\pi/N}$. The concept of the discrete Fourier Transform is illustrated in Figure 4.3.

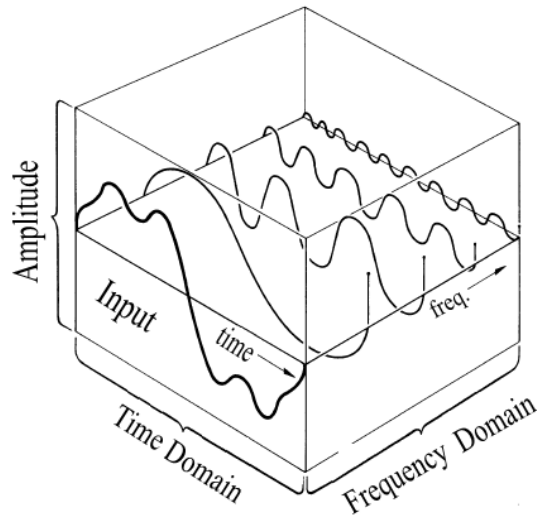


Figure 4.3 Discrete Fourier transform concept (Allemang 1999).

During the process of fast Fourier transform, some problems may occur, such as leakage. Leakage is the unwanted distortion caused by artificial truncation of sampled data (Maia et al. 1997). A common tool used to overcome the leakage problem is windowing. This function consists of a process of ‘weighting’ the original time history data to reduce the noise distortion and the effect of leakage. There are a few developed window functions, such as uniform, hamming, hanning, force and exponential windows. The latter two were used in this research and are briefly described below.

A force window is usually applied to the impact excitation to remove noise from the impulse signal. Ideally, the impulse signal is non-zero for the small time period of the excitation (e.g. hammer hit) and zero for the remaining time. Therefore, any non-zero data following the impulse signal is assumed to be noise and thus is considered to be zero, as illustrated in Figure 4.4 (a). Exponential windows are commonly used for response signals, to ensure that the transient signal decays sufficiently at the end of the sampling period, as depicted in Figure 4.4 (b). This decay is employed by introducing artificial damping into the measurement data. (Schwarz & Richardson 1999)

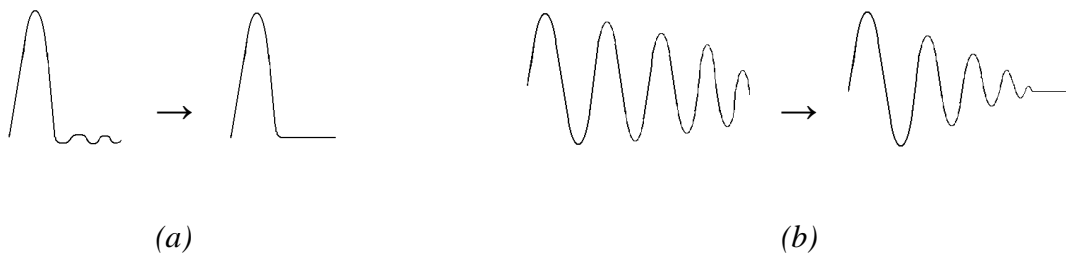


Figure 4.4 Windowing functions (a) force window and (b) exponential window.

4.2.2 Frequency Response Function

FRFs are widely used for dynamic system identification in many industries, including the automotive, machine tool and structural engineering industries. The general procedure for utilising FRFs for system identification is shown in Figure 4.5.

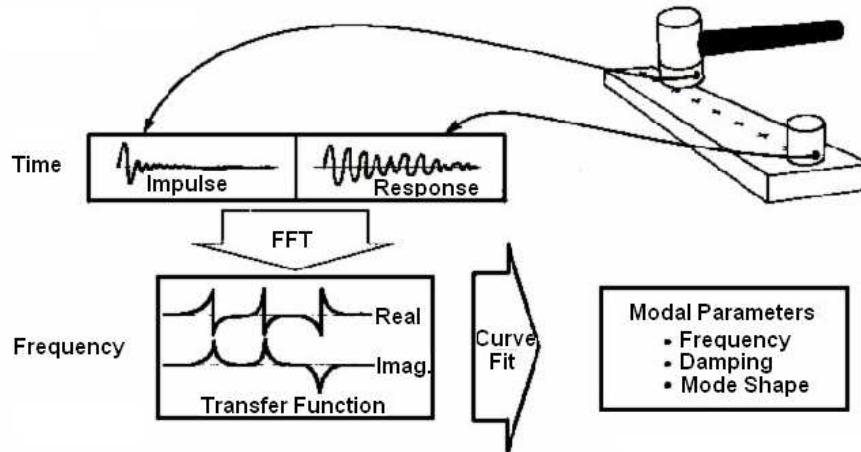


Figure 4.5 Transfer function method (AgilentTechnologies 2000)

FRFs are used to describe the input-output (force-response) relationship of a system. To obtain FRF data, transducers (e.g. accelerometers) record an electric output signal from the test structure, while the input signal is obtained from the source of excitation. For example, the input signal $f(\omega)$ with respect to frequency ω is the force applied to the structure (e.g. with a modal hammer) and the output signal $g(\omega)$ is the response motion signal obtained from the accelerometers attached to the system. The FRF ($H(\omega)$) for each point on a system is the ratio of the output to the input after Fourier transformation, as shown in equation (4.4).

$$H(\omega) = \frac{\text{output}}{\text{input}} = \frac{g(\omega)}{f(\omega)} \quad (4.4)$$

In real life testing, FRF data can be estimated from measured data by two methods. The first method normalises the cross input-output spectrum $G_{fg}(\omega)$ by the input auto-spectrum $G_{ff}(\omega)$, described as:

$$H_1(\omega) = \frac{G_{fg}(\omega)}{G_{ff}(\omega)} \quad (4.5)$$

where $G_{fg}(\omega) = f(\omega) \times g(\omega)$ is the cross spectrum, while $G_{ff}(\omega) = f(\omega) \times f(\omega)$ is the input auto-spectrum. And the second method normalises the auto spectrum of the output $G_{gg}(\omega)$ by the cross input-output spectrum $G_{fg}(\omega)$, defined as:

$$H_2(\omega) = \frac{G_{gg}(\omega)}{G_{fg}(\omega)} \quad (4.6)$$

where $G_{gg}(\omega) = g(\omega) \times g(\omega)$ is the output auto-spectrum.

FRF can be presented in rectangular coordinates (real part vs frequency, and imaginary part vs frequency) or in polar coordinates (amplitude vs frequency, and phase vs frequency). At resonance, in the rectangular presentation, the imaginary part is a maximum and the real part is zero. In the polar system, the magnitude reaches a maximum at resonance, while the phase lag approaches 90° . This is shown for a single-degree-of-freedom (SDOF) system in Figure 4.6. These characteristics enable the identification of the modal parameters of a structure from the FRF.

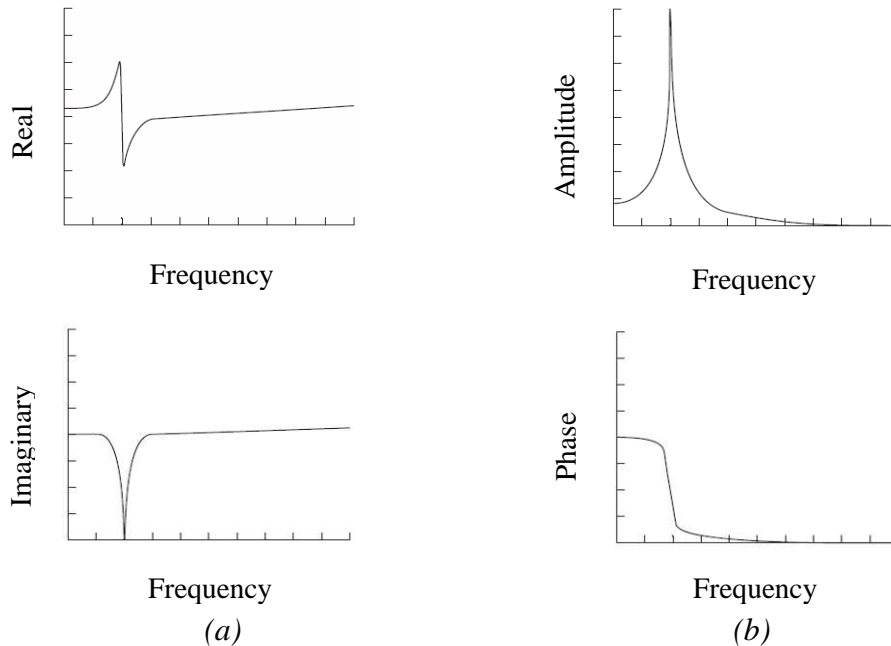


Figure 4.6 FRF graphs in (a) rectangular and (b) polar coordinates for a single-degree-of-freedom system.

4.2.3 Modal Parameter Estimation

In general, a systems modal parameters (natural frequencies, damping and mode shapes) can be estimated through three different approaches. In analytical systems, the modal parameters are determined from the system matrices by formulating the eigensolution of the system. In experimental modal analysis (EMA), the modal parameters are extracted either from the FRF in the frequency domain, or from the impulse response function (IRF) in the time domain. The three different methods of modal parameter estimation are illustrated in Figure 4.7.

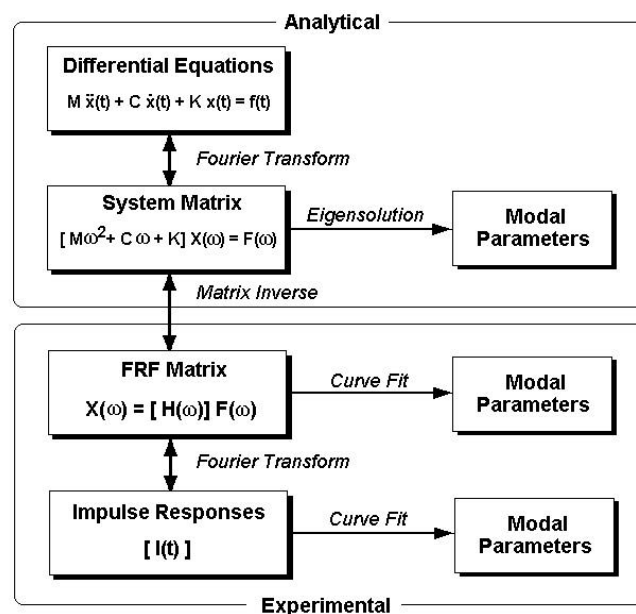


Figure 4.7 Modal parameter estimation methods (Schwarz & Richardson 1999).

In EMA, the modal parameters are mainly estimated in the frequency domain by means of FRFs and curve fitting techniques. Generally, curve fitting is a process of matching a mathematical model to a set of measured data points. This is done by minimising the squared error (or squared difference) between the analytical function and the measured input-output data. All curve fitting methods fall into one of four categories: local single degree of freedom (SDOF) method, local multiple degree of freedom (MDOF) method, global method and multi-reference (poly reference) method (listed in order of increasing complexity). SDOF methods estimate modal parameters one mode at a time, whereas MDOF, global and multi-reference methods can estimate modal parameters for two or more modes simultaneously (Schwarz & Richardson 1999).

In early applications of EMA, frequency domain modal parameter estimation was typically performed using simple local single-degree-of-freedom (SDOF) curve fitting methods. Such methods were able to extract all three modal parameters (frequency, damping and mode shape) directly from a set of FRF measurements.

Nowadays, most EMA methods are based on MDOF methods, which also use curve-fitting methods to determine the modal parameters. Many of these methods use numerical techniques that separate the contributions of individual modes of vibration in measured FRFs by estimating the individual SDOF contributions to the MDOF measurement. This concept is graphically illustrated in Figure 4.8.

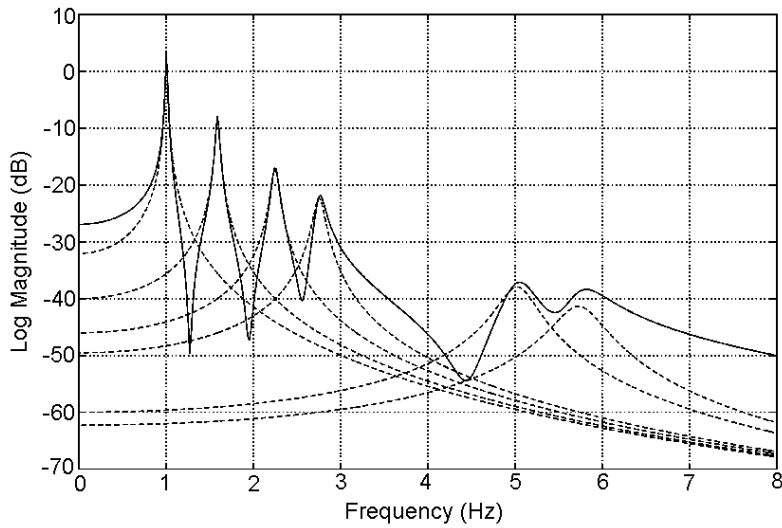


Figure 4.8 MDOF – SDOF Superposition (Allemang 1999).

A number of MDOF-based methods were developed over the past decades, such as the complex exponential, rational fraction polynomial, polyreference frequency domain and matrix decomposition methods. In this study, a method called frequency domain direct parameter identification (FDPI) is used to estimate the modal parameters. This technique is a MDOF method that is also capable of polyreference analysis. The principle of the FDPI method is briefly described as follows. Given is the equation of motion of a linear and time-invariant structure:

$$M \ddot{y}(t) + C \dot{y}(t) + K y(t) = f(t) \quad (4.7)$$

When transformed into the frequency domain, this equation can be reformulated in terms of measured FRFs:

$$\left[-\omega^2 I + j\omega A_1 + A_0 \right] \left[H(\omega) \right] = j\omega B_1 + B_0 \quad (4.8)$$

where ω = frequency variable, $A_0 = M^{-1}K$ (the mass modified stiffness matrix), $A_1 = M^{-1}C$ (the mass modified damping matrix), $H(\omega)$ = matrix of FRF's, and B_0, B_1 are the force distribution matrices. When equation (4.8) is assembled for all available FRFs the unknown matrix coefficients A_0, A_1, B_0 and B_1 can be estimated from $H(\omega)$. Hence, measurement data $H(\omega)$ can be described by a second order linear model with constant matrix coefficients. For the identified matrices, the system's poles (natural frequencies) and mode shapes can be estimated via an eigenvalue and eigenvector decomposition of the system matrix.

$$\begin{bmatrix} -A_1 & -A_0 \\ I & 0 \end{bmatrix} \quad (4.9)$$

This will yield the diagonal matrix $[A]$ of poles and a matrix Ψ of eigenvectors. In the final step, the modal participation factors are estimated from another least squares problem, using the obtained $[A]$ and Ψ matrices (CADA-X 1996).

4.3 EXPERIMENTAL SET UP AND TESTING OF LABORATORY BEAMS

4.3.1 The Test Beams

In this study, the first structure to be investigated experimentally was the pin-pin supported steel beam. A photo of the beam and its test set up is depicted in Figure 4.9. In total four identical beams were tested to study single damage cases at four different locations. The dimensions of the beams were 12 mm by 32 mm by 2,400 mm. According to the manufacturer's specifications the modulus of elasticity was $200,000 \times 10^6 \text{ N/m}^2$, the Poisson's ratio was 0.3 and the density was $7,850 \text{ kg/m}^3$. A specially designed support system was used to connect the beams with the concrete supports to provide well-defined boundary conditions, which are very close to a pin-pin connection.

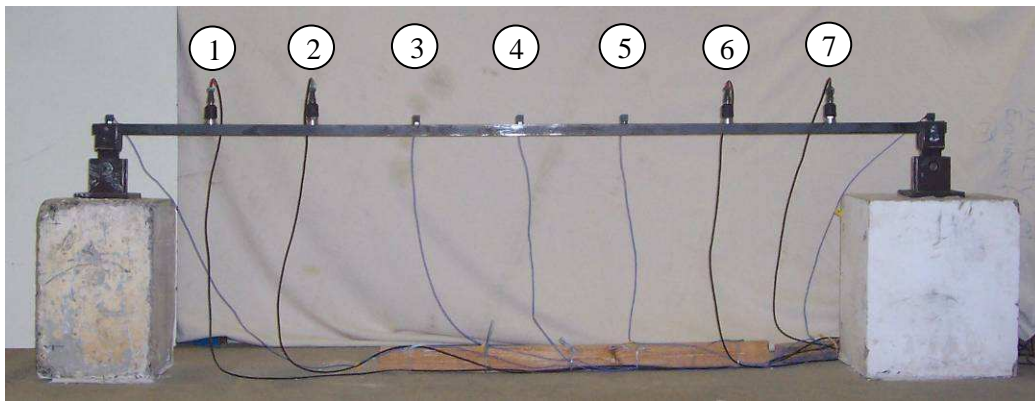


Figure 4.9 Experimental test set up.

To study damage scenarios at different locations and of various intensities, a total of 16 single damage cases were investigated. These relate to damage at four different locations each having four levels of severity. The four damage locations were at $4/8^{\text{th}}$, $5/8^{\text{th}}$, $6/8^{\text{th}}$ and $7/8^{\text{th}}$ of the span length and are referred to in the following as '4', '5', '6' and '7' (as shown in Figure 4.9). (Only these four locations were studied as the beam structure is symmetric and no additional information is gained by investigating damage cases across the entire length of the beam.) The four damage severities, termed as extra light (XL), light (L), medium (M) and severe (S), are of notch type with 1 mm notch width and lengths of 1 mm, 4 mm, 8 mm and 12 mm, respectively. These damage extents correspond to a cross-section loss of the second moment of area, I , of 9.09%, 33.01%, 57.81% and 75.59%, respectively. Damage was gradually inflicted by a saw

cut from the soffit of the beam. The four damage severities are depicted in Figure 4.10. All damage cases are listed in Table 4.1.

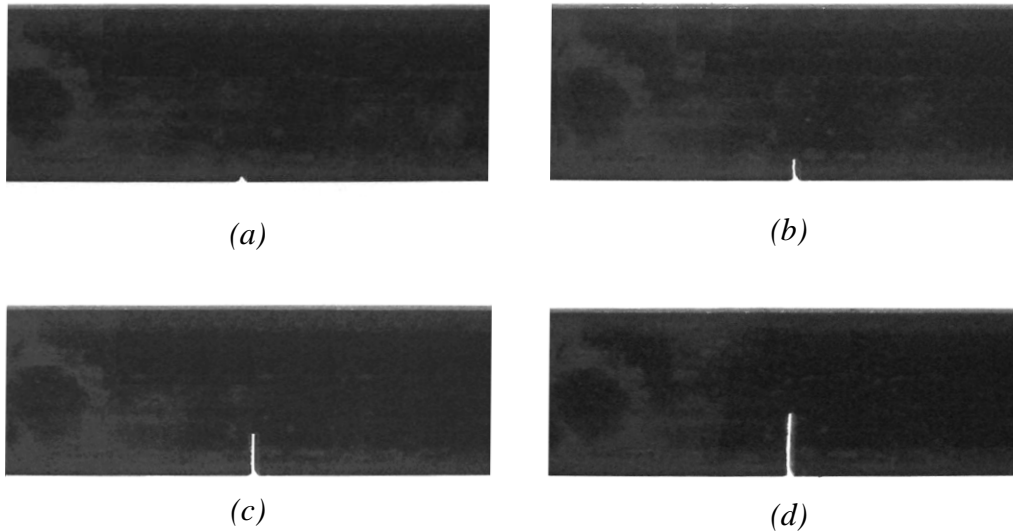


Figure 4.10 Experimental damage (a) 1 mm, (b) 4 mm, (c) 8 mm and (d) 12 mm cut.

Table 4.1 Experimental damage cases.

	Damage Cases			
Beam 1	4XL	4L	4M	4S
Beam 2	5XL	5L	5M	5S
Beam 3	6XL	6L	6M	6S
Beam 4	7XL	7L	7M	7S

Note: 4XL = damage at location '4' ($4/8^{\text{th}}$ of the span length) with damage severity 'XL'.

4.3.2 Modal Test Set Up

To identify the dynamic properties of the steel beams, MT&EMA was performed. In modal testing, the beams were excited by a modally tuned impact hammer at a certain reference point and the responses of the beams were measured by accelerometers. In experimental modal analysis, the converted signals from the hammer and the accelerometers were analysed and the modal parameters of the beams were determined. Each of the four test beams was tested in its undamaged state and in each of the four damage states. The set up of the MT&EMA is shown in Figure 4.11.

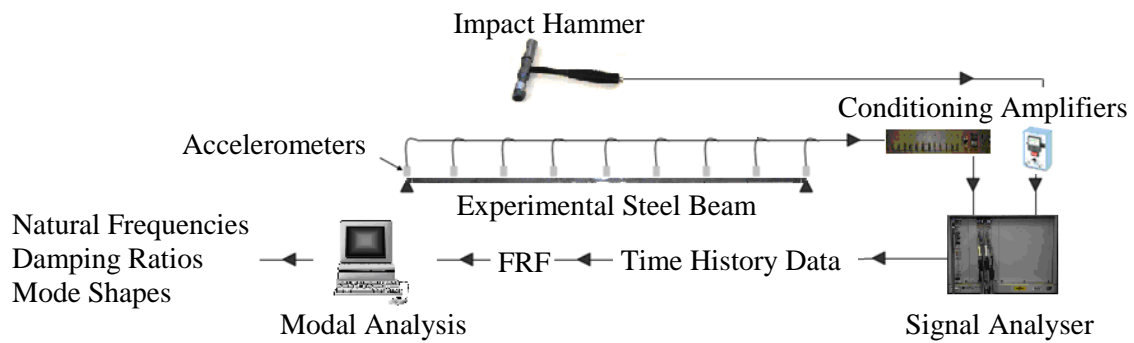


Figure 4.11 Schematic diagram of MT&EMA.

The impact hammer used to excite the beams was a PCB model HP 086C05, which is shown in Figure 4.13 (a). The reference point was situated at location ‘3’ (see Figure 4.9). This position was chosen for the following reasons:

- None of the first seven flexural mode shapes has a node point at location ‘3’. (If a node point of a mode is located at the reference point then this mode is not excited and hence cannot be identified; e.g. locations ‘2’, ‘4’ and ‘6’ have node points of modes ‘2’, ‘4’ and ‘6’. The mode shapes of the first seven flexural modes and their node points along the beam length are illustrated in Figure 4.12.)
- Location ‘3’ was chosen over location ‘1’ as it is farther away from the supports, and thereby, provided better excitation and less interference from the supports.

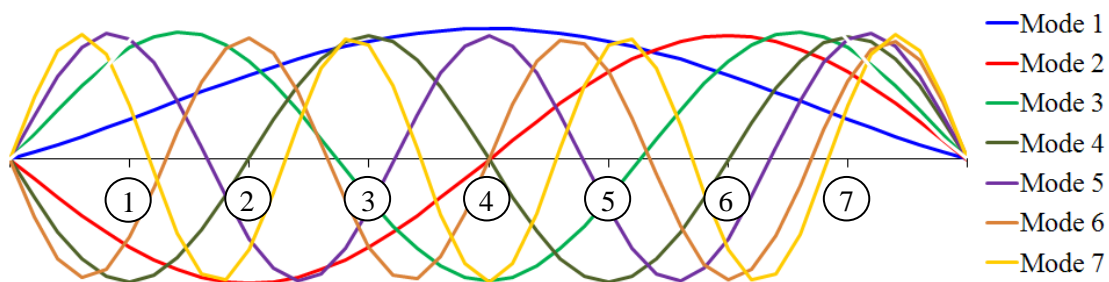


Figure 4.12 The first seven flexural mode shapes and their node points.

The beams’ responses were measured by nine equally spaced low impedance piezoelectric accelerometers, which were mounted on the top surface of the beams. The accelerometers were PCB model 356A08 and model 337A26 (shown in Figure 4.13 (b) and (c)), having a sensitivity range from 94 mV/g to 100 mV/g. The accelerometers were located at each end of the beam (in line with the supports) and at the locations ‘1’ to ‘7’. The time history signals of the impact hammer and the accelerometers were amplified and conditioned by signal conditioners. For the input signal of the hammer a

battery powered signal conditioner (PCB model 480E06, depicted in Figure 4.13 (d)) was used and the response signals were processed using a multi-channel signal conditioner (PCB model 483B03 as illustrated in Figure 4.13 (e)).

The main data acquisition system consisted of a Hewlett Packard state-of-the-art dynamic analyser (model E1432A) Vxi system equipped with two HP Vxi 16 channel 51.2 kHz digitisers with anti-aliasing filter and a digital signal processor in a C-sized frame (see Figure 4.13 (f)). The data acquisition system was connected to a personal computer equipped with the LMS CADA-X signal acquisition and post-processing software for experimental modal analysis.

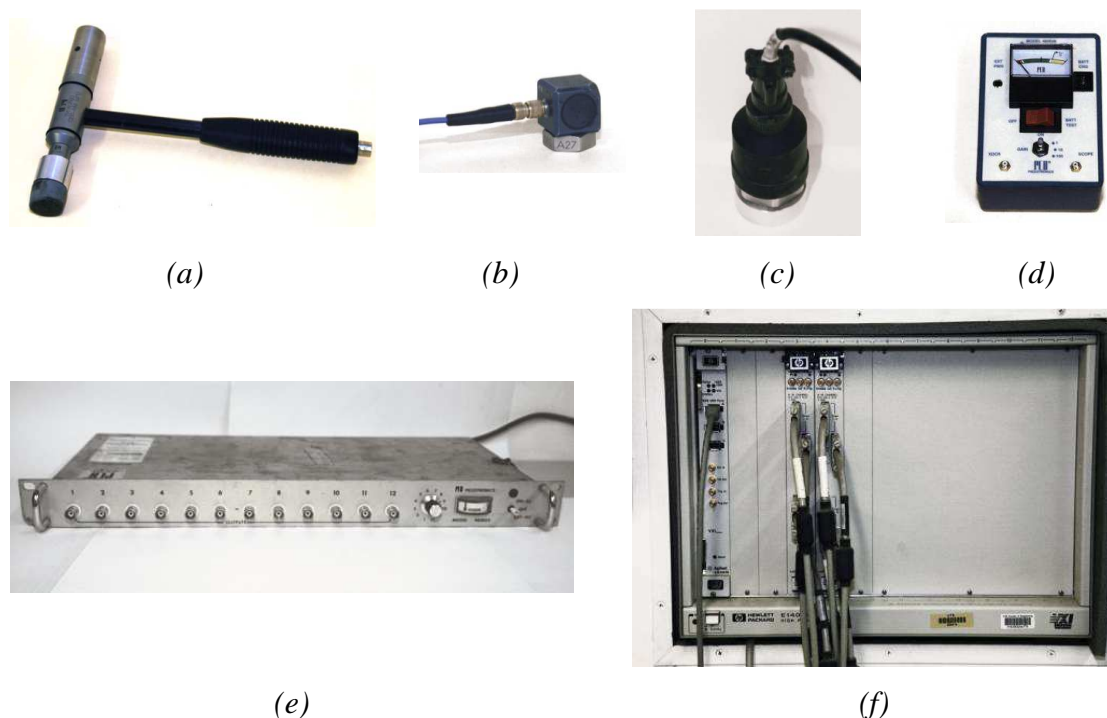


Figure 4.13 Test equipment (a) Modal hammer, (b) accelerometer model PCB 356A08, (c) accelerometer model PCB 337A26 (d) battery powered signal conditioner (e) multi-channel signal conditioner and (f) data acquisition system E1432A.

For each test, the sampling rate was set to 10,000 Hz with 16,384 time domain data points being recorded. In the frequency domain, this corresponds to a frequency range of 5,000 Hz with 8,192 FRF data points, thus giving a frequency resolution of 0.61 Hz per data point. To reduce the interference of noise, averaging of three ensembles per test was employed. To further improve the quality of the time history measurements, the following signal processing techniques were applied. (These features are integrated in the LMS CADA-X signal acquisition module.)

- A pre-trigger delay was used to ensure that the entire impact excitation signal was captured.
- A force window was applied to the excitation channel (impact hammer force) to remove noise from the impulse signal and to thereby minimise spectral leakage.
- An exponential window was used for the response channels (accelerometer measurements) to ensure that the transient signals showed sufficient decay at the end of the sampling period.

The acquired impact and response time history signals (amplitude versus time) were then converted into frequency spectra (amplitude versus frequency) using the Fourier transform, as described in section 4.2.1. By dividing the Fourier transform signals of the accelerometers (output) by the Fourier transform signal of the hammer impact (input), the FRFs were obtained. For each state of the beam (undamaged state and each damaged state), five averaged FRFs (from 15 different hammer hits) were recorded. Thereby 25 test measurements were obtained from each steel beam and 100 measurements from the entire test series.

4.3.3 Modal Testing and Experimental Modal Analysis Results of Beams

From MT&EMA, the dynamic properties of the steel beams (FRFs, natural frequencies, damping ratios and mode shapes) were determined at each undamaged and damaged state. FRFs were directly obtained from the LMS CADA-X software, and the modal parameters (natural frequencies, damping ratios and mode shapes) were extracted from the FRFs by means of experimental modal analysis procedures, which were described in detail in section 4.2.3.

Undamaged Test Beams

Before damage was introduced to the test beams, each of the four steel beams was tested firstly in its intact state to determine the dynamic characteristics of the individual baseline structures. Although specimens were nearly identical, each beam was tested individually in order to consider minor discrepancies in the boundary conditions, which could be introduced from differences in the setup and clamping of the beam supports. A typical FRF summation function obtained by adding up the FRFs of all nine sensors

from beam 1 in its intact state is shown in Figure 4.14. In the FRF graph distinct frequency peaks are visible, which describe the first seven flexural modes. In the displayed frequency bandwidth, ranging from 0 Hz to 700 Hz, additional peaks are observed. These peaks indicate other modes (probably torsional or transversal modes), which cannot be clearly identified with the chosen sensor setup.

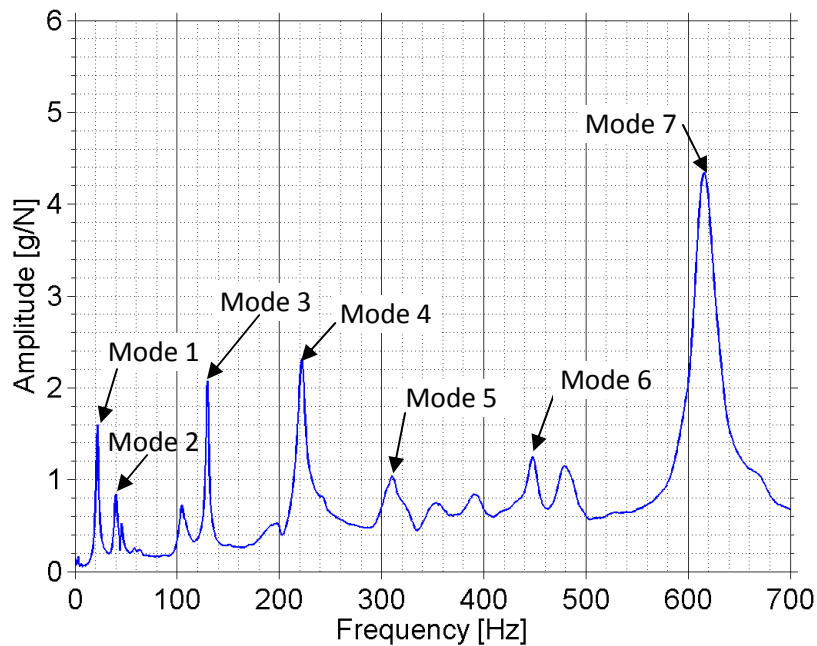


Figure 4.14 FRF summation function of undamaged beam 1.

By employing frequency direct parameter identification (FDPI) (see Section 4.2.3), the modal parameters (natural frequencies, damping ratios and mode shapes) of the intact steel beams were extracted from the FRFs utilising the post-processing module in LMS CADA-X software. In Table 4.2, the natural frequencies of the first seven flexural modes of beams 1 to 4 are listed. The corresponding frequency peaks of these modes are marked with an arrow in the FRF of Figure 4.14. From the frequency table it is observed that the modal frequencies of the four intact beams show discrepancies, even though they are supposed to be the same. With standard deviations of 0.55 Hz, 0.47 Hz, 2.35 Hz, 4.9 Hz, 4.4 Hz, 15.7 Hz and 4.7 Hz for modes 1 to 7, respectively, it is noted that the frequency differences are larger when the mode is higher. The large discrepancy of mode 6 is due to the fact that the determination of mode 6 from the FRFs was extremely difficult as the hammer impact point was very close to a node point of that mode.

Table 4.2 Natural frequencies of the first seven flexural modes of beams 1 to 4.

	Natural frequencies [Hz]						
	Mode 1	Mode 2	Mode 3	Mode 4	Mode 5	Mode 6	Mode 7
Beam 1	21.60	40.07	129.37	221.49	310.39	448.69	614.30
Beam 2	20.27	40.71	125.02	215.96	302.79	477.86	616.27
Beam 3	21.09	40.21	127.86	218.05	307.09	483.94	616.62
Beam 4	21.01	39.56	124.41	209.65	300.44	476.46	606.48

The damping ratios of the first seven flexural modes of beams 1 to 4 are listed in Table 4.3. Here the standard deviations are 0.56%, 0.4%, 0.43%, 0.32%, 0.64%, 0.25% and 0.27% for modes 1 to 7, respectively. A general trend between the damping ratios and the modal frequencies is not observed.

Table 4.3 Damping ratios of the first seven flexural modes of beam 1 to 4.

	Damping ratios [%]						
	Mode 1	Mode 2	Mode 3	Mode 4	Mode 5	Mode 6	Mode 7
Beam 1	1.17	0.43	0.57	1.14	2.67	0.87	1.64
Beam 2	2.17	1.30	1.21	1.60	2.09	1.18	1.38
Beam 3	2.31	1.01	1.52	1.93	1.21	1.48	1.64
Beam 4	1.41	1.25	0.76	1.55	1.56	1.23	1.05

Figure 4.15 displays the mode shapes of the captured modes of beam 1. Whereas the deformations of mode shapes 1 to 3 are as expected, the shapes of modes 4 to 7 show abnormalities at the support ends of the beams. While in theory, the mode deformations should be zero at the beam ends (as visible for modes 1 to 3), an uplifting motion is noted for mode shapes 4 to 7. This phenomenon was repeatedly observed for all four steel beams and may be due to resonance interferences of the supports, which occur at higher frequencies. However, as this study investigates differences in dynamic characteristics of structures before and after damage such mode shape discrepancies are irrelevant for the developed damage identification methods.

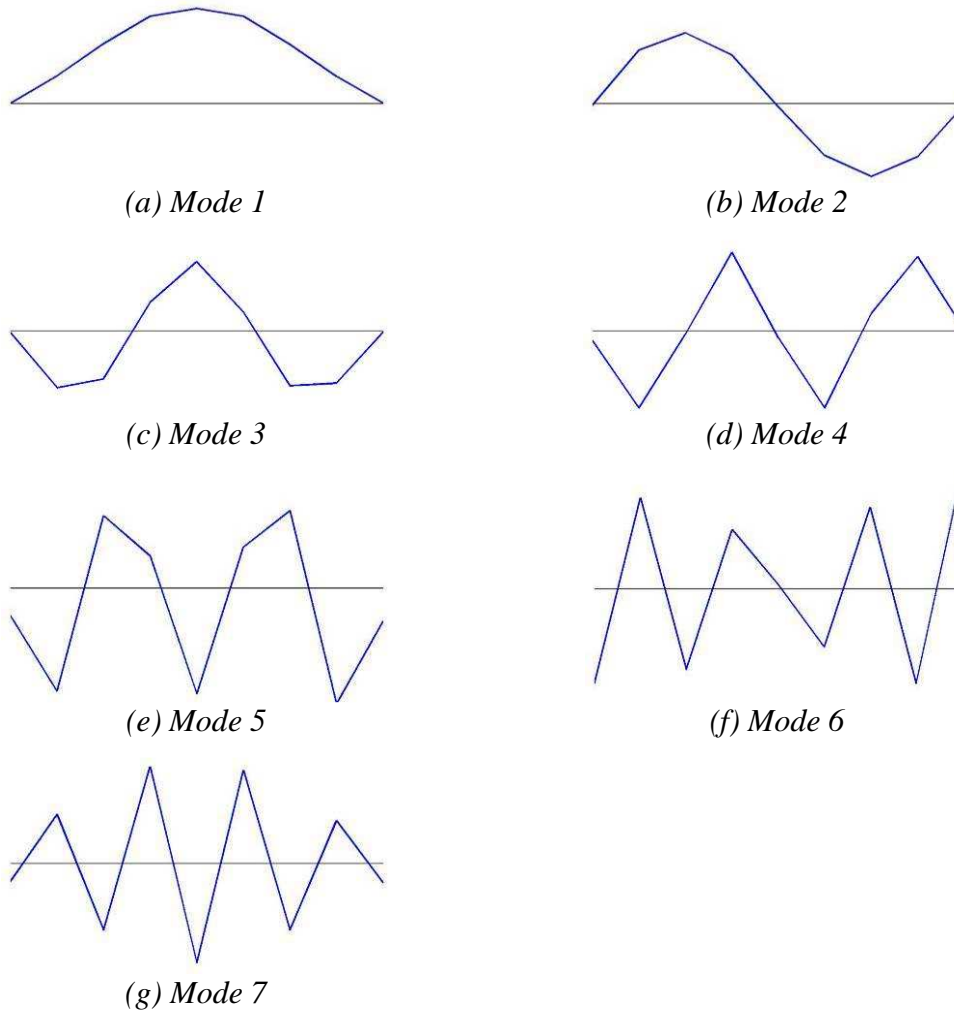


Figure 4.15 First seven flexural mode shapes of beam 1.

Damaged Test Beams

When physical modifications occur in a structure, its dynamic properties change. These changes are the basis for the developed damage identification methods. The changes of the dynamic properties due to damage are demonstrated by the analytical solution for natural frequency of a linear vibratory system. For a bi-pinned beam, the analytical solution for natural frequencies are given as (Geradin & Rixen 1997):

$$\omega_n^2 = (n\pi)^4 \frac{EI}{\bar{m}L^4} \quad (4.10)$$

where ω_n is the circular natural frequency of the n^{th} mode of the system with modulus of elasticity E , moment of inertia I , mass per unit length \bar{m} and span length L . From equation (4.10), a reduction in stiffness (EI) (e.g. caused by damage) leads to a drop in the natural frequencies. These frequency reductions reflect in the FRF data by shifts and

magnitude changes of frequency peaks. Further, as natural frequencies drop, damping ratios ζ , which represent the ratio of coefficient c to critical damping coefficient c_{cr} , increase and thereby indicate changes to the structure.

Natural Frequency Changes of Laboratory Beams

As stated above, theoretically, the natural frequencies of a structure drop when damage is inflicted. For the laboratory beams, Table A.1 (APPENDIX A) lists the results of the captured first seven natural frequencies of all undamaged and damaged beams. To show changes in the frequency values, Figure A.1 (APPENDIX A) illustrates the corresponding drop in natural frequencies between frequencies of the intact and damaged data. As example, for beam 1, the natural frequency values and their reductions are also shown in Table 4.4 and Figure 4.16, respectively. From the tables as well as the graphs, the following is observed. The frequency values of the first and second flexural modes only experience very minor or no changes for all four beams. For all higher modes, however, a general increase in the reduction in natural frequencies for all beams is noted as the severity of damage increases (although there are small fluctuations). Further, if damage is located at a node point of a certain mode, the frequency of that mode does not change. This phenomenon can be demonstrated by damage at mid-span (location '4'), which is node point for modes 2, 4 and 6 (see Figure 4.16). Here, only minor frequency changes were observed for these modes.

Table 4.4 Natural frequencies [Hz] of the first seven flexural modes of the intact state and all damaged states of beam 1.

Beam 1 - Natural frequencies [Hz]							
	Mode 1	Mode 2	Mode 3	Mode 4	Mode 5	Mode 6	Mode 7
Undamaged	21.60	40.07	129.37	221.49	310.39	448.69	614.30
4XL	21.62	40.09	129.27	221.64	310.78	448.97	615.41
4L	21.49	40.12	129.43	222.06	310.15	449.24	613.78
4M	21.44	40.07	128.03	221.33	307.18	448.65	610.25
4S	21.37	40.05	126.50	220.68	305.34	448.62	601.10

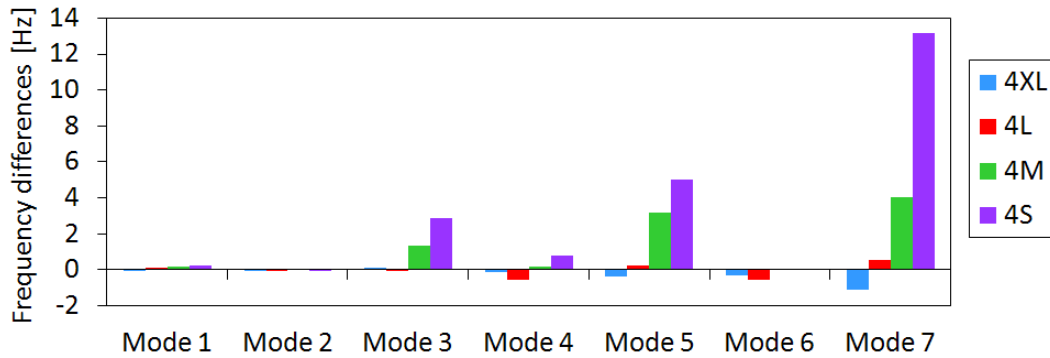


Figure 4.16 Comparison of reduction in natural frequencies [Hz] of different severities of damage at location '4' (beam 1).

Damping Ratio Changes of Laboratory Beams

Damping ratios, which accompany the captured modes, are another dynamic quantity that changes due to damage. Theoretically, the damping ratios should increase as damage increases. Table A.2 and Figure A.2 (APPENDIX A) show the damping ratios and differences of damping ratios for the undamaged and damaged states of all laboratory beams. As example, for beam1, damping ratios and their corresponding differences are also shown in Table 4.5 and Figure 4.17. With damping ratios ranging from 0.38% to 3.42% and damping ratio differences fluctuating between -1.09% and 1.94%, a rather inconsistent trend is observed. In about half of the damage cases, the damping ratio is even decreasing as the damage severity increases. Studies conducted by Kato and Shimada (1986) and Salawu and Williams (1995b) observed similar inconsistencies and concluded that, unlike for natural frequencies, a reasonably consistent trend could not be established for damping ratios before and after damage. The reason for such inconsistency is that damping is difficult to evaluate accurately due to measurement errors and uncertainties.

Table 4.5 Damping ratios [%] of the first seven flexural modes of the intact state and all damaged states of beam 1.

Beam 1 – Damping ratios [%]							
	Mode 1	Mode 2	Mode 3	Mode 4	Mode 5	Mode 6	Mode 7
Undamaged	1.17	0.43	0.57	1.14	2.67	0.87	1.64
4XL	1.45	0.51	0.61	1.12	1.96	0.97	1.56
4L	1.36	0.82	0.55	1.18	2.90	1.06	1.39
4M	1.20	0.58	0.38	1.35	1.87	1.50	1.43
4S	1.17	0.75	0.52	1.19	1.58	1.05	1.11

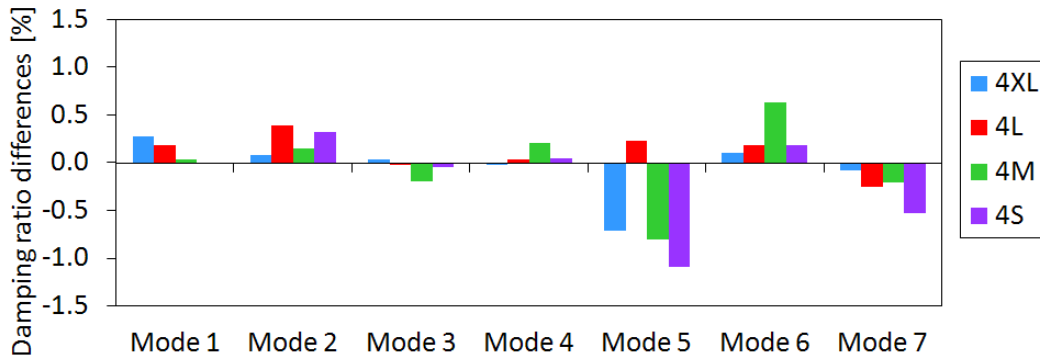
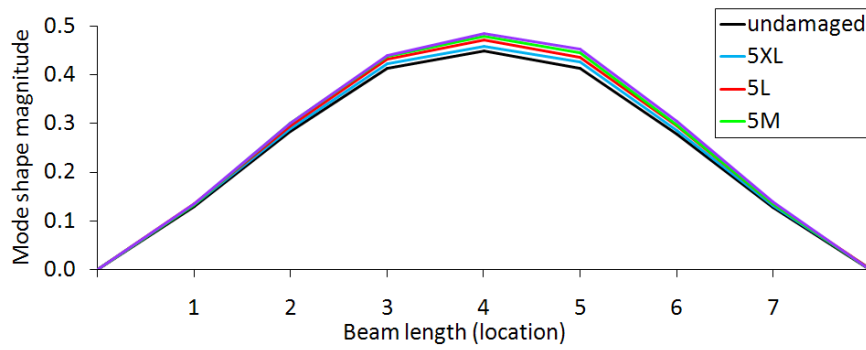


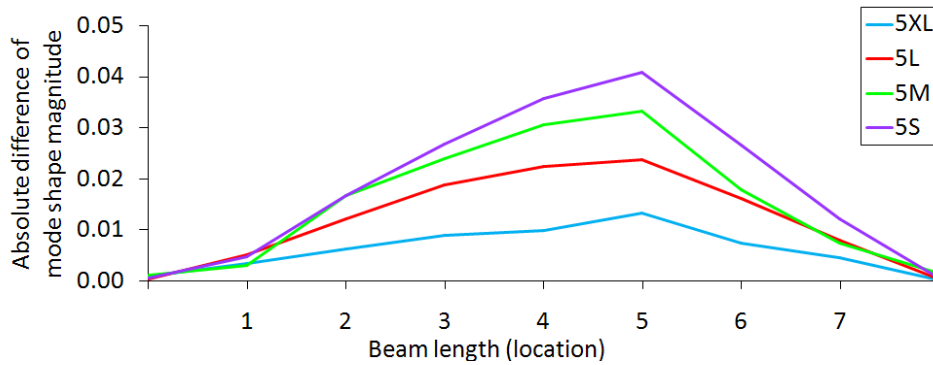
Figure 4.17 Comparison of increase in damping ratios [%] of different severities of damage at location ‘4’ (beam 1).

Mode Shape Changes of Laboratory Beams

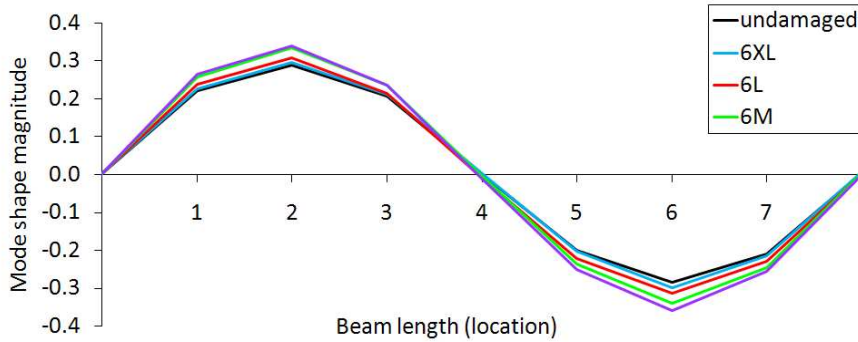
It is commonly acknowledged that local damage will cause changes to the mode shapes in the vicinity of the damage. These mode shape changes are the basis of one of the presented damage identification methods utilising damage index (DI) values, which are based on mode shape curvature differences between the undamaged and the damaged structures. For the laboratory beams, due to the nature of damage introduced (i.e. saw-cut damage), the captured mode shapes of the first seven flexural modes showed only small changes. Figure 4.18 illustrates some good examples of mode shapes and corresponding absolute differences of mode shapes between intact and damaged beams of different damage scenarios. Figure 4.18 (a) and (b) show mode 1 of damage severities XL to S of beam 2, which is damaged at location ‘5’, and (c) and (d) display mode 2 of different damage severities of a beam damaged at location ‘6’. From the figures, changes of mode shape vectors are clearly visible. Figures (b) and (d) demonstrate the high sensitivity of mode shapes to local damage; it is noted from the figures that the absolute mode shape differences are the largest in the vicinity of damage, i.e. near location ‘5’ for Figure 4.18 (b), and close to location ‘6’ for Figure 4.18 (d). Furthermore, it is observed that damages of higher severity cause larger mode shape changes (see Figure 4.18 (b) and (d)). As mentioned earlier, one of the proposed damage identification methods utilise damage indices from the DI method, which is based on mode shape curvature changes, as damage fingerprints. By analysing the curvatures of mode shapes, the observed local mode shape changes are further enhanced giving better and more robust damage identification results.



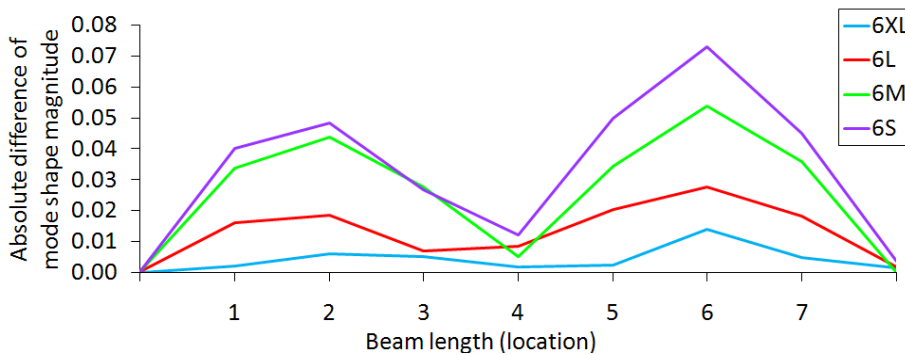
(a) Mode shape of mode 1 of a beam damaged at location '5'



(b) Absolute mode shape differences of mode 1 of a beam damaged at location '5'



(c) Mode shape of mode 2 of a beam damaged at location '6'



(d) Absolute mode shape differences of mode 2 of a beam damaged at location '6'

Figure 4.18 Mode shapes ((a) and (c)) and absolute mode shape differences ((b) and (d)) of various damage severities. (a) and (b) display mode 1 of beam 2 damaged at location '5' and (c) and (d) illustrate mode 2 of beam 3 damaged at location '6'.

Frequency Response Function Changes of Laboratory Beams

FRFs are directly measured data and are therefore very sensitive to any kind of change. When damage occurs in a structure, the frequency peaks of the FRFs shift and their amplitudes change. Depending on the severity and the type of structural modification/damage, new frequency peaks can occur and other peaks can disappear. In addition, frequency peaks of various modes behave differently depending on the location of the damage site; whereas some modes are very sensitive to a specific damage location, others stay unchanged, which is, for example, the case if damage is located at a node point of a given mode. Figure 4.19 and Figure 4.20 show FRF summation functions of the experimental steel beams in the undamaged state and various damaged states. Figure 4.19 shows the effect of different damage severities and Figure 4.20 illustrates the impact of various damage locations to the FRF summation function. Subfigures (a) display a frequency range from 0 Hz to 700 Hz and subfigures (b) show a close-up of the frequency peak of mode 7 ranging from 570 Hz to 650 Hz. From Figure 4.19 (b) it can be seen that with an increase in the damage severity, the FRF peaks of mode 7 shift to the left (indicating a drop of the natural frequency of mode 7) and the amplitudes increase, which is a general trend for all frequency peaks. For the different damage locations displayed in Figure 4.20 (a) and (b), the FRF peaks also change in amplitude and position; here, however, no general trend can be observed. Such damage induced changes of FRFs are the basis for the second proposed damage identification method. Residual FRFs, which are differences in FRF data from the undamaged structure and the damaged structures, are used as damage fingerprints in the second proposed method.

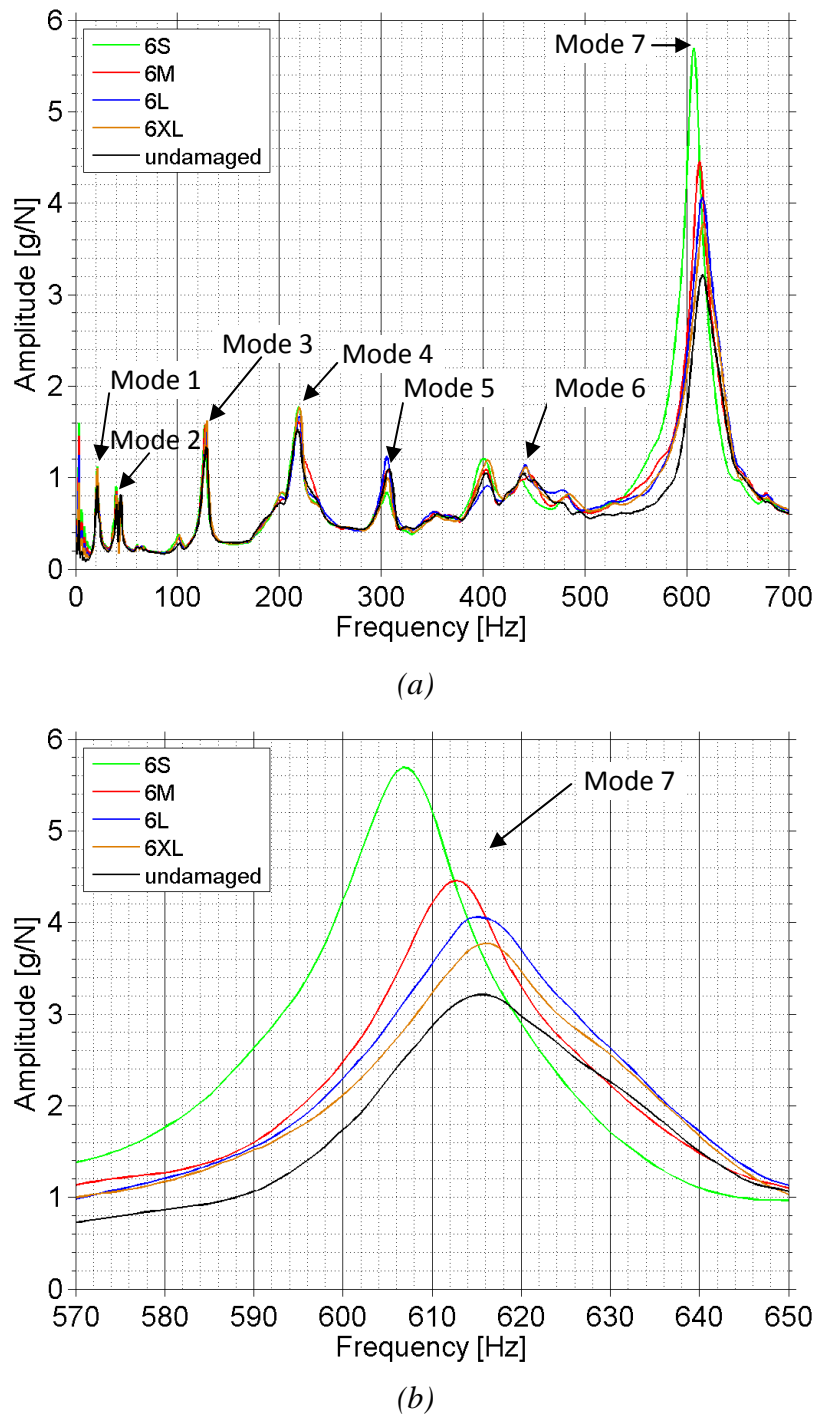


Figure 4.19 Effects of different damage severities on FRF data. Displayed are FRF summation functions from beam 3 in the undamaged state and damaged states with defects at location '6' of severities extra-light (6XL), light (6L), medium (6M) and severe (6S) with subfigure (a) displaying a frequency range from 0 Hz to 700 Hz and subfigure (b) illustrating a close-up of the frequency peak of mode 7.

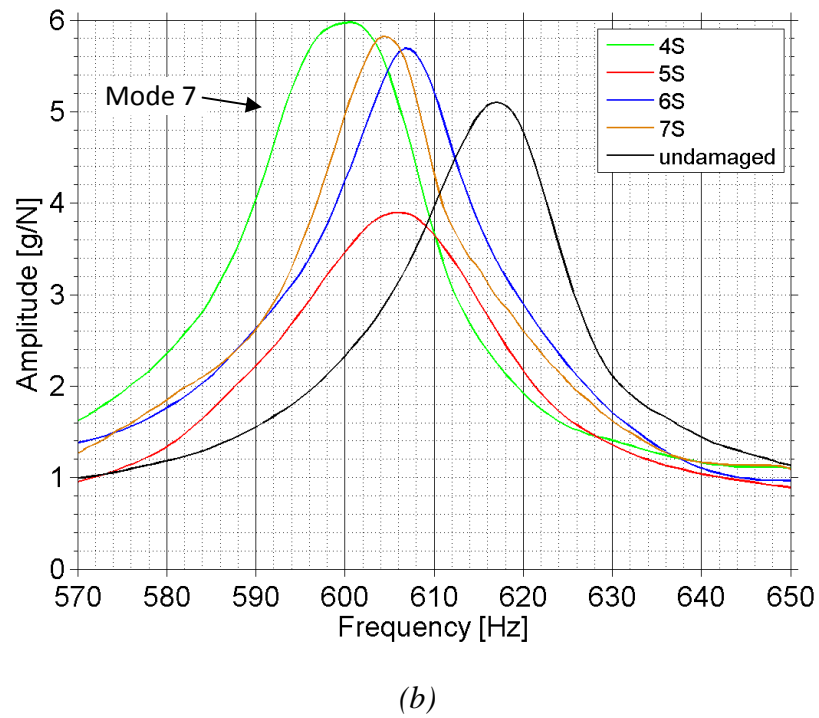
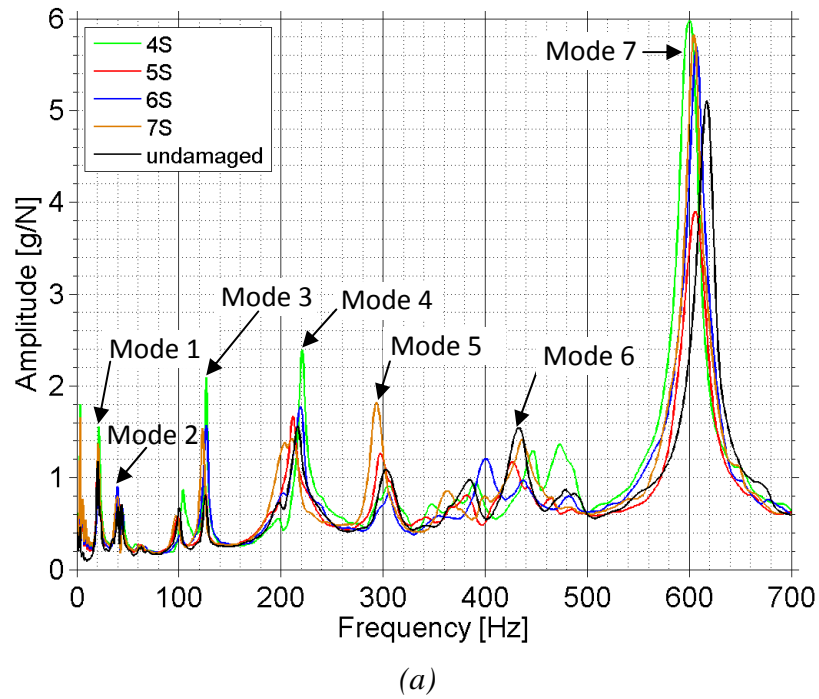


Figure 4.20 Effects of different damage locations on FRF data. Displayed are FRF summation functions of undamaged beam and damaged beams 1 to 4 with defects of severe extent at locations '4' to '7' (4S to 7S) with subfigure (a) displaying a frequency range from 0 Hz to 700 Hz and subfigure (b) illustrating a close-up of the frequency peak of mode 7.

4.4 EXPERIMENTAL SET UP AND TESTING OF LABORATORY TWO-STOREY FRAMED STRUCTURE

4.4.1 The Two-Storey Framed Structure

A two-storey framed structure was manufactured in the UTS Metal Workshop to experimentally validate the proposed damage identification method on a more complicated structure. A photo of the steel framed structure is shown in Figure 4.21.

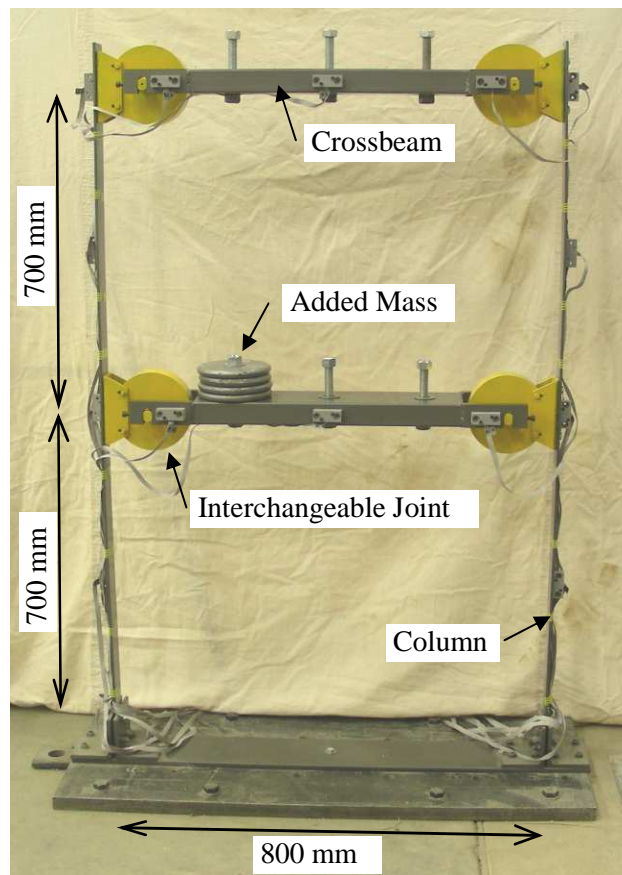
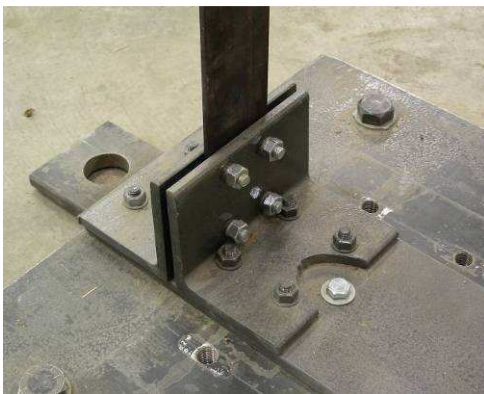


Figure 4.21 Laboratory two-storey framed structure.

The structure consisted of two columns, two crossbeam and four joint elements. The columns were made of flat steel with a cross-section of $65 \text{ mm} \times 5.5 \text{ mm}$ and a height of 1600 mm and mounted to a steel base with a fixed connection (see Figure 4.22 (a)). The distance between the two columns was 800 mm. The two crossbeams were specially designed to allow an exchange of the joint elements such as rigid joints, pin joints and semi-rigid joints. The main body consisted of a box section of $150 \text{ mm} \times 50 \text{ mm}$ and a wall thickness of 3 mm. On each end of the crossbeams, solid steel

sections were welded to link the crossbeams to the joint elements. Through a straight-sided notch shaft connection (see Figure 4.22 (b)), the crossbeams were firmly fixed to the joint elements with a screw preventing the loosening of the connection. The crossbeams were located 700 mm and 1400 mm above the steel base connection, respectively and there was a spacing of 700 mm between the steel base connection and the lower beam, and between the two crossbeams. Two types of joint elements were considered in this investigation. One is a rigid joint element and the other is a pinned connection. By interchanging these two joint elements, one can simulate the change of boundary conditions caused by damage. The joint elements were screwed to the columns allowing for a fixed connection. A photo of the column-joint-crossbeam connection is shown in Figure 4.22 (b). In order to investigate different added mass scenarios, each crossbeam was fitted with three stubs to provide for the mounting of additional mass. The steel had the following material characteristics: the modulus of elasticity was $200,000 \times 10^6 \text{ N/m}^2$, the Poisson's ratio was 0.3 and the density was $7,850 \text{ kg/m}^3$.



(a)



(b)

Figure 4.22 Connection details (a) steel base - column connection (b) column - joint - crossbeam connection.

4.4.2 Damage/Added Mass Scenarios in Two-Storey Framed Structure

The goal of this study was to identify different kinds of changes in a complex structure. The two-storey framed structure was introduced with the following three damage/added mass scenarios:

- 1) Changes of boundary condition: the conditions of the four joints (J1 to J4, see Figure 4.23) that connected the crossbeams with the columns were changed from fixed to pinned. Single and multiple joint changes were investigated.
- 2) Added mass: extra mass was added to the crossbeams of the structure at six different locations, M1 to M6 (see Figure 4.23).
- 3) Changes of column cross-section: Single damage was inflicted to a column by cutting a notch on a column at two locations (C1 and C3, see Figure 4.23). Three different severities of section losses were studied.

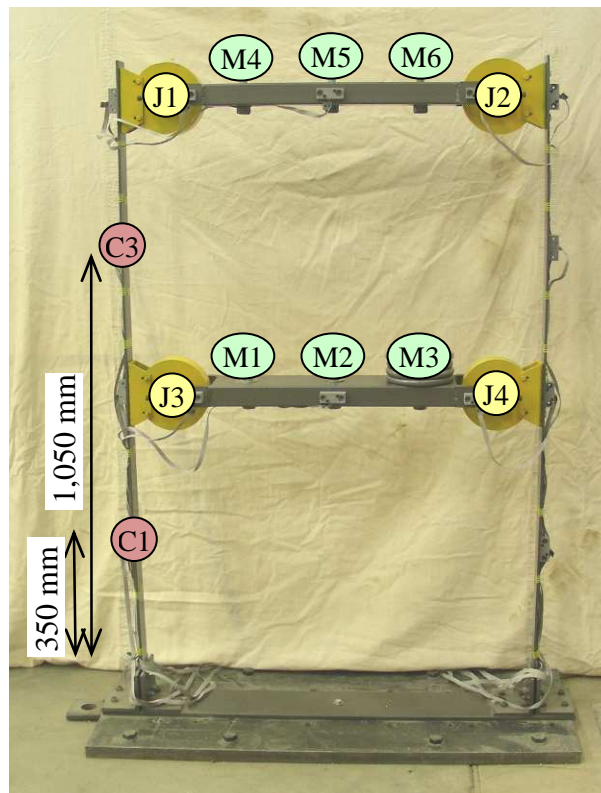


Figure 4.23 Modified elements of the two-storey framed structure.

For damage scenarios due to boundary imperfections, a total of ten different boundary changes were investigated. The changes on the boundaries were used to simulate damage caused by environmental or ageing decay such as corrosion or loosening of

connections. Joints connecting the crossbeams with the columns behave as either a fixed or a pinned connection (through interchanging the two types of joint elements). A photo of a fixed and a pinned joint is shown in Figure 4.24. For the fixed joint, the shaft was welded to the body of the joint, providing a rigid connection. For the pinned joint, a roll bearing was built on the shaft allowing the pin to rotate freely.

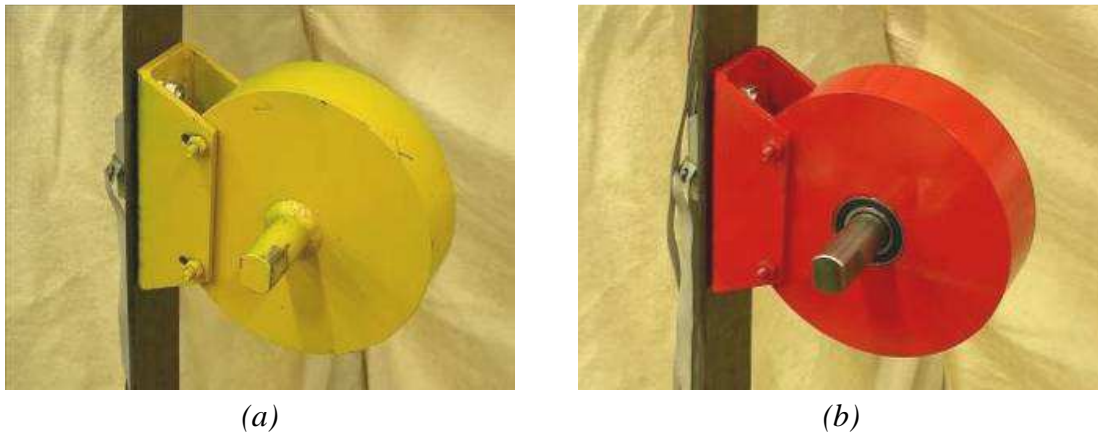


Figure 4.24 (a) Fixed joint (b) pinned joint.

For the initial baseline state of the structure, the fixed connections were used for all four joints (termed FFFF). Four scenarios of single joint changes were studied by swapping one of the four fixed joints with a pinned joint at a time. Six multiple joint alterations with two joints swapped each from fixed to pinned were also explored. All boundary changes are listed in Table 4.6.

Table 4.6 Boundary change scenarios.

Boundary case	Boundary scenario	Joint conditions			
		J1	J2	J3	J4
1	PFFF	P	F	F	F
2	FPPF	F	P	F	F
3	FFPF	F	F	P	F
4	FFFP	F	F	F	P
5	PPFF	P	P	F	F
6	FFPP	F	F	P	P
7	FPPF	F	P	F	P
8	PFPF	P	F	P	F
9	FPPF	F	P	P	F
10	PFFP	P	F	F	P

Note: F indicates a fixed joint and P a pinned joint

For the added mass scenarios, six different mass locations were studied. Added mass is widely used to study alterations of mass and to simulate frequency changes due to damage. The following researchers utilised mass in damage identification studies: (Carden & Fanning 2003; Cattarius & Inman 1997; Doebling et al. 1997; Liberatore & Carman 2004; Ostachowicz, Krawczuk & Cartmell 2002; Parloo et al. 2002; Paul & Carden 2004; Verboven et al. 2002; Vieira De Moura & Steffen 2006; Yan et al. 2005). For the two-storey framed structure, four disks of 2.3 kg each were placed on one of the six stubs of the crossbeams. A screw connection ensured that the mass was tightly bound to the structure, as shown in Figure 4.25. With the entire structure having a mass of approximately 87 kg, the added mass equals an additional mass of 10.5%. The six added mass scenarios were termed after the location of the masses M1 to M6 (see Figure 4.23).

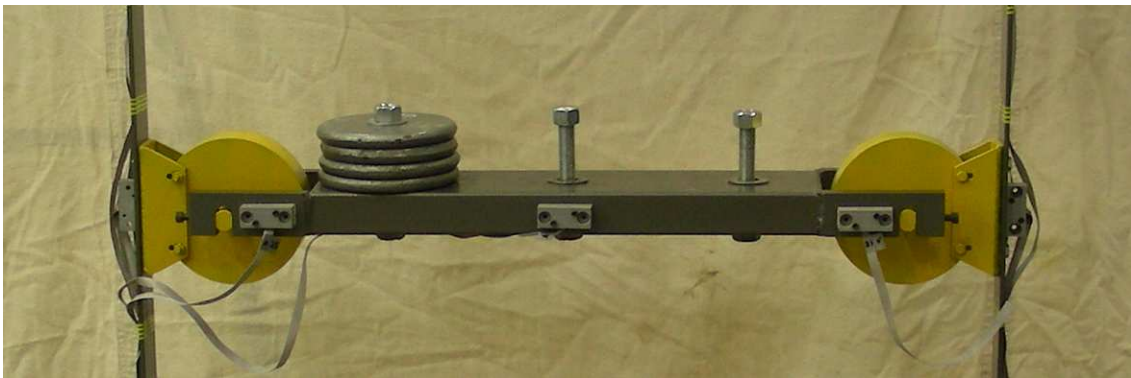


Figure 4.25 Added mass at location M1.

For scenarios of damage on columns due to cross-section reduction, a column was inflicted with progressive severities of single notch type damage at two locations. Locations C1 and C3 of Figure 4.23, which are 350 mm and 1,050 mm above the steel base connection, respectively, were chosen as damage sites. These two locations are the mid-spans of the upper and the lower column halves. At each location, damage of three severities were gradually inflicted to the column with a disc grinder (see Figure 4.26).



Figure 4.26 Cutting of damage using a disk grinder.

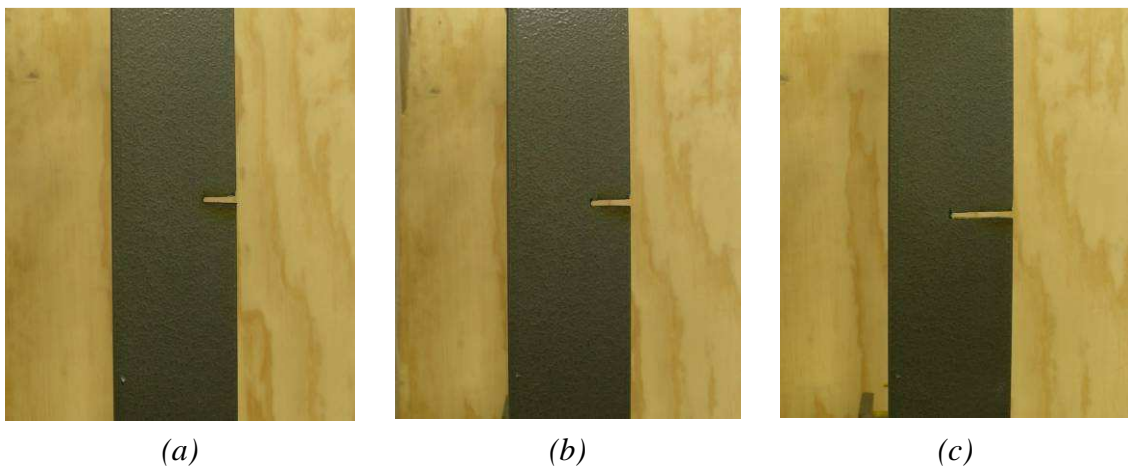


Figure 4.27 Section loss of (a) 16.25 mm, (b) 21.7 mm and (c) 32.5 mm width and 4 mm height.

The three levels of damage severities termed light (L), medium (M) and severe (S), were introduced corresponding to a section loss of 4 mm in notch width and 16.25 mm, 21.7 mm and 32.5 mm in notch depth, respectively. These section losses correspond to a cross-section loss of the second moment of area, I , of 25%, 33.33% and 50%, respectively. The three damage severities are depicted in Figure 4.27. All section reduction scenarios are listed in Table 4.7.

Table 4.7 Section reduction scenarios.

Section reduction case	Section reduction scenario	Location	Severity
1	1L	C1	L
2	1M	C1	M
3	1S	C1	S
4	3L	C3	L
5	3M	C3	M
6	3S	C3	S

Note: C1 and C3 indicate the mid-span of the lower and upper column half, respectively.

L, M and S denote light, medium and severe damage, respectively.

4.4.3 Modal Test Set Up

The dynamic properties of the two-storey framed structure were again determined using MT&EMA. In modal testing, the structure was excited with the same modally tuned impact hammer as used for the testing of the steel beams (see Figure 4.13 (a)). The reference point for the hammer was located at the upper end of a column indicated with a red cross and noted as H5 in Figure 4.28 (a). The hammer strike was executed in the horizontal direction resulting in a lateral excitation of the structure. The responses of the column and the crossbeam members were measured by 14 accelerometers. The locations of the sensors are also depicted in Figure 4.28 (a). In experimental modal analysis, the acquired signals from the impact hammer and the 14 accelerometers were analysed and the modal parameters of the structure determined.

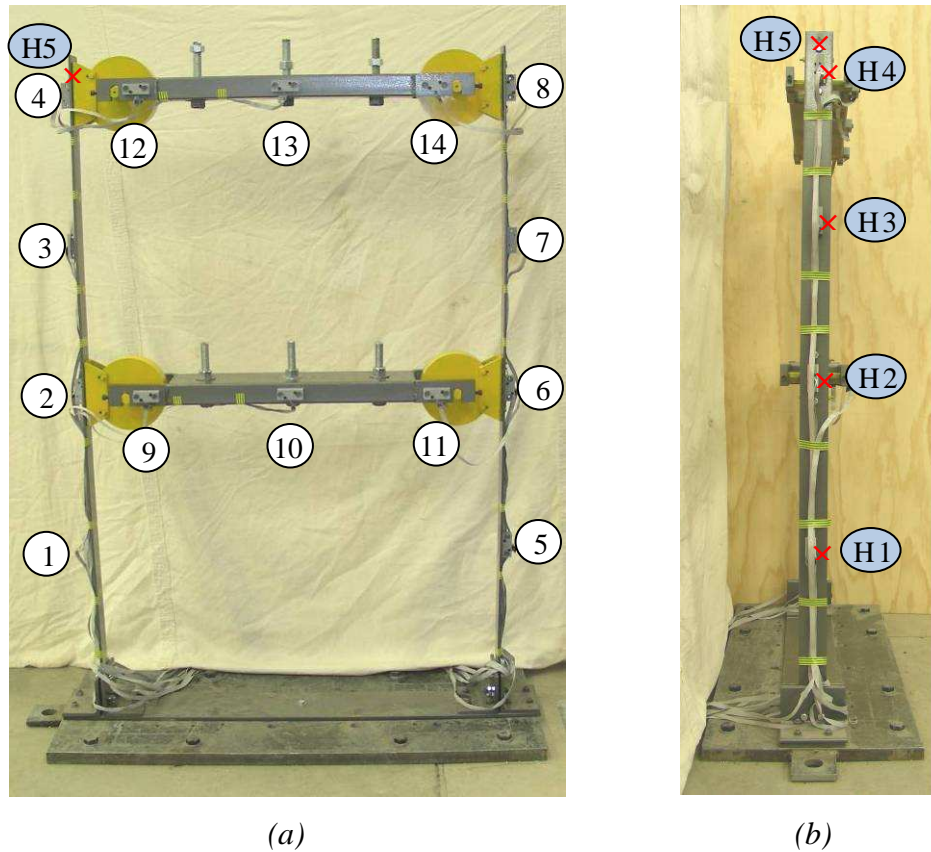


Figure 4.28 (a) Accelerometer locations and (b) hammer impact points of the two-storey framed structure.

The accelerometers at locations ‘1’ to ‘8’ were mounted on the centreline of the columns and were set up to measure horizontal accelerations. As the crossbeams experienced negligible horizontal deformation, the accelerometers of locations ‘9’ to ‘14’, mounted to one side of the crossbeams, measured acceleration in the vertical direction. The identification of damage/added mass scenarios by measuring vertical accelerations is however very challenging as the structure was only excited in the horizontal direction, experiencing very small vertical accelerations due to secondary effects.

As the testing of the two-storey framed structure required 14 accelerometers, different accelerometers were chosen compared to the testing of the steel beams (see section 4.3.2). The accelerometers used for the testing of the two-storey framed structure were 14 low cost dual-axis piezoresistive accelerometers of model ADXL320 having a bandwidth of 0.5 Hz to 2.5 kHz. The accelerometers were supplied with a 5 V DC power excitation measuring a range of ± 5 g. As the purchased accelerometers were only in a form of circuit board (see Figure 4.29 (a)), they were encased into a

specially designed housing (depicted in Figure 4.29 (b)). The data acquisition system used was an Iotech Daqbook 260 equipped with 2×16 input channels (see Figure 4.29 (c)). The software Daqview controlled the data acquisition system. While the ADXL320 accelerometers were inexpensive (only sensor circuit boards without encasing were purchased) they are of high accuracy, with a sensitivity range of 154 to 194 mV/g (compared to 94 to 100 mV/g for the PCB accelerometers used for the beam structures). Before the actual testing, preliminary tests were conducted to compare the performance of the ADXL320 accelerometers against that of the PCB accelerometers. From these preliminary tests, the accuracy of the ADXL320 accelerometers was found to be precise and comparable to the performance of the PCB accelerometers. These findings are of particular interest for the testing of real large-size structures where a larger number of (preferably low cost) accelerometers are necessary to assess the damage state of the structures.

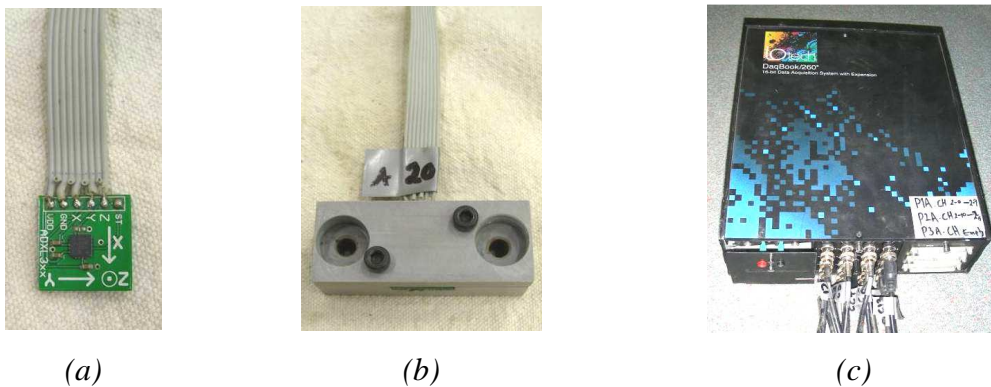


Figure 4.29 (a) Accelerometer chip ADXL320 (b) accelerometer with housing and (c) data acquisition system Iotech Daqbook 260.

For each test, the sampling rate was set to 1,000 Hz capturing a frequency range of 500 Hz and 8,192 data points, thus giving a frequency resolution of 0.061 Hz per data point. The acquired time domain signals from the impact hammer and the 14 accelerometers were processed in MATLAB (The MathWorks 2007) using the fast Fourier transform (FFT) to produce FRFs data in the frequency domain. Using the modal analysis module of the LMS CADA-X software, the natural frequencies, damping ratios and corresponding mode shapes were extracted from the FRF data. The details of experimental modal analysis can be found in section 4.2. Each damage/added mass state of the two-storey framed structure was tested 15 times. By combining and

averaging the FRFs of three tests at a time, five averaged FRF recordings are obtained for each state of the structure.

4.4.4 Impact Point Determination

The reference point of the impact hammer was determined after performing a series of tests considering five impact locations. The tested impact points are shown in Figure 4.28 (b) and are noted as H1 to H5. Impact locations H1 to H4 were situated at locations '1' to '4' just to the right of the accelerometers. Impact point H5 was located at location '4' above the sensor. The selection criteria for the reference point were that it should excite global and local modes in equal measure and as clearly as possible. Figure 4.30 shows FRF summation functions of horizontal acceleration responses (from accelerometers at locations '1' to '8') from all five hammer impact points.

In the FRF graphs, the first two frequency peaks (2.2 Hz and 6.9 Hz) are global modes corresponding to 2 DOF lumped mass model and the remaining peaks are local modes of the columns (a description of the mode shapes is given in section 4.4.5). As can be seen from the FRF graphs, reference points H2 and H4 mainly excite the two global modes of the structure (Figure 4.30 (b) and (c)). These two impact points are located at the end of and along the crossbeams of the structure and therefore induce only minor effects on the local column modes. Reference points H1, H3 and H5 can excite global and local mode shapes (see Figure 4.30 (a), (d) and (e)). For an excitation at points H1 and H3, however, the local modes of the columns are excited more than the global modes, as these impact points are at the mid-spans of the two column halves. Hammer location H5 equally excites global and local mode shapes (as seen in Figure 4.30 (e)) and was therefore chosen as the impact point for all tests in the following study. Further, as location H5 is chosen in the centreline of the column, no torsional effects are introduced. The execution of the actual hammer hit is also easier as impact point H5 is at a comfortable height of 1,600 mm above the steel base and the risk of inadvertently hitting an accelerometer is lower.

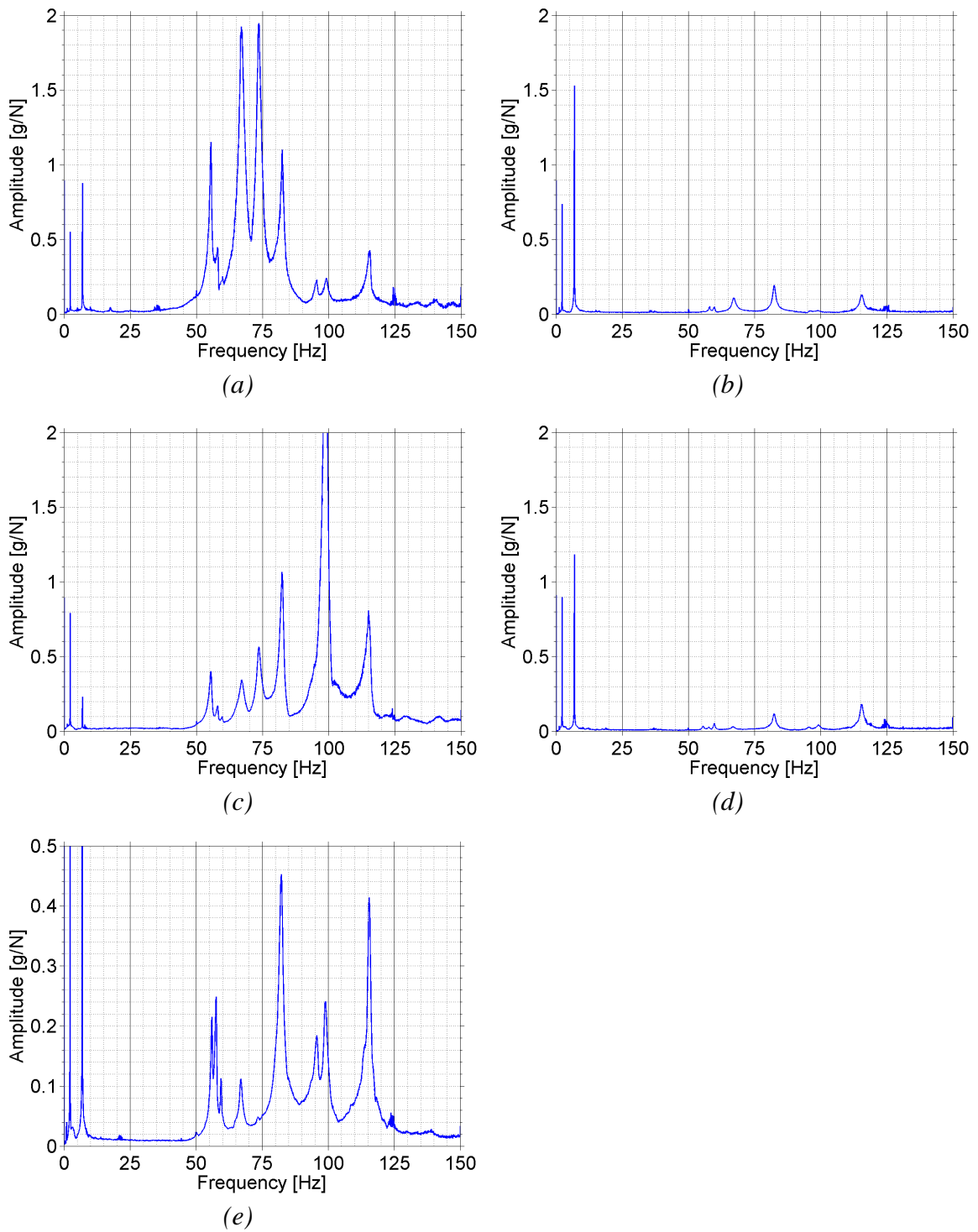


Figure 4.30 FRF summation functions of impact points (a) H1, (b) H2, (c) H3, (d) H4 and (e) H5.

4.4.5 Experimental Modal Testing and Analysis Results of Laboratory Two-Storey Framed Structure

Baseline Structure

From MT&EMA, seven flexural vibration modes with a frequency range from 2.2 Hz to 115.4 Hz were captured for the baseline structure (with four fixed joints). These seven modes were the maximum number of flexural modes that could be captured with the chosen sensor set up. The horizontal FRF summation function (resulting from the summation of the FRFs of accelerometers at locations ‘1’ to ‘8’, which capture horizontal accelerations) of the baseline structure is displayed in Figure 4.31. From the FRF results, the frequency peaks of the seven flexural modes are clearly visible and are labelled with arrows. Frequency peaks that are not marked are either torsional or transverse modes, which cannot be captured accurately with the available sensor network. The frequencies and damping ratios are listed in Table 4.8, and the corresponding mode shapes of the captured modes are illustrated in Figure 4.32. Both, the experimentally and numerically obtained mode shapes (see CHAPTER 5) are displayed in Figure 4.32 for better illustration and comparison purposes.

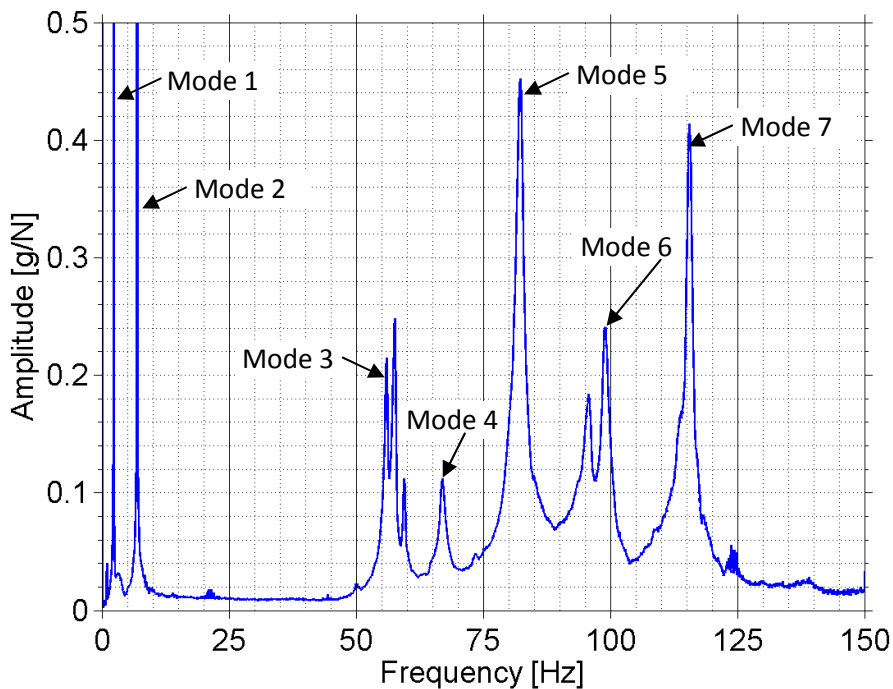


Figure 4.31 Horizontal FRF summation function of baseline structure.

As can be seen from the mode shape figures, modes 1 and 2 are global modes and modes 3 to 7 are local modes. Mode 1 and mode 2 describe the shapes of the first and second flexural modes of a cantilever, respectively. Modes 3 to 7 have different combinations of local column deformations, which all describe shapes similar to the first flexural mode of a beam.

Table 4.8 Frequencies of the first seven flexural modes.

	Natural Frequency [Hz]	Damping ratio [%]
Mode 1	2.2	0.46
Mode 2	6.9	0.16
Mode 3	56.1	0.35
Mode 4	67.0	0.86
Mode 5	82.1	0.88
Mode 6	98.9	0.58
Mode 7	115.4	0.74

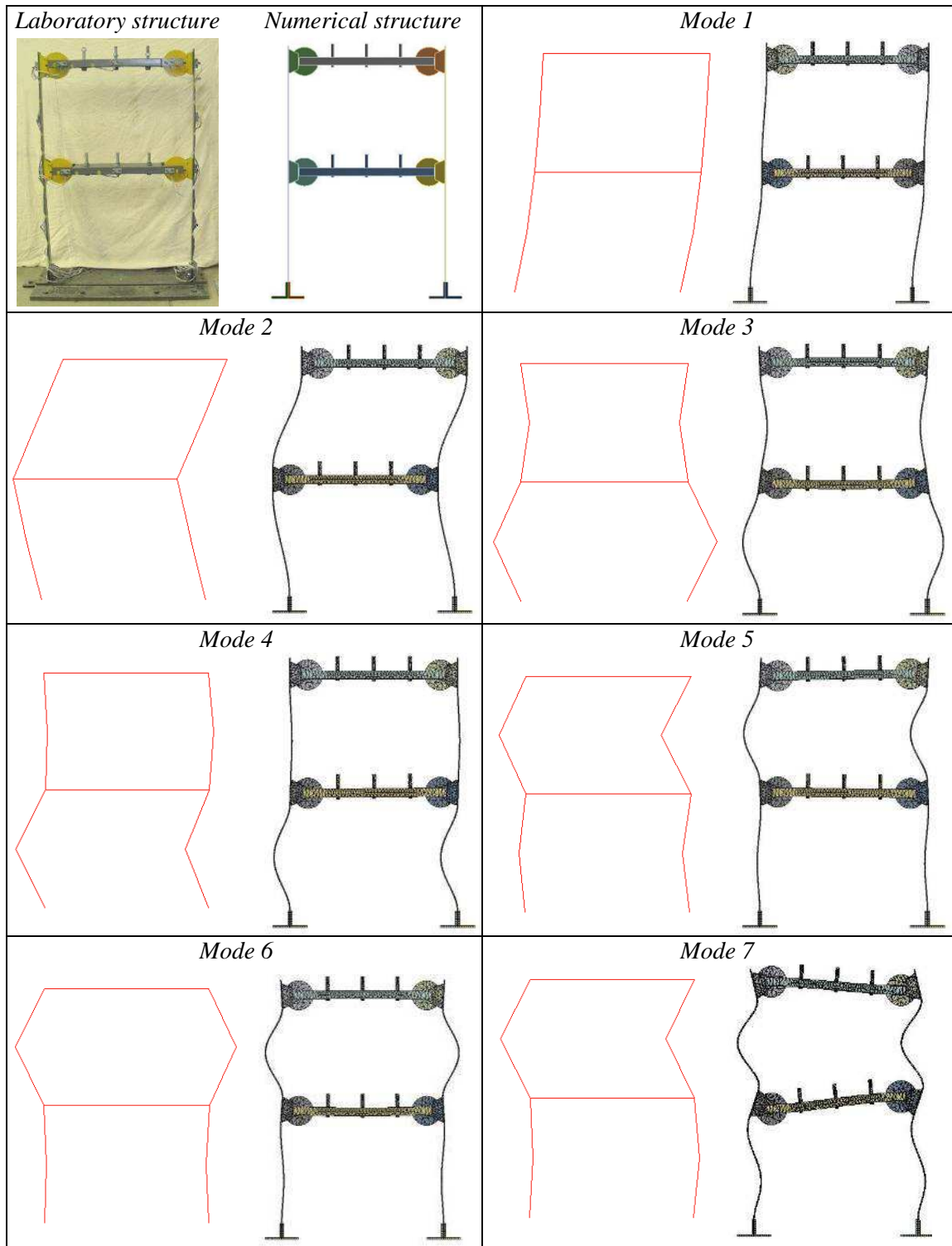


Figure 4.32 First seven flexural mode shapes of laboratory and numerical baseline two-storey framed structure.

Boundary Condition Changes

Changes in the boundary conditions of the two-storey framed structure resulted in major changes of the structure's dynamic properties, e.g. FRFs, natural frequencies and mode shapes (damping ratio changes were not evaluated). In Figure 4.33 and Figure 4.34, horizontal FRF summation functions of the baseline structure (denoted as FFFF) and different multiple and single boundary condition scenarios are depicted, respectively.

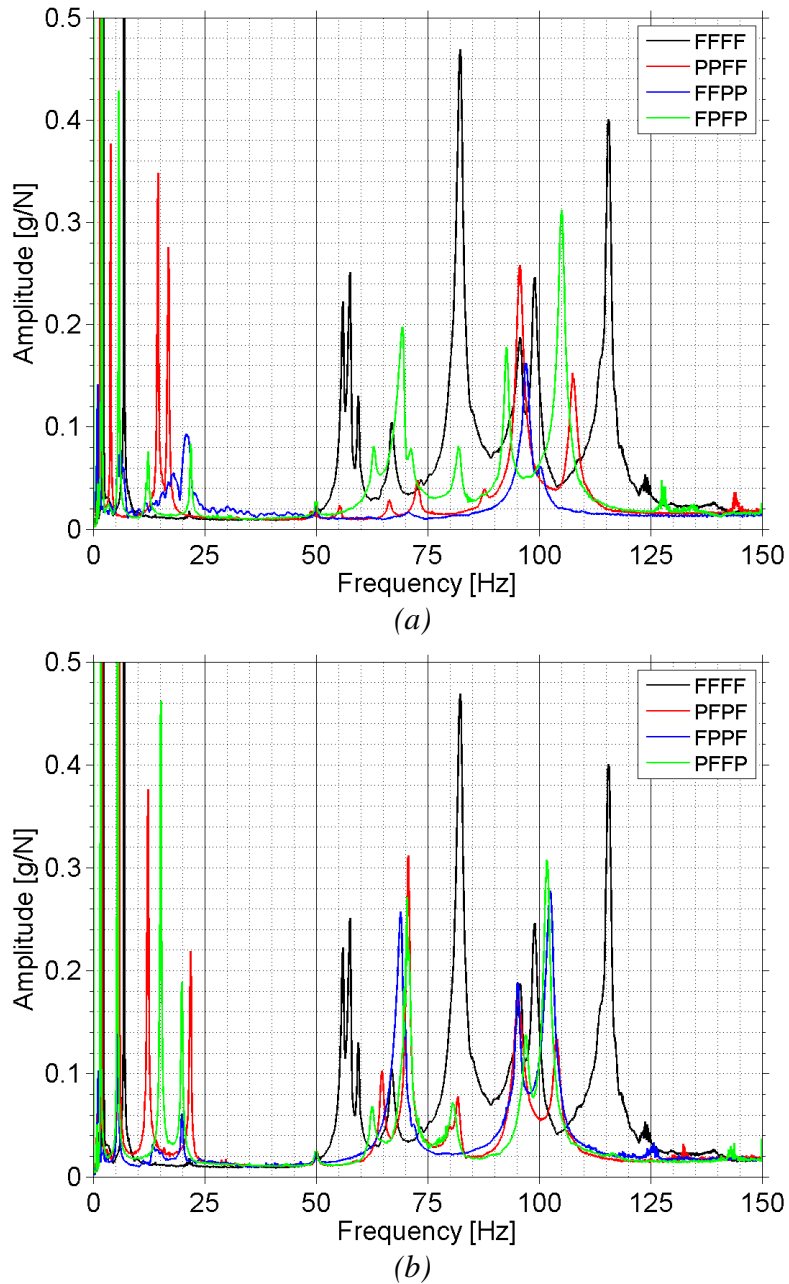


Figure 4.33 Horizontal FRF summation functions of baseline structure (FFFF) and different multiple boundary condition scenarios.

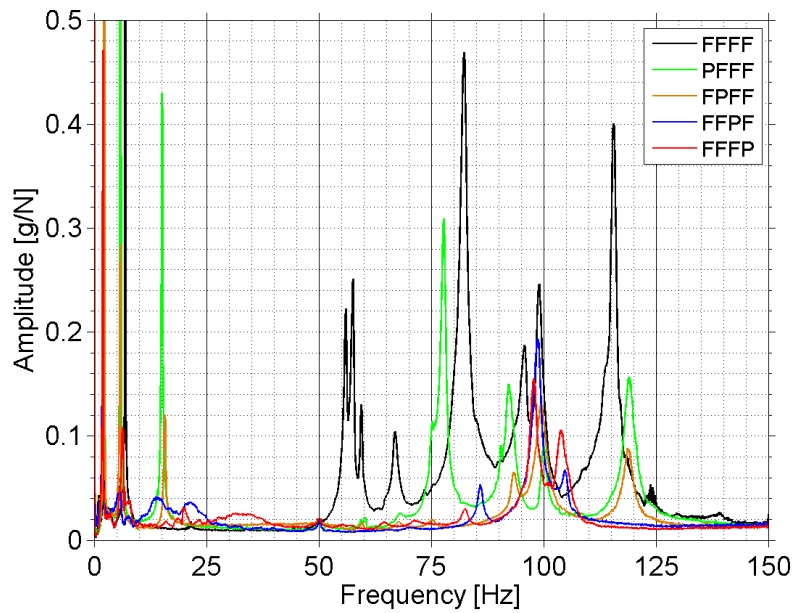


Figure 4.34 Horizontal FRF summation functions of baseline structure (FFFF) and different single boundary condition scenarios.

From the figures, it can clearly be seen that the FRFs of the structure with modified boundary configurations are very distinct from one another. Frequency peaks not only shift or change amplitude, but also the various FRFs show completely new patterns with new peaks emerging and others disappearing. The changes of the frequency peaks in the FRFs reflect changes in the vibrational modes of the structure. Whereas in some modes only the natural frequencies change, in others the mode shape also changes. In a couple of boundary condition scenarios, new modes emerge which describe new modal deformations. To demonstrate these changes, boundary scenario PFFF (with a pinned connection at joint J1 and fixed connections at joints J2 to J4) was chosen as an example. In the following two figures, the horizontal FRF summation functions (Figure 4.35), and the corresponding frequencies and mode shapes (Figure 4.36) of the PFFF set up as well as the baseline structure (for comparison) are presented.

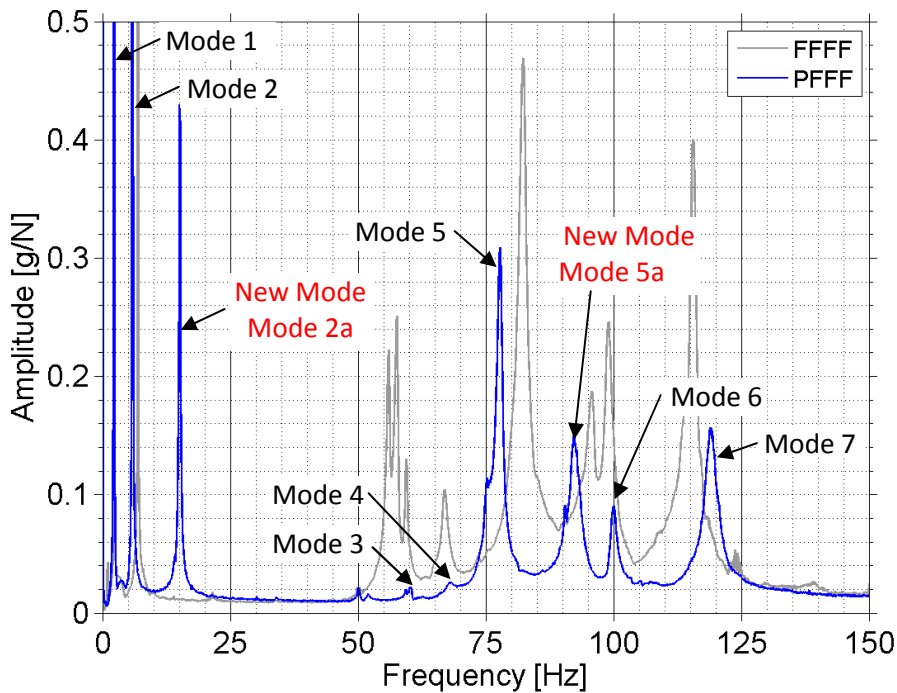


Figure 4.35 Horizontal FRF summation functions of baseline structure (FFFF) and structure with boundary configuration PFFF.

From the FRF and the mode shape figures it is observed that the global modes, mode 1 and mode 2, experience only minor changes. The natural frequency and the mode shape of mode 1 are essentially the same. For mode 2, the frequency decreases by 1.1 Hz and the shape of the upper half of the left column (where the joint was replaced) changes slightly. At 15.1 Hz a new frequency peak (mode 2a) emerges in the FRF of the modified structure constituting a local mode of the left upper column half, which was introduced by changing joint J1 to a pinned connection (see Figure 4.36). The shapes of mode 3 and mode 4, which are mainly local modes of the lower column halves, are very similar to the modes of the baseline structure with an increase in the frequencies of 4.1 Hz and 0.1 Hz, respectively. It is noted that the amplitudes in the FRF of these two modes are significantly lower. At 92.5 Hz a further new mode appears (mode 5a, see Figure 4.36), this mode is also a local mode of the upper left column half introduced by the pinned joint at J1. The basic modes 5 to 7 are all local modes of the upper column halves; hence, the mode shape deformations of the ‘damaged’ structure (PFFF) are different to the shapes of the baseline structure. Whereas modes 5 to 7 of the ‘undamaged’ structure (FFFF) show symmetric deformations, the structure with the pinned connection at J1 shows asymmetric mode behaviour.

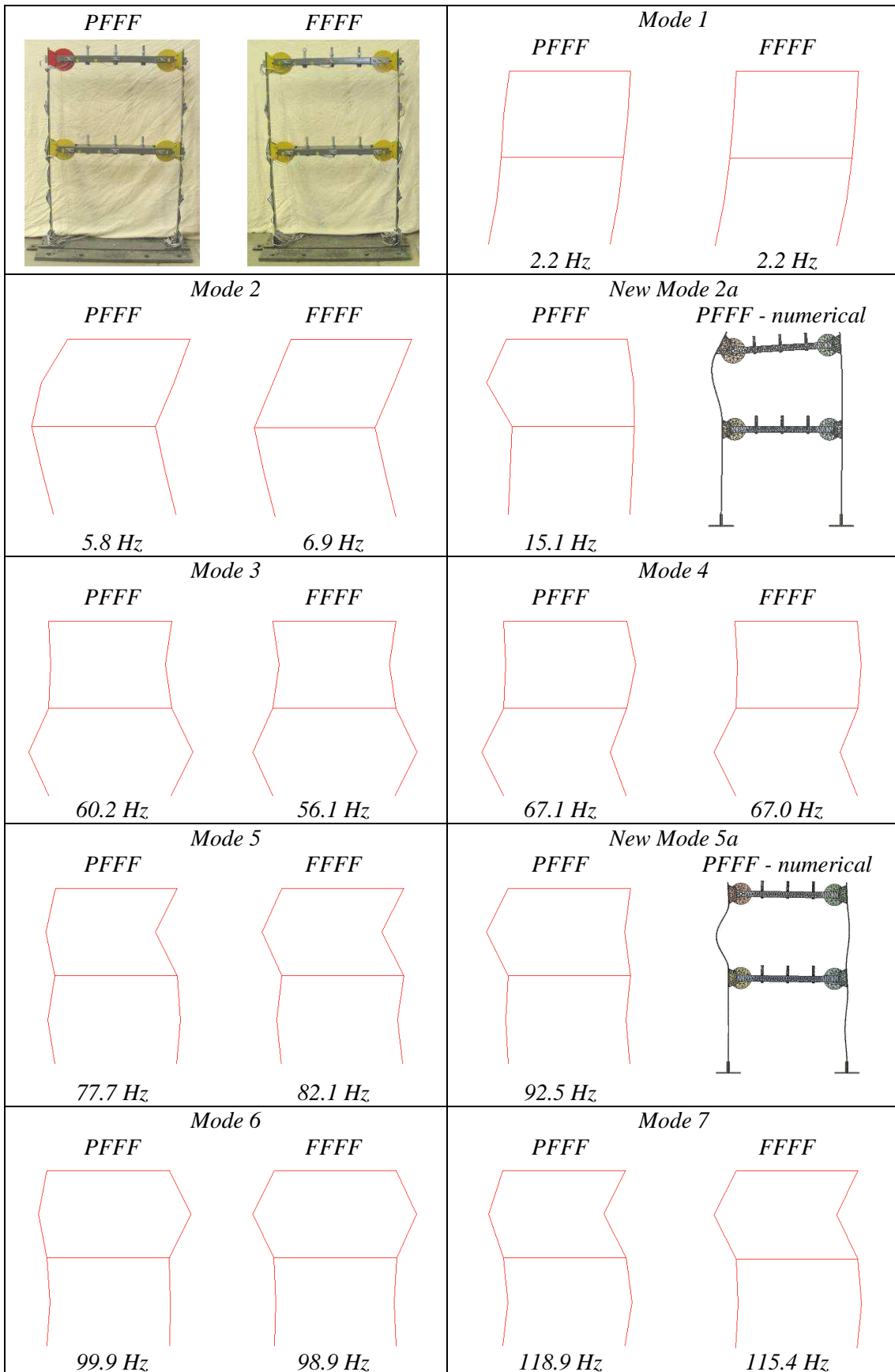


Figure 4.36 Mode shapes of two-storey framed structure with boundary configuration *PFFF* and baseline structure (*FFFF*).

As mentioned above, the natural frequencies of the modes change with varying boundary conditions. Table 4.9 lists the frequencies of the first seven flexural modes of the baseline structure and the frequencies of the corresponding modes of all boundary condition scenarios. In addition, Figure 4.37 displays the corresponding drops in frequencies of the boundary condition cases when compared against the baseline structure. From the table and the figure it can be seen that modes 3, 5 and 7 experience the biggest frequency changes. In the cases of modes 3 and 5, major mode shape changes also occur. Each boundary condition scenario shows individual changes in the structure’s dynamic characteristics. The reader is referred to APPENDIX B, which presents the horizontal FRF summation functions, natural frequencies and mode shapes of all changed boundary cases.

Table 4.9 Natural frequencies of the first seven flexural modes of the baseline structure and all boundary condition scenarios.

Natural frequencies [Hz]							
	Mode 1	Mode 2	Mode 3	Mode 4	Mode 5	Mode 6	Mode 7
Baseline	2.2	6.9	56.1	67.0	82.1	98.9	115.4
PFFF	2.2	5.8	60.2	67.1	92.5	99.9	118.9
FFFF	2.2	5.5	59.6	67.8	93.2	99.6	118.9
FFFP	1.8	5.7	63.4	70.0	85.9	98.4	104.8
FFFP	1.9	6.1	64.3	71.1	82.5	97.8	104.1
PPFF	1.5	3.9	55.4	66.4	87.9	95.7	107.6
FFPP	1.0	5.6	18.2	67.6	89.9	97.1	100.1
FPPF	1.9	5.7	21.8	62.9	90.0	92.7	105.0
PFPP	1.9	5.7	21.7	64.6	81.3	95.2	103.7
FPPF	1.1	5.4	19.9	70.0	81.9	94.1	103.4
PFFP	1.6	5.4	19.8	62.5	80.9	96.9	101.8

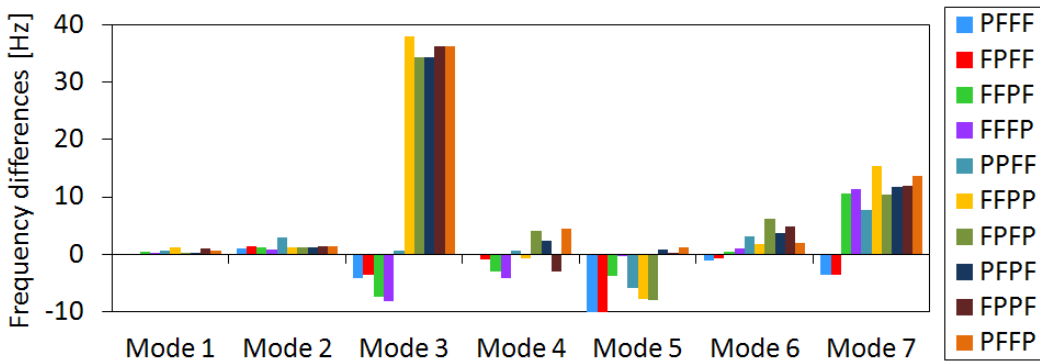


Figure 4.37 Drop in natural frequencies of all boundary condition scenarios.

Mass Changes

For the changed mass scenarios, the dynamic characteristics of the two-storey framed structure also change. These changes are, however, of smaller magnitude when compared to the boundary condition scenarios. From the FRFs of the changed mass cases (depicted in Figure 4.38 and Figure 4.39) variations in the frequency peaks are again visible. Here, however, the changes are restricted mainly to frequency shifting and amplitude change of the peaks. For the added mass cases of the lower crossbeam (see Figure 4.38), the seven mode shapes of the baseline structure remain almost the same with only small frequency changes. For the added mass scenarios of the upper beam, however, a new mode around frequency 50 Hz appears (mode 2a), which describes symmetric deformations of both upper column halves. The mode shape of the new mode is depicted for the experimental and the numerical structure (see CHAPTER 5) in Figure 4.40.

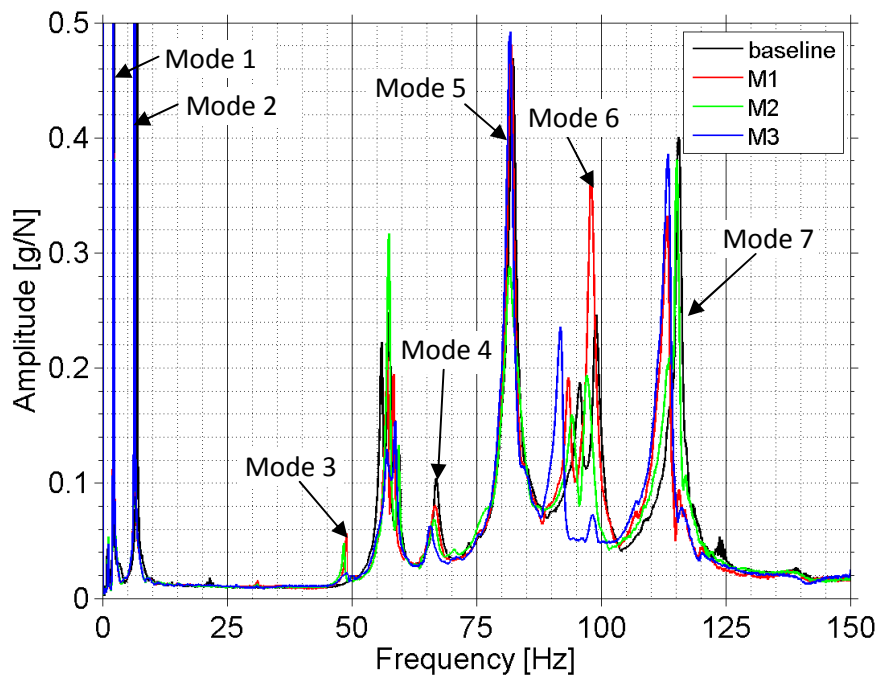


Figure 4.38 Horizontal FRF summation functions of baseline structure and structure with mass added to the lower crossbeam at locations M1, M2 or M3.

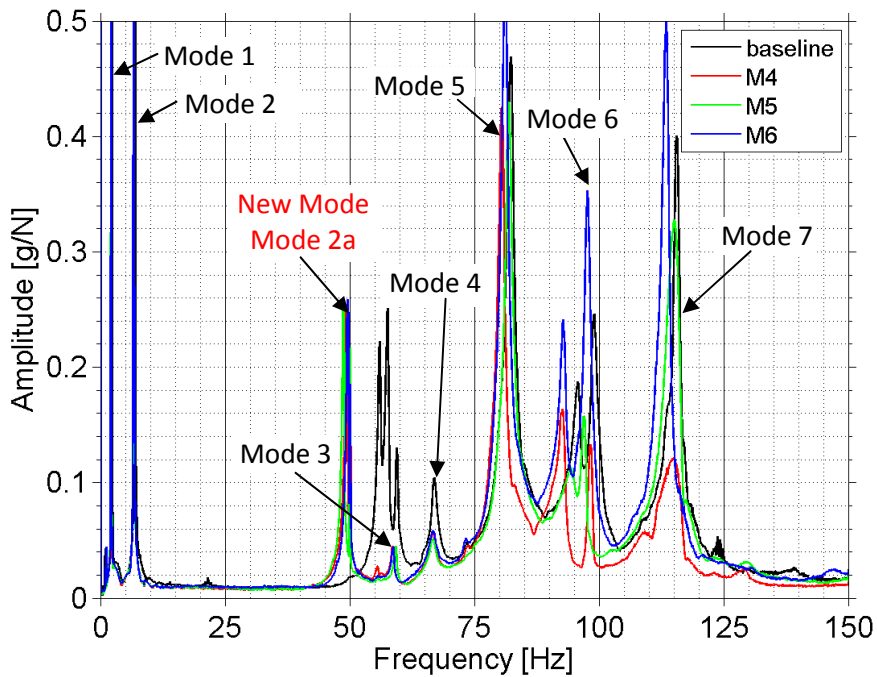


Figure 4.39 Horizontal FRF summation functions of baseline structure and structure with mass added to the upper crossbeam at locations M4, M5 or M6.

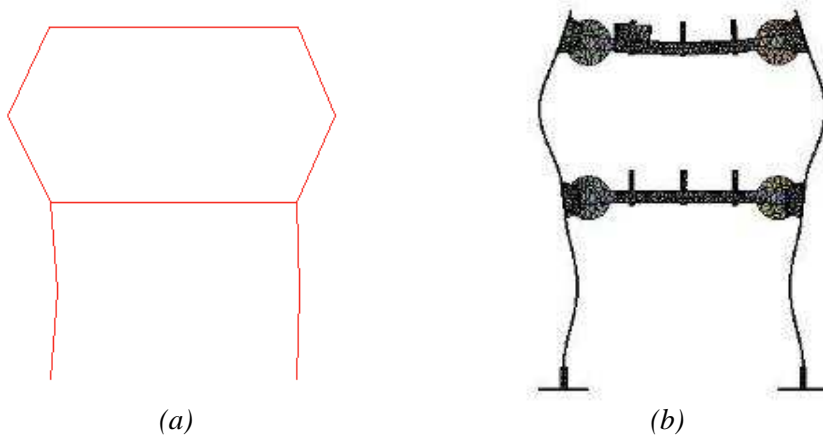


Figure 4.40 New mode (mode 2a) of the two-storey framed structure when mass is added to the upper crossbeam, (a) experimental and (b) numerical mode shape.

To compare the natural frequencies of the added mass cases against the frequencies of the baseline structure, a table listing all frequencies (see Table 4.10) and a graph displaying frequency changes (see Figure 4.41) are shown below. It is observed that for the first three modes, the frequencies of the added mass cases of the lower crossbeam are distinct from those of the upper crossbeam. This is especially visible for mode 3, which ranges between 48.3 Hz and 49.9 Hz for added mass cases of the lower crossbeam and between 58.3 Hz and 59.1 Hz for the upper crossbeam cases. The

dynamic characteristics (FRFs, frequencies and mode shapes) of all added mass scenarios are also presented in APPENDIX B.

Table 4.10 Natural frequencies of the first seven flexural modes of the baseline structure and all added mass scenarios.

Natural frequencies [Hz]							
	Mode 1	Mode 2	Mode 3	Mode 4	Mode 5	Mode 6	Mode 7
Baseline	2.2	6.9	56.1	67.0	82.1	98.9	115.4
M1	2.2	6.4	48.8	66.8	81.6	98.0	113.2
M2	2.2	6.4	48.3	66.4	81.6	97.6	115.1
M3	2.2	6.4	49.9	66.6	81.5	98.3	113.2
M4	2.1	6.6	58.3	66.6	80.2	98.2	114.5
M5	2.1	6.6	59.1	66.4	81.9	96.9	115.3
M6	2.1	6.6	58.5	66.4	80.7	97.6	113.4

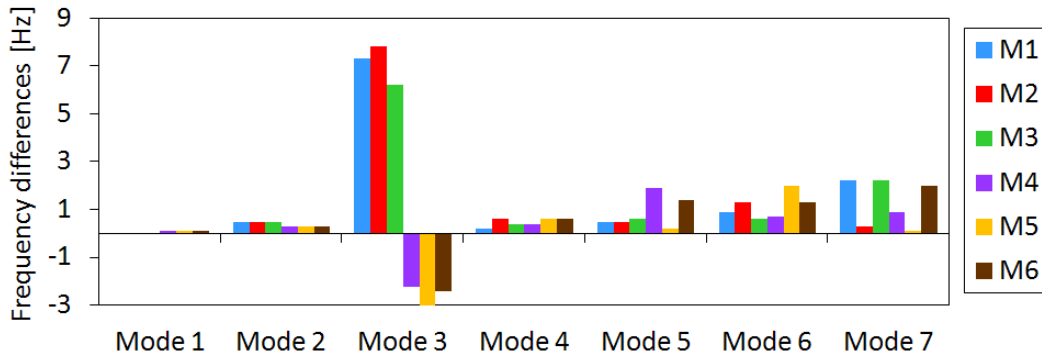


Figure 4.41 Drop in natural frequencies of all added mass scenarios.

Loss of Column Cross-Section

For the cross-section reduction cases, the dynamic properties change only slightly. From the horizontal FRF summation functions of the different saw cut scenarios (see Figure 4.42 and Figure 4.43), only small amplitude and frequency changes of the peaks are observed. Likewise, it was found that the mode shapes experience only minor alterations.

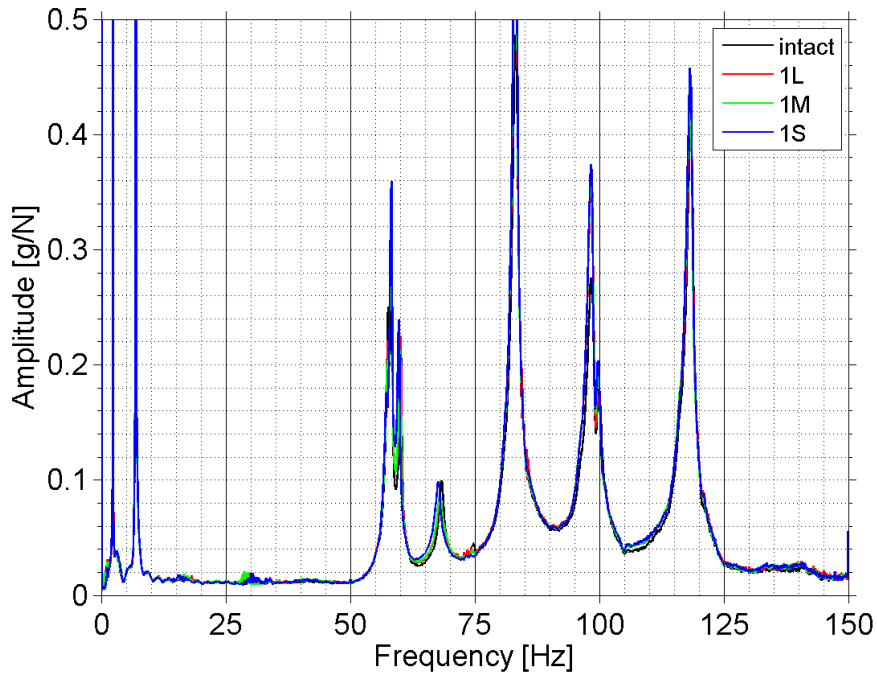


Figure 4.42 Horizontal FRF summation functions of baseline structure (intact) and structure with light, medium and severe cross-section reductions at location C1.

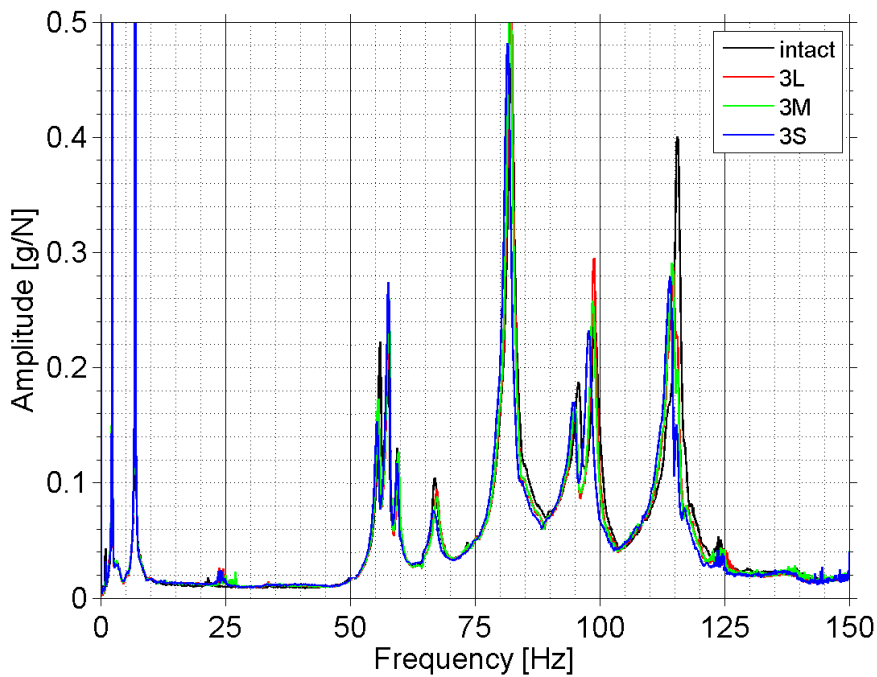


Figure 4.43 Horizontal FRF summation functions of baseline structure (intact) and structure with light, medium and severe cross-section reductions at location C3.

The frequencies of the different cross-section reduction cases and their corresponding baseline structures are shown in Table 4.11, and the related frequency drops are presented in Figure 4.44. It is observed that with increasing section loss the frequencies

consistently drop. Also, the natural frequencies change according to the shape of the mode. For example, for mode 7, which is a local mode of the upper two column halves, the frequencies of the structure damaged at location C3, which is located at the mid-span of the upper column halves, experience larger changes than for the damage cases of the lower column halves. Likewise, for mode 3, which is a local mode of the lower column halves, the frequencies of damage cases 1L, 1M and 1S drop by a larger value than the frequencies of cases 3L, 3M and 3S.

Table 4.11 Natural frequencies of the first seven flexural modes of the baseline structures and all section reduction scenarios.

Natural frequencies [Hz]							
	Mode 1	Mode 2	Mode 3	Mode 4	Mode 5	Mode 6	Mode 7
Baseline2	2.3	6.9	60.5	68.3	83.1	98.8	118.2
1L	2.3	6.9	59.9	68.0	83.1	98.6	118.1
1M	2.3	6.8	59.9	68.0	83.1	98.4	118.0
1S	2.3	6.8	59.6	67.6	83.1	98.2	118.0
Baseline1	2.2	6.9	56.1	67.0	82.1	98.9	115.4
3L	2.2	6.9	55.6	67.2	82.1	98.7	114.6
3M	2.2	6.9	55.6	67.2	82.0	98.5	114.5
3S	2.2	6.9	55.3	66.6	81.7	97.7	114.1

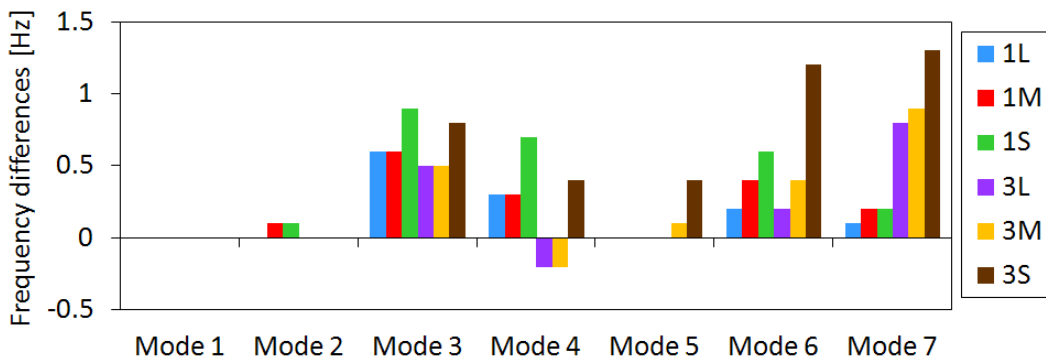


Figure 4.44 Drop in natural frequencies of all section reduction scenarios.

4.5 SUMMARY

This chapter presented MT&EMA procedures and results of the two test structures (the beam and the two-storey framed structure). Some background information on MT&EMA techniques were given. The test structures and different damage/added mass cases were presented and modal testing procedures described. The modal tests were successfully executed and from the modal analysis results it was observed that the modal parameter and the FRFs of the different damage/added mass cases changed

according to the damage/added mass scenario, damage/added mass location and damage severity.

For the steel beam structure, the following was observed:

- In the FRFs of the different damage scenarios, the frequency peaks shifted and the peak amplitudes changed. Increasing damage severities caused a shift of the frequency peaks towards the lower end of the frequency spectrum.
- The natural frequencies generally dropped with increasing damage size. In addition, it was noticed that the drop was larger for the higher modes. When damage was located at a node point of a mode, no or only minor frequency changes occurred for that mode.
- Small changes in the mode shapes were observed. The differences of mode shape vectors were the largest in the vicinity of the damage and increased with increasing damage size.
- Damping ratio changes showed inconsistent trends.

For the two-storey framed structure, the following was noticed:

- The FRFs responded significantly to changes of boundary conditions, such as displaying new patterns with new frequency peaks emerging and others disappearing. For the added mass cases, FRF features changed slightly. Whereas the added mass scenarios of the upper crossbeam caused the appearance of a new frequency peak, no additional peak emerged for added mass cases of the lower beam. The cross-section reductions of the column caused only minor changes in the FRF.
- For the natural frequencies, a general drop in frequencies was observed for all three damage/added mass changes. The first and second natural frequencies (global modes) experienced only minimal changes, whereas the higher frequencies (local modes) generally decreased more markedly.
- The mode shapes responded to alterations of the different boundary condition scenarios significantly. New mode shape deformations were introduced by the modified joint conditions from rigid fixed to fully pinned. Each boundary condition scenario exhibited unique mode shape patterns. For the added mass cases, a new mode shape having local deformations at the two upper column halves appeared for added mass scenarios of the upper crossbeam. No visible mode shape changes were observed for the cross-section reduction cases.

CHAPTER 5

FINITE ELEMENT MODELLING

5.1 INTRODUCTION

This chapter presents the finite element modelling of the beam structure and the two-storey framed structure to represent the laboratory structures described in the previous chapter. Numerical models are created in order to generate vibrational data for thorough investigation of the proposed damage identification method without uncertainties from experimental imperfections (i.e. manufacturing faults, laboratory testing inaccuracies and signal processing disturbances). A numerical model allows the study of a multitude of damage scenarios without being significantly more labour intensive (compared to laboratory testing). Further, by polluting numerical data with different levels of noise (to simulate real testing), thorough investigations on the influence of measurement noise can be undertaken.

In this chapter, for each test structure (the beam structure and the two-storey framed structure), the finite element modelling of the baseline structures using ANSYS Classic and ANSYS Workbench are first presented. Second, the modelling of the different damage/added mass scenarios is described. Third, procedures on the execution of transient analysis with subsequent noise pollution and modal parameter extraction are explained. Fourth, a correlation analysis based on natural frequencies and mode shapes is conducted to validate the numerical models. Fifth, the derived dynamic properties of the baseline structures are described and their changes due to structural modification presented.

5.2 NUMERICAL MODELLING OF BEAM STRUCTURE

5.2.1 Finite Element Modelling of Intact Beam

To create a numerical model of the tested laboratory steel beams (see section 4.3), the commercial finite element (FE) analysis package ANSYS Classic (ANSYS Inc 2007a) is used. The dimensions of the numerical beam model are based on the measurements of

the laboratory beams: 12 mm wide by 32 mm high by 2,400 mm long. The element type used is SOLID45, which is an orthotropic three-dimensional structural solid defined by eight nodes having translations in the nodal x , y and z directions. This element is chosen as it is recommended by ANSYS Classic documentation (ANSYS Inc 2007c) for three-dimensional modelling of solid structures and because saw-cut damage can easily be modelled for this element. The geometric properties of element type SOLID45 are illustrated in Figure 5.1.

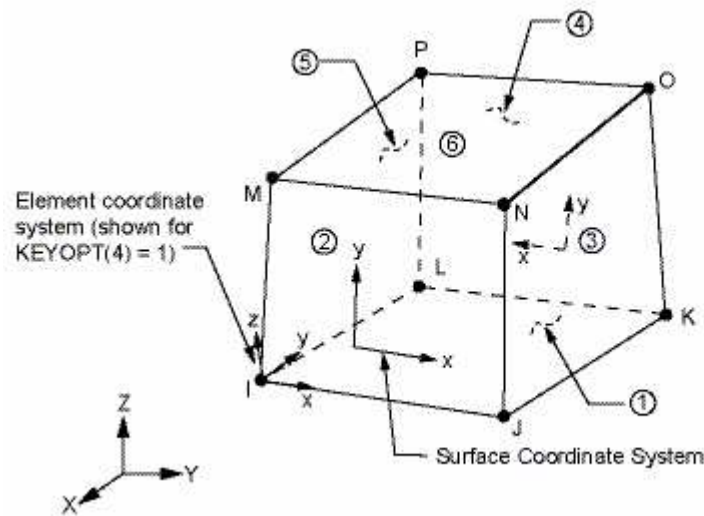


Figure 5.1 Geometric properties of SOLID45 (ANSYS Inc 2007c).

The cross-section of the beam is modelled with 4 elements across the height (8 mm each element) and 4 elements along the width (3 mm each element). A division into 201 nodes and 200 elements (12 mm each element) in the longitudinal direction of the model is chosen in accordance with previous sensitivity studies undertaken by Choi et al. (2007). In total, the FE model consists of 5,025 nodes and 3,200 elements. With this mesh configuration, the beam model has 15,075 degrees of freedom (DOF). According to the manufacturer's specifications of the laboratory steel beams, the modulus of elasticity is set to $200,000 \times 10^6 \text{ N/m}^2$, the Poisson's ratio to 0.3 and the density to $7,850 \text{ kg/m}^3$. The support conditions are set as pin-pin. A schematic model of the numerical beam is shown in Figure 5.2.

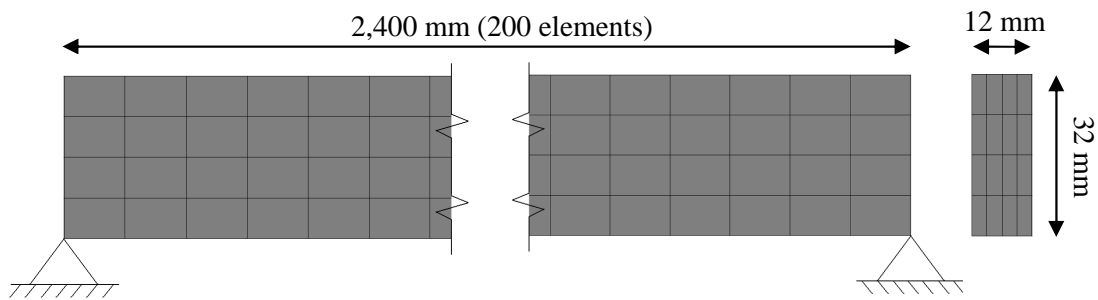


Figure 5.2 Finite element modelling of a pin-pin supported steel beam.

5.2.2 Simulation of Damage in Beam Model

For the numerical model, the same damage scenarios are studied as for the laboratory beams, which are 16 notch type damage cases of four locations and four severities. The four different damage locations are again situated at $4/8^{\text{th}}$, $5/8^{\text{th}}$, $6/8^{\text{th}}$ and $7/8^{\text{th}}$ of the beam length (denoted as '4', '5', '6' and '7') and the four different damage severities correspond to a loss of the second moment of area, I , of 9.09%, 33.01%, 57.81% and 75.59% (termed as extra light (XL), light (L), medium (M) and severe (S)). The damage locations are illustrated in Figure 5.3.

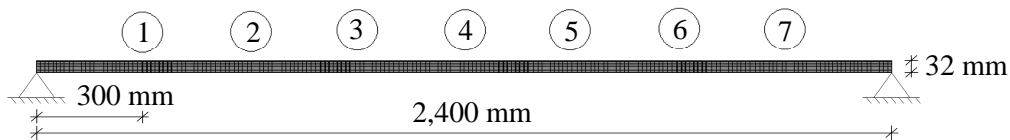


Figure 5.3 Damage locations of numerical beam model.

The inflicted damage cases are notch types of 1 mm in length and 1 mm, 4 mm, 8 mm and 12 mm in height. Damage is modelled by rectangular openings from the soffit of the beam. The mesh density is refined in the vicinity of the defect, as displayed in Figure 5.4.

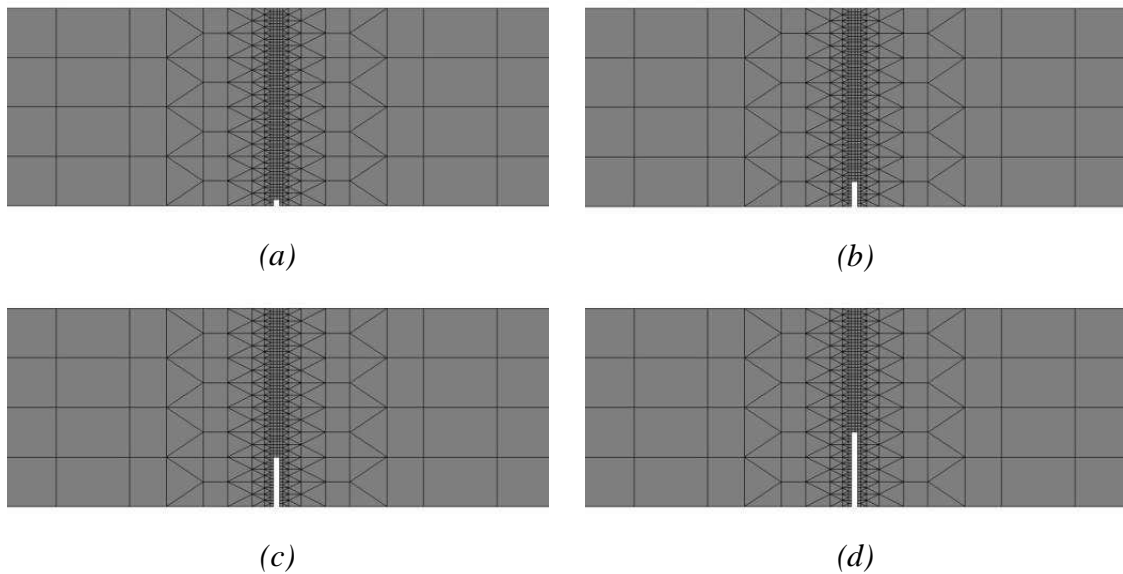


Figure 5.4 Finite element modelling of damage with a width of 1 mm and varying heights of (a) 1 mm, (b) 4 mm, (c) 8 mm and (d) 12 mm.

5.2.3 Transient Analysis and Noise Pollution

From the numerical beam models, vibrational characteristics are acquired from two types of data, i.e. noise-free and noise-polluted data. Noise-free data are used to investigate the performance of the proposed DI-based damage identification method on directly extracted mode shape data without uncertainties from experimental modal analysis and measurement noise. Noise-polluted data are used to simulate real testing conditions and to study the influence of noise and modal extraction errors on both proposed damage identification methods. For noise-free data, the modal parameters are directly extracted from the numerical models by solving the eigenvalue problem using the modal analysis module in ANSYS Classic. By directly solving the eigenvalue problem, only natural frequencies and mode shapes are extracted but not the frequency response functions (FRFs). However, for the proposed DI-based damage identification method, only mode shape vectors are of interest and it is therefore sufficient to directly solve the eigenvalue problem.

The following overview describes the steps undertaken to generate dynamic properties from noise-polluted data. First, transient analysis is performed using ANSYS Classic. By executing transient analysis, response time history data of the beam models under impulse loading are generated. Second, the impact loading and response time histories from the transient analysis are polluted with different levels of white Gaussian noise.

Third, the noise-polluted time history data are transformed into the frequency spectrum, generating FRF data. Last, by performing experimental modal analysis, the modal parameters of the beams are determined. The procedure of generating vibrational characteristics from numerical noise-polluted data is illustrated in Figure 5.5.

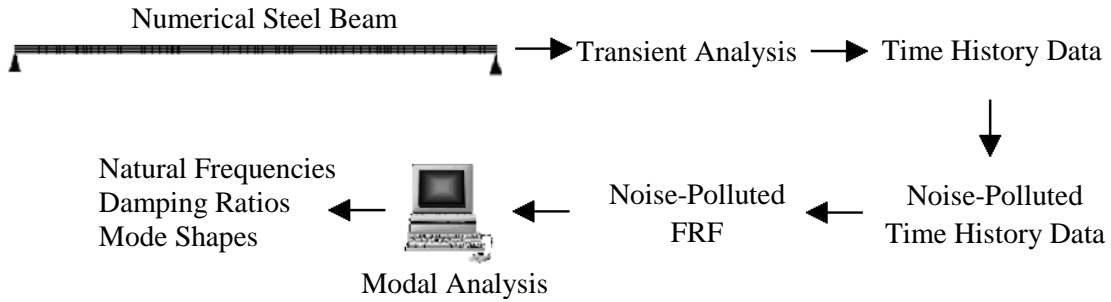


Figure 5.5 Generation of noise-polluted numerical data with subsequent determination of the modal parameters.

As described above, in order to generate noise-polluted numerical data, transient analysis is performed to obtain response time histories for the beam models. In general, transient analysis is a numerical technique that is used to determine the dynamic response of a structure under the action of any general time-dependent load. It can be used to determine time-varying displacements, strains, stresses and forces in a structure as it responds to any combination of static and transient loads. A simple formulation of the technique is given below (ANSYS Inc 2007c).

The basic equation of motion solved by transient dynamic analysis is:

$$M \ddot{y}(t) + C \dot{y}(t) + K y(t) = f(t) \quad (5.1)$$

where M is the mass matrix, C the damping matrix, K the stiffness matrix, y the nodal displacement vector, \dot{y} the nodal velocity vector, \ddot{y} the nodal acceleration vector and $f(t)$ the load vector. At any given time, t , equation (5.1) can be thought of as a 'static' equilibrium equation that also takes into account inertia forces $M \ddot{y}(t)$ and damping forces $C \dot{y}(t)$. In this study, the Newmark time integration method is used to solve equation (5.1) at discrete time points. The Newmark method uses finite difference expansions in the time interval Δt , in which it is assumed that:

$$\dot{y}(t+1) = \dot{y}(t) + \left[(1-\delta) \ddot{y}(t) + \delta \ddot{y}(t+1) \right] \Delta t \quad (5.2)$$

$$y(t+1) = y(t) + \dot{y}(t)\Delta t + \left[\left(\frac{1}{2} - \alpha \right) \ddot{y}(t) + \alpha \ddot{y}(t+1) \right] \Delta t^2 \quad (5.3)$$

where α and δ are Newmark integration parameters. Since the primary aim is the computation of displacement $y(t+1)$, the governing equation (5.1) is evaluated at time $t+1$ as:

$$M \ddot{y}(t+1) + C \dot{y}(t+1) + K y(t+1) = f(t) \quad (5.4)$$

The solution for the displacement at time $t+1$ is obtained by first rearranging equations (5.2) and (5.3) such that:

$$\ddot{y}(t+1) = a_0 [y(t+1) - y(t)] - a_2 \dot{y}(t) - a_3 \ddot{y}(t) \quad (5.5)$$

$$\dot{y}(t+1) = \dot{y}(t) + a_6 \ddot{y}(t) - a_7 \ddot{y}(t+1) \quad (5.6)$$

with $a_0 = \frac{1}{\alpha \Delta t^2}$, $a_2 = \frac{1}{\alpha \Delta t}$, $a_3 = \frac{1}{2\alpha} - 1$, $a_6 = \Delta t(1 - \delta)$ and $a_7 = \delta \Delta t$. Noting that

$\ddot{y}(t+1)$ in equation (5.5) can be substituted into equation (5.6), equations for $\ddot{y}(t+1)$ and $\dot{y}(t+1)$ can be expressed in terms of only one unknown, $y(t+1)$. The equations for $\ddot{y}(t+1)$ and $\dot{y}(t+1)$ are then combined with equation (5.4) to form:

$$(a_0 M + a_1 C + K) y(t+1) = \dots \quad (5.7)$$

$$f(t) + M [a_0 y(t) + a_2 \dot{y}(t) + a_3 \ddot{y}(t)] + C [a_4 y(t) + a_4 \dot{y}(t) + a_5 \ddot{y}(t)]$$

with $a_1 = \frac{\delta}{\alpha \Delta t}$, $a_4 = \frac{\delta}{\alpha} - 1$, $a_5 = \frac{\Delta t}{2} \left(\frac{\delta}{\alpha} - 2 \right)$

Once a solution is obtained for $y(t+1)$, velocities and accelerations are updated as described in equations (5.5) and (5.6).

For the beam structure, transient analysis is performed for the intact beam and all damaged beam models. As a solution method, the 'full method' is chosen in ANSYS Classic, which uses the full system matrices to calculate the transient responses (ANSYS Inc 2007c). A force of 800 N, which is a typical impact force observed from experimental hammer excitation, is applied at a reference point (here at location '3'; see

Figure 5.3). The loading curve of the impact hammer is illustrated in Figure 5.6 (a). The response time histories of the beam are recorded at nine equally spaced points, which represent the measurement sensors from experimental testing (see section 4.3.1). To resemble the sampling rate from laboratory testing, the total number of time steps is set to 16,385 with an integration time step of 0.0001 s (giving a total record time of 1.6385 s). A proportional damping model is adopted in the numerical calculation in which damping is specified by the mass matrix multiplier for damping ALPHAD and the stiffness matrix multiplier for damping BETAD. The specific values for ALPHAD and BETAD are calculated for each beam based on the damping values determined from experimental testing, which are presented in Table 4.3. As an example, the generated displacement response time history from location ‘5’ of an intact beam is shown in Figure 5.6 (b).

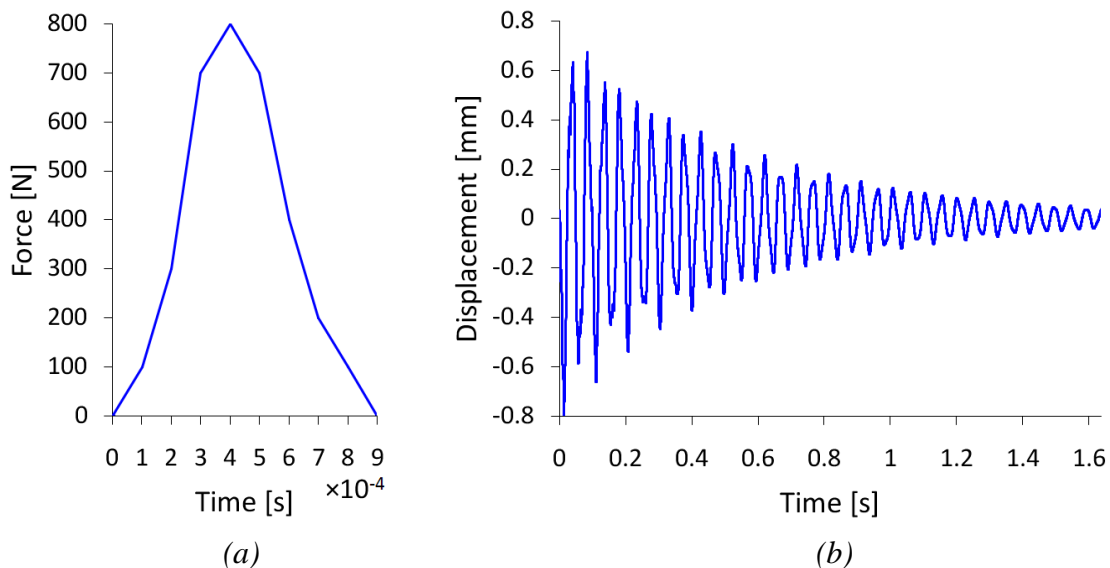


Figure 5.6 (a) Hammer impact force and (b) displacement response time history of location ‘5’ of the beam structure.

To simulate measurement noise interferences experienced during experimental testing, acceleration data is polluted with noise. First, acceleration time histories are calculated from the displacement time histories obtained from ANSYS by double differentiation. Then, white Gaussian noise of four intensities (i.e. 1%, 2%, 5% and 10% noise-to-signal-ratio) is added to both the impact force signal and the acceleration response time histories. The Matlab function *awgn* (The MathWorks 2009a) with the noise-to-signal-ratio function $20 \log_{10}(\text{ratio})$ is used to calculate noise-polluted data for the ratios of 0.01, 0.02, 0.05 and 0.1, which correspond to the noise intensity levels of 1%, 2%, 5%

and 10%, respectively. For each level of noise, three sets of noise-contaminated data are generated to simulate three repeated tests.

Next, the noise-polluted acceleration time history data are transformed into the frequency spectrum using the Fast Fourier Transform (FFT). The FRFs are estimated by dividing cross-spectra between the input and output with auto-spectra of the input (see section 4.2.2). In order to capture the first seven vibrational modes and to synchronise the frequency resolution of the numerical simulations with the resolution obtained from experimental testing, FRFs are generated which comprise 1638 spectral lines in a frequency range of 0-1000 Hz with a frequency resolution of 0.61 Hz. Next, the modal parameters of the first seven flexural modes are identified by performing experimental modal analysis (EMA) procedures using the same software as for laboratory testing (i.e. LMS CADA-X) (see section 4.2.3). Therefore, the generated FRFs are imported into CADA-X and, by using the frequency direct parameter identification (FDPI) method (see section 4.2.3), the modal parameters are extracted from the FRFs.

5.2.4 Dynamic Characteristics of the Numerical Beam Structure

Correlation Analysis and Dynamic Characteristics of the Undamaged Numerical Beam Structure

To validate the numerical beam model, a correlation analysis between numerical and experimental beam data is conducted for the undamaged beam. In general, correlation analysis is a technique to examine quantitatively and qualitatively the correspondence and difference between analytically and experimentally obtained modal parameters (Brownjohn & Xia 1999). This analysis gives a platform for modal parameter selection related to dynamic responses for modal updating. In this study, dynamic responses, namely natural frequencies and mode shapes, are used as the indices for the objective function (*OF*) for the correlation analysis. The goal of updating or calibrating the numerical model is to minimise the objective function. The global objective function used is given as:

$$OF = f(NError, MACError) \quad (5.8)$$

with *NError* being the error function for natural frequencies and *MACError* the error function for mode shape vectors (both functions are discussed below).

For natural frequencies, the relative error (*NError*) between frequencies obtained from numerical simulations and experimental testing is used to check their correlation. The *NError* function is given as:

$$NError = \frac{|\omega_{Exp} - \omega_{Num}|}{\omega_{Exp}} \times 100 \quad (5.9)$$

where ω_{Exp} is the natural frequency of the experimental structure and ω_{Num} the frequency of the numerical model. The *NError* values of the natural frequencies of the first seven flexural modes are listed in Table 5.1. Next to the *NError* values, also displayed are the actual frequencies of the numerical model (from noise-free data) and of the experimental test beams, as well as the absolute differences between numerically and experimentally obtained frequencies. From the table, it is noted that the *NError* values are in general less than 9%, except for mode 2. Overall, it is concluded from Table 5.1 that the natural frequency values match very well and that the numerical model is able to represent the experimental model well in that regard.

Table 5.1 Comparison of natural frequencies between numerical and laboratory beam.

	Mode 1	Mode 2	Mode 3	Mode 4	Mode 5	Mode 6	Mode 7
Numerical beam [Hz]	20.55	51.98	128.08	205.89	334.21	452.46	631.88
Laboratory beam [Hz]	20.99	40.14	126.67	216.29	305.18	471.74	613.42
Absolute difference [Hz]	0.44	11.84	1.41	10.40	29.03	19.28	18.46
<i>NError</i> [%]	2.14	22.78	1.10	5.05	8.69	4.26	2.92

For the mode shape vectors, the Modal Assurance Criterion (*MAC*) is adopted for comparison between the numerical and experimental mode shapes. *MAC* is one of the most popular measures for correlating two sets of mode shapes (Allemang & Brown 1982). This parameter provides a measure of the least-squares deviation of the points from the straight-line correlation. The *MACError* uses *MAC* values for indicating the correlation between numerical and experimental model results, as given in:

$$MACError(\varphi_{Exp}, \varphi_{Num}) = 1 - \frac{(\varphi_{Exp}^T \varphi_{Num})^2}{(\varphi_{Exp}^T \varphi_{Exp})(\varphi_{Num}^T \varphi_{Num})} \quad (5.10)$$

with φ_{Exp} being the mode shape vector of the experimental structure and φ_{Num} the mode shape vector of the numerical model. A *MACError* value close to 1 indicates poor

correlation between the mode shapes, whilst a value close to 0 indicates good correlation. The extent of calibration can be determined through evaluating the change in the correlation between the mode shapes. Table 5.2 lists *MAC* and *MACError* in actual values and percentages for experimental and numerical mode shapes. (For the numerical model, mode shape vectors of noise-free data of nine data points are used, which are the locations of the nine measurement sensors in experimental testing, see section 4.3.1.) For visualisation, the extracted mode shapes derived from the eigenvalue solution of the numerical model are illustrated in Figure 5.7.

Table 5.2 Mode shape correlation between numerical and laboratory beams.

	Mode 1	Mode 2	Mode 3	Mode 4	Mode 5	Mode 6	Mode 7
<i>MAC</i>	0.9987	0.9985	0.9690	0.9585	0.9648	0.9605	0.9868
<i>MAC</i> [%]	99.87	99.85	96.90	95.85	96.48	96.05	98.68
<i>MACError</i>	0.0013	0.0015	0.0310	0.0415	0.0352	0.0395	0.0132
<i>MACError</i> [%]	0.13	0.15	3.10	4.15	3.52	3.95	1.32

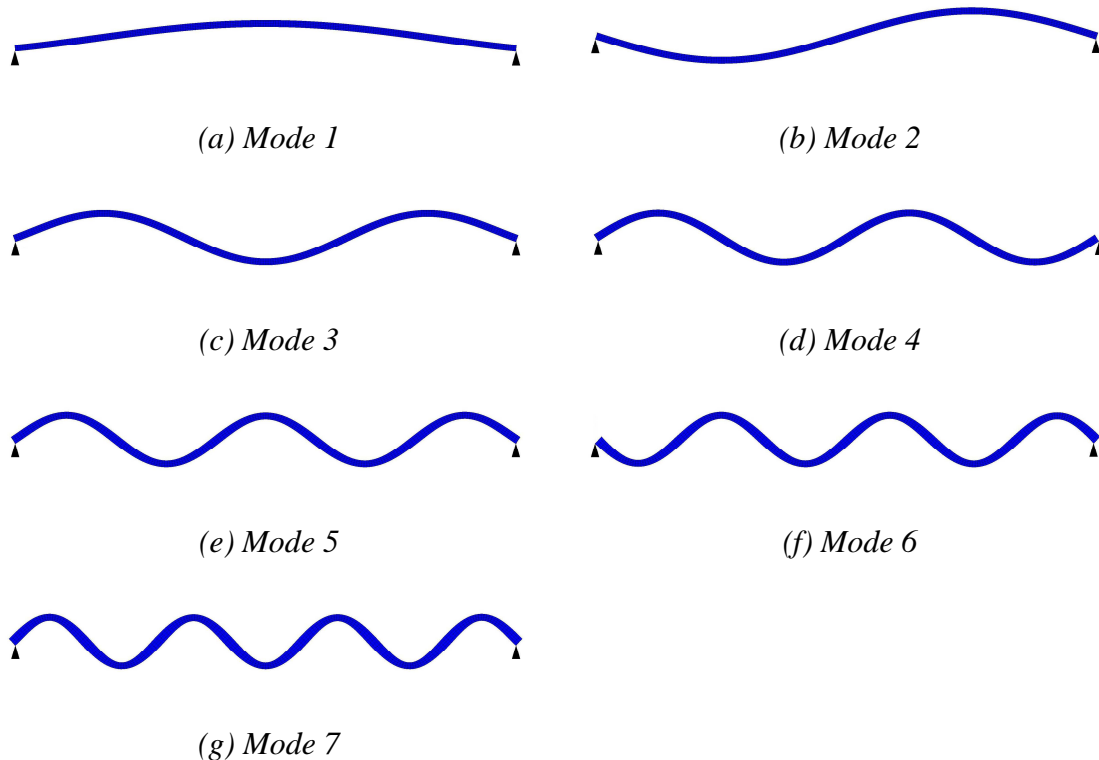


Figure 5.7 First seven flexural mode shapes of numerical beam model derived from the eigenvalue solution.

As can be seen from Table 5.2, for all seven modes, the *MACError* values are below 5%. This means that both sets of mode shapes match very well. (*MACError* values of less than 10% (or 90% for *MAC*) are considered acceptable according to Brownjohn and Xia (1999) and Maia et al. (1997).) For the first two modes, the *MACError* values are extremely low with values of 0.13% and 0.15%. The slightly higher *MACError* values of modes 3 to 7 are caused by the ‘uplifting motion’ at the beam-ends of the experimental beams due to resonance interferences of the supports (see section 4.3.3). These mode shape discrepancies are, however, only of small magnitude and therefore cause only small *MACError* values.

From the results of the *NError* and *MACError* values, it is inferred that the numerical model simulates the experimental model quite well. Therefore, this numerical model can be used in this study as a representation of the experimental beam structures for application of the proposed damage identification methods.

From the validated numerical model, the natural frequencies and mode shapes are determined either from the eigenvalue solution (for noise-free numerical data) or from results of transient analysis and EMA (for noise-polluted numerical data) (see above). To compare the extracted resonance frequencies derived from the eigenvalue solution against those generated from transient analysis and EMA, Table 5.3 lists the frequency values of the first seven flexural modes for noise-free and noise-polluted data. From the table, it is noted that natural frequencies generated from the eigenvalue solution (data of 0% noise pollution) almost perfectly match with the frequencies obtained from transient analysis and EMA (data of 1% to 10% noise pollution). The minor discrepancies, which are smaller than 0.1 Hz, result from experimental modal analysis errors and uncertainties from noise contamination of the noise-polluted data.

Table 5.3 Comparison of natural frequencies [Hz] of numerical beams.

	Mode 1	Mode 2	Mode 3	Mode 4	Mode 5	Mode 6	Mode 7
Noise pollution 0%	20.55	51.98	128.08	205.89	334.21	452.46	631.88
Noise pollution 1%	20.55	51.96	128.08	205.89	334.22	452.45	631.90
Noise pollution 2%	20.54	51.96	128.08	205.89	334.24	452.49	631.87
Noise pollution 5%	20.51	51.99	128.08	205.90	334.25	452.39	631.78
Noise pollution 10%	20.59	51.95	128.10	205.82	334.12	452.39	631.79

For FRFs, Figure 5.8 displays the FRF summation functions of the undamaged beam model generated from transient analysis of data with 1% noise pollution (Figure 5.8 (a)) and data with 10% noise pollution (Figure 5.8 (b)).

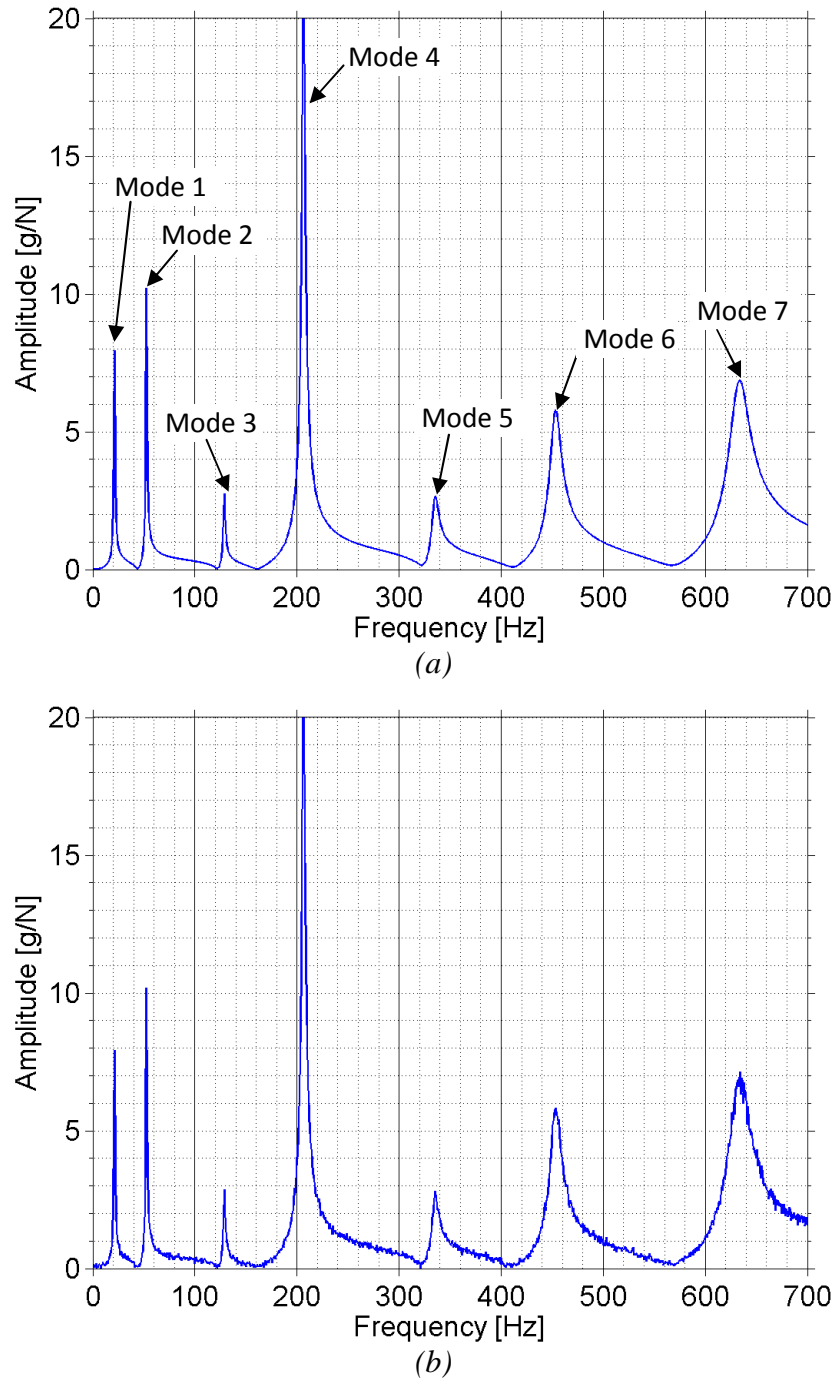


Figure 5.8 FRF summation function of undamaged numerical beam of (a) 1% noise-polluted data and (b) 10% noise-polluted data.

From the figure, clear indications of the first seven flexural modes are visible. Whereas for the FRFs of the laboratory beams, frequency peaks of other modes (e.g. torsional or

transverse modes) are also observed (see section 4.3.3); for the numerical simulations, only the flexural modes are indicated. (In laboratory testing, it is extremely difficult to avoid the appearance of non-flexural modes in the FRF data due to inaccuracies resulting from the hammer hit, which cannot be carried out in a perfectly straight manner, as well as from manufacturing imperfections of the test structure and its supports.) From Figure 5.8 (b), the effect of noise pollution on the generated FRF summation function is clearly visible. It is noted that these irregularities in the FRF increase with ascending frequency.

Dynamic Characteristics of the Damaged Numerical Beams

For the different damage scenarios of the numerical beam models, changes in the dynamic properties are observed. Similar to the results of the experimental beams, the natural frequencies drop when damage is inflicted. The first seven captured flexural frequencies of all 16 damage cases and the undamaged beam are listed in Table C.1 (APPENDIX C). Graphs illustrating the change of natural frequency due to damage are also shown in Figure C.1 (APPENDIX C). As an example, listed in Table 5.4 are the natural frequencies of a beam damaged at location ‘4’ with four severities (extra-light to severe, denoted at ‘4XL’ to ‘4S’); also listed are the frequencies of the undamaged beam for comparison. The corresponding illustration of the differences in frequencies is shown in Figure 5.9. From the table and the figure, the frequencies are observed to drop according to the severity of the damage (i.e. the larger the damage size, the larger the frequency reduction). In the numerical simulations, the modelled beam structure has perfect measures; therefore, for damage at location ‘4’, which is a node point for modes 2, 4 and 6, the natural frequencies have zero change for these modes, as demonstrated in Figure 5.9.

Table 5.4 Natural frequencies [Hz] of the first seven flexural modes of the intact state and all damaged states of a beam damaged at location ‘4’.

Natural frequencies [Hz]							
	Mode 1	Mode 2	Mode 3	Mode 4	Mode 5	Mode 6	Mode 7
Undamaged	20.55	51.98	128.08	205.89	334.21	452.46	631.88
4XL	20.55	51.98	128.05	205.89	334.20	452.46	631.77
4L	20.55	51.98	127.77	205.89	333.79	452.46	630.37
4M	20.52	51.98	126.70	205.89	332.36	452.46	625.95
4S	20.47	51.98	124.63	205.89	329.94	452.46	618.00

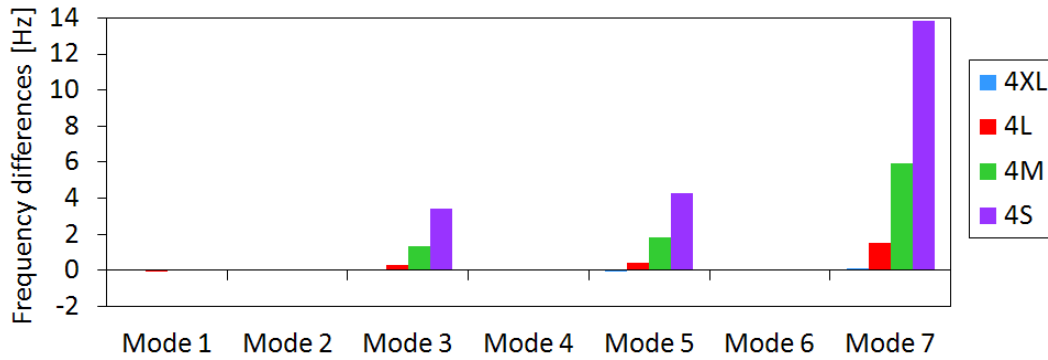
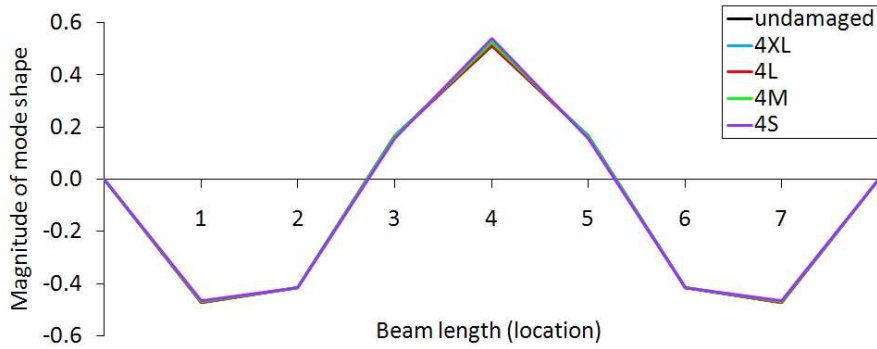
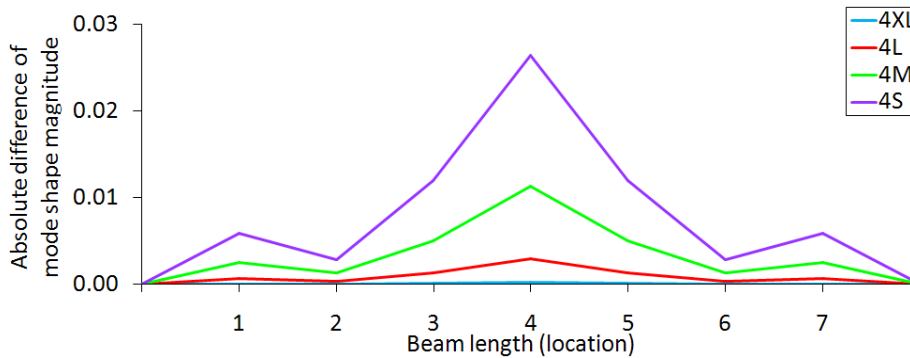


Figure 5.9 Comparison of reduction in natural frequencies of the numerical beam model of different severities of damage at location ‘4’.

As with natural frequencies, mode shapes also change when damage is inflicted. For example, Figure 5.10 displays mode shapes (Figure 5.10 (a)) and absolute mode shape differences (Figure 5.10 (b)) of mode 3 of a numerical beam damaged at location ‘4’ with various damage severities. From the figure, changes of the mode shape vectors are clearly visible. The high sensitivity of mode shapes to local damage is again noted from Figure 5.10 (b), which shows the largest mode shape differences in the vicinity of the damage, i.e. near location ‘4’. Further, a progressive change in the mode shapes is observed with increasing damage size. Moreover, it is noted that for extra-light damage, the mode shape shows hardly any change. This finding indicates that the detection of extra-light damage might lead to complications in identifying damage based on mode shape changes (e.g. damage identification with the first proposed method, which is based on changes in mode shape curvatures).



(a) Mode shape of mode 3 of a numerical beam damaged at location '4'



(b) Absolute mode shape differences of mode 3 of a beam damaged at location '4'

Figure 5.10 (a) Mode shapes and (b) absolute mode shape differences of mode 3 of a numerical beam damaged at location '4' with various damage severities.

FRFs are the third vibrational characteristics of interest. Being direct derivatives from transient analysis, numerically obtained FRF data demonstrate high sensitivity to any kind of structural change. As can be seen from Figure 5.11 and Figure 5.12, which illustrate FRF summation functions of the intact beam and of different damage scenarios, a clear change in the frequency peaks of FRF data is observed. From Figure 5.11, which displays the effects of different damage severities on FRF data (damage at location '5' of sizes extra-light to severe), it is noted that with increasing damage extent a gradual increase in amplitude and a leftward shift of the frequency peaks occur. The gradual leftward shift of the frequency peaks confirms the earlier finding of a reduction in natural frequencies for advancing damage. It is further noted that for extra-light damage, the FRF data experiences hardly any change (see Figure 5.11 (b)). A similar observation was made when studying the effects of damage on mode shape vectors (see above). For Figure 5.12, which displays the impact of different damage locations on FRF data, a change in frequency peaks is also observed. However, similar to the findings of the experimental beams, no general trend can be observed.

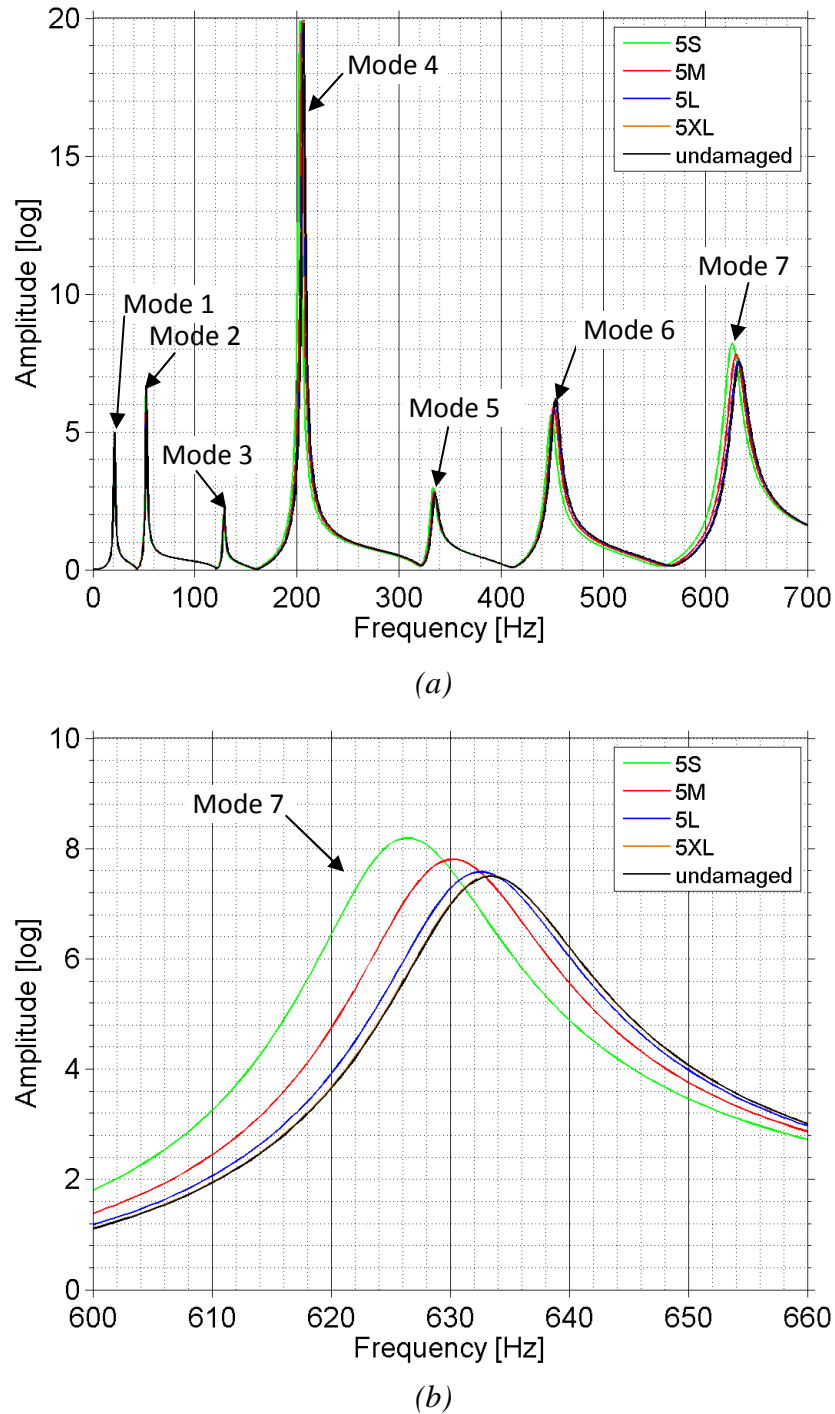


Figure 5.11 Effects of different damage severities on FRF data. Displayed are FRF summation functions from the numerical beam in the undamaged state and different damaged states with defects at location '5' of severities extra-light (5XL), light (5L), medium (5M) and severe (5S), with subfigure (a) displaying a frequency range from 0 Hz to 700 Hz and subfigure (b) illustrating a close-up of the frequency peak of mode 7.

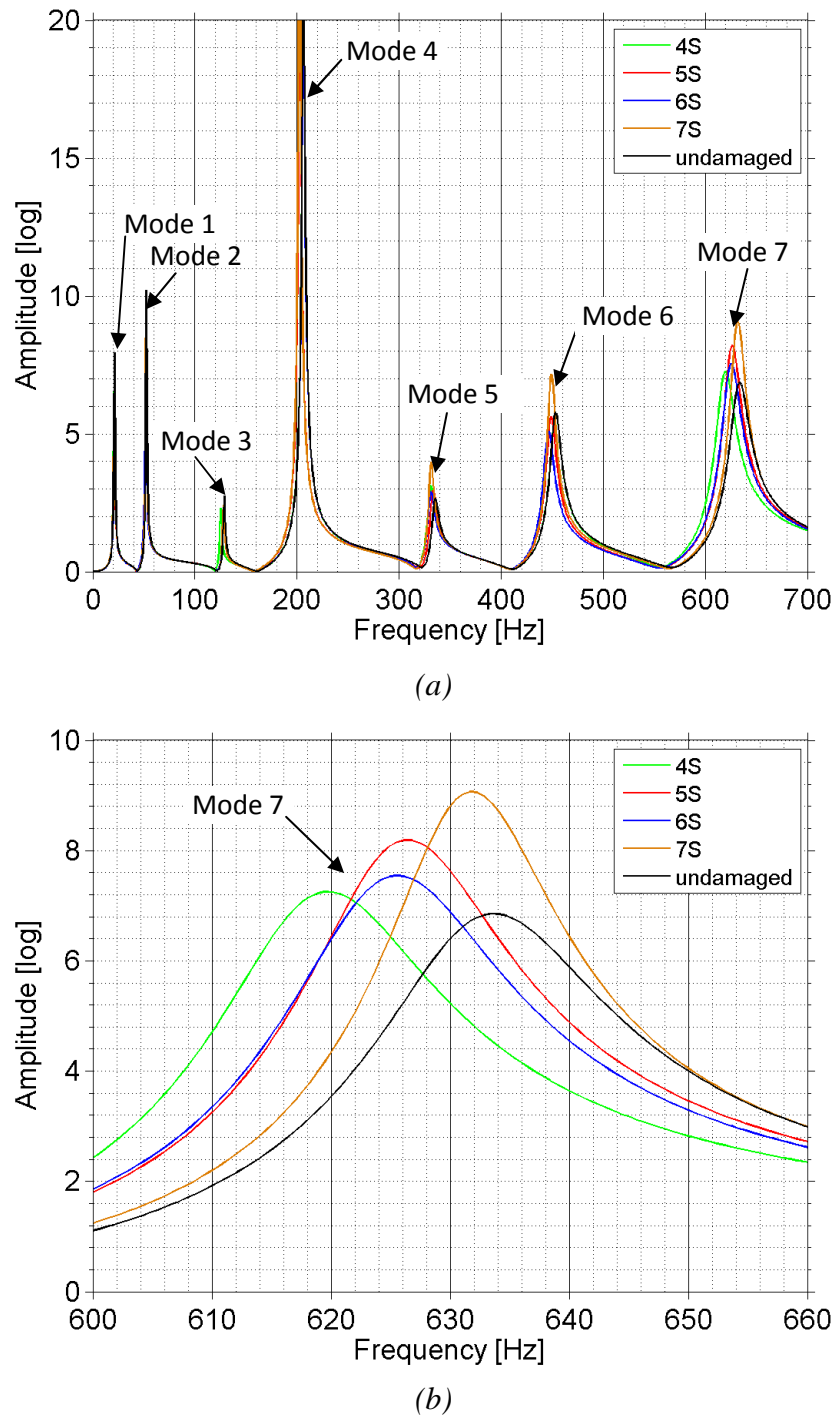


Figure 5.12 Effects of different damage locations on FRF data. Displayed are FRF summation functions from the numerical beam in the undamaged state and different damaged states with defects of severe extent at locations '4' to '7' (4S to 7S), with subfigure (a) displaying a frequency range from 0 Hz to 700 Hz and subfigure (b) illustrating a close-up of the frequency peak of mode 7.

5.3 NUMERICAL MODELLING OF TWO-STOREY FRAMED STRUCTURE

5.3.1 Finite Element Modelling of Two-Storey Framed Structure

The objective for the finite element modelling of the two-storey framed structure is to create a model that represents the actual laboratory structure as closely as possible. Therefore, instead of creating a simplified model an attempt is made here to accurately replicate all geometric features of the structure. Due to the complexity of the two-storey framed structure, ANSYS Workbench (ANSYS Inc 2007b) rather than ANSYS Classic (ANSYS Inc 2007a) is used to model the geometry of the structure. ANSYS Workbench has very user-friendly features for creating complex geometric models and for generating meshes for multifaceted bodies. Further, a link between ANSYS Workbench and ANSYS Classic allows the creation of a geometric model with subsequent meshing in ANSYS Workbench and enables the user to import the meshed model to ANSYS Classic for subsequent transient analysis.

The geometric features of the two-storey framed structure are modelled with the DesignModeler module of ANSYS Workbench. In this module, the four main bodies of the structure (i.e. column, crossbeam, joint element and base connection) are created. Figure 5.13 (a) illustrates the assembled structure, consisting of two columns, two crossbeams, four joints and four base connections. A close-up of a crossbeam and a joint element is displayed in Figure 5.13 (b) and (c), respectively. The column is modelled as a solid body with a cross-section of $65 \text{ mm} \times 5.5 \text{ mm}$ and a height of 1600 mm . The crossbeam is a composite of a hollow box ($150 \text{ mm} \times 50 \text{ mm} \times 575 \text{ mm}$), two solid cap elements (one on each side), four solid extension elements, two horizontal shafts (to link the crossbeam to the joint elements) and three vertical shaft elements (for the attachment of the additional masses). The joint element is composed of a solid round disc ($50 \text{ mm wide} \times 180 \text{ mm diameter}$ with a round opening of 20 mm in diameter) and a fitting shoe. The base connection consists of two L-shaped elements of $100 \text{ mm} \times 100 \text{ mm}$. (The dimensions of all elements equal those of the laboratory structure.)

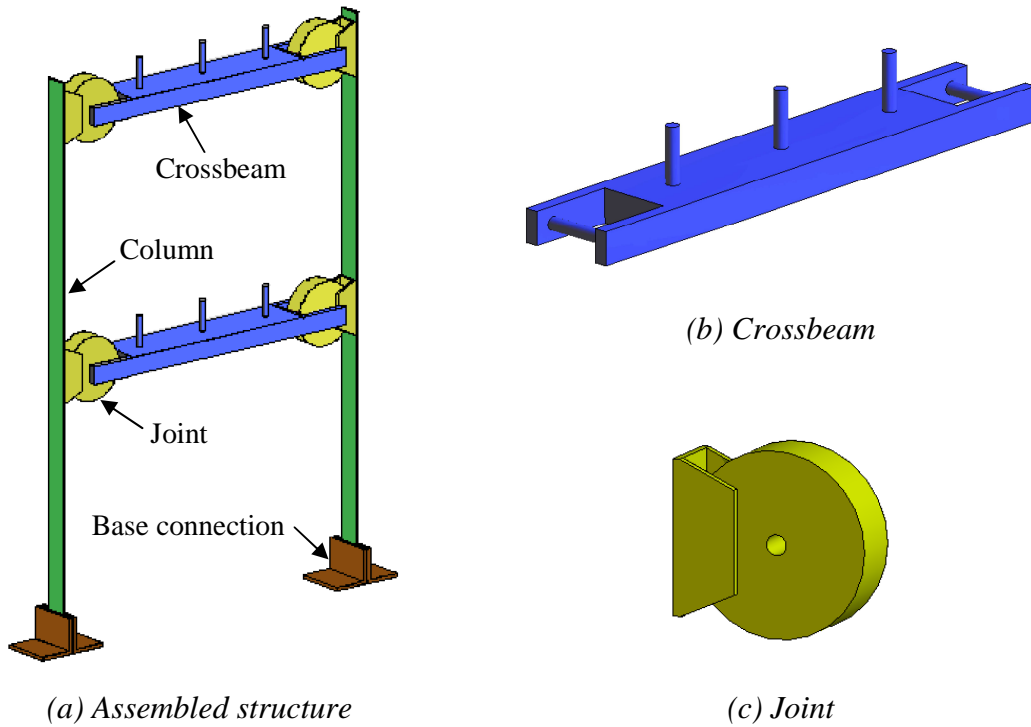


Figure 5.13 Geometric model of numerical two-storey framed structure.

To connect the individual bodies of the two-storey framed structure and to mesh all elements, the Simulation module of ANSYS Workbench is used. Before meshing, all contact regions between the individual body parts are defined. For the connection faces between column and joint elements as well as column and base connection elements, the contact regions are defined as a fixed bond, which allows no sliding (sliding tolerance is set to zero) or separation between the faces. For the connection between crossbeams and joint elements, the surfaces of the horizontal shafts of the crossbeams are also tightly bonded to the inner surfaces of the joint discs, creating a fixed connection between the crossbeams and joints (for the boundary damage scenarios, this connection will be modified). To define the support conditions, the bottom faces of the base connections are set as fixed connections. Figure 5.14 illustrates all contact regions (in red) and the support faces (in blue) of the numerical model of the two-storey framed structure.

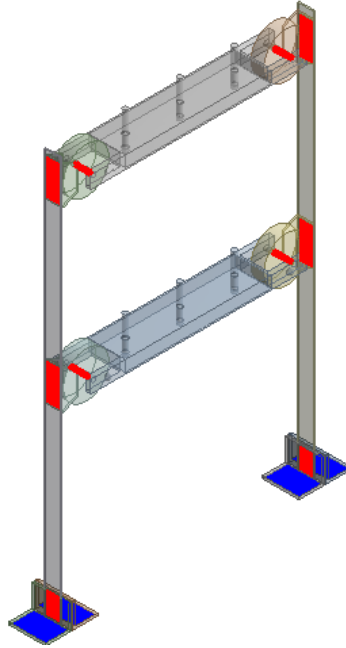


Figure 5.14 Contact regions (red) and support faces (blue) of the two-storey framed structure.

After defining the connection regions, all body parts are meshed. As the crossbeams and the joint elements have very complex features, the bodies are meshed with a tetrahedral mesh. As element type, SOLID187 is chosen, which is a tetrahedral structural solid defined by ten nodes having three degrees of freedom at each node (i.e. translations in the nodal x , y and z directions). SOLID187 is recommended in ANSYS Classic documentation (ANSYS Inc 2007c) as being well suited to modelling irregular meshes. The geometric properties of element type SOLID187 are illustrated in Figure 5.15.

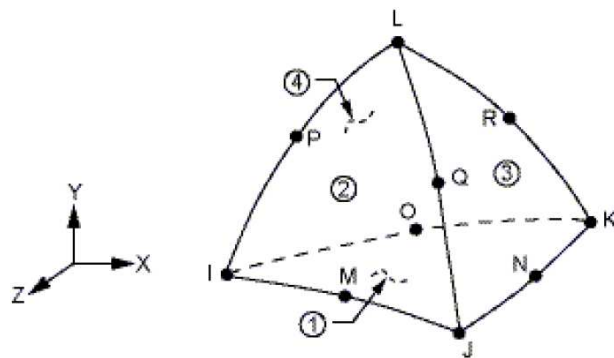


Figure 5.15 Geometric properties of SOLID187 (ANSYS Inc 2007c).

The tetrahedral meshing of the body parts is performed by an inbuilt patch independent algorithm defined by the following features. Physics preference: mechanical; relevance: 100 (for columns), -100 (for crossbeams and joints) and -50 (for base connection);

relevance centre: fine; maximum element size: 20 mm; shape checking: standard mechanical; solid element midside nodes: program controlled; straight sided elements: no; initial size seed: full assembly; smoothing: low; and transition: fast.

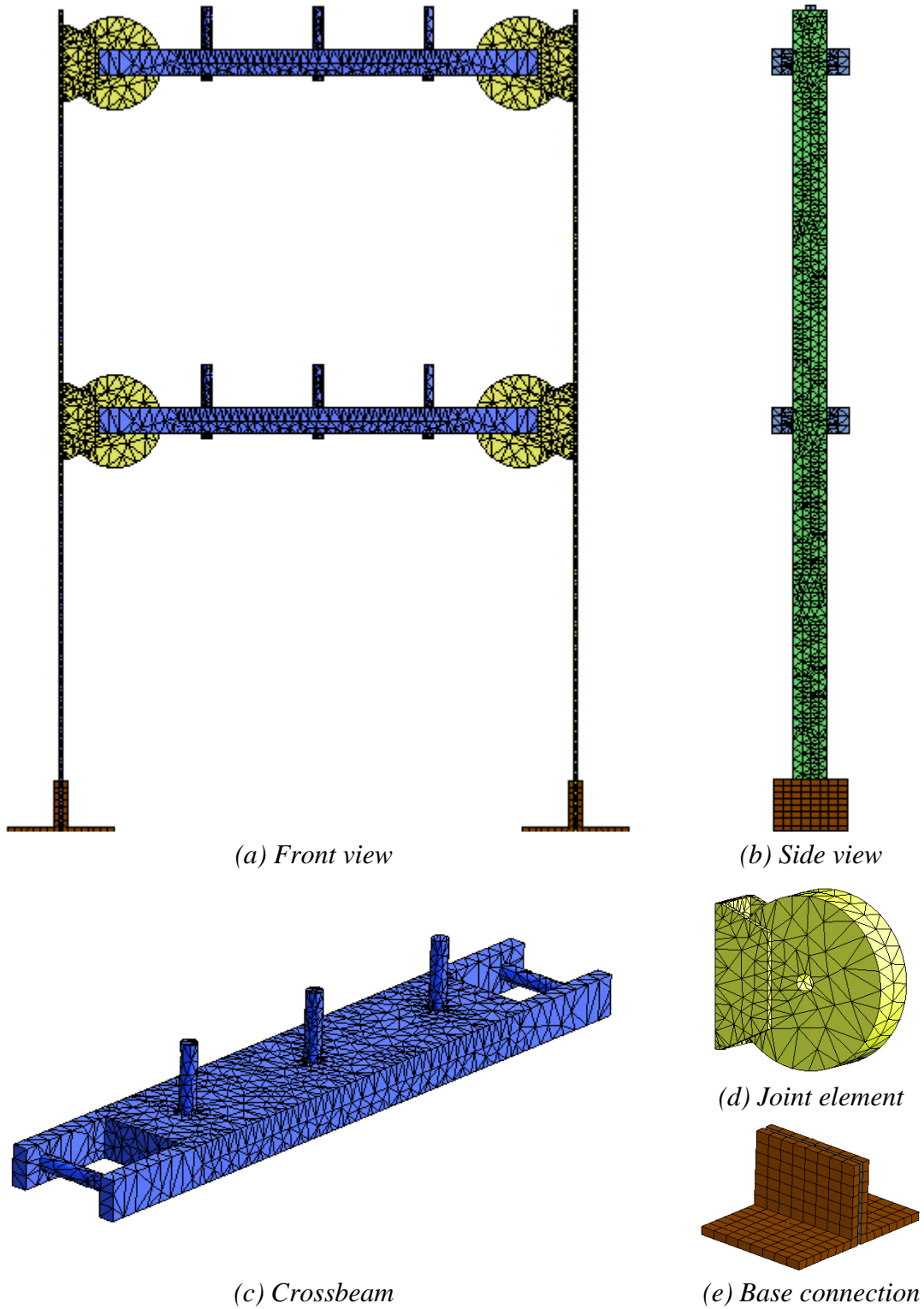


Figure 5.16 Meshed two-storey framed structure.

For the undamaged structure, a total of 63,025 nodes and 29,205 elements are created. The fully meshed structure (in front and side view) and detailed views of a crossbeam, a joint element and two base connections are illustrated in Figure 5.16. The material of all bodies is set to structural steel with a modulus of elasticity of $200,000 \times 10^6 \text{ N/m}^2$, a Poisson's ratio of 0.3 and a density of $7,850 \text{ kg/m}^3$, which reflect the values of the laboratory structure.

5.3.2 Simulation of Damage/Added Mass Scenarios

Three types of structural modifications are modelled, i.e. changes in the joint connection from fixed to pinned, addition of mass and section reduction damage of the column.

For the modelling of the pinned connection between crossbeam and joint element, the horizontal shaft of the crossbeam is deleted and replaced by a revolute joint connection. The revolute joint is constrained in five local degrees of freedom (UX, UY, UZ, ROTX, ROTY) and free in ROTZ, which allows free rotation around the longitudinal axis of the deleted horizontal shaft. An illustration of a revolute connection simulating a pinned joint is shown in Figure 5.17. For this study, four single joint scenarios are created by modelling one of the four fixed joint elements as a revolute connection. Also, six multiple joint scenarios are modelled by replacing two of the four fixed joints with revolute connections.

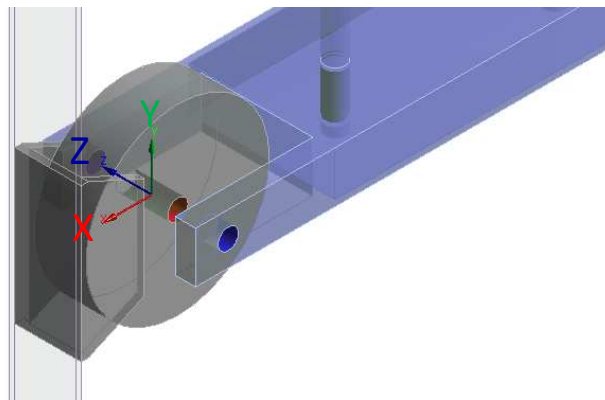


Figure 5.17 Pinned joint modelled as revolute connection.

For the modelling of the added mass, the crossbeam is extended by a cylinder shaped element of 150 mm in diameter and 68 mm in height. The mass of the added element is equal to the weight of the four disks used in experimental testing, i.e. approximately 9.2 kg (see section 4.4.2). Figure 5.18 illustrates the modelling of added mass at location

'10' of the crossbeam (i.e. the midspan of the lower crossbeam; see section 4.4.3). In total, six added mass configurations are modelled by adding cylindrical elements to locations '9' to '14' of the two crossbeams.

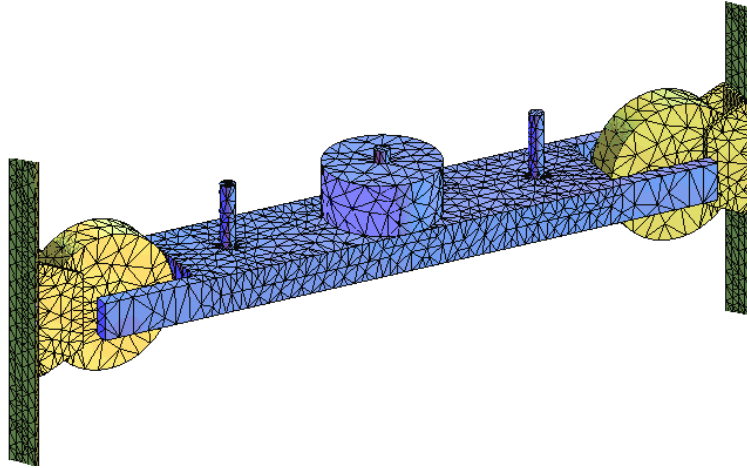


Figure 5.18 Modelling of added mass.

For damage due to cross-section reduction of the column, rectangular openings from one side of the column are modelled. Three severities of notch type damage – termed 'L', 'M' and 'S' – are created; they are of 4 mm notch width and 16.25 mm, 21.7 mm and 32.5 mm in notch depth, respectively. The corresponding reductions in the second moment of area, I , are 25%, 33.33% and 50%. The three damage severities are illustrated in Figure 5.19 (a) to (c). For the numerical study, six damage locations are investigated, i.e. locations '1a', '1b' and '1c' of the lower column half and locations '3a', '3b', and '3c' of the upper column half. Locations '1a' and '3a' are at the midspans of the column halves and are equal to locations '1' and '3' of the laboratory structure (see section 4.4.3). Locations '1b' and '3b' are positioned at one third of the column halves and locations '1c' and '3c' are at one quarter of the column halves. All six locations are illustrated in Figure 5.19 (d). At each of the six locations, damage of three severities is modelled, resulting in a total of 18 different damage cases.

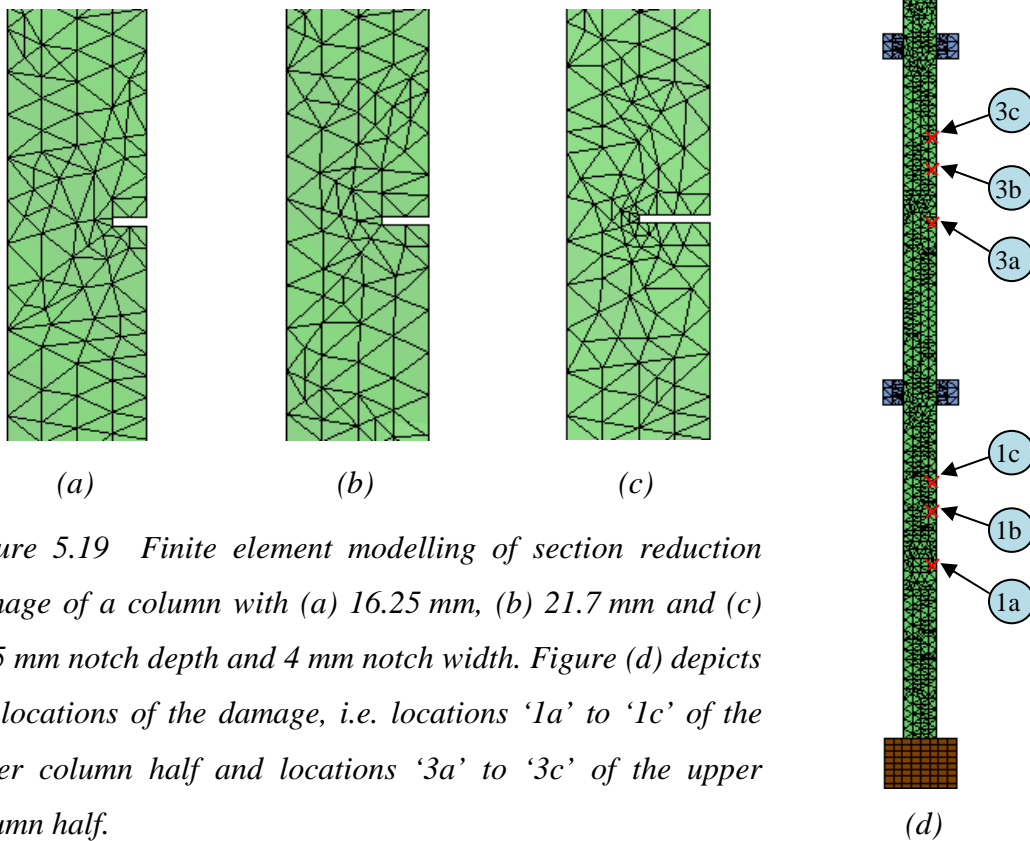


Figure 5.19 Finite element modelling of section reduction damage of a column with (a) 16.25 mm, (b) 21.7 mm and (c) 32.5 mm notch depth and 4 mm notch width. Figure (d) depicts the locations of the damage, i.e. locations ‘1a’ to ‘1c’ of the lower column half and locations ‘3a’ to ‘3c’ of the upper column half.

5.3.3 Transient Analysis and Noise Pollution

For the numerical two-storey framed structure, the dynamic properties are also determined by both eigenvalue solution and transient analysis. For both methods, the meshed models of the different scenarios of the two-storey framed structure are exported from ANSYS Workbench (ANSYS Inc 2007b) to ANSYS Classic (ANSYS Inc 2007a) for subsequent processing. The modal parameters determined by solving the eigenvalue problem are used to validate the numerical models and the FRFs obtained from transient analysis are used as damage fingerprints for damage identification. As for the beam structure, noise-polluted FRF data are generated by polluting time history data from transient analysis with different levels of white Gaussian noise.

For transient analysis, an impact force of 500 N is applied at location H5, which is the impact point of the hammer in experimental testing (see section 4.4.4). The loading curve of the excitation force is illustrated in Figure 5.20 (a) and reflects a typical hammer hit observed in laboratory testing. In transient analysis, the response of the two-storey framed structure is recorded for 16.385 s in integration time steps of 0.001 s, resembling the sampling rate from experimental testing. The ‘full method’ is again

chosen in ANSYS Classic (ANSYS Inc 2007a) to calculate the transient responses. From the finite element model, 14 different displacement response time histories are sampled from measurement locations '1' to '14' (see Figure 4.28 of section 4.4.3). At locations '1' to '8' (on the columns), the time histories are recorded in the horizontal direction, and at locations '9' to '14' (on the crossbeams), the time history data are sampled in the vertical direction. As an example, the generated displacement response time history from transient analysis of location '4' is shown in Figure 5.20 (b).

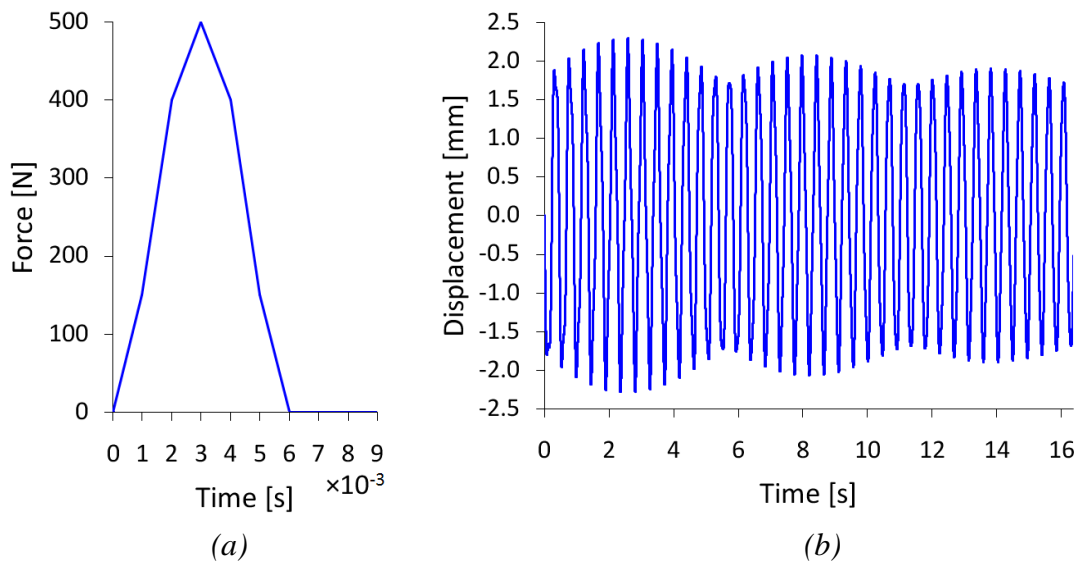


Figure 5.20 (a) Hammer impact force and (b) displacement response time history of location '4' of the two-storey framed structure.

As with the numerical beam structure, the generated time history data are polluted with white Gaussian noise to simulate measurement noise interferences experienced during experimental testing. Therefore, the recorded displacement time histories are first double differentiated to obtain acceleration time history data. Then, the acceleration response time histories and the excitation force signal of the impact hammer are polluted with different intensities of white Gaussian noise by using the 'awgn' function in Matlab (The MathWorks 2009a). By employing the noise-to-signal ratio function $20\log_{10}(\text{ratio})$ with ratios of 0.01, 0.02, 0.05 and 0.1, data of noise pollution levels of 1%, 2%, 5% and 10% are generated. To simulate five repeated tests (as executed in laboratory testing), for each level of noise, five different sets of noise contaminated data are generated by polluting data with different signals of white Gaussian noise.

Next, FRFs are calculated from the noise-polluted impact force signals and the noise-polluted acceleration response time histories, following the procedures described in section 4.2.2. The generated FRFs capture a frequency range of 0–500 Hz and comprise 8,192 spectral lines, resulting in a frequency resolution of 0.061 Hz per data point, which equals the resolution obtained from experimental testing.

5.3.4 Dynamic Characteristics of the Two-Storey Framed Structure

Correlation Analysis and Dynamic Characteristics of Baseline Structure

As with the beam structure, a correlation analysis is conducted for the finite element model of the two-storey framed structure to validate the numerical model against data from the laboratory structure. The indices for the objective function, OF , of the correlation analysis are the natural frequencies ($NError$) and mode shapes ($MACError$). The respective equations for OF , $NError$ and $MACError$ are found in section 5.2.4.

For the correlation of the natural frequencies, Table 5.5 lists the first seven natural frequencies of the numerical and laboratory structure, their absolute differences and $NError$ values. From the table, it is seen that $NError$ is in general smaller than 10%, except for mode 7. Very good correlations are achieved for modes 1, 3 and 6, with $NError$ values under 3%.

Table 5.5 Comparison of natural frequencies between numerical and laboratory two-storey framed structure.

	Mode 1	Mode 2	Mode 3	Mode 4	Mode 5	Mode 6	Mode 7
Numerical structure [Hz]	2.23	6.50	66.07	72.56	90.20	101.53	130.30
Laboratory structure [Hz]	2.26	6.89	67.03	67.03	82.10	98.90	115.39
Absolute difference [Hz]	0.03	0.39	0.96	5.53	8.1	2.63	14.91
$NError$ [%]	1.33	5.66	1.43	8.25	9.87	2.66	12.92

For mode shapes, MAC and $MACError$ values are used to compare the mode shape vectors of the numerical structure with those of the experimental structure. Table 5.6 presents MAC and $MACError$ values of experimental and numerical mode shapes. (For the numerical structure, mode shape vectors of 14 data points are used, representing the 14 measurement sensors in laboratory testing.) From the table, it is seen that the mode shapes correlate very well, giving a maximum $MACError$ value of 1.28% for mode 5. These excellent results are well below the acceptable threshold value of 10% nominated

by Brownjohn and Xia (1999) and Maia et al. (1997). A graphical comparison is illustrated in Figure 5.21, which shows the first seven flexural mode shapes of the finite element model and the laboratory structure. As can be seen, the mode shapes match very well.

Table 5.6 Mode shape correlation between numerical and laboratory two-storey framed structure.

	Mode 1	Mode 2	Mode 3	Mode 4	Mode 5	Mode 6	Mode 7
<i>MAC</i>	0.9994	0.9973	0.9956	0.9944	0.9872	0.9990	0.9978
<i>MAC [%]</i>	99.94	99.73	99.56	99.44	98.72	99.90	99.78
<i>MACerror</i>	0.0006	0.0027	0.0044	0.0056	0.0128	0.0010	0.0022
<i>MACerror [%]</i>	0.06	0.27	0.44	0.56	1.28	0.10	0.22

From the outcomes of the correlation analysis, it is concluded that the finite element model of the two-storey framed structure is a good representation of the laboratory test structure, and therefore, model updating is not necessary for the purpose of this study.

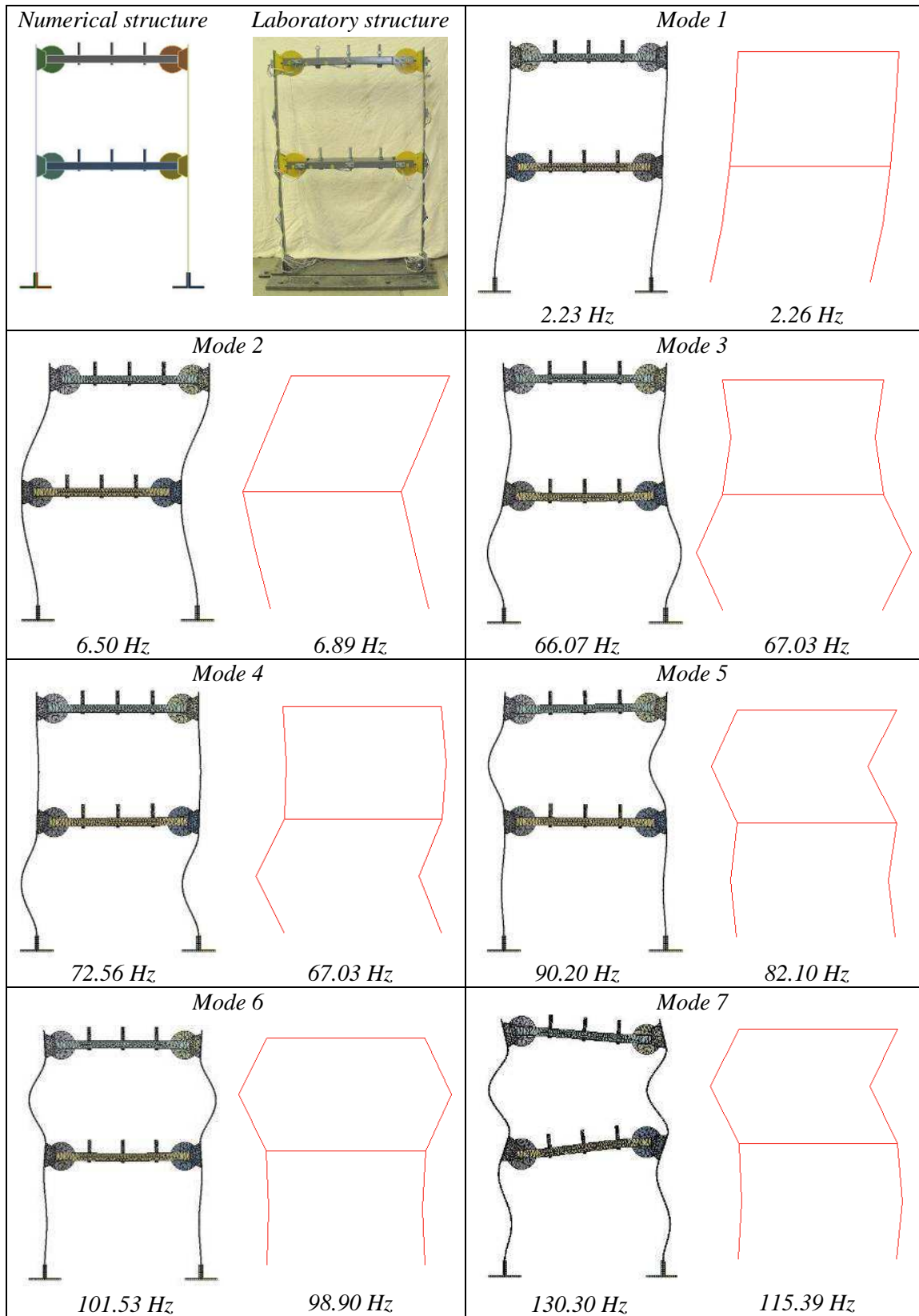


Figure 5.21 First seven flexural mode shapes of laboratory and numerical baseline two-storey framed structure.

For the validated numerical model, Figure 5.22 illustrates the horizontal FRF summation function, which is calculated by summing FRFs from locations '1' to '8'. In the figure, frequency peaks of all seven modes are visible. It is, however, noted that modes 3 and 6 are indicated with only very small humps. This suggests that modes 3 and 6 make only a small modal contribution.

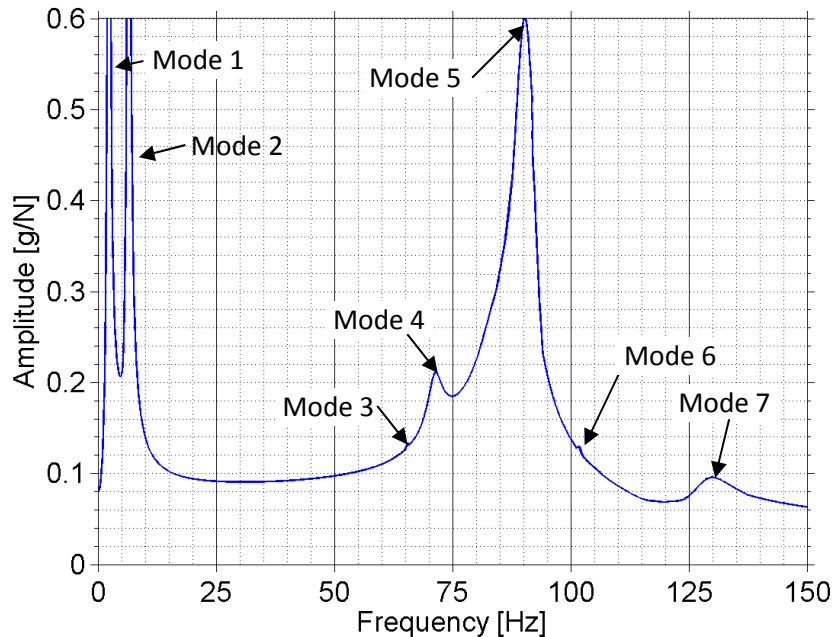


Figure 5.22 Horizontal FRF summation function of baseline structure of numerical two-storey framed structure.

Next, the individual FRFs of the 14 measurement locations are studied. From this investigation, it is found that FRFs from locations '2', '4', '6' and '8' (positioned on the columns at the height of the crossbeams; see Figure 4.28 in section 4.4.3) are less sensitive to the local modes of the columns, which are modes 3 to 7 (see Figure 5.21). As an example, individual FRFs of measurement locations '2', '3', '4' and '9' are illustrated in Figure 5.23. From figures (a) and (c), which show FRFs of locations '2' and '4', it is observed that predominantly modes 1 and 2 are indicated, only a very small hump is visible for mode 5 and none of the higher modes are represented. For the FRFs of locations '3' and '9', however, all local modes are indicated with distinctive peaks (even though for some modes the peaks are small). The low sensitivity to local modes in FRF data of locations '2', '4', '6' and '8' may result in a low susceptibility to damage of FRFs of these locations, as FRF data are primarily sensitive to changes in the proximity of frequency peaks.

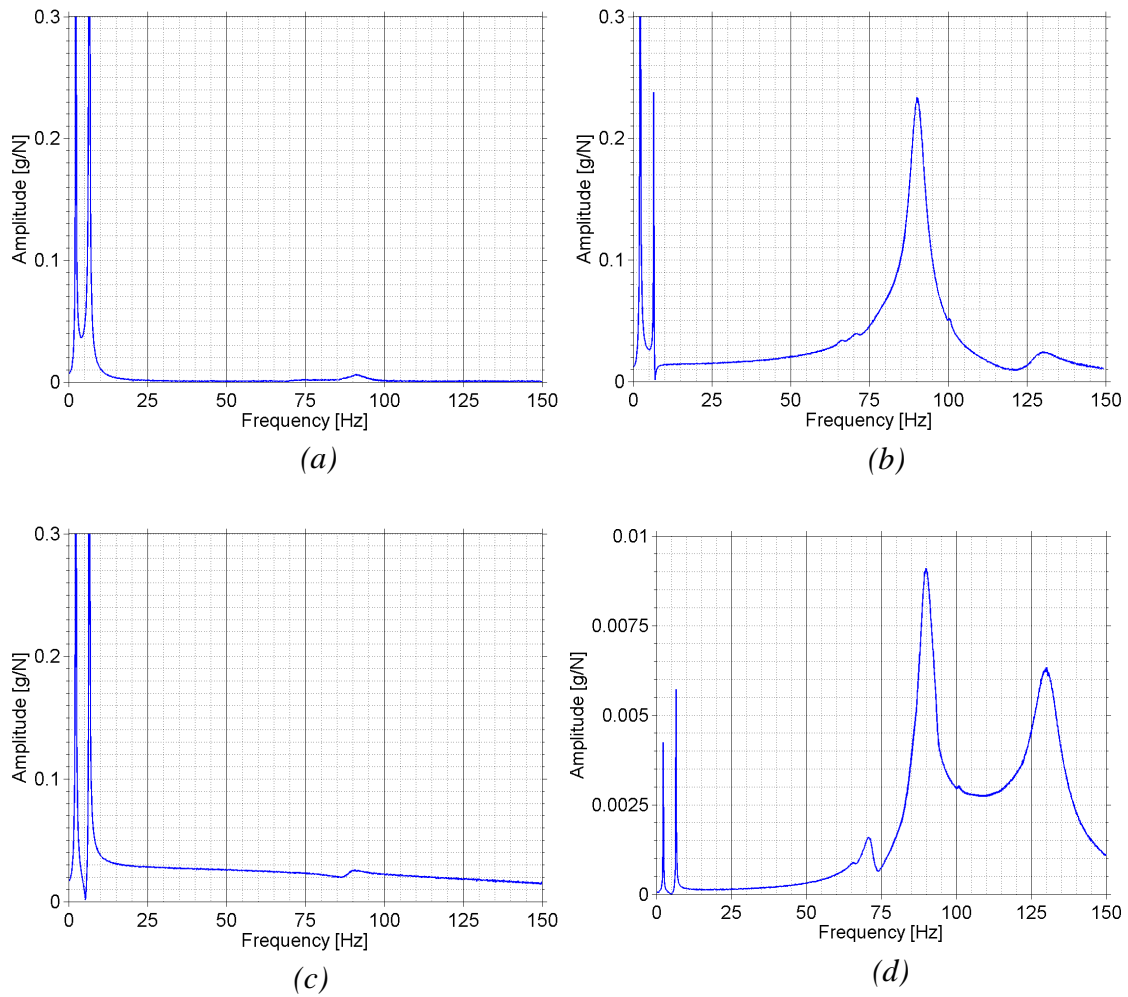


Figure 5.23 FRFs of (a) location '2', (b) location '3', (c) location '4' and (d) location '9'.

Dynamic Characteristics of Structure with Boundary Condition Changes

For the different boundary condition scenarios of the numerical two-storey framed structure, changes in the dynamic characteristics (natural frequencies, mode shapes and FRFs) are observed. For FRF data, Figure 5.24 and Figure 5.25 illustrate horizontal FRF summation functions of the baseline structure (FFFF) and different multiple and single boundary condition changes. From the figures, distinctive changes in amplitude and positioning of the frequency peaks are noted. Similar to the laboratory structure, additional frequency peaks emerge for some scenarios, indicating new modes. The reader is referred to Figure D.1 to Figure D.11 of APPENDIX D, which illustrate the mode shapes of the baseline structure and all boundary condition scenarios of the two-storey framed structure. As an example, new mode shapes of boundary scenarios PPF

and FFPP are shown in Figure 5.26. The new mode shapes clearly show deformations introduced by the change of the joint conditions from fixed to pinned.

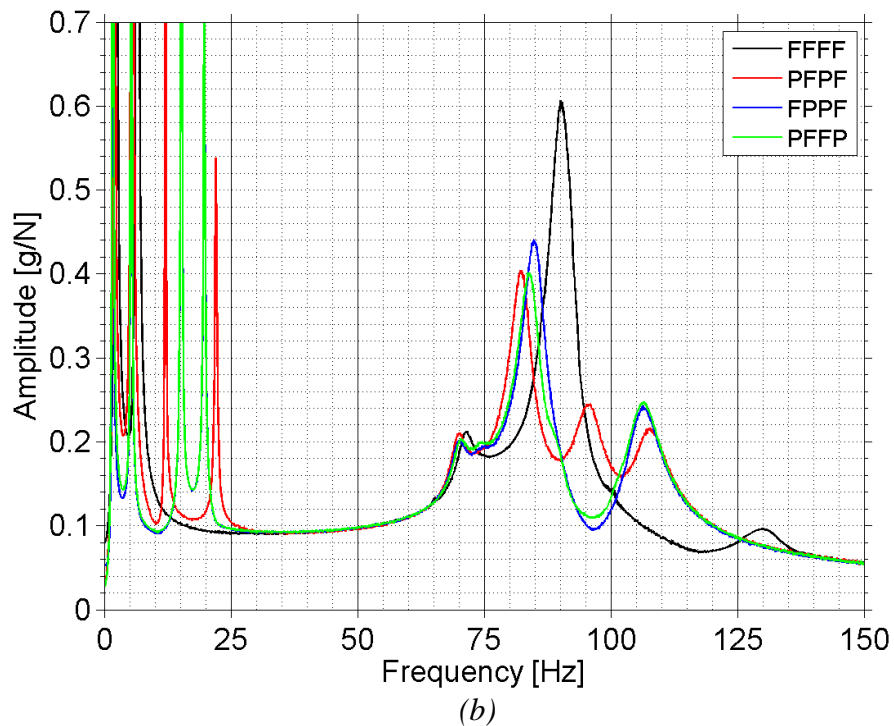
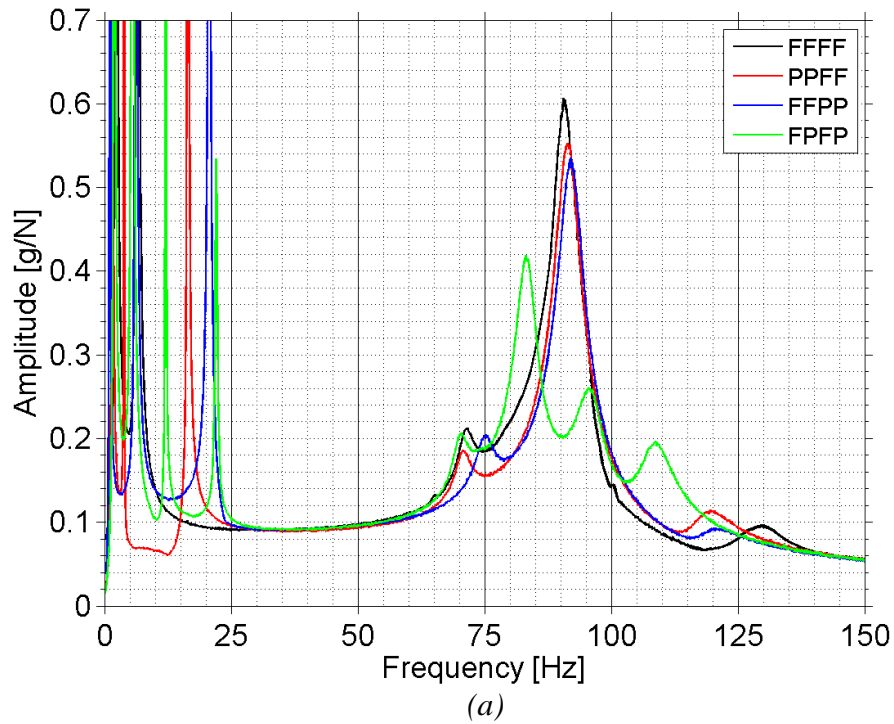


Figure 5.24 Horizontal FRF summation functions of baseline structure (FFFF) and different multiple boundary condition scenarios of numerical two-storey framed structure.

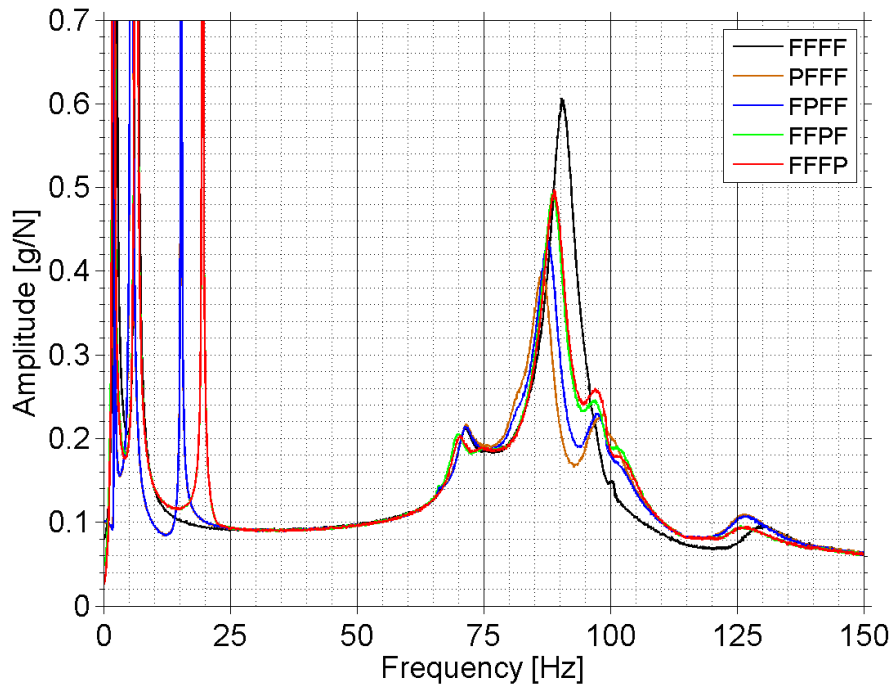


Figure 5.25 Horizontal FRF summation functions of baseline structure (FFFF) and different single boundary condition scenarios of numerical two-storey framed structure.

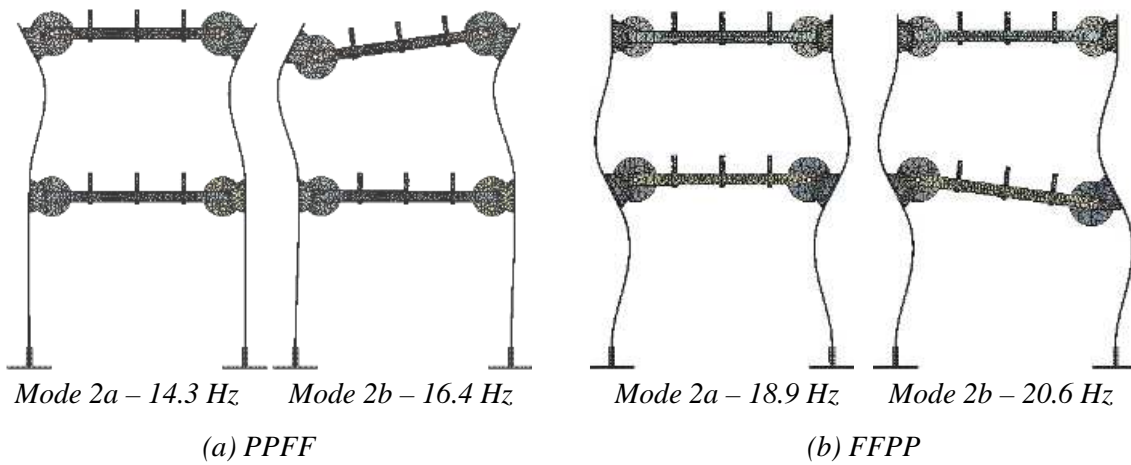


Figure 5.26 New mode shapes of (a) boundary scenario PPF and (b) boundary scenario FFPP of numerical two-storey framed structure.

To investigate changes in natural frequencies, Table 5.7 lists the first seven resonant frequencies of the baseline structure and all boundary condition scenarios. An accompanying graph (Figure 5.27) illustrates the reduction in frequencies of the boundary condition scenarios when compared against the baseline structure. Large changes in frequencies occur for the higher modes (modes 5 to 7) as well as for mode 3. The actual increase of the frequency of mode 3 is related to a switch between mode 3

and mode 4 (the order of the two modes changed). For boundary scenario FFFP, for example, mode 3 is at a frequency of 75.6 Hz, while mode 4 is at 71.3 Hz.

Table 5.7 Natural frequencies of the first seven flexural modes of the baseline structure and all boundary condition scenarios.

Natural frequencies [Hz]							
	Mode 1	Mode 2	Mode 3	Mode 4	Mode 5	Mode 6	Mode 7
Baseline	2.2	6.5	66.1	72.6	90.2	101.5	130.3
PFFF	2.1	5.5	66.2	72.6	86.1	98.4	126.6
FPFF	2.1	5.5	66.2	72.6	87.2	98.7	126.7
FFPF	1.8	6.4	66.2	71.0	88.2	98.4	125.7
FFFP	1.9	6.4	75.9	71.3	88.5	98.7	125.8
PPFF	1.5	3.7	65.5	71.9	94.0	99.2	124.3
FFPP	1.0	6.2	75.6	76.6	94.7	100.0	125.2
FPPF	1.9	5.5	75.8	71.4	85.4	99.0	112.6
PFPP	1.9	5.7	71.2	64.6	82.0	95.2	103.7
FPPF	1.1	5.4	75.6	70.0	77.2	94.1	103.4
PFFP	1.6	5.2	75.7	71.4	86.2	91.9	110.2

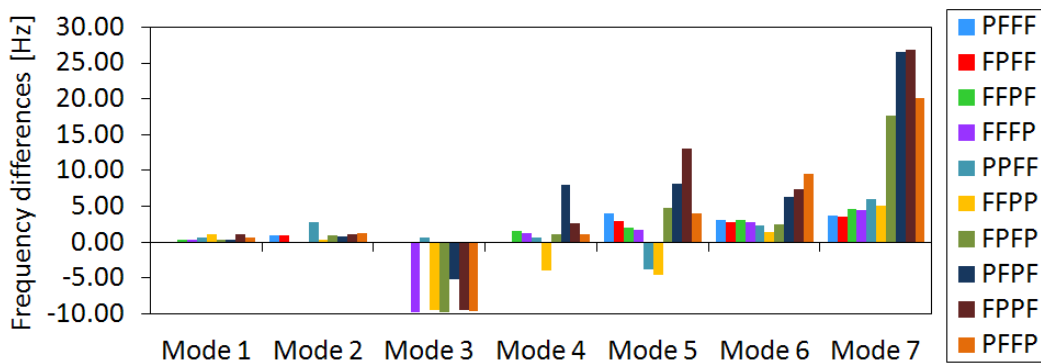


Figure 5.27 Changes in natural frequencies of all boundary condition scenarios of the numerical two-storey framed structure.

Dynamic Characteristics of the Two-Storey Framed Structure with Added Mass

Next, changes in the dynamic properties for the added mass scenarios are investigated. From the horizontal summation FRFs of different added mass cases (depicted in Figure 5.28 and Figure 5.29), it is seen that changes in FRF data are rather small when compared to the boundary condition scenarios. If mass is added to the lower crossbeam, the FRFs hardly change. For additional mass at the upper crossbeam, a shift of FRF magnitudes is noted. Further, a new mode emerges at 64.2 Hz (for scenario M4), 60.9 Hz (for M5) and 62.8 Hz (for M6). A picture of the new mode is illustrated in Figure 5.30 for added mass scenario M4. From the FRF graphs of Figure 5.29, it is

furthermore observed that the FRF of M4 experiences larger changes than the FRFs of M5 and M6, especially in the frequency bandwidth between 60 Hz and 70 Hz. These changes are because the new mode (mode 2a) is a local deformation of the upper column halves and is therefore largely influenced by additional mass close to the column. Further, the excitation point of the structure for transient analysis is close to the added mass location M4 and hence, M4 experiences larger changes than M5.

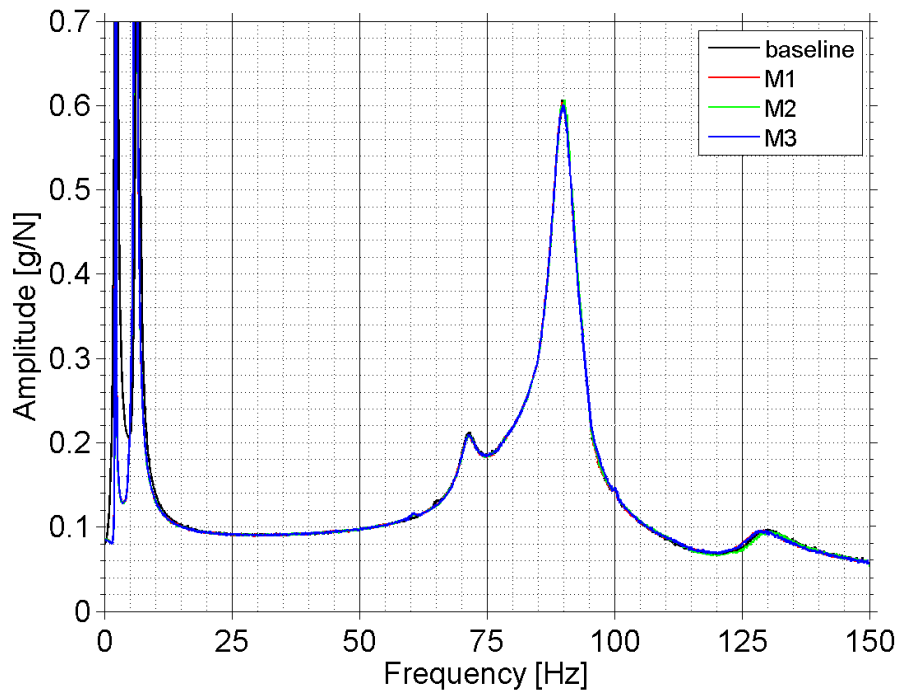


Figure 5.28 Horizontal FRF summation functions of baseline structure and structure with mass added to the lower crossbeam at locations M1, M2 or M3 of numerical two-storey framed structure.

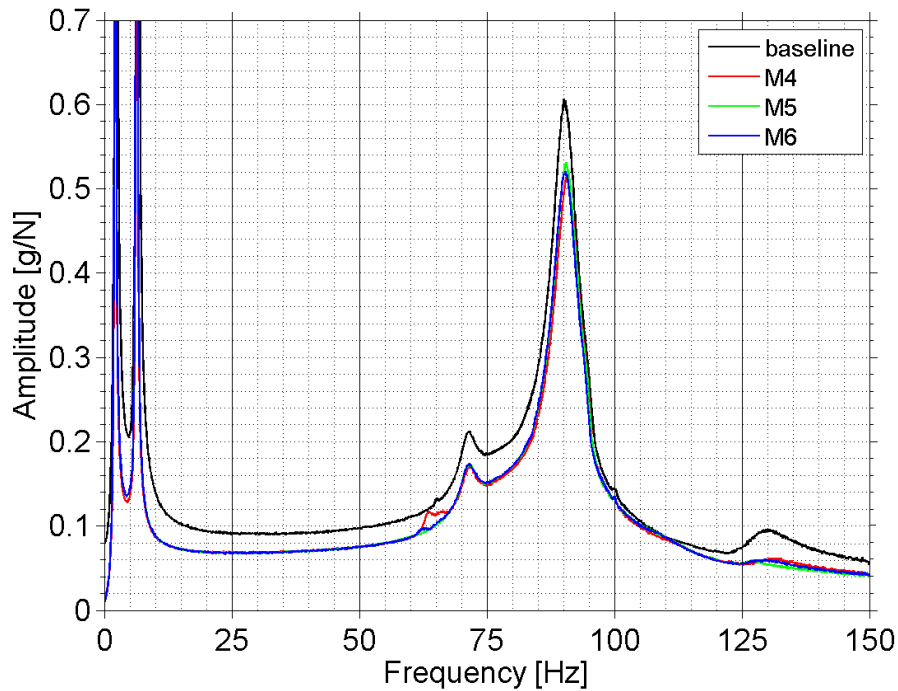


Figure 5.29 Horizontal FRF summation functions of baseline structure and structure with mass added to the upper crossbeam at locations M4, M5 or M6 of numerical two-storey framed structure.



Figure 5.30 New mode (mode 2a) of numerical two-storey framed structure that emerges when mass is added to the upper crossbeam.

For changes in natural frequencies, Table 5.8 lists the frequencies of the baseline structure and all six added mass scenarios. In addition, Figure 5.31 illustrates the corresponding changes (reductions) in natural frequencies of the added mass cases when compared to the baseline structure. From the table and the figure, it is noted that large changes in the frequencies of mode 3 occur for added mass scenarios of the lower crossbeam. Such changes are because mode 3 is a local mode of the lower crossbeam

halves and therefore experiences the most dramatic changes from additional mass at the lower crossbeam. Moderate frequency changes of modes 6 and 7 are further noted.

Table 5.8 Natural frequencies of the first seven modes of the baseline structure and all added mass scenarios.

Natural frequencies [Hz]							
	Mode 1	Mode 2	Mode 3	Mode 4	Mode 5	Mode 6	Mode 7
Baseline	2.2	6.5	66.1	72.6	90.2	101.5	130.3
M1	2.1	6.1	60.9	72.5	90.1	99.6	129.0
M2	2.1	6.1	59.4	72.6	90.2	99.3	130.7
M3	2.1	6.1	60.9	72.6	90.1	99.6	129.1
M4	2.1	6.3	66.9	72.7	90.7	100.2	131.1
M5	2.1	6.3	66.3	72.9	90.4	99.7	130.3
M6	2.1	6.3	66.4	72.6	90.3	100.0	129.0

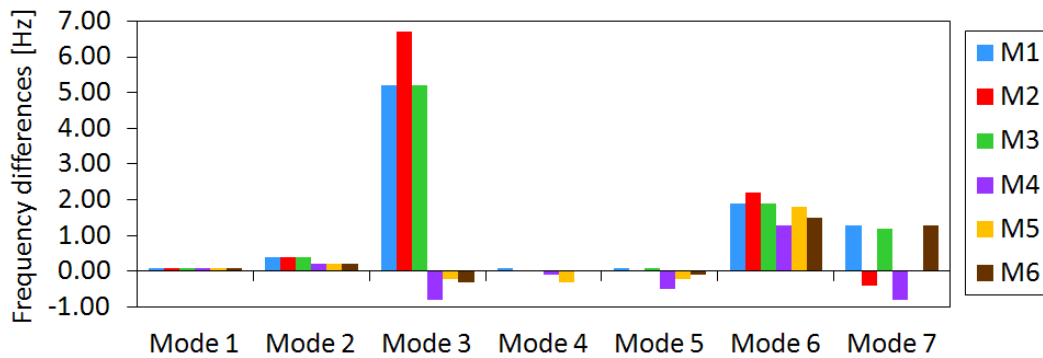
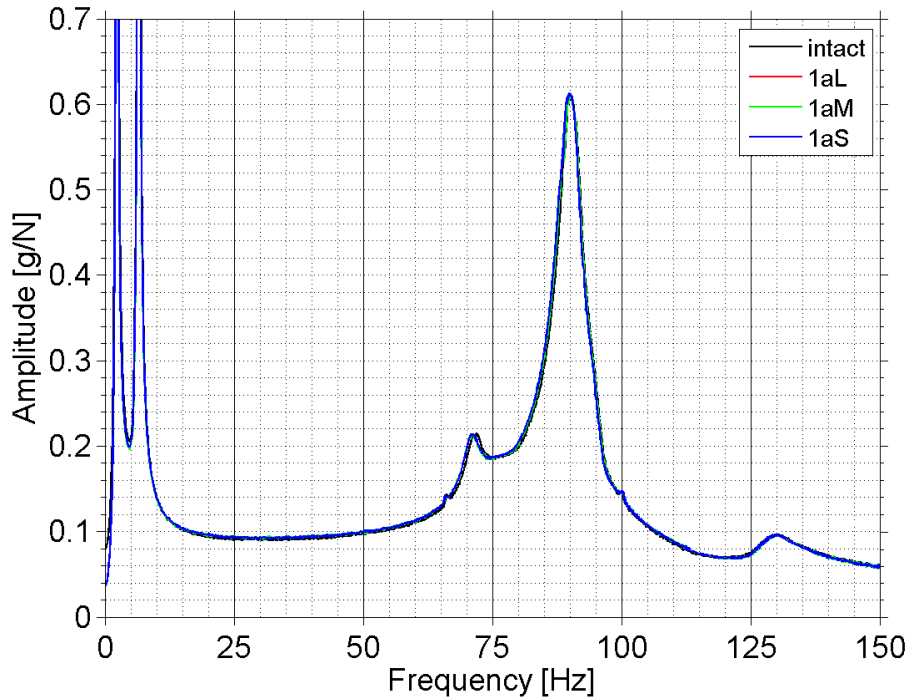


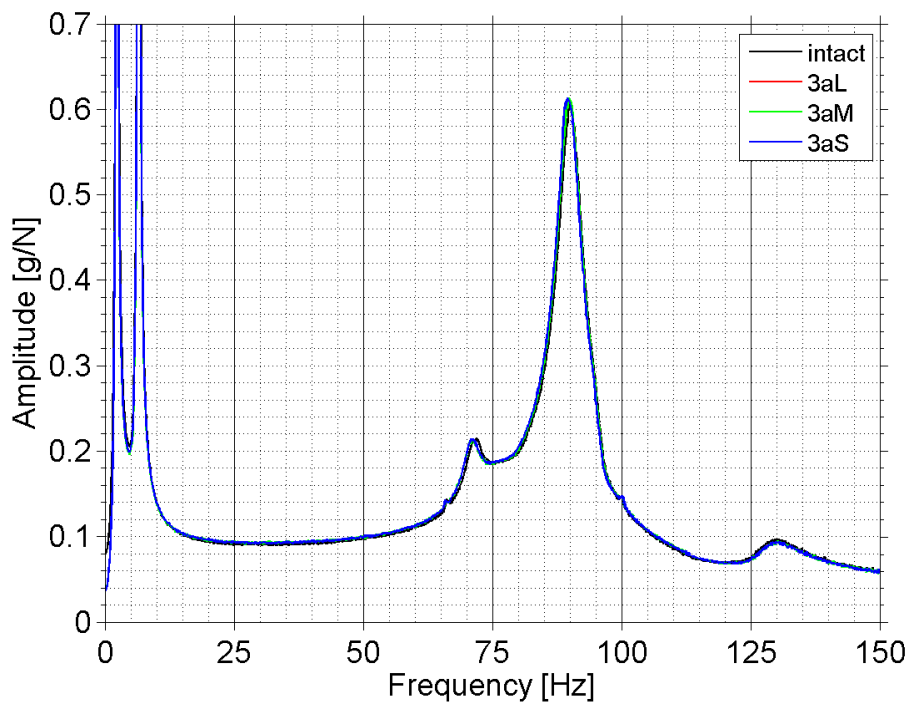
Figure 5.31 Changes in natural frequencies of all added mass scenarios of the numerical two-storey framed structure.

Dynamic Characteristics of the Two-Storey Framed Structure with Section Reduction Damage

For the cross-section reduction scenarios of the numerical two-storey framed structure, 18 different damage cases are modelled (damage of three severities at six locations). For these section reduction cases, the dynamic properties change only slightly. As can be seen from Figure 5.32, the horizontal FRF summation functions of damage at locations 1a and 3a, which coincide with the damage locations ‘1’ and ‘3’ of experimental testing, shift only marginally.



(a)



(b)

Figure 5.32 Horizontal FRF summation functions of baseline structure (intact) and structure with light, medium and severe section reduction damage at (a) location 1a and (b) location 3a.

To investigate changes in natural frequencies, Table 5.9 lists the first seven frequencies of all section reduction cases and Figure 5.33 illustrates frequency reductions for

damage at locations '1a' and '3a'. From the table and the figure, it is noted that frequency reductions are larger for damage of larger severity. Further, a relationship between frequency drop, the shape of a particular mode and the damage location is observed. For example, for modes 5 and 6, which are local modes of the upper column halves, the frequency differences for damage at location 3a (positioned at the midspan of the upper column half) are larger than for damage at location 1a (positioned at the midspan of the lower column half).

Table 5.9 Natural frequencies of the first seven modes of the baseline structure and all section reduction scenarios.

Natural frequencies [Hz]							
	Mode 1	Mode 2	Mode 3	Mode 4	Mode 5	Mode 6	Mode 7
Baseline	2.2	6.5	66.1	72.6	90.2	101.5	130.3
1aL	2.2	6.5	65.6	72.2	90.2	101.4	130.3
1aM	2.2	6.5	65.6	72.2	90.2	101.4	130.3
1aS	2.2	6.5	65.2	72.1	90.1	101.3	130.3
1bL	2.2	6.5	65.7	72.3	90.2	101.4	130.3
1bM	2.2	6.5	65.7	72.2	90.2	101.4	130.3
1bS	2.2	6.5	65.7	72.2	90.2	101.4	130.3
1cL	2.2	6.5	65.7	72.2	90.2	101.4	130.3
1cM	2.2	6.5	65.7	72.2	90.2	101.4	130.3
1cS	2.2	6.5	65.7	72.2	90.2	101.4	130.3
3aL	2.2	6.5	65.7	72.2	90.0	101.2	130.3
3aM	2.2	6.5	65.7	72.2	89.8	101.0	130.3
3aS	2.2	6.5	65.6	72.2	89.0	100.4	129.9
3bL	2.2	6.5	65.7	72.0	90.2	101.4	130.3
3bM	2.2	6.5	65.7	72.0	90.2	101.4	130.3
3bS	2.2	6.5	65.7	71.9	90.0	101.2	130.2
3cL	2.2	6.5	65.7	72.3	90.1	101.3	130.3
3cM	2.2	6.5	65.7	72.0	90.1	101.3	130.3
3cS	2.2	6.4	65.7	71.9	90.0	101.1	130.1

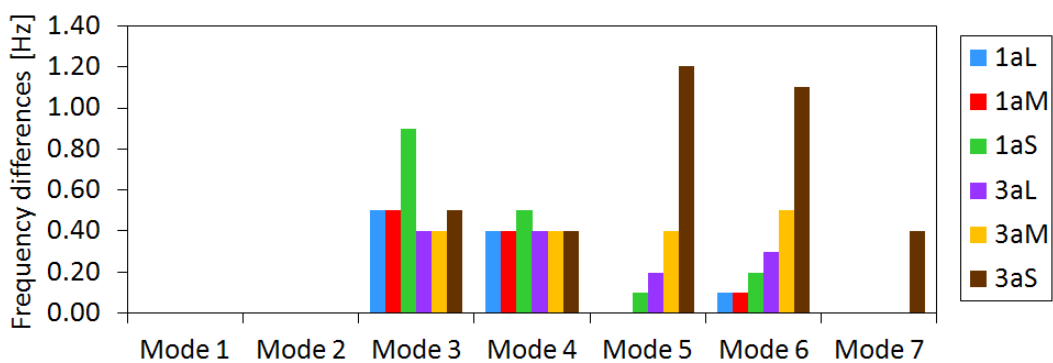


Figure 5.33 Reduction in natural frequencies of section reduction scenarios at locations '1a' and '3a' of the numerical two-storey framed structure.

Even though changes of the vibrational characteristics of the cross-section reduction scenarios are very small when compared against changes due to boundary damage or added mass, each section reduction case exhibits individual modifications of the dynamic properties, which can be used to identify the individual damage scenario.

5.4 SUMMARY

This chapter presented procedures relating to the numerical modelling of the beam structure and the two-storey framed structure using ANSYS Classic and ANSYS Workbench. A correlation analysis was undertaken for both structures to validate the numerical models in terms of vibrational characteristics against results from the laboratory test structures. Background information was given on the execution of transient analysis, which was performed to obtain response time history data of the structures, and details on the pollution of acquired time history data with white Gaussian noise were described. The derived dynamic properties of the intact structures and their changes due to structural modification were presented. For the numerical models, the characteristics of the changes of the vibrational properties were very similar to those obtained from the laboratory structures. Such changes were, for example: an increasing drop in natural frequencies when damage size increases (for the beam structure and section reduction scenarios of the two-storey framed structure); enlarged mode shape changes in the vicinity of the damage location (for the beam structure); newly emerging modes due to changed boundary conditions (for boundary damage of the two-storey framed structure); and larger changes in FRF data for boundary damage than for added mass and section reduction scenarios (for the two-storey framed structure). Further, it was observed that due to the ideal conditions of the finite element simulations, numerically obtained FRF data only indicated flexural modes; whereas for laboratory testing, other modes, such as torsional or transverse modes, were also indicated. It was further noted that for the two-storey framed structure, some flexural modes were only indicated with very small humps in the FRF curves, indicating a small modal contribution of the modes. In addition, for the two-storey framed structure, individual FRF data of certain measurement locations (locations '2', '4' '6' and '8') demonstrated a very low sensitivity to local modes (modes 3 to 7), which was exhibited by marginal or no indications of these modes in the FRF data.

CHAPTER 6

METHODOLOGY OF DAMAGE IDENTIFICATION

METHODS

6.1 INTRODUCTION

This chapter presents the theory, background and methodology of two novel vibration-based damage identification schemes. The core of both schemes is the use of artificial neural network (ANN) techniques for pattern recognition and noise reduction. One scheme is a modal parameter method (based on the damage index (DI) method), and the other scheme is a frequency response function (FRF) method. To enhance damage signatures and to reduce the size of input data to neural networks, principal component analysis (PCA) techniques are employed. A hierarchical network training based on network ensembles is proposed to take advantage of individual characteristics of damage indicators derived from different sources.

For the modal-parameter-based method, first, theoretical background information is given on utilising the DI method for damage identification. Second, a mode shape reconstruction technique based on cubic spline interpolation is presented. This technique refines mode shape vectors from coarse sensor networks in order to obtain improved damage identification results. Third, limitations of the DI method are discussed. Fourth, PCA is applied to DI values and its effects on damage features and uncertainties, such as noise and modal analysis errors, are studied. Fifth, damage identification by means of PCA-compressed DI values and ANNs is proposed. Last, advantages are discussed on separating PCA-compressed DI values according to the mode shapes they are derived from and analysing the separated input features in individual networks based on hierarchical network ensemble training.

For the FRF-based method, firstly, advantages on utilising FRF data over modal parameter data for damage identification are presented. Secondly, a damage fingerprint termed as ‘residual FRF’, which represents the differences between undamaged and

damaged FRF data, is analysed and proposed as a damage indicator for FRF-based damage detection. Thirdly, to overcome dimension issues of large size FRF data, PCA is applied to the damage fingerprint. The benefits of using PCA for data reduction, feature extraction and noise filtering are discussed. Fourthly, it is proposed to utilise PCA-compressed residual FRF data as input features for ANNs to identify damage characteristics. Finally, network training based on network ensembles is suggested, which individually analyses FRF-based damage indicators separated by sensor location.

6.2 PROPOSED METHOD 1: DAMAGE IDENTIFICATION BASED ON DAMAGE INDEX METHOD

The first damage identification scheme proposed in this thesis is developed based on the DI method (Stubbs, Kim & Topole 1992). The DI method is a modal parameter method, which is based on changes in modal strain energy caused by damage. Compared to frequency-or damping-based methods, the DI method is more robust in the presence of noise and environmental influences. Further, it is a global technique that is able to assess the condition of the entire structure simultaneously. Many researchers have successfully applied the DI method in various fields and applications, and several modifications of the algorithm have been developed and verified by analytical and experimental studies (see section 2.7).

Despite the reported successful applications of the algorithm, the method has several shortcomings. For example, if damage is located close to a node point of a given mode, the defect stays undetected unless other modes are used for detection. In addition, when multiple mode shapes are used, it often produces false positive damage detection especially when only limited measurements are available. These issues lead to major challenges when the method is applied to real structures under real testing conditions. The accuracy and reliability of damage detection are greatly jeopardised due to, for example, measurement noise interferences, limited number of sensors, experimental modal analysis uncertainties and environmental influences.

The successes as well as the challenges of the DI method sparked the interest in utilising and further developing this technique for improved damage identification. In conjunction with ANNs and their robust capability of pattern recognition and noise filtering, this thesis investigates a novel damage identification scheme that has the

potential to overcome the problems of the DI method and of delivering desired damage identification results for field application. By employing mode shape reconstruction and PCA techniques, further improvements of the damage identification outcomes are anticipated. A unique contribution of this thesis is the design and training of neural networks in a network ensemble scheme that takes advantage of unique individual features of the mode shapes and characteristics of PCA-compressed DI values derived from different vibrational modes.

The proposed method is verified by a numerical and a laboratory simply supported steel structure. In order to incorporate field-testing conditions, the issue of limited number of sensors is considered by allowing only a small number of measurement points for the numerical as well as the experimental structure. Further, white Gaussian noise is added to the numerical data to simulate field conditions in the numerical simulations.

6.2.1 Theory of Damage Identification using Damage Index Method

The DI method was developed by Stubbs, Kim and Topole in 1992 (Stubbs, Kim & Topole 1992). This method utilises an indicator based on modal strain energies, which are a function of relative changes in mode shape curvatures of a structure before and after damage, to detect, locate and quantify damage. Considering a general Euler-Bernoulli beam, the strain energy stored in a system is expressed by,

$$U_i = \frac{1}{2} \int_0^L EI (w''(x))^2 dx \quad (6.1)$$

where EI is the flexural rigidity of the beam and w the beam deflection. Similarly, the energy in modal space associated with a particular mode shape ϕ_i is calculated from,

$$U_i = \frac{1}{2} \int_0^L EI (\phi_i''(x))^2 dx \quad (6.2)$$

where ϕ_i'' is the second derivative or curvature of mode shape ϕ_i , with respect to x . If the Euler-Bernoulli beam is subdivided into N elements, the modal strain energy associated with the j^{th} element for the i^{th} mode is given by,

$$U_{ij} = \frac{1}{2} \int_j (EI)_j (\phi_i''(x))^2 dx \quad (6.3)$$

The fractional energy of the j^{th} element, denoted as F_{ij} , is therefore,

$$F_{ij} = \frac{U_{ij}}{U_i} = \frac{\frac{1}{2} \int_j (EI)_j (\phi_i''(x))^2 dx}{\frac{1}{2} \int_0^L EI (\phi_i''(x))^2 dx} \quad (6.4)$$

By assuming that the fraction of modal energy is the same for damaged (indicated by *) and undamaged structures, it is found that,

$$\frac{\frac{1}{2} \int_j (EI)_j (\phi_i''(x))^2 dx}{\frac{1}{2} \int_0^L EI (\phi_i''(x))^2 dx} = \frac{\frac{1}{2} \int_j (EI)_j^* (\phi_i''^*(x))^2 dx}{\frac{1}{2} \int_0^L EI^* (\phi_i''^*(x))^2 dx} \quad (6.5)$$

When rearranging equation (6.5), the damage indicator of mode i and member j , β_{ij} , is obtained from,

$$\beta_{ij} = \frac{(EI)_j}{(EI)_j^*} = \frac{\int_j (\phi_i''^*(x))^2 dx \int_0^L (\phi_i''(x))^2 dx}{\int_j (\phi_i''(x))^2 dx \int_0^L (\phi_i''^*(x))^2 dx} \quad (6.6)$$

Here it is assumed that the flexural rigidity $(EI)_j$ of the damaged and undamaged modes is constant over the entire length of the element j . To establish a comparative basis for different modes, the DI β_{ij} is transformed into the standard normal space, and the normalised damage indicator Z_{ij} is given by,

$$Z_{ij} = \frac{\beta_{ij} - \mu_{\beta_{ij}}}{\sigma_{\beta_{ij}}} \quad (6.7)$$

with $\mu_{\beta_{ij}}$ being the mean and $\sigma_{\beta_{ij}}$ the standard deviation of the β_{ij} values for all j elements. The estimation of the damage severity for element j is expressed by,

$$\alpha_{ij} = 1 - \frac{1}{\beta_{ij}} \quad (6.8)$$

with α_{ij} being the severity estimator.

Positive Z_{ij} and α_{ij} values indicate the possibility of damage and can therefore be utilised to locate and quantify defects, respectively. As an example, the damage indicators Z_j and α_j of the numerical beam structure are shown in Figure 6.1 and Figure 6.2, respectively. The illustrated damage indices are derived from mode 1 of noise-free numerical beam simulations of 41 data points. In the figures, the horizontal axis shows the length of the beam, with '1' to '7' indicating the seven investigated damage locations, and the vertical axis the damage indices Z_j and α_j , respectively. The actual damage location is marked with a straight line. Figure 6.1 shows the damage indicator Z_j of beams with defects at locations '4', '5' and '6'. Here, a clear indication of the damage location is visible. Besides the actual damage, some false detections appear close to the supports (indicated by positive Z_j values). The magnitudes of Z_j for the spurious damage locations are, however, significantly smaller when compared to the values of the actual damage. The existence of these false indications is inherent to the DI method and is usually overcome by summing up DI values of several modes and thereby enhancing the magnitude of the indices at the actual damage site. Further, the issue of spurious damage can be dealt with by introducing a threshold value, i.e. only DI values above a certain threshold value (e.g. Z_j values above 0.5) indicate damage. The illustrations of Figure 6.2 depict the severity estimator α_j of beams damaged at location '4' with damage severities of light, medium and severe extent. The varying magnitude of α_j clearly indicates different damage extents. The phenomenon of spurious damage is also observed for the severity estimator α_j .

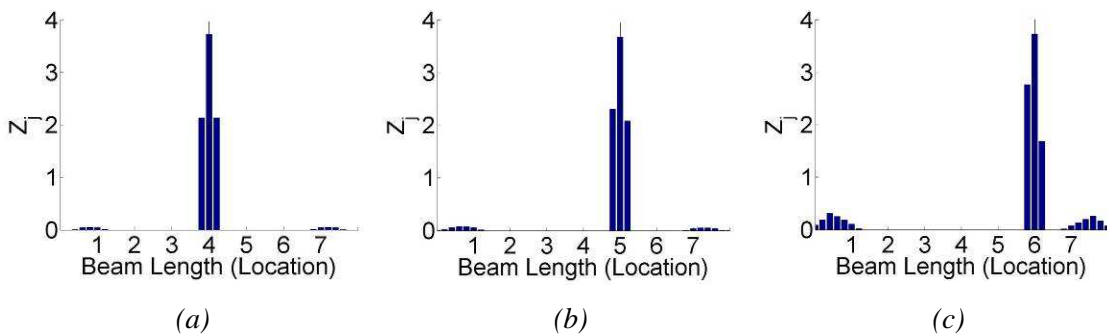


Figure 6.1 Damage indicator Z_j derived from mode 1 of noise-free numerical simulations. Damage is situated at (a) location '4', (b) location '5' and (c) location '6'.

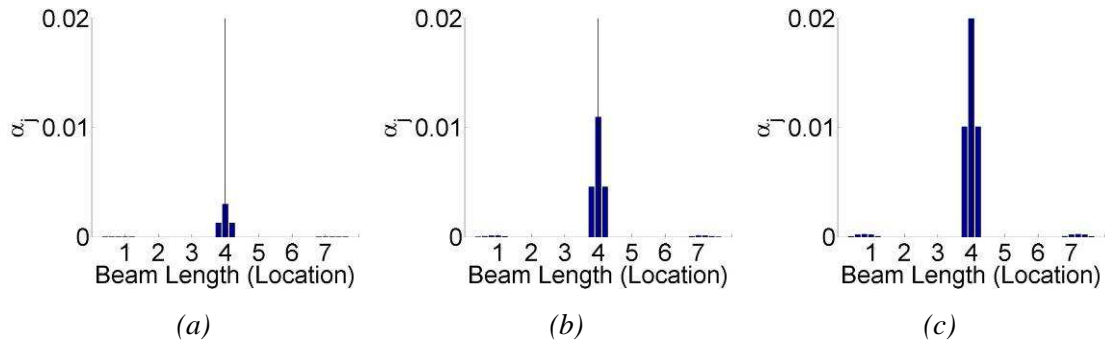


Figure 6.2 Severity estimator α_j derived from mode 1 of noise-free numerical simulations. Damage is situated at location '4' with severity (a) light, (b) medium and (c) severe.

6.2.2 Reconstruction of Mode Shapes

The reliability and accuracy of damage identification is closely related to the density of measurement points (sensors) especially for modal-based damage identification methods (Stubbs & Park 1996; Wang & Zong 2002). The more measurement data available (the finer the sensor network) the more accurate the damage diagnosis. For practical applications, however, it is important for both cost and practicality to be able to obtain reliable damage identification results from only a few sensors. When the collected data are below a certain quantity, the damage detection results inevitably become unreliable. An optimal damage detection scheme is therefore able to give more reliable and precise identification results from a minimal number of sensors. For the DI method, one way of achieving improved damage identification with a small number of measurement points is to refine mode shape vectors utilising data interpolation techniques. The approach of mode shape reconstruction for improved damage detection is reported in several publications. Park and Stubbs (1995) and Stubbs and Park (1996) utilised Shannon's sampling theorem combined with the DI method to locate damage with fewer sensor data points. Worden, Manson and Allman (2001) applied a cubic convolution polynomial interpolation to refine mode shapes for strain-energy-based damage detection. Choi (2007) compared cubic spline interpolation techniques against Shannon's sampling theorem techniques for mode shape reconstruction and subsequent damage identification based on the DI method. Choi concluded that utilising cubic spline interpolation for mode shape refinement is more effective in improving damage identification results than using Shannon's sampling theorem.

In this study, experimental testing of the steel beams is conducted utilising a reduced number of 9 measurement sensors (see section 4.3) giving mode shape vectors of 9 data points. To enhance the quality and effectiveness of damage identification, a reconstruction of the mode shape vectors from 9 to 41 points is performed. Based on the results and recommendations of Choi (2007), the cubic spline technique is used for interpolation. MATLAB (The MathWorks 2007) provides an easy access to data interpolation using the Spline function. In the operation, a tri-diagonal linear system is solved to describe the coefficients of various cubic polynomials, which make up the interpolating spline. From the original 9 data points mode shapes and the reconstructed mode shape vectors (containing 41 data points) damage indices Z_j and α_j are derived.

To show the effectiveness of mode shape reconstruction, damage indices Z_j of an experimental beam derived from mode shapes of 9 and 41 data points are illustrated in Figure 6.3. Depicted are DI values derived from modes 2 to 4 of a beam with medium damage at location '5'. It is noted that the figures only display positive Z_j values, which indicate the possibility of damage. From the Z_j values of mode 2 (Figure 6.3 (a) and (d)), it is observed that the actual damage at location '5' is correctly indicated for both DI values. Both figures also show positive Z_j values of a spurious damage around location '1'. The damage locator derived from the 41 data point mode shape, however, enhances the magnitude of the actual damage from 1.6 to 2.5, while the magnitude of the spurious damage stays about the same. An enhancement of the DI value at the actual damage site is important to establish the existence of damage at that location with higher confidence and to dismiss other false damage indications. For the DI values of mode 3 (Figure 6.3 (b) and (e)), the Z_j figure of 9 data points indicates a damage at location '7' and some minor damage at locations '4' to '6'. When establishing a threshold value of about 0.5, the actual damage would stay undetected, which could have significant consequences. Utilising mode shape reconstruction techniques, the magnitude of damage at location '5' is enhanced (see Figure 6.3 (e)). Even though a spurious damage at location '6' is still shown, the actual damage site is indicated and cannot be dismissed. For the figures of mode 4 (Figure 6.3 (c) and (f)), the Z_j values derived from the original 9 data point mode shape totally dismiss the actual damage with no positive Z_j values near the damage location, which will certainly result in an oversight of the present damage. Instead, false damage is shown at both supports. By

reconstructing the mode shape, the missing damage at location ‘5’ resurfaces as a well defined peak locating the damage correctly (see Figure 6.3 (f)). Some spurious damage is still indicated for the 41 data point values; however, their magnitudes are notably smaller.

From these figures, the effectiveness and significance of mode shape reconstruction for DI-based damage identification with a limited number of sensors is shown. Even though in some cases the reconstruction technique may not provide better results, it at least performs equally as well compared to merely using the limited original mode shape data. In most cases, however, the quality of damage identification is significantly improved, resulting in more precise and more reliable damage detection.

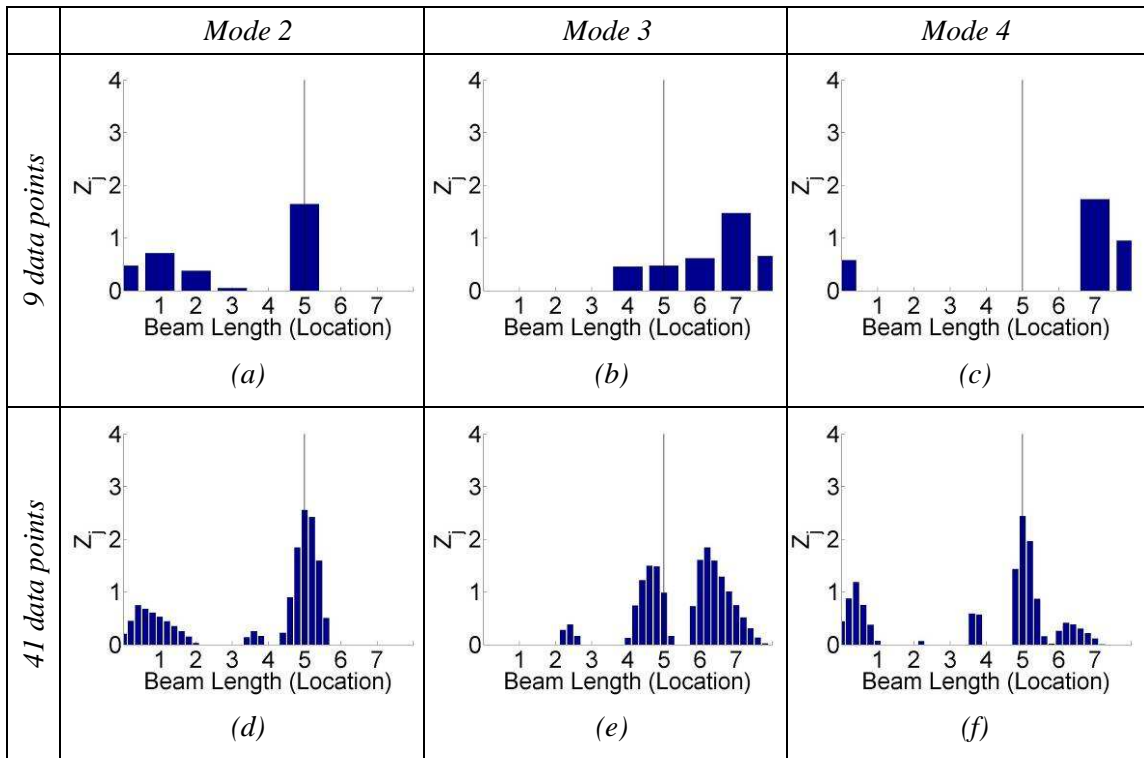


Figure 6.3 Z_j values derived from mode shapes with 9 and 41 data points, respectively. The DI values are derived from modes 2 to 4 of an experimental beam with medium damage at location ‘5’.

For finite element modelling, the density of the mode shape coordinates is linked to the mesh (see section 5.2). For numerical simulations of the beams, 201 node points are modelled in the longitudinal direction, giving mode shape vectors with 201 coordinates. To be comparable with experimental measurements with 9 sensors (see above), the number of numerical mode shape coordinates is reduced to 41 (corresponding to case

41a) and 9 data points. Then, using cubic spline interpolation technique the 9 data point mode shapes are expanded to 41 data points (corresponding to case 41b). Mode shape vectors of 41a data points are used to compare results from reconstructed mode shapes of a coarse sensor network (41b) against those obtained directly from a finer sensor network (41a). From the mode shape vectors of 9 and 41 points (both 41a and 41b cases), the damage indices Z_j and α_j are again derived.

Figure 6.4 shows a comparison between the damage indices Z_j of mode shapes with 9, 41b and 41a data point cases obtained from numerical modelling of the steel beams. Similar to Figure 6.3, damage indicators of a beam damaged at location '5' derived from modes 2, 3 and 4 (of noise-free simulations) are illustrated. This comparison shows again the effectiveness of mode shape reconstruction using cubic spline interpolation techniques as well as the impact of different sensor densities to damage indices. It is stressed that the depicted DI values are derived from numerical simulations with no noise pollution, which means that all spurious detections are inherent issues of the DI method (which will be discussed in more detail in section 6.2.3).

From the Z_j values of 9 and 41b data points (see Figure 6.4 (a) to (f)), the effect of mode shape refinement is again clearly visible. For modes '2' and '4' (Figure 6.4 (a) and (d), and (c) and (f)), the magnitude of the Z_j values at the actual damage location increases from 1.7 to 2.8 and 1.8 to 3.3, respectively, reinforcing reliability of the identification of the damage at location '5'. Similar to the results of experimental testing, a reconstruction of mode shape 3 prevents the missing of the actual damage by enhancing the peak at location '5' (see Figure 6.4 (b) and (e)). When comparing the directly derived DI values from different sensor densities (i.e. 9 and 41 (case 41a) sensors), the significance of the number of sensors in DI-based damage identification becomes clear. The DIs derived from mode shapes of 9 data points produce not only correct location identifications but also a number of false damage indications (sometimes with magnitudes even larger than the peak at the actual damage site), while the Z_j values of 41 sensors (case 41a) show very sharp and clear peaks at the correct damage location and smaller indications at spurious damage sites.

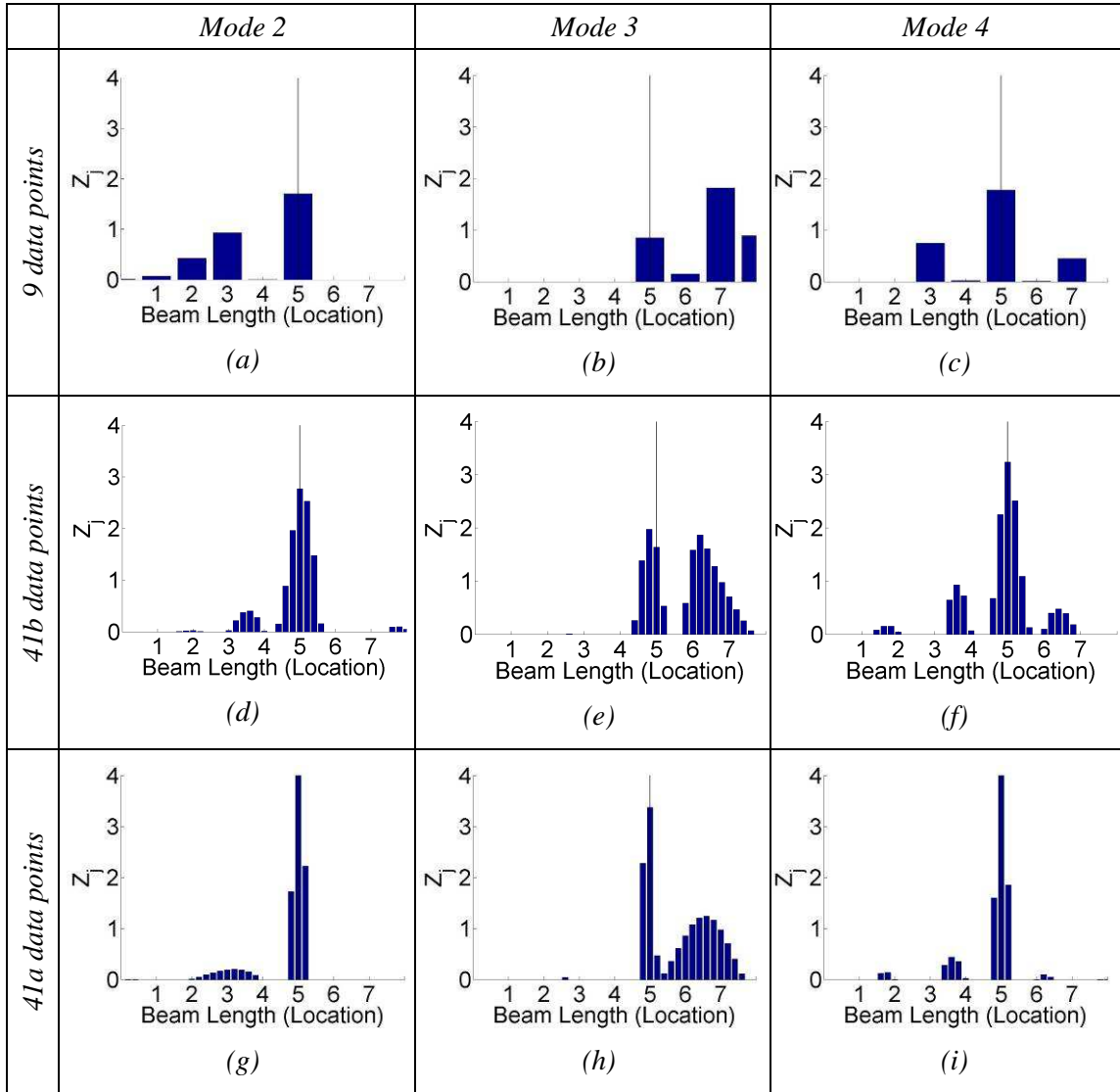


Figure 6.4 Z_j values derived from mode shapes with 9, 41b and 41a data points, respectively. The DI values are based on modes 2, 3 and 4 from noise-free numerical simulations of a beam with medium damage at location ‘5’.

These results show that an increased number of sensors in measurements significantly improves the accuracy and reliability of DI-based damage detection. By reconstructing mode shapes from a small number of sensors utilising cubic spline interpolation, important information can be regained and damage identification results improved (as it is observed from the Z_j values derived from refined mode shapes of 41b data points). Although the damage detection results of reconstructed mode shapes (of 41b data points) are inferior to results obtained from direct mode shape vectors of a large number of sensors (41a data points), the enhancement of damage indices can prevent an oversight of damage cases and deliver more precise and robust detection results.

Therefore, it is always recommended to reconstruct mode shape vectors for damage identification unless data from a very fine sensor network are available. In general, the accuracy of damage localisation outcomes is inversely proportional to the distance between two sensors. Thus, if a finer resolution than the available sensor distribution is required, mode shape reconstruction is essential. Some guidelines on the determination of the ratio between original and reconstructed data points as well as on other available reconstruction techniques can be found in (Choi 2007).

In the following discussions, DI values of all numerical and experimental beam data are derived from reconstructed mode shape vectors of 41b data points utilising cubic spline interpolation techniques. The necessity of using limited sensors in field applications is thereby considered and advantage is taken of the improved damage identification capability arising from reconstructed mode shapes. (The full set of DI values Z_j and α_j of noise-free numerical beam simulations derived from reconstructed mode shapes of 41b data points is illustrated in APPENDIX E.)

6.2.3 Limitations of Damage Index Method

A number of issues are encountered with the DI method. These issues are either associated with the DI algorithm itself or to limitations such as coarse sensor networks, incomplete modal data, modal analysis errors, noise interferences or environmental uncertainties such as temperature and humidity fluctuations. As outlined in CHAPTER 2, many efforts have been made to overcome these problems, for example, by modifying the original DI method or by introducing techniques that either enhance the damage indicators or reduce uncertainties. Some of the limitations associated with the DI method are discussed below.

Firstly, node points of mode shapes may create singularities in the calculation of the DI values (see equations (6.4) to (6.6)). These singularities result in exceptionally large DI values at (and in the proximity of) the node points, which lead to the false indication of damage (Shi, Law & Zhang 1998). This phenomenon is illustrated in Figure 6.5 for Z_j values of modes 3, 6 and 7 of noise-free numerical simulations of a beam damaged at location '6'. Figure 6.5 (a) to (c) display damage indices derived from fine mode shapes of 41a data points and Figure 6.5 (d) to (f) show values from reconstructed mode shapes of 41b data points. In Figure 6.5 (a) to (c), spurious node point indications are clearly

visible. For mode 3, two additional peaks appear in the proximity of the two node points (see Figure 6.5 (a)); likewise for the Z_j values of modes 6 and 7, false damage indications appear close to the node points of these two modes (see Figure 6.5 (b) and (c)). When only a coarse network of sensors is used (see Figure 6.5 (d) to (f)), these false damage indications are enhanced, resulting in more uncertainties. Due to these spurious indications, which become worse at higher modes (more node points), techniques such as the summation of DI values of different modes are crucial to ensure reliable damage diagnosis.

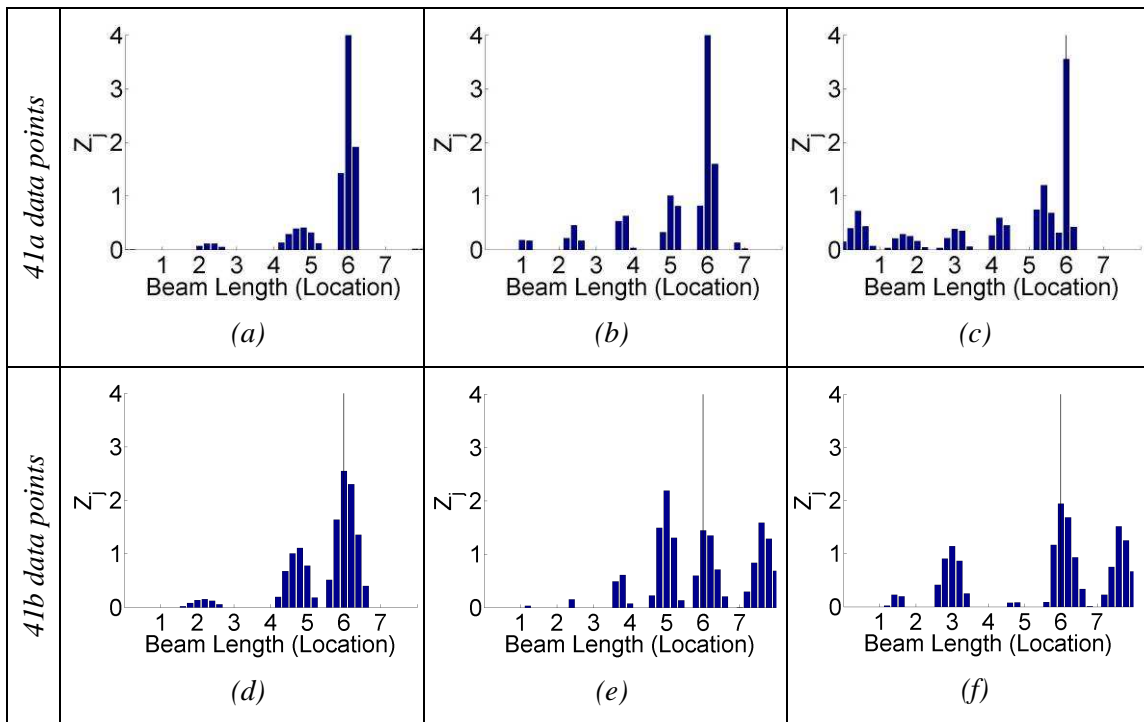


Figure 6.5 Z_j values from noise-free numerical simulations of a beam with medium damage at location '6' derived from (a) to (c) fine mode shapes of 41a data points, and (d) to (f) reconstructed mode shapes of 41b data points. DI values are calculated from (a) and (d) mode 3, (b) and (e) mode 6, and (c) and (f) mode 7.

Secondly, node points of mode shapes may create an undetectable situation in some cases, i.e. when damage is situated at the actual location of a node point, it cannot be detected. This is demonstrated in Figure 6.6, which shows damage indicator Z_j derived from modes 2, 4 and 6 of a noise-free numerical beam damaged at mid-span (location '4'). As location '4' is a node point for these three modes, modal amplitude at this node point location is zero resulting in zero value of Z_j even with damage occurring at that location. Due to the normalisation process that transforms β_j to Z_j (see equation (6.7))

spurious damage indications appear for the Z_j indicator (see Figure 6.6). For the severity estimator α_j , the DI values indicate no damage at all (see Figure E.5 to Figure E.12 in APPENDIX E).

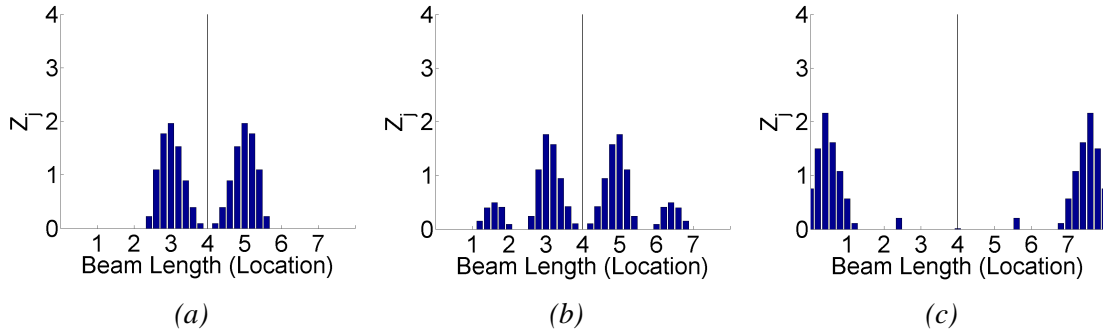


Figure 6.6 Z_j values from reconstructed mode shapes of noise-free numerical simulations of a beam with medium damage at location '4' derived from (a) mode 2, (b) mode 4 and (c) mode 6.

Thirdly, DI values close to the beam supports are very susceptible to uncertainties causing false indications of damage. Examples of spurious damage peaks in the proximity of the beam-ends are illustrated for damage at locations '5' and '6' in Figure 6.7 (a) and (b). Here, besides the correct damage peaks, false damage indications close to the support at the right beam-end are produced. Next, if damage is situated close to the beam-ends (e.g. at location '7', see Figure 6.7 (c)), the actual damage peak is shifted towards the support, giving mislocated damage indications.

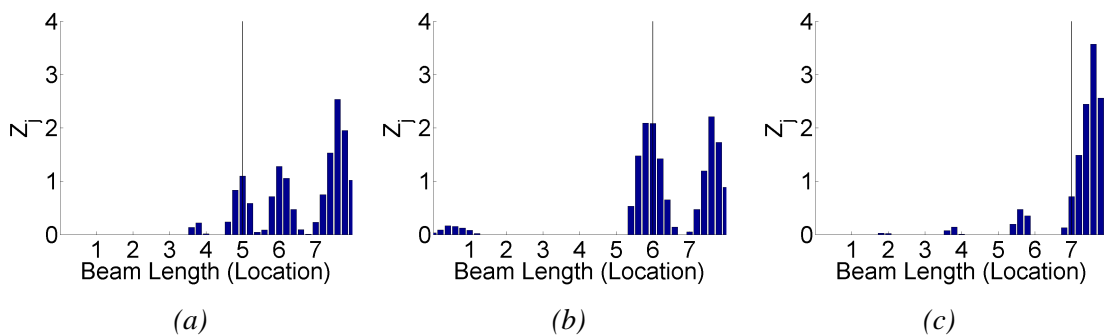


Figure 6.7 Z_j values from reconstructed mode shapes of noise-free numerical simulations of beams with medium damage at (a) location '5' (data derived from mode 6), (b) location '6' (mode 1) and (c) location '7' (mode 3).

Furthermore, the most important issue is related to the susceptibility of the DI method to uncertainties such as noise interferences, modal analysis errors and environmental influences (e.g. temperature or humidity fluctuations). Noise can be caused by many

sources such as testing procedures, noisy environment and electronic systems during measurement (e.g. sensors, cables and acquisition systems). The vulnerability of the DI values to noise is illustrated in Figure 6.8, which displays damage indicator Z_j derived from mode 1 and mode 5, based on numerical simulations polluted with three different random signals of white Gaussian noise at 2% noise to signal ratio. Here, light damage is present at location '4'. Figure 6.8 (a) and (d) depict Z_j values that almost perfectly match the indices obtained from noise-free simulations (i.e. noise uncertainties did not influence these two damage indices). The DI values of Figure 6.8 (b), (c), (e) and (f), however, display additional spurious damage indications as well as shifted peaks of the actual damage. This displays clearly the vulnerability of the damage indices to noise. The susceptibility to noise influences is naturally larger when the damage is less severe or the noise level is higher.

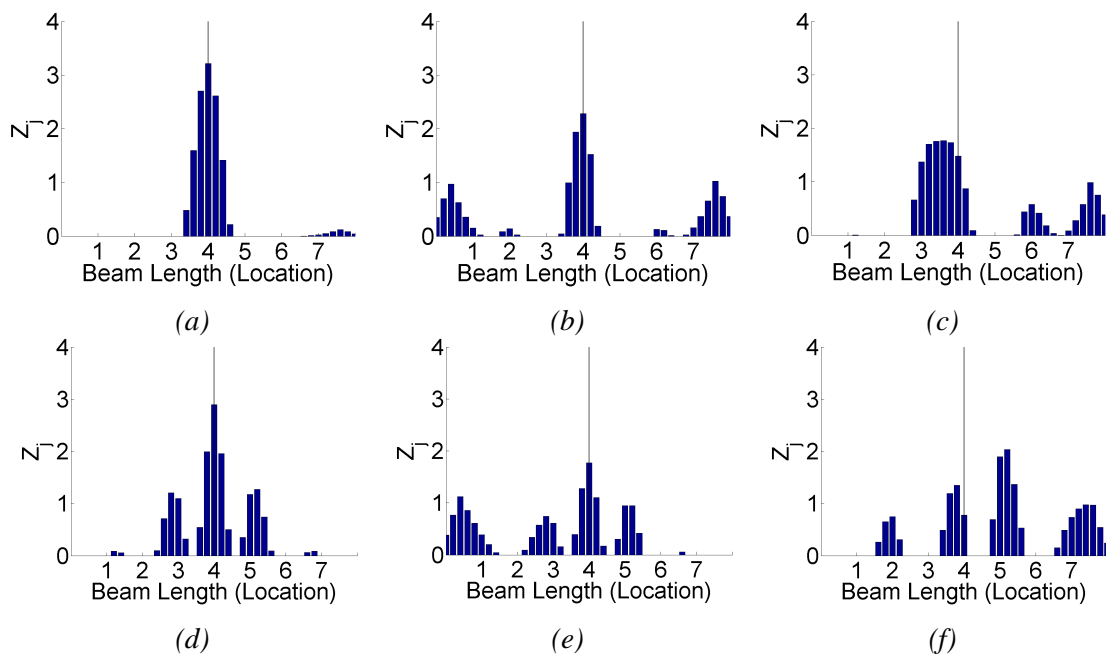


Figure 6.8 Z_j values from numerical simulations of a beam with light damage at location '4'. Data polluted with three different signals of 2% white Gaussian noise derived from (a) to (c) mode 1, and (d) to (f) mode 5.

The issues described above compromise the reliability and effectiveness of the DI method in diagnosing damage. Some problems can be improved by summing the DI values of different modes. However, the performance of the method is still greatly dependent on the number and quality of the available modes (Pereyra et al. 1999).

6.2.4 Principal Component Analysis for Damage Index Values

As outlined above, the big drawback of the DI method is its susceptibility to uncertainties such as measurement noise, modal analysis errors and environmental fluctuations. PCA is known for its capability to reduce the dimension of data as well as its ability to reduce the influence of uncertainties by filtering unrepeatable random features (see section 3.4). Measurement noise, modal analysis errors and environmental uncertainties are random features, which should not be correlated with the global characteristics of the DI values. Therefore, by projecting DI data onto the most important principal components (PCs) and disregarding PCs of low power, only the most dominant characteristics of the data are extracted, and uncorrelated features of noise, modal analysis and environmental uncertainties can be reduced, if not eliminated.

Based on the equations of section 3.4, the 'princomp' function in MATLAB (The MathWorks 2009b) is utilised to transfer the damage indices into the principal component space. For each mode, the DI values Z_j and α_j of the noise-free and the noise-polluted numerical data and the laboratory beam data are separately arranged in matrices of $m \times k$, where m is the number of observations (number of sampled damage cases) and k the dimension of the observations (41 DI data points of Z_j and of α_j obtained from reconstructed mode shapes). For the noise-polluted numerical simulations, data from all four noise levels are transformed together in order to extract the main characteristics from the entire data set and to obtain comparable results among data polluted with different levels of noise. Thereby, for noise-free numerical data 16 cases are available, 576 samples are available for each mode of the noise-polluted numerical beam data and 400 sampled data cases for each mode of the laboratory beams (see Table 6.1). After the projection, each observation is represented by 41 PCs.

Table 6.1 Specifications for PCA transformation of DI data from numerical and laboratory beam structure.

	Sampled cases [m]	DI data points [k]	Remarks
Noise-free numerical data	16	41	16 damage scenarios (4 locations \times 4 severities)
Noise-polluted numerical data	576	41	16 damage scenarios (4 locations \times 4 severities) \times 3 undamaged data cases \times 3 damaged data cases \times 4 noise levels
Laboratory beams	400	41	16 damage scenarios (4 locations \times 4 severities) \times 5 undamaged data cases \times 5 damaged data cases

The derived PCs represent a certain contribution of the data set. As an example, Figure 6.9 shows a plot of the individual and the cumulative contribution of all 41 PCs of Z_j indices of mode 5 of numerical beam data. From the graph, it can be seen that the individual contribution of each of the first seven PCs is 72.5%, 21.2%, 3.6%, 0.8%, 0.7%, 0.6% and 0.2%. That is, the first seven PCs account for 99.6% of the information of the original data.

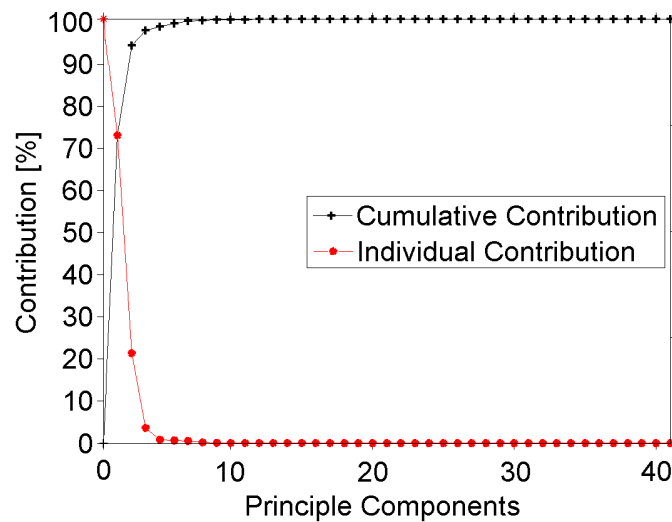


Figure 6.9 Individual and cumulative contribution of the 41 PCs of Z_j values derived from mode 5 of noise-polluted numerical beam simulations.

The individual contributions of the first ten PCs of all seven modes of the noise-polluted numerical and the experimental beam structures are listed in Table 6.2 and Table 6.3. It is noted that due to different characteristics of the seven captured modes, the individual contributions of the PCs vary among the different modes. In general, however, it is

observed that the first few PCs contain over 99% of the information from the original data. Further, from the eighth PC onwards the individual contribution is less than 1% for PCs of all modes.

Table 6.2 Individual contributions of PCs of noise-polluted numerical beam simulations.

	Individual contribution of PCs derived from Z_j in [%]									
	PC 1	PC 2	PC 3	PC 4	PC 5	PC 6	PC 7	PC 8	PC 9	PC 10
Mode 1	35.60	24.82	19.69	11.59	2.24	1.92	1.30	0.85	0.72	0.50
Mode 2	35.73	24.27	14.97	12.73	7.20	1.58	1.09	0.76	0.59	0.34
Mode 3	40.54	34.43	9.84	7.85	3.63	1.24	0.77	0.46	0.31	0.26
Mode 4	57.01	29.75	8.57	2.06	0.88	0.65	0.36	0.20	0.12	0.09
Mode 5	72.54	21.21	3.57	0.83	0.71	0.58	0.17	0.12	0.05	0.05
Mode 6	54.24	28.81	10.70	2.91	1.55	0.52	0.36	0.26	0.15	0.12
Mode 7	45.77	27.99	17.56	5.20	0.88	0.76	0.26	0.16	0.12	0.06
	Individual contribution of PCs derived from α_j in [%]									
	PC 1	PC 2	PC 3	PC 4	PC 5	PC 6	PC 7	PC 8	PC 9	PC 10
Mode 1	37.22	19.81	16.21	12.63	7.93	1.75	1.16	0.95	0.60	0.45
Mode 2	52.64	21.09	14.02	6.05	2.98	1.78	0.54	0.31	0.23	0.14
Mode 3	58.43	23.57	13.15	2.22	1.28	0.72	0.25	0.09	0.07	0.05
Mode 4	66.55	33.28	0.09	0.05	0.01	0.01	0.01	0.01	0.01	0.01
Mode 5	76.02	18.88	4.84	0.20	0.02	0.01	0.01	0.01	0.01	0.01
Mode 6	89.31	10.54	0.09	0.04	0.01	0.01	0.01	0.01	0.01	0.01
Mode 7	64.12	27.68	6.70	0.85	0.38	0.13	0.05	0.03	0.01	0.01

Table 6.3 Individual contributions of PCs of laboratory beams.

	Individual contribution of PCs derived from Z_j in [%]									
	PC 1	PC 2	PC 3	PC 4	PC 5	PC 6	PC 7	PC 8	PC 9	PC 10
Mode 1	64.11	15.49	9.13	3.53	2.69	1.39	1.30	0.57	0.44	0.40
Mode 2	42.53	30.66	13.92	4.73	3.05	1.61	0.98	0.81	0.67	0.29
Mode 3	38.97	22.85	13.42	9.35	5.78	3.37	2.14	1.46	0.85	0.46
Mode 4	32.79	28.12	24.94	6.02	4.59	1.21	0.60	0.35	0.30	0.26
Mode 5	59.99	20.59	10.52	3.90	2.29	1.12	0.43	0.27	0.20	0.18
Mode 6	54.55	22.81	15.45	3.00	1.71	0.68	0.48	0.36	0.30	0.18
Mode 7	51.46	24.49	15.21	5.43	1.49	0.90	0.29	0.20	0.14	0.08
	Individual contribution of PCs derived from α_j in [%]									
	PC 1	PC 2	PC 3	PC 4	PC 5	PC 6	PC 7	PC 8	PC 9	PC 10
Mode 1	57.61	30.56	6.74	2.40	0.93	0.66	0.41	0.18	0.15	0.11
Mode 2	46.29	30.19	8.37	6.84	3.11	1.94	1.42	0.59	0.46	0.28
Mode 3	48.32	18.94	11.03	9.21	5.05	2.81	1.76	1.10	0.61	0.45
Mode 4	39.60	30.06	13.81	8.59	3.66	1.63	1.23	0.71	0.21	0.12
Mode 5	57.86	18.63	12.80	6.92	2.16	0.79	0.29	0.14	0.11	0.06
Mode 6	51.83	23.13	15.36	6.45	1.15	0.91	0.47	0.27	0.13	0.06
Mode 7	66.83	13.16	9.95	6.56	2.25	0.69	0.29	0.06	0.05	0.03

To determine the optimal number of PCs that contain sufficient data for damage identification, a study on the sensitivity of the PCs to different damage scenarios and noise is undertaken. For the noise-polluted numerical beam simulations, Figure 6.10 illustrates the first ten PCs of Z_j and α_j derived from mode 5 and mode 7 of different damage scenarios of numerical data polluted with 1% white Gaussian noise. Figure 6.10 (a) and (c) display PCs of Z_j of medium size damage at locations '4', '5', '6' and '7', and Figure 6.10 (b) and (d) show PCs of α_j of damage at location '5' of severities 'XL', 'L', 'M' and 'S'. For each damage scenario, three different data cases, each polluted with random signals of 1% white Gaussian noise, are displayed. From the figures, it is seen that the PCs of the various damage scenarios have clearly distinguishable patterns up to the seventh PC. The PC values from the eighth component onwards are very small, indicating their insignificant contribution to the damage cases investigated. Further, the three data cases of each damage scenario group together, and thus they are represented by the same PCs. It is noted that PCs derived from DI values of mode 5 are significantly different to those of mode 7. This is due to the different nature of damage indices of the individual modes.

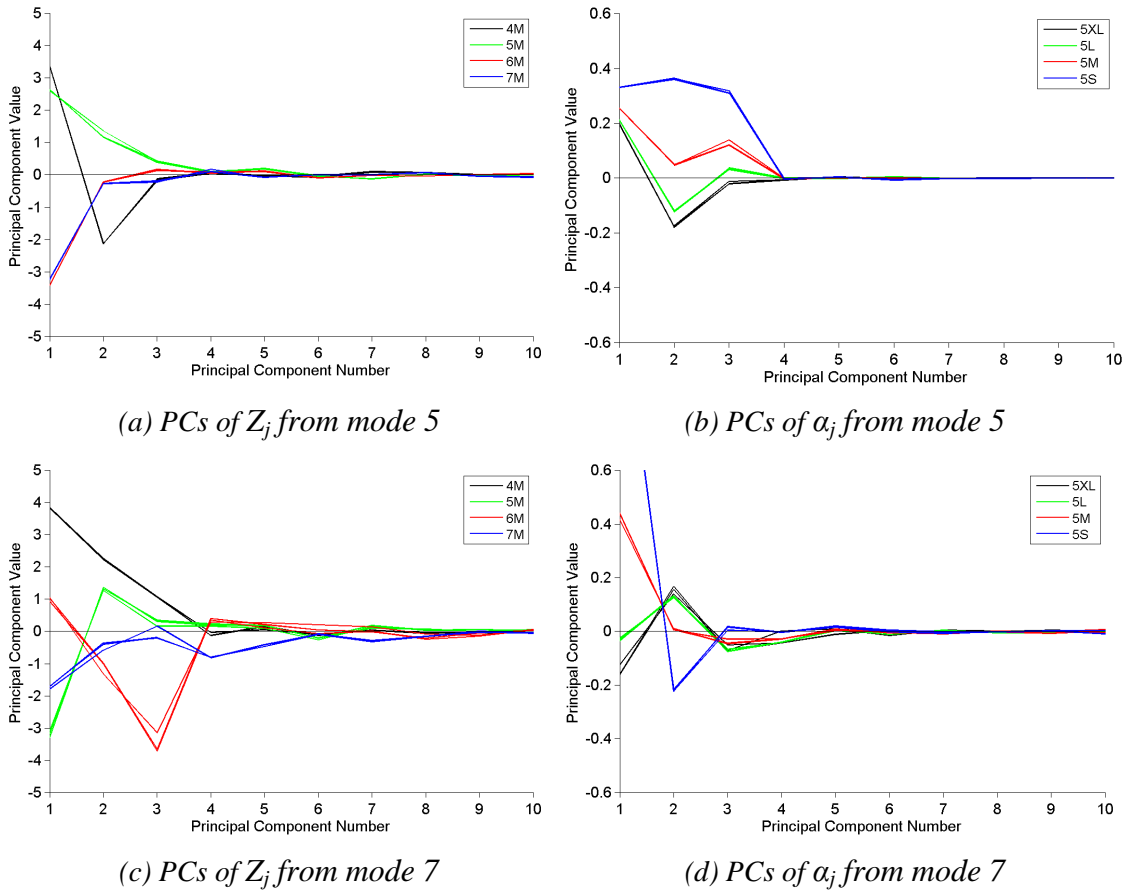


Figure 6.10 The first ten PCs derived from Z_j and α_j of (a) and (b) mode 5 and (c) and (d) mode 7 from numerical beam simulations polluted with 1% white Gaussian noise of (a) and (c) different damage locations and (b) and (d) different damage severities.

For the laboratory beams, the first ten PCs of Z_j and α_j of the same damage scenarios (as presented in Figure 6.10) are illustrated in Figure 6.11. Each damage scenario is represented by three different data cases, each resulting from different hammer hits. From the figures, it is observed that the PCs of the different damage scenarios again show distinguishable patterns. Also, the three data cases of each damage scenario group together; however, the deviation is larger for the laboratory data when compared to data obtained from numerical simulations with 1% noise pollution (see Figure 6.10). It is further noted that the patterns of the PC values of the laboratory data are significantly different to the PCs of the numerical data. The reason for this phenomenon is that, firstly, the DI values of the experimental beams have slightly different features due to differences in mode shape characteristics (see section 4.3.3). Secondly, there are whole ranges of uncertainties encountered in laboratory testing, such as measurement noise, testing and support imperfections, while only noise (assumed to be white Gaussian) is

considered in the numerical simulations. Thirdly, PCs of the laboratory and the numerical data are derived in individual matrices, which further enhance different features of the two data sets.

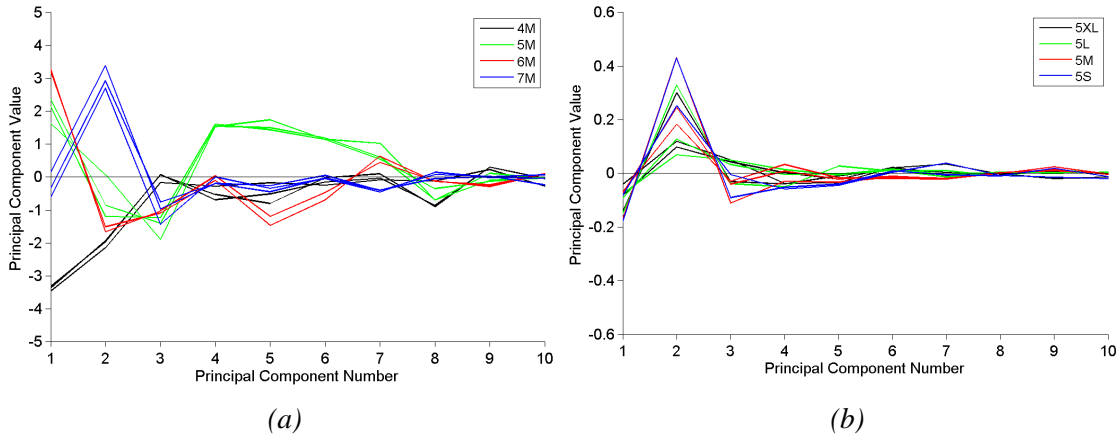


Figure 6.11 The first ten PCs derived from (a) Z_j and (b) α_j of mode 3 from laboratory beams of (a) different damage locations and (b) different damage severities.

To investigate the influence of noise on the numerical beam simulations, Figure 6.12 illustrates the plots of the PCs of Z_j derived from mode 3 of one damage scenario (medium damage at location ‘5’) for the noise levels of 1%, 2%, 5% and 10%. In each graph, five different data cases are shown. Each set is contaminated with randomly generated noise of the same intensity. From the graphs, it is observed that for a noise level of 1%, the first ten PCs of different data cases group together. For a noise intensity of 2%, however, the PCs of different data cases have slightly varying values (see Figure 6.12 (b)); a noise pollution level of 5% results in even larger variations (see Figure 6.12 (c)). For 10% noise pollution, the PCs are entirely dissimilar. For example, for the second PC, values between -1 and -3 are obtained for data of 1% to 5% noise pollution (see Figure 6.12 (a) and (c)); whereas, for a noise level of 10%, the values of the second PC range between +0.5 and +2.5 (see Figure 6.12 (d)). It is noted that PCs derived from 10% noise polluted data do not only differ greatly in the range of the actual values but also in variance between the different data cases.

From these observations, it is found that noise has a profound influence on the PCs of the Z_j values. With an increasing level of noise, not only are PCs of lower power affected, but the most dominant PCs are also influenced. Therefore, by disregarding PCs of lower power, the effects of noise can only be reduced, not eliminated. It is noted that

besides noise pollution, modal analysis errors also have a strong influence on the accuracy of the damage indices and thereby on the PC values. These modal extraction errors have an elevated effect on damage indices as noise pollution level increases. Thereby, PCs of higher power are largely affected by modal analysis errors resulting from high levels of noise.

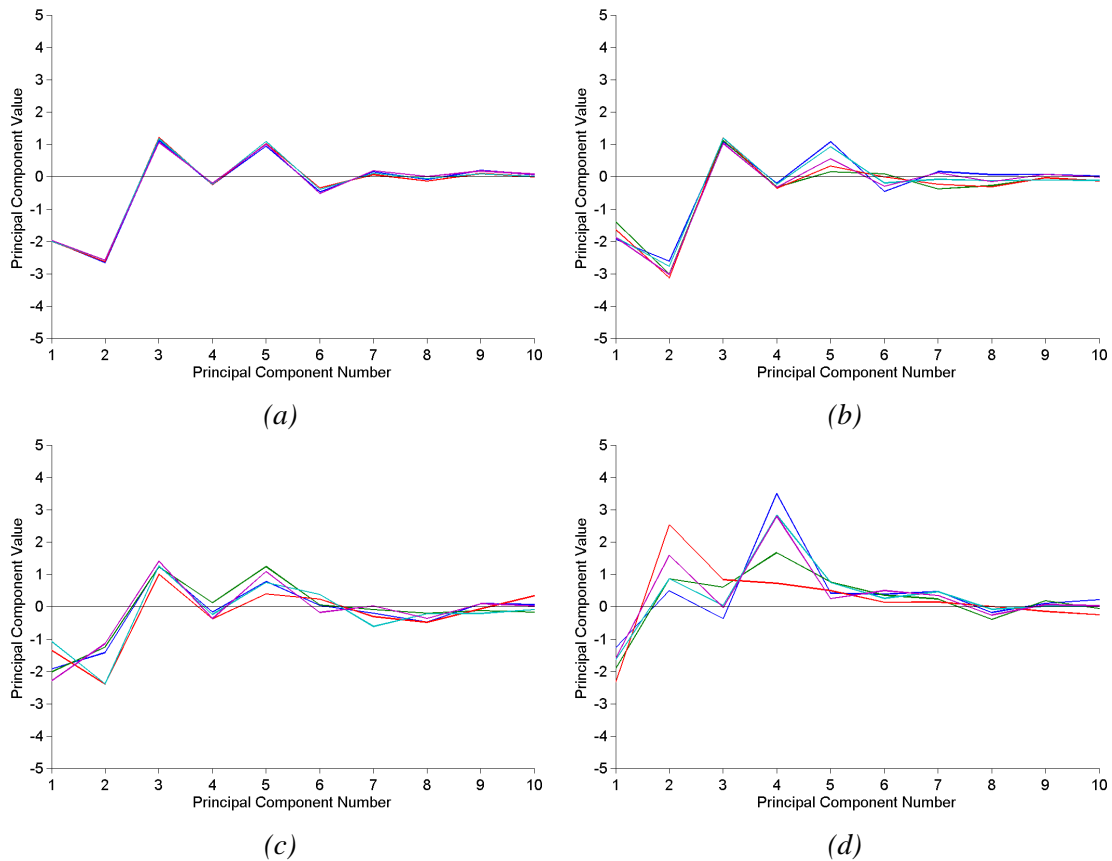


Figure 6.12 The first ten PCs derived from Z_j of mode 3 from numerical beam simulations polluted with (a) 1%, (b) 2%, (c) 5% and (d) 10% white Gaussian noise of a beam with medium size damage at location '5'.

As presented above, PCA has the capability of representing main damage characteristics that are embedded in damage indices Z_j and α_j by a reduced number of PC data. By utilising only the most dominant PCs, the data size is minimised and effects of measurement noise are reduced. From the observations of different PC contributions and the study on sensitivities of PCs to different damage scenarios and noise, it is concluded that for the noise-free and noise-polluted numerical beam structures, the first seven PCs contain the most relevant information on different damage characteristics. For the laboratory structure, the first nine PCs are considered the most important.

6.2.5 Methodology of Neural-Network-Based Damage Identification using Damage Index Method

The DI method is a vibration-based damage detection method that identifies locations and severities of damage based on changes in modal strain energy. As outlined in a previous section (section 6.2.3), there are serious drawbacks with the DI method that result in faulty damage detection jeopardising the reliability and the effectiveness of the DI method and hindering its application in real life situations. On the other hand, it was noted that the patterns of the false indices (especially of those associated with issues of the DI method itself) are of a recurring nature. ANNs, with their capability to recognise patterns, are therefore an ideal tool to complement the DI method and to eliminate/reduce the impact of such faults. Further, the filtering ability of neural networks can help to diminish the uncertain effects of measurement noise, modal analysis errors and environmental fluctuations. Instead of directly feeding the DI values into neural networks, it is beneficial to first transfer the damage indices into the principal component space and to then utilise only the most dominant PCs as input features for neural network training. Such an approach further reduces the impacts of uncertainties (e.g. measurement noise), and moreover damage features are enhanced due to the capability of PCA to project the most dominant features of a data set onto its most important PCs. In addition, the training efficiency of the neural networks is improved due to a reduced number of input nodes and clearer patterns of the input data.

PCs derived from DI values of different modes have dissimilar features (see section 6.2.4). These differences are due to unique patterns of the DI values of the different modes. The unique DI patterns result from individual modal characteristics and the varying susceptibilities of different mode shapes to various damage scenarios. Due to these unique features, it would be a great loss to feed the PCs of all modes together into one network without separation of modes. Such an approach would lead to inefficient network training in which the network would have to learn a multitude of patterns, which not only leads to slower network convergence but also to less reliable outcomes due to the complexity and diversity of input features. Therefore, instead of utilising a single neural network for damage identification, an approach based on neural network ensembles (see section 3.3.4) is proposed. In the network ensemble, first, PCs separated by individual mode shape are evaluated in individual neural networks, then

the outcomes of the individual networks are fused in the ensemble. Such multi-stage network training takes advantage of unique features of PCA-compressed DI values derived from different vibrational modes. By fusing the outcomes of the individual networks in the network ensemble, the proposed technique further considers individual characteristics of different mode shapes, in terms of sensitivity to damage and disturbances. For example, if the outcomes of the individual networks were simply to be averaged, the contribution of each mode in the damage identification process would be considered equal. However, in reality, different modes have different sensitivities to damage (e.g. mode shapes with larger curvatures are more susceptible to damage) and to uncertainties (e.g. mode shapes of higher frequency are more vulnerable to noise than mode shapes of lower frequency), which results in differences in accuracy and reliability of the damage identification outcomes of these modes. Therefore, an intelligent fusion is needed, such as the network ensemble that evaluates the outcomes of the individual networks and gives a final conclusive identification of damage based on the performances of the individual networks. The concept of utilising a neural network ensemble for damage identification is illustrated in Figure 6.13.

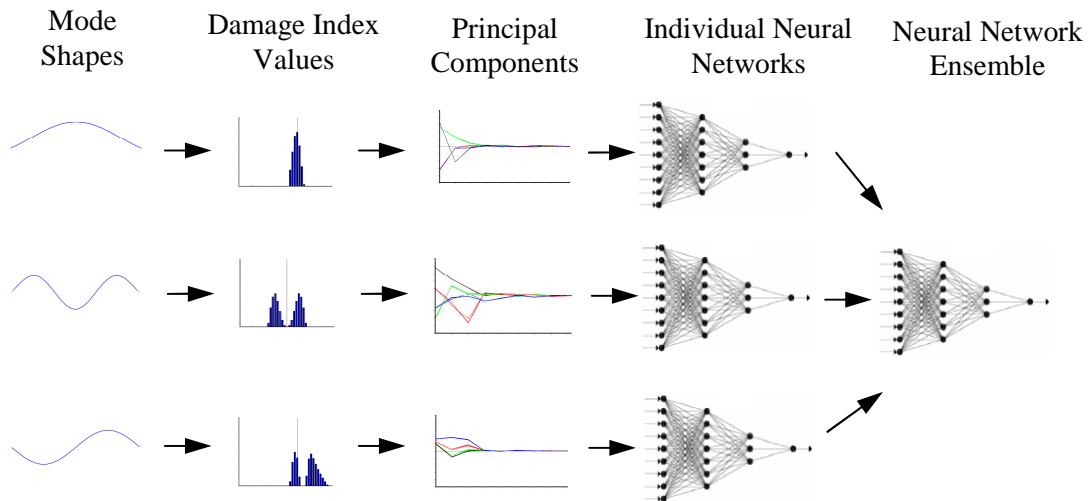


Figure 6.13 Concept of utilising neural network ensembles for damage identification. Input features of individual neural networks are separated by mode shapes in order to take advantage of the unique features of PCA-compressed DI values.

The following methodology for improved DI-based damage identification is proposed.

- First, by means of modal testing (or transient analysis in numerical analysis) and subsequent experimental modal analysis, mode shapes are extracted from the structure (see section 4.2).
- Second, to enhance embedded damage features, measured coarse mode shapes are reconstructed by utilising cubic spline interpolation techniques (see section 6.2.2).
- Third, DI values Z_j and α_j are determined by relating mode shape curvature values (from reconstructed mode shapes) of the undamaged structure to those of the damaged structure following calculations of the DI method (see section 6.2.1).
- Fourth, the damage indices are transformed into the principal component space by employing PCA techniques (see section 3.4).
- Fifth, the most dominant PCs of mode-separated Z_j and α_j values are utilised as input patterns for individual neural network training (see section 3.3).
- Last, the outcomes of the individual networks are fused in a network ensemble that estimates locations and severities of damage (see section 3.3.4). A flow cart of the proposed procedure is shown in Figure 6.14.

The proposed method combines the DI method with ANNs and PCA techniques in order to overcome the issues associated with the DI method and to improve damage identification results. The method considers limited availability of sensors by allowing a minimal number of measurement points. Cubic spline interpolation techniques are utilised to enhance damage features in coarse mode shape vectors. Filtering and feature extracting abilities of PCA are utilised to reduce uncertainties and to improve neural network efficiency. ANNs are used to identify unique damage patterns in PCA-compressed damage indices and further filter uncorrelated uncertainties. By employing network ensemble techniques and separating PCs based on their mode shape origin, unique features of mode-separated PCs are taken advantage of. The network ensemble further considers individual sensitivities of different mode shapes and gives final damage identification predictions based on the outcomes of the individual networks.

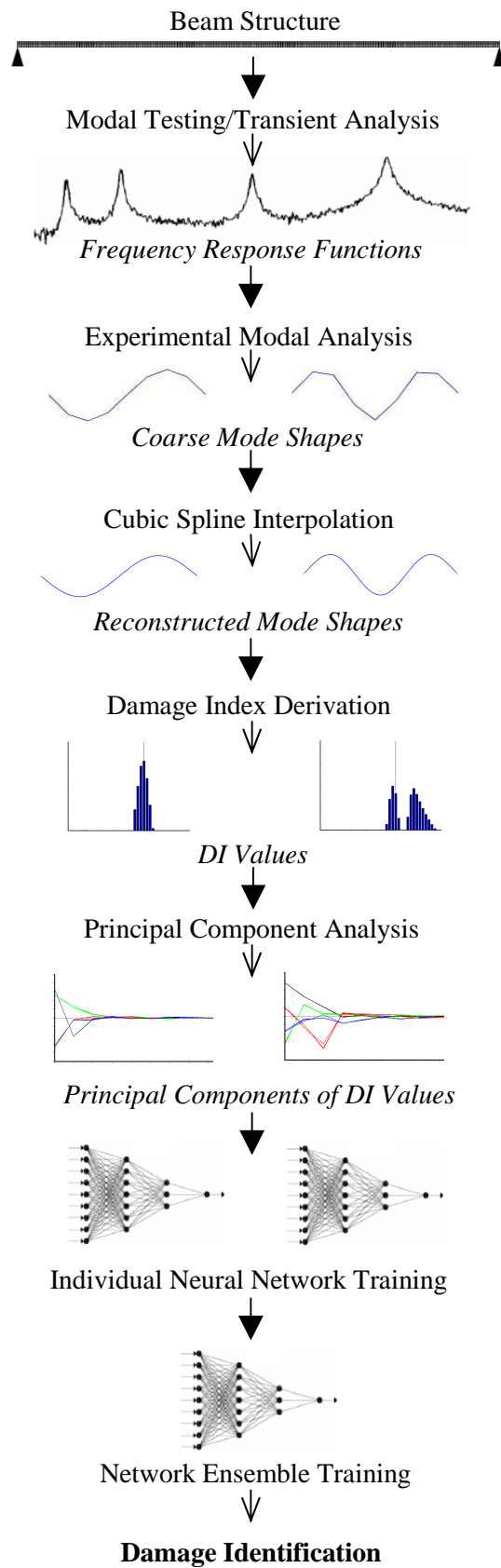


Figure 6.14 Procedure of damage identification based on DI method.

6.3 PROPOSED METHOD 2: DAMAGE IDENTIFICATION METHOD BASED ON FREQUENCY RESPONSE FUNCTIONS

The second proposed damage identification scheme is based on measured FRFs. FRF data are directly measured data and are one of the easiest to obtain in real-time as they require only a small number of sensors and very little human involvement (Fang & Tang 2005). FRFs are normalised complex quantities that specify how vibration is transmitted as a function of frequency between points on the structure (see section 4.2.2). Measured FRF data are usually the most compact form of data obtained from vibration tests of structures. They provide an abundance of information on the structure's dynamic behaviour at a considerable number of degrees of freedom (DOF) and over a range of frequency of interest, whereas modal data are only sub-sets of FRF data (Huynh, He & Tran 2005). Compared to modal parameter methods, FRF-based damage detection techniques do not require extensive post-data analysis such as experimental modal analysis (see section 4.2.3), which involves intensive labour and is very susceptible to human error.

As FRF data are sensitive to structural changes, they have been used as indicators in various forms to detect damage (see section 2.8). In particular, the use of residual FRFs, which are differences between FRF data of the undamaged and the damaged structure, have revealed very promising results (Trendafilova & Heylen 2003). Using as a damage indicator FRF differences instead of directly measured FRF data enhances damage fingerprints and thereby improves detection results. Damage identification based on residual FRFs can be considered as a type of pattern recognition problem as it is looking into discrepancy between two or more signal categories, e.g. before and after a structure is damaged, or differences in damage levels or locations. By utilising ANNs with their powerful pattern recognition and classification ability, damage characteristics, such as damage locations and severities, can be effectively determined from measured residual FRFs.

One of major obstacles in using FRFs for damage identification is the large size of the FRF data. Utilising full-size FRFs in neural networks will result in a large number of input nodes, which will cause problems in training convergence and computational efficiency. If only partial sets of FRF data are used, an improper selection of data points

from frequency windows will result in a loss of important information, and errors will be introduced to the detection scheme (Ni, Zhou & Ko 2006). PCA is again an effective technique for achieving dimensional data reduction (see section 3.4). By projecting data onto the most important PCs, the data's size can be greatly reduced without a significant loss of its most important features. Further, it is a powerful tool in reducing the effects of measurement noise and other random uncertainties (see section 6.2.4).

A further challenge in utilising FRF data for damage identification is the influence of measurement points (Trendafilova & Heylen 1998). While FRFs from some points of a structure are very susceptible to damage, others may not. Likewise, measurement noise has different effects on FRF data at different points of a structure. Naturally, the distance between sensors and the damage is an important factor, but structural dynamic behaviour at the measurement location also plays an important role. In order to respect such individual characteristics of different measurement points, a neural network training approach based on network ensembles is proposed. By analysing FRFs from different measurement points separately in individual neural networks, unique characteristics from different sensor signals (of different measurement points) will be retained. Further, by intelligently fusing outcomes of the individual networks in a network ensemble, an optimal result is obtained. Training neural networks in a hierarchy of network ensembles creates a detection scheme that is less dependent on the completeness of FRF measurements and is therefore more robust in identifying damage.

In this proposed damage identification method, differences in FRF data between the intact and the damaged structure (termed 'residual FRFs') are utilised as damage fingerprints to identify defects. Pattern changes in residual FRF data are analysed by ANNs that map unique damage fingerprints to locations and severities of damage. To obtain suitable input data for network training and to filter uncertainties such as measurement noise, the residual FRFs are compressed to a few PCs using PCA techniques. A hierarchy of neural network ensembles is utilised to take advantage of different characteristics obtained by individual measurements from various sensor locations. Thereby a more robust and improved damage identification scheme is obtained.

The proposed method is verified by two types of structures: a simply supported beam structure and a two-storey framed structure. For both structures, the method is applied to

numerical and laboratory models. First, the technique is thoroughly tested and refined for the beam structure, and then, the two-storey framed structure is utilised to verify the refined method on a more complex structure with various damage scenarios. Issues of limited sensor availability are considered in both structures. Further, to simulate field-testing conditions, white Gaussian noise is added to the numerical data and a noise sensitivity study is conducted for both structures to investigate the robustness of the developed damage detection technique in relation to noise.

6.3.1 Damage Fingerprints in Frequency Response Functions

FRFs are sensitive to structural changes. When damage occurs in a structure, its dynamic behaviours will change; thus the amplitudes and shapes of the FRF data alter. For the beam structure and the two-storey framed structure, such changes in FRF data are discussed in CHAPTER 4 and CHAPTER 5. In the proposed method, residual FRFs will be used as a damage indicator to determine both damage locations and severities. Residual FRF data are defined as:

$$ResH(\omega) = H_d(\omega) - H_{und}(\omega) \quad (6.9)$$

where $H_d(\omega)$ is the FRF data from the damaged structure and $H_{und}(\omega)$ is the FRF data from the undamaged structure.

For the beam structure, Figure 6.15 illustrates such residual FRFs (from the FRF summation function) of numerical beam simulations of 1% noise pollution for different damage scenarios. Figure 6.15 (a) shows the effect of damage at different locations (location '4', location '5', location '6' and location '7' of a medium size damage) and Figure 6.15 (b) depicts the impact of damage of various severities (extra-light, light, medium and severe damage at location '5'). From the figures it is noted that the residual FRF values closest to the frequency peaks are most affected by the damage, or in other words, the frequency ranges in-between the resonant frequencies are not affected by the defects. Further, some frequencies appear to be more sensitive than others. This is particularly visible for the fourth resonant frequency of 205 Hz, which shows the largest amplitude change.

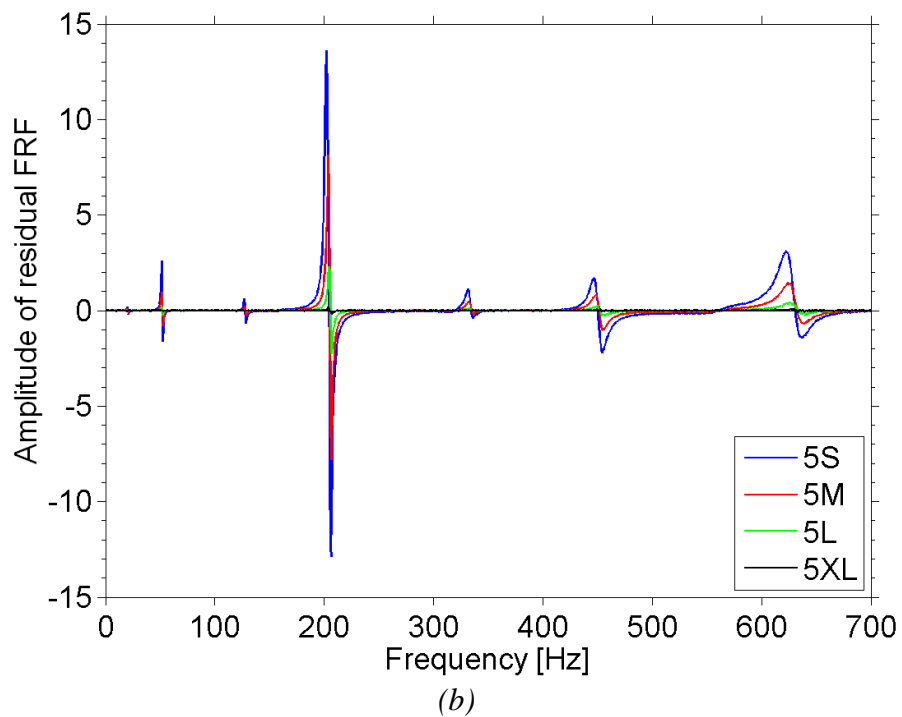
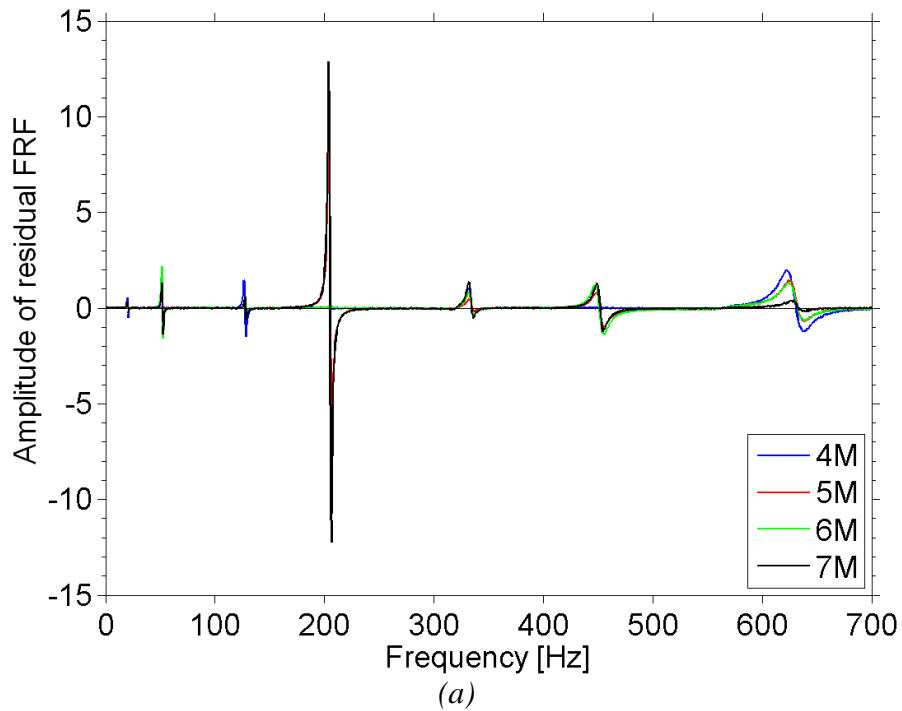


Figure 6.15 Effects of (a) different damage locations and (b) different damage severities to residual FRFs of numerical beam simulations polluted with 1% white Gaussian noise.

The observation of the insensitivity of FRF data in-between frequency peaks leads to the proposal of a second FRF-based damage indicator, termed as ‘compressed normalised residual FRF’ (CNR-FRF). This indicator is a condensed form of the residual FRF and contains only damage sensitive data. Here, only residual FRF values around the frequency peaks are considered. For the FRF data of the beam structure, a frequency band of 10 Hz for the first two natural frequencies and 25 Hz for the third to the seventh frequency is considered. In addition, the residual FRFs of each selected frequency range are normalised by their maximum value. Thereby, differences in amplitude changes between different resonant frequencies are compensated. Besides the advantages of enhanced damage fingerprints and improved data processing, the CNR-FRF has the further benefit of adjusting differences between the FRFs of numerical and laboratory structures. By focusing on frequency bandwidths around resonant peaks, differences in the actual frequency values of the numerical and experimental resonant frequencies become insignificant.

The CNR-FRFs of the previously discussed damage cases are displayed in Figure 6.16. In the graphs, changes in the CNR-FRFs to different damage scenarios are clearly visible and distinguishable. The different damage severities of Figure 6.16 (a) show an explicit amplitude change (a larger damage extent corresponds to a bigger amplitude change). Also, the different damage locations of Figure 6.16 (b) show specific alterations. Here, however, the changes exhibit a more complicated relationship. For example, for the fifth frequency, a medium size damage at location ‘7’ causes the largest amplitude change, followed by damage at location ‘4’, then location ‘6’, and the smallest shift is seen for damage at location ‘5’. For the frequency band around the seventh mode, however, medium damage at location ‘4’ causes the greatest change in amplitude, then damage at location ‘5’, then location ‘6’, and lastly location ‘7’.

It is noted that in the presented example, only frequency peaks from flexural modes are present due to the impact excitation and the response recordings of the structure in one direction. If torsional or transverse modes were also excited and recorded, additional peaks would appear in the FRF. Depending on the type and location of damage, these torsional or transverse peaks would also reflect individual damage characteristics and could therefore be used to detect damage in the same way as peaks from flexural modes.

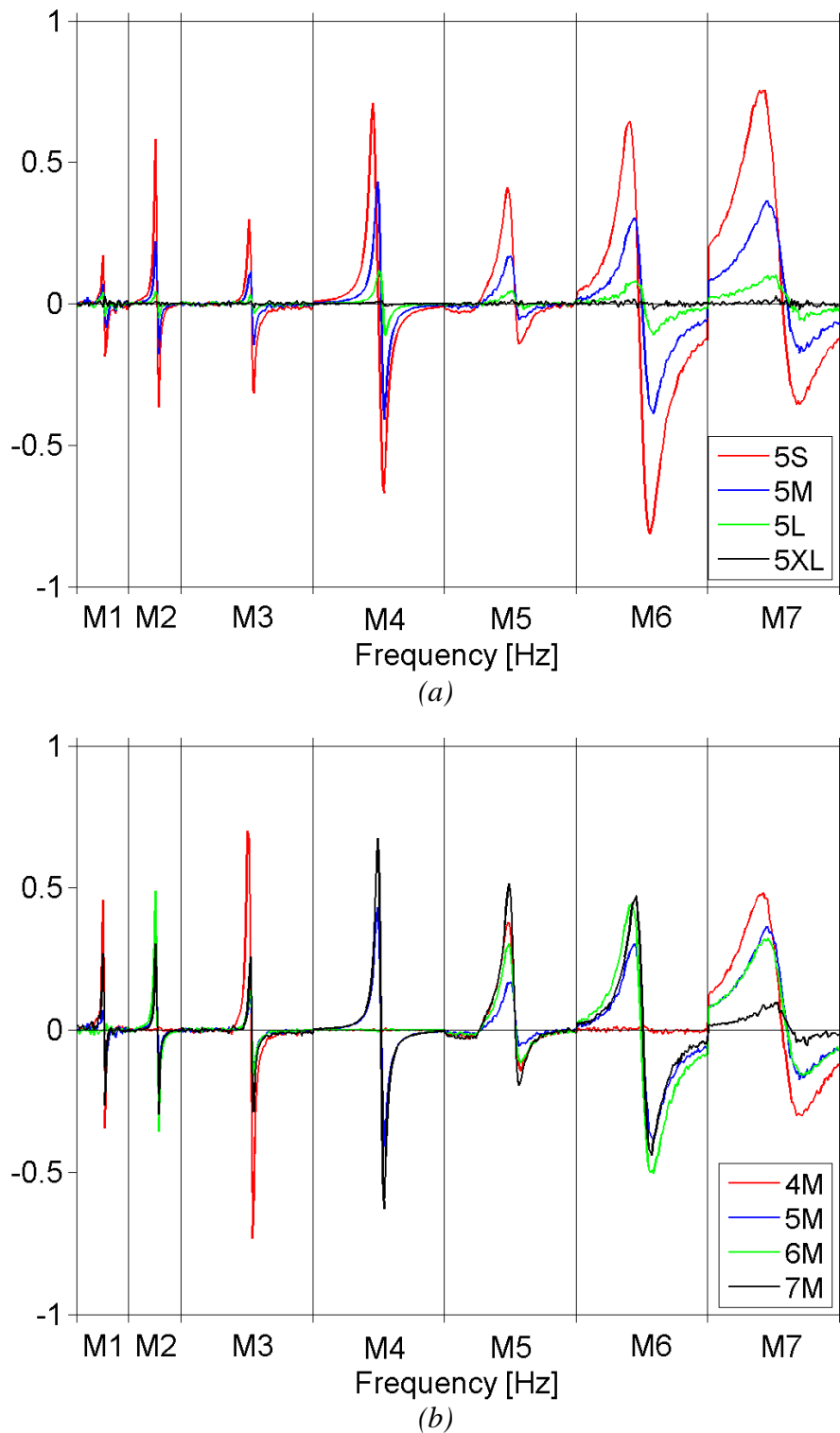


Figure 6.16 Effects of (a) different damage severities and (b) different damage locations to CNR-FRFs from numerical beam simulations polluted with 1% white Gaussian noise.

In general, a very complex pattern of residual FRF changes, such as altering amplitudes, shifting peaks and varying shapes, which relate to different damage locations and damage severities, is observed for the damage scenarios of the beam structure. For the two-storey framed structure, a similar complex pattern of change in the residual FRFs is observed. These unique patterns form the basis of the proposed damage identification method. For the beam structure, both damage indicators (the direct residual FRFs and the CNR-FRFs) are utilised to identify damage of the numerical and laboratory beams. The identification of the different damage/added mass scenarios of the two-storey framed structure is only performed with the direct residual FRF data. (CNR-FRF data are disregarded for the two-storey framed structure, as damage identification results of the beam structure revealed that residual FRFs and CNR-FRFs give almost identical outcomes.)

6.3.2 Principal Component Analysis for Frequency-Response-Function-Based Damage Identification

As mentioned in a previous section, the large size of FRF data is a major obstacle for neural network training. To produce damage indices that are feasible for neural network training, the size of the damage quantities (residual FRFs and CNR-FRFs) must be greatly reduced. For the beam structure, in this study, a full-size residual FRF, which covers a frequency range of 0 to 700 Hz (capturing the first seven flexural modes), contains 1,146 spectral lines (see section 4.3). This would mean 1,146 input nodes in the neural network. The already compressed CNR-FRFs still comprise 481 spectral lines. For the two-storey framed structure used in this study, a frequency bandwidth of 0 to 150 Hz with 2,458 spectral lines is considered (see section 4.4). Such large numbers of input points cause severe problems in training convergence. Therefore, PCA is applied to the selected damage quantities (residual FRFs and CNR-FRFs) to reduce their size and to filter noise.

Similar to the transformation of the DI values into the principal component space (see section 6.2.4), for the residual FRFs or the CNR-FRFs, the ‘princomp’ function in MATLAB is utilised to project the damage fingerprints onto their PCs. For the beam structure, the sampled data cases of the numerical and the laboratory structure are projected in two separate matrices of $m \times k$ – one for the noise-polluted numerical data

(all noise levels combined) and one for the experimental data. Table 6.4 lists the numbers of sampled data cases (observations) and the corresponding numbers of FRF data points (for residual FRFs and CNR-FRFs (in brackets)) for the numerical and the laboratory data. After the projection, each of the observations is represented by 1,146 and 481 PCs (for residual FRFs and CNR-FRFs, respectively). For each damage case, FRF data is acquired at nine measurement points (see section 4.3). In addition, a summation FRF, which is obtained by adding up the FRFs of all nine measurement points, is calculated. Therefore, for each of the ten FRF sources, two PCA transformation matrices are formed.

Table 6.4 Specifications for PCA transformation of FRF-based data from numerical and laboratory beam structure. FRF data points refer to residual FRF spectral lines and CNR-FRF data points (in brackets), respectively.

	Sampled cases [m]	FRF data points [k]	Remarks
Numerical beams	576	1,146 (481)	16 damage scenarios (4 locations \times 4 severities) \times 3 undamaged data cases \times 3 damaged data cases \times 4 noise levels
Laboratory beams	400	1,146 (481)	16 damage scenarios (4 locations \times 4 severities) \times 5 undamaged data cases \times 5 damaged data cases

For the two-storey framed structure, the three damage/added mass scenarios of the numerical and experimental structure (boundary condition scenario, added mass scenario and section reduction scenario) are analysed separately. Therefore, six separate matrices are formed, extracting the most important features from each of the three damage/added mass types for the numerical and the laboratory structures. Details on sampled cases and FRF spectral lines are listed in Table 6.5. After PCA projection, all sampled cases of the two-storey framed structure are represented by 2,458 PCs. (For the two-storey framed structure, FRFs are measured at 14 different locations (see section 4.4), and two additional horizontal and vertical summation FRFs are calculated. Therefore, for each of the sixteen FRF sources, six different matrices are formed.)

Table 6.5 Specifications for PCA transformation of FRF-based data from numerical and laboratory two-storey framed structure.

	Scenario	Sampled cases [m]	FRF data points [k]	Remarks
Numerical two-storey framed structure	Boundary condition scenarios	1,000	2,458	10 boundary condition scenarios \times 5 undamaged data cases \times 5 damaged data cases \times 4 noise levels
	Added mass scenarios	600	2,458	6 added mass scenarios \times 5 baseline data cases \times 5 added mass data cases \times 4 noise levels
	Section reduction scenarios	1,800	2,458	18 section reduction scenarios (6 locations \times 3 severities) \times 5 undamaged data cases \times 5 damaged data cases \times 4 noise levels
Laboratory two-storey framed structure	Boundary condition scenarios	250	2,458	10 boundary condition scenarios \times 5 undamaged data cases \times 5 damaged data cases
	Added mass scenarios	150	2,458	6 added mass scenarios \times 5 baseline data cases \times 5 added mass data cases
	Section reduction scenarios	150	2,458	18 section reduction scenarios (6 locations \times 3 severities) \times 5 undamaged data cases \times 5 damaged data cases

The individual contributions that are obtained from the projection of the residual FRFs of the numerical and experimental beam structures are listed in Table 6.6 and Table 6.7. The tables present the first ten PCs for locations ‘1’ to ‘7’ and the FRF summation function. From the tables it is observed that the PC contributions of the residual FRF from different measurement locations and the FRF summation function are all very similar. For example, for the numerical data, the contributions of the first five PCs from different measurement sources are all about 20.0%, 8.5%, 5%, 2.5% and 0.8%. It is also noted that for the numerical data, PCs of rank 5 and higher have a low contribution of less than 1%; whereas for the experimental data, up to the tenth PC the contribution is higher than 2%. Further, it is found that the summation of the first ten PCs of numerical data accounts for about 40% of the information, while that of experimental data accounts for about 80%. These findings are expected since experimental testing gives rise to more complex features in residual FRF data, which are reflected in larger contributions of higher PCs. (In the ideal environment where structures are numerically simulated by finite element modelling only changes from damage together with noise interferences from artificial noise pollution are present in the residual FRFs and are therefore projected with a large contribution onto the highest PCs.) Hence, to seek only

PCs with a large contribution is not sufficient as PCs reflect information pertaining to the entire data set and not only characteristics of damage.

For damage identification based on DI values, such clear differences between PCs obtained from numerical and laboratory data are not observed (see section 6.2.4). The reasoning for this is that DI values are indirectly measured data, and by performing experimental modal analysis, such direct correlations are suppressed. This is a clear evidence that FRF data are more suitable for damage indication than modal-based data where additional uncertainties could be induced by processing such as experimental modal analysis.

Table 6.6 Individual contributions of PCs from residual FRFs of numerical beams for measurement locations '1' to '7' and the FRF summation function ('Sum').

Individual contribution of PCs derived from residual FRFs in [%]											
	PC 1	PC 2	PC 3	PC 4	PC 5	PC 6	PC 7	PC 8	PC 9	PC 10	$\sum_{i=1}^{10} PC_i$
'1'	19.75	7.73	4.70	2.70	0.82	0.79	0.74	0.73	0.71	0.70	39.37
'2'	22.06	7.00	4.25	1.88	0.88	0.83	0.82	0.76	0.74	0.73	39.95
'3'	20.10	7.75	4.04	2.44	0.88	0.84	0.82	0.79	0.79	0.77	39.22
'4'	24.01	5.50	4.65	2.19	0.80	0.78	0.77	0.77	0.75	0.71	40.93
'5'	17.76	9.85	5.64	2.35	0.81	0.75	0.74	0.74	0.71	0.69	40.04
'6'	18.11	10.61	4.74	2.44	0.85	0.81	0.79	0.76	0.73	0.69	40.53
'7'	14.61	9.96	5.61	2.77	0.85	0.80	0.78	0.75	0.73	0.72	37.58
'Sum'	24.06	10.86	5.61	2.72	0.95	0.92	0.89	0.85	0.84	0.82	48.52

Table 6.7 Individual contributions of PCs from residual FRFs of laboratory beams for measurement locations '1' to '7' and the FRF summation function ('Sum').

Individual contribution of PCs derived from residual FRFs in [%]											
	PC 1	PC 2	PC 3	PC 4	PC 5	PC 6	PC 7	PC 8	PC 9	PC 10	$\sum_{i=1}^{10} PC_i$
'1'	22.22	17.25	12.01	7.86	4.98	3.95	3.30	3.16	2.56	2.34	79.63
'2'	30.07	17.36	12.96	6.92	5.38	4.82	2.88	2.21	2.11	2.03	86.74
'3'	22.01	15.40	12.62	9.91	5.55	4.97	3.58	3.07	2.51	2.41	82.03
'4'	20.23	15.73	14.26	11.06	5.38	4.56	3.23	2.90	2.41	2.01	81.77
'5'	25.21	13.79	10.31	8.58	5.16	4.65	3.90	3.06	2.74	2.12	79.52
'6'	21.56	12.20	10.62	10.05	6.97	6.05	4.95	2.97	2.63	2.35	80.35
'7'	38.19	11.32	9.58	7.42	6.28	4.80	2.86	2.42	2.22	2.03	87.12
'Sum'	29.95	14.07	10.31	7.81	5.35	3.91	3.43	3.19	2.48	2.12	82.62

To closely examine PCs from the numerical beam structure, Figure 6.17 illustrates the first ten PCs of residual FRFs (obtained from the FRF summation function) of different damage scenarios from numerical beam simulations polluted with 1% noise. Graph (a) presents damage at different locations (medium size damage at locations ‘4’, ‘5’, ‘6’ and ‘7’) and graph (b) shows damage of different severities (damage at location ‘5’ of severities ‘XL’, ‘L’, ‘M’ and ‘S’). Each damage scenario is represented by three different data cases (each polluted with 1% random white Gaussian noise). Similar to the PCs obtained from DI values, clearly distinguishable patterns are observed for the first four PCs. From the fifth PC onwards, PC values are smaller (in absolute terms) and very similar for all damage scenarios. The three data cases of each damage scenario cluster together and are represented by the same PCs. Such clustering behaviour and the distinct patterns of the different damage scenarios are ideal conditions for neural-network-based pattern recognition.

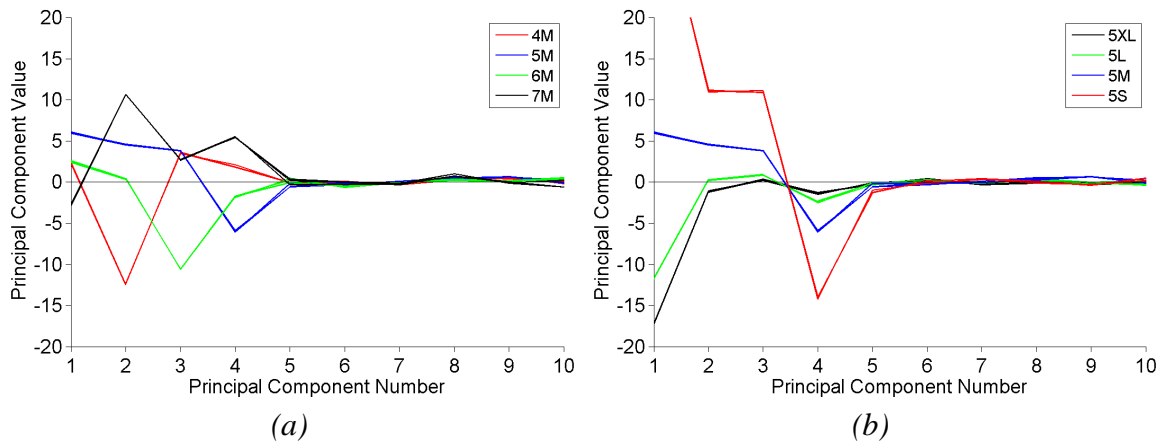


Figure 6.17 The first ten PCs of residual FRFs (from the FRF summation function) of numerical beam data polluted with 1% white Gaussian noise of (a) different damage locations and (b) different damage severities.

For the laboratory beam structures, Figure 6.18 illustrates the first ten PCs from residual FRFs of the same damage cases. Again, specific patterns and clustering effects of different damage scenarios are observed from the figures. It is noted that the first few PCs are least affected by noise and uncertainties. Data cases of the same damage scenario group together for the first five PCs, but appear more scattered from the sixth PC onwards. (Such behaviour is typical for data in the principal component space as noise is a random feature and should therefore be represented by PCs of lower power.)

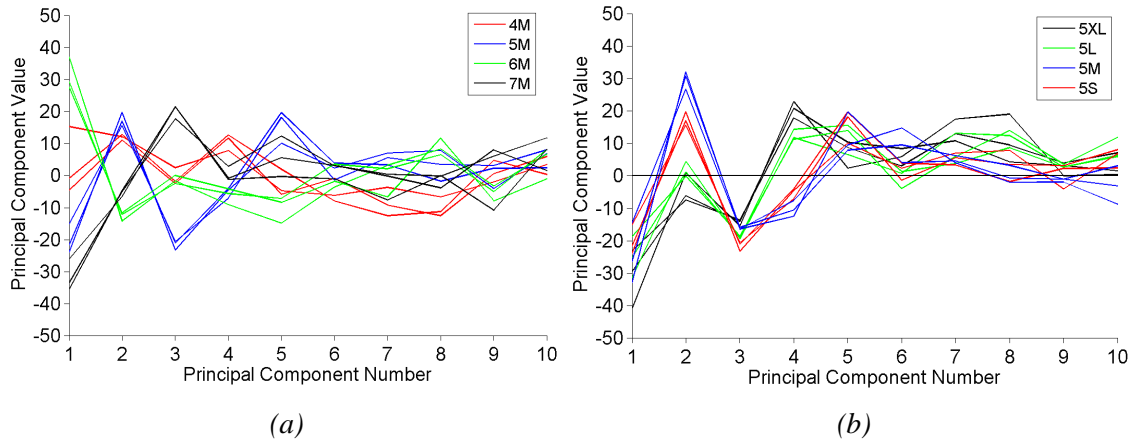


Figure 6.18 The first ten PCs derived from residual FRFs (from the FRF summation function) from laboratory beams of (a) different damage locations and (b) different damage severities.

At this point, a further study on the influence of noise on PCs from residual FRFs of noise polluted numerical beam simulations is conducted. In Figure 6.19, PCs from residual FRFs (obtained from the FRF summation function) of numerical beam structures of one damage scenario (medium damage at location ‘5’) are plotted for the noise levels of 1%, 2%, 5% and 10%. In each graph, 15 different data cases, all polluted with the same intensity but different generations of noise, are shown. From the four graphs, it is observed that up to a noise level of 5% the first ten PCs of the different data cases show only minor variations. For a noise intensity of 10%, however, the PCs of rank five and higher have significantly different values. This clearly shows that the component values from the fifth PC onwards reflect noise patterns, which confirms the findings of the laboratory data. By disregarding the PCs of lower power (from the fifth PC onwards), noise effects will therefore be greatly reduced, which should result in improved damage identification results. In comparison to PCs obtained from DI values (see Figure 6.12), for the PCs of residual FRFs, the most dominant PCs are less sensitive to noise (even at 10% noise pollution, the first four PCs of the different data cases still keep the same trend). At the same time, the PCs from residual FRFs of lower power are more susceptible to noise (see Figure 6.19 (d)). The reason for such behaviour is that residual FRFs are directly measured quantities and noise therefore has a direct influence on the data. DI values, however, are obtained from FRFs after executing experimental modal analysis procedures. (Therefore, noise has a less direct effect on the DI values resulting in error prone PC values of higher power.) These

different impacts of noise on the damage indicators (DI values and residual FRFs) further highlight the advantage of utilising directly measured FRFs instead of modal parameter data such as DI values for damage detection.

From the observations above, it is concluded that for the numerical beam structures, the first four PCs represent the most dominant features in the data set with respect to damage characteristics. Therefore, only the first four PCs will be used as an input feature for neural network training. For the laboratory beam structures, even though a scattering effect is noted from the sixth PC onwards, the high individual contributions of the first ten PCs lead to the decision to use all of the first ten PCs for network training.

For the two-storey framed structure, relevant tables and figures of PCs from residual FRFs from the numerical and the laboratory structure are presented in APPENDIX F. Table F.1 to Table F.6 list individual contributions of the first 30 PCs of the numerical and the laboratory two-storey framed structure. Figure F.1 to Figure F.4 illustrate PCs of different damage/added mass scenarios of the numerical and the laboratory structure.

In general, the determination of the optimal number of PCs is dependent on the quality of damage patterns embedded in a data set as well as the level of noise pollution. Therefore, for the selection of PCs, a sensitivity study on the PC contributions of damage characteristics and noise levels must be undertaken. As a general guideline, indications on dominant features of a data set are given by individual and cumulative contributions of PCs. For example, if the first 10 PCs account for more than 99% of the information of the original data, then a selection of more than 10 PCs for damage identification is probably unnecessary as the information gained by including higher PCs is negligible.

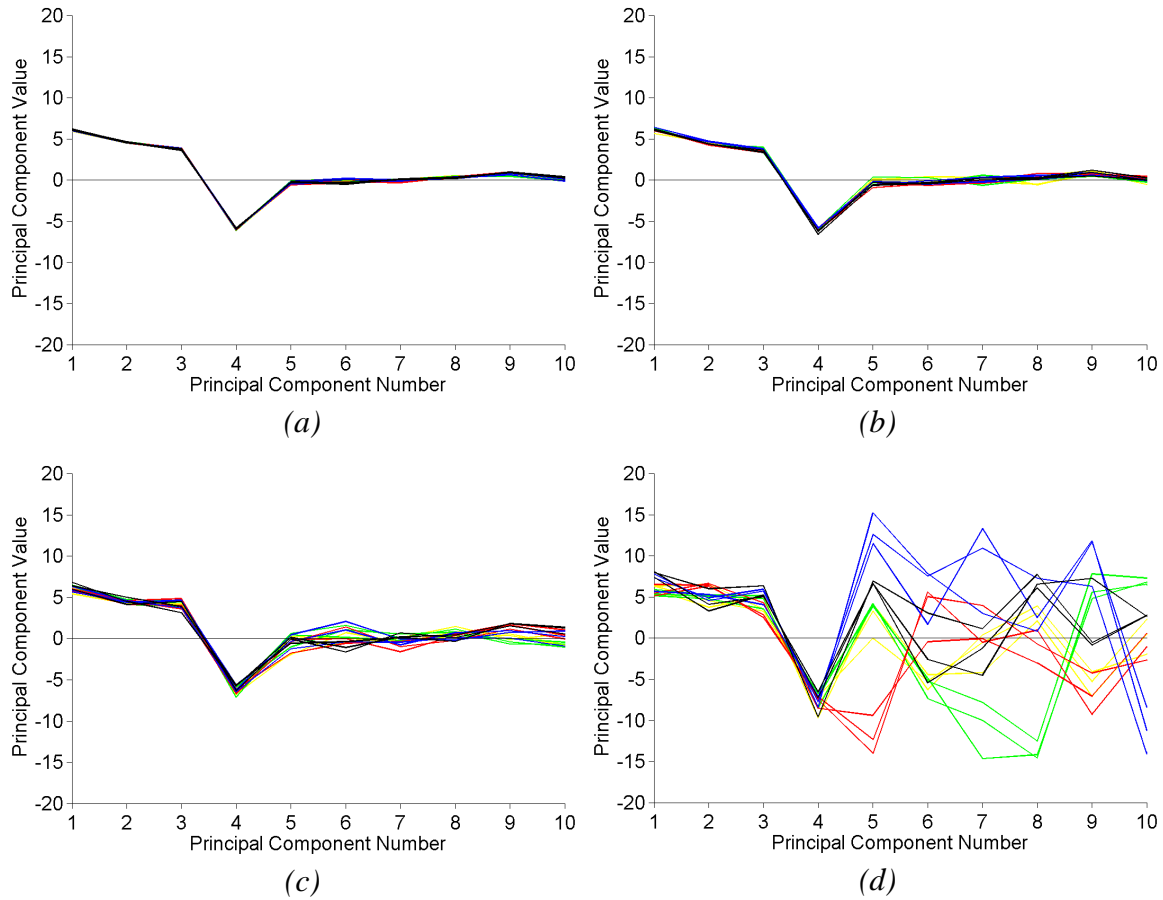


Figure 6.19 First ten PCs obtained from residual FRFs of numerical beam simulations polluted with (a) 1%, (b) 2%, (c) 5% and (d) 10% white Gaussian noise of a medium size damage at location '5'.

6.3.3 Methodology of Neural-Network-Based Damage Identification using Frequency Response Function Data

Identifying damage based on damage fingerprints from FRF data has several advantages. FRFs are directly measured data that are easy to obtain without post-processing that needs human involvement. FRF data provide an abundance of information and are less error prone than modal data, which require human operated experimental modal analysis procedures. By utilising residual FRFs as damage indicators, damage fingerprints from FRF data are enhanced. Damage patterns in residual FRFs can be identified by ANNs that map changes in residual FRFs to damage characteristics such as damage types, damage locations and damage severities. The utilisation of neural networks has the further benefit of reducing noise influences in damage detection. Using PCA, large size residual FRF data can be compressed to a few

PCs. In addition, random uncertainties, such as measurement noise, are reduced by disregarding PCs of lower power. Due to the different characteristics of FRF data from various measurement locations, neural network training based on network ensemble techniques is proposed. By first training individual neural networks with PCA-compressed residual FRFs separated by sensor location and then fusing the outcomes of the individual networks in a network ensemble, advantage is taken of individual characteristics from different sensor signals, and training efficiency is improved.

For FRF-based damage identification the following procedure is proposed.

- First, time history data are extracted from the structure. Therefore, modal testing is conducted for the laboratory structure (see CHAPTER 4), and transient analysis with subsequence noise pollution is performed for the numerical structure (see CHAPTER 5).
- Second, from the time history data, FRFs are determined by relating input forces to response forces of the structure (see section 4.2.2).
- Third, by subtracting FRF values of the intact structure from FRFs of the damage structure, residual FRF data are obtained.
- Fourth, by adopting PCA techniques, residual FRFs are compressed and the most important PCs identified (see section 3.4).
- Fifth, sets of individual sensor neural networks are trained and tested with PCA-compressed residual FRFs separated by sensor location (see section 3.3).
- Finally, a neural network ensemble fuses the outcomes of the individual networks, and an overall damage prediction is obtained (see section 3.3.4). A flow cart of the proposed FRF-based damage identification scheme is shown in Figure 6.20.

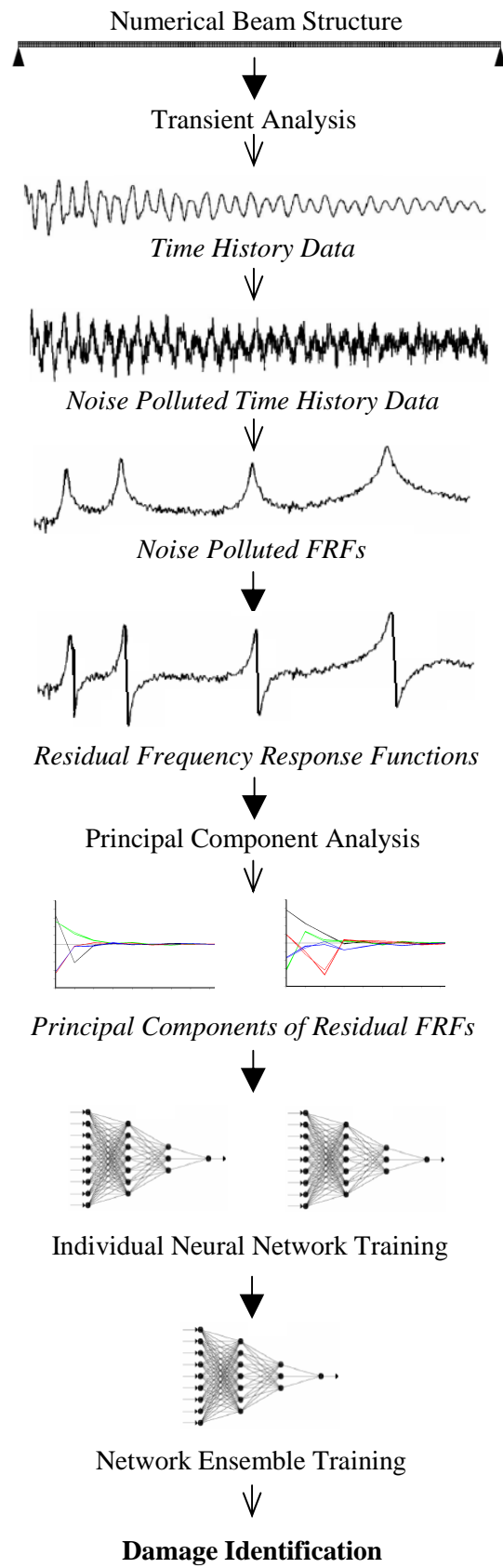


Figure 6.20 Procedure of damage identification based on FRFs.

6.3.4 Summary

This chapter presented the theory, background and methodology of two proposed damage identification schemes. The first damage detection method is based on modal parameters (i.e. DI values) and the second method is based on changes in FRFs. Both methods utilise PCA and neural network techniques to extract damage features from vibrational data and to reduce uncertainties. The proposal of a neural network training scheme based on network ensembles is a novel contribution of this work to both damage identification algorithms.

For the modal parameter method, which is based on damage patterns in DI values, problems related to the DI method were discussed. These problems are related either to the DI method itself (such as singularities at mode shape node points) or to the susceptibility of the DI method to uncertainties such as measurement noise, modal analysis errors and environmental influences. Considering overcoming sensor limitations in measurement, discussions were made in reconstructing coarse mode shape vectors to finer mode shapes utilising cubic spline interpolation techniques. The capabilities of PCA to extract damage features from DI values and to reduce the effects of noise and modal analysis uncertainties were demonstrated. Damage identification utilising the pattern recognition capabilities of ANNs was proposed. A novel neural network training concept using individual networks with network ensembles was presented. The technique is able to reduce/overcome problems associated with the DI method and is capable of reducing uncertainties. In the network ensemble, PCA-compressed DI values are first separated based on their mode shape origin and then fed to individual networks that predict locations and severities of damage. A network ensemble then fuses the outcomes of the individual networks, and final damage identifications are obtained. Such multi-stage network training takes advantage of unique features and differing sensitivities of mode separated PCA-compressed DI values.

For the FRF-based damage identification scheme, first, advantages of utilising direct FRF measurements versus modal parameters were discussed. It was concluded that FRF data are easy to obtain, less dependent to sensor numbers and require little human involvement, which make them ideal damage indicators for structural health monitoring. They provide an abundance of information and are less error prone than

modal parameters, as they do not require the execution of experimental modal analysis. It was highlighted that utilising residual FRFs, which are FRF differences between damaged and undamaged structures, instead of direct FRFs as a damage indicator provides enhanced damage fingerprints and thereby improves detection outcomes. The implementation of PCA techniques was suggested to overcome the obstacle of the large size of FRF data. Besides data reduction, PCA also has the capability of noise reduction and damage feature extraction. The use of ANNs to map PCA-compressed residual FRF data to damage characteristics was proposed. It was shown that instead of using one single network, there are advantages in training several networks in a network ensemble that analyse data from different measurement locations individually. By applying hierarchical network training, individual characteristics of FRF data from different measurement locations are retained and network training efficiency is improved.

CHAPTER 7

DAMAGE IDENTIFICATION OF BEAM STRUCTURE

7.1 INTRODUCTION

This chapter presents numerical and experimental investigations of the two novel damage identification methods, proposed in the last chapter, on a simple beam structure. Both methods are studied using beam data obtained from numerical simulations and laboratory testing. To take advantage of individual characteristics of damage patterns obtained from different sources (different vibrational modes for the DI-based method and different sensor locations for the FRF-based method), a neural network training approach based on network ensembles is employed. The damage identification results obtained from the individual networks and the network ensembles are evaluated according to the difference between desired and actual network output. Differences in the performance of individual networks are analysed and correlations between damage size and network outcome accuracies investigated. For data from noise-polluted numerical simulations, noise sensitivity studies are performed to assess the influence of different noise levels on the identification results.

The structure of this chapter is as follows. First, details of the designed artificial neural networks (ANNs) are described. Second, results of the DI-based damage identification method obtained from numerical simulations and laboratory beam testing are discussed. Finally, for the FRF-based method, network outcomes from numerical and experimental beam data are presented.

7.2 ARTIFICIAL NEURAL NETWORK DESIGN

For both damage identification methods, a number of feed-forward multi-layer neural networks are created, mapping damage fingerprints to damage characteristics, i.e. damage locations and damage severities. The NeuroIntelligence software (Alyuda Research Inc 2006a) is adopted in this project to design and train all neural networks. The inputs to the networks are the most dominant principal components (PCs), either of damage indices Z_j and α_j , or of residual FRFs and CNR-FRFs. (For damage indices Z_j

and α_j , these are seven PCs for numerical beam data and nine PCs for laboratory data (see section 6.2.4), and for residual FRFs and CNR-FRFs these are four PCs for numerical data and ten PCs for laboratory data (see section 6.3.2.) To take advantage of unique individual characteristics of PCs derived from different sources (i.e. DI values of individual vibrational modes and FRF data from each individual sensor, respectively), a network training approach based on network ensembles is employed. For the DI-based method, in each ensemble, seven individual networks are trained with PCs from damage indices separated by their mode shape origin (each individual network is trained with data derived from one of the seven captured vibrational modes). For the FRF-based method, eight individual networks are created; seven of them are trained with FRF-based data from one of the measurements of locations '1' to '7', and the eighth is trained with data acquired from summation FRFs (which are obtained by summing the FRFs of measurement locations '1' to '7'). An ensemble network then fuses the outcomes of the seven individual networks (of measurement locations '1' to '7') giving merged outcome results. The outcomes of the network trained with data from summation FRFs are then compared against the outcomes of the neural network ensemble to demonstrate the advantages of the network ensemble.

Beam data of three categories are evaluated, i.e. noise-free numerical data (only for DI-based method), noise-polluted numerical data and laboratory data. For each of the three categories, two network ensembles are created: one for the identification of damage location and the other for the estimation of damage severity. The number of input samples for the individual networks differs according to the data category; for noise-free numerical data, 16 data cases are available (from the 16 damage scenarios), for noise-polluted numerical data, a total of 576 data cases are captured (16 damage scenarios \times 3 undamaged data cases \times 3 damaged data cases \times 4 noise levels) and for the laboratory beams, 400 data cases are available (16 damage scenarios \times 5 undamaged data cases \times 5 damaged data cases).

For each data category, the input samples are divided into three sets: a training, a validation and a testing set. While the network adjusts its weights from the training samples, its performance is supervised utilising the validation set to avoid overfitting. The network training stops when the error of the validation set reaches a minimum and begins to increase. At this point, while the error of the training set continues to decrease,

the generalisation ability of the network is lost and overfitting occurs. The available input samples of the three data categories are divided into the three sets (training, validation and testing) according to a partitioning system termed chessboard selection. For the laboratory data, the chessboard selection principle is illustrated in Table 7.1. To calculate damage indices Z_j and α_j , as well as residual FRFs and CNR-FRFs, a set of undamaged data is correlated to a set of damaged data (see section 6.2.1 and section 6.3.1). In laboratory testing, each undamaged and damaged state was tested five times. Therefore, by correlating each undamaged state with each damaged state, a total of 25 data cases are obtained for each damage scenario. When partitioning data into sets for training ('train'), validation ('val') and testing ('test'), it is important to select a diverse range of data for each set; this can be accomplished by selecting data along a diagonal line, as illustrated in Table 7.1. For the laboratory data, each damage case is divided into sets of 15 samples for training, 5 samples for validation and 5 samples for testing. Thereby, for the entire data set of 400 laboratory samples, 240 are allocated for training, and 80 each for validation and testing.

Table 7.1 Chessboard selection for laboratory beam data. Table 7.2 Chessboard selection for noise-free numerical beam data.

		Undamaged data				
		U1	U2	U3	U4	U5
Damaged data	D1	Train	Val	Train	Train	Test
	D2	Test	Train	Val	Train	Train
	D3	Train	Test	Train	Val	Train
	D4	Train	Train	Test	Train	Val
	D5	Val	Train	Train	Test	Train

		Damage location			
		4	5	6	7
Damage severity	XL	Test	Train	Val	Train
	L	Train	Test	Train	Val
	M	Val	Train	Test	Train
	S	Train	Val	Train	Test

For the noise-free numerical data, only 16 samples are available (one sample for each damage scenario). Here the chessboard selection principle is applied to the entire data set of 16 samples, as presented in Table 7.2. The numbers of samples for the training, validation and testing sets for all three data categories are listed in Table 7.3.

Table 7.3 Training, validation and testing partitioning of numerical and laboratory beam structure.

Data category	Set	Samples	Remarks
Noise-free numerical data (only for DI-based method)	Training	8	8 damage scenarios (4L, 4S, 5XL, 5M, 6L, 6S, 7XL, 7M)
	Validation	4	4 damage scenarios (4M, 5S, 6XL, 7L)
	Testing	4	4 damage scenarios (4XL, 5L, 6M, 7S,)
Noise-polluted numerical data	Training	320	16 damage scenarios (4 locations \times 4 severities) \times 5 samples \times 4 noise levels
	Validation	128	16 damage scenarios (4 locations \times 4 severities) \times 2 samples \times 4 noise levels
	Testing	128	16 damage scenarios (4 locations \times 4 severities) \times 2 samples \times 4 noise levels
Laboratory data	Training	240	16 damage scenarios (4 locations \times 4 severities) \times 15 samples
	Validation	80	16 damage scenarios (4 locations \times 4 severities) \times 5 samples
	Testing	80	16 damage scenarios (4 locations \times 4 severities) \times 5 samples

As mentioned above, for each data category, two network ensembles are created estimating either the location (in length along the beam) or the severity (in loss of the second moment of area, I) of the damage cases. The corresponding target output values for all damage scenarios for both network types are listed in Table 7.4.

Table 7.4 Neural network target output values.

Damage scenario	Network output	Network output
	– Damage location [m]	– Damage severity [%]
4XL	1.2	9.09
4L	1.2	33.01
4M	1.2	57.81
4S	1.2	75.59
5XL	1.5	9.09
5L	1.5	33.01
5M	1.5	57.81
5S	1.5	75.59
6XL	1.8	9.09
6L	1.8	33.01
6M	1.8	57.81
6S	1.8	75.59
7XL	2.1	9.09
7L	2.1	33.01
7M	2.1	57.81
7S	2.1	75.59

Before each data set is presented to the network, the input and output data are scaled to a range from -1 to $+1$ following equation (3.16). Data scaling is important to ensure that the distance measure accords equal weight to each sample. Without scaling, the sample with the largest scale will dominate the measure. Furthermore, the input and output data must comply with the transfer function of the hidden layer and output layer. For this study, the hyperbolic tangent sigmoid transfer function, which operates in the range of -1 to $+1$, is selected for all layers.

The number of hidden layers and neurons is chosen in accordance with the geometric pyramid rule, which states that neurons in the hidden layer should decrease in number from the input towards the output layer. As the NeuroIntelligence software (Alyuda Research Inc 2006a) has a built-in overfitting regulation, a large number of hidden neurons can be employed. For the DI-based method, the individual networks of the numerical beam data are designed with: one input layer of seven nodes, representing the first seven PCs of the damage indices; three hidden layers of six, four and two nodes; and one output node estimating the damage location or severity (denoted as a 7-6-4-2-1 network). For the laboratory data of the DI-based method, the input layer comprises nine nodes (from the nine most dominant PCs), four hidden layers of eight, six, four and two nodes, and one output node (denoted as a 9-8-6-4-2-1 network). For the FRF-based method, the individual networks of numerical data are designed as 4-3-2-1 networks and the individual networks of laboratory data as 10-8-6-4-2-1 networks. For both identification methods, the ensemble networks are created with: seven input nodes, which are the outputs of the seven individual networks; three hidden layers of six, four and two nodes; and one output node for the location or severity predictions (also termed a 7-6-4-2-1 network).

For the convergence algorithm, NeuroIntelligence offers a wide range of functions. Due to the size of the data sets and the chosen number of nodes, in this study, one of the following three functions is used: the quick propagation function, the conjugate gradient descent function and the online backpropagation function. The best performing algorithm is determined by trial and error. Each network configuration is trained several times with different initial weight and bias values to obtain the best network results (each network is trained up to 50 times, depending on the network performance).

Details on the chosen convergence algorithm and the network design are presented in subsequent sections.

NeuroIntelligence assesses the training performance of the networks by absolute error (AE), which is defined as:

$$AE = |current\ output\ values - target\ output\ values| \quad (7.1)$$

Training is stopped either manually or automatically after a set number of iterations. A built-in overtraining control in NeuroIntelligence is set to retrain and restore the network with the lowest testing set AE . During training, the network performance is monitored by a real-time AE performance graph. An example of an AE performance graph is shown in Figure 7.1. In the figure, it can be seen that the overtraining control in NeuroIntelligence determines the point of the best network performance at 3,176 iterations. Although carrying out more iterations further reduces the absolute error for the training set, the error of the validation set increases, which means that the network starts overfitting the data and thereby loses its generalisation ability.

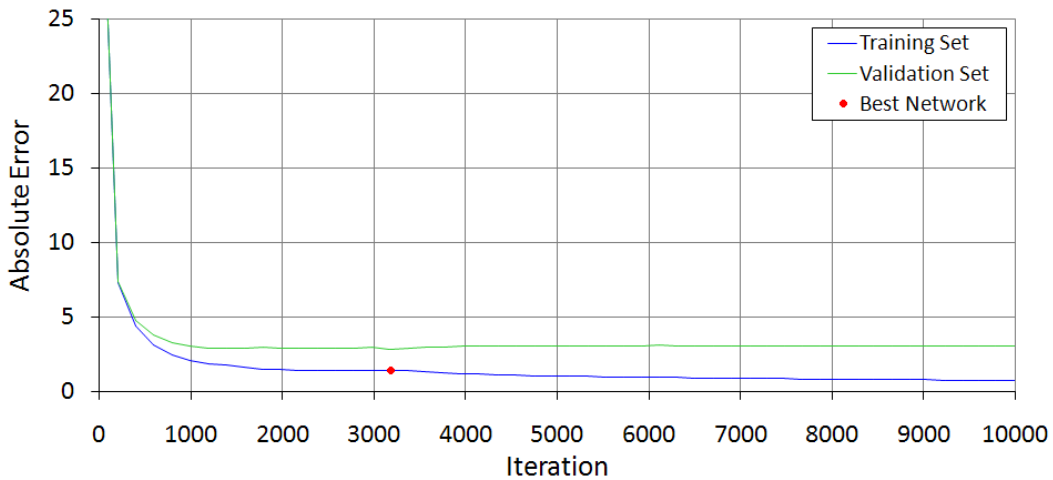


Figure 7.1 AE performance graph.

To assess the outcomes of the neural networks, the damage location and severity predictions are evaluated by normalised errors (NE_{loc} for damage location and NE_{sev} for damage severity), which are defined as:

$$NE_{loc} = \frac{(T_d - O_d)}{L_{max}} \quad \text{and} \quad NE_{sev} = \frac{(T_d - O_d)}{S_{max}} \quad (7.2)$$

where d is the damage case, T_d the target value of d , O_d the network output value of d , L_{max} the total length of the beam (here 2.4 m) and S_{max} the maximum severity of damage (here 100% loss of the second moment of area, I).

7.3 DAMAGE IDENTIFICATION BASED ON DAMAGE INDEX METHOD

7.3.1 Results of Damage-Index-Based Damage Identification Method Applied to Numerically Simulated Beam

The DI-based damage identification method is firstly applied to data obtained from numerical beam models to explore the problems of the DI method. The proposed procedure is tested on two types of numerical data: noise-free data and data polluted with different levels of white Gaussian noise. The study on noise-free numerical data investigates the feasibility of the proposed method to deal with issues of the DI method. As presented in section 6.2.3, some problems are inherent to the DI method such as those associated with singularities at mode shape node points, a limited number of sensors or interferences of boundaries. By applying pattern recognition techniques such as PCA and neural networks, such inherent issues of a recurring nature are expected to be overcome. For the study on noise-polluted data, the susceptibility of the proposed method to uncertainties such as measurement noise and modal analysis errors is investigated. It is expected that the filtering capabilities of PCA and neural networks are able to reduce the influence of these disturbances. The proposed method is applied to both data types to predict damage locations and to estimate damage severities.

Neural Network Outcomes of Damage-Index-Based Method to Locate Damage of Numerically Simulated Beam

Neural Network Outcomes of Damage-Index-Based Method Applied to Noise-Free Numerical Beam Simulations to Identify Damage Locations

Table 7.5 presents details on network specifications and performance for neural networks trained with PCA-compressed Z_j values of noise-free numerical data to identify damage locations. The table lists results of all seven individual networks (networks of ‘Mode 1’ to ‘Mode 7’) and of the network ensemble (‘Ens’), including the number of neurons of the input, hidden and output layers (‘Network design’); the

chosen convergence algorithm; the number of iterations (until the network is either stopped manually or reached the best possible results); and the performance of the training, validation and testing sets (in absolute mean of normalised error (AMNE)).

From the network performance of Table 7.5, it is observed that the location predictions of all networks are precise for all damage cases, giving AMNEs from <0.01% up to 0.03% for training, validation and testing sets. These impressive results clearly demonstrate the pattern recognition ability of neural networks combined with PCA. These findings show that the proposed method is capable of successfully overcoming the inherent problems of the DI method, such as node point singularities, limited number of sensor nets and interferences of boundaries. Whereas the network of mode 7 reached optimal performance after 5,367 iterations, the training of all other networks is stopped manually after 50,000 iterations (very good network results with AMNEs of 0.01% and lower are already achieved).

Table 7.5 Neural network specifications and performance (in AMNE) trained with PCA-compressed Z_j values from noise-free numerical beam simulations to identify damage locations.

Network	Network design	Convergence algorithm	Iteration	Training performance (AMNE [%])	Validation performance (AMNE [%])	Testing performance (AMNE [%])
Mode 1	7-6-4-2-1	Obp	50,000	<0.01	<0.01	<0.01
Mode 2	7-6-4-2-1	Obp	50,000	<0.01	<0.01	0.01
Mode 3	7-6-4-2-1	Obp	50,000	<0.01	0.01	<0.01
Mode 4	7-6-4-2-1	Obp	50,000	<0.01	<0.01	<0.01
Mode 5	7-6-4-2-1	Obp	50,000	<0.01	<0.01	<0.01
Mode 6	7-6-4-2-1	Obp	50,000	0.01	0.01	0.01
Mode 7	7-6-4-2-1	Obp	5,367	0.01	0.02	0.03
Ens	7-6-4-2-1	Obp	50,000	<0.01	<0.01	<0.01

Note: Obp = Online backpropagation function

In this and subsequent sections, detailed network outcomes of all damage cases are illustrated by network output graphs such as the one presented in Figure 7.2, which displays normalised errors of all damage cases of the ensemble network ('Ens') trained with noise-free numerical data to identify damage locations.

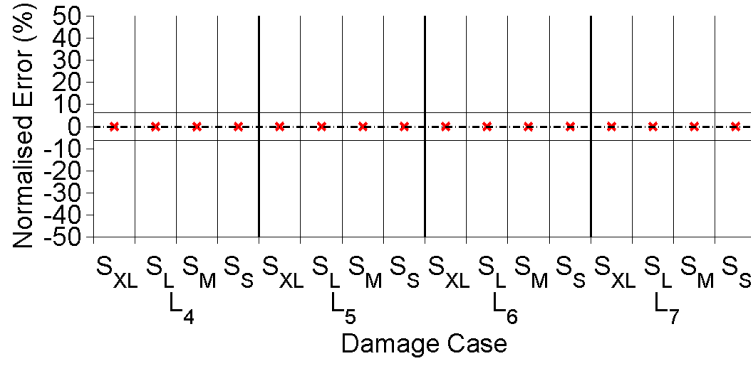


Figure 7.2 Outcomes of ensemble network trained with PCA-compressed Z_j values of noise-free numerical beams to identify damage locations.

In the figure, the horizontal axis represents the damage cases sorted by their locations (L_4 , L_5 , L_6 and L_7) and their severities (S_{XL} , S_L , S_M and S_S); the vertical axis displays the normalised errors of the network localisation outcomes (or, for damage severity estimation, the network quantification outcomes). A marked band around the 0% error line symbolises the area in which the network estimations should fall in order to correctly categorise the damage. For damage localisation, the band ranges from -6.25% to $+6.25\%$ normalised error, representing the midpoints in-between two damage locations, determined by:

$$NE_{loc} = \pm \frac{0.15 \text{ m}}{2.4 \text{ m}} = \pm 6.25\% \quad (7.3)$$

The band for damage severity quantification ranges from -12% to $+12\%$ normalised error, which specifies averaged midpoints in-between two severity levels, calculated as:

$$NE_{sev} = \pm \frac{\text{mean}\left(\frac{33.33\% - 9.09\%}{2} + \frac{57.81\% - 33.33\%}{2} + \frac{75.59\% - 57.81\%}{2}\right)}{100\%} = \pm 12\% \quad (7.4)$$

From Figure 7.2, it is seen that the ensemble network precisely locates all damage cases, with normalised errors of $<0.01\%$. The output figures of all individual networks (and the ensemble network) trained with PCA-compressed Z_j values from noise-free numerical data are presented in Figure G.1 in APPENDIX G.

Neural Network Outcomes of Damage-Index-Based Method Applied to Noise-Polluted Numerical Beam Simulations to Identify Damage Locations

For noise-polluted numerical data, Table 7.6 lists specifications and performance of individual networks and their ensemble trained with data of all four noise pollution levels (1%, 2%, 5% and 10%) to locate damage. From the network performance (AMNEs), it is observed that the network predictions are significantly worse than those of the networks trained with noise-free numerical data (see above). This finding highlights the major influence of noise on the damage identification scheme. It is noted that the performance of the different networks varies considerably among each other. For example, the individual network of mode 1 attains AMNEs of 8.05%, 9.29% and 10.03% (for training, validation and testing set, respectively), while the performances of the network of mode 7 are 1.70%, 3.94% and 2.75%. The best performance of all trained networks is achieved with the ensemble network, giving AMNEs of 1.08%, 2.42% and 1.89%.

Table 7.6 Neural network specifications and performance (in AMNE) trained with PCA-compressed Z_j values from noise-polluted numerical beam simulations to identify damage locations.

Network	Network design	Convergence algorithm	Iteration	Training performance (AMNE [%])	Validation performance (AMNE [%])	Testing performance (AMNE [%])
Mode 1	7-6-4-2-1	Qp	1,358	8.05	9.29	10.03
Mode 2	7-6-4-2-1	Qp	4,589	4.10	6.52	6.63
Mode 3	7-6-4-2-1	Qp	7,851	3.71	5.27	5.15
Mode 4	7-6-4-2-1	Qp	5,846	3.85	6.68	6.63
Mode 5	7-6-4-2-1	Qp	9,872	1.62	2.96	2.84
Mode 6	7-6-4-2-1	Qp	8,125	3.99	5.48	4.91
Mode 7	7-6-4-2-1	Qp	8,479	1.70	3.94	2.75
Ens	7-6-4-2-1	Cgd	1,973	1.08	2.42	1.89

Note: Qp = Quick propagation function

Cgd = Conjugate gradient descent function

For assessing the capabilities of the proposed damage identification method, the most meaningful information is given by the network outcomes of the testing set. As discussed above, neural networks utilise the samples of the training set to adjust the weights and biases of the network. Input samples of the validation set are used to supervise the training process to avoid overfitting, and samples of the testing set are utilised to test the networks with hitherto unseen data. Hence, the network outcomes of

the testing set give the true and realistic information on the actual performance of the networks. To discuss the testing set outcomes in more detail, Figure 7.3 presents the testing set results (in AMNE) of all eight networks subdivided by damage cases of different severities. Next to the graphical illustration, a table lists the corresponding AMNE values. From the figure and the table, it is found that the prediction errors of lighter damage cases are larger than the errors of more severe damage cases. This trend is noted for all networks, and it demonstrates that noise has a greater influence on the identification of lighter damage cases (as the signal-to-noise ratio is low). Further, performance differences between the various individual networks (and the ensemble network) are again observed. The individual networks of modes 3, 5 and 7 seem to deliver better performance, whereas the networks of modes 1, 2, 4 and 6 perform rather poorly.

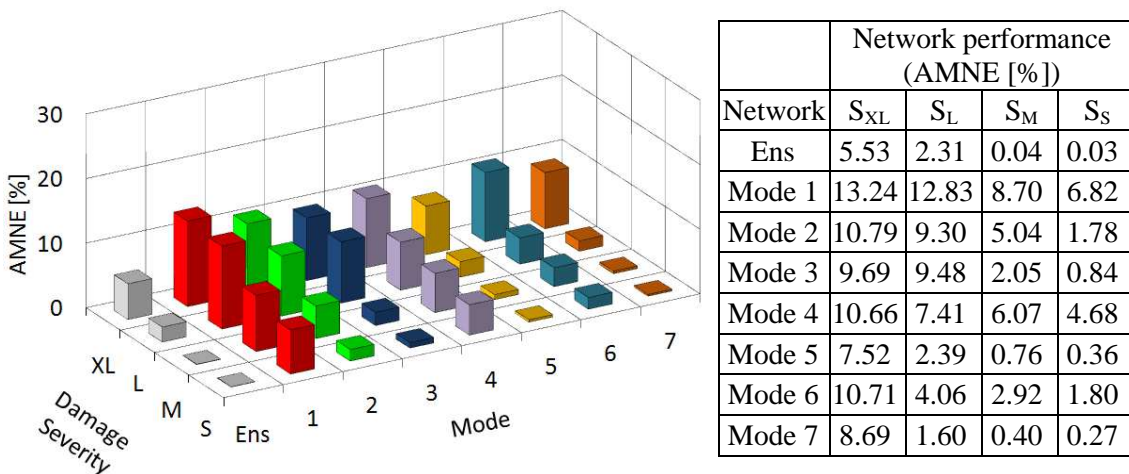


Figure 7.3 Neural network testing set performance (in AMNE) subdivided by damage severities trained with PCA-compressed Z_j values from noise-polluted numerical beams to localise damage.

To further investigate the observed error differences between different networks, Figure 7.4 shows detailed network outcomes of 1% noise polluted data for networks of modes 1, 4, 5 and the ensemble network (the full set of output figures of all networks and all noise pollution levels is presented in Figure G.2 to Figure G.5 in APPENDIX G). The displayed figures show the results of the 32 testing set samples (two samples per damage case). The outcomes of the network of mode 1 (Figure 7.4 (a)) show large errors for damage at all four locations. It is believed that the small curvature of the mode shape of mode 1 causes a lower sensitivity to damage, and therefore, noise has a greater effect on the curvature data, resulting in erroneous damage identifications for

this mode. From the outcomes of mode 4 (Figure 7.4 (b)), it is seen that the network falsely locates many damage cases of locations '4' and '6', whereas the predictions for damage cases of locations '5' and '7' are all classified correctly (all lie within the marked band). This is caused by the node points of mode 4, which coincide with locations '4' and '6', as explained earlier. Similar findings (of faulty predictions of damage cases at node point locations) are observed for the network outcomes of mode 2 and mode 6 (see Figure G.2 to Figure G.5 in APPENDIX G), which explains the poor AMNE results of these modes. Even though the networks of modes 2, 4 and 6 when trained with noise-free data correctly identify all damage cases (and thereby overcome the node point singularity issue of the DI method, as discussed above), noise seems to have a great influence on DI values at node points, which results in false network predictions. For the network outcomes of mode 5 (Figure 7.4 (c)), only extra-light damage cases (of all four damage locations) produce large errors; the localisation outcomes of all light, medium and severe damage cases are correct, with only minor deviations of some samples. The network ensemble of Figure 7.4 (d) shows the best network outcomes for data of 1% noise pollution, with only one wrong detection of extra-light damage at location '4'.

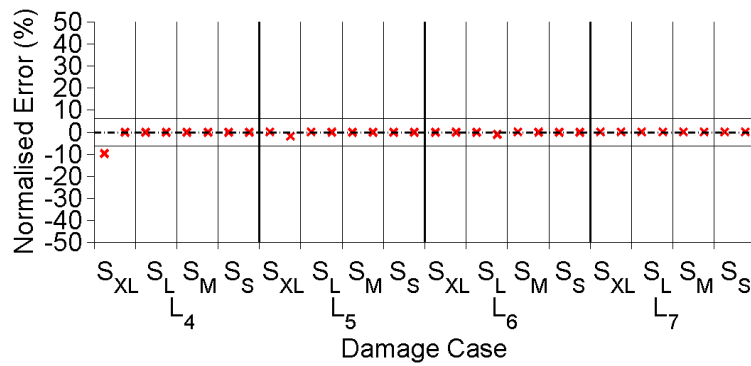
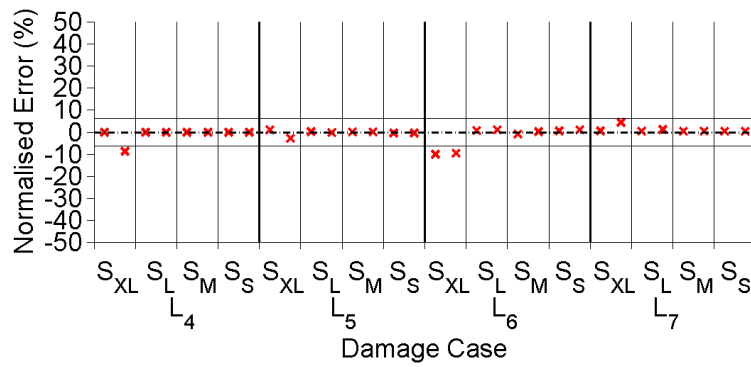
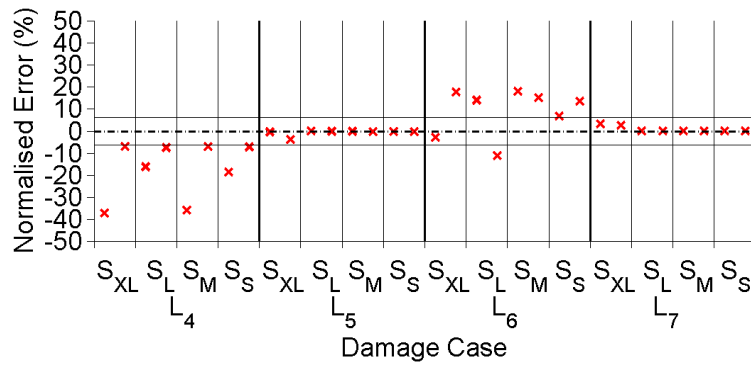
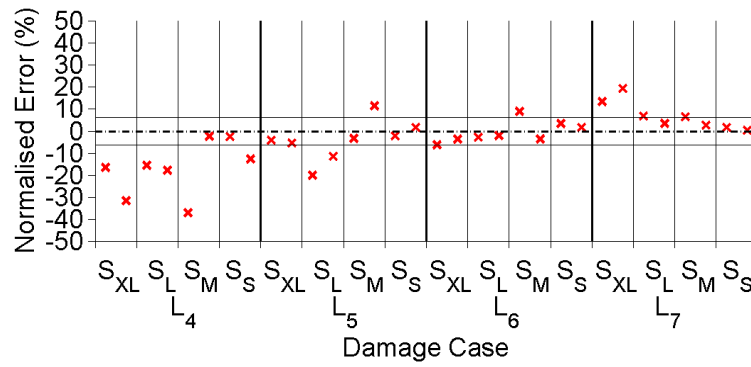


Figure 7.4 Neural network testing set outcomes of networks from (a) mode 1, (b) mode 4, (c) mode 5 and (d) the ensemble network trained with PCA-compressed Z_j values to locate damage of numerical data polluted with 1% noise.

To study the influence of different noise levels on the damage identification approach, the network outcomes are separated according to the noise pollution level of the input data. As an example, Figure 7.5 illustrates testing set results (in AMNE) of networks trained with data from modes 1, 2, 5 and the ensemble network, subdivided by noise pollution level and damage severity. (Figures of all networks are presented in Figure G.6 in APPENDIX G). From the network outcomes of modes 2 and 5 (Figure 7.5 (b) and (c)) as well as the ensemble network (Figure 7.5 (d)), a clear dependency of identification accuracy on noise pollution level and damage severity is seen, i.e. the network outcomes are more erroneous the higher the noise pollution level and the smaller the size of the damage. A similar trend is observed for the networks of modes 3, 4, 6 and 7 (see Figure G.6 in APPENDIX G). For the network of mode 1 (see Figure 7.5 (a)), however, such dependency is not as clear. This result indicates that the mode shape of mode 1 is highly sensitive to experimental modal analysis uncertainties and noise influences (i.e. even 1% noise intensity level can overshadow damage fingerprints contained in the mode shapes of mode 1). From the final outcomes of the network ensemble, it is seen that up to a noise level of 2%, all light, medium and severe damage cases are successfully located. For data of 5% and 10% noise pollution, the network ensemble still gives precise locations for all medium and severe damage cases.

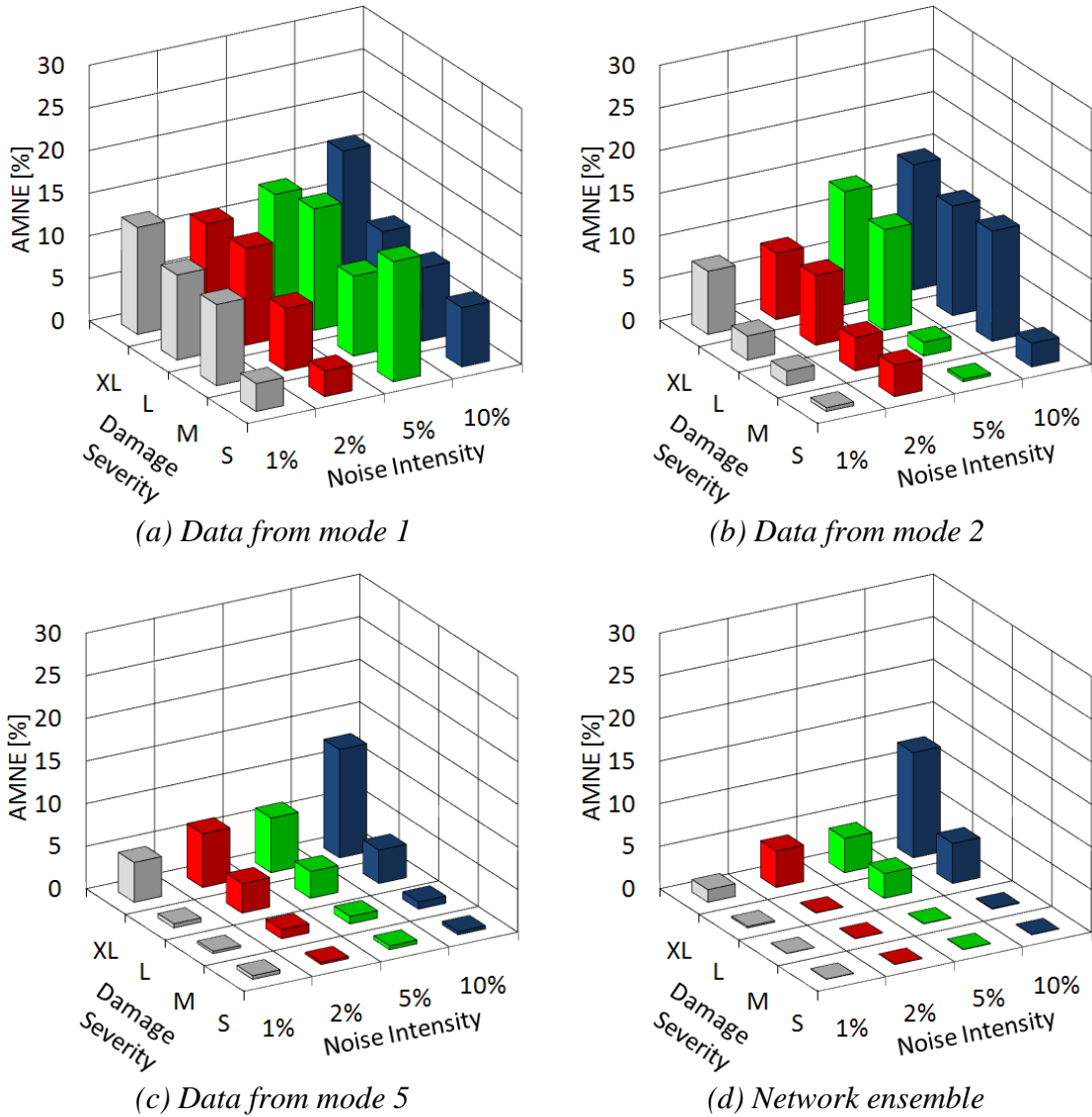


Figure 7.5 Comparison of testing set outcomes of networks trained with PCA-compressed Z_j values to identify damage locations of noise-polluted numerical beams subdivided by damage severity and noise pollution level.

The outcomes presented above clearly show that noise has a major influence on the identification of damage locations. Even though PCA and neural network techniques have filtering capacities, the effects of noise and modal analysis errors can only be reduced, not eliminated. The main reason for this phenomenon is that noise features are indirect errors embedded in mode shape measurements. These embedded inaccuracies result from erroneous mode shape extractions from experimental modal analysis procedures caused by noise. For noise filtering tools (such as PCA and neural networks), it is therefore very challenging to separate these embedded noise features from the damage indices. In addition, the level of damage severity contributes greatly to

the outcomes of the identification. Furthermore, the unique characteristics of damage fingerprints derived from different modes play an important role in the damage identification.

Neural Network Outcomes of Damage-Index-Based Method to Identify Damage Severities of Numerically Simulated Beams

Neural Network Outcomes of Damage-Index-Based Method Applied to Noise-Free Numerical Beam Simulations to Identify Damage Severities

For damage severity estimations, in this section, PCA-compressed α_j damage indices are determined from noise-free numerical data and fed to neural networks. Specifications and performance of the trained networks are listed in Table 7.7. It is noted that with noise-free numerical data, the network performance of damage severity estimations are significantly worse than the performance of networks trained to locate damage (see section 7.3.1). Whereas for damage location prediction all networks precisely identified all damage cases, for damage severity estimations, error values reached up to 18.74% AMNE in the predictions with individual modes.

Table 7.7 Neural network specifications and performance (in AMNE) trained with PCA-compressed α_j values from noise-free numerical beam simulations to identify damage severities.

Network	Network design	Convergence algorithm	Iteration	Training performance (AMNE [%])	Validation performance (AMNE [%])	Testing performance (AMNE [%])
Mode 1	7-6-4-2-1	Cgd	16,351	0.05	0.67	4.78
Mode 2	7-6-4-2-1	Cgd	4,458	12.78	13.07	6.17
Mode 3	7-6-4-2-1	Cgd	8,652	1.39	3.46	3.15
Mode 4	7-6-4-2-1	Cgd	3,251	12.65	18.15	18.74
Mode 5	7-6-4-2-1	Cgd	9,245	0.83	2.08	2.67
Mode 6	7-6-4-2-1	Cgd	2,595	8.23	13.23	8.04
Mode 7	7-6-4-2-1	Cgd	5,324	2.20	3.63	4.58
Ens	7-6-4-2-1	Obp	23,548	0.10	0.15	0.69

Note: Cgd = Conjugate gradient descent function

Obp = Online backpropagation function

When observing Figure 7.6, which illustrates the testing set outcomes separated by damage severity, it is noted that the individual networks trained with modes 2, 4 and 6 give the largest errors. These erroneous outcomes are caused by node point singularities of these modes. As demonstrated in section 6.2.3, when damage is located at node

points, damage indices Z_j (for damage localisation) indicate false damage peaks (caused by the normalisation of β_j); damage indices α_j (for damage severity estimation), however, give no indication of damage at all (α_j values are all close to zero). Therefore, for location identification with damage index Z_j , the networks of modes 2, 4 and 6 can successfully locate all damage cases due to false but ‘unique’ damage peaks. For severity estimation, however, the network outcomes of modes 2, 4 and 6 give large errors because α_j values do not give any information for damage cases located at node points of these modes.

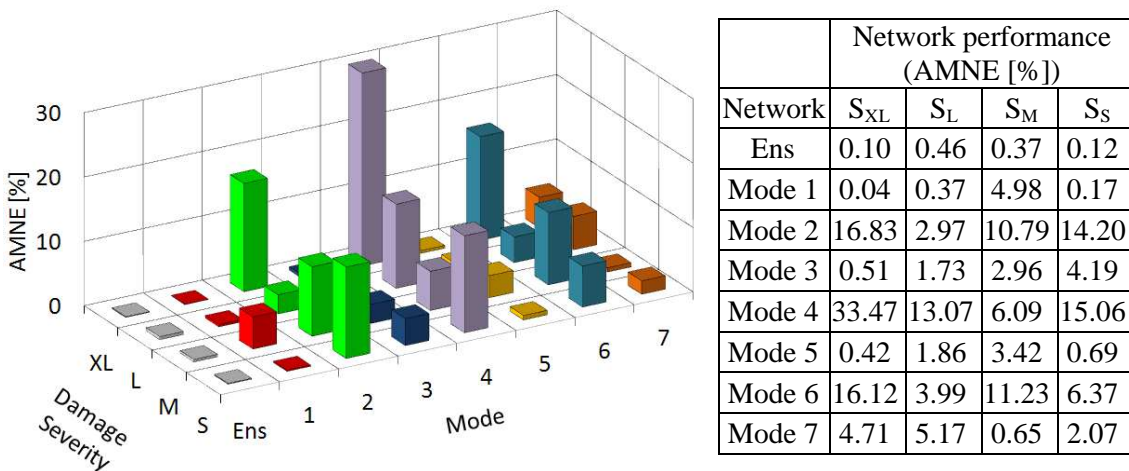


Figure 7.6 Neural network testing set performance (in AMNE) subdivided by damage severity trained with PCA-compressed α_j values from noise-free numerical beams to identify damage severities.

Due to the small number of input samples, a correlation between damage severity and outcome accuracy of the networks is difficult to observe from Figure 7.6. For noise-free cases, despite of poor results of severity estimations from some individually trained networks, the performance of the ensemble network produces still very good results with AMNE values of 0.10%, 0.15% and 0.69% for the training, validation and testing sets. (Figure G.7 in APPENDIX G displays the detailed outcomes of all individual networks and the network ensemble trained with α_j values of noise-free numerical beam simulations to estimate damage severities.)

Neural Network Outcomes of Damage-Index-Based Method Applied to Noise-Polluted Numerical Beam Simulations to Identify Damage Severities

The influence of noise on the proposed severity estimation scheme is studied in this section. Networks are trained with PCA-compressed α_j values obtained from polluted data with different intensities of white Gaussian noise. Specifications and performance of the respective networks are listed in Table 7.8. To investigate the relationship between network predictions and damage size, Figure 7.7 illustrates the network errors of the testing set outcomes, separated by damage severity. From the table and the figure, it is again observed that the network trained from mode 1 produces large errors for damage severity estimation. Similar to the identification of damage location with Z_j , the small curvature values of the mode shape of mode 1, in combination with uncertainties from modal analysis and noise effects are believed to be the cause for these errors. It is further noted that the networks trained with data of modes 2, 4, and 6 also perform poorly, due to node point singularities of these modes. The outcomes of the individual networks of modes 3, 5 and 7, however, produce reasonably good results, with the maximum testing set AMNE at 5.12%. Damage cases at larger severity levels produce results with better accuracy than those of smaller damage size (see Figure 7.7). The best results for severity estimations are obtained with the ensemble network, which gives a testing set performance of 0.44%. These results again demonstrate the effectiveness of network training in a network ensemble.

Table 7.8 Neural network specifications and performance (in AMNE) trained with PCA-compressed α_j values from noise-polluted numerical beam simulations to identify damage locations.

Network	Network design	Convergence algorithm	Iteration	Training performance (AMNE [%])	Validation performance (AMNE [%])	Testing performance (AMNE [%])
Mode 1	7-6-4-2-1	Obp	1,253	15.47	18.09	17.61
Mode 2	7-6-4-2-1	Obp	2,658	10.13	11.22	11.76
Mode 3	7-6-4-2-1	Obp	15,264	1.40	4.07	5.12
Mode 4	7-6-4-2-1	Obp	3,265	12.32	14.17	13.30
Mode 5	7-6-4-2-1	Obp	17,593	0.20	0.22	0.52
Mode 6	7-6-4-2-1	Obp	5,471	8.89	9.94	8.55
Mode 7	7-6-4-2-1	Obp	14,658	0.03	1.79	2.05
Ens	7-6-4-2-1	Cgd	8,786	0.13	0.21	0.44

Note: Obp = Online backpropagation function

Cgd = Conjugate gradient descent function

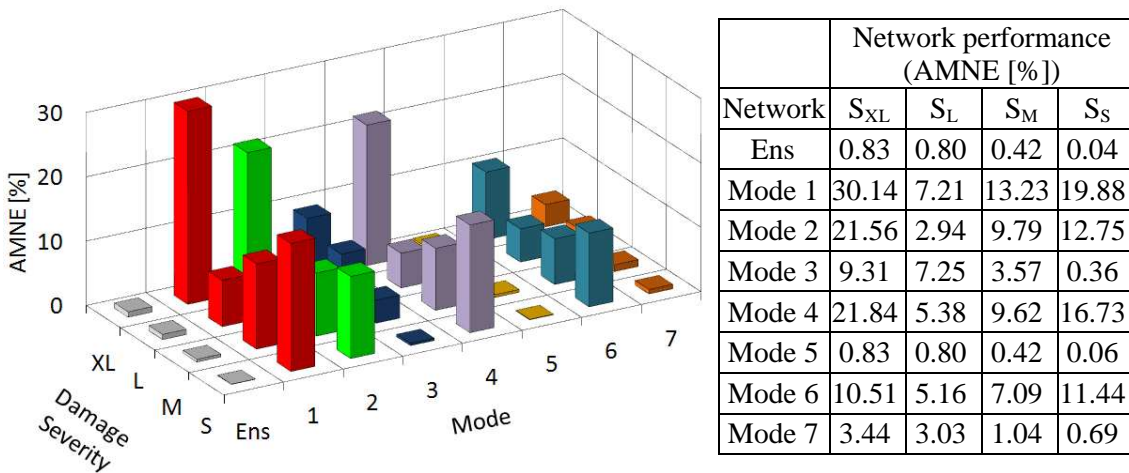


Figure 7.7 Neural network testing set performance (in AMNE) subdivided by damage severity trained with PCA-compressed α_j values from noise-polluted numerical beams to identify damage severity.

To investigate the noise sensitivity on damage severity estimations, all trained networks are studied according to the noise pollution intensity of the input data. As an example, Figure 7.8 illustrates network outcome errors (in AMNE), subdivided by noise intensity level and damage severity, of networks trained with data from modes 1, 2 and 7 and the network ensemble. (All results are presented in Figure G.12 in APPENDIX G.) For the network of mode 1 (Figure 7.8 (a)), an uncorrelated behaviour of noise level and network performance demonstrates the high sensitivity to both noise and modal analysis errors for this mode (similar findings were previously obtained for damage localisation results). For mode 2 (Figure 7.8 (b)), the large errors due to node point singularity distort the network results of this mode and thereby lead to uncorrelated network outcomes (similar observations are found for modes 4 and 6). For the figures of mode 7 and the network ensemble (Figure 7.8 (c) and (d)), although there are some discrepancies, a correlation between damage identification accuracy and the level of noise pollution is observed. From the final severity predictions obtained by the ensemble network, it is seen that up to a noise level of 5%, all damage cases are precisely identified. For 10% noise intensity, the ensemble network still correctly quantifies all damage cases of medium and severe size (see Figure G.11 in APPENDIX G). These results highlight again the importance of the hierarchical network training in a network ensemble, by which results of the best individual networks are retained and the poor outcomes of underperforming individual networks (e.g. networks of modes 1, 2, 4 and 6) are disregarded.

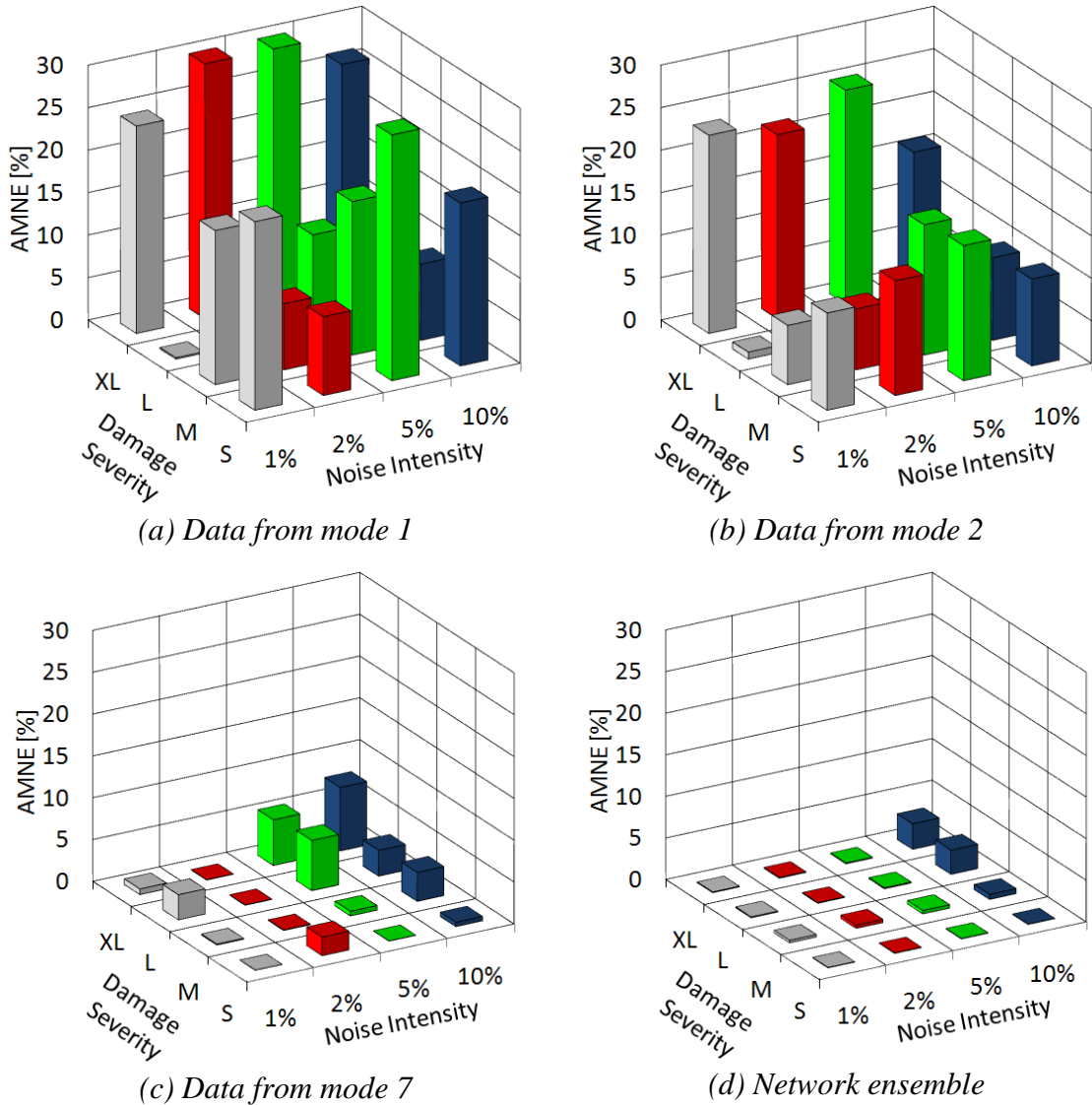


Figure 7.8 Comparison of testing set outcomes of networks trained with PCA-compressed α_j values to identify damage severities of noise-polluted numerical beams subdivided by damage severity and noise pollution level.

7.3.2 Results of Damage-Index-Based Damage Identification Method Applied to Laboratory Test Beams

To validate the proposed damage identification method on a real structure, it is applied on data obtained from experimental testing of the laboratory beams. From modal testing and experimental modal analysis (MT&EMA) of the laboratory beams, mode shape data are obtained and used to calculate damage indices Z_j and α_j . The damage indices are compressed utilising PCA techniques, and the most dominant features are selected for neural network inputs to identify locations and severities of damage.

Neural Network Outcomes of Damage-Index-Based Method Applied to Laboratory Beams to Identify Damage Locations

For damage location identification of the laboratory beams, specifications and performance of the trained individual networks and the network ensemble are listed in Table 7.9. Figure 7.9 illustrates for the testing set the network errors separated by damage size.

Table 7.9 Neural network specifications and performance (in AMNE) trained with PCA-compressed Z_j values from laboratory beams to identify damage locations.

Network	Network design	Convergence algorithm	Iteration	Training performance (AMNE [%])	Validation performance (AMNE [%])	Testing performance (AMNE [%])
Mode 1	9-8-6-4-2-1	Obp	8,654	0.01	0.04	0.04
Mode 2	9-8-6-4-2-1	Obp	4,574	0.11	0.27	0.24
Mode 3	9-8-6-4-2-1	Obp	7,516	0.02	0.03	0.02
Mode 4	9-8-6-4-2-1	Obp	15,248	0.01	0.01	0.01
Mode 5	9-8-6-4-2-1	Obp	3,574	1.30	2.66	2.24
Mode 6	9-8-6-4-2-1	Obp	1,985	2.51	3.34	3.35
Mode 7	9-8-6-4-2-1	Obp	859	3.26	5.36	5.01
Ens	7-6-4-2-1	Obp	9,303	0.01	0.01	0.01

Note: Obp = Online backpropagation function

From Table 7.9, it is found that the networks of modes 1 to 4 produce very good location predictions, with the largest AMNEs being 0.11%, 0.27% and 0.24% for the training, validation and testing sets of the network of mode 2. The network ensemble produces the best results, as expected, with errors of 0.01% for all three input sets. For the networks of modes 5 to 7, however, larger errors are obtained (the worst performance being 3.26%, 5.36% and 5.01% for the training, validation and testing sets of the network of mode 7).

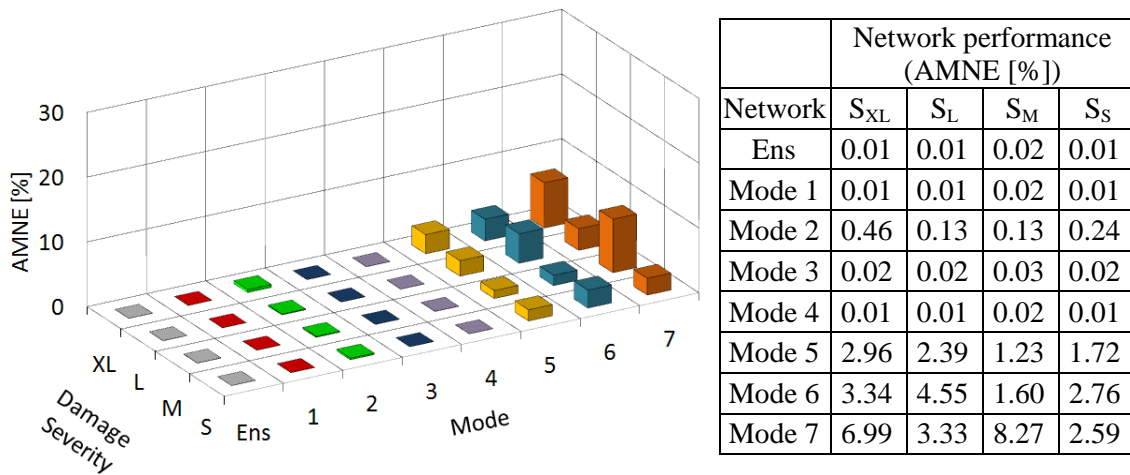


Figure 7.9 Neural network testing set performance (in AMNE) subdivided by damage severity trained with PCA-compressed Z_j values from laboratory beams to identify damage locations.

The reason for the poor performance of the networks of modes 5 to 7 is that during experimental modal analysis, the extraction of the modal parameters from such higher modes became more difficult and therefore the obtained mode shapes are often more error-prone. It is further noted that unlike the outcomes from noise-polluted numerical data (see section 7.3.1), problems with the network of mode 1, which is highly sensitive to noise and experimental modal analysis errors, or the networks of modes 2 and 4, which are affected by node point singularity, did not appear. There are two possible reasons for this phenomenon. First, the noise level during laboratory testing is lower than 1%, rather than 5% and 10% of extreme cases simulated. Hence, the network outcomes from laboratory data are closer to the results from noise-free numerical data. The second possibility is that for laboratory testing, damage indices for damage localisation are enhanced due to the testing of different experimental beams for different damage locations. Thereby, patterns in Z_j values do not only reflect damage but also unique features obtained from the testing of different laboratory beams. Hence, these additional features assist in the identification of damage locations and consequently result in improved detection outcomes.

From Figure 7.9, no clear correlation is found between damage size and prediction accuracy. In addition, from the detailed network outcomes (see Figure 7.10 and Figure G.13 in APPENDIX G), it is seen that the erroneous damage predictions of the networks of the higher modes are scattered and show no correlation to damage severity

or damage location. It is believed that uncertainty errors due to the extraction of the higher modes during experimental modal analysis are responsible for such problem.

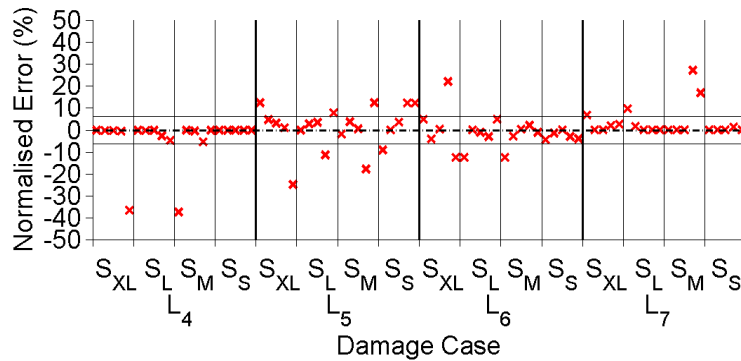


Figure 7.10 Neural networks testing set outcomes of network trained with PCA-compressed Z_j values of mode 7 to identify damage locations of laboratory beams.

Neural Network Outcomes of Damage-Index-Based Method Applied to Laboratory Beams to Identify Damage Severities

For the damage severity estimation of the laboratory beams, network specifications and performance are listed in Table 7.10. From the table, it is noted that the network performance is slightly poor. For severity estimation, the networks of all modes produce large errors, with the higher modes producing worse results. The poor outcomes of the higher modes are again due to uncertainty errors in extracting mode shapes during experimental modal analysis.

Table 7.10 Neural network specifications and performance (in AMNE) trained with PCA-compressed α_j values from laboratory beams to identify damage severities.

Network	Network design	Convergence algorithm	Iteration	Training performance (AMNE [%])	Validation performance (AMNE [%])	Testing performance (AMNE [%])
Mode 1	9-8-6-4-2-1	Obp	2,658	4.04	7.20	7.25
Mode 2	9-8-6-4-2-1	Obp	5,379	2.85	5.64	3.94
Mode 3	9-8-6-4-2-1	Obp	8,459	1.17	4.12	2.02
Mode 4	9-8-6-4-2-1	Obp	5,985	2.95	4.06	3.96
Mode 5	9-8-6-4-2-1	Obp	2,154	6.78	9.25	9.22
Mode 6	9-8-6-4-2-1	Obp	3,741	5.47	7.43	8.25
Mode 7	9-8-6-4-2-1	Obp	3,265	6.71	8.56	8.30
Ens	7-6-4-2-1	Obp	25,367	1.02	3.21	1.74

Note: Obp = Online backpropagation function

These larger errors in severity estimation are expected as the identification of damage severity with the DI value α_j is extremely challenging for experimental structures.

Unlike for damage localisation with DI value Z_j , for damage severity estimation, a precise amplitude specification is necessary to produce correct quantification results. Amplitude values of α_j are, however, very sensitive to all kinds of interferences resulting in larger severity estimation errors for laboratory beams. Further, additional features in α_j values (resulting from the testing of different experimental beams) make the estimation of damage severity even more difficult.

When examining the network performance in the context of damage size (see Figure 7.11), a clear correlation between damage severity and identification accuracy is observed (especially for the networks of modes 1 to 4). Due to large mode shape extraction errors of the higher modes (modes 5 to 7), this correlation is to some extent disturbed. It is further noted that the networks of modes 2 and 4 give worse outcomes than the network of mode 3, which again indicates the high sensitivity of α_j to node point singularities. From the outcomes of the network ensemble, it is seen that all damage cases of light, medium and severe size are eventually identified correctly.

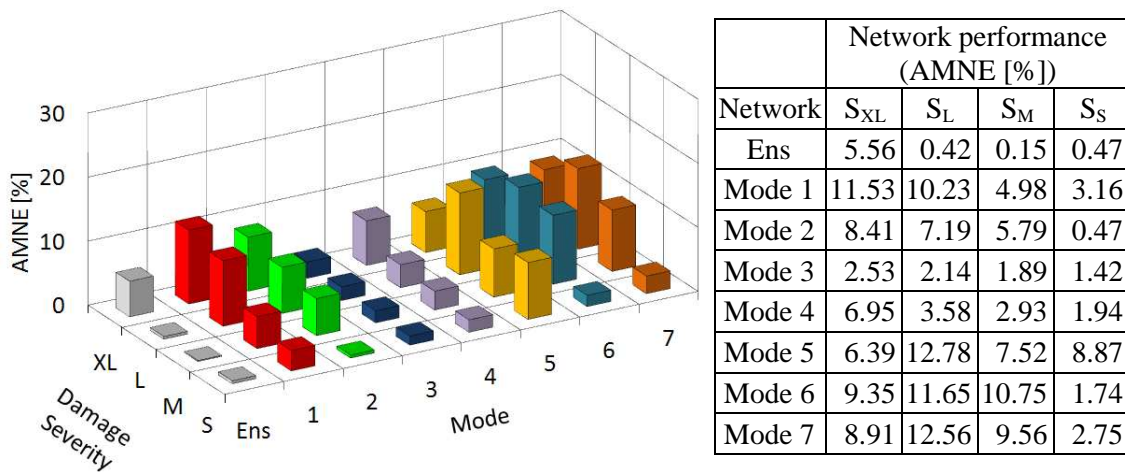


Figure 7.11 Neural network testing set performance (in AMNE) subdivided by damage severity trained with PCA-compressed α_j values from laboratory beams to identify damage severity.

When observing the detailed network outcomes of the higher modes (Figure 7.12 and Figure G.14 in APPENDIX G), a scattered pattern of erroneous damage detections is noted. This observation is similar to the finding from the localisation outcomes of the laboratory beams (see section 7.3.2), and it is believed that errors from mode shape extraction and noise interferences are the cause for these uncorrelated network outcomes.

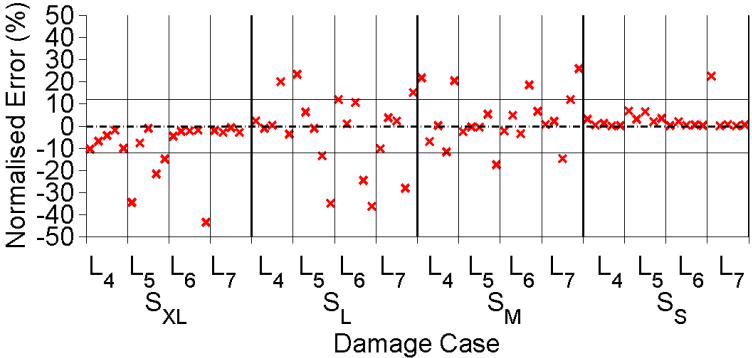


Figure 7.12 Neural network testing set outcomes for the network of mode 7 trained with PCA-compressed α_j values to identify damage severities of laboratory beams.

7.4 DAMAGE IDENTIFICATION BASED ON FREQUENCY RESPONSE FUNCTIONS

This section presents results of the proposed FRF-based damage identification method applied to numerical and laboratory beam data. As previously discussed, FRF data are less processed data that contain an abundance of information on the structural dynamic behaviour. Unlike modal-based damage identification methods (such as the DI method), FRF-based damage detection techniques do not require experimental modal analysis procedures that are very susceptible to human error. By using directly measured FRF data for damage detection, uncertainties and errors can be greatly reduced and information loss will be better preserved. Due to the large amount of information that is contained in the FRF data, problems associated with node point singularities can be avoided.

In this section, first, the feasibility of the FRF-based method is tested on beam data obtained from numerical simulations, and then the method is verified on data obtained from laboratory testing. The effectiveness of two types of FRF-based damage indicators is investigated, i.e. residual FRFs and CNR-FRFs (see section 6.3.1). Both indices are compressed using PCA techniques, and only the most dominant PCs are used as input parameters for ANNs to identify locations and severities of damage. For each identification task, a total of eight individual networks are created; seven of these are trained with data obtained from the measurement locations ‘1’ to ‘7’, and one network is trained with data from summation FRFs. A network ensemble then fuses the outcomes of the seven individual networks (of measurement locations ‘1’ to ‘7’) and gives final damage predictions.

After analysing the results obtained from the two damage indices (residual FRF and CNR-FRF), it was observed that the identification results of both indices are very similar in terms of accuracies for both damage localisation and damage severity estimations. Therefore, only the results obtained from residual FRF data are discussed in this section. The outcomes from CNR-FRFs are presented in APPENDIX I.

7.4.1 Results of Frequency-Response-Function-Based Damage Identification Method Applied to Numerically Simulated Beam

In this section, the proposed FRF-based damage identification method is applied for detecting damage in the numerically simulated beam. To incorporate ‘real life’ issues of measurement noise interferences, numerically acquired acceleration data are polluted with four levels of white Gaussian noise. Studies are then undertaken to analyse the influence of different noise levels on damage identification and to investigate the effectiveness of the noise filtering capabilities of PCA and neural networks.

Neural Network Outcomes of Frequency-Response-Function-Based Method Applied to Numerically Simulated Beam to Identify Damage Locations

Table 7.11 shows specifications and performance of the proposed neural networks trained with PCA-compressed residual FRFs for damage localisation using noise-polluted numerical data. Figure 7.13 illustrates the correlating testing set performance of the networks, subdivided by damage severity.

Table 7.11 Neural network specifications and performance (in AMNE) trained with PCA-compressed residual FRFs from noise-polluted numerical beams to identify damage locations.

Network	Network design	Convergence algorithm	Iteration	Training performance (AMNE [%])	Validation performance (AMNE [%])	Testing performance (AMNE [%])
‘1’	4-3-2-1	Qp	7,783	1.55	2.31	1.74
‘2’	4-3-2-1	Qp	3,982	1.79	2.71	2.56
‘3’	4-3-2-1	Qp	6,298	0.77	1.49	1.59
‘4’	4-3-2-1	Qp	5,923	1.40	1.73	1.49
‘5’	4-3-2-1	Qp	4,956	1.54	1.88	1.71
‘6’	4-3-2-1	Qp	8,733	0.90	1.53	2.16
‘7’	4-3-2-1	Qp	5,302	1.10	1.33	2.36
Sum	4-3-2-1	Qp	4,910	1.21	1.51	1.76
Ens	7-6-4-2-1	Obp	16,589	0.07	0.09	0.98

Note: Qp = Quick propagation function

Obp = Online backpropagation function

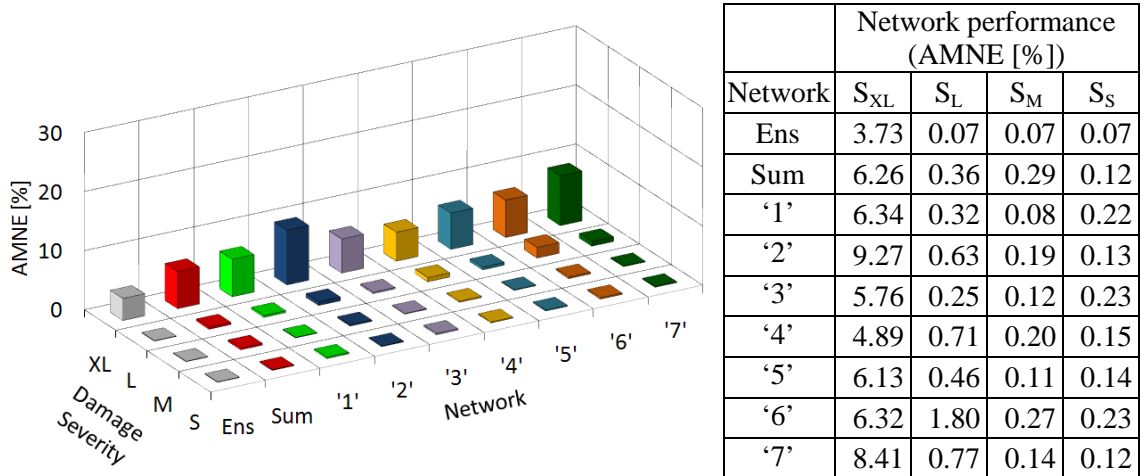


Figure 7.13 Neural network testing set performance (in AMNE) subdivided by damage severity trained with PCA-compressed residual FRFs from noise-polluted numerical beams to identify damage locations.

From the table and the figure, it can be seen that for damage cases of light, medium and severe size, all networks correctly identify all damage locations. For extra-light damage cases large errors occurred for all networks. However, it is worth noticing that there is a significant improvement of the outcomes, when comparing these results with the localisation outcomes from the DI-based method (see section 7.3.1). For the DI-based identification method, as discussed previously, errors in prediction are largely introduced by the modal extraction process from experimental modal analysis, as well as by singularity of mode shape node points, mode shape reconstruction and noise sensitivity issues. For the FRF-based method, the aforementioned problems are avoided and thereby better identification results are expected. Further, the excellent localisation results of the FRF-based method for cases of light, medium and severe damage demonstrate the noise filtering capability of PCA and neural networks for FRF data with direct noise features. As found in section 6.3.2, noise only affected PCs of lower power. Therefore, by disregarding these lower power PCs, noise is successfully reduced and hence has minimum effect on damage identification. However, for damage cases of extra-light severity, noise does have a significant impact on the damage localisation outcomes (as the signal-to-noise ratios is low). In other words, damage fingerprints of extra-light damage are so small that they are overshadowed by noise disturbances. Hence, noise patterns are effectively included in PCs of higher power and thus result in faulty damage localisations.

From the performance of the individual networks, it is noted that the network trained with data from summation FRFs provides improved but not necessarily the best identification outcomes (e.g. the network trained with data from location '3' gives smaller AMNE values for the training, validation and testing sets). As expected, among all trained networks, the best results are obtained with the ensemble network, giving AMNEs of 0.07%, 0.09% and 0.98% for the training, validation and testing sets, respectively. It is further noted that the difference in damage detection results from each individual network is very small. This observation suggests that even with measurements from a single sensor, using the FRF-based method, accurate and reliable damage identification can be obtained. This finding is further evidence to the superiority of the FRF-based damage identification method in comparison with the DI-based method, which is found to produce individual network outcomes with varying accuracies due to the sensitivity of DI values to individual vibrational mode characteristics, such as node points and low curvature values.

To investigate the influence of various noise levels on the damage localisation outcomes, Figure 7.14 illustrates the testing set outcomes of different networks separated by noise-pollution level and damage severity. (Corresponding figures of all networks are displayed in Figure H.5 in APPENDIX H.)

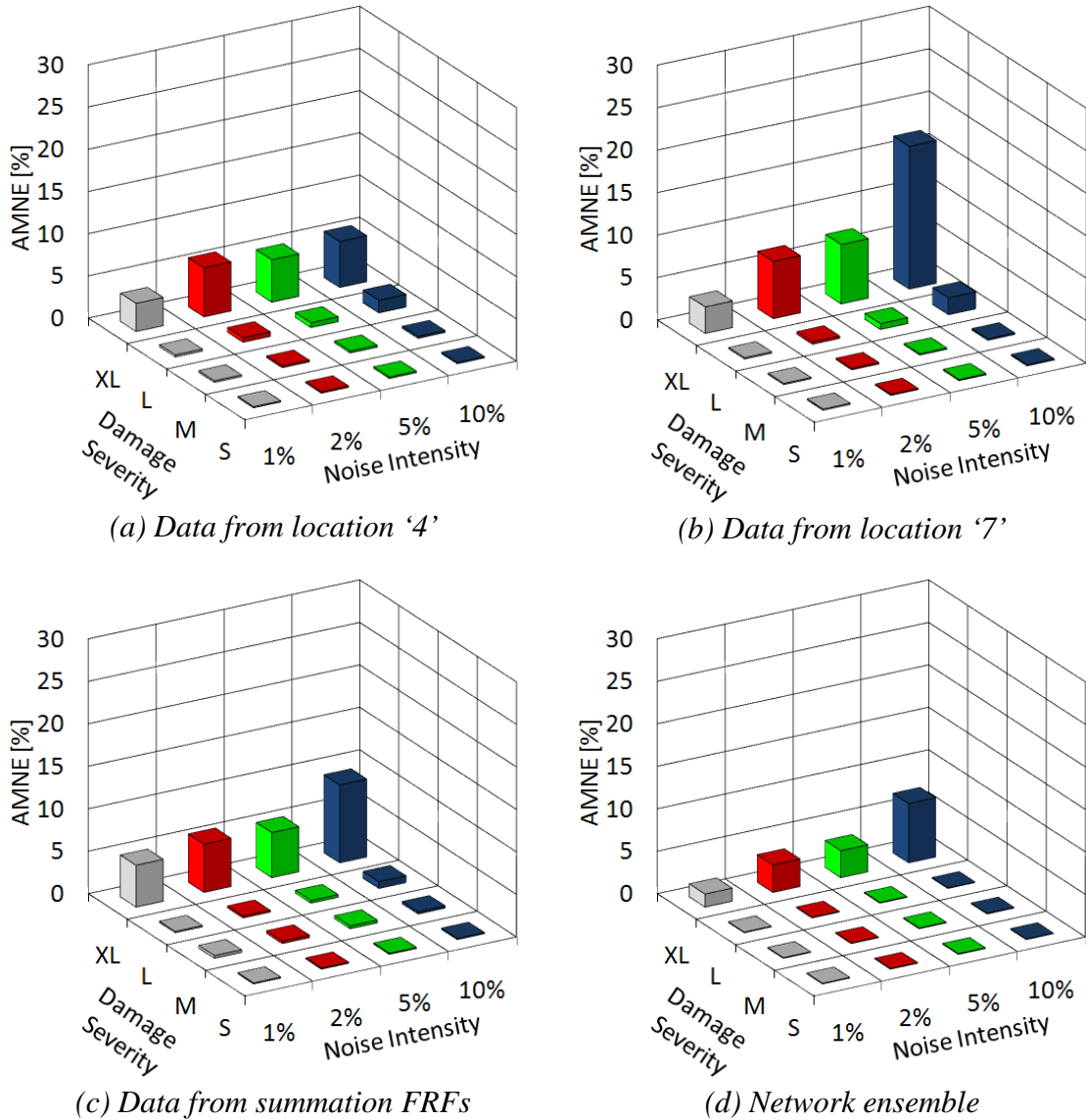


Figure 7.14 Comparison of testing set outcomes of networks trained with PCA-compressed residual FRFs to identify damage locations of noise-polluted numerical beams subdivided by damage severity and noise pollution levels.

From the figures, a clear correlation between noise pollution level and network localisation accuracy is observed. For example, for the ensemble network, the AMNE value for extra-light damage cases of 1% noise polluted data is only 1.54%, whereas the errors for 2% and 5% noise are about 3.20%, and for 10% noise pollution level an AMNE of 6.98% is obtained. The detailed localisation outcomes of all individual networks and the network ensemble are found in Figure H.1 to Figure H.4 in APPENDIX H. From the detailed outcomes of the network ensemble, it is found that up to a noise pollution level of 2%, all damage cases are estimated correctly within the

decisive error band of $\pm 6.25\%$. For damage cases of 5% and 10% noise pollution, however, some cases of extra-light severity produce larger error.

Neural Network Outcomes of Frequency-Response-Function-Based Method Applied to Numerically Simulated Beam to Identify Damage Severities

For damage severity estimations, Table 7.12 lists specifications and performance of all networks trained with noise-polluted numerical beam data. From the table it is seen that for severity identification, all networks produce good results, with a maximum testing set AMNE of 0.04% for the networks of locations '2' and '4'. From the testing set results of Figure 7.15 (separated by damage severity) and the detailed identification outcomes illustrated in Figure H.6 to Figure H.9 in APPENDIX H, it is found that all networks correctly estimate the severities of all damage cases for all noise pollution levels. From the table in Figure 7.15, it is further noted that identification errors of damage cases of smaller size are slightly larger than predictions of more severe cases. These results demonstrate the potential of using FRF data for identifying damage severities. As mentioned above, in contrast to the DI-based method, FRF-based damage identification eliminates problems associated with errors introduced during experimental modal analysis procedures, and it avoids issues with node point singularity of mode shapes and noise sensitivity issues caused by small mode shape curvature values and interferences of boundaries. It is noted that for FRF-based damage identification, the damage severity estimations are even better than the damage localisation results.

Table 7.12 Neural network specifications and performance (in AMNE) trained with PCA-compressed residual FRFs from noise-polluted numerical beams to identify damage severities.

Network	Network design	Convergence algorithm	Iteration	Training performance (AMNE [%])	Validation performance (AMNE [%])	Testing performance (AMNE [%])
'1'	4-3-2-1	Obp	1,437	0.01	0.01	0.01
'2'	4-3-2-1	Obp	1,586	0.02	0.06	0.04
'3'	4-3-2-1	Obp	1,835	0.01	0.02	0.02
'4'	4-3-2-1	Obp	946	0.03	0.04	0.04
'5'	4-3-2-1	Obp	1,196	0.02	0.02	0.02
'6'	4-3-2-1	Obp	1,376	0.02	0.03	0.02
'7'	4-3-2-1	Obp	1,464	0.01	0.03	0.02
Sum	4-3-2-1	Obp	856	0.02	0.02	0.03
Ens	7-6-4-2-1	Obp	13,765	0.01	0.01	0.01

Note: Obp = Online backpropagation function

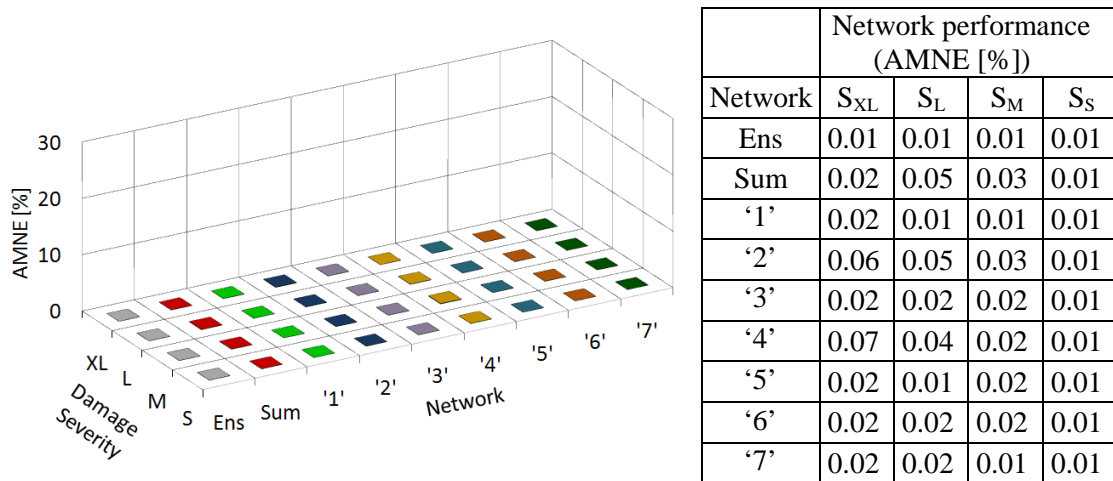


Figure 7.15 Neural network testing set performance (in AMNE) subdivided in damage severities trained with PCA-compressed residual FRFs from noise-polluted numerical beams to identify damage severities.

7.4.2 Results of Frequency-Response-Function-Based Damage Identification Method Applied to Laboratory Test Beams

In this section, the proposed FRF-based damage identification method is verified with real beam structures. Influences of the real environment, such as measurement noise and effects of structure and boundary imperfections, on the proposed method are thereby considered. Direct measurements of FRF data are used to form damage fingerprints for the identification of damage locations and severities. The outcomes of neural networks trained with PCA-compressed residual FRFs of laboratory beams are presented.

Neural Network Outcomes of Frequency-Response-Function-Based Method Applied to Laboratory Beams to Identify Damage Locations

For damage location identification, Table 7.13 lists specifications and performance of networks trained with data from the laboratory beams. From the network performance, it is seen that for laboratory data, all damage cases are precisely located by all trained networks, with a maximum AMNE of 0.02%. For some individual networks (networks of locations ‘1’, ‘5’, ‘6’ and ‘7’) as well as the ensemble network, even AMNE values of 0.01% are obtained for all three data sets (the training, validation and testing sets). When comparing the localisation results from laboratory beam data to the outcomes obtained from noise-polluted numerical data, it is noted that the networks trained with laboratory data give better predictions, especially for extra-light damage cases. A similar trend is observed for damage location identification using the DI-based method (see section 7.3.2). These improved localisation outcomes are due to a lower level of noise in experimental testing (usually below 1%) and an enhancement of damage patterns in dynamic characteristics resulting from the testing of different experimental beams for different damage locations.

From severity separated testing set results presented in Figure 7.16, it is observed that extra-light damage cases also give larger errors than for the light to severe damage cases (which is similar to the results obtained from noise-polluted numerical data). Detailed network outcomes are illustrated in Figure H.11 in APPENDIX H.

Table 7.13 Neural network specifications and performance (in AMNE) trained with PCA-compressed residual FRFs from laboratory beams to identify damage locations.

Network	Network design	Convergence algorithm	Iteration	Training performance (AMNE [%])	Validation performance (AMNE [%])	Testing performance (AMNE [%])
‘1’	10-8-6-4-2-1	Obp	15,266	0.01	0.01	0.01
‘2’	10-8-6-4-2-1	Obp	12,147	0.01	0.02	0.02
‘3’	10-8-6-4-2-1	Obp	13,256	0.01	0.01	0.02
‘4’	10-8-6-4-2-1	Obp	10,268	0.01	0.02	0.02
‘5’	10-8-6-4-2-1	Obp	15,487	0.01	0.01	0.01
‘6’	10-8-6-4-2-1	Obp	12,483	0.01	0.01	0.01
‘7’	10-8-6-4-2-1	Obp	13,695	0.01	0.01	0.01
Sum	10-8-6-4-2-1	Obp	15,826	0.01	0.02	0.02
Ens	7-6-4-2-1	Obp	16,191	0.01	0.01	0.01

Note: Obp = Online backpropagation function

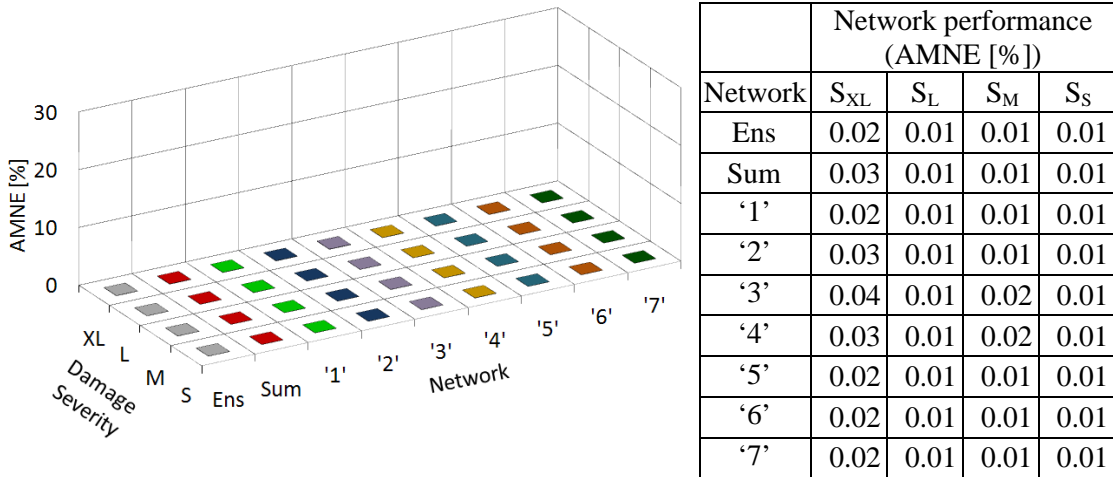


Figure 7.16 Neural network testing set performance (in AMNE) subdivided in damage severities trained with PCA-compressed residual FRFs from laboratory beams to identify damage locations.

Neural Network Outcomes of Frequency-Response-Function-Based Method Applied to Laboratory Beams to Identify Damage Severities

Specifications and performance of networks trained to estimate damage severities of laboratory structures are shown in Table 7.14. From the table, it can be seen that the proposed method produces very good results in terms of severity estimations. Although the results may not be as good as the localisation outcomes presented above, severities for all damage cases of the laboratory beams are correctly identified by all networks. The ensemble network produces even better results with AMNE values of 0.01% for the training, validation and testing sets, which is similar to damage localisation. From the detailed severity estimation results (Figure H.12 in APPENDIX H), it is observed that some individual networks give minor errors for a few damage cases. These small discrepancies are, however, scattered among the different damage cases and are believed to be caused by measurement noise interferences.

Table 7.14 Neural network specifications and performance (in AMNE) trained with PCA-compressed residual FRFs from laboratory beams to identify damage severities.

Network	Network design	Convergence algorithm	Iteration	Training performance (AMNE [%])	Validation performance (AMNE [%])	Testing performance (AMNE [%])
'1'	10-8-6-4-2-1	Obp	10,268	0.01	0.02	0.03
'2'	10-8-6-4-2-1	Obp	9,582	0.01	0.03	0.04
'3'	10-8-6-4-2-1	Obp	8,825	0.02	0.10	0.05
'4'	10-8-6-4-2-1	Obp	9,114	0.03	0.09	0.06
'5'	10-8-6-4-2-1	Obp	8,246	0.04	0.08	0.07
'6'	10-8-6-4-2-1	Obp	7,824	0.05	0.11	0.11
'7'	10-8-6-4-2-1	Obp	8,353	0.08	0.10	0.06
Sum	10-8-6-4-2-1	Obp	10,588	0.03	0.04	0.03
Ens	7-6-4-2-1	Obp	16,829	0.01	0.01	0.01

Note: Obp = Online backpropagation function

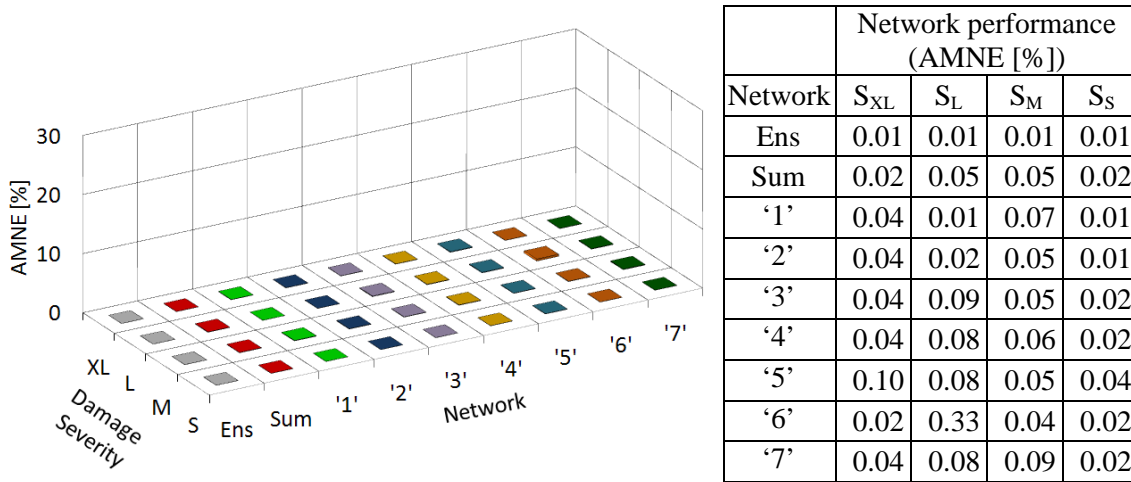


Figure 7.17 Neural network testing set performance (in AMNE) subdivided in damage severities trained with PCA-compressed residual FRFs from laboratory beams to identify damage severities.

7.5 SUMMARY

This chapter presented results of the two proposed damage identification schemes applied to the beam structure. One scheme was based on damage patterns obtained from the DI method and the other was based on damage fingerprints from FRF data. Both methods were firstly tested on numerically simulated data from finite element modelling and then verified on data obtained from laboratory testing. ANNs were the core element for both methods in identifying locations and severities of damage. For the DI-based identification scheme, PCA-compressed damage indices (Z_j and α_j values) were used as network inputs; for the FRF-based method, PCA-compressed residual FRFs were used

as input patterns for the networks. To take advantage of individual characteristics of damage patterns obtained from different sources, i.e. either vibrational modes for the DI-based method or individual sensors for the FRF-based method, a network training approach based on network ensembles was employed. The outcomes from individual networks and the ensemble network were analysed in terms of the accuracies of damage predictions. Differences in performance of individual networks were evaluated and correlations between damage severity and outcome accuracies investigated. For noise-polluted numerical data, noise sensitivity studies were carried out to assess the influence of different noise intensities on damage identification results.

For the DI-based identification scheme, the following observations are made:

- For damage localisation using data from noise-free numerical simulations, all trained networks (individual networks and the network ensemble) precisely located all damage cases. These results are evidence that the proposed DI-based damage identification scheme is capable of successfully overcoming inherent problems of the original DI method, such as issues related to node point singularities, sensitivity to limited number of sensors and boundary conditions.
- From the damage localisation results of networks trained with noise-polluted numerical data, there is a significant influence of noise and modal analysis errors on the identification results. Mode shape data appeared to be highly sensitive to noise and resulted in large prediction errors. A clear correlation between noise pollution level and location identification accuracy was observed.
- For damage severity estimations of noise-free numerical data, the results utilising severity indicator α_j were highly influenced by modal node points. The outcomes of the remaining networks were reasonably good.
- From the damage severity results of noise-polluted numerical data, problems related to node point singularities were again observed (for the networks of modes 2, 4 and 6). A correlation between noise pollution intensity and severity estimation accuracy was observed for the networks of modes 3, 5, 7 and the network ensemble.
- For the damage localisation using laboratory data, excellent identification results were obtained for individual networks of lower modes. These good results are due to

a lower level of noise during experimental testing (usually below 1%) and an enhancement of damage patterns obtained from laboratory testing of different test beams for different damage locations. The individual networks of higher modes gave large identification errors due to difficulties faced in the extraction of the mode shapes during experimental modal analysis. The network ensemble precisely located all damage cases.

- For the severity identifications of laboratory test data, the obtained results were similar to the severity outcomes of networks trained with noise-polluted numerical data. However, for the laboratory data, individual networks of the higher modes produced large errors due to difficulties in experimental modal analysis.

For the FRF-based identification scheme, the following observations are made:

- For severity and location identification of noise-polluted numerical data, all trained networks precisely estimated severities of all damage cases, and locations were successfully identified for all light, medium and severe damage cases. These excellent outcomes demonstrate the advantages of the FRF-based method, which avoids errors from experimental modal analysis and reduces the influences of node point singularities. Further, these outcomes show the noise filtering capabilities of PCA and neural networks, which were found to give correct results even for data of 10% noise pollution.
- For laboratory data, all individual networks and the network ensemble precisely identified the locations and severities of all damage cases.

From the damage identification outcomes of both methods, the following conclusions are drawn. For the DI-based identification scheme, noise influences have profound impacts on the identification results for damage locations and severities. While for noise-free data, inherent problems of the original DI method can be successfully overcome by the proposed method, in the presence of noise, the errors/problems are amplified. Further, some errors may be caused by mode shape reconstruction and mode shape node points. In addition, the level of noise pollution and the severity of damage have some influence on the accuracy of the damage identifications. The proposed network ensemble training approach was found to be successful in filtering error-prone damage identifications from networks trained with ‘critical’ modes and it produced

much improved final damage identifications. For the FRF-based identification scheme, the filtering capabilities of PCA and neural networks were shown to successfully remove noise up to level of at least 10% (noise-to-signal ratio). Networks trained with data from any measurement location can produce accurate and robust identifications of all damage locations (except for extra-light damage cases) and damage severities. As a result, it can be concluded that the FRF-based damage identification scheme is superior to the DI-based identification scheme in locating and identifying severity of damage. For the FRF-based method, problems from experimental modal analysis are avoided, influences of individual characteristics from different measurement sources are reduced, and noise influences are successfully filtered out. The proposed FRF-based damage identification scheme provides an accurate and robust identification method that requires only a small number of sensors.

CHAPTER 8

DAMAGE IDENTIFICATION OF TWO-STOREY FRAMED STRUCTURE BASED ON FREQUENCY RESPONSE FUNCTIONS

8.1 INTRODUCTION

This chapter presents application of the proposed frequency-response-function (FRF)-based damage identification method on a more complicated structure, i.e. the two-storey framed structure. The proposed method uses dynamic fingerprints from residual FRFs in combination with principal component analysis (PCA) and artificial neural networks (ANNs) to identify damage inflicted to the two-storey framed structure. Three types of structural changes are investigated: boundary damage, added mass changes and section reduction damage. For damage prediction, neural networks of two kinds are created; one categorises structural changes into set categories (e.g. for boundary damage and added mass changes) and the other gives numerical output values (e.g. for section reduction damage). The neural network tasks for damage identification are as follows:

- Boundary condition identification: identify current types of boundary condition.
- Added mass identification: identify location of added mass.
- Section reduction damage identification: identify location and severity of damage.

The chapter begins by describing the design features of the created ANNs; next, the results of the damage/added mass identifications of the numerical two-storey framed structure are discussed; and lastly, the outcomes of the experimental damage/added mass cases are presented.

8.2 ARTIFICIAL NEURAL NETWORK DESIGN

For the identification of structural changes of the two-storey framed structure, a number of multi-layer backpropagation neural networks are created. 16 individual networks and one network ensemble are designed for each of the three numerical and experimental damage/added mass scenarios. The individual networks are trained with principal components (PCs) of residual FRFs. Out of the 16 individual networks, 14 are trained with data obtained from the 14 sensor locations (see Figure 8.1 (a)) and two are trained with data derived from horizontal and vertical summation FRFs. (FRFs of horizontal accelerations (from sensor locations ‘1’ to ‘8’) and FRFs of vertical accelerations (from sensor locations ‘9’ to ‘14’) are added up to give horizontal and vertical summation FRFs, respectively.) The network ensemble is trained with the outcomes of the 14 individual sensor networks. Similar to the evaluation of the beam results, the outcomes of the horizontal and vertical summation FRF networks are compared against the results of the neural network ensemble.

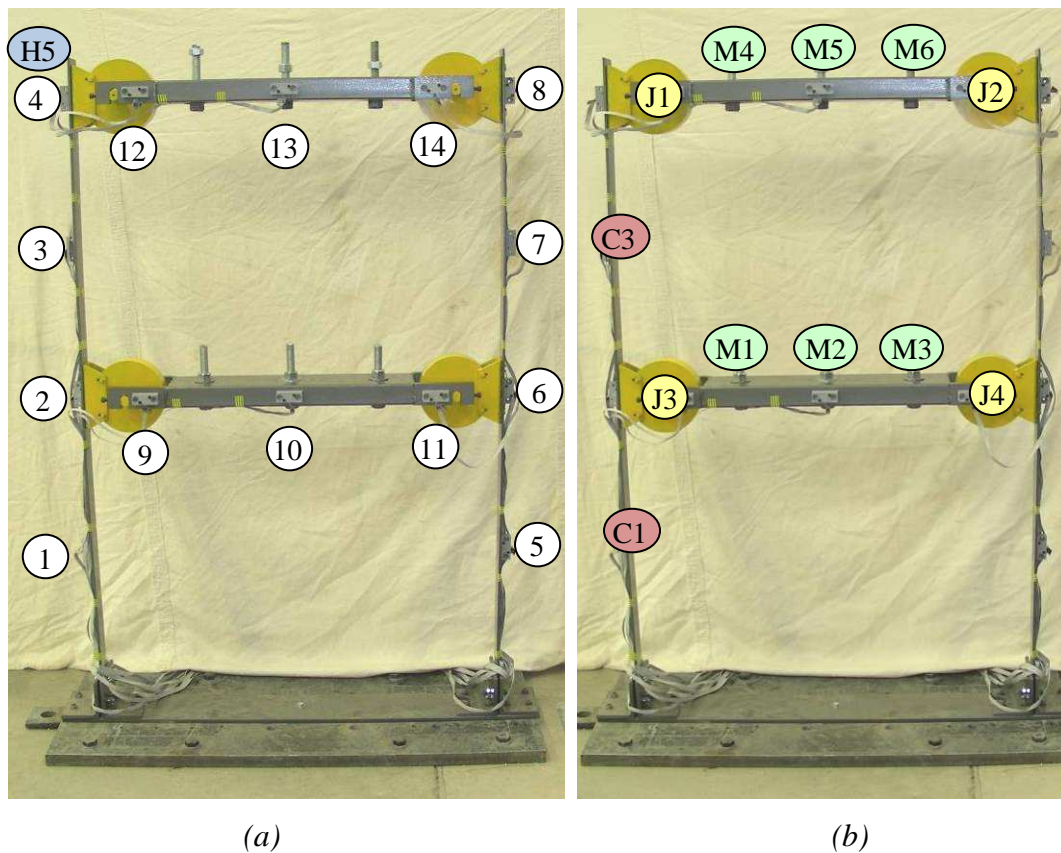


Figure 8.1 (a) Measurement sensor locations ‘1’ to ‘14’ and hammer impact point H5, and (b) damage/added mass scenarios of the two-storey framed structure.

For the classification of the boundary condition and added mass scenarios, the networks are designed to categorise the damage/added mass cases into one of the ten boundary condition scenarios or one of the six added mass locations in a winner-takes-all fashion. The section reduction damage cases are identified by precise numerical location and severity measures (similar to the beam damage cases in CHAPTER 7).

To avoid overfitting, the data of the three structural change types are again separated into training, validation and testing sets. For each structural state (the undamaged and all damaged/added mass states), five sets of FRF measurements are available for the laboratory and the numerical two-storey framed structure. (For the laboratory structure, each state was tested five times, and for the numerical model, acceleration data was polluted with five sets of different noise signals for each noise pollution level.) To calculate residual FRFs, the five samples of FRF data from the damaged/added mass states are correlated to each of the five samples of FRFs obtained from the baseline (undamaged) state. Therefore, a total of 25 residual FRFs (and consequently 25 neural network input samples) are available for each damage/added mass scenario. Following the chessboard selection (see section 7.2), each damage/added mass scenario is separated into 15 training, 5 validation and 5 testing samples. Table 8.1 and Table 8.2 list the numbers of all damage/added mass samples of the training, validation and testing sets for the numerical and the experimental structure.

Table 8.1 Training, validation and testing partitioning of damage/added mass scenarios for the numerical two-storey framed structure.

Scenario	Set	Samples	Remarks
Boundary condition scenarios	Training	600	10 boundary condition scenarios \times 15 samples \times 4 noise levels
	Validation	200	10 boundary condition scenarios \times 5 samples \times 4 noise levels
	Testing	200	10 boundary condition scenarios \times 5 samples \times 4 noise levels
Added mass scenarios	Training	360	6 added mass scenarios \times 15 samples \times 4 noise levels
	Validation	120	6 added mass scenarios \times 5 samples \times 4 noise levels
	Testing	120	6 added mass scenarios \times 5 samples \times 4 noise levels
Section reduction scenarios	Training	1080	18 section reduction scenarios (6 locations \times 3 severities) \times 15 samples \times 4 noise levels
	Validation	360	18 section reduction scenarios (6 locations \times 3 severities) \times 5 samples \times 4 noise levels
	Testing	360	18 section reduction scenarios (6 locations \times 3 severities) \times 5 samples \times 4 noise levels

Table 8.2 Training, validation and testing partitioning of damage/added mass scenarios for the laboratory two-storey framed structure.

Scenario	Set	Samples	Remarks
Boundary condition scenarios	Training	150	10 boundary condition scenarios × 15 samples
	Validation	50	10 boundary condition scenarios × 5 samples
	Testing	50	10 boundary condition scenarios × 5 samples
Added mass scenarios	Training	90	6 added mass scenarios × 15 samples
	Validation	30	6 added mass scenarios × 5 samples
	Testing	30	6 added mass scenarios × 5 samples
Section reduction scenarios	Training	90	6 section reduction scenarios (2 locations × 3 severities) × 15 samples
	Validation	30	18 section reduction scenarios (2 locations × 3 severities) × 5 samples
	Testing	30	6 section reduction scenarios (6 locations × 3 severities) × 5 samples

The network output categories of the boundary condition and added mass scenarios are encoded using the 1-of-N encoding method (Alyuda Research Inc 2006b). This technique converts N categories into a set of N numerical output neurons. For each category, one of the N output neurons is set to 1 and the others to 0. The network output encoding for all boundary condition and added mass scenarios is shown in Table 8.3 and Table 8.4, respectively.

Table 8.3 Neural network output encoding of boundary condition scenarios. Table 8.4 Neural network output encoding of added mass scenarios.

Boundary condition scenario	Network output
PFFF	{1,0,0,0,0,0,0,0,0}
FPFF	{0,1,0,0,0,0,0,0,0}
FFPF	{0,0,1,0,0,0,0,0,0}
FFFP	{0,0,0,1,0,0,0,0,0}
PPFF	{0,0,0,0,1,0,0,0,0}
FFPP	{0,0,0,0,0,1,0,0,0}
FPFP	{0,0,0,0,0,0,1,0,0}
PFPF	{0,0,0,0,0,0,0,1,0}
FPPF	{0,0,0,0,0,0,0,0,1}
PFFP	{0,0,0,0,0,0,0,0,0,1}

Added mass scenario	Network output
M1	{1,0,0,0,0,0}
M2	{0,1,0,0,0,0}
M3	{0,0,1,0,0,0}
M4	{0,0,0,1,0,0}
M5	{0,0,0,0,1,0}
M6	{0,0,0,0,0,1}

Note: P = Pinned
F = Fixed

The network outputs of the section reduction cases are either the locations (in height above the steel base connection) or the severities (in loss of the second moment of area, I) of damage. Target output location and severity values are listed for all numerical and experimental (in brackets) section reduction cases in Table 8.5.

Table 8.5 Neural network target output of section reduction cases.

Section reduction scenario	Network output - Damage location [m] (measured from steel base connection)	Network output - Damage severity [%] (in loss of the second moment of area, I)
1aL (1L)	0.350	25.0
1aM (1M)	0.350	33.3
1aS (1S)	0.350	50.0
1bL	0.467	25.0
1bM	0.467	33.3
1bS	0.467	50.0
1cL	0.525	25.0
1cM	0.525	33.3
1cS	0.525	50.0
3aL (3L)	1.050	25.0
3aM (3M)	1.050	33.3
3aS (3S)	1.050	50.0
3bL	1.167	25.0
3bM	1.167	33.3
3bS	1.167	50.0
3cL	1.225	25.0
3cM	1.225	33.3
3cS	1.225	50.0

The input and output data are scaled to a range from -1 to $+1$ (see equation (3.16)) to suit the hyperbolic tangent sigmoid transfer function, which is chosen for all layers. For the convergence algorithm, one of the following three functions is used: the quick propagation function, the conjugate gradient descent function and the online backpropagation function. The best performing algorithm is determined by trial and error. For the three damage/added mass types, different numbers of hidden layers and neurons are created following the geometric pyramid rule. Details on the exact numbers of hidden layers and neurons, as well as the chosen convergence algorithms are presented for each created network in subsequent sections.

For the numerical networks (for section reduction scenarios), NeuroIntelligence assesses the training performance by absolute error (AE) (see equation (7.1) in section 7.2), for

the categorical networks (for boundary condition and added mass scenarios) the training performance is supervised by the correct classification rate (CCR). The CCR is defined as:

$$CCR = \frac{\text{Number of correctly recognised cases}}{\text{Total number of cases}} \quad (8.1)$$

Training of the networks is stopped by either manual control or after a set number of iterations. The built-in overtraining control in NeuroIntelligence is set to retain and restore the network with the lowest testing AE (for section reduction scenarios) or the highest testing CCR (for boundary condition and added mass scenarios). During training, network performance is monitored by the real-time AE performance graph and the real-time CCR performance graph, respectively. The CCR performance graph of a network reaching a CCR of 100% after 36 iterations is shown in Figure 8.2.

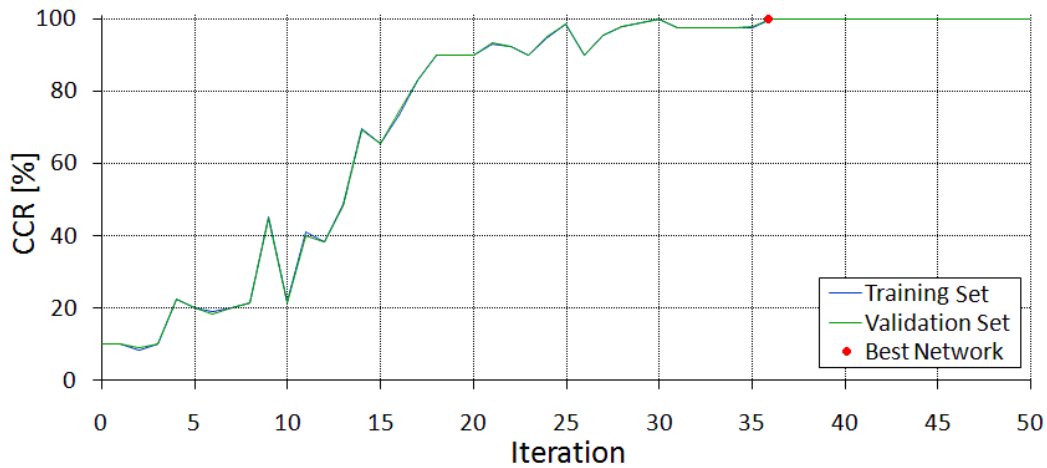


Figure 8.2 CCR performance graph.

8.3 DAMAGE IDENTIFICATION RESULTS USING DATA FROM NUMERICAL SIMULATIONS OF THE TWO-STOREY FRAMED STRUCTURE

8.3.1 Boundary Condition Identification

The specifications and performance of networks trained to identify the boundary conditions of the numerical two-storey framed structure are shown in Table 8.6, which presents the 16 individual networks and the network ensemble ('Ens'). The individual networks '1' to '14' are trained with data from the 14 sensor locations and the networks SumH and SumV with data derived from horizontal and vertical summation FRFs, respectively. The table lists the number of neurons per input-hidden-output layer (Network design); the convergence algorithms; the number of iterations until the optimum network performance is reached ('Iteration'); and the training, validation and testing performance of the networks in mean correct classification rate (MCCR).

From the network performance, it is observed that all networks, except those trained with data from locations '2', '4', '6' and '8', correctly identify the boundary conditions of all training, validation and testing cases. It is noted that these networks reach their optimum performance (100% MCCR) after only a few dozen of iterations. For the networks of locations '2', '4', '6' and '8', however, some damage cases are incorrectly identified. As already observed from the direct FRF measurements, vibrational data of locations '2', '4', '6' and '8' are insensitive to local modes due to the fixed bonding of the joint elements to the columns (see section 5.3.4). Hence, the damage patterns in FRFs of these locations are limited and therefore lead to false damage identifications. For the individual networks of the horizontal and vertical summation FRFs as well as the network ensemble, all boundary damage cases are classified correctly with MCCR values of 100% for all training, validation and testing data. It is emphasised that even though some individual networks give incorrect estimations, the network ensemble eventually precisely identifies all boundary condition cases.

Table 8.6 Neural network specifications and performance (in MCCR) trained with data from the numerical two-storey framed structure with different boundary conditions.

Net-work	Network design	Convergence algorithm	Iteration	Training performance (MCCR [%])	Validation performance (MCCR [%])	Testing performance (MCCR [%])
'1'	10-16-14-12-10	Qp	24	100	100	100
'2'	10-16-14-12-10	Qp	1126	99.8	97.0	97.0
'3'	10-16-14-12-10	Qp	35	100	100	100
'4'	10-16-14-12-10	Qp	2458	97.8	98.0	97.0
'5'	10-16-14-12-10	Qp	34	100	100	100
'6'	10-16-14-12-10	Qp	3159	97.8	97	95.5
'7'	10-16-14-12-10	Qp	26	100	100	100
'8'	10-16-14-12-10	Qp	3685	98.2	94	94
'9'	10-16-14-12-10	Qp	24	100	100	100
'10'	10-16-14-12-10	Qp	62	100	100	100
'11'	10-16-14-12-10	Qp	26	100	100	100
'12'	10-16-14-12-10	Qp	25	100	100	100
'13'	10-16-14-12-10	Qp	42	100	100	100
'14'	10-16-14-12-10	Qp	17	100	100	100
SumH	10-16-14-12-10	Qp	142	100	100	100
SumV	10-16-14-12-10	Qp	34	100	100	100
Ens	14-13-12-11-10	Cgd	41	100	100	100

Note: Qp = Quick propagation function

Cgd = Conjugate gradient descent function

To study the influence of different noise levels on the damage identification results, Table 8.7 shows a detailed listing of testing set MCCRs of networks trained with data from locations '2', '4', '6' and '8' broken down into individual boundary condition cases and into the four noise pollution levels (1%, 2%, 5% and 10%). It is observed that for the networks of locations '2' and '4' only cases with 10% noise pollution are misclassified (see Table 8.7 (a) and (b)). Data from locations '6' and '8', however, lead to incorrect identification of boundary damage cases for all four levels of noise pollution. The reasoning for this is that locations '2' and '4' are on the same column as the hammer impact point, which results in stronger excitation and higher signal-to-noise ratio, i.e. noise has a negligible effect on the signals. The misclassifications of the testing cases are more or less equally distributed among the different boundary condition scenarios (every boundary scenario is misidentified by at least one network).

Table 8.7 MCCRs [%] of boundary condition predictions of networks trained with data from the numerical structure of locations (a) ‘2’, (b) ‘4’, (c) ‘6’ and (d) ‘8’. Tables present testing data of noise intensities from 1% to 10% (N 1% to N 10%).

(a) Data from location ‘2’

	N 1%	N 2%	N 5%	N 10%
PFFF	100	100	100	80
FPPF	100	100	100	80
FFPF	100	100	100	100
FFFP	100	100	100	100
PPFF	100	100	100	100
FFPP	100	100	100	100
FPPF	100	100	100	80
PFPF	100	100	100	100
FPPF	100	100	100	40
PFPF	100	100	100	100

(b) Data from location ‘4’

	N 1%	N 2%	N 5%	N 10%
PFFF	100	100	100	100
FPPF	100	100	100	60
FFPF	100	100	100	60
FFFP	100	100	100	100
PPFF	100	100	100	100
FFPP	100	100	100	100
FPPF	100	100	100	80
PFPF	100	100	100	100
FPPF	100	100	100	100
PFPF	100	100	100	80

(c) Data from location ‘6’

	N 1%	N 2%	N 5%	N 10%
PFFF	100	100	100	80
FPPF	100	100	100	100
FFPF	100	100	80	100
FFFP	100	100	100	100
PPFF	100	100	100	80
FFPP	100	100	100	80
FPPF	100	100	80	100
PFPF	100	100	100	80
FPPF	80	100	80	80
PFPF	100	100	100	100

(d) Data from location ‘8’

	N 1%	N 2%	N 5%	N 10%
PFFF	100	100	100	100
FPPF	100	100	60	80
FFPF	100	100	80	100
FFFP	100	100	100	80
PPFF	100	100	100	100
FFPP	100	100	100	80
FPPF	100	80	100	100
PFPF	100	100	60	80
FPPF	80	100	100	80
PFPF	100	100	80	100

8.3.2 Added Mass Identification

For identification of the added mass locations, the network specifications and performance are listed in Table 8.8. From the table, a similar trend is observed in the performance of the networks for added mass identification as for boundary condition identification. Again, all networks besides those trained with data from locations ‘2’, ‘4’, ‘6’ and ‘8’ (and the network of the horizontal summation FRF data) correctly locate all training, validation and testing cases. It is noted that the iterations of the networks of locations ‘1’, ‘3’, ‘5’ and ‘7’ (trained with data of horizontal accelerations) are four times lower than the iterations of the networks of locations ‘9’ to ‘14’ (trained with data of vertical accelerations). This indicates that for added mass identification, FRFs from horizontal accelerations (of locations ‘1’, ‘3’, ‘5’ and ‘7’) are more sensitive to mass changes of the crossbeams than FRFs derived from vertical accelerations (of locations ‘9’ to ‘14’).

Table 8.8 Neural network specifications and performance (in MCCR) trained with data from the numerical two-storey framed structure with different added mass scenarios.

Net-work	Network design	Convergence algorithm	Iteration	Training performance (MCCR [%])	Validation performance (MCCR [%])	Testing performance (MCCR [%])
'1'	10-9-8-7-6	Qp	25	100	100	100
'2'	10-9-8-7-6	Qp	3125	44.6	45.0	44.2
'3'	10-9-8-7-6	Qp	35	100	100	100
'4'	10-9-8-7-6	Qp	4456	51.9	52.5	45.0
'5'	10-9-8-7-6	Qp	37	100	100	100
'6'	10-9-8-7-6	Qp	2259	49.7	50.8	47.5
'7'	10-9-8-7-6	Qp	34	100	100	100
'8'	10-9-8-7-6	Qp	1625	47.5	46.7	39.2
'9'	10-9-8-7-6	Qp	123	100	100	100
'10'	10-9-8-7-6	Qp	124	100	100	100
'11'	10-9-8-7-6	Qp	129	100	100	100
'12'	10-9-8-7-6	Qp	142	100	100	100
'13'	10-9-8-7-6	Qp	126	100	100	100
'14'	10-9-8-7-6	Qp	135	100	100	100
SumH	10-9-8-7-6	Qp	4682	100	98.3	97.5
SumV	10-9-8-7-6	Qp	226	100	100	100
Ens	14-12-10-8-6	Cgd	46	100	100	100

Note: Qp = Quick propagation function

Cgd = Conjugate gradient descent function

It is further observed that the performance of the networks of locations '2', '4', '6' and '8' are very low (around 50% MCCR). A detailed presentation of the testing outcomes of these networks is shown in Table 8.9. For all four networks, added mass cases of all noise pollution levels and of all locations are incorrectly identified. Some added mass cases have MCC rates ranging from 0% to 100% with increasing noise level (see Table 8.9 (c)). This indicates that the network outcomes are rather random and that the input data to the networks of locations '2', '4', '6' and '8' contain no relevant information on the location of the added masses. This lack of information is again due to the insensitivity of FRF data from these locations to local modes.

Due to the low MCCR values of these networks, the network trained with data derived from horizontal summation FRFs misidentifies some added mass cases of 5% and 10% noise pollution (see Table 8.9 (e)). The network of the vertical summation FRFs correctly classifies all added mass cases. It is again noted that the network ensemble gives precise identifications despite the bad performance of the individual networks of locations '2', '4', '6' and '8'.

Table 8.9 MCCRs [%] of added mass localisations of networks trained with data from the numerical two-storey framed structure of locations '1' to '8'. Tables present testing data of noise intensities from 1% to 10% (N 1% to N 10%).

(a) Data from location '2'

	N 1%	N 2%	N 5%	N 10%
M1	0	20	40	60
M2	20	0	0	0
M3	100	100	100	40
M4	100	100	20	20
M5	100	20	0	0
M6	0	0	0	60

(b) Data from location '4'

	N 1%	N 2%	N 5%	N 10%
M1	60	100	60	80
M2	20	20	60	0
M3	40	60	0	60
M4	40	60	20	60
M5	100	40	40	40
M6	0	60	20	40

(c) Data from location '6'

	N 1%	N 2%	N 5%	N 10%
M1	0	0	0	0
M2	0	20	40	100
M3	80	80	40	20
M4	100	80	100	100
M5	60	60	0	60
M6	60	40	20	20

(d) Data from location '8'

	N 1%	N 2%	N 5%	N 10%
M1	0	0	60	40
M2	80	60	20	40
M3	20	60	40	40
M4	60	60	20	0
M5	0	0	0	60
M6	100	40	40	100

(e) Data from horizontal summation FRFs

	N 1%	N 2%	N 5%	N 10%
M1	100	100	80	80
M2	100	100	100	100
M3	100	100	100	80
M4	100	100	100	100
M5	100	100	100	100
M6	100	100	100	100

8.3.3 Section Reduction Damage Identification

For the section reduction scenarios, neural networks are trained to identify the locations and the severities of the different damage cases. As with the network outcome evaluations of the beam damage cases (see CHAPTER 7) normalised error values are calculated. The normalised error (NE) of the location and the severity results are:

$$NE_{loc} = \frac{(T_d - O_d)}{L_{max}} \quad \text{and} \quad NE_{sev} = \frac{(T_d - O_d)}{S_{max}} \quad (8.2)$$

respectively, where d is the damage case, T_d the target value of d , O_d the network output value of d , L_{max} the total length of the column (i.e. 1.4 m) and S_{max} the maximum severity of damage (i.e. 100% loss of the second moment of area, I). The acceptable error band of location estimates ranges here from -3.125% to $+3.125\%$ normalised

error, which represents the average midpoints in-between two damage locations determined by:

$$NE_{loc} = \pm \frac{\frac{0.525 \text{ m} - 0.467 \text{ m}}{2} + \frac{0.467 \text{ m} - 0.35 \text{ m}}{2}}{2 \times 1.4 \text{ m}} = \pm 3.125\% \quad (8.3)$$

The band of the damage quantifications ranges from -6.25% to $+6.25\%$ normalised error, specifying averaged midpoints in-between two damage quantifications, calculated as:

$$NE_{sev} = \pm \frac{\frac{50\% - 33.33\%}{2} + \frac{33.33\% - 25\%}{2}}{2 \times 100\%} = \pm 6.25\% \quad (8.4)$$

Localisation of Section Reduction Damage

For damage location identification, the specifications and performance of the trained networks are listed in Table 8.10. In the table, the network performance is given in absolute mean of normalised error (AMNE), which is similar to the outcome presentation of the beam results. An illustration of the testing set outcomes subdivided by damage cases of different severities is displayed in Figure 8.3. Next to the graphical illustration, a table lists the corresponding AMNE values. (The detailed presentation of the outcomes of all samples of the testing set is given in Figure J.3 to Figure J.10 in APPENDIX J.)

Table 8.10 Neural network specifications and performance (in AMNE) trained with data from the numerical two-storey framed structure of different cross-section reductions to identify damage locations.

Net-work	Network design	Convergence algorithm	Iteration	Training performance (AMNE [%])	Validation performance (AMNE [%])	Testing performance (AMNE [%])
'1'	10-8-6-4-2-1	Cgd	986	0.03	0.22	0.28
'2'	10-8-6-4-2-1	Cgd	348	1.84	3.22	3.22
'3'	10-8-6-4-2-1	Cgd	460	0.32	0.85	0.79
'4'	10-8-6-4-2-1	Cgd	707	6.34	7.02	6.87
'5'	10-8-6-4-2-1	Cgd	446	3.06	4.39	4.76
'6'	10-8-6-4-2-1	Cgd	869	8.51	9.52	9.50
'7'	10-8-6-4-2-1	Cgd	592	6.18	6.80	5.23
'8'	10-8-6-4-2-1	Cgd	478	6.20	7.12	7.37
'9'	10-8-6-4-2-1	Cgd	986	1.18	1.29	1.31
'10'	10-8-6-4-2-1	Cgd	816	0.06	0.08	0.09
'11'	10-8-6-4-2-1	Cgd	869	1.03	1.64	1.12
'12'	10-8-6-4-2-1	Cgd	973	1.02	1.22	1.25
'13'	10-8-6-4-2-1	Cgd	957	0.39	0.40	0.41
'14'	10-8-6-4-2-1	Cgd	993	0.60	0.92	1.23
SumH	10-8-6-4-2-1	Cgd	835	0.21	0.90	0.86
SumV	10-8-6-4-2-1	Cgd	893	0.25	0.42	0.50
Ens	14-10-8-6-4-2-1	Obp	5000	0.06	0.16	0.23

Note: Cgd = Conjugate gradient descent function

Obp = Online backpropagation function

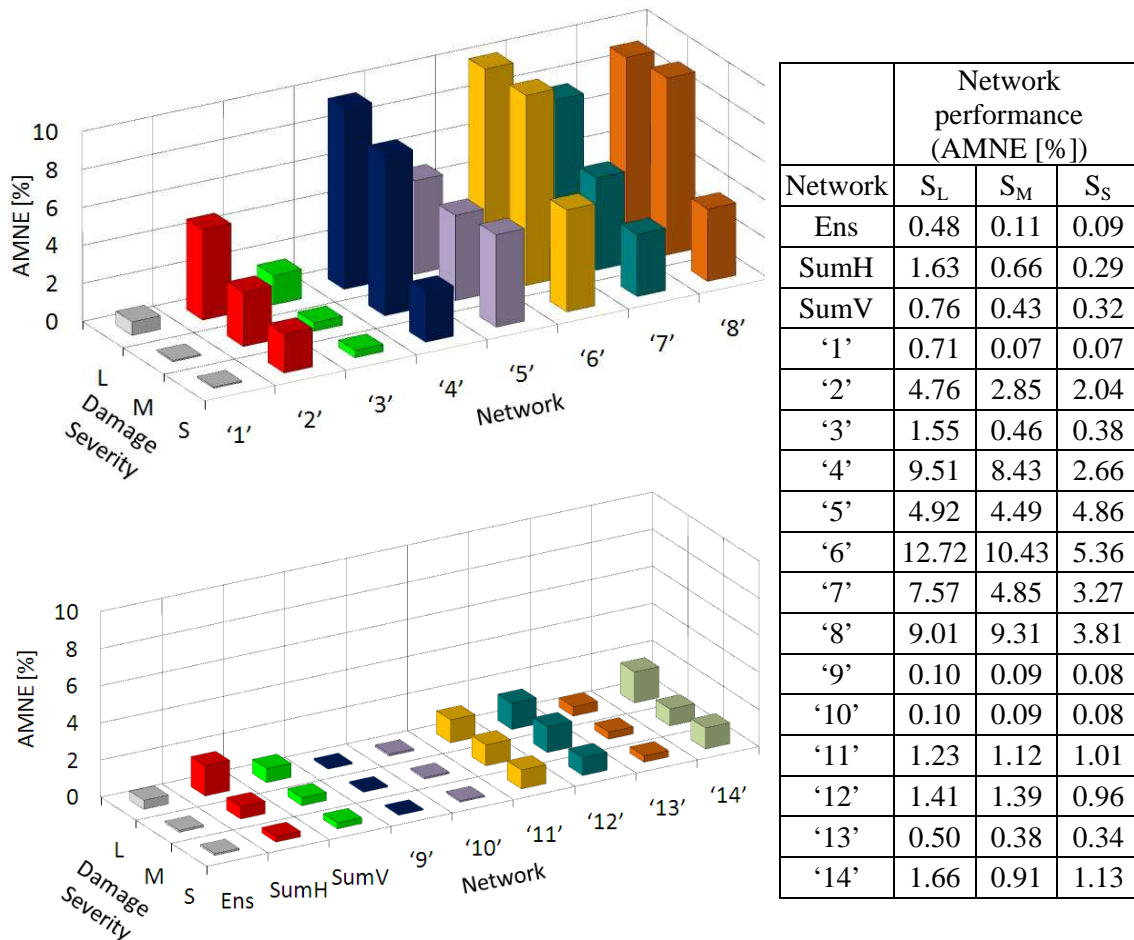


Figure 8.3 Neural network testing set performance (in AMNE) subdivided by damage severities trained with data from noise-polluted numerical simulations to locate section reduction damage.

From the outcomes of the damage localisation networks, it is observed that among the networks trained with horizontal data (networks of locations '1' to '8'), the networks of locations '1' and '3' perform the best, with testing set AMNE values of only 0.28% and 0.79%, respectively. These two networks correctly identify all damage locations up to a noise level of 2% and only a few light and medium cases are falsely located for noise intensities of 5% and 10% (the misidentified cases fall outside the acceptable bandwidth of $\pm 3.125\%$). Figure 8.4 (a) and (b) display graphs illustrating the testing set outcomes of the networks of locations '1' and '3' separated by noise pollution level and damage severity. (The respective outcome graphs from all networks are shown in Figure J.1 and Figure J.2 in APPENDIX J.) The network of location '2' performs reasonably well, with a testing set AMNE of 3.22%. Up to a noise pollution level of 2%, this network misallocates only two light damage cases of locations '1a' and '3a' (see Figure J.3 and

Figure J.5 in APPENDIX J). The good results of these networks (networks of locations ‘1’ to ‘3’) are due to their close proximity of the actual damage sites.

For the networks trained with data of locations ‘4’ to ‘8’, however, poor performance is obtained, with AMNE values up to 9.50%. The poor outcomes of the networks of locations ‘4’, ‘6’ and ‘8’ are again a result of the low sensitivity of FRF data to local modes of these points (see section 5.3.4). The networks of locations ‘5’ and ‘7’ give incorrect identifications due to the large distance to the damage sites. For these two networks, a clear relation between the localisation accuracy and the damage size as well as the noise-pollution level is observed (see Figure 8.4 (c)).

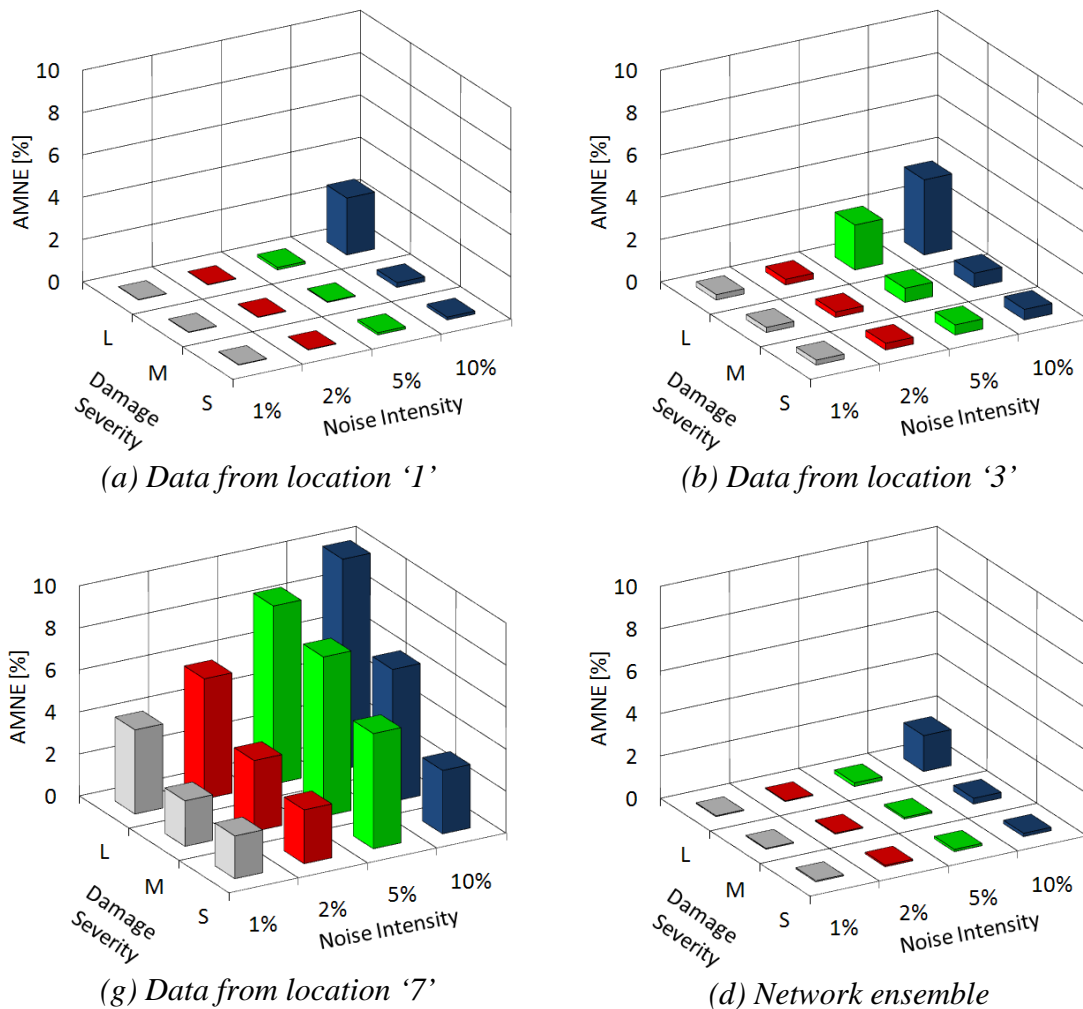


Figure 8.4 Comparison of testing set outcomes of networks trained with PCA-compressed residual FRFs to identify damage locations of noise-polluted numerical beams subdivided by damage severity and noise pollution level.

For the networks trained with vertical data from the crossbeams (networks of locations '9' to '14'), good damage localisation outcomes are obtained. The networks of locations '10' and '13' give correct locations for all except one light damage case (AMNE is 0.09% and 0.41%, respectively).

The network trained with data from horizontal summation FRFs gives correct localisations for damage cases polluted with a noise level of up to 2%, and only one light damage case is misidentified with 5% noise pollution. The SumV network correctly locates all cases up to 5% noise pollution. The network ensemble provides the best network outcomes with precise damage localisations up to 5% noise pollution level (AMNE is 0.23%). For a noise level of 10%, only two light damage cases of locations '1a' and '3a' are misidentified.

It is noted that for damage localisation of the section reduction scenarios, the individual networks are trained with the conjugate gradient descent function, while the network ensemble is trained with the online backpropagation function. In comparison with the categorisation of boundary or added mass scenarios (using the quick propagation and the conjugate gradient descent function), for damage localisation a much larger number of iterations is needed to obtain the best network convergence.

8.3.3.1 Quantification of Section Reduction Damage

The specifications and performance of the networks trained to estimate the severity of damage cases due to section reduction are listed in Table 8.11. The network performance are again given in AMNE. Illustrations of the testing set outcomes separated by damage severities are shown in Figure 8.5. (Detailed results of all testing set results are presented in Figure J.13 to Figure J.20 in APPENDIX J).

Table 8.11 Neural network specifications and performance (in AMNE) trained with data from the numerical two-storey framed structure of different cross-section reductions to identify damage severities.

Net-work	Network design	Convergence algorithm	Iteration	Training performance (AMNE [%])	Validation performance (AMNE [%])	Testing performance (AMNE [%])
'1'	10-8-6-4-2-1	Cgd	968	0.02	0.14	0.11
'2'	10-8-6-4-2-1	Cgd	826	1.17	1.21	1.20
'3'	10-8-6-4-2-1	Cgd	973	0.11	0.37	0.50
'4'	10-8-6-4-2-1	Cgd	819	2.38	2.86	2.90
'5'	10-8-6-4-2-1	Cgd	946	0.74	1.12	1.17
'6'	10-8-6-4-2-1	Cgd	759	3.57	4.49	4.45
'7'	10-8-6-4-2-1	Cgd	859	1.21	1.63	1.72
'8'	10-8-6-4-2-1	Cgd	947	2.11	2.88	2.80
'9'	10-8-6-4-2-1	Cgd	812	1.18	1.48	1.39
'10'	10-8-6-4-2-1	Cgd	943	1.24	1.23	1.28
'11'	10-8-6-4-2-1	Cgd	782	2.16	2.53	2.73
'12'	10-8-6-4-2-1	Cgd	839	2.06	2.61	2.63
'13'	10-8-6-4-2-1	Cgd	986	0.36	0.37	0.36
'14'	10-8-6-4-2-1	Cgd	824	2.11	2.35	2.36
SumH	10-8-6-4-2-1	Cgd	953	0.41	0.53	0.56
SumV	10-8-6-4-2-1	Cgd	935	0.59	1.02	0.93
Ens	14-10-8-6-4-2-1	Obp	5000	0.01	0.09	0.04

Note: Cgd = Conjugate gradient descent function

Obp = Online backpropagation function

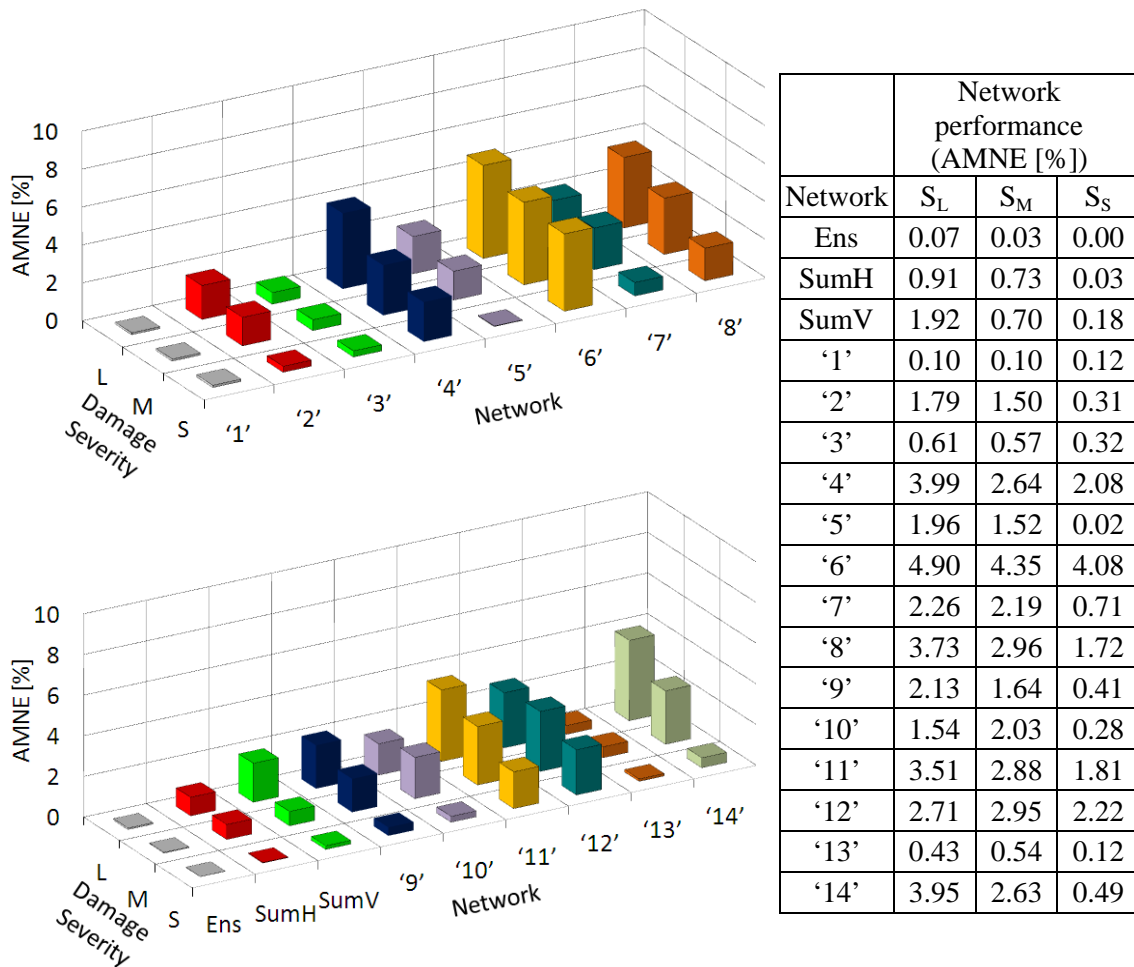


Figure 8.5 Neural network testing set performance (in AMNE) subdivided by damage severities trained with data from noise-polluted numerical simulations to estimate severities of section reduction damage.

For damage quantification, the individual networks trained with data of locations '1' and '3' give the best outcomes, with AMNE values of only 0.11% and 0.46%, respectively. These results are very similar to the localisation outcomes of the section reduction cases. For these two networks, all testing cases up to a noise pollution level of 2% are quantified correctly. As an example, the testing set results of the network of location '3', separated by noise pollution level, are illustrated in Figure 8.6 (b). (The respective graphs of network results from all trained networks are displayed in Figure J.11 and Figure J.12 in APPENDIX J.) The network of location '2' also performs well, with an AMNE value of 1.20%. Here, all severe damage cases are identified correctly for all noise pollution levels (see Figure 8.6 (a)). Reasonably good outcomes are also obtained from the networks of locations '5' and '7'. The worst damage quantifications are given by the networks trained with data of locations '4', '6' and '8'. Again, the low

sensitivity of FRF data to local modes is the reason for the poor performance of these networks.

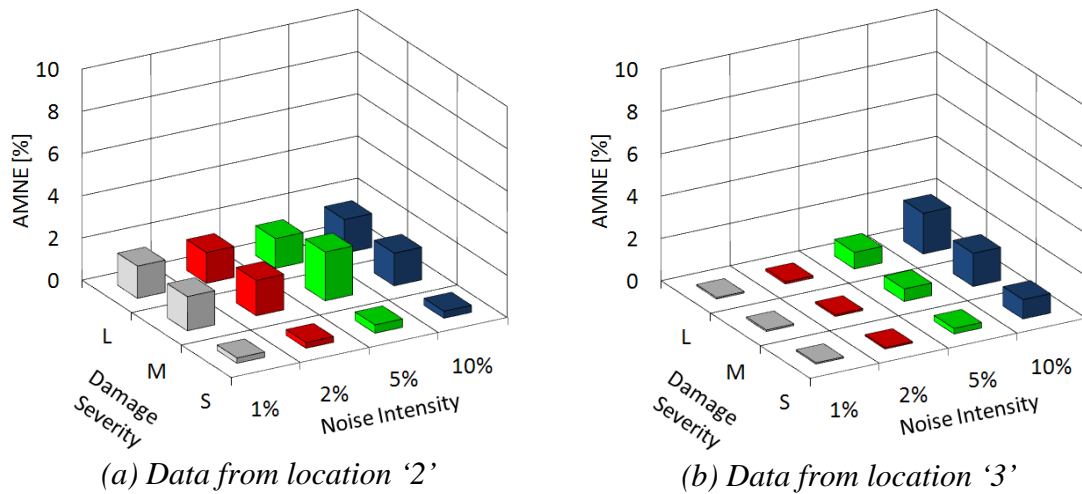


Figure 8.6 Comparison of testing set outcomes of networks trained with PCA-compressed residual FRFs to identify damage locations of noise-polluted numerical beams subdivided by damage severity and noise pollution level.

For the networks trained with data derived from vertical accelerations (networks of locations '9' to '14'), reasonably good quantification outcomes are obtained. At up to 2% noise pollution, almost all damage cases are quantified correctly.

The damage quantification results of the networks trained with horizontal and vertical summation FRFs are good, with testing set AMNE values of 0.56% and 0.93%, respectively. Also, these two networks predict the severity of damage correctly up to 2% noise pollution. With an AMNE of 0.04%, the network ensemble gives the best quantification outcomes among all networks. For all noise pollution levels, the network ensemble precisely quantifies all damage cases except one case where there is light severity with 10% noise pollution. These results stress again the superiority of the network ensemble, which gives results that are better than the outcomes of any of the individual networks.

It is further noted that for section reduction damage, the results for damage quantification are better than the results for damage localisation. Similar outcomes were obtained for the FRF-based damage identification of the beam structure, which gave many incorrect results for damage localisation of extra-light cases, while the severity estimations were precise for all damage cases (see section 7.4.1).

8.4 DAMAGE IDENTIFICATION RESULTS USING EXPERIMENTAL DATA FROM THE LABORATORY TWO-STOREY FRAMED STRUCTURE

8.4.1 Boundary Condition and Added Mass Identification

For the boundary condition and added mass predictions of the laboratory two-storey framed structure, the neural networks produce excellent outcomes. All boundary damage and all added mass cases are correctly categorised by all networks. The network specifications and performance are listed in Table 8.12 and Table 8.13. It is noted that again only a few dozen iterations are necessary to reach good network convergence using the quick propagation algorithm for the individual networks and the conjugate gradient descent function for the network ensembles, which is similar to the boundary condition and added mass identifications of the numerical structure.

Table 8.12 Neural network specifications and performance (in MCCR) trained with data from the laboratory two-storey framed structure of different boundary condition changes.

Net-work	Network design	Convergence algorithm	Iteration	Training performance (MCCR [%])	Validation performance (MCCR [%])	Testing performance (MCCR [%])
'1'	10-16-14-12-10	Qp	26	100	100	100
'2'	10-16-14-12-10	Qp	28	100	100	100
'3'	10-16-14-12-10	Qp	19	100	100	100
'4'	10-16-14-12-10	Qp	35	100	100	100
'5'	10-16-14-12-10	Qp	28	100	100	100
'6'	10-16-14-12-10	Qp	35	100	100	100
'7'	10-16-14-12-10	Qp	27	100	100	100
'8'	10-16-14-12-10	Qp	45	100	100	100
'9'	10-16-14-12-10	Qp	32	100	100	100
'10'	10-16-14-12-10	Qp	28	100	100	100
'11'	10-16-14-12-10	Qp	29	100	100	100
'12'	10-16-14-12-10	Qp	31	100	100	100
'13'	10-16-14-12-10	Qp	25	100	100	100
'14'	10-16-14-12-10	Qp	32	100	100	100
SumH	10-16-14-12-10	Qp	35	100	100	100
SumV	10-16-14-12-10	Qp	26	100	100	100
Ens	14-13-12-11-10	Cgd	32	100	100	100

Note: Qp = Quick propagation function

Cgd = Conjugate gradient descent function

Table 8.13 Neural network specifications and performance (in MCCR) trained with data from the laboratory two-storey framed structure of different added mass changes.

Net-work	Network design	Convergence algorithm	Iteration	Training performance (MCCR [%])	Validation performance (MCCR [%])	Testing performance (MCCR [%])
'1'	10-9-8-7-6	Qp	72	100	100	100
'2'	10-9-8-7-6	Qp	69	100	100	100
'3'	10-9-8-7-6	Qp	75	100	100	100
'4'	10-9-8-7-6	Qp	68	100	100	100
'5'	10-9-8-7-6	Qp	81	100	100	100
'6'	10-9-8-7-6	Qp	75	100	100	100
'7'	10-9-8-7-6	Qp	83	100	100	100
'8'	10-9-8-7-6	Qp	73	100	100	100
'9'	10-9-8-7-6	Qp	82	100	100	100
'10'	10-9-8-7-6	Qp	78	100	100	100
'11'	10-9-8-7-6	Qp	84	100	100	100
'12'	10-9-8-7-6	Qp	75	100	100	100
'13'	10-9-8-7-6	Qp	79	100	100	100
'14'	10-9-8-7-6	Qp	85	100	100	100
SumH	10-9-8-7-6	Qp	74	100	100	100
SumV	10-9-8-7-6	Qp	84	100	100	100
Ens	14-12-10-8-6	Cgd	28	100	100	100

Note: Qp = Quick propagation function

Cgd = Conjugate gradient descent function

8.4.2 Section Reduction Damage Identification

For the damage cases due to section reduction, networks are again trained to locate and quantify the damage. For the laboratory two-storey framed structure, only two damage sites, locations '1' and '3' (equivalent to locations '1a' and '3a' of the numerical cases), are considered. At each of the two locations, damage cases of severity levels light, medium and severe are investigated.

Localisation of Section Reduction Damage

The specifications and performance of the networks trained to locate laboratory damage are listed in Table 8.14. Two accompanying graphs and a table present the testing set outcomes separated by damage severity (see Figure 8.7). (Detailed results of the testing set of all damage cases are shown in Figure J.21 and Figure J.22 in APPENDIX J.) From the table and the figures, it is seen that the locations of all damage cases are correctly identified by all networks. As the performance of the networks had already reached a very low error (very good performance) after a few hundred iterations, the

training was manually stopped after 5000 iterations. The network ensemble, which reached an AMNE of 0.01% after 5000 iterations, gives the best network outcomes.

Table 8.14 Neural network specifications and performance (in AMNE) trained with data from the laboratory two-storey framed structure of different section reduction damage cases to identify damage locations.

Net-work	Network design	Convergence algorithm	Iteration	Training performance (AMNE [%])	Validation performance (AMNE [%])	Testing performance (AMNE [%])
'1'	10-8-6-4-2-1	Obp	5000	0.03	0.03	0.03
'2'	10-8-6-4-2-1	Obp	5000	0.04	0.04	0.04
'3'	10-8-6-4-2-1	Obp	5000	0.04	0.04	0.04
'4'	10-8-6-4-2-1	Obp	5000	0.02	0.02	0.02
'5'	10-8-6-4-2-1	Obp	5000	0.06	0.06	0.06
'6'	10-8-6-4-2-1	Obp	5000	0.05	0.05	0.05
'7'	10-8-6-4-2-1	Obp	5000	0.05	0.05	0.05
'8'	10-8-6-4-2-1	Obp	5000	0.05	0.05	0.05
'9'	10-8-6-4-2-1	Obp	5000	0.05	0.05	0.05
'10'	10-8-6-4-2-1	Obp	5000	0.05	0.05	0.05
'11'	10-8-6-4-2-1	Obp	5000	0.04	0.04	0.04
'12'	10-8-6-4-2-1	Obp	5000	0.05	0.05	0.05
'13'	10-8-6-4-2-1	Obp	5000	0.06	0.06	0.12
'14'	10-8-6-4-2-1	Obp	5000	0.06	0.06	0.06
SumH	10-8-6-4-2-1	Obp	5000	0.03	0.03	0.03
SumV	10-8-6-4-2-1	Obp	5000	0.05	0.05	0.05
Ens	14-10-8-6-4-2-1	Obp	5000	0.01	0.01	0.01

Note: Obp = Online backpropagation function

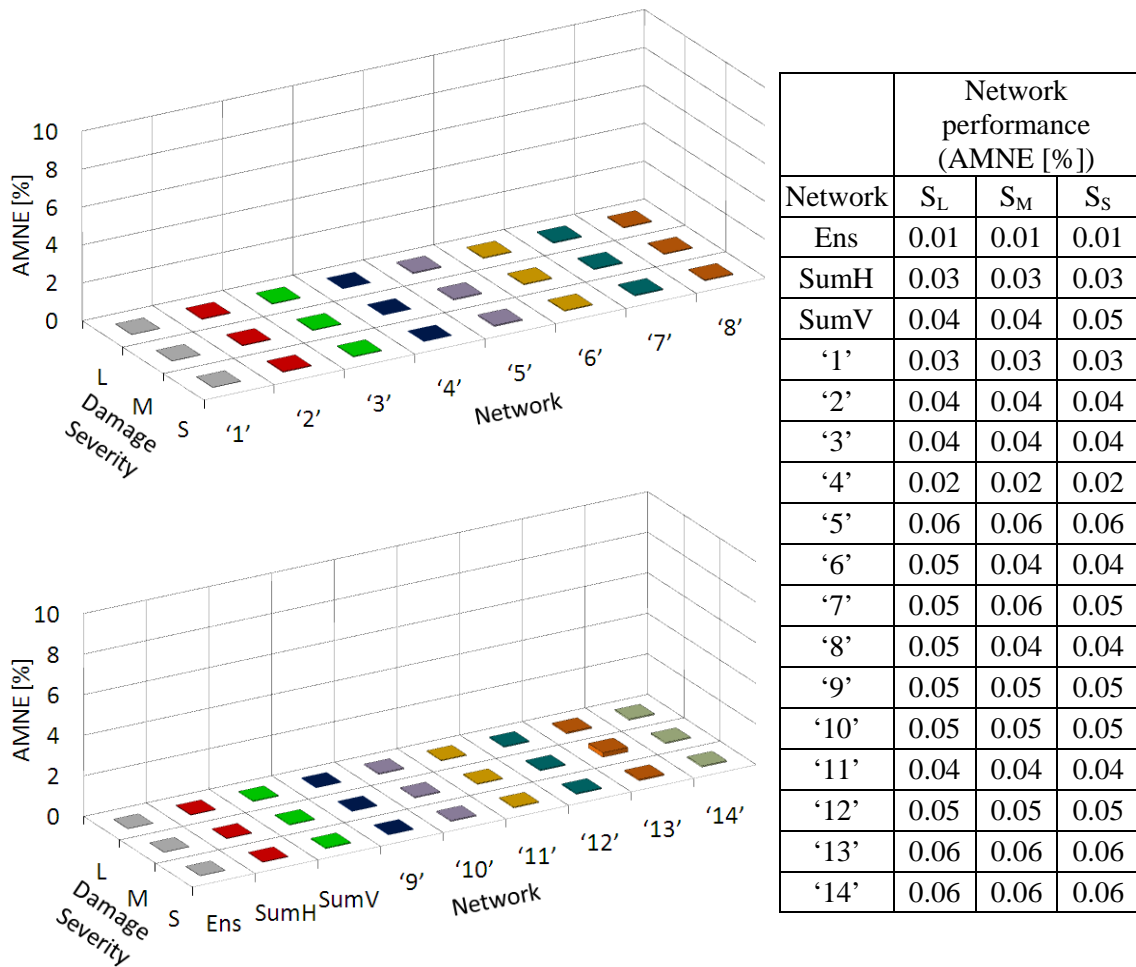


Figure 8.7 Neural network testing set performance (in AMNE) trained with data from the laboratory two-storey framed structure subdivided by damage severities to identify locations of section reduction damage.

Quantification of Section Reduction Damage

For the damage severity predictions of the laboratory two-storey framed structure, network specifications and performance are given in Table 8.15. The results of the testing set are illustrated in Figure 8.8. (In addition, Figure J.23 and Figure J.24 of APPENDIX J present the detailed network outcomes of all section reduction cases of the testing set.) From the network results, it is observed that, as with the quantification outcomes of the numerical damage cases, the networks of locations '1' and '3', with AMNE values of 0.02%, perform the best among the networks trained with horizontal acceleration data. This result is expected as locations '1' and '3' are the sites of the inflicted damage. The networks of locations '5' and '7' also give correct severity predictions for all damage cases, with AMNE values of 0.26% and 0.54%.

Table 8.15 Neural network specifications and performance (in AMNE) trained with data from the laboratory two-storey framed structure of different section reduction damage cases to identify damage severities.

Net-work	Network design	Convergence algorithm	Iteration	Training performance (AMNE [%])	Validation performance (AMNE [%])	Testing performance (AMNE [%])
'1'	10-10-8-6-4-2-1	Obp	5000	0.01	0.31	0.02
'2'	10-10-8-6-4-2-1	Obp	1652	1.57	3.11	3.50
'3'	10-10-8-6-4-2-1	Obp	5000	0.01	0.02	0.02
'4'	10-10-8-6-4-2-1	Obp	2245	3.89	3.58	4.67
'5'	10-10-8-6-4-2-1	Obp	5000	0.01	0.15	0.26
'6'	10-10-8-6-4-2-1	Obp	1256	4.46	3.96	3.74
'7'	10-10-8-6-4-2-1	Obp	1526	0.01	1.27	0.54
'8'	10-10-8-6-4-2-1	Obp	993	5.04	4.91	5.19
'9'	10-10-8-6-4-2-1	Obp	5000	0.03	0.08	0.03
'10'	10-10-8-6-4-2-1	Obp	5000	0.02	0.08	0.10
'11'	10-10-8-6-4-2-1	Obp	5000	0.01	0.02	0.02
'12'	10-10-8-6-4-2-1	Obp	5000	0.01	0.01	0.02
'13'	10-10-8-6-4-2-1	Obp	1269	0.26	0.91	1.12
'14'	10-10-8-6-4-2-1	Obp	4583	0.16	0.54	0.57
SumH	10-10-8-6-4-2-1	Obp	5000	0.01	0.11	0.09
SumV	10-10-8-6-4-2-1	Obp	5000	0.01	0.04	0.03
Ens	14-10-8-6-4-2-1	Obp	5000	0.01	0.03	0.01

Note: Obp = Online backpropagation function

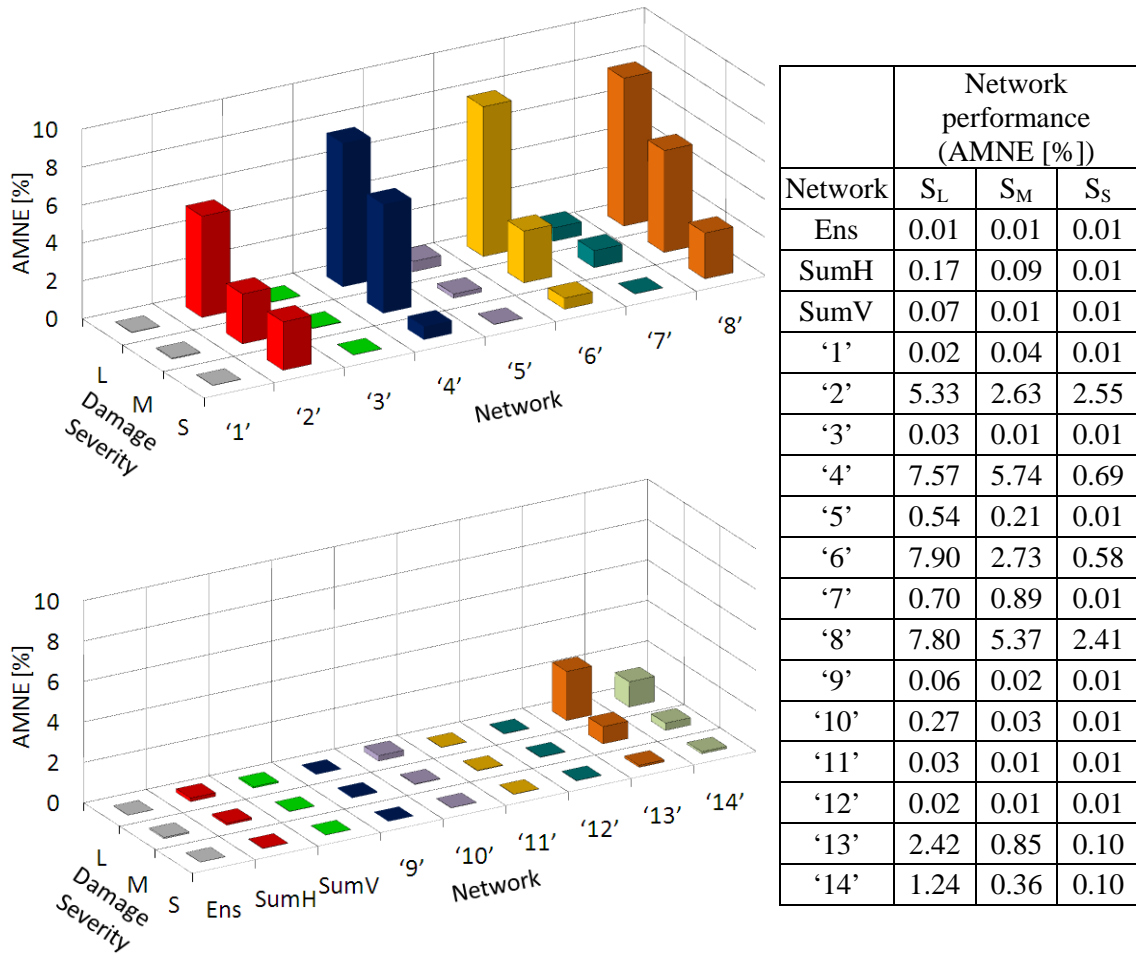


Figure 8.8 Neural network testing set performance (in AMNE) trained with data from the laboratory two-storey framed structure subdivided by damage severities to identify severities of section reduction damage.

For the networks of locations '2', '4', '6' and '8', rather poor performance are obtained with testing set AMNE values ranging from 3.50% to 5.19%. For these networks, all severe damage cases are correctly quantified (the predictions lie inside the acceptable error band of $\pm 6.25\%$); however, for medium and light cases many false estimations are obtained. The reason for the poor performance of these networks is again the low sensitivity of FRF data to local modes of these locations.

For the networks trained with vertical acceleration data, good results are obtained. The networks of locations '9' to '12' correctly quantify all testing damage cases, with AMNE values from 0.02% to 0.10%. For the networks trained with data of locations '13' and '14', some light and medium cases are falsely identified.

Correct severity estimations of all damage cases are obtained from the SumH and SumV networks. The best quantification outcomes, however, are obtained by the network ensemble, which gives AMNE values of 0.01% for all light, medium and severe cases of the testing set (see the table next to Figure 8.8). These excellent results of the network ensemble demonstrate again the efficiency and importance of the ensemble approach, which filters poor results from bad performing networks and gives better outcomes than any of the individual networks.

8.5 SUMMARY

This chapter presented results of the proposed FRF-based damage identification method applied to the numerical and the experimental two-storey framed structure. A hierarchy of ANNs were trained with PCs of residual FRFs to identify three types of structural change (i.e. boundary damage, added mass and section reduction damage). For boundary condition and added mass identification, the networks categorised damage/added mass changes in a winner-takes-all fashion. For identification of section reduction damage, the networks gave numerical outputs determining the locations and severities of damage. Final damage estimations were obtained from the predictions of network ensembles that fused the outcomes of individually trained networks for better damage identification.

From the results of the numerical two-storey framed structure, the following was observed:

- For boundary condition and added mass identification, the individual networks trained with data derived from horizontal accelerations of locations '1', '3', '5' and '7' and vertical accelerations of locations '9' to 14' gave correct classifications for all damage/added mass cases. The networks of locations '2', '4', '6' and '8', however, wrongly identified some boundary condition cases and many (about 50%) added mass cases. The reason for the poor performance of these networks is that at locations '2', '4', '6' and '8' FRF data have low sensitivity to local modes. This greatly diminishes the damage fingerprints in FRF data of these locations and results in bad identification outcomes. While the noise pollution level played an important role in the misclassification of boundary damage, for added mass identification, wrong predictions were obtained for all noise levels, indicating the low sensitivity of

global modes to added mass changes for these locations. Despite the poor performance of some networks, the network ensemble still produced precise predictions for all boundary damage and all added mass cases.

- For the location and severity identification of the section reduction cases, the networks trained with data from locations that were in close proximity to the actual damage sites, i.e. data of locations ‘1’ to ‘3’, gave the best localisation and quantification outcomes among the networks trained with horizontal data. Likewise, good outcomes were obtained from networks trained with data derived from vertical accelerations (i.e. from locations ‘9’ to ‘14’). Whereas the networks of locations ‘5’ and ‘7’ performed well in quantifying damage, for damage localisation many false predictions were obtained. Similar to the boundary damage and added mass cases, networks of locations ‘2’, ‘4’, ‘6’ and ‘8’ demonstrated poor performance. While the SumH and SumV networks gave reasonably good outcomes, the network ensembles gave excellent identification results, correctly locating and quantifying all damage cases except a few light cases of 10% noise pollution.

From the results of the laboratory two-storey framed structure, the following was noted:

- For boundary condition and added mass identification, all individual networks and the network ensembles precisely categorised all damage cases. Likewise, for localisation of the section reduction damage cases, all networks correctly identified all damage cases. For the severity estimation, only the networks of locations ‘1’, ‘3’, ‘5’ and ‘9’ to ‘12’ gave accurate predictions. The networks trained with data of locations ‘2’, ‘4’, ‘6’ and ‘8’, as well as ‘13’ and ‘14’, falsely predicted the severities of many light and medium damage cases. The individual SumH and SumV networks gave correct quantifications of all damage cases. The network ensemble was again the network with the best results, giving precise severity identifications for all damage cases.

The proposed FRF-based damage identification method proved to be accurate and robust in the identification of different types of structural change inflicted to a more complicated structure, i.e. the two-storey framed structure. For the numerical as well as the laboratory structure, precise identifications were obtained for almost all cases of boundary damage, added mass changes and section reduction damage. The proposed

neural network ensemble approach was found to be highly efficient in filtering bad estimation outcomes from poorly performing networks and giving identification results that were generally better than the outcomes of any of the individual networks. In addition, the network ensemble proved to be more accurate than the networks trained with data obtained from summation FRFs, which highlights the superiority of the network ensemble technique against the approach of simply summing FRF data from different measurement locations. The study further showed that it is crucial to capture FRF data from different locations of the structure, as at some locations, i.e. locations '2', '4', '6' and '8', FRF data turned out to have a low sensitivity to local modes, resulting in error-prone damage identifications for networks trained with data of these locations. For the two-storey framed structure, ideal sensor placements were found to be the midpoints of the column halves (measuring horizontal acceleration) and any location on the crossbeams (measuring vertical acceleration); locations on the columns that are at the same height as the crossbeams are to be avoided.

CHAPTER 9

CONCLUSIONS AND RECOMMENDATIONS

9.1 SUMMARY AND CONCLUSIONS

This thesis dealt with artificial neural networks (ANNs) in vibration-based damage identification and their application in civil structures. Two novel damage identification schemes were proposed. The first scheme is a modal-parameter-based method and the second a frequency-response-function (FRF)-based method. Both methods use neural network techniques and principal component analysis (PCA) for damage feature extraction and noise reduction. To verify the proposed damage identification procedures, numerical and experimental studies were undertaken on two types of structures: a simple beam structure and a two-storey framed structure. Field testing conditions were considered by incorporating measurement noise and a limited number of sensors. To investigate the robustness of the methods to noise, noise sensitivity studies were conducted on numerical models of both structures.

Proposed Method 1: Damage Identification Based on Damage Index Method

The literature review has shown that the damage index (DI) method is an effective and promising technique for locating structural damage. However, despite some reports on successful applications of the algorithm, the method has been found to suffer some serious drawbacks. These problems are mainly associated either with the DI method itself (such as node point singularities of mode shapes) or with susceptibilities of the algorithm to uncertainties such as measurement noise interferences, experimental modal analysis errors or environmental effects. Consequently, these drawbacks produce faulty damage identification, jeopardising the reliability and effectiveness of the method and hindering its application in real life situations. The successes as well as the challenges of the DI method sparked an interest in using and further developing this technique for improved damage detection.

The first proposed damage identification scheme in this thesis was, therefore, based on the DI method. The ANNs, with their capability to recognise patterns and to reduce

uncertainties, formed the core of this new method. Further, PCA techniques were implemented to extract damage features from DI values, to filter noise and to improve neural network training efficiency. To consider the effects posed by a limited number of sensors, cubic spline interpolation techniques were employed to reconstruct coarse mode shape vectors and enhance embedded damage features in measured data. Instead of using a single neural network for damage identification, an approach based on network ensembles was proposed. In the neural network ensemble, first, principal components (PCs) of DI values were separated by individual mode shapes and analysed in individual neural networks; then, the outcomes of the individual networks were fused in a network ensemble to give a final conclusive damage evaluation. Such multi-stage network training takes advantage of unique features of PCA-compressed DI values derived from different vibrational modes. By fusing the outcomes of the individual networks in the network ensemble, the developed procedure further considers different sensitivities of individual mode shapes to uncertainties and damage characteristics.

The following steps summarise the first proposed damage identification scheme based on the DI method:

1. Mode shapes are extracted from data obtained from either modal testing or transient analysis for finite element modelling by means of experimental modal analysis.
2. Obtained coarse mode shapes are reconstructed and refined by utilising cubic spline interpolation techniques.
3. The DI values, Z_j and α_j , are calculated from change of modal strain energy from reconstructed mode shapes of the structure before and after damage.
4. The DI values are transformed into the principal component space by employing PCA techniques.
5. The most dominant PCs of mode-separated DI values are selected as input to individual neural networks for identification of damage characteristics.
6. The outcomes of the individual networks are fused in a network ensemble to give final predictions on locations and severities of damage.

For verification, the proposed DI-based ANN method was applied to numerical and experimental models of the beam structure to identify locations and severities of notch type damage. From the identification results, the following observations were made and conclusions drawn.

- In noise-free numerical simulations, the network ensembles successfully identified both locations and severities of all damage cases. The success demonstrated that the proposed DI-based damage detection scheme is capable of successfully overcoming inherent problems of the DI method including issues with node point singularities and limited number of sensors. Whereas, for damage localisation, all individual networks precisely identified all damage cases, for damage severity prediction, some individual networks gave large errors. The individual networks of modes 2, 4 and 6 exhibited an insensitivity of damage indicator α_j at node points, which resulted in erroneous damage detection. Through the proposed network ensemble technique, the faulty results of these problematic individual networks were filtered and final precise severity predictions obtained.
- For noise-polluted numerical data, damage detection results from the neural networks were significantly influenced by noise and experimental modal analysis errors. Inherent problems in mode shapes, such as small curvature values of low modes or mode shape node point singularities, amplified noise sensitivity and resulted in large errors of individual networks for damage detection. With the network ensemble, however, precise severity estimations can be achieved for all damage cases. For damage localisation, small errors were obtained from the network ensemble for extra-light and light damage cases (with absolute mean of normalised error (AMNE) values of 5.53% and 2.31%). A clear correlation between the level of noise pollution, the damage size and the accuracy of the damage identification was observed.
- For the laboratory experiments, the individual networks of higher modes (modes 5, 6 and 7) produced larger identification errors due to difficulties in the extraction of the higher mode shapes via experimental modal analysis. For damage localisation, the individual networks of lower modes and the network ensemble correctly identified all damage cases. These unexpectedly good results were, however, partially owing to better data patterns obtained from laboratory testing due to individual setting of each beam specimen including its boundary conditions. For severity estimations, the obtained results were similar to the severity results of the noise-polluted numerical data, displaying large errors for individual networks trained with problematic mode shapes. The network ensemble, however, gave correct severity predictions for all

light, medium and severe damage cases; for extra-light cases small errors of 5.56% AMNE were obtained.

The proposed DI-based ANN damage identification scheme has successfully improved the original DI method. The results showed that in combining ANNs and PCA, problems of the original DI method could effectively be overcome. Even though uncertainties from sources such as measurement noise and experimental modal analysis resulted in erroneous outcomes for some individual networks, the proposed hierarchical network ensemble training compensates for outcomes of those networks and offers satisfactory damage identification outcomes. Some final false estimations only occur for data of small size damage with high noise pollution level.

Proposed Method 2: Damage Identification Based on Frequency Response Functions

The second proposed method for damage identification, in this thesis, was based on measured FRF data. FRFs are directly measured data and one of the easiest to obtain in real-time as they require only a small number of sensors and very little human involvement (Fang & Tang 2005). They provide an abundance of information on the structure's dynamic behaviour. Compared to modal parameter methods, FRF-based damage detection techniques do not require extensive post-data analysis such as experimental modal analysis, which involves intensive labour and is very susceptible to human error. These characteristics make FRF data particularly attractive in the field of dynamic-based damage detection.

In the proposed method, residual FRFs, which are differences in FRF data between the intact and the damaged structure, were utilised as indicators to identify damage. Using residual FRFs instead of direct FRF measurements enhances damage fingerprints and improves detection outcomes. Damage identification based on residual FRFs can be considered as a type of pattern recognition problem as it looks into discrepancy between two or more signal categories, e.g. before and after a structure is damaged, or differences in damage levels or locations. Therefore, in the proposed procedure, ANNs with their powerful pattern recognition and classification ability were used to extract damage information from residual FRFs and to provide estimations of damage characteristics such as damage type, locations or severities. To overcome the obstacle of

the large size of FRF data, the implementation of PCA techniques was suggested. Besides data reduction, PCA also offers the benefit of noise reduction and damage feature extraction, which further assists to reduce uncertainties from sources such as measurement noise and environmental fluctuations. Due to the different characteristics of FRF data from different measurement locations, neural network training based on network ensemble techniques was proposed. By first training individual neural networks with PCA-compressed residual FRFs separated by sensor locations and then fusing the outcomes of the individual networks in a network ensemble, advantage is taken of individual characteristics from different sensor signals, and training efficiency is improved.

The following steps summarise the second proposed damage identification scheme based on FRF data:

1. FRFs are obtained from structures by means of modal testing or transient analysis for finite element modelling.
2. Residual FRFs are determined by subtracting FRF values of a structure before and after damage.
3. Residual FRFs are projected onto their principal component space by employing PCA techniques.
4. Individual neural networks are trained and tested with the most dominant PCs of the residual FRFs, separated by sensor location for identification of damage.
5. A network ensemble fuses the outcomes of the individual networks and gives final predictions on damage characteristics such as damage type, location or severity.

To investigate the performance of the proposed FRF-based damage identification method, it was applied to the beam structure as well as the two-storey framed structure. For both structures, numerical and laboratory models were used to verify the method. First, the proposed technique was thoroughly studied and refined on the beam structure, and then, the refined method was applied to the two-storey framed structure for verification. From the results, the following observations were made and conclusions drawn.

Results of the beam structure:

- For numerical simulations with noise-polluted data, all individual networks and the network ensemble successfully identified the severities of all damage cases. For damage localisation, all networks (individual networks and network ensemble) also precisely estimated all light, medium and severe damage cases. Only extra-light damage cases were falsely located by the networks with an AMNE value of 3.73% for the network ensemble. These exceptionally good outcomes clearly demonstrated the noise filtering capabilities of PCA and neural networks, which produce precise predictions even for data containing up to 10% noise pollution.
- For laboratory data, the locations and severities of all damage cases were precisely identified by all individual networks as well as the network ensemble. The successful localisations of extra-light damage cases for laboratory data was likely due to better FRF patterns obtained from the testing of different laboratory beams for different damage locations.

Results of the two-storey framed structure:

- For the classification of boundary types of damage and mass change scenarios of the numerical models, most individual networks produced precise identifications for all investigated cases. Some problems were encountered with individual networks that analysed data derived from horizontal accelerations from locations on the columns that are at the same height as the crossbeams (locations '2', '4', '6' and '8'). The reason for the poor performance of these networks is that these measurement locations are not sensitive to the captured vibrational modes resulting in large degrading of damage fingerprints in FRF data at these locations. Despite the poor performance of these individual networks, the network ensemble is able to correctly identify all numerical boundary damage and mass change scenarios.
- For the location and severity identification of section reduction scenarios of numerical models, good results were again obtained for most individual networks. Similar to the boundary damage and mass change cases, the networks of locations '2', '4', '6' and '8' had poor performance. While reasonably good outcomes were obtained from the individual networks of the horizontal and vertical summation FRFs, the network ensembles produced excellent identification results, correctly

locating and quantifying all damage cases except for a few light cases with 10% noise pollution.

- For the laboratory structure, the boundary damage and added mass scenarios were precisely categorised by all individual networks and the network ensembles. Likewise, for the localisation of the section reduction damage cases, all networks correctly identified all damage cases. For the severity estimation, problems were again encountered with individual networks of locations '2', '4', '6' and '8', which produced false damage identification for light and medium damage cases. The network ensembles delivered the best results, precisely identifying all experimental damage cases.

The proposed FRF-based damage identification scheme proved to be accurate and robust in the identification of damage in a simple and a more complicated structure. For numerical and laboratory structures, precise identifications were obtained for almost all cases of boundary damage, mass changes and section reduction cases. The proposed hierarchical network training in a network ensemble was found to be highly efficient in filtering undesired estimation outcomes from poorly performing networks and giving identification results that were generally better than the outcomes of any of the individual networks. In addition, the network ensemble proved to be more accurate than the networks trained with data obtained from summation FRFs, which highlights the superiority of the network ensemble technique against the approach of simply summing FRF data from different measurement locations. The study further showed that it is crucial to capture FRF data from different locations of the structure, as at some locations, FRF data turned out to have low sensitivity to local vibrational modes, resulting in error-prone damage identifications for networks trained with data of these locations.

From the findings, it can be concluded that the FRF-based damage identification scheme is superior to the DI-based identification procedure. For the FRF-based method, errors from experimental modal analysis are avoided, influences of individual characteristics from different measurement sources are reduced, and noise influences are successfully filtered out.

9.2 CONTRIBUTION TO KNOWLEDGE

In this thesis, the main contributions to knowledge are listed as follows:

1. A novel modal-based ANN damage identification scheme was developed, capable of overcoming limitations of the original DI method. The proposed damage detection procedure combines the original DI method with ANN, PCA and data interpolation techniques and thereby produces improved damage identification results.

This was achieved by the following:

- A thorough study on the characteristics of DI values Z_j and α_j and their effects on damage, measurement noise and number of measurement locations led to understanding of the performance of individual damage indices and identified the challenges of the DI method. This study provided the basis for the newly proposed DI-based ANN damage identification scheme.
- By introducing the cubic spline interpolation technique and reconstructing measured coarse mode shapes, embedded damage features in mode shape vectors were enhanced resulting in improved DI values. It was demonstrated on mode shape data of a beam structure that this enhancement of damage indices can regain crucial information and can thereby prevent an oversight of damage cases.
- By projecting the damage indices onto their principal component space and only using the most dominant PCs as input features for neural networks, uncertainties from sources such as measurement noise, experimental modal analysis and limited number of sensors, were partially reduced and network training was optimised.
- By separating the DI values of the DI method, based on their mode shape origin and analysing them in individual networks, advantage was taken of unique characteristics of damage indices for each mode. It was shown that with this procedure, damage indices (such as those influenced by node point insensitivities or small curvature values of low mode shapes) were separated from indices with clear damage features and thereby providing optimal input data for subsequent network ensemble training.
- With the use of ANN's pattern recognition capability, faulty damage indices can be better managed. Due to the recurring nature of these faulty patterns, ANNs were able to identify the faulty damage indices. For noise-free mode shape data of numerical beam simulations, it was shown that the individual networks from

problematic modes precisely identified locations and severities of all investigated damage cases.

- By fusing the outcomes of the individual networks with a network ensemble, optimal results can be obtained in terms of damage identifications. It was found that the networks ensemble was highly efficient in filtering error-prone outcomes from problematic individual networks and produced results that were in general better or at least as good as the outcomes of the best performing individual network.
2. A second ANN damage identification scheme was developed based on damage fingerprints in FRF data. This proposed method, which combines FRF measurements with ANN and PCA techniques, is capable of producing accurate and robust damage identification results even under conditions of high noise intensity.

This was achieved by the following:

- An extensive study on the characteristics of FRF data from different measurement locations as well as FRF summation functions led to understanding the effects of damage from different locations and varying severities on individual FRF data. This understanding provided the basis for the proposed FRF-based damage identification scheme.
- Residual FRFs, rather than direct FRF measurements, were used as damage indices. By calculating residual FRFs, which are differences between FRF data from the damaged and the intact structure, hidden features related to damage in FRF data were revealed and excessive information was reduced.
- In order to reduce the large size of FRF data and to form suitable inputs for ANNs, PCA techniques were adopted. By projecting FRF data to obtain the most important PCs, the data's size was greatly reduced without major loss of information, and noise influences were significantly reduced. A study on the noise filtering capabilities of PCA showed that up to 10% noise intensity can be effectively removed from FRF data by PCA techniques.
- In addition to simply use FRF features from the FRF summation function as input patterns for ANNs, a number of individual networks were also created that utilised FRF features from individual FRFs as input data. With this approach, advantage was taken of individual characteristics from different measurement locations. Results from the two-storey framed structure showed that FRFs from

some measurement locations were less sensitive to damage and hence may produce false damage identifications.

- A network ensemble was again used to fuse the outcomes of the individual networks. It was found that the network ensemble results were superior to the outcomes produced by all individual networks, including the networks trained with summation FRFs.
3. The two proposed methods were verified on numerical and experimental models of two different structures, i.e. a simply supported beam structure and a two-storey framed structure.

This was achieved by the following:

- Finite element models were created for a beam structure and a two-storey framed structure. To consider real life testing conditions, issues such as limited number of measurement sensors and measurement noise with different intensities were incorporated in the numerical modelling.
- Different types of damage scenarios were simulated in the two numerical structures. Both proposed damage detection methods were applied to the numerically produced vibration response data to identify various damage.
- In an extensive experimental program, four steel beams and a two-storey framed structure were physically tested in the laboratory. Acquired data were processed by means of various post-processing procedures including experimental modal analysis and then were employed to identify the damage.

9.3 RECOMMENDATIONS AND FUTURE WORK

Based on the literature review and the research of this thesis, the following recommendations for future research work in the area of dynamic and neural-network-based damage identification are given.

1. As stated in many research publications, a crucial factor influencing dynamic-based damage identification is changing environmental conditions. Although the proposed methods, in this thesis, already demonstrated their efficiency in reducing uncertainties from sources such as measurement noise and experimental modal analysis, it is of great value to investigate the performance of the methods under fluctuating environmental conditions such as changing temperature or humidity.

2. It will be beneficial to further investigate the application of other types of ANNs (such as perceptron networks or Bayesian networks) or other types of artificial intelligence (such as genetic algorithms or fuzzy logic), in order to further improve damage identification results.
3. To broaden the range of applications, it is of interest to apply the proposed methods to different types of structures such as plate-like structures or space frame structures.
4. It will further be of interest to undertake a sensitivity study regarding the smallest size of damage that can reliably and accurately be detected by the two proposed methods.
5. It is also useful to investigate the performance of the proposed methods to structures of different materials such as timber or reinforced concrete structures. Thereby, the influence of inhomogeneous materials on the accuracy of the identification outcomes can be studied. It is also essential to apply the proposed methods to real field structures in order to evaluate their capabilities to cope with real life uncertainties.
6. There is a need to scrutinise the performance of the proposed methods in the case of multiple damage scenarios. There is further value in studying the performance of the methods in detecting damage that is positioned in-between trained damage cases.
7. To further reduce uncertainties and to enhance damage features, it is recommended to investigate the implementation of statistical methods in the proposed schemes.
8. To make this research work feasible for practical applications, it is crucial to investigate the feasibility of finite element model updating techniques to deliver numerical models that accurately model the dynamic characteristics (especially mode shapes and FRFs) of real structures. It is vital to have a precise numerical model available to be used for the generation of input pattern for neural network training.
9. It is of interest to explore the use of other vibration-based damage indicators such as damage fingerprints in time domain data for neural-network-based damage

detection. It is further recommended to investigate the use of a combination of different dynamic-based damage indicators in a neural-network-ensemble-based identification scheme.

10. To allow a comparison between the developed methods and other damage identification techniques, it is necessary to apply them to benchmark structures such as the ASCE four-story benchmark building, the UCF Benchmark Bridge Structure or the Guangzhou New TV Tower.

REFERENCES

- Abdul Rahman, A.G. 1999, *Notes of signal processing*, Mechanical Engineering Department, Faculty of Engineering, University of Malaya.
- Abdul Razak, H. & Choi, F.C. 2001, 'The effect of corrosion on the natural frequency and modal damping of reinforced concrete beams', *Engineering Structures*, vol. 23, no. 9, pp. 1126-1133.
- Abdul Razak, H., Teng, S.L., Ismail, Z. & Abdul Rahman, A.G. 2001, 'Crack detection in a simply supported RC beam using simplified Laplacian', *Proceedings of the 14th International Modal Analysis Conference*, vol. 2, Kissimmee, FL, US, pp. 1344-1350.
- Adams, R.D., Cawley, P., Pye, C.J. & Stone, B.J. 1978, 'A vibration technique for non-destructively assessing the integrity of structures', *Journal of Mechanical Engineering Science*, vol. 20, pp. 93-100.
- Agilent Technologies 2000, *The fundamentals of modal testing*, Agilent Technologies, Application Note 243-3.
- Allemang, R.J. 1999, *Experimental modal analysis*, Report Number UC-SDRL-RJA, University of Cincinnati, Cincinnati, OH, US.
- Allemang, R.J. & Brown, D.L. 1982, 'A correlation coefficient for modal vector analysis,' *Proceedings of the 1st International Modal Analysis Conference*, Society for Experimental Mechanics, Orlando, Florida, pp. 690-695.
- Alyuda Research Inc 2006a, *Alyuda NeuroIntelligence*, version 2.2
- Alyuda Research Inc 2006b, 'Alyuda NeuroIntelligence Help Manual', version 2.2
- ANSYS Inc 2007a, *ANSYS*, release 11.0.
- ANSYS Inc 2007b, *ANSYS Workbench*, release 11.0.
- ANSYS Inc 2007c, 'Documentation for ANSYS', release 11.0, Canonburg, PA, US.
- Avitabile, P. 2002, 'Twenty years of structural dynamic modification - a review', *Proceedings of the IMAC-XX: A Conference on Structural Dynamics*, vol. 1, Society for Experimental Mechanics, Los Angeles, CA, US, pp. 356-372.
- Azom, F. 2000, 'Biologically inspired modular neural networks', PhD Thesis, Virginia Tech, Blacksburg, VA, US.
- Bakhary, N. 2008, 'Structural condition monitoring and damage identification with artificial neural network', PhD thesis, University of Western Australia, Perth, WA, Australia.
- Barroso, L.R. & Rodriguez, R. 2004, 'Damage detection utilizing the damage index method to a benchmark structure', *Journal of Engineering Mechanics*, vol. 130, no. 2, pp. 142-151.
- Bernal, D. 2002, 'Load vectors for damage localisation', *Journal of Engineering Mechanics*, vol. 128, no. 1, pp. 7-14.
- Bishop, C.M. 1994, 'Neural networks and their applications', *Review of Scientific Instruments*, vol. 65, no. 6, pp. 1803-1832.
- Breiman, L. 1996, 'Bagging predictors', *Machine Learning*, vol. 24, no. 2, pp. 123 -140.

- Brownjohn, J.M.W. & Xia, P. 1999, 'Finite element model updating of a damaged structure', *Proceedings of the 17th International Modal Analysis Conference*, Society for Experimental Mechanics, Kissimmee, FL, US, pp. 457-462.
- CADA-X 1996, 'Modal analysis manual', *LMS International*, Belgium.
- Carden, E.P. & Fanning, P.J. 2003, 'An added mass identification algorithm based on frequency response functions', *Proceedings of the 2nd M.I.T. Conference in Computational Fluid and Solid Mechanics*, Boston, MA, US, pp. 1880-1882.
- Carden, P., E & Fanning, P. 2004, 'Vibration based condition monitoring: a review', *Structural Health Monitoring*, vol. 3, no. 4, pp. 355-377.
- Casas, J.R. & Aparicio, A.C. 1994, 'Structural damage identification from dynamic-test data', *Journal of Structural Engineering*, vol. 120, no. 8, pp. 2437-2450.
- Cattarius, J. & Inman, D.J. 1997, 'Time domain analysis for damage detection in smart structures', *Mechanical Systems and Signal Processing*, vol. 11, no. 3, pp. 409-423.
- Chen, H.L., Spyrakos, C.C. & Venkatesh, G. 1995, 'Evaluating structural deterioration by dynamic response', *Journal of Structural Engineering*, vol. 121, no. 8, pp. 1197-1204.
- Chen, J., Xu, Y.L. & Zhang, R.C. 2004, 'Modal parameter identification of Tsing Ma suspension bridge under typhoon Victor: EMD-HT method', *Journal of Wind Engineering and Industrial Aerodynamics*, vol. 92, no. 10, pp. 805-827.
- Ching, J. & Beck, J.L. 2004, 'Bayesian analysis of the Phase II IASC-ASCE structural health monitoring experimental benchmark data', *Journal of Engineering Mechanics*, vol. 130, no. 10, pp. 1233-1244.
- Choi, F.C. 2007, 'Assessment of the structural integrity of bridges using dynamic approaches', PhD thesis, University of Technology Sydney, NSW, Australia.
- Choi, F.C., Li, J., Samali, B. & Crews, K. 2007, 'An experimental study on damage detection of structures using a timber beam', *Journal of Mechanical Science and Technology - MOVIC Special Edition*, vol. 21, pp. 903-907.
- Choi, F.C., Li, J., Samali, B. & Crews, K. 2008, 'Application of the modified damage index method to timber beams', *Engineering Structures*, vol. 30, no. 4, pp. 1124-1145.
- Choi, S., Park, S. & Stubbs, N. 2005, 'Nondestructive damage detection in structures using changes in compliance', *International Journal of Solids and Structures*, vol. 42, no. 15, pp. 4494-4513.
- Chong, K.P., Carino, N.J. & Washer, G. 2003, 'Health monitoring of civil infrastructures', *Smart Materials and Structures*, vol. 12, no. 3, pp. 483-493.
- Choudhury, A.R. 1996, 'Damage detection in structures using measured frequency response function data', PhD thesis, Victoria University of Technology, Melbourne, VIC, Australia.
- Demuth, H.B. & Beale, M. 2002, *Neural network toolbox user's guide*, The MathWorks, Natick, MA, US.
- Doebling, S.W., Farrar, C.R. & Prime, M.B. 1998, 'Summary review of vibration-based damage identification methods', *Shock and Vibration Digest*, vol. 30, no. 2, pp. 91-105.

- Doebbling, S.W., Farrar, C.R., Prime, M.B. & Shevitz, D.W. 1996, *Damage identification and health monitoring of structural and mechanical systems from changes in their vibration characteristics: a literature review*, Los Alamos National Laboratory Report LA-13070-MS, Los Alamos, NM, US.
- Doebbling, S.W., Hemez, F.M., Peterson, L.D. & Farhat, C. 1997, 'Improved damage location accuracy using strain energy-based mode selection criteria', *AIAA Journal*, vol. 35, no. 4, pp. 693-699.
- Døssing, O. 1988, *Structural testing - part 2: modal analysis and simulation*, Brüel and Kjær, Nærum, Denmark.
- Efron, B. & Tibshirani, R. 1993, *An introduction to the bootstrap*, Chapman & Hall, New York, NY, US.
- Elkordy, M., Chang, K.C. & Lee, G.C. 1992, 'Application of neural network classifier in vibrational signature analysis', *Proceedings of the 8th Annual Conference of Computation in Civil Engineering*, ASCE, pp. 1066-1073.
- Elkordy, M.F., Chang, K.C. & Lee, G.C. 1993, 'Neural networks trained by analytically simulated damage states', *Journal of Computing in Civil Engineering*, vol. 7, no. 2, pp. 130-145.
- Fang, X., Luo, H. & Tang, J. 2005, 'Structural damage detection using neural network with learning rate improvement', *Computers and Structures*, vol. 83, no. 25-26, pp. 2150-2161.
- Fang, X. & Tang, J. 2005, 'Frequency response based damage detection using principal component analysis', *Proceedings of the IEEE International Conference on Information Acquisition*, Hong Kong and Macau, China, pp. 407-412.
- Farrar, C.R. & Doebbling, S.W. 1997, 'Lessons learned from applications of vibration-based damage identification methods to a large bridge structure', *Proceedings of the International Workshop on Structural Health Monitoring*, Stanford, CA, US, pp. 351-370.
- Farrar, C.R. & Jauregui, D.A. 1998, 'Comparative study of damage identification algorithms applied to a bridge: I. experiment', *Smart Materials and Structures*, vol. 7, no. 5, pp. 704-719.
- Fausett, L. 1994, *Fundamentals of neural networks: architecture, algorithms, and applications*, Prentice Hall, Upper Saddle River, NJ, US.
- Friswell, M.I. & Mottershead, J.E. 2001, 'Inverse methods in structural health monitoring', *Proceedings of the 4th International Conference on Damage Assessment of Structures*, Trans Tech Publications, Cardiff, Wales, UK, pp. 201-210.
- Funahashi, K. 1989, 'On the approximate realization of continuous mappings by neural networks', *Neural Networks*, vol. 2, no. 3, pp. 183-192.
- Furukawa, A., Otsuka, H. & Kiyono, J. 2006, 'Structural damage detection method using uncertain frequency response functions', *Computer-Aided Civil and Infrastructure Engineering*, vol. 21, no. 4, pp. 292-305.
- Garesci, F., Catalano, L. & Petrone, F. 2006, 'Experimental results of a damage detection methodology using variations in modal parameters', *Experimental Mechanics*, vol. 46, pp. 441-451.

- Gately, E. 1996, *Neural networks for financial forecasting*, John Wiley and Sons, New York, NY, US.
- Geradin, M. & Rixen, D. 1997, *Mechanical vibrations: theory and application to structural dynamics*, John Wiley and Sons, New York, NY, US.
- Gonzalez, M.P. & Zapico, J.L. 2008, 'Seismic damage identification in buildings using neural networks and modal data', *Computers and Structures*, vol. 86, no. 3-5, pp. 416-426.
- Hagan, M.T., Demuth, H.B. & Beale, M. 1996, *Neural network design*, PWS Publishing, Boston, MA, USA.
- Hagan, M.T. & Menhaj, M. 1994, 'Training feedforward networks with the Marquardt algorithm', *IEEE Transaction of Neural Networks*, vol. 5, no. 6, pp. 989-993.
- Hamey, C.S., Lestari, W., Qiao, P. & Song, G. 2004, 'Experimental damage identification of carbon/epoxy composite beams using curvature mode shapes', *Structural Health Monitoring*, vol. 3, no. 4, pp. 333-353.
- Hansen, L.K. & Salamon, P. 1990, 'Neural network ensembles', *IEEE Transactions on Pattern Analysis and Machine Intelligence*, vol. 12, no. 10, pp. 993 -1001.
- Harvey, A.C. 1989, *Forecasting, structural time series models and the Kalman filter*, Cambridge University Press, New York, NY, US.
- Hassibi, B. & Stork, D.G. 1993, 'Second order derivatives for network pruning: optimal brain surgeon', *Proceedings of the Advances in Neural Information Processing Systems 5*, San Mateo, CA, US.
- Hotelling, H. 1933, 'Analysis of a complex of statistical variables into principal components', *Journal of Educational Psychology*, vol. 24, pp. 417-441.
- Housner, G.W., Bergman, L.A., Caughey, T.K., Chassiakos, A.G., Claus, R.O., Masri, S.F., Skelton, R.E., Soong, T.T., Spencer, B.F. & Yao, J.T.P. 1997, 'Structural control: Past, present, and future', *Journal of Engineering Mechanics*, vol. 123, no. 9, pp. 897-971.
- Hu, C. & Afzal, M.T. 2006, 'A statistical algorithm for comparing mode shapes of vibration testing before and after damage in timbers', *Journal of Wood Science*, vol. 52, pp. 348-352.
- Hu, S.J., Wang, S. & Li, H. 2006, 'Cross-modal strain energy method for estimating damage severity', *Journal of Engineering Mechanics*, vol. 132, no. 4, pp. 429-437.
- Huynh, D., He, J. & Tran, D. 2005, 'Damage location vector: a non-destructive structural damage detection technique', *Computers and Structures*, vol. 83, no. 28-30, pp. 2353-2367.
- Ismail, Z., Abdul Razak, H. & Abdul Rahman, A.G. 2006, 'Determination of damage location in RC beams using mode shape derivatives', *Engineering Structures*, vol. 28, pp. 1566-1573.
- Kao, C.-Y. & Hung, S.-L. 2005, 'A neural network-based approach for detection of structural damage', *Proceedings of the 16th IASTED Conference on Modelling and Simulation*, Cancun, Mexico.
- Kato, M. & Shimada, S. 1986, 'Vibration of PC bridge during failure process', *Journal of Structural Engineering*, vol. 112, no. 7, pp. 1692-1703.

- Kessler, S.S., Spearing, S.M., Atalla, M.J., Cesnik, C.E.S. & Soutis, C. 2002, 'Damage detection in composite materials using frequency response methods', *Composites Part B: Engineering*, vol. 33, no. 1, pp. 87-95.
- Kim, B.H., Park, T. & Voyiadjis, G.Z. 2006, 'Damage estimation on beam-like structures using the multi-resolution analysis', *International Journal of Solids and Structures*, vol. 43, no. 14-15, pp. 4238-4257.
- Kim, J.-T., Park, J.-H. & Lee, B.-J. 2007, 'Vibration-based damage monitoring in model plate-girder bridges under uncertain temperature conditions', *Engineering Structures*, vol. 29, no. 7, pp. 1354-1365.
- Kim, J.-T., Ryu, Y.-S., Cho, H.-M. & Stubbs, N. 2003, 'Damage identification in beam-type structures: frequency-based method vs mode-shape-based method', *Engineering Structures*, vol. 25, no. 1, pp. 57-67.
- Kim, J.-T. & Stubbs, N. 2003, 'Crack detection in beam-type structures using frequency data', *Journal of Sound and Vibration*, vol. 259, no. 1, pp. 145-160.
- Kim, J.T. & Stubbs, N. 2002, 'Improved damage identification method based on modal information', *Journal of Sound and Vibration*, vol. 252, no. 2, pp. 223-238.
- Ko, J.M., Sun, Z.G. & Ni, Y.Q. 2002, 'Multi-stage identification scheme for detecting damage in cable-stayed Kap Shui Mun Bridge', *Engineering Structures*, vol. 24, no. 7, pp. 857-868.
- Kosslyn, S.M. 1994, *Image and brain*, MIT Press, Cambridge, MA, US.
- Krogh, A. & Hertz, J.A. 1995, 'A simple weight decay can improve generalization', *Proceedings of the Advances in Neural Information Processing Systems 5*, San Mateo, CA, US.
- Krogh, A. & Vedelsby, J. 1995, 'Neural network ensembles, cross validation, and active learning', in *Advances in Neural Information Processing Systems*, vol. 7, MIT, Cambridge, MA, US, pp. 231-238.
- Lee, J.J., Lee, J.W., Yi, J.H., Yun, C.B. & Jung, H.Y. 2005, 'Neural networks-based damage detection for bridges considering errors in baseline finite element models', *Journal of Sound and Vibration*, vol. 280, no. 3-5, pp. 555-578.
- Lee, J.J. & Yun, C.B. 2006, 'Damage diagnosis of steel girder bridges using ambient vibration data', *Engineering Structures*, vol. 28, no. 6, pp. 912-925.
- Li, H., Yang, H. & Hu, S.L.J. 2006, 'Modal strain energy decomposition method for damage localization in 3D frame structures', *Journal of Engineering Mechanics*, vol. 132, no. 9, pp. 941-951.
- Liberatore, S. & Carman, G.P. 2004, 'Power spectral density analysis for damage identification and location', *Journal of Sound and Vibration*, vol. 274, no. 3-5, pp. 761-776.
- Lifshitz, J.M. & Rotem, A. 1969, 'Determination of reinforcement unbonding of composites by a vibration technique', *Journal of Composite Materials*, vol. 3, no. 3, pp. 412-423.
- Maeck, J. 2003, 'Damage assessment of civil engineering structures by vibration monitoring', PhD thesis, Katholieke Universiteit Leuven, Belgium.

- Maeck, J. & De Roeck, G. 2002, 'Damage assessment of a gradually damaged RC beam using dynamic system identification', *Proceedings of the 20th International Modal Analysis Conference*, Society for Experimental Mechanics, Los Angeles, CA, US, pp. 1560-1566.
- Maia, N.M.M., Silva, J.M.M., Almas, E.A.M. & Sampaio, R.P.C. 2003, 'Damage detection in structures: from mode shape to frequency response function methods', *Mechanical Systems and Signal Processing*, vol. 17, no. 3, pp. 489-498.
- Maia, N.M.M., Silva, J.M.M., He, J., Lieven, N.A.J., Lin, R.M., Skingle, G.W., To, W.M. & Urgueira, A.P.V. 1997, *Theoretical and experimental modal analysis*, Research Studies Press, Baldock, Hertfordshire, England.
- Maren, A.J., Jones, D. & Franklin, S. 1990, 'Configuring and optimizing the backpropagation network', in *Handbook of Neural Computing Applications*, Academic Press, San Diego, CA, US.
- Marwala, T. 2000, 'Damage identification using committee of neural networks', *Journal of Engineering Mechanics-ASCE*, vol. 126, no. 1, pp. 43-50.
- Marwala, T. & Hunt, H.E.M. 1999, 'Fault identification using finite element models and neural networks', *Mechanical Systems and Signal Processing*, vol. 13, pp. 475-490.
- Masri, S.F., Nakamura, M., Chassiakos, A.G. & Caughey, T.K. 1996, 'Neural network approach to detection of changes in structural parameters', *Journal of Engineering Mechanics*, vol. 122, no. 4, pp. 350-360.
- Masri, S.F., Smyth, A.W., Chassiakos, A.G., Caughey, T.K. & Hunter, N.F. 2000, 'Application of neural networks for detection of changes in nonlinear systems', *Journal of Engineering Mechanics-ASCE*, vol. 126, no. 7, pp. 666-676.
- Masters, T. 1993, *Practical neural network recipes in C++*, Academic Press, London, UK.
- McCulloch, W.S. & Pitts, W. 1943, 'A logical calculus of the ideas immanent in nervous activity', *Journal Bulletin of Mathematical Biology*, vol. 52, no. 1-2, pp. 115-133.
- Mehrjoo, M., Khaji, N., Moharrami, H. & Bahreininejad, A. 2008, 'Damage detection of truss bridge joints using artificial neural networks', *Expert Systems with Applications*, vol. 35, no. 3, pp. 1122-1131.
- Minsky, M.L. & Papert, S.A. 1969, *Perceptrons*, MIT Press, Cambridge, MA, US.
- Mufti, A.A. 2001, *Guidelines for structural health monitoring: design manual*, vol. 1, ISIS Canada, Winnipeg, MB, Canada.
- Ndambi, J.M., Vantomme, J. & Harri, K. 2002, 'Damage assessment in reinforced concrete beams using eigenfrequencies and mode shape derivatives', *Engineering Structures*, vol. 24, no. 4, pp. 501-515.
- Ni, Y.Q., Zhou, X.T. & Ko, J.M. 2006, 'Experimental investigation of seismic damage identification using PCA-compressed frequency response functions and neural networks', *Journal of Sound and Vibration*, vol. 290, no. 1-2, pp. 242-263.
- Omenzetter, P. & Brownjohn, J.M.W. 2006, 'Application of time series analysis for bridge monitoring', *Smart Materials and Structures*, vol. 15, pp. 129-138.

- Opitz, D.W. & Shavlik, J.W. 1996, 'Actively searching for an effective neural-network ensemble', *Connection Science*, vol. 8, pp. 337-353.
- Ostachowicz, W., Krawczuk, M. & Cartmell, M. 2002, 'The location of a concentrated mass on rectangular plates from measurements of natural vibrations', *Computers and Structures*, vol. 80, no. 16-17, pp. 1419-1428.
- Owolabi, G.M., Swamidas, A.S.J. & Seshadri, R. 2003, 'Crack detection in beams using changes in frequencies and amplitudes of frequency response functions', *Journal of Sound and Vibration*, vol. 265, no. 1, pp. 1-22.
- Pandey, A.K. & Biswas, M. 1994, 'Damage detection in structures using changes in flexibility', *Journal of Sound and Vibration*, vol. 169, no. 1, pp. 3-17.
- Pandey, A.K., Biswas, M. & Samman, M.M. 1991, 'Damage detection from changes in curvature mode shapes', *Journal of Sound and Vibration*, vol. 145, no. 2, pp. 321-332.
- Park, S. & Stubbs, N. 1995, 'Reconstruction of mode shapes using Shannon's sampling theorem and its application to the nondestructive damage localization algorithm', *Proceedings of Smart Structures and Materials: Smart Systems for Bridges, Structures, and Highways*, vol. 2446, Society of Photo-Optical Instrumentation Engineers, San Diego, CA, US, pp. 280-292.
- Parloo, E., Verboven, P., Guillaume, P. & Van Overmeire, M. 2002, 'Autonomous structural health monitoring - part II: vibration-based in-operation damage assessment', *Mechanical Systems and Signal Processing*, vol. 16, no. 4, pp. 659-675.
- Partridge, D. 1996, 'Network generalization differences quantified', *Neural Networks*, vol. 9, no. 2, pp. 263-271.
- Patjawit, A. & Kanok-Nukulchai, W. 2005, 'Health monitoring of highway bridges based on a global flexibility index', *Engineering Structures* vol. 27, no. 9, pp. 1385-1391.
- Paul, J.F. & Carden, E.P. 2004, 'Experimentally validated added mass identification algorithm based on frequency response functions', *Journal of Engineering Mechanics*, vol. 130, no. 9, pp. 1045-1051.
- Pearson, K. 1901, 'On lines and planes of closest fit to systems of points in space', *Philosophical Magazine*, vol. 2, no. 6, pp. 559-572.
- Pereyra, L.R., Osegueda, R.A., Carrasco, C.J. & Ferregut, C.M. 1999, 'Damage detection in a stiffened plate using modal strain energy differences', *Proceedings of the Nondestructive Evaluation of Aging Aircraft, Airports, and Aerospace Hardware III*, vol. 3586, Society of Photo-Optical Instrumentation Engineers, Newport Beach, CA, US, pp. 211-222.
- Perrone, M.P. & Cooper, L.N. 1993, 'When networks disagree: ensemble methods for hybrid neural networks', in *Artificial Neural Networks for Speech and Vision*, Chapman and Hall, London, UK, pp. 126-142.
- Prechelt, L. 1995, 'Automatic early stopping using cross validation: quantifying the criteria', *Neural Networks*, vol. 11, no. 4, pp. 761-767.
- Qu, F., Zou, D. & Wang, X. 2004, 'Substructural damage detection using neural networks and ICA', in *Lecture Notes in Computer Science*, vol. 3173, Springer Verlag, Berlin, Germany, pp. 750-754.

- Ramsey, K.A. 1982, 'Experimental modal analysis, structural modifications and FEM analysis on a desktop computer', *Proceedings of the 1st International Modal Analysis Conference*, Society for Experimental Mechanics, Orlando, FL, US.
- Ratcliffe, C.P. 1997, 'Damage detection using a modified Laplacian Operator on mode shape data', *Journal of Sound and Vibration*, vol. 204, no. 3, pp. 505-517.
- Ratcliffe, C.P. 2000, 'A frequency and curvature based experimental method for locating damage in structures', *Journal of Vibration and Acoustics*, vol. 122, pp. 324-329.
- Ratcliffe, C.P. & Bagaria, W.J. 1998, 'Vibration technique for locating delamination in a composite beam', *AIAA Journal*, vol. 36, no. 6, pp. 1074-1077.
- Rosenblatt, F. 1958, 'The perceptron: a probabilistic model for information storage and organization in the brain', *Psychological Review* vol. 65, pp. 386-408.
- Rumelhart, D.E., Hinton, G.E. & Williams, R.J. 1986, *Parallel distributed processing: explorations in the microstructure of cognition*, vol. 1-3, MIT Press, Cambridge, MA, US.
- Rytter, A. 1993, 'Vibration based inspection of civil engineering structures', PhD thesis, Aalborg University, Aalborg, Denmark.
- Sahin, M. & Sheno, R.A. 2003, 'Vibration-based damage identification in beam-like composite laminates by using artificial neural networks', *Journal of Mechanical Engineering Science*, vol. 217, no. 6, p. 661.
- Salane, H.J. & Baldwin, J.W. 1990, 'Identification of modal properties of bridges', *Journal of Structural Engineering*, vol. 116, no. 7.
- Salawu, O.S. 1997, 'Detection of structural damage through changes in frequency: a review', *Engineering Structures*, vol. 19, no. 9, pp. 718-723.
- Salawu, O.S. & Williams, C. 1995a, 'Bridge assessment using forced-vibration testing', *Journal of Structural Engineering*, vol. 121, no. 2, pp. 161-172.
- Salawu, O.S. & Williams, C. 1995b, 'Review of full-scale testing of bridge structures', *Engineering Structures*, vol. 17, no. 2, pp. 113-121.
- Sampaio, R.P.C., Maia, N.M.M. & Silva, J.M.M. 1999, 'Damage detection using the frequency-response-function curvature method', *Journal of Sound and Vibration*, vol. 226, no. 5, pp. 1029-1042.
- Sánchez, J.C.H. 2005, 'Evaluation of structural damage identification methods based on dynamic characters', PhD thesis, University of Puerto Rico, Puerto Rico, US.
- Sarle, W.S. 1995, 'Stopped training and other remedies for overfitting', *Proceedings of the 27th Symposium on the Interface of Computing Science and Statistics*, Pittsburgh, PA, US, pp. 352-360.
- Savov, K. & Wenzel, H. 2005, 'System identification and damage detection using wavelet analysis: applications in frame structures', *1st International Operational Modal Analysis Conference*, Copenhagen, Denmark.
- Schapire, R.E. 1990, 'The strength of weak learnability', *Machine Learning*, vol. 5, no. 2, pp. 197 - 227.
- Schwarz, B.J. & Richardson, M.H. 1999, 'Experimental modal analysis', *CSI Reliability Week*, Orlando, FL, USA, p. 12.

- Sharkey, A.J.C. 1996, 'Combining artificial neural nets: modular approaches', *Connection Science*, vol. 8, no. 3-4.
- Shi, Z.Y., Law, S.S. & Zhang, L.M. 1998, 'Structural damage localization from strain energy change', *Journal of Sound and Vibration*, vol. 218, no. 5, pp. 825-844.
- Shi, Z.Y., Law, S.S. & Zhang, L.M. 2000, 'Damage localization by directly using incomplete mode shapes', *Journal of Engineering Mechanics*, vol. 126, no. 6, pp. 656-660.
- Shi, Z.Y., Law, S.S. & Zhang, L.M. 2002, 'Improved damage quantification from elemental modal strain energy change', *Journal of Engineering Mechanics*, vol. 128, no. 5, pp. 521-529.
- Sohn, H., Farrar, S.R., Hemez, F.N., Shunk, D., Stinemates, D.W. & Nader, B.R. 2003, *A review of structural health monitoring literature 1996-2001*, Los Alamos National Laboratory Report, LA-13976-MS, Los Alamos, NM, US.
- Sollich, P. & Krogh, A. 1996, 'Learning with ensembles: how overfitting can be useful', in, *Advances in Neural Information Processing Systems 8*, MIT Press, Denver, CO, US, pp. 190-196.
- Stubbs, N., Kim, J.-T. & Topole, K. 1992, 'An efficient and robust algorithm for damage localization in offshore platforms', *Proceedings of the 10th Structures Congress*, ASCE, Antonio, LA, USA, pp. 543-546.
- Stubbs, N., Kim, J.T. & Farrar, C.R. 1995, 'Field verification of a nondestructive damage localization and severity estimation algorithm', *Proceedings of the 13th International Modal Analysis Conference*, vol. 2460, Society of Photo-Optical Instrumentation Engineers, Nashville, TN, pp. 210-218.
- Stubbs, N. & Park, S. 1996, 'Optimal sensor placement for mode shapes via Shannon's sampling theorem', *Microcomputers in Civil Engineering.*, vol. 11, no. 6, pp. 411-419.
- Stubbs, N.S. & Osegueda, R.A. 1990a, 'Global damage detection in solids - experimental verification', *The International Journal of Analytical and Experimental Modal Analysis*, vol. 5, no. 2, pp. 81-97.
- Stubbs, N.S. & Osegueda, R.A. 1990b, 'Global nondestructive damage evaluation in solids', *The International Journal of Analytical and Experimental Modal Analysis*, vol. 5, no. 2, pp. 67-79.
- Su, Z. & Ye, L. 2004, 'Lamb wave-based quantitative identification of delamination in CF/EP composite structures using artificial neural algorithm', *Composite Structures*, vol. 66, no. 1-4, pp. 627-637.
- Sumitomo Australia Pty Ltd 2009, 'Bridge Repair Market Statistics', assessed internet on 25-Nov-2009, <<http://www.iceng.com.au/files/link/Bridge-market-statistics.pdf>>.
- The MathWorks, I. 2007, *Matlab 2007b*.
- The MathWorks, I. 2009a, 'Communications Toolbox 4', *User's Guide*.
- The MathWorks, I. 2009b, 'Statistics Toolbox 7', *User's Guide*.
- Trendafilova, I. 2005, 'A study on vibration-based damage detection and location in an aircraft wing scaled model', *Applied Mechanics and Materials*, vol. 3-4, pp. 309-314.

- Trendafilova, I. & Heylen, W. 1998, 'Fault localization in structures from remote FRF measurements - influence of the measurement points', *Proceedings of the 23rd International Conference on Noise and Vibration*, Leuven, Belgium, pp. 149-156.
- Trendafilova, I. & Heylen, W. 2003, 'Categorisation and pattern recognition methods for damage localisation from vibration measurements', *Mechanical Systems and Signal Processing*, vol. 17, no. 4, pp. 825-836.
- U.S. Department of Transportation 2006, *Status of the nation's highways, bridges, and transit: conditions & performance*, Report, Federal Highway Administration, Washington, DC, US.
- Unger, J.F., Teughels, A. & De Roeck, G. 2005, 'Damage detection of a prestressed concrete beam using modal strains', *Journal of Structural Engineering*, vol. 131, no. 9, pp. 1456-1463.
- Verboven, P., Parloo, E., Guillaume, P. & Van Overmeire, M. 2002, 'Autonomous structural health monitoring - part I: modal parameter estimation and tracking', *Mechanical Systems & Signal Processing*, vol. 16, no. 4, pp. 637-657.
- Vieira De Moura, J.D.R. & Steffen, V. 2006, 'Impedance-based health monitoring: frequency band evaluation', *Journal of Intelligent Material Systems and Structures*, vol. 17, no. 11, pp. 1023-1036.
- Wahab, M.M.A. & De Roeck, G. 1999, 'Damage detection in bridges using modal curvatures: application to a real scenario', *Journal of Sound and Vibration*, vol. 226, no. 2, pp. 217-235.
- Wang, T.-L. & Zong, Z. 2002, *Improvement of evaluation method for existing highway bridges*, Research Report No. FL/DOT/RMC/6672-818, Florida International University, Tallahassee, FL, US.
- Wang, Z., Lin, R.M. & Lim, M.K. 1997, 'Structural damage detection using measured FRF data', *Computer Methods in Applied Mechanics and Engineering*, vol. 147, no. 1-2, pp. 187-197.
- White, P.R., Tan, M.H. & Hammond, J.K. 2006, 'Analysis of the maximum likelihood, total least squares and principal component approaches for frequency response function estimation', *Journal of Sound and Vibration*, vol. 290, no. 3-5, pp. 676-689.
- Worden, K. & Dulieu-Barton, J.M. 2004, 'An overview of intelligent fault detection in systems and structures', *Structural Health Monitoring*, vol. 3, no. 1, pp. 85-98.
- Worden, K., Manson, G. & Allman, D. 2001, 'An experimental appraisal of the strain energy damage location method', *Proceedings of the International Conference on Damage Assessment of Structures*, Cardiff, UK, pp. 35-46.
- Wu, X., Ghaboussi, J. & Garrett, J.H., Jr. 1992, 'Use of neural networks in detection of structural damage', *Computers & Structures*, vol. 42, no. 4, pp. 649-659.
- Xu, H. 2005, 'Application of artificial neural networks in vibration-based damage identification', PhD thesis, Carleton University, Ottawa, Canada.
- Xu, H. & Humar, J. 2006, 'Damage detection in a girder bridge by artificial neural network technique', *Computer-Aided Civil and Infrastructure Engineering*, vol. 21, no. 6, pp. 450-464.

- Xu, Y.L. & Chen, J. 2004, 'Structural damage detection using empirical mode decomposition: experimental investigation', *Journal of Engineering Mechanics*, vol. 130, no. 11, pp. 1279-1288.
- Xu, Y.L., Chen, S.W. & Zhang, R.C. 2003, 'Modal identification of Di Wang Building under typhoon York using the Hilbert-Huang transform method', *The Structural Design of Tall and Special Buildings*, vol. 12, no. 1, pp. 21-47.
- Yam, L.H., Yan, Y.J. & Jiang, J.S. 2003, 'Vibration-based damage detection for composite structures using wavelet transform and neural network identification', *Composite Structures*, vol. 60, no. 4, pp. 403-412.
- Yan, A.M., Kerschen, G., De Boe, P. & Golinval, J.C. 2005, 'Structural damage diagnosis under varying environmental conditions - part I: a linear analysis', *Mechanical Systems and Signal Processing*, vol. 19, no. 4, pp. 847-864.
- Yang, J.N., Lei, Y., Lin, S. & Huang, N. 2004, 'Hilbert-Huang based approach for structural damage detection', *Journal of Engineering Mechanics*, vol. 130, no. 1, pp. 85-95.
- Yeung, W.T. & Smith, J.W. 2005, 'Damage detection in bridges using neural networks for pattern recognition of vibration signatures', *Engineering Structures*, vol. 27, no. 5, pp. 685-698.
- Ying, Z., Jun, G. & Xuezhi, Y. 2005, 'A survey of neural network ensembles', *Proceedings of the International Conference on Neural Networks and Brain*, vol. 1, Beijing, China, pp. 438-442.
- Yoon, M.K., Heider, D., Gillespie, J.W.J., Ratcliffe, C.P. & Crane, R.M. 2001, 'Local damage detection using a global fitting method on mode shape data', *14th International Modal Analysis Conference*, Society for Experimental Mechanics, Inc., Kissimmee, Florida, US, pp. 231-237.
- Zang, C., Friswell, M.I. & Imregun, M. 2003a, 'Structural health monitoring and damage assessment using measured FRFs from multiple sensors: part I: the indicator of correlation criteria', *Proceedings of the 5th International Conference on Damage Assessment of Structures* vol. 245-246, Key Engineering Materials, Southampton, Hampshire, UK, pp. 131-140.
- Zang, C., Friswell, M.I. & Imregun, M. 2003b, 'Structural health monitoring and damage assessment using measured FRFs from multiple sensors: part II: decision making with RBF networks', *Proceedings of the 5th International Conference on Damage Assessment of Structures*, vol. 245-246, Key Engineering Materials, Southampton, Hampshire, UK, pp. 141-148.
- Zang, C., Friswell, M.I. & Imregun, M. 2007, 'Structural health monitoring and damage assessment using frequency response correlation criteria', *Journal of Engineering Mechanics*, vol. 133, no. 9, pp. 981-993.
- Zang, C. & Imregun, M. 2001a, 'Combined neural network and reduced FRF techniques for slight damage detection using measured response data', *Archive of Applied Mechanics (Ingenieur Archiv)*, vol. 71, no. 8, pp. 525-536.
- Zang, C. & Imregun, M. 2001b, 'Structural damage detection using artificial neural networks and measured FRF data reduced via principal component projection', *Journal of Sound and Vibration*, vol. 242, no. 5, pp. 813-827.

- Zapico, J.L., Worden, K. & Molina, F.J. 2001, 'Vibration-based damage assessment in steel frames using neural networks', *Smart Materials and Structures*, vol. 10, no. 3, pp. 553-559.
- Zhao, J. & DeWolf, J.T. 1999, 'Sensitivity study for vibrational parameters used in damage detection', *Journal of Structural Engineering*, vol. 125, no. 4, pp. 410-416.
- Zhou, Z.-H., Wu, J. & Tang, W. 2002, 'Ensembling neural networks: many could be better than all', *Artificial Intelligence*, vol. 137, no. 1-2, pp. 239-263.
- Zhu, X.Q. & Law, S.S. 2006, 'Wavelet-based crack identification of bridge beam from operational deflection time history', *International Journal of Solids and Structures*, vol. 43, pp. 2299-2317.
- Zou, Y., Tong, L. & Steven, G.P. 2000, 'Vibration-based model-dependent damage (delamination) identification and health monitoring for composite structures - a review', *Journal of Sound and Vibration*, vol. 230, no. 2, pp. 357-378.
- Zurada, J.M. 1992, *Introduction to artificial neural systems*, West Publishing Company, Boston, MA, US.

APPENDICES

APPENDIX A

NATURAL FREQUENCY AND DAMPING RATIO

CHANGES OF LABORATORY BEAMS

Table A.1 Natural frequencies of the first seven flexural modes of the intact state and all damaged states of beams 1 to 4.

Beam 1 - Natural frequencies [Hz]							
	Mode 1	Mode 2	Mode 3	Mode 4	Mode 5	Mode 6	Mode 7
Undamaged	21.60	40.07	129.37	221.49	310.39	448.69	614.30
4XL	21.62	40.09	129.27	221.64	310.78	448.97	615.41
4L	21.49	40.12	129.43	222.06	310.15	449.24	613.78
4M	21.44	40.07	128.03	221.33	307.18	448.65	610.25
4S	21.37	40.05	126.50	220.68	305.34	448.62	601.10

Beam 2 - Natural frequencies [Hz]							
	Mode 1	Mode 2	Mode 3	Mode 4	Mode 5	Mode 6	Mode 7
Undamaged	20.27	40.71	125.02	215.96	302.79	477.86	616.27
5XL	20.23	40.64	125.24	216.01	302.89	478.99	617.39
5L	20.18	40.69	125.40	215.78	300.58	480.03	616.65
5M	20.30	40.36	125.70	213.47	299.06	477.59	612.14
5S	20.29	40.31	126.05	212.24	298.52	476.78	604.19

Beam 3 - Natural frequencies [Hz]							
	Mode 1	Mode 2	Mode 3	Mode 4	Mode 5	Mode 6	Mode 7
Undamaged	21.09	40.21	127.86	218.05	307.09	483.94	616.62
6XL	20.97	40.04	128.31	218.39	305.22	480.56	616.08
6L	21.04	40.15	128.04	218.91	305.12	478.01	615.37
6M	21.04	39.98	127.64	218.24	304.85	480.37	613.17
6S	20.93	39.54	126.64	218.34	304.54	479.66	607.02

Beam 4 - Natural frequencies [Hz]							
	Mode 1	Mode 2	Mode 3	Mode 4	Mode 5	Mode 6	Mode 7
Undamaged	21.01	39.56	124.41	209.65	300.44	476.46	606.48
7XL	20.94	39.41	123.94	205.22	299.19	476.37	609.10
7L	20.77	39.58	123.91	208.80	298.54	476.57	607.12
7M	20.77	39.50	123.59	207.33	297.83	472.93	605.13
7S	20.77	39.16	123.20	206.50	292.96	471.89	604.05

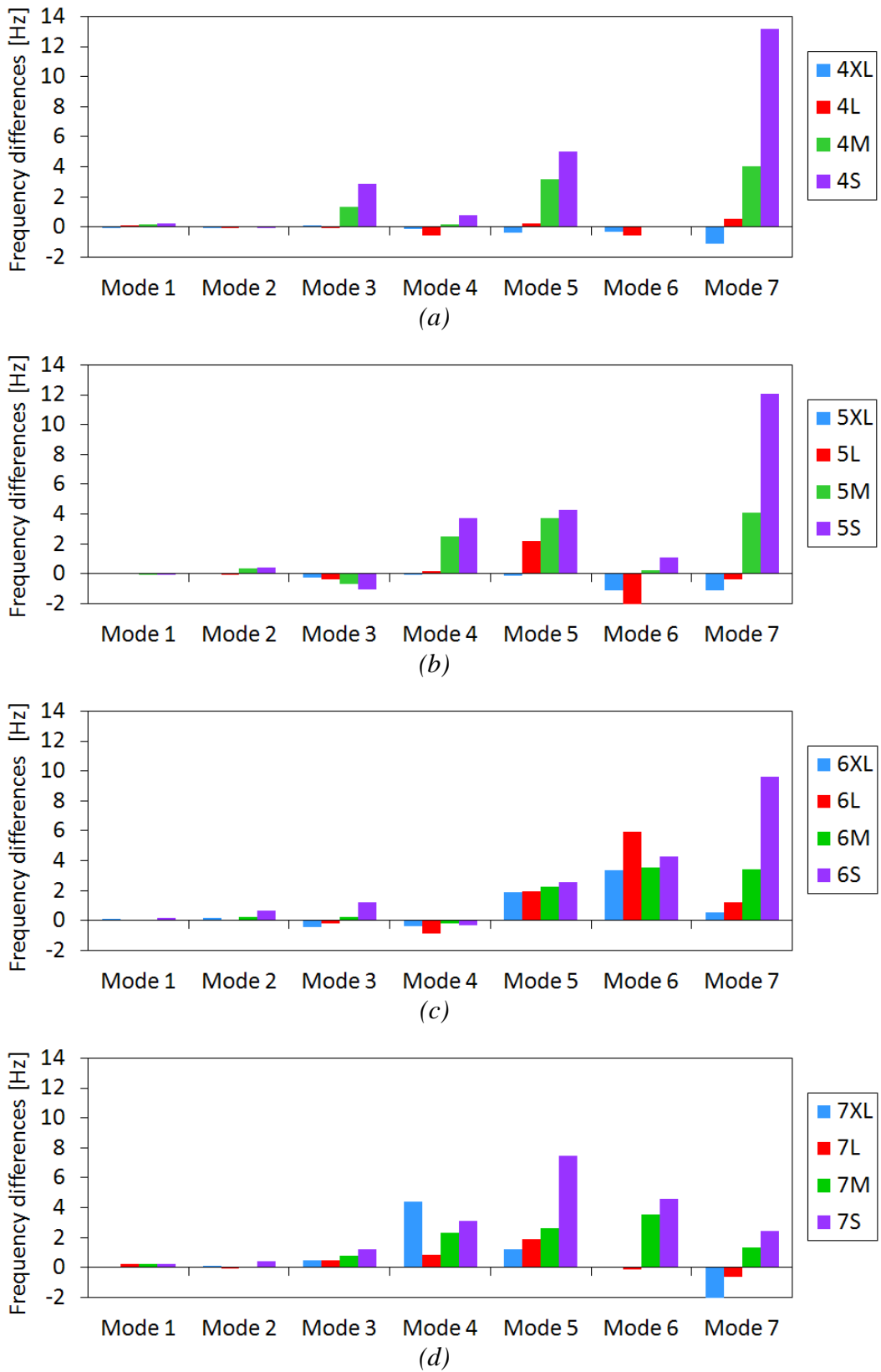


Figure A.1 Comparison of reduction in natural frequencies [%] of various damage cases of (a) beam 1, (b) beam 2, (c) beam 3 and (d) beam 4.

Table A.2 Damping ratios of the first seven flexural modes of the intact state and all damaged states of beams 1 to 4.

Beam 1 – Damping ratios [%]							
	Mode 1	Mode 2	Mode 3	Mode 4	Mode 5	Mode 6	Mode 7
Undamaged	1.17	0.43	0.57	1.14	2.67	0.87	1.64
4XL	1.45	0.51	0.61	1.12	1.96	0.97	1.56
4L	1.36	0.82	0.55	1.18	2.90	1.06	1.39
4M	1.20	0.58	0.38	1.35	1.87	1.50	1.43
4S	1.17	0.75	0.52	1.19	1.58	1.05	1.11

Beam 2 – Damping ratios [%]							
	Mode 1	Mode 2	Mode 3	Mode 4	Mode 5	Mode 6	Mode 7
Undamaged	2.17	1.30	1.21	1.60	2.09	1.18	1.38
5XL	2.51	1.78	2.15	1.64	2.22	0.75	1.12
5L	2.58	1.50	1.24	1.69	2.19	0.94	0.91
5M	2.06	1.36	1.30	0.92	1.70	0.44	1.29
5S	2.55	1.48	0.76	1.15	1.65	0.57	1.78

Beam 3 – Damping ratios [%]							
	Mode 1	Mode 2	Mode 3	Mode 4	Mode 5	Mode 6	Mode 7
Undamaged	2.31	1.01	1.52	1.93	1.21	1.48	1.64
6XL	2.09	1.14	1.31	1.80	1.54	3.42	1.62
6L	2.26	0.89	1.09	1.21	1.46	2.21	1.46
6M	1.93	1.01	1.09	2.37	1.91	2.63	1.24
6S	2.18	1.54	1.09	1.63	1.95	2.52	1.04

Beam 4 – Damping ratios [%]							
	Mode 1	Mode 2	Mode 3	Mode 4	Mode 5	Mode 6	Mode 7
Undamaged	1.41	1.25	0.76	1.55	1.56	1.23	1.05
7XL	1.33	1.21	0.81	2.09	2.00	2.33	1.04
7L	1.37	1.62	0.79	1.46	0.99	0.97	1.10
7M	1.72	0.82	0.76	0.95	1.69	1.02	1.13
7S	1.64	1.13	1.00	0.92	2.04	1.40	1.01

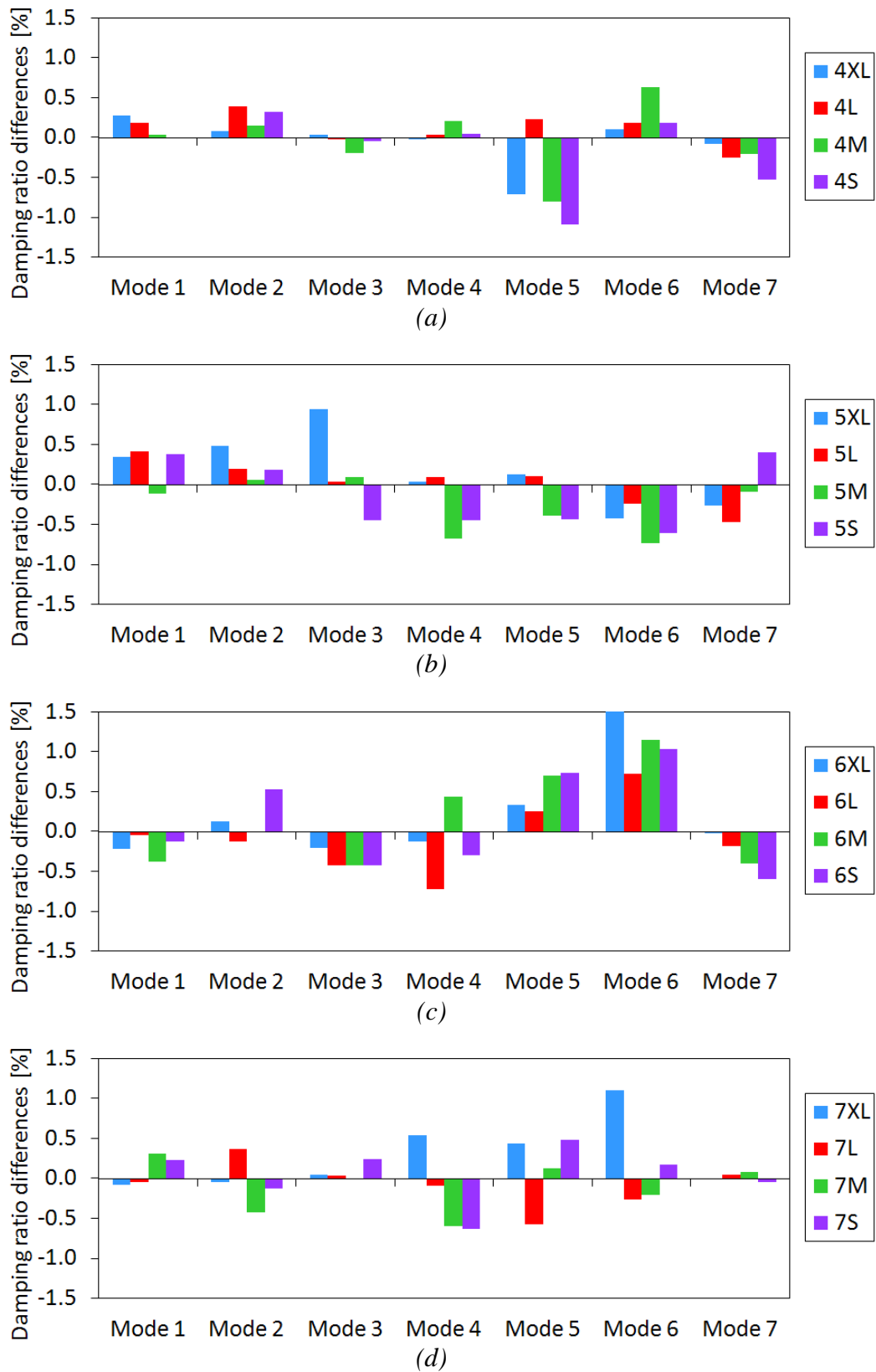
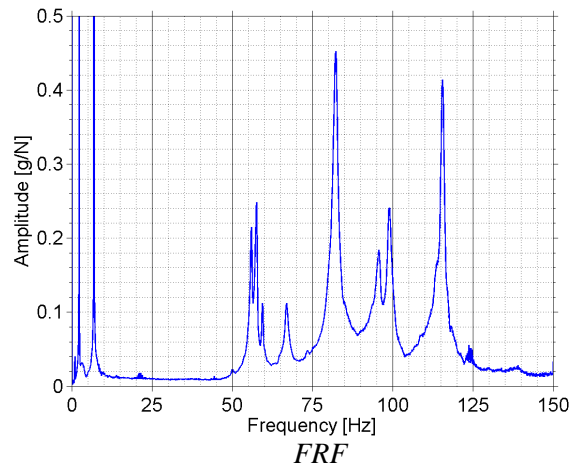
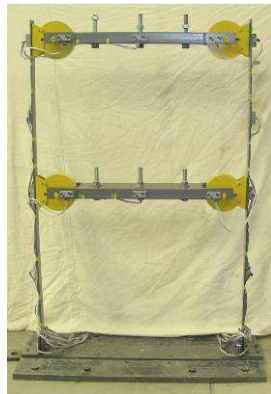


Figure A.2 Comparison of increase in damping ratios of various damage cases of (a) beam 1, (b) beam 2, (c) beam 3 and (d) beam 4.

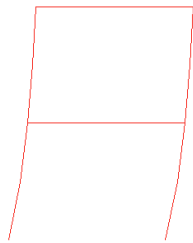
APPENDIX B

VIBRATIONAL MODES OF LABORATORY TWO- STOREY FRAMED STRUCTURE

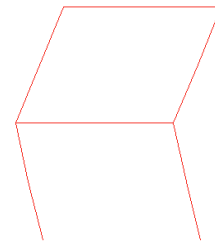


FFFF

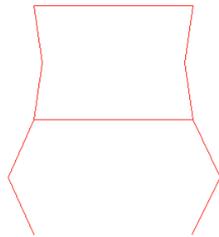
FRF



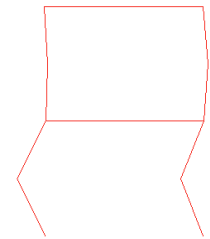
Mode 1 - 2.2 Hz



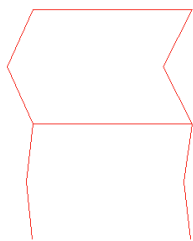
Mode 2 - 6.9 Hz



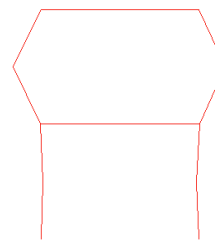
Mode 3 - 56.1 Hz



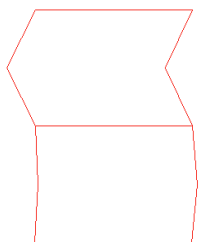
Mode 4 - 67.0 Hz



Mode 5 - 82.1 Hz

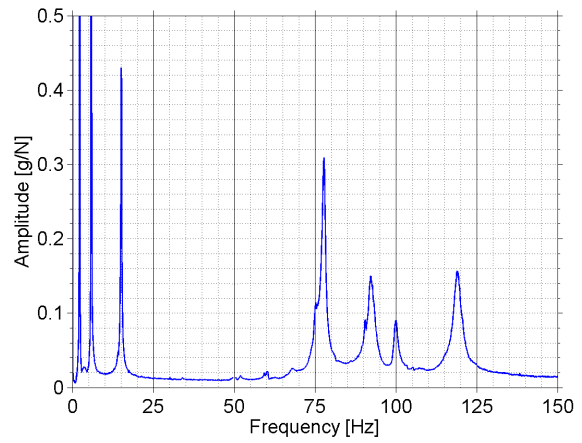
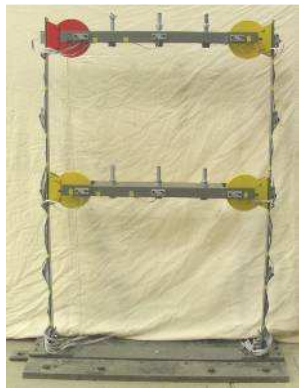


Mode 6 - 98.9 Hz



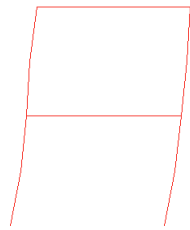
Mode 7 - 115.4 Hz

Figure B.1 Dynamic characteristics of laboratory baseline structure (FFFF).

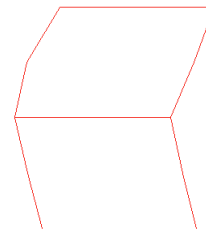


PFFF

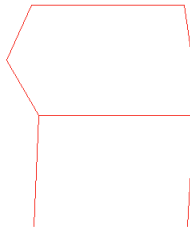
FRF



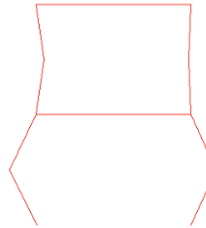
Mode 1 - 2.2 Hz



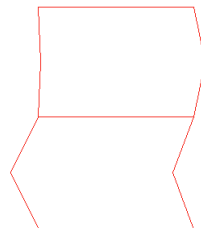
Mode 2 - 5.8 Hz



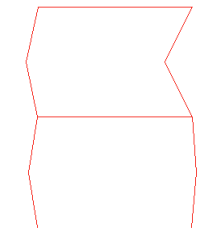
Mode 2a - 15.1 Hz



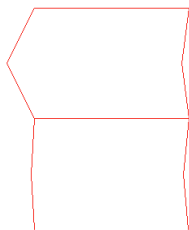
Mode 3 - 60.2 Hz



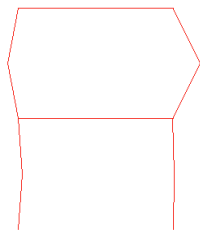
Mode 4 - 67.1 Hz



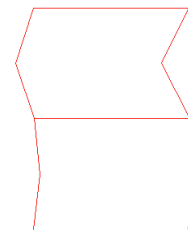
Mode 5 - 77.7 Hz



Mode 5a - 92.5 Hz

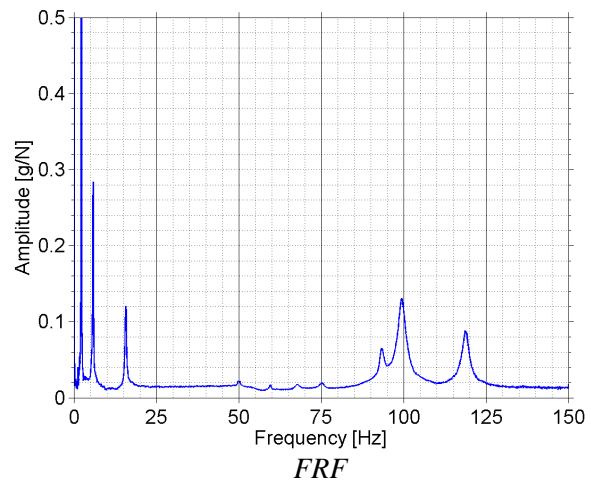
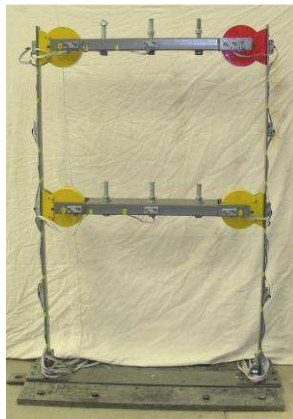


Mode 6 - 99.9 Hz



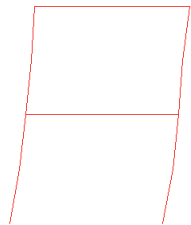
Mode 7 - 118.9 Hz

Figure B.2 Dynamic characteristics of laboratory structure PFFF.

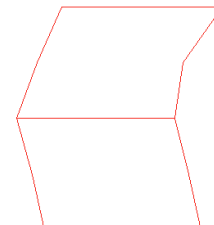


FPFF

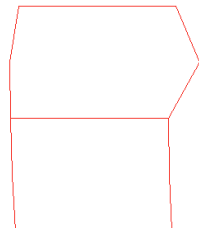
FRF



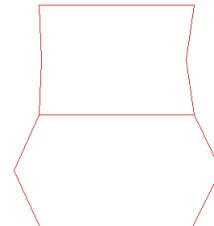
Mode 1 - 2.2 Hz



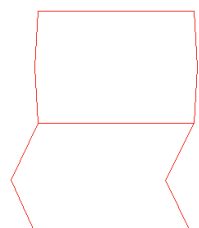
Mode 2 - 5.5 Hz



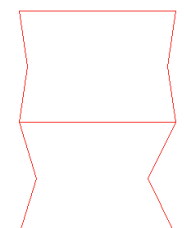
Mode 2a - 15.6 Hz



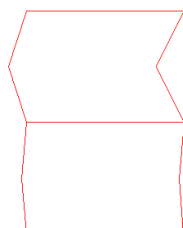
Mode 3 - 59.6 Hz



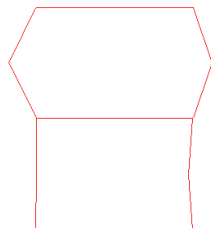
Mode 4 - 67.8 Hz



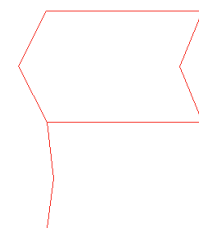
Mode 4a - 74.1 Hz



Mode 5 - 93.2 Hz

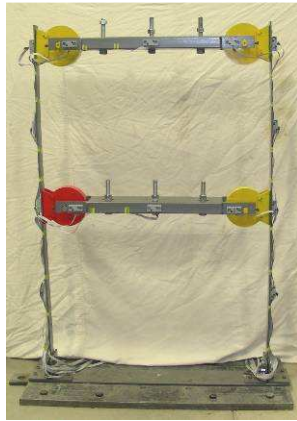


Mode 6 - 99.6 Hz

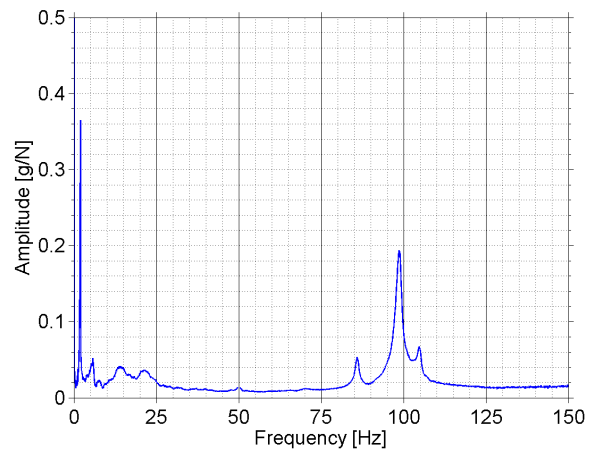


Mode 7 - 118.9 Hz

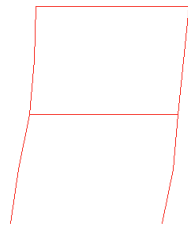
Figure B.3 Dynamic characteristics of laboratory structure FPFF.



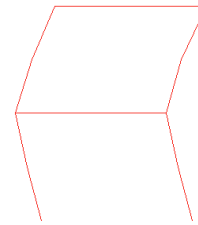
FFPF



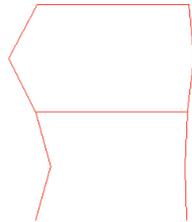
FRF



Mode 1 – 1.8 Hz



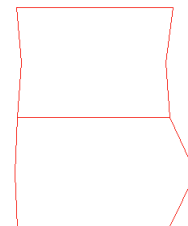
Mode 2 – 5.7 Hz



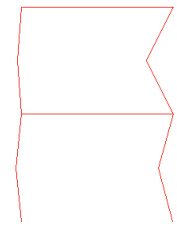
Mode 2a – 16.1 Hz



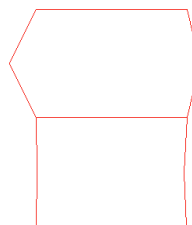
Mode 4 – 63.4 Hz



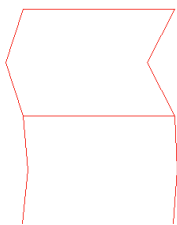
Mode 3 – 70.0 Hz



Mode 5 – 85.9 Hz

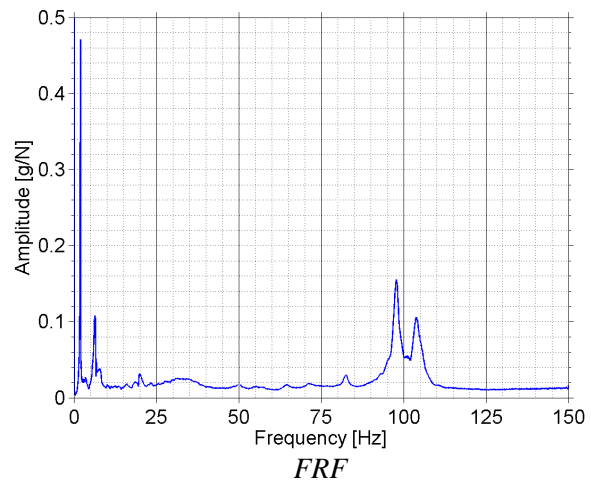
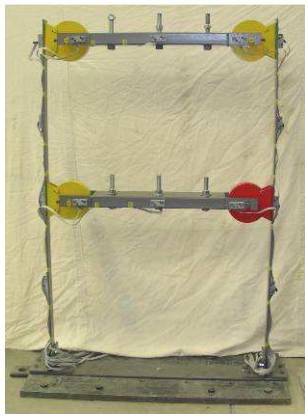


Mode 6 – 98.4 Hz



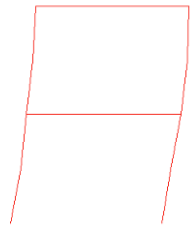
Mode 7 – 104.8 Hz

Figure B.4 Dynamic characteristics of laboratory structure FFPF.

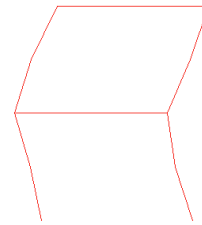


FFFP

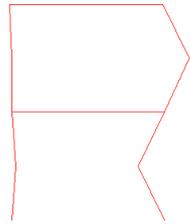
FRF



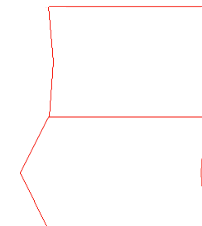
Mode 1 – 1.9 Hz



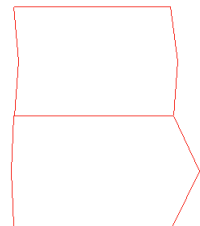
Mode 2 – 6.1 Hz



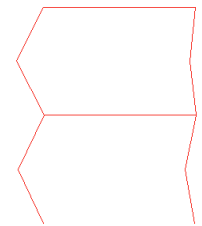
Mode 2a – 19.8 Hz



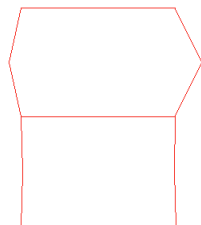
Mode 4 – 64.3 Hz



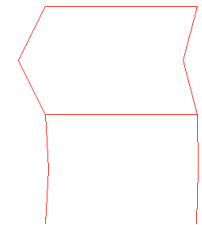
Mode 3 – 71.1 Hz



Mode 5 – 82.5 Hz

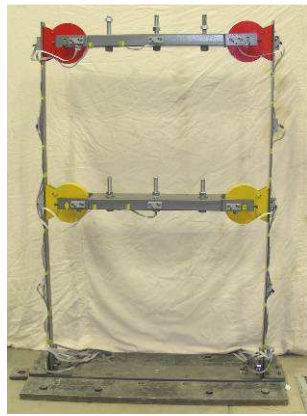


Mode 6 – 97.8 Hz

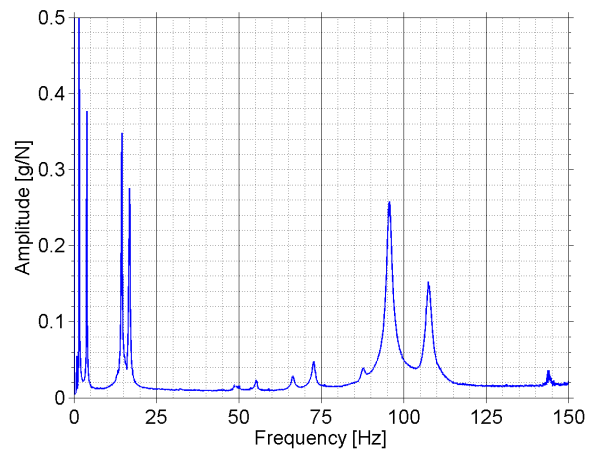


Mode 7 – 104.1 Hz

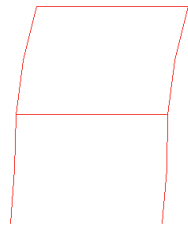
Figure B.5 Dynamic characteristics of laboratory structure FFFP.



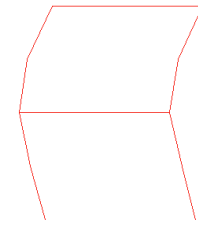
PPFF



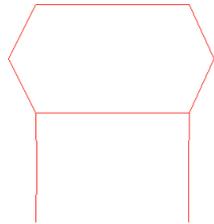
FRF



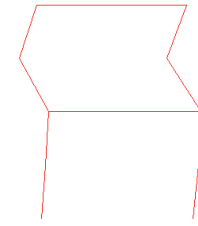
Mode 1 – 1.5 Hz



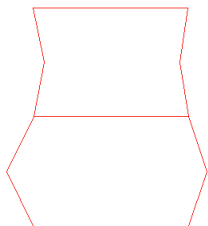
Mode 2 – 3.9 Hz



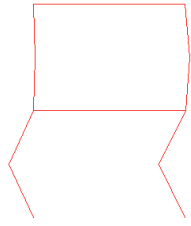
Mode 2a – 14.4 Hz



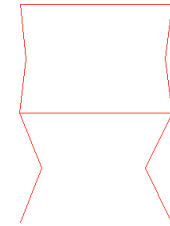
Mode 2b – 16.8 Hz



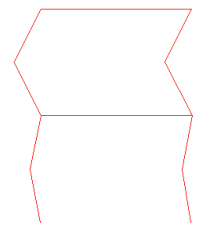
Mode 3 – 55.4 Hz



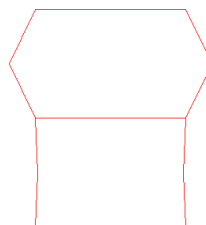
Mode 4 – 66.4 Hz



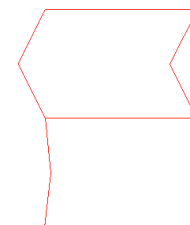
Mode 4a – 72.4 Hz



Mode 5 – 87.9 Hz



Mode 6 – 95.7 Hz

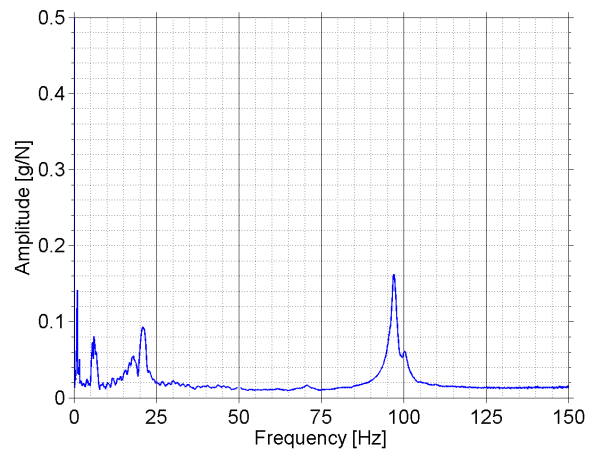


Mode 7 – 107.6 Hz

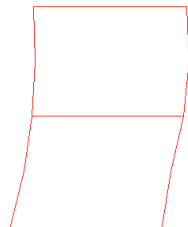
Figure B.6 Dynamic characteristics of laboratory structure PPFF.



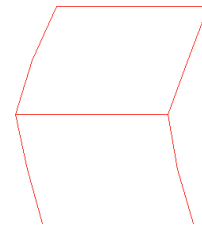
FFPP



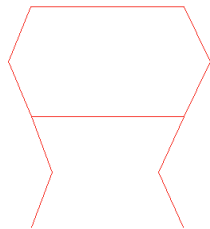
FRF



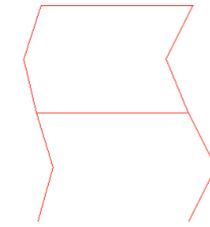
Mode 1 – 1.0 Hz



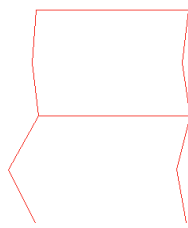
Mode 2 – 5.6 Hz



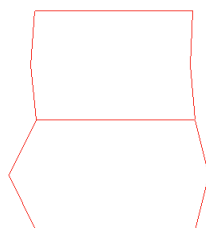
Mode 2a – 18.2 Hz



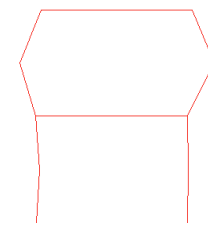
Mode 2b – 20.5 Hz



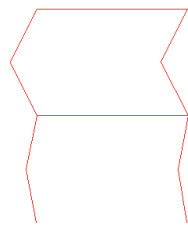
Mode 4 – 67.6 Hz



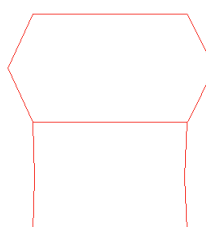
Mode 3 – 70.6 Hz



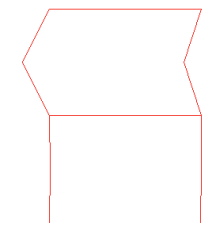
Mode 4a – 73.5 Hz



Mode 5 – 89.9 Hz

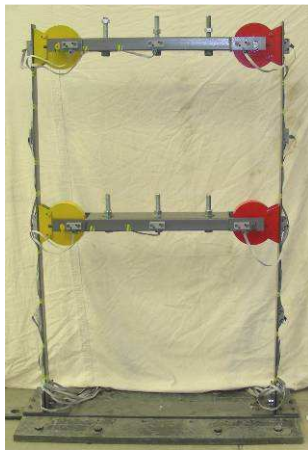


Mode 6 – 97.1 Hz

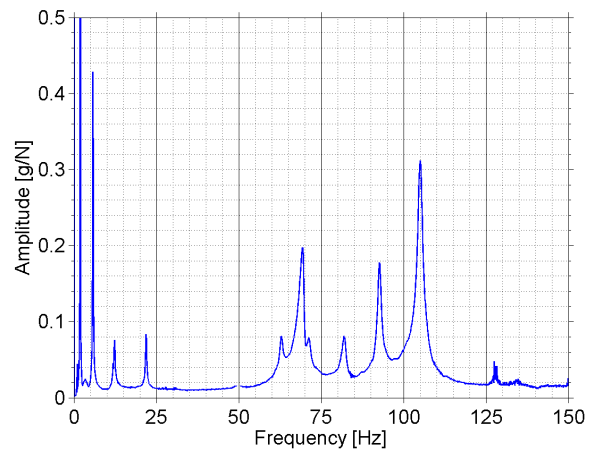


Mode 7 – 100.1 Hz

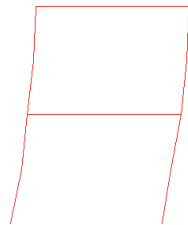
Figure B.7 Dynamic characteristics of laboratory structure FFPP.



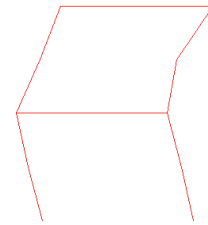
FPFP



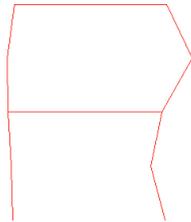
FRF



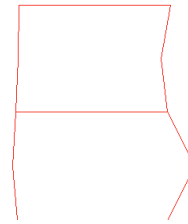
Mode 1 – 1.9 Hz



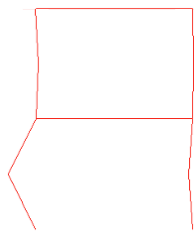
Mode 2 – 5.7 Hz



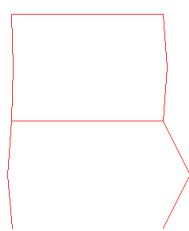
Mode 2a – 12.1 Hz



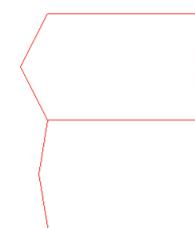
Mode 2b – 21.8 Hz



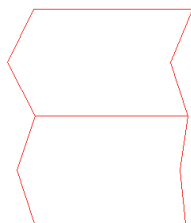
Mode 4 – 62.9 Hz



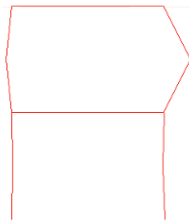
Mode 3 – 68.9 Hz



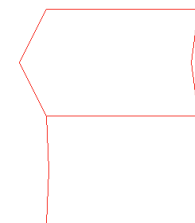
Mode 4a – 71.3 Hz



Mode 5 – 90.0 Hz



Mode 6 – 92.7 Hz

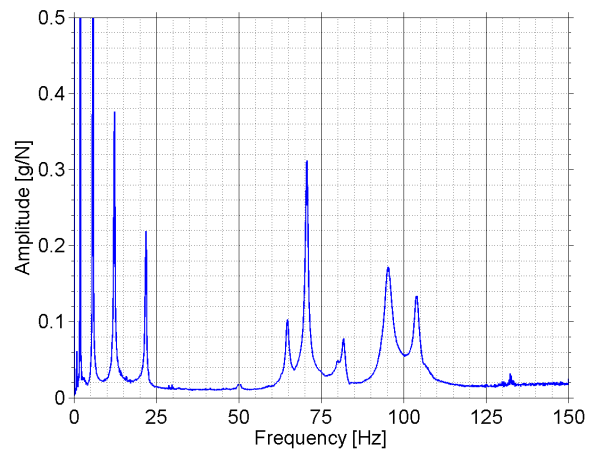


Mode 7 – 105.0 Hz

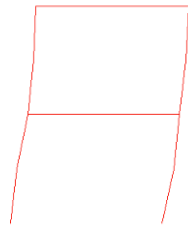
Figure B.8 Dynamic characteristics of laboratory structure FPFP.



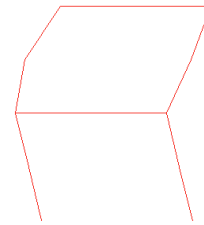
PFPP



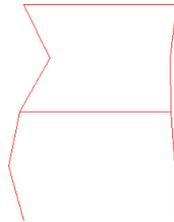
FRF



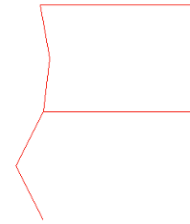
Mode 1 – 1.9 Hz



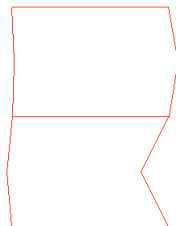
Mode 2 – 5.7 Hz



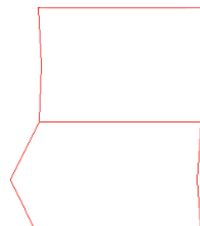
Mode 2a – 12.2 Hz



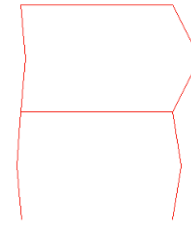
Mode 2b – 21.7 Hz



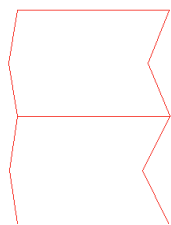
Mode 4 – 64.6 Hz



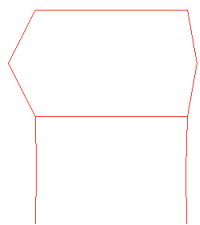
Mode 3 – 71.2 Hz



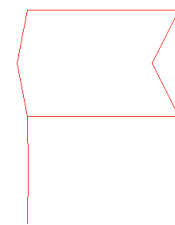
Mode 4a – 82.0 Hz



Mode 5 – 81.3 Hz

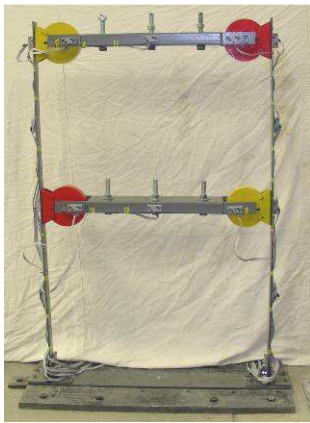


Mode 6 – 95.2 Hz

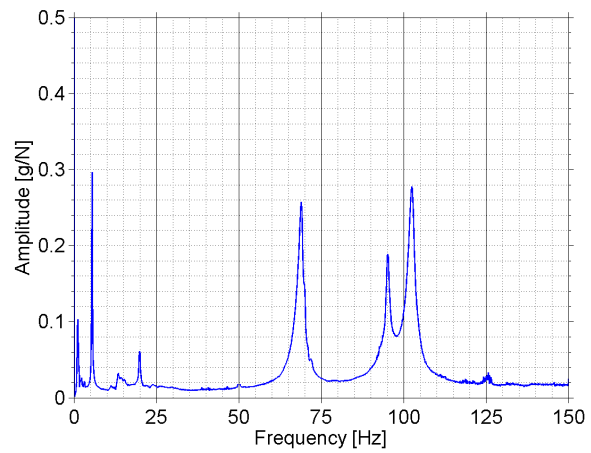


Mode 7 – 103.7 Hz

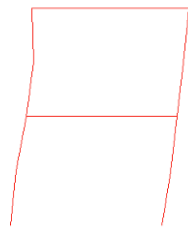
Figure B.9 Dynamic characteristics of laboratory structure PFPP.



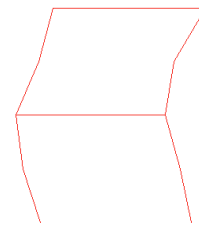
FPPF



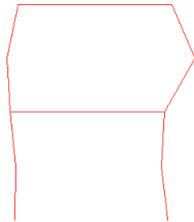
FRF



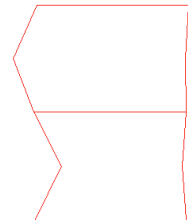
Mode 1 – 1.1 Hz



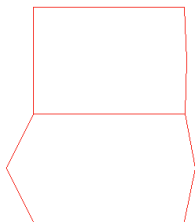
Mode 2 – 5.4 Hz



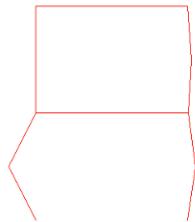
Mode 2a – 14.4 Hz



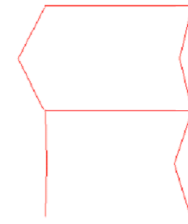
Mode 2b – 19.9 Hz



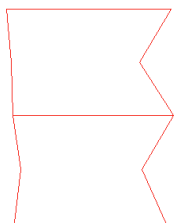
Mode 3 – 70.0 Hz



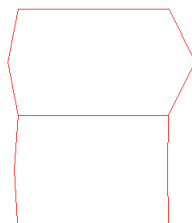
Mode 3a – 75.6 Hz



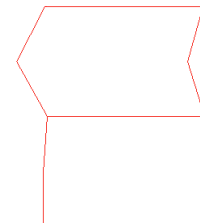
Mode 4 – 77.2 Hz



Mode 5 – 81.9 Hz

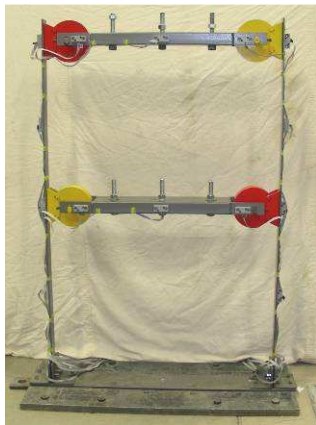


Mode 6 – 94.1 Hz

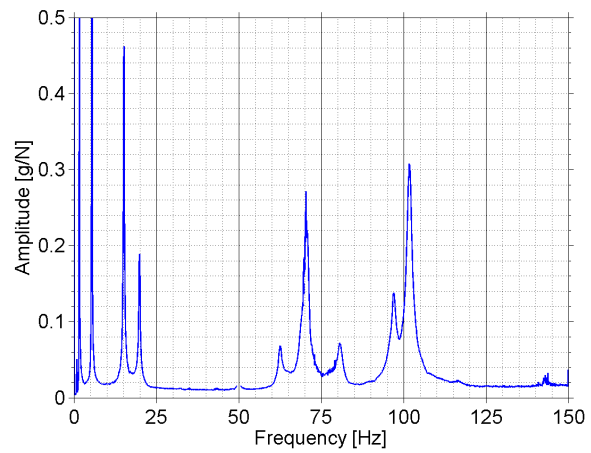


Mode 7 – 103.4 Hz

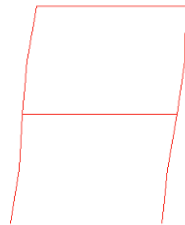
Figure B.10 Dynamic characteristics of laboratory structure FPPF.



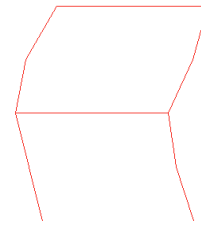
PFFP



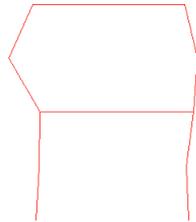
FRF



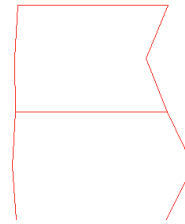
Mode 1 – 1.6 Hz



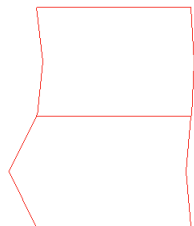
Mode 2 – 5.4 Hz



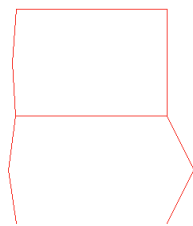
Mode 2a – 15.1 Hz



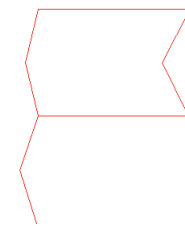
Mode 2b – 19.8 Hz



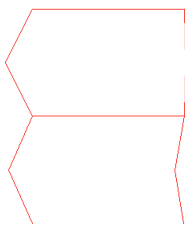
Mode 4 – 62.5 Hz



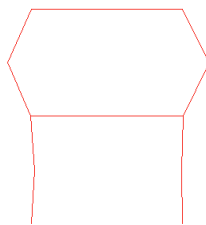
Mode 3 – 70.6 Hz



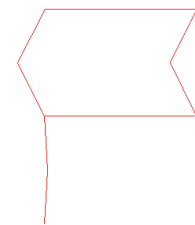
Mode 4a – 73.2 Hz



Mode 5 – 80.9 Hz



Mode 6 – 96.9 Hz

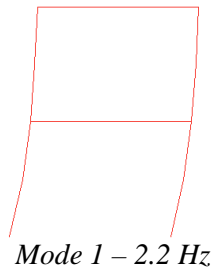
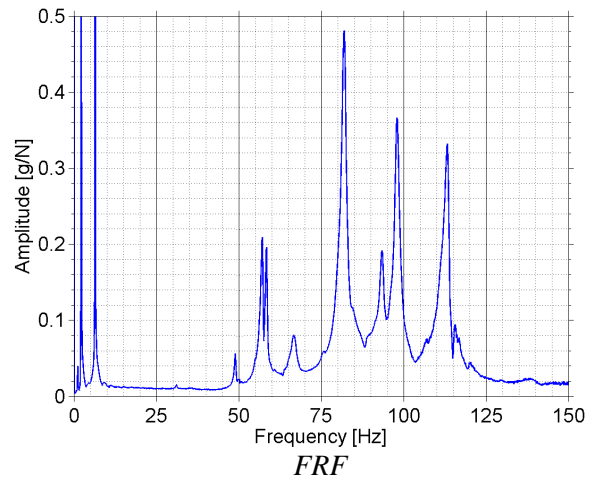


Mode 7 – 101.8 Hz

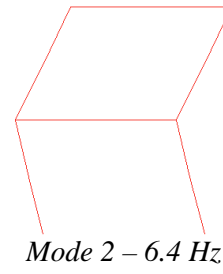
Figure B.11 Dynamic characteristics of laboratory structure PFFP.



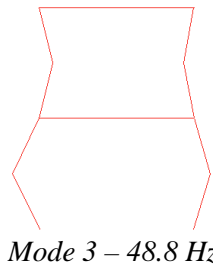
M1



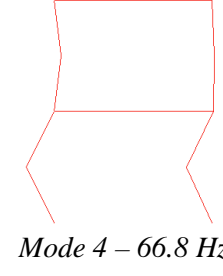
Mode 1 – 2.2 Hz



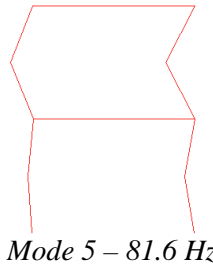
Mode 2 – 6.4 Hz



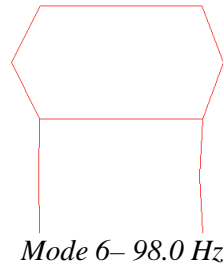
Mode 3 – 48.8 Hz



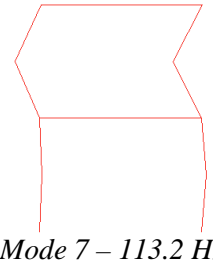
Mode 4 – 66.8 Hz



Mode 5 – 81.6 Hz



Mode 6 – 98.0 Hz



Mode 7 – 113.2 Hz

Figure B.12 Dynamic characteristics of laboratory structure with added mass at M1.



M2

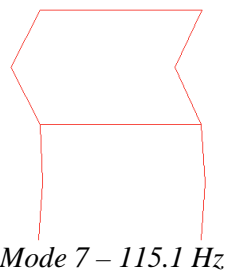
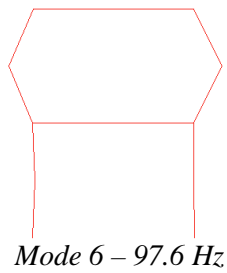
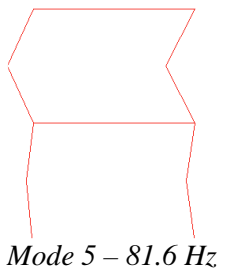
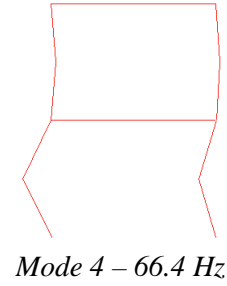
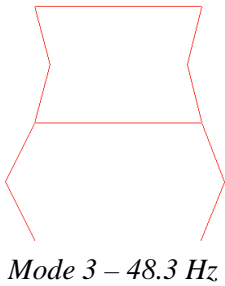
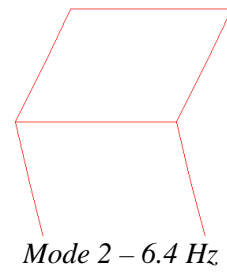
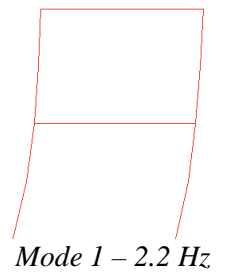
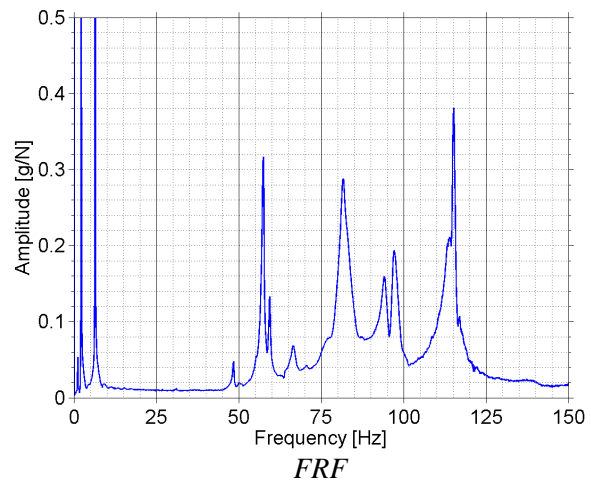
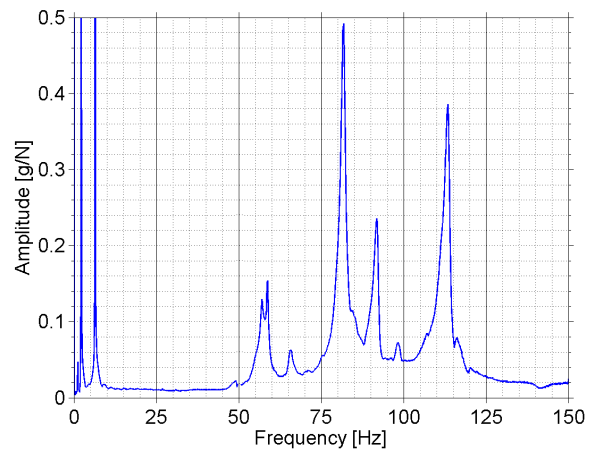


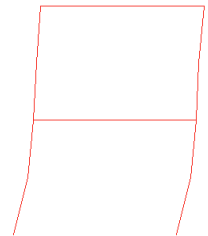
Figure B.13 Dynamic characteristics of laboratory structure with added mass at M2.



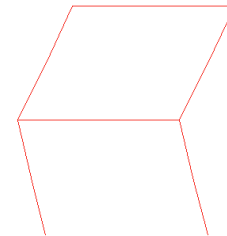
M3



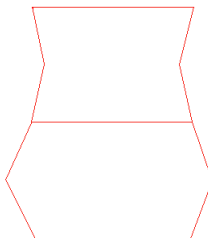
FRF



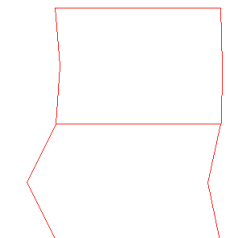
Mode 1 – 2.2 Hz



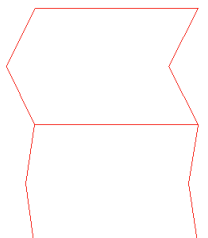
Mode 2 – 6.4 Hz



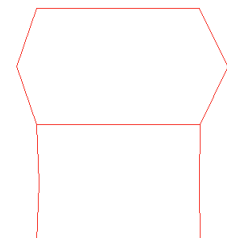
Mode 3 – 49.9 Hz



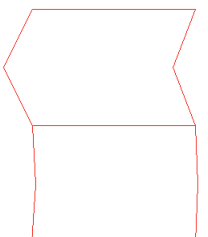
Mode 4 – 66.6 Hz



Mode 5 – 81.5 Hz

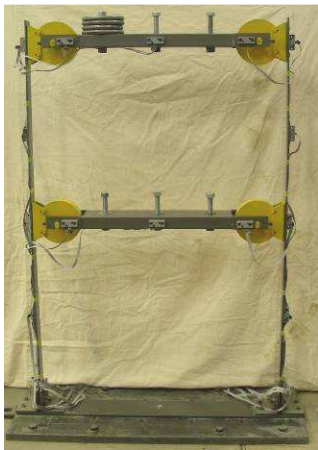


Mode 6 – 98.3 Hz

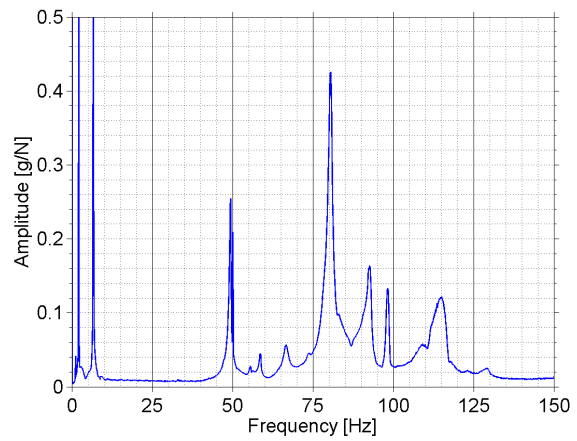


Mode 7 – 113.2 Hz

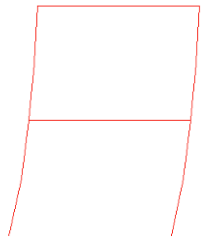
Figure B.14 Dynamic characteristics of laboratory structure with added mass at M3.



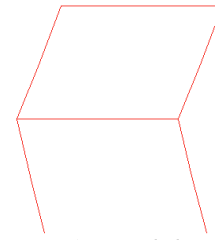
M4



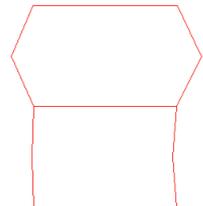
FRF



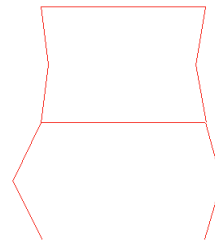
Mode 1 – 2.1 Hz



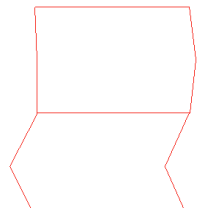
Mode 2 – 6.6 Hz



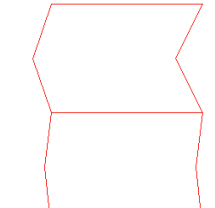
Mode 2a – 49.3 Hz



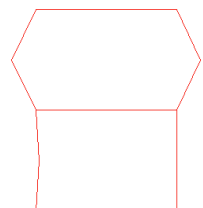
Mode 3 – 58.8 Hz



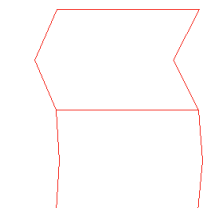
Mode 4 – 66.6 Hz



Mode 5 – 80.2 Hz



Mode 6 – 98.2 Hz

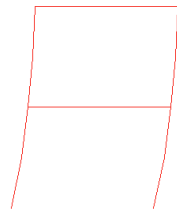
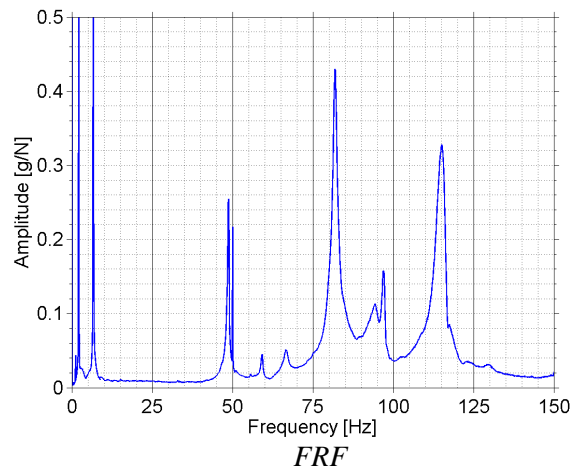


Mode 7 – 114.5 Hz

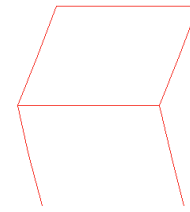
Figure B.15 Dynamic characteristics of laboratory structure with added mass at M4.



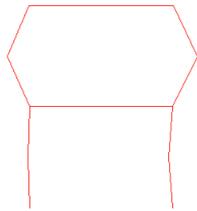
M5



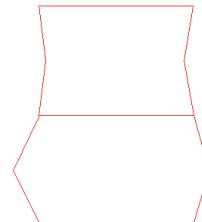
Mode 1 – 2.1 Hz



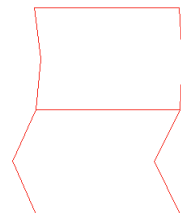
Mode 2 – 6.6 Hz



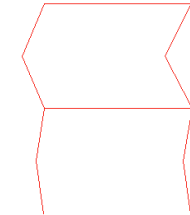
Mode 2a – 48.6 Hz



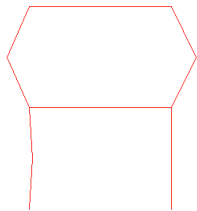
Mode 3 – 59.1 Hz



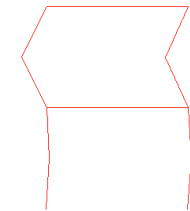
Mode 4 – 66.4 Hz



Mode 5 – 81.9 Hz



Mode 6 – 96.9 Hz

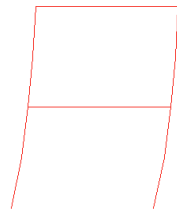
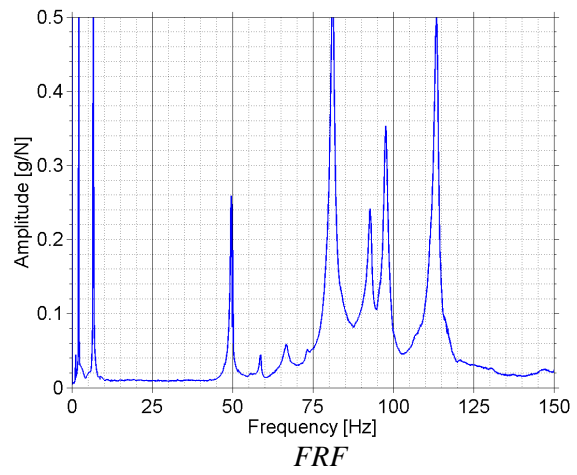


Mode 7 – 115.3 Hz

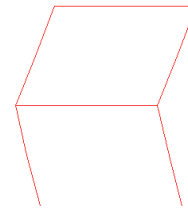
Figure B.16 Dynamic characteristics of laboratory structure with added mass at M5.



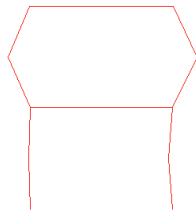
M6



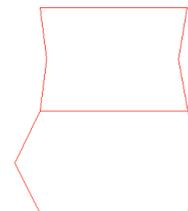
Mode 1 – 2.1 Hz



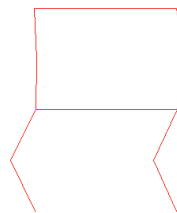
Mode 2 – 6.6 Hz



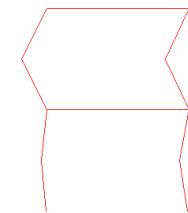
Mode 2a – 49.4 Hz



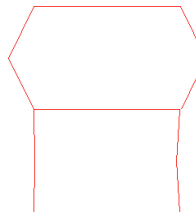
Mode 3 – 58.5 Hz



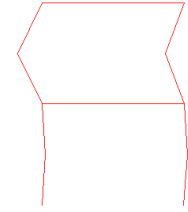
Mode 4 – 66.4 Hz



Mode 5 – 80.7 Hz



Mode 6 – 97.6 Hz



Mode 7 – 113.4 Hz

Figure B.17 Dynamic characteristics of laboratory structure with added mass at M6

APPENDIX C

NATURAL FREQUENCY CHANGES OF NUMERICAL BEAMS

Table C.1 Natural frequencies of the first seven flexural modes of the intact state and all damaged states of the numerical beams.

Numerical beam 1 - Natural frequencies [Hz]							
	Mode 1	Mode 2	Mode 3	Mode 4	Mode 5	Mode 6	Mode 7
Undamaged	20.55	51.98	128.08	205.89	334.21	452.46	631.88
4XL	20.55	51.98	128.05	205.89	334.20	452.46	631.77
4L	20.55	51.98	127.77	205.89	333.79	452.46	630.37
4M	20.52	51.98	126.70	205.89	332.36	452.46	625.95
4S	20.47	51.98	124.63	205.89	329.94	452.46	618.00

Numerical beam 2 - Natural frequencies [Hz]							
	Mode 1	Mode 2	Mode 3	Mode 4	Mode 5	Mode 6	Mode 7
Undamaged	20.55	51.98	128.08	205.89	334.21	452.46	631.88
5XL	20.55	51.97	128.08	205.86	334.20	452.42	631.81
5L	20.55	51.92	128.02	205.47	334.02	451.97	631.02
5M	20.53	51.77	127.80	204.27	333.42	450.57	628.71
5S	20.51	51.47	127.35	202.09	332.26	448.07	624.97

Numerical beam 3 - Natural frequencies [Hz]							
	Mode 1	Mode 2	Mode 3	Mode 4	Mode 5	Mode 6	Mode 7
Undamaged	20.55	51.98	128.08	205.89	334.21	452.46	631.88
6XL	20.55	51.95	128.07	205.89	334.20	452.35	630.22
6L	20.55	51.88	128.05	205.89	333.55	451.78	629.29
6M	20.55	51.57	127.83	205.89	332.89	450.44	626.81
6S	20.55	51.27	127.44	205.89	332.01	448.39	622.16

Numerical beam 4 - Natural frequencies [Hz]							
	Mode 1	Mode 2	Mode 3	Mode 4	Mode 5	Mode 6	Mode 7
Undamaged	20.55	51.98	128.08	205.89	334.21	452.46	631.88
7XL	20.54	51.88	127.96	205.14	333.67	452.19	630.19
7L	20.53	51.77	127.80	204.46	332.61	451.74	629.62
7M	20.50	51.67	127.40	203.32	330.57	450.52	629.22
7S	20.46	51.47	127.35	202.16	328.53	449.45	628.98

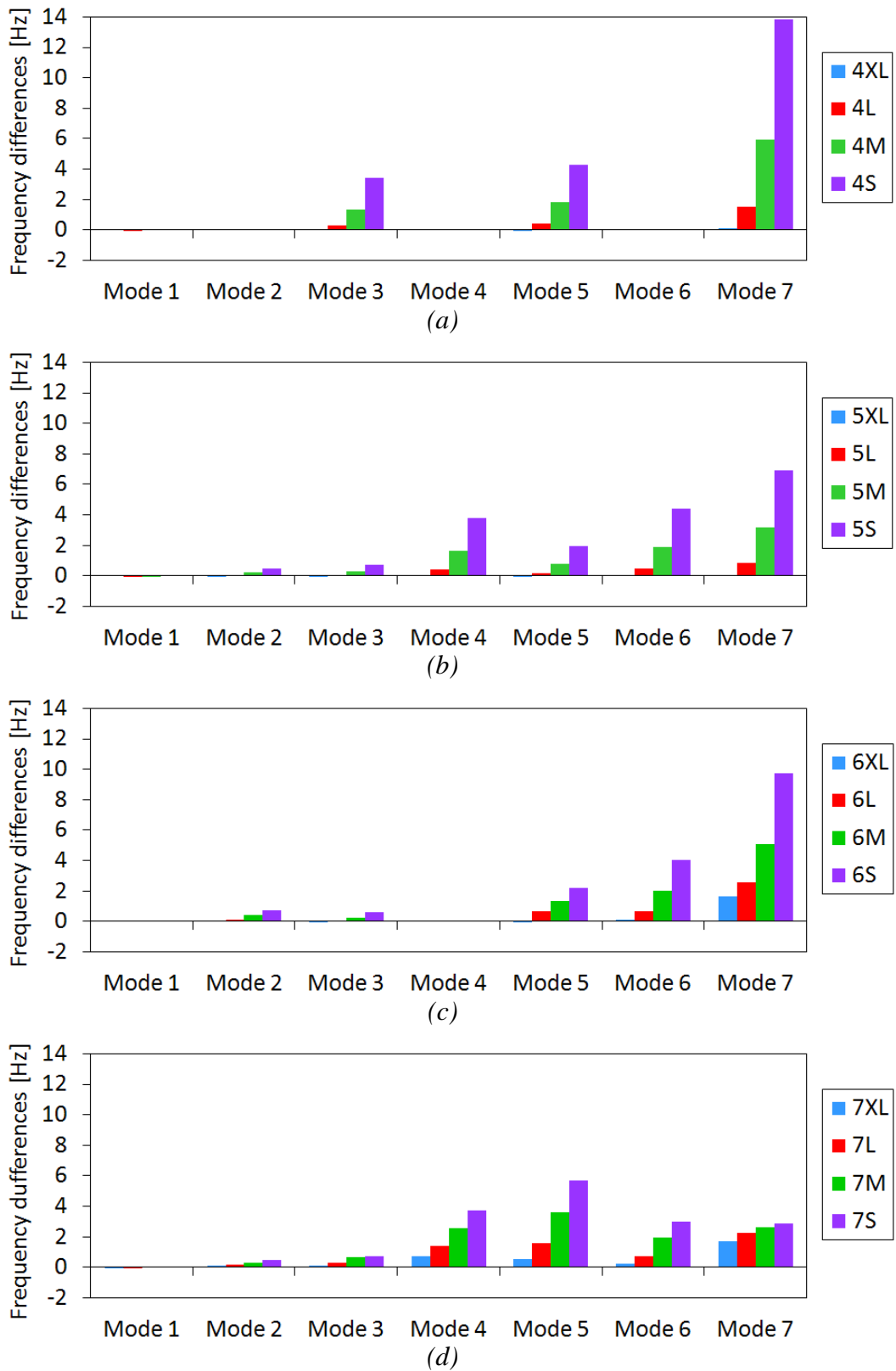


Figure C.1 Comparison of reduction in natural frequencies [%] of various damage cases of the numerical beam damaged at (a) location '4' (b) location '5', (c) location '6' and (d) location '7'.

APPENDIX D

VIBRATIONAL MODES OF NUMERICAL TWO- STOREY FRAMED STRUCTURE

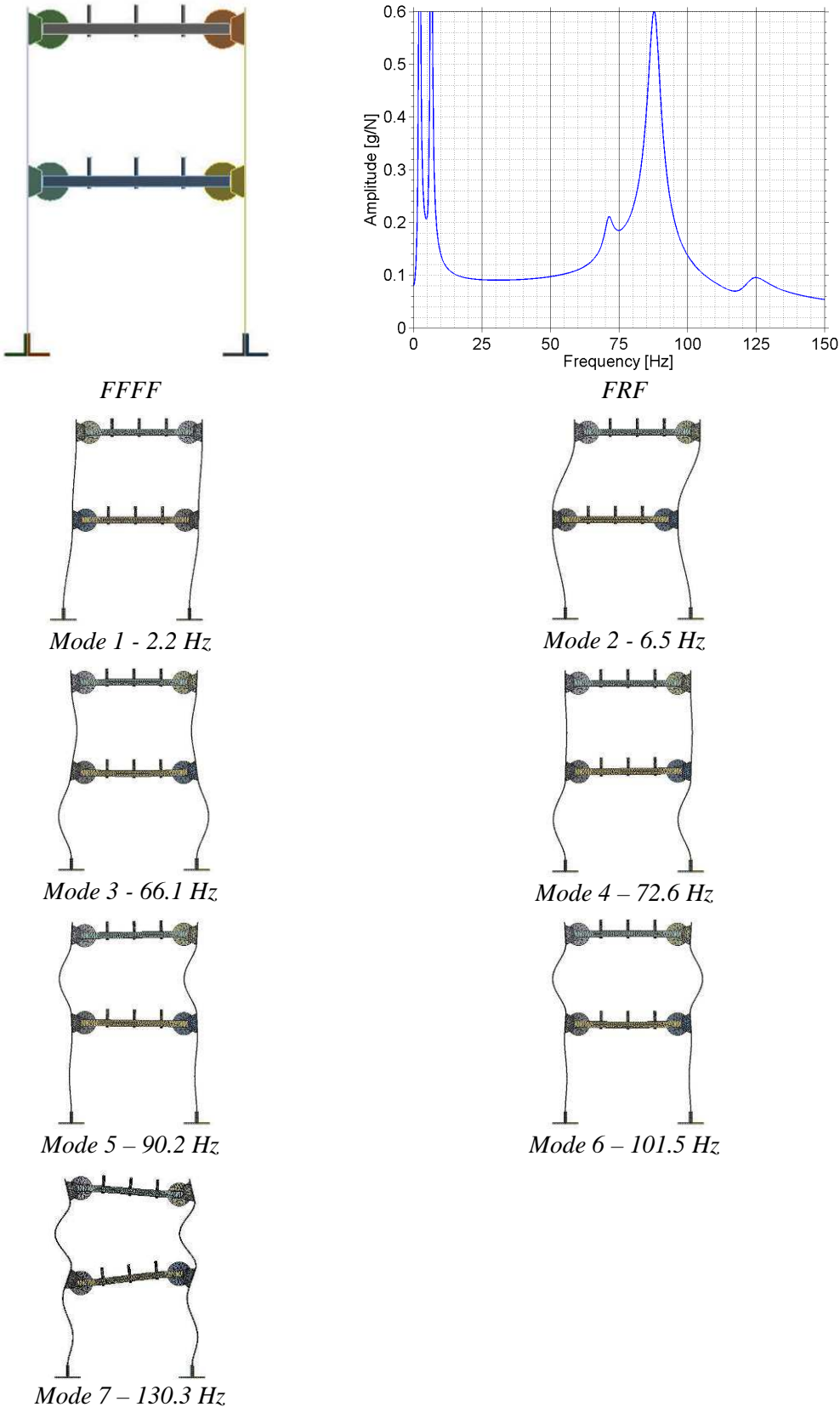


Figure D.1 Dynamic characteristics of numerical baseline structure (FFFF).

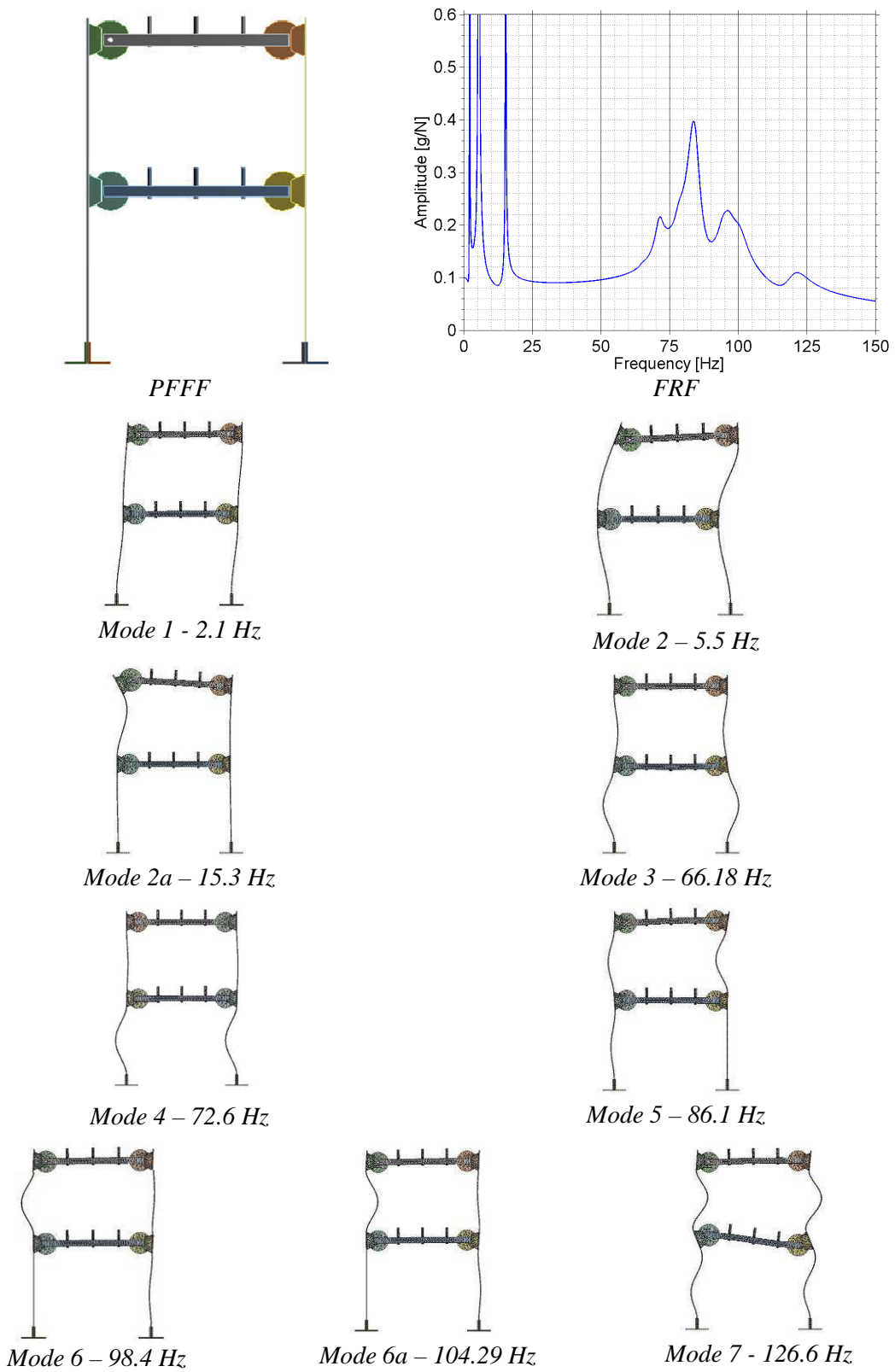


Figure D.2 Dynamic characteristics of numerical structure PFFF.

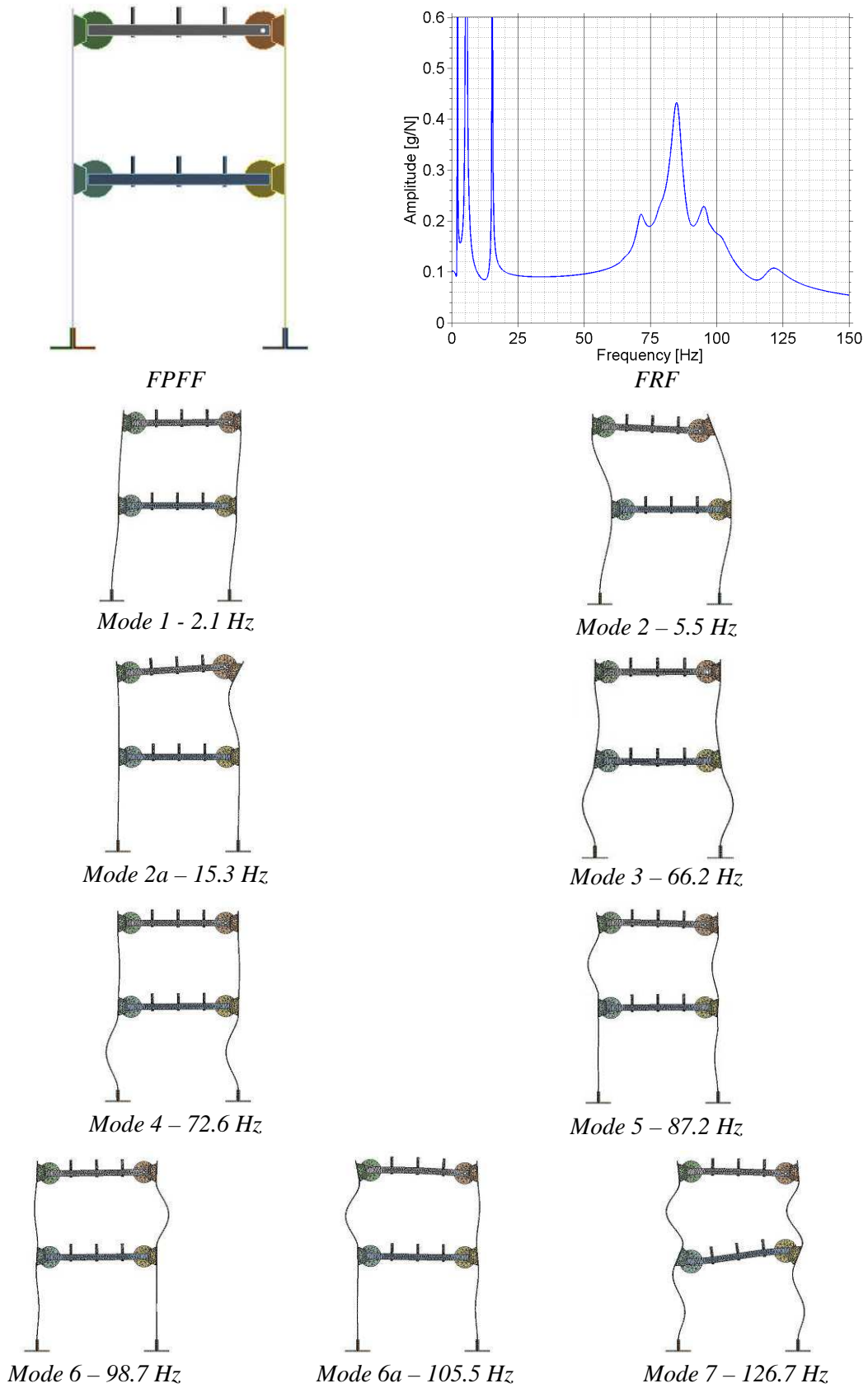


Figure D.3 Dynamic characteristics of numerical structure FPF.

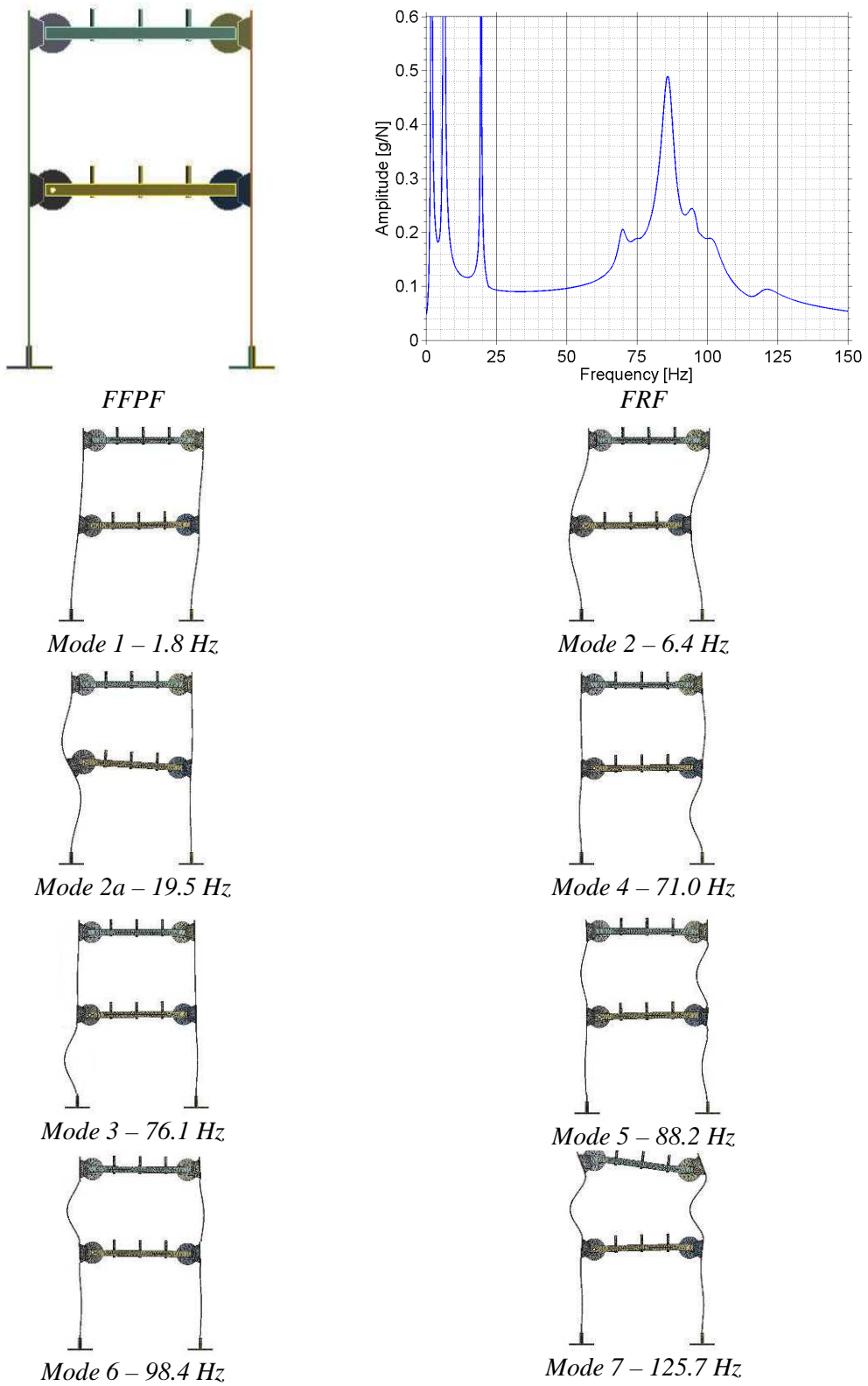


Figure D.4 Dynamic characteristics of numerical structure FFPF.

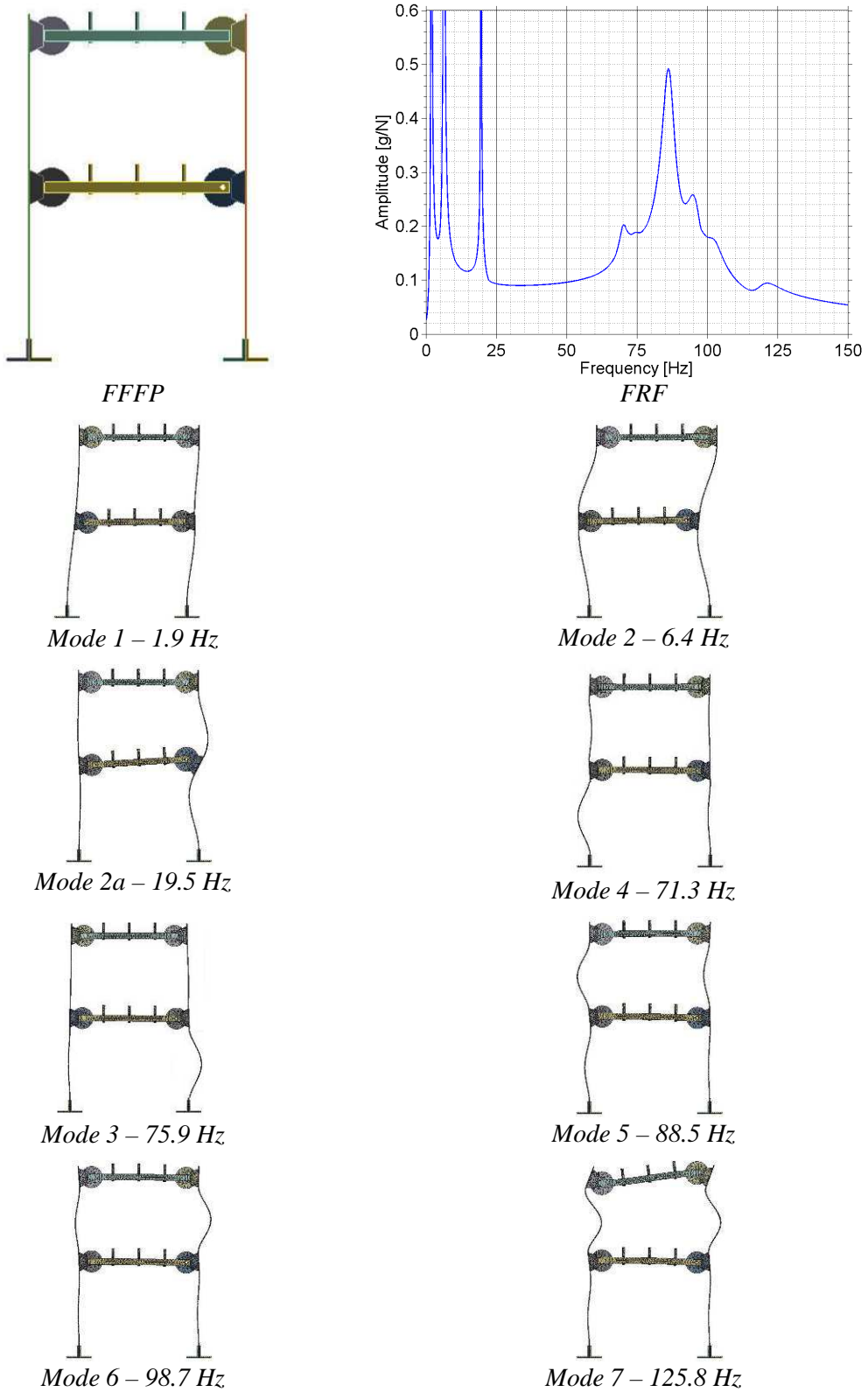


Figure D.5 Dynamic characteristics of numerical structure FFFP.

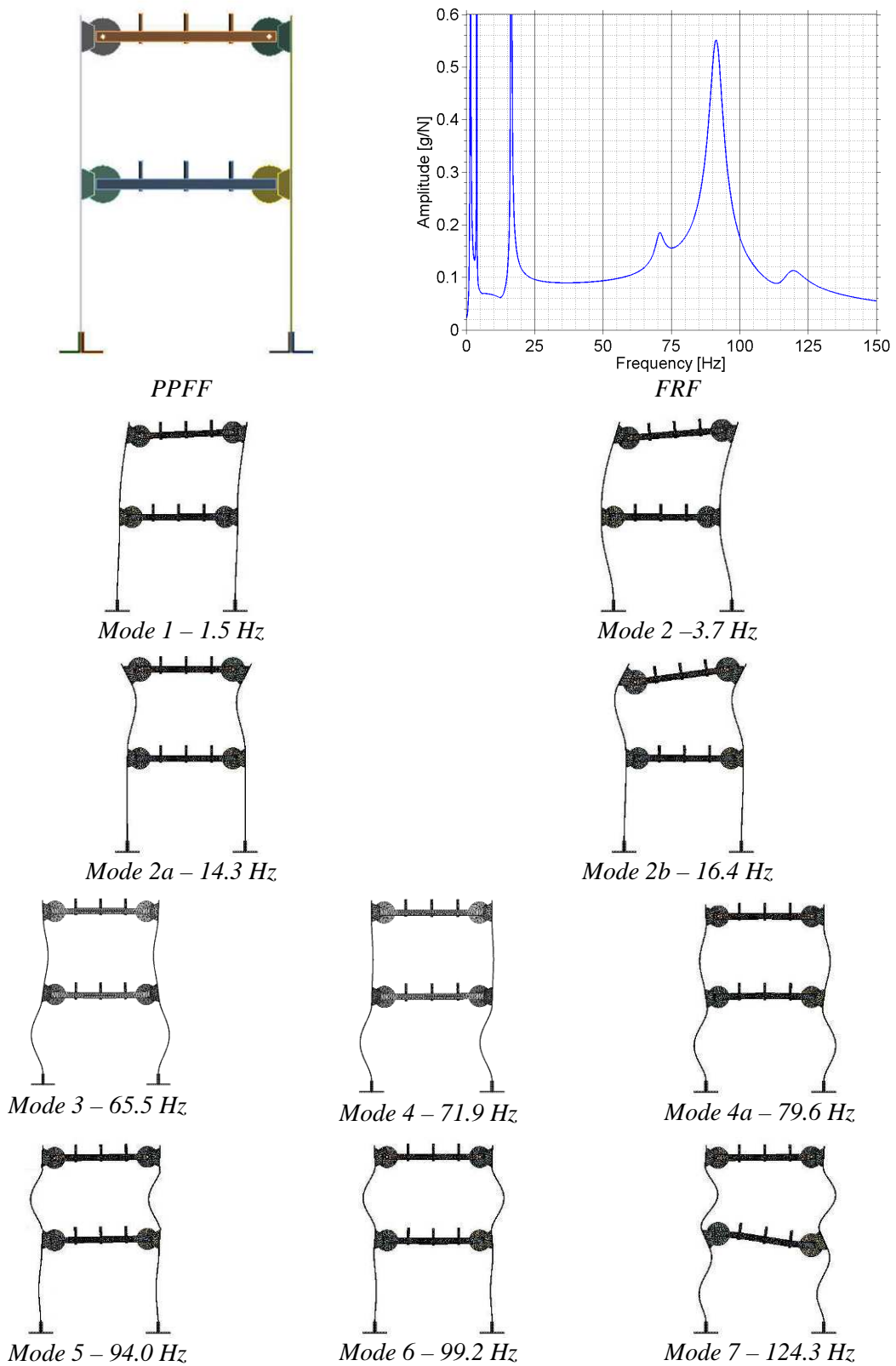


Figure D.6 Dynamic characteristics of laboratory structure PPF.

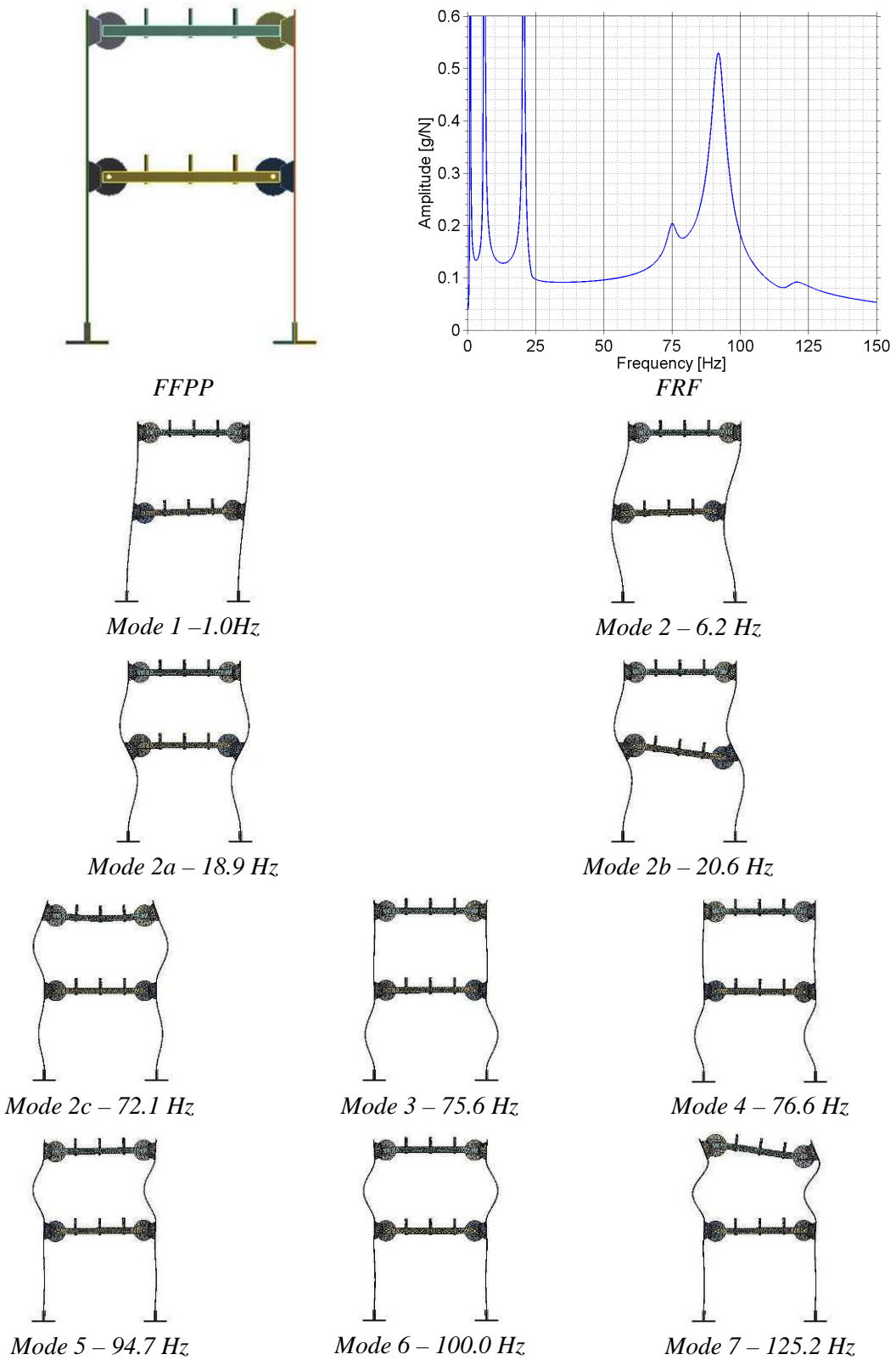


Figure D.7 Dynamic characteristics of laboratory structure FFPP.

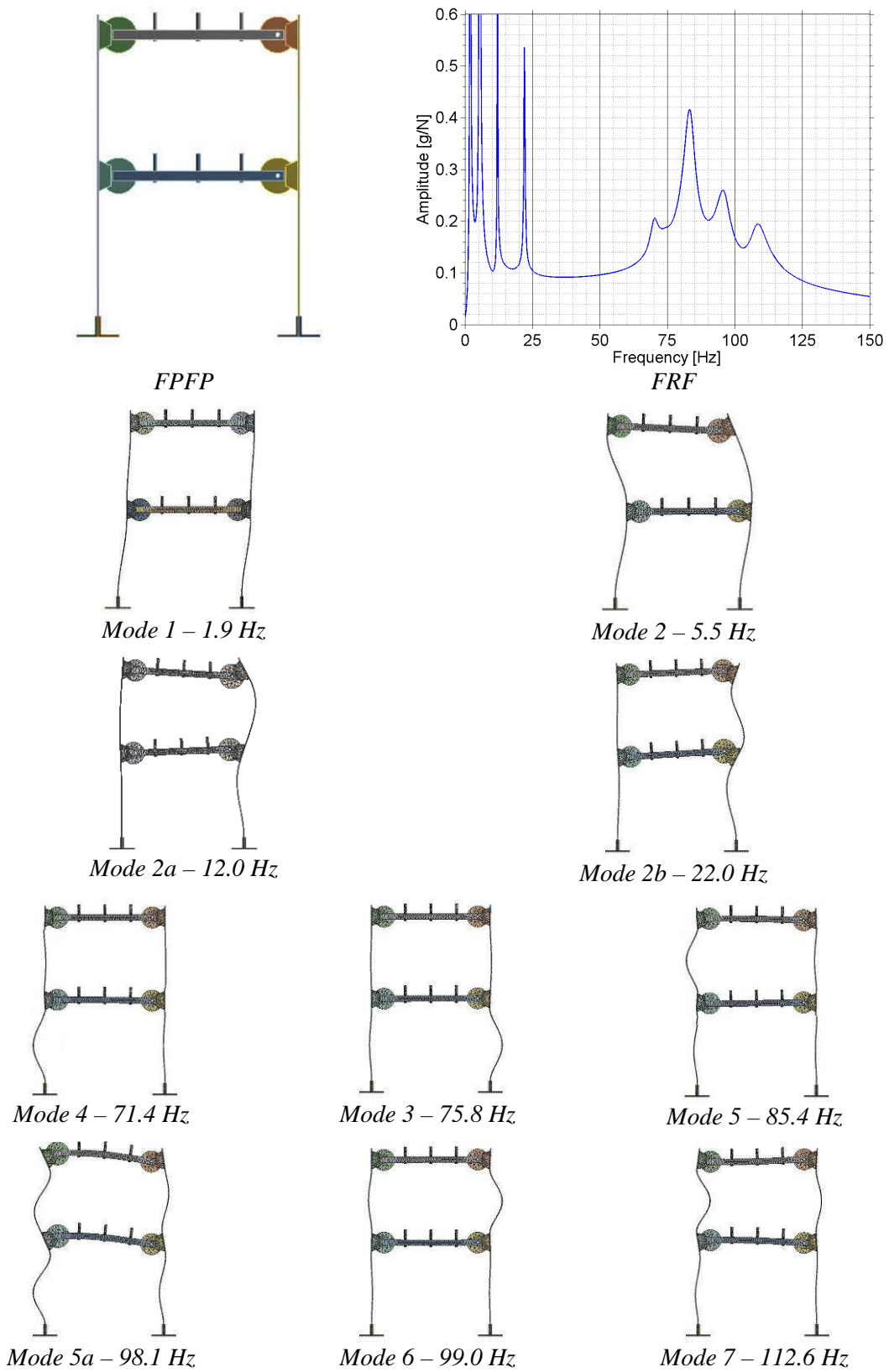


Figure D.8 Dynamic characteristics of numerical structure FFPF.

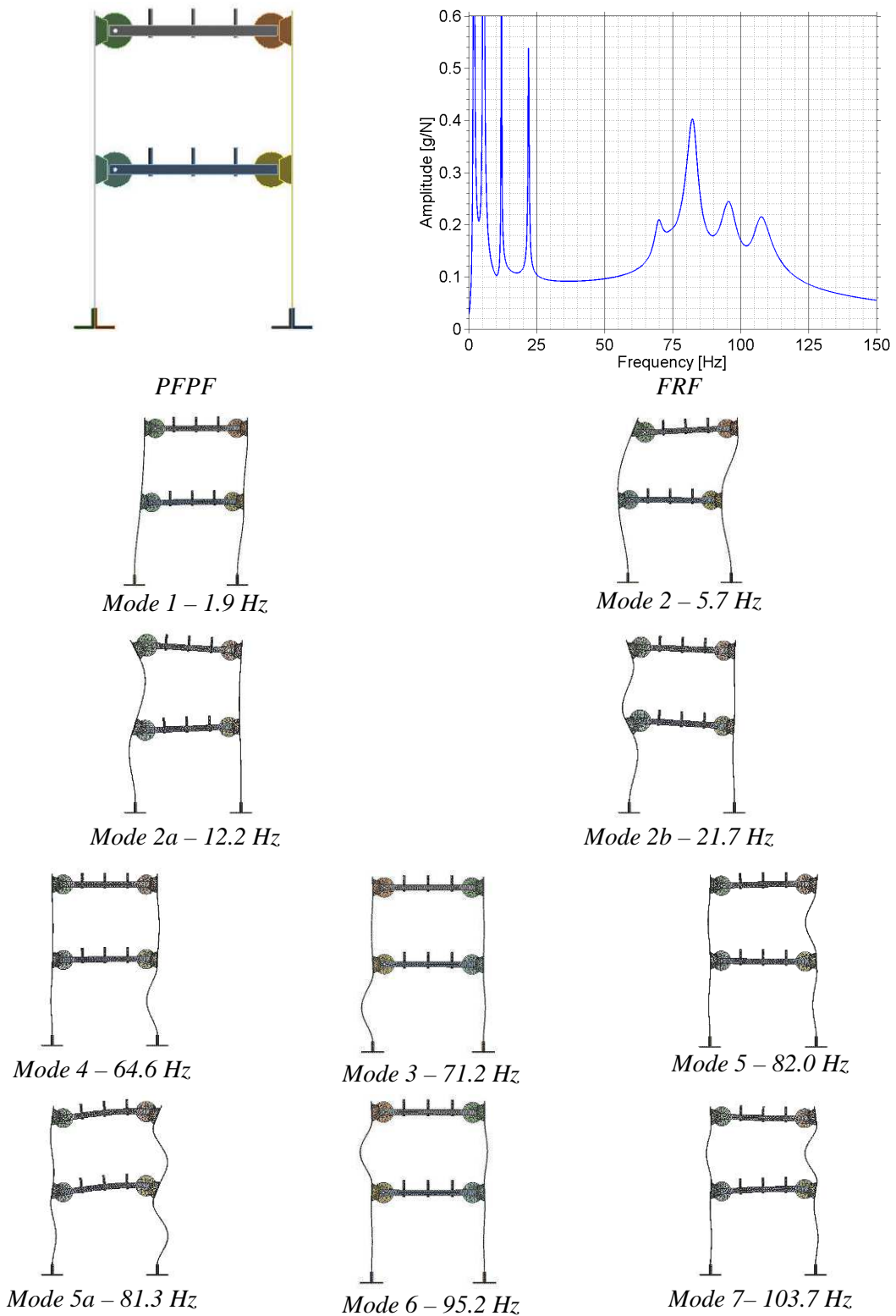


Figure D.9 Dynamic characteristics of numerical structure PFPF.

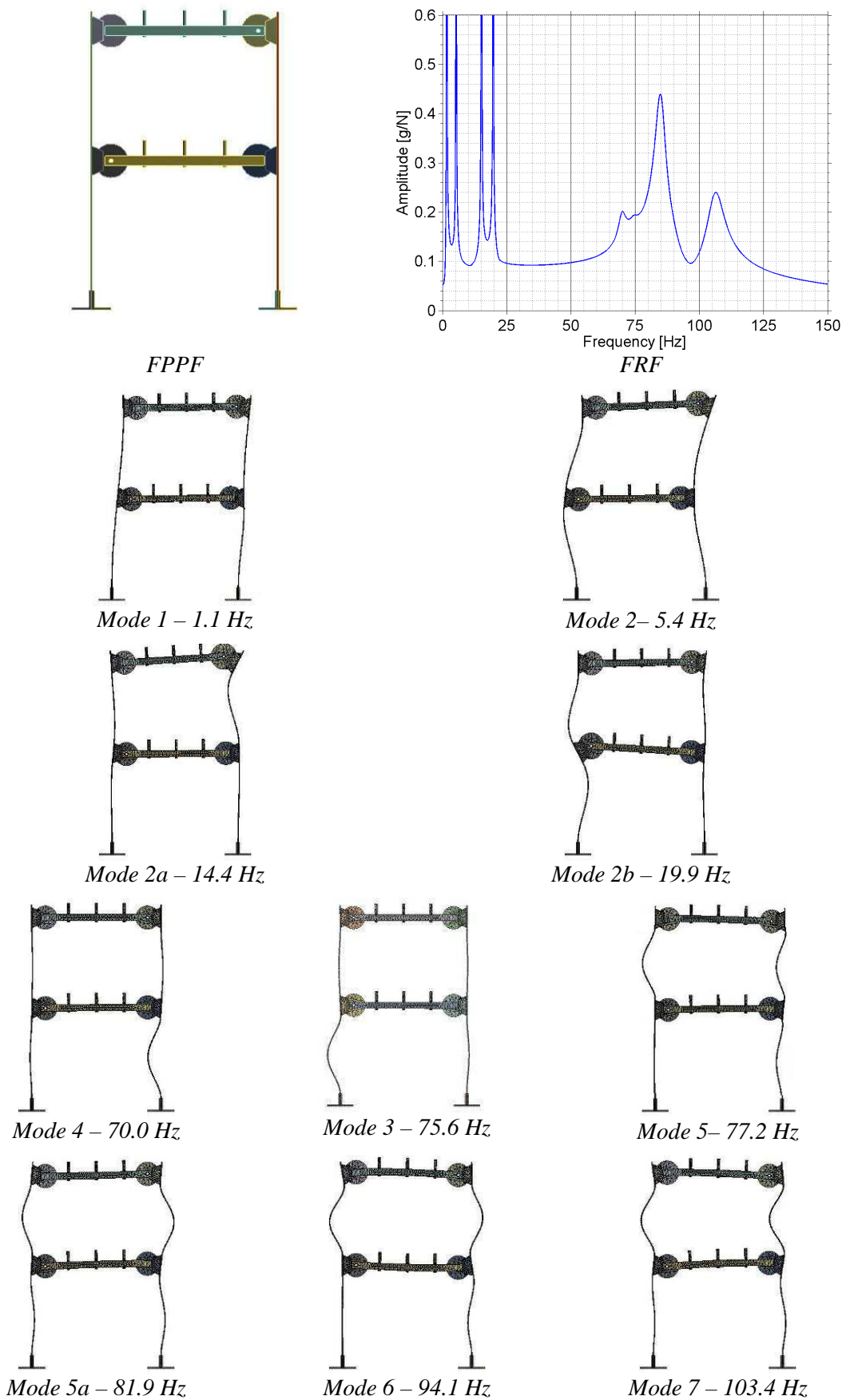


Figure D.10 Dynamic characteristics of numerical structure FPPF.

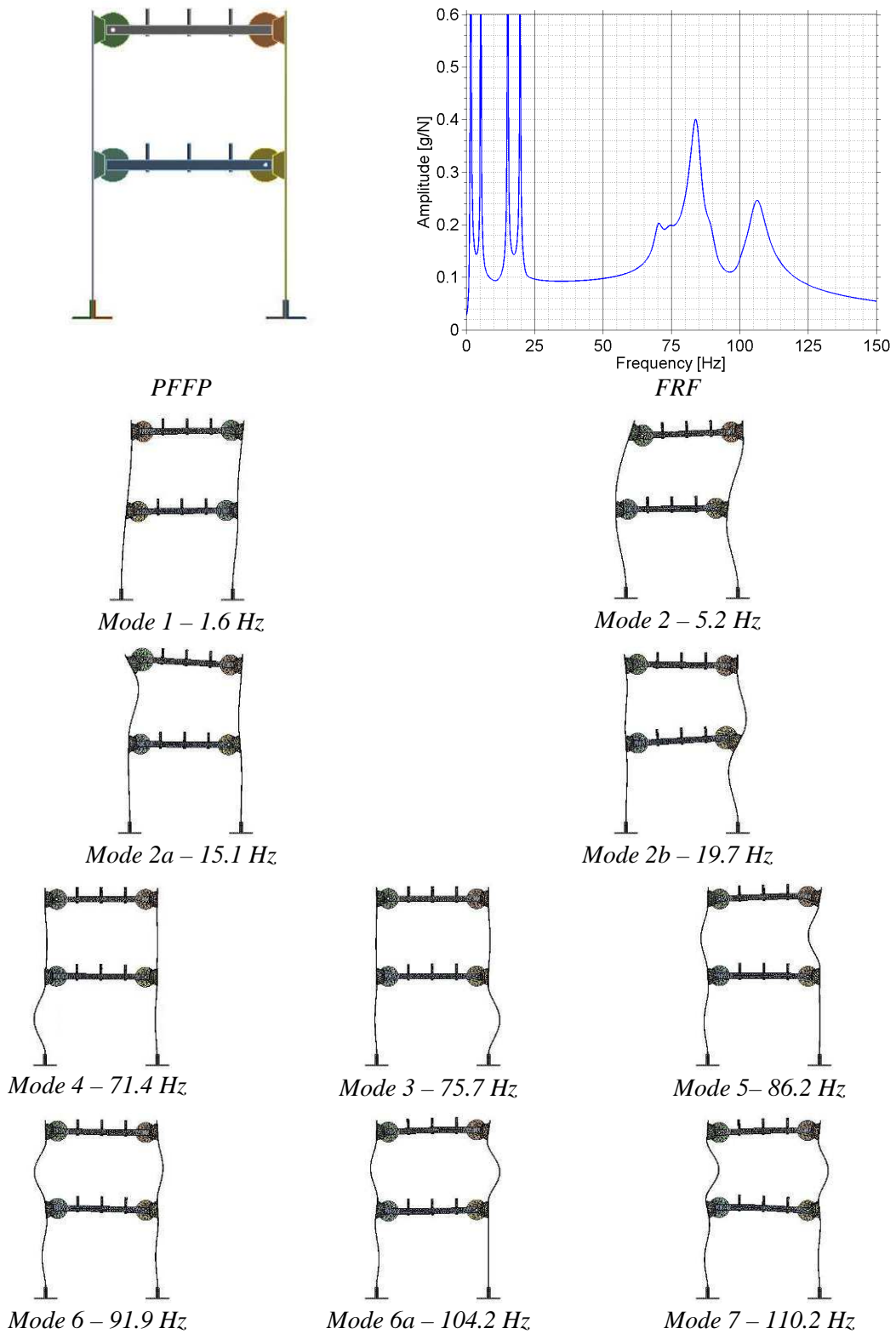


Figure D.11 Dynamic characteristics of numerical structure PFFP.

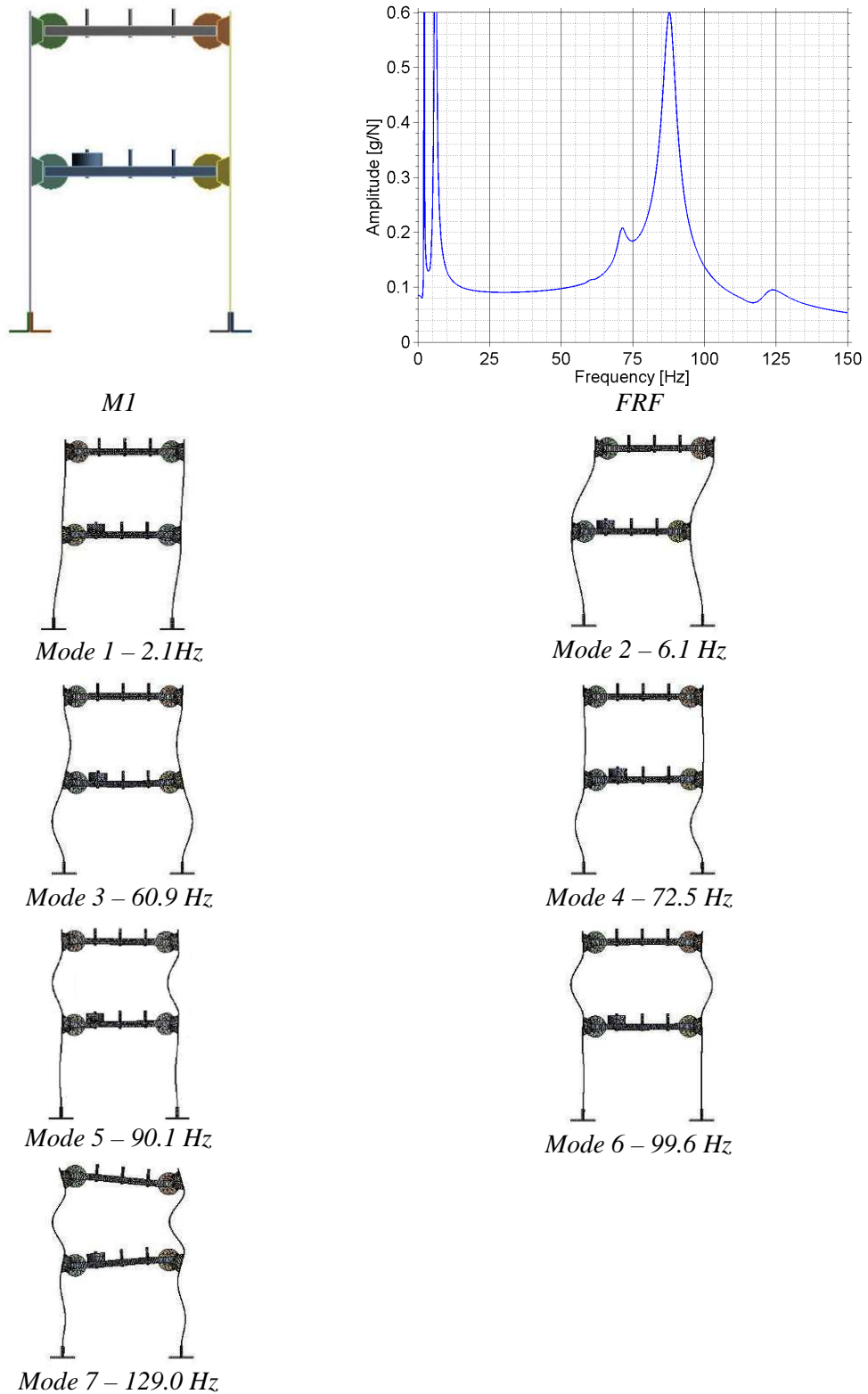
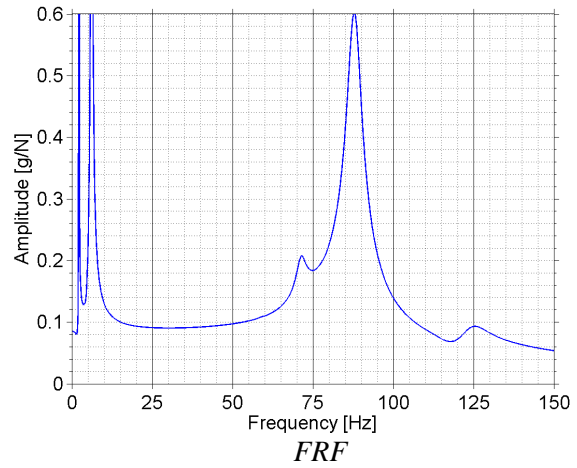
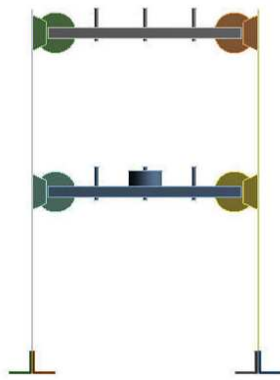
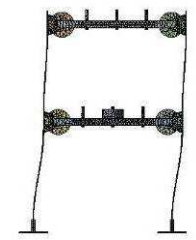


Figure D.12 Dynamic characteristics of numerical structure with added mass at M1.

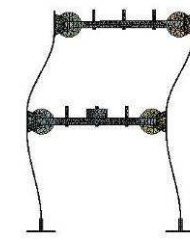


M2

FRF



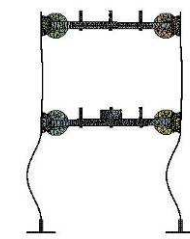
Mode 1 – 2.1 Hz



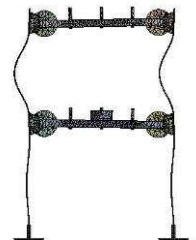
Mode 2 – 6.1 Hz



Mode 3 – 59.4 Hz



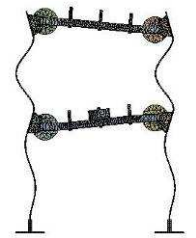
Mode 4 – 72.6 Hz



Mode 5 – 90.2 Hz



Mode 6 – 99.3 Hz



Mode 7 – 130.7 Hz

Figure D.13 Dynamic characteristics of numerical structure with added mass at M2.

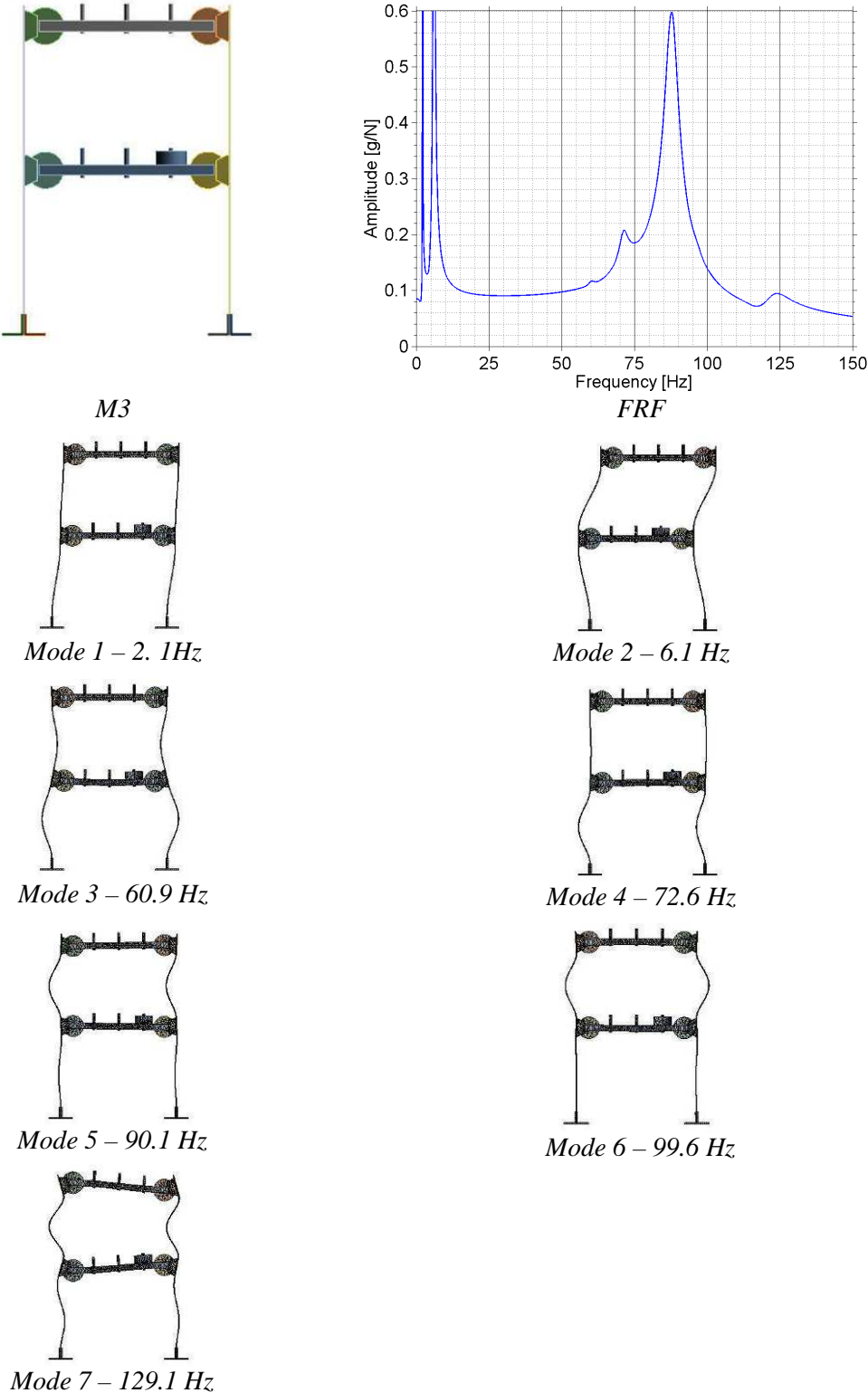
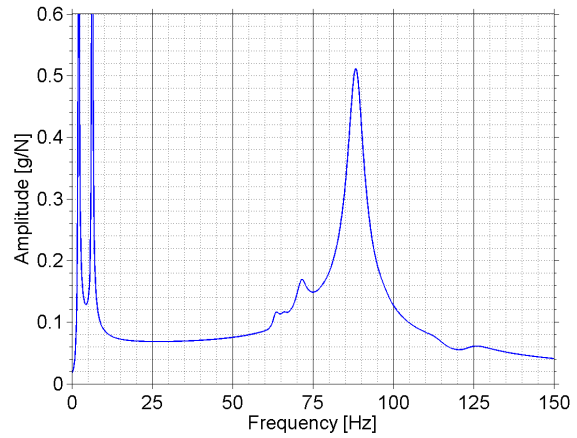
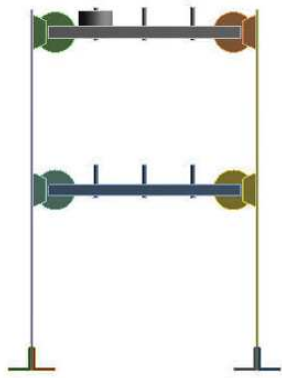


Figure D.14 Dynamic characteristics of numerical structure with added mass at M3.



M4

FRF

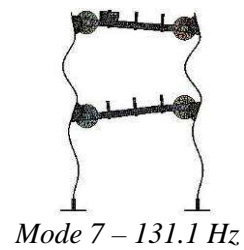
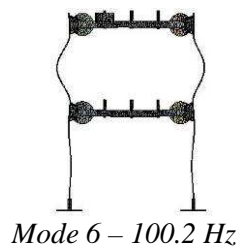
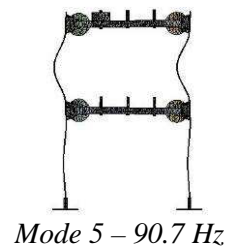
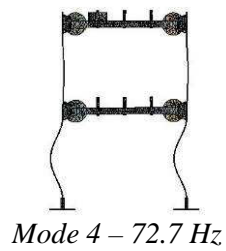
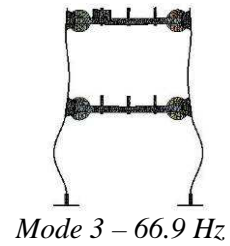
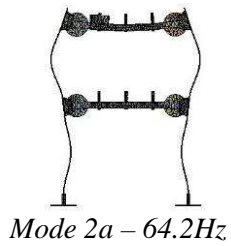
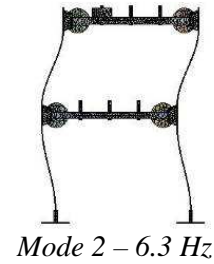
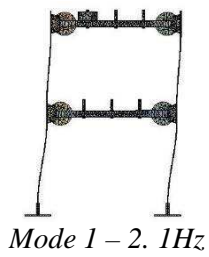


Figure D.15 Dynamic characteristics of numerical structure with added mass at M4.

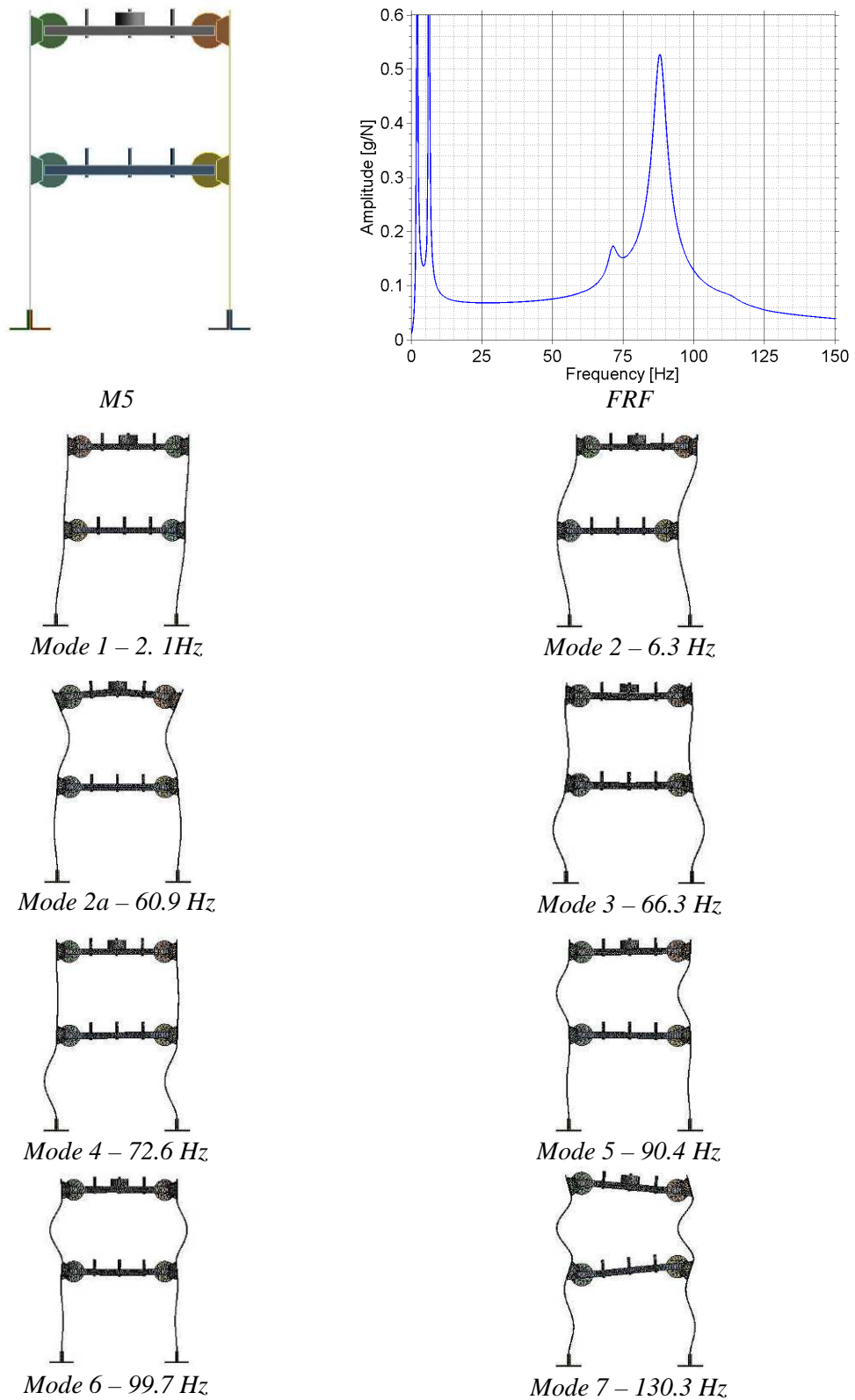
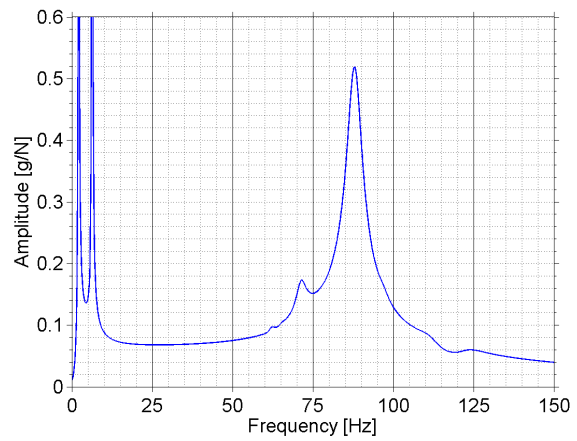
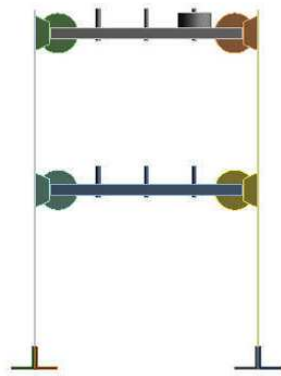
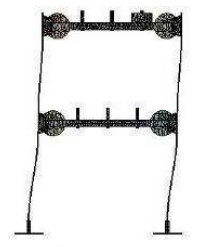


Figure D.16 Dynamic characteristics of numerical structure with added mass at M5.

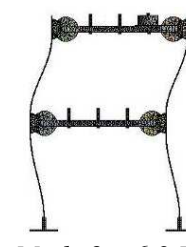


M6

FRF



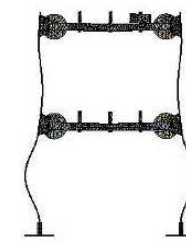
Mode 1 – 2.1 Hz



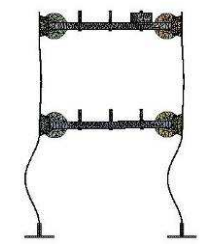
Mode 2 – 6.3 Hz



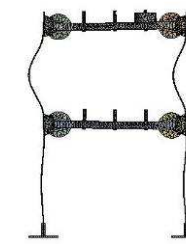
Mode 2a – 62.8 Hz



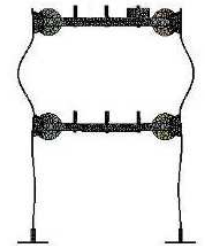
Mode 3 – 66.4 Hz



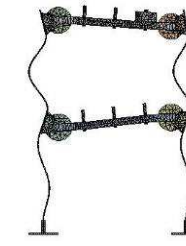
Mode 4 – 72.6 Hz



Mode 5 – 90.3 Hz



Mode 6 – 100.0 Hz



Mode 7 – 129.0 Hz

Figure D.17 Dynamic characteristics of numerical structure with added mass at M6.

APPENDIX E

DAMAGE INDEX VALUES OF NUMERICAL NOISE-FREE BEAM SIMULATIONS

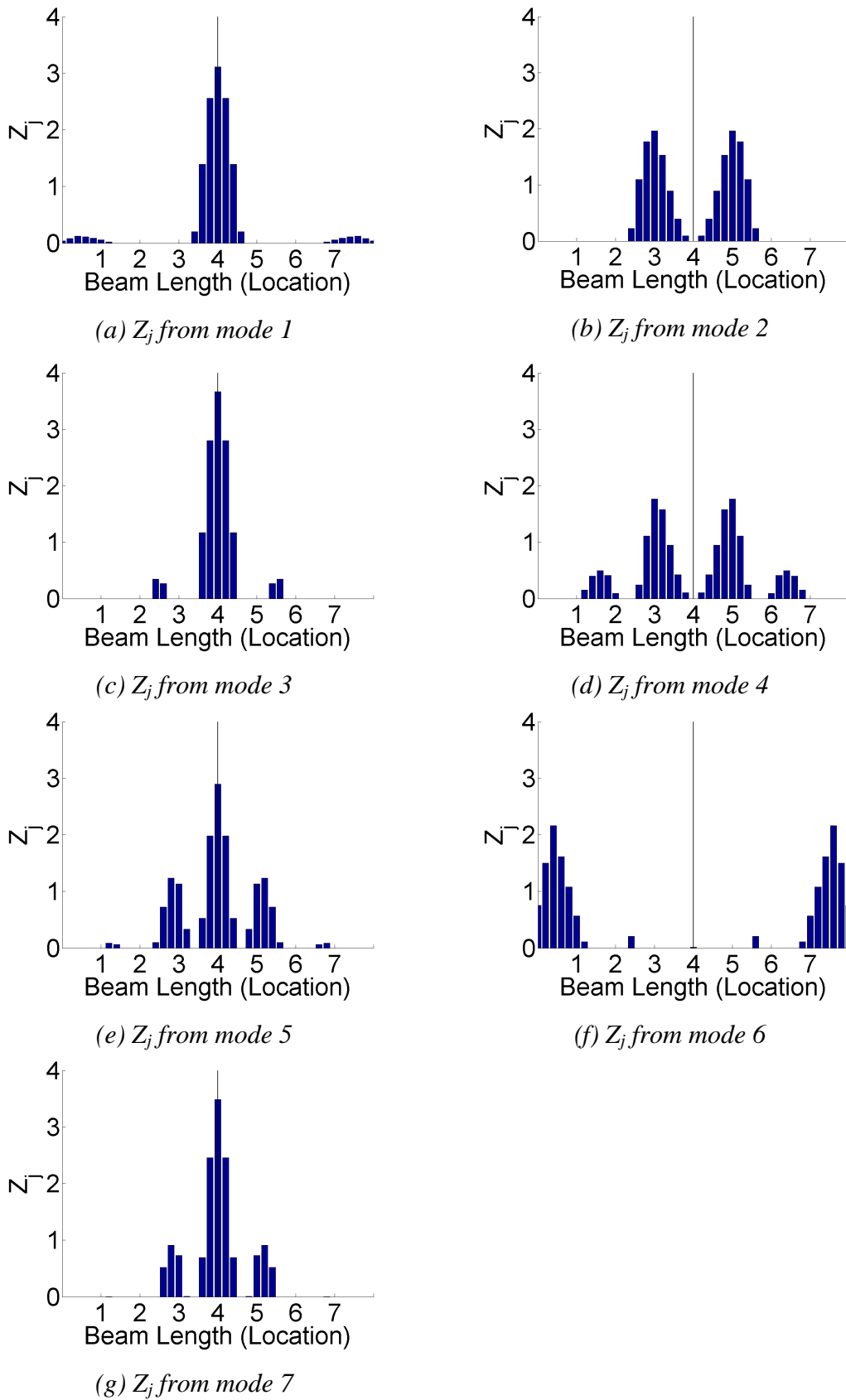


Figure E.1 Z_j values derived from modes 1 to 7 of numerical noise-free simulations of a beam with medium size damage at location '4'.

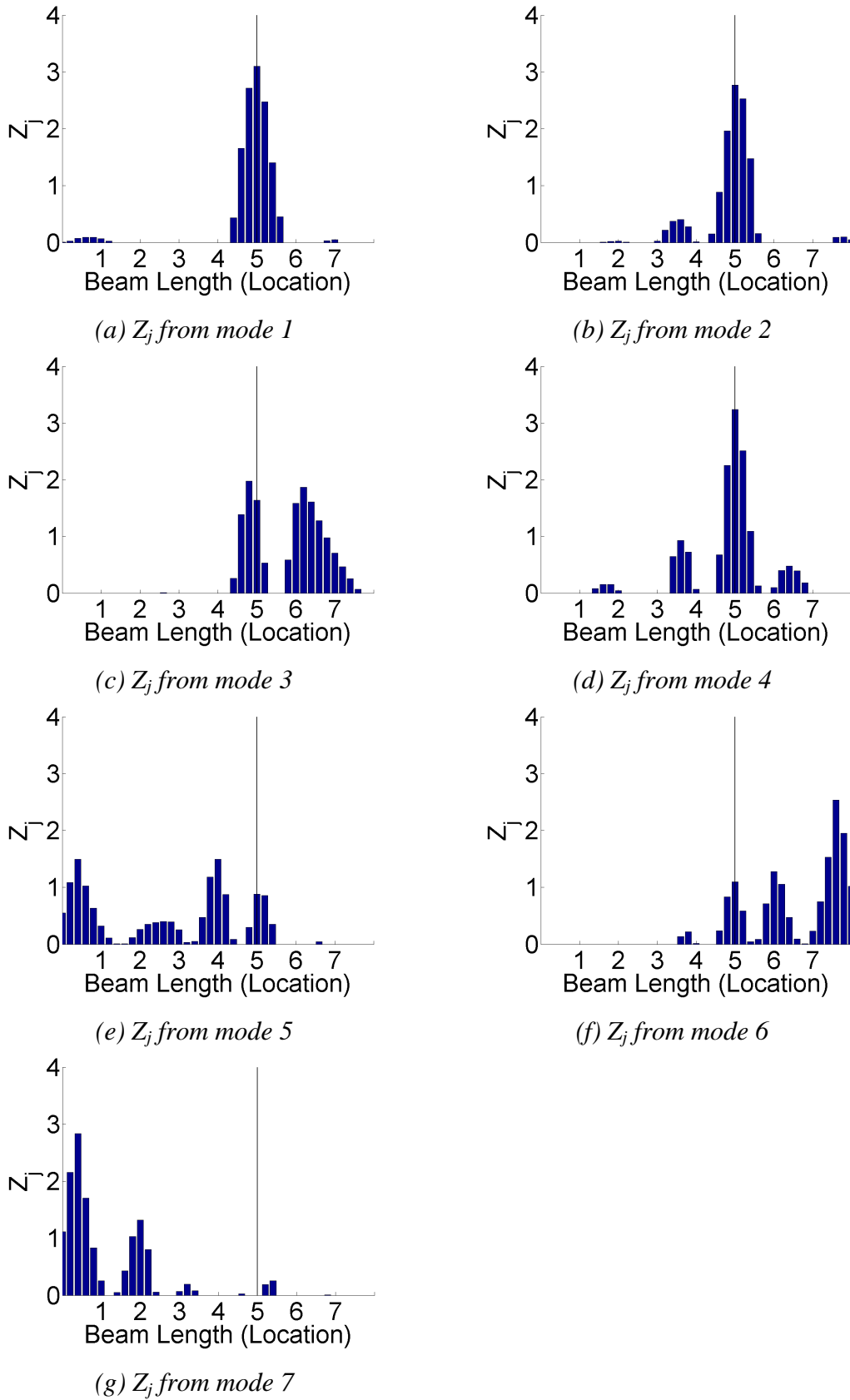


Figure E.2 Z_j values derived from modes 1 to 7 of numerical noise-free simulations of a beam with medium size damage at location '5'.

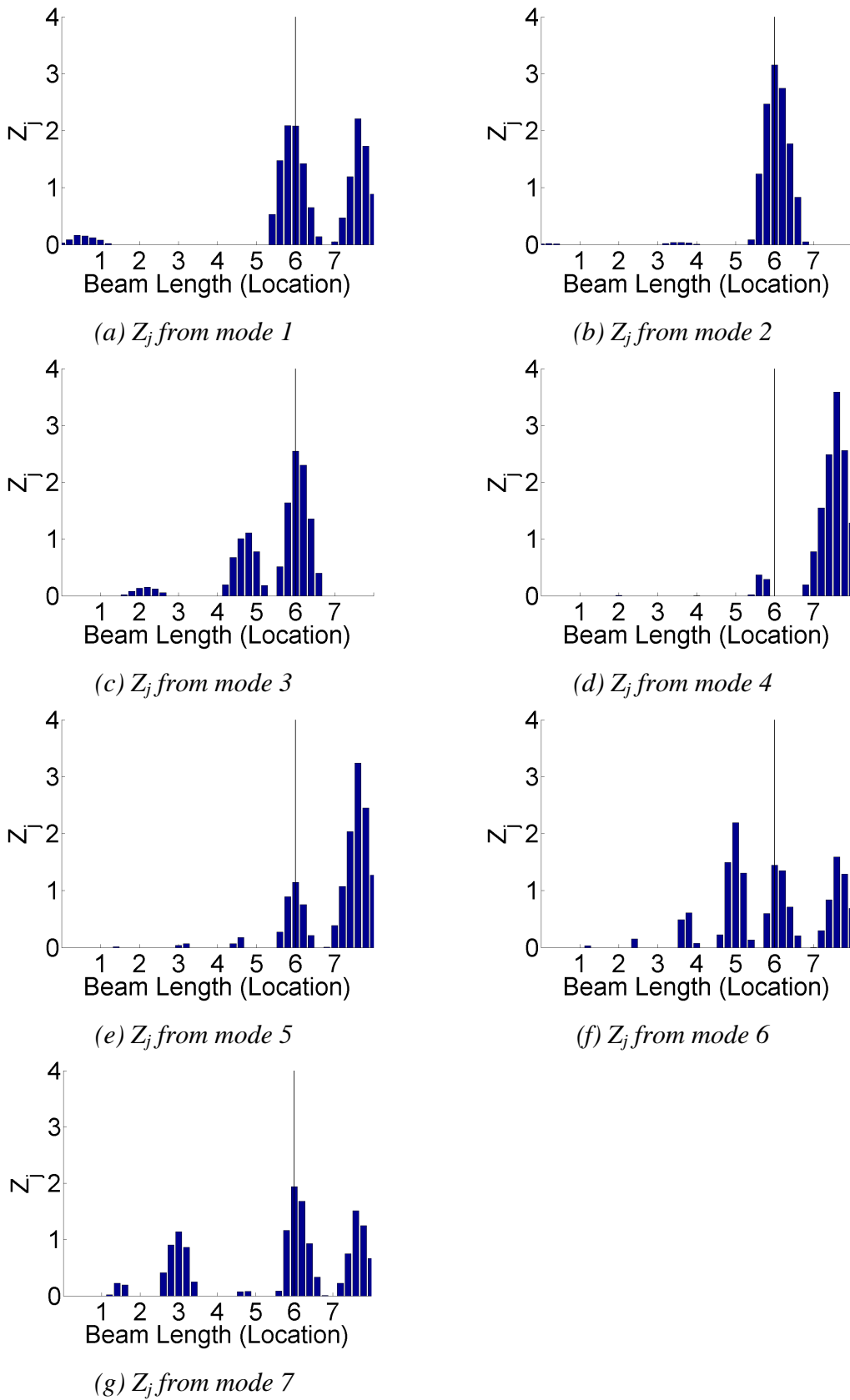


Figure E.3 Z_j values derived from modes 1 to 7 of numerical noise-free simulations of a beam with medium size damage at location '6'.

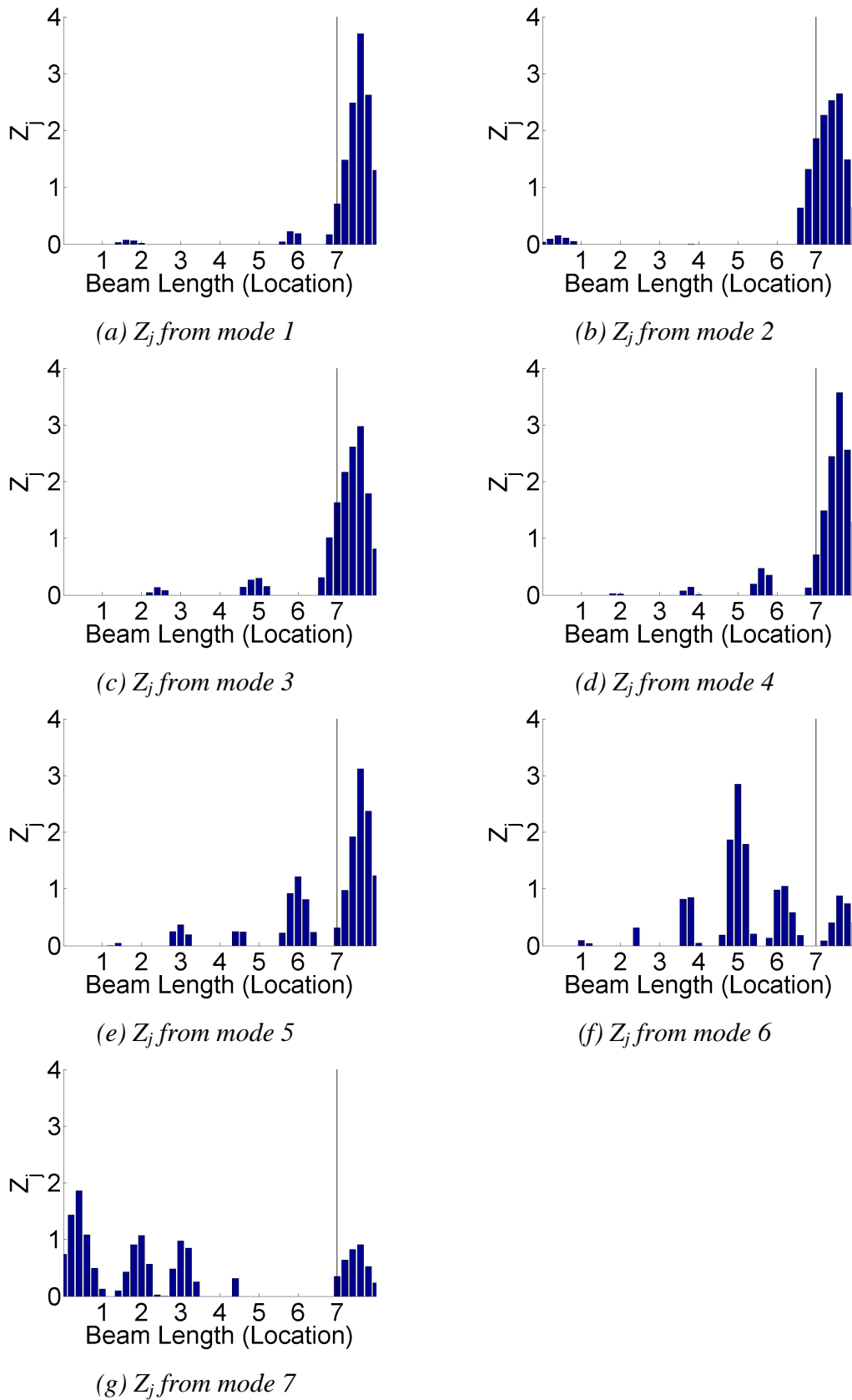


Figure E.4 Z_j values derived from modes 1 to 7 of numerical noise-free simulations of a beam with medium size damage at location '7'.

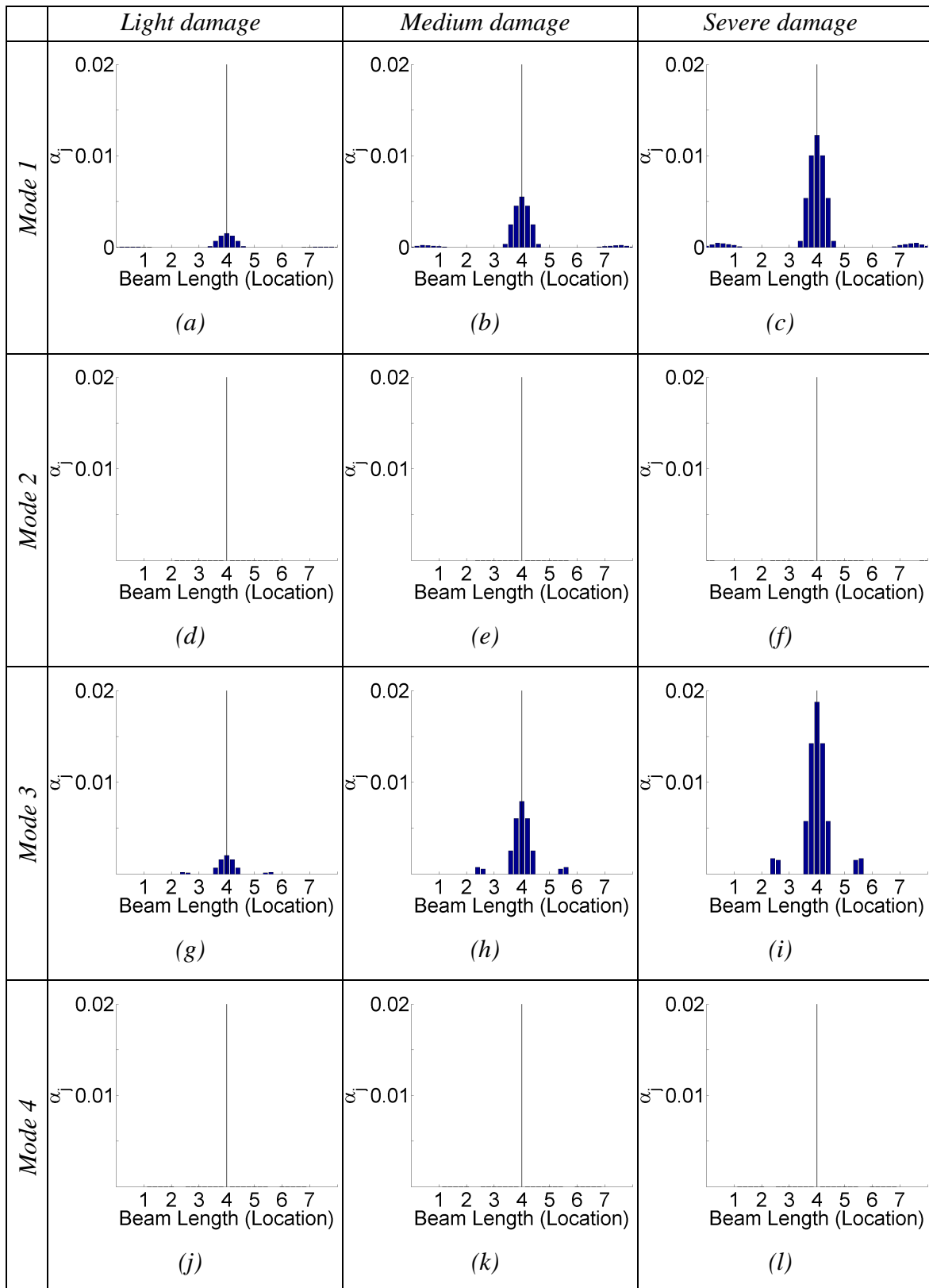


Figure E.5 a_j values of numerical noise-free simulations of a beam damaged at location '4' of light, medium and severe size, respectively. a_j values are derived from (a) to (c) mode 1, (d) to (f) mode 2, (g) to (i) mode 3, and (j) to (l) mode 4.

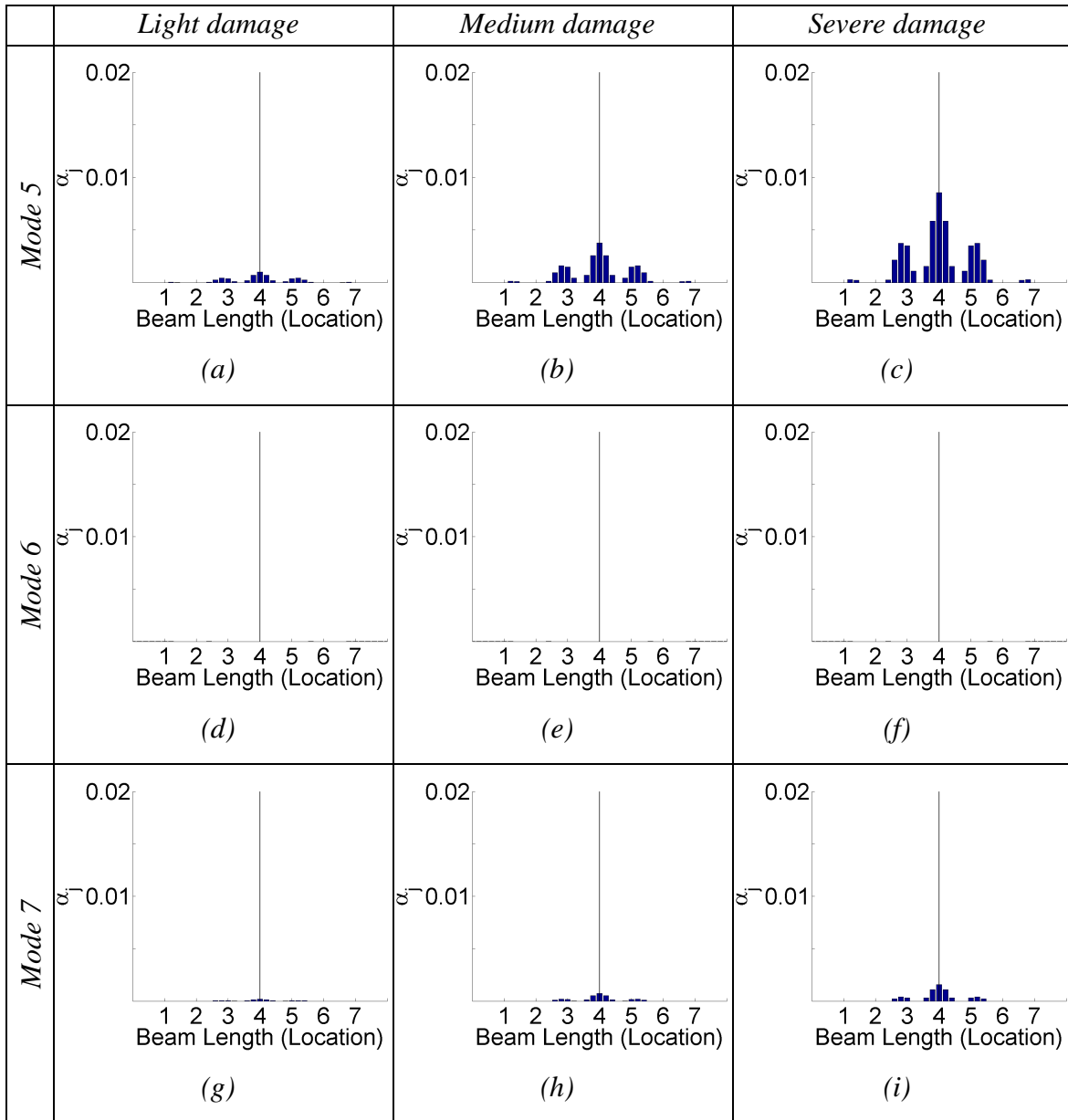


Figure E.6 α_j values of numerical noise-free simulations of a beam damaged at location '4' of light, medium and severe size, respectively. α_j values are derived from (a) to (c) mode 5, (d) to (f) mode 6, and (g) to (i) mode 7.

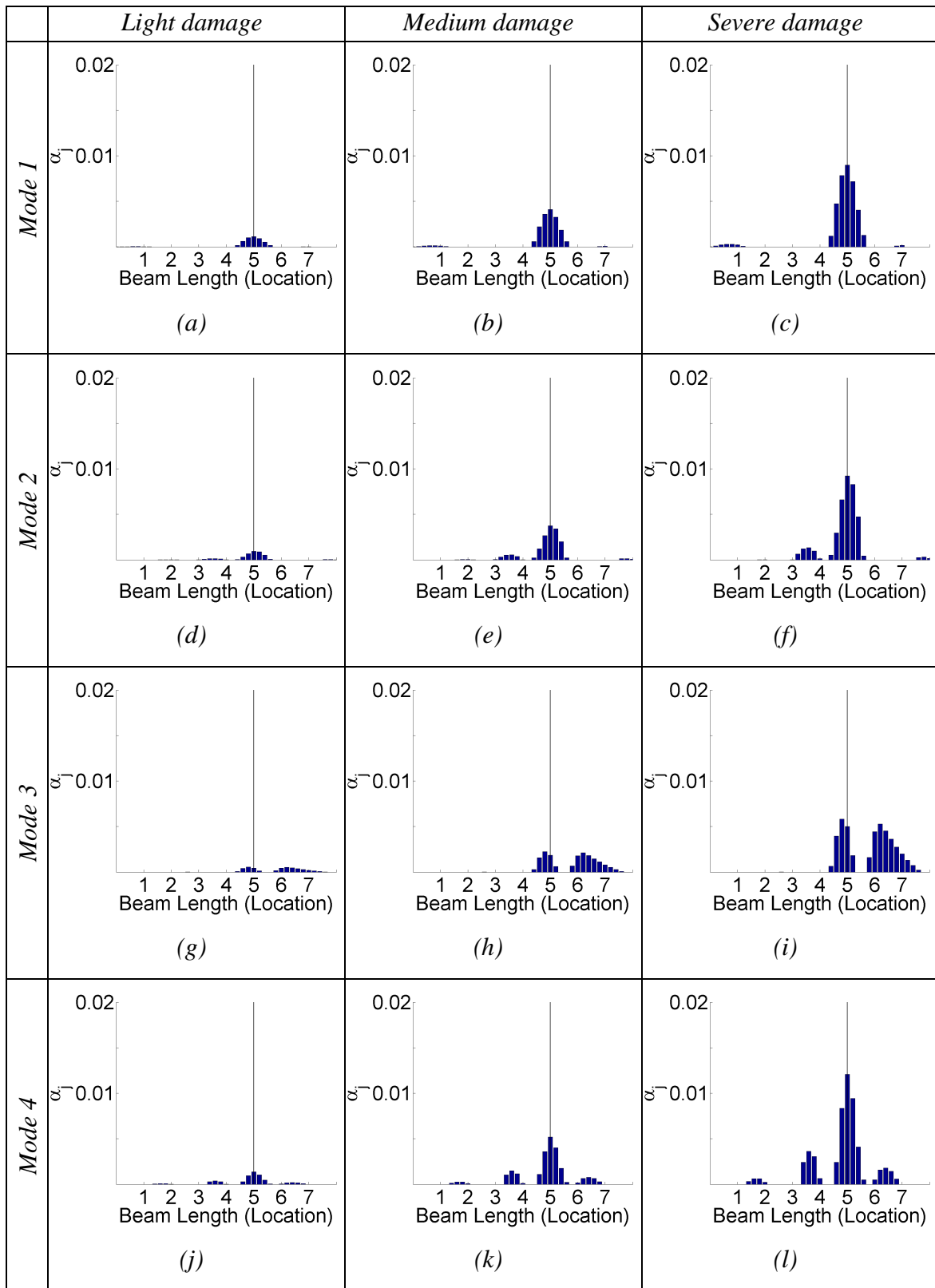


Figure E.7 α_j values of numerical noise-free simulations of a beam damaged at location '5' of light, medium and severe size, respectively. α_j values are derived from (a) to (c) mode 1, (d) to (f) mode 2, (g) to (i) mode 3, and (j) to (l) mode 4.

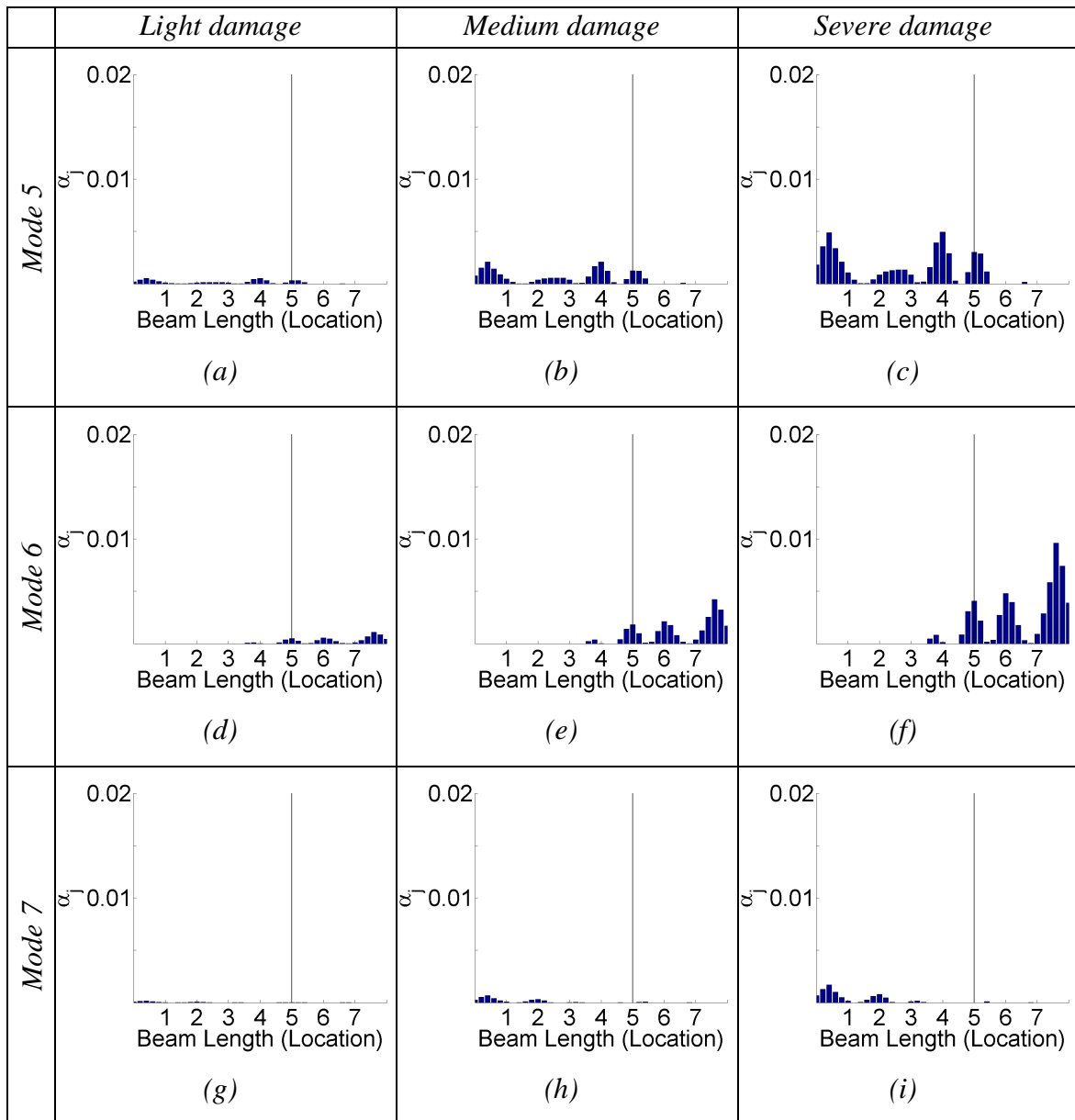


Figure E.8 α_j values of numerical noise-free simulations of a beam damaged at location '5' of light, medium and severe size, respectively. α_j values are derived from (a) to (c) mode 5, (d) to (f) mode 6, and (g) to (i) mode 7.

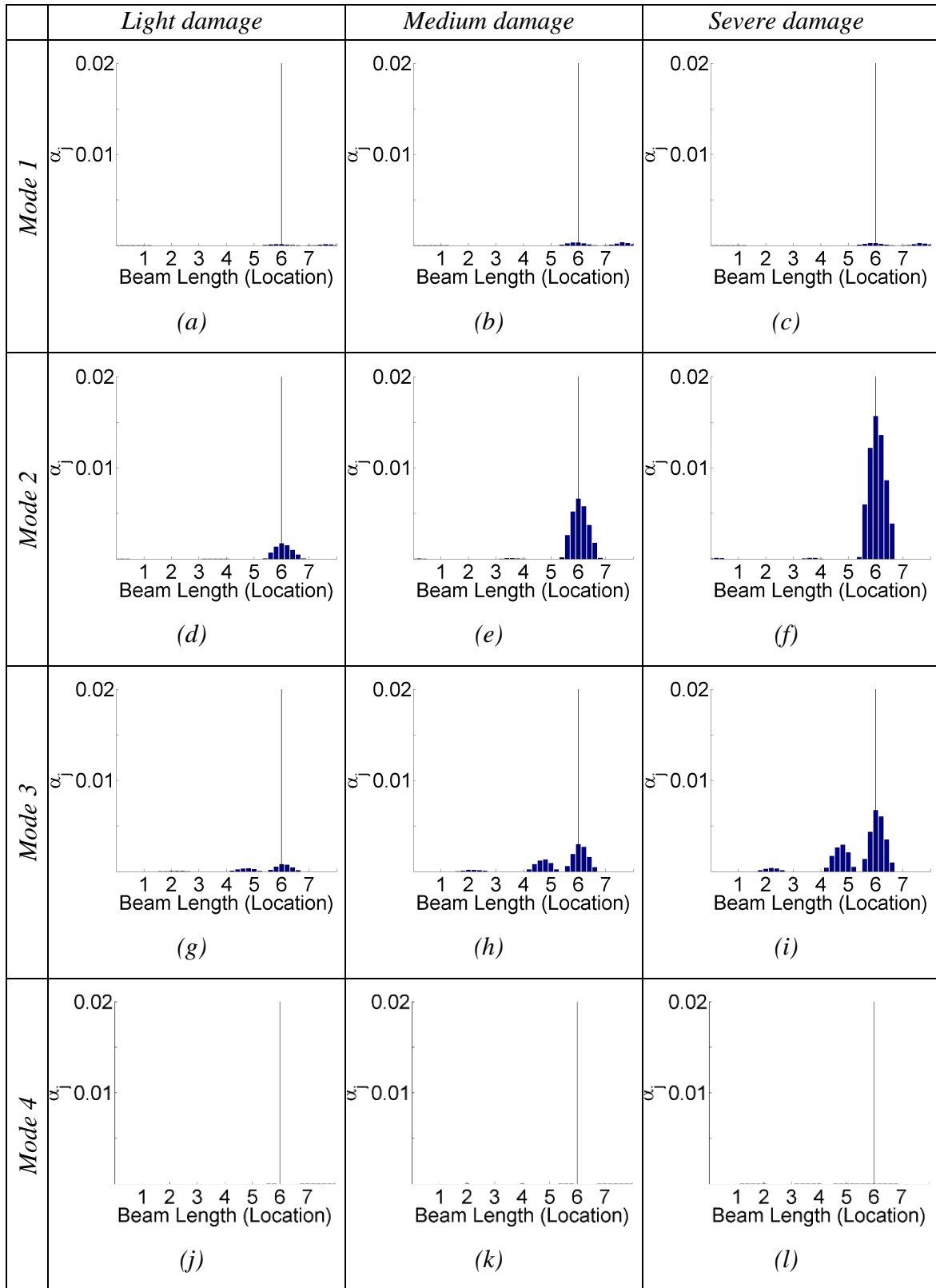


Figure E.9 α_j values of numerical noise-free simulations of a beam damaged at location '6' of light, medium and severe size, respectively. α_j values are derived from (a) to (c) mode 1, (d) to (f) mode 2, (g) to (i) mode 3, and (j) to (l) mode 4.

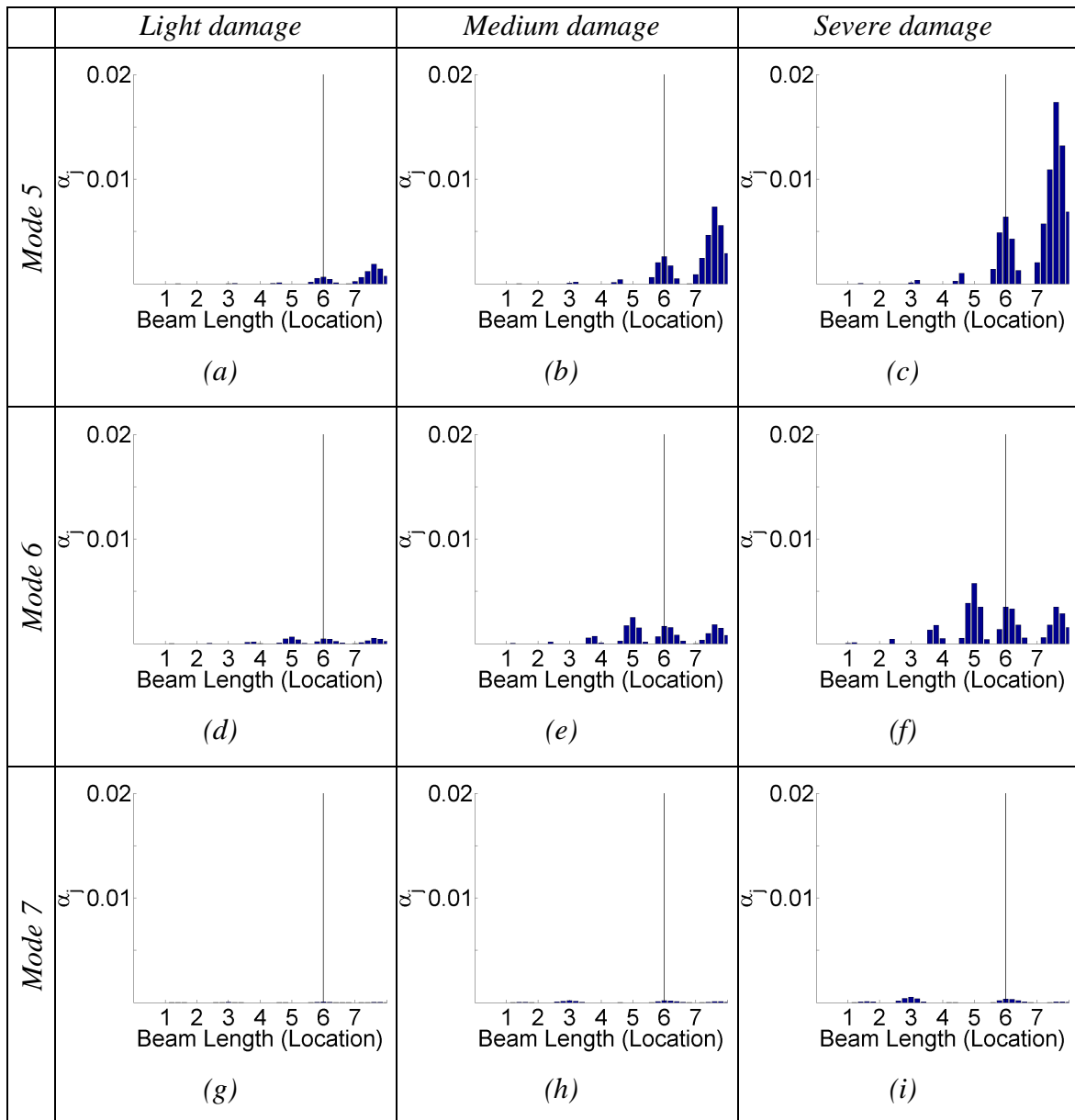


Figure E.10 α_j values of numerical noise-free simulations of a beam damaged at location '6' of light, medium and severe size, respectively. α_j values are derived from (a) to (c) mode 5, (d) to (f) mode 6, and (g) to (i) mode 7.

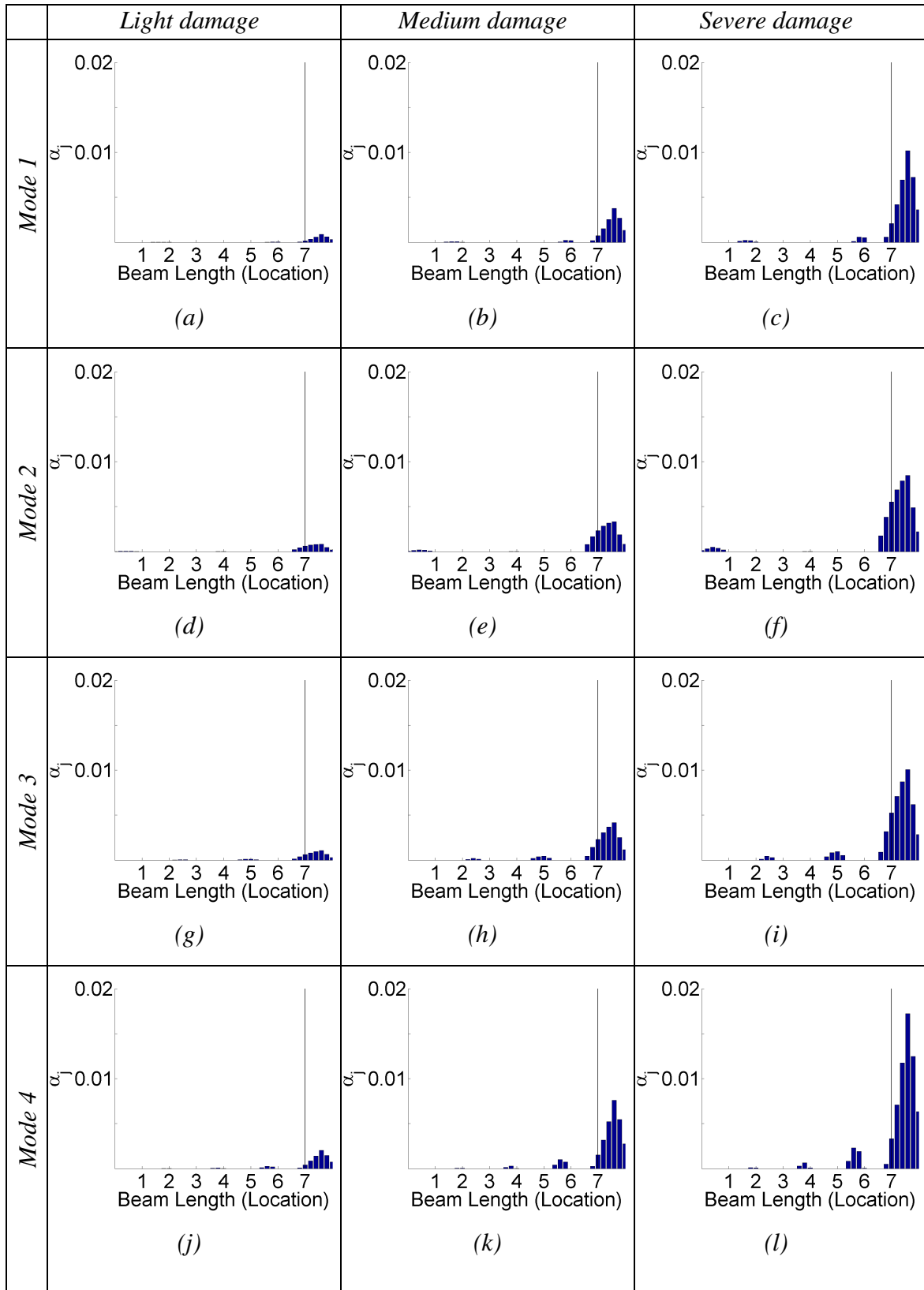


Figure E.11 α_j values of numerical noise-free simulations of a beam damaged at location '6' of light, medium and severe size, respectively. α_j values are derived from (a) to (c) mode 1, (d) to (f) mode 2, (g) to (i) mode 3, and (j) to (l) mode 4.

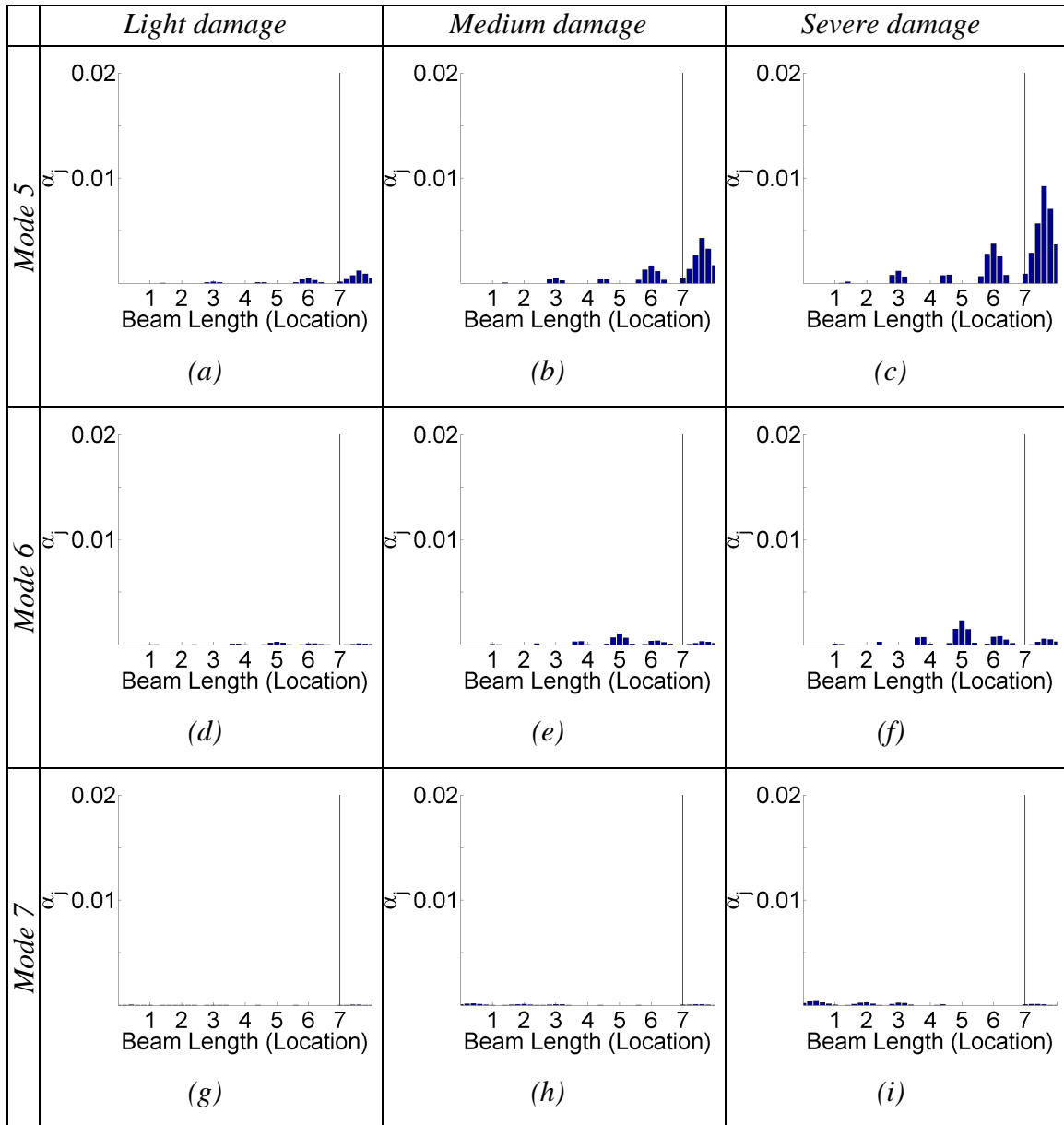


Figure E.12 α_j values of numerical noise-free simulations of a beam damaged at location '7' of light, medium and severe size, respectively. α_j values are derived from (a) to (c) mode 5, (d) to (f) mode 6, and (g) to (i) mode 7.

APPENDIX F

PRINCIPAL COMPONENTS OF TWO-STOREY FRAMED STRUCTURE

Table F.1 Individual contributions of first 30 PCs from residual FRFs of numerical two-storey framed structure of different boundary conditions for measurement locations '1' to '14' and horizontal and vertical summation FRFs (SumH and SumV).

	Individual contribution of PCs derived from residual FRFs in [%]															SumH	SumV
	'1'	'2'	'3'	'4'	'5'	'6'	'7'	'8'	'9'	'10'	'11'	'12'	'13'	'14'			
PC 1	30.1	13.7	27.9	7.4	30.7	13.5	28.7	7.4	46.0	73.6	80.5	38.1	61.4	37.4	22.5	64.6	
PC 2	15.2	6.8	13.7	7.4	15.4	6.6	13.6	7.2	22.2	10.2	4.3	19.3	10.3	20.4	10.4	12.6	
PC 3	6.5	6.5	10.1	7.1	6.2	6.3	9.1	7.1	5.9	4.2	2.0	9.8	7.2	9.8	8.1	7.9	
PC 4	4.6	6.4	5.3	6.7	4.4	6.3	5.3	6.7	4.2	2.8	1.6	5.3	3.8	5.1	7.8	3.1	
PC 5	3.6	6.2	3.5	6.4	3.5	6.0	3.4	6.4	3.3	1.5	1.5	4.8	2.0	4.9	4.5	2.0	
PC 6	2.8	6.0	3.0	6.4	2.7	5.8	3.0	5.8	2.4	0.4	1.5	2.4	0.5	2.2	4.0	1.4	
PC 7	2.7	3.9	2.8	3.8	2.6	4.0	3.0	3.8	1.7	0.4	1.5	1.7	0.5	1.5	3.9	1.2	
PC 8	2.6	3.0	2.7	3.3	2.6	3.0	2.8	3.4	1.1	0.4	1.2	1.0	0.5	0.9	3.7	1.1	
PC 9	2.5	2.1	2.6	2.5	2.5	2.2	2.7	2.5	1.0	0.4	0.9	0.8	0.5	0.9	3.5	1.1	
PC 10	2.3	2.1	2.6	2.3	2.4	2.1	2.6	2.3	0.5	0.3	0.8	0.8	0.5	0.9	3.4	1.1	
PC 11	2.2	2.0	2.4	2.2	2.3	2.0	2.6	2.2	0.5	0.3	0.6	0.7	0.4	0.9	1.3	0.8	
PC 12	1.9	1.9	1.8	2.2	2.2	2.0	1.8	2.2	0.5	0.3	0.6	0.7	0.4	0.9	1.3	0.4	
PC 13	1.1	1.9	1.2	2.1	1.2	1.9	1.1	2.1	0.4	0.2	0.5	0.7	0.4	0.8	1.2	0.4	
PC 14	0.9	1.9	1.1	2.0	1.1	1.9	1.1	2.1	0.4	0.2	0.5	0.7	0.4	0.7	1.2	0.4	
PC 15	0.9	1.7	1.0	2.0	1.0	1.8	1.0	2.0	0.4	0.2	0.5	0.6	0.4	0.7	1.1	0.3	
PC 16	0.9	1.6	0.9	1.9	0.9	1.7	1.0	2.0	0.4	0.2	0.4	0.6	0.4	0.7	1.0	0.3	
PC 17	0.8	1.6	0.9	1.8	0.9	1.6	1.0	1.9	0.4	0.2	0.3	0.6	0.4	0.7	1.0	0.2	
PC 18	0.8	1.6	0.8	1.8	0.9	1.6	0.8	1.8	0.4	0.2	0.1	0.6	0.4	0.7	1.0	0.1	
PC 19	0.8	1.4	0.8	1.6	0.8	1.5	0.8	1.6	0.4	0.2	0.1	0.6	0.4	0.6	0.9	0.1	
PC 20	0.7	1.2	0.7	1.3	0.8	1.2	0.8	1.4	0.4	0.2	0.1	0.5	0.4	0.6	0.9	0.1	
PC 21	0.7	1.0	0.7	1.1	0.8	0.9	0.7	1.2	0.3	0.2	0.1	0.5	0.4	0.6	0.7	0.1	
PC 22	0.7	0.8	0.6	1.1	0.7	0.9	0.6	1.0	0.3	0.2	0.1	0.5	0.4	0.6	0.7	0.1	
PC 23	0.6	0.8	0.6	0.8	0.7	0.8	0.6	0.8	0.3	0.2	0.1	0.4	0.4	0.4	0.6	0.1	
PC 24	0.6	0.7	0.5	0.8	0.7	0.8	0.5	0.8	0.3	0.2	0.1	0.4	0.3	0.3	0.5	0.0	
PC 25	0.4	0.7	0.5	0.8	0.4	0.8	0.5	0.8	0.3	0.2	0.0	0.4	0.3	0.3	0.5	0.0	
PC 26	0.4	0.7	0.4	0.8	0.4	0.7	0.4	0.8	0.3	0.2	0.0	0.4	0.3	0.3	0.5	0.0	
PC 27	0.4	0.6	0.4	0.8	0.3	0.6	0.4	0.7	0.3	0.1	0.0	0.4	0.3	0.3	0.4	0.0	
PC 28	0.4	0.6	0.4	0.7	0.3	0.6	0.3	0.7	0.2	0.1	0.0	0.4	0.3	0.3	0.4	0.0	
PC 29	0.4	0.6	0.4	0.7	0.3	0.6	0.3	0.7	0.2	0.1	0.0	0.3	0.3	0.3	0.4	0.0	
PC 30	0.3	0.6	0.3	0.7	0.3	0.6	0.3	0.7	0.2	0.1	0.0	0.2	0.3	0.2	0.4	0.0	

Table F.2 Individual contributions of first 30 PCs from residual FRFs of numerical two-storey framed structure of different added mass scenarios for measurement locations '1' to '14' and horizontal and vertical summation FRFs (SumH and SumV).

	Individual contribution of PCs derived from residual FRFs in [%]														SumH	SumV
	'1'	'2'	'3'	'4'	'5'	'6'	'7'	'8'	'9'	'10'	'11'	'12'	'13'	'14'		
PC 1	19.0	8.0	50.1	62.2	16.9	7.9	48.2	62.1	36.8	55.2	33.5	37.3	62.1	38.2	69.6	48.8
PC 2	6.5	7.7	11.0	3.5	9.3	7.5	12.1	3.4	14.9	12.7	21.2	29.4	14.5	25.0	2.6	15.7
PC 3	6.0	7.6	3.2	3.4	6.0	7.4	3.2	3.3	8.0	10.6	6.4	5.3	7.1	9.1	2.4	9.2
PC 4	5.8	7.5	2.9	3.2	5.8	7.0	3.1	3.2	3.4	5.2	3.5	3.2	6.6	4.0	2.3	2.7
PC 5	5.7	6.8	2.9	3.1	5.7	7.0	3.0	3.1	3.1	2.5	2.8	2.0	2.4	1.9	2.3	2.3
PC 6	5.3	6.7	2.8	2.7	5.5	6.8	3.0	2.9	3.0	0.8	2.6	1.9	0.8	1.8	2.1	1.8
PC 7	5.0	2.5	2.7	0.9	5.0	2.6	2.9	1.0	2.8	0.7	2.6	1.8	0.6	1.7	1.5	1.6
PC 8	3.9	2.4	2.6	0.9	2.4	2.4	2.6	0.9	2.6	0.7	2.4	1.7	0.6	1.7	1.0	1.6
PC 9	2.0	2.4	1.4	0.9	1.9	2.3	1.5	0.9	2.4	0.7	2.3	1.6	0.5	1.6	0.7	1.6
PC 10	1.9	2.3	0.8	0.8	1.9	2.2	0.9	0.8	1.6	0.7	2.0	0.7	0.5	0.7	0.6	1.1
PC 11	1.8	2.0	0.8	0.7	1.8	2.1	0.9	0.7	0.9	0.6	0.9	0.6	0.4	0.6	0.6	0.6
PC 12	1.8	1.4	0.8	0.7	1.6	1.4	0.8	0.7	0.9	0.5	0.8	0.6	0.4	0.6	0.6	0.5
PC 13	1.5	1.4	0.7	0.7	1.6	1.3	0.8	0.6	0.8	0.5	0.8	0.6	0.4	0.6	0.5	0.5
PC 14	1.2	1.3	0.6	0.6	1.5	1.3	0.7	0.6	0.8	0.5	0.8	0.6	0.3	0.6	0.5	0.5
PC 15	1.0	1.3	0.6	0.6	1.2	1.3	0.6	0.6	0.8	0.5	0.7	0.6	0.3	0.5	0.5	0.5
PC 16	1.0	1.2	0.6	0.6	1.0	1.2	0.6	0.6	0.7	0.4	0.7	0.5	0.2	0.4	0.5	0.4
PC 17	1.0	1.2	0.6	0.6	1.0	1.2	0.5	0.6	0.7	0.4	0.7	0.5	0.2	0.4	0.4	0.4
PC 18	1.0	1.2	0.5	0.6	1.0	1.2	0.5	0.6	0.7	0.4	0.6	0.4	0.2	0.4	0.4	0.3
PC 19	0.9	1.2	0.5	0.6	1.0	1.2	0.5	0.6	0.6	0.4	0.6	0.4	0.2	0.4	0.4	0.3
PC 20	0.9	1.2	0.5	0.6	0.9	1.2	0.5	0.6	0.6	0.4	0.5	0.4	0.2	0.4	0.4	0.3
PC 21	0.9	1.1	0.5	0.6	0.9	1.1	0.5	0.6	0.5	0.3	0.5	0.4	0.1	0.4	0.4	0.3
PC 22	0.9	1.1	0.5	0.5	0.9	1.1	0.5	0.6	0.5	0.3	0.5	0.4	0.1	0.3	0.4	0.3
PC 23	0.9	1.1	0.5	0.5	0.9	1.1	0.5	0.5	0.5	0.3	0.5	0.3	0.1	0.3	0.4	0.3
PC 24	0.9	1.1	0.5	0.5	0.9	1.1	0.5	0.5	0.5	0.3	0.5	0.3	0.1	0.3	0.4	0.3
PC 25	0.8	1.0	0.5	0.5	0.8	1.1	0.4	0.5	0.5	0.3	0.5	0.3	0.1	0.3	0.4	0.3
PC 26	0.8	1.0	0.4	0.4	0.8	1.1	0.4	0.4	0.4	0.2	0.4	0.3	0.1	0.3	0.4	0.3
PC 27	0.8	1.0	0.4	0.4	0.8	1.0	0.4	0.4	0.4	0.2	0.4	0.3	0.0	0.3	0.3	0.3
PC 28	0.8	1.0	0.4	0.3	0.8	1.0	0.4	0.4	0.4	0.2	0.4	0.3	0.0	0.3	0.3	0.3
PC 29	0.7	1.0	0.4	0.3	0.8	1.0	0.4	0.4	0.4	0.2	0.4	0.3	0.0	0.3	0.3	0.3
PC 30	0.7	1.0	0.4	0.3	0.8	1.0	0.4	0.3	0.4	0.2	0.4	0.3	0.0	0.3	0.3	0.3

Table F.3 Individual contributions of first 30 PCs from residual FRFs of numerical two-storey framed structure of different section reduction cases for measurement locations '1' to '14' and horizontal and vertical summation FRFs (SumH and SumV).

	Individual contribution of PCs derived from residual FRFs in [%]														SumH	SumV
	'1'	'2'	'3'	'4'	'5'	'6'	'7'	'8'	'9'	'10'	'11'	'12'	'13'	'14'		
PC 1	84.8	84.7	9.5	7.3	6.6	7.1	8.4	47.2	12.8	46.1	11.4	12.1	45.2	15.1	58.1	15.3
PC 2	2.3	2.2	6.7	7.2	6.3	6.7	6.8	3.9	6.5	12.2	6.0	6.7	14.8	6.5	7.4	6.0
PC 3	0.9	1.0	6.3	6.9	6.2	6.7	6.6	3.8	6.2	9.1	5.9	6.5	8.9	6.3	3.4	5.9
PC 4	0.9	0.9	6.2	6.6	6.0	6.3	6.4	3.7	6.2	1.8	5.6	6.1	3.8	6.3	2.4	5.9
PC 5	0.8	0.9	6.0	6.4	5.9	6.1	6.3	3.5	5.6	1.7	5.5	6.0	2.4	6.0	2.3	5.5
PC 6	0.8	0.9	5.6	4.2	5.5	4.1	5.9	3.3	5.5	1.6	5.4	5.9	1.2	5.6	2.2	5.4
PC 7	0.7	0.8	3.0	2.4	3.5	2.6	3.0	2.2	5.3	1.4	3.8	2.5	1.2	2.3	2.1	3.8
PC 8	0.7	0.8	2.3	2.4	3.0	2.5	2.4	1.4	2.2	1.3	2.2	2.3	1.1	2.2	2.0	2.2
PC 9	0.5	0.3	2.3	2.3	2.4	2.4	2.3	1.3	2.2	1.1	2.1	2.2	1.0	2.2	0.9	2.1
PC 10	0.3	0.3	2.1	2.3	2.3	2.3	2.2	1.3	2.1	0.8	2.1	2.2	1.0	2.1	0.8	2.0
PC 11	0.3	0.3	2.0	2.2	2.2	2.2	2.2	1.2	2.0	0.8	2.0	2.1	0.9	2.0	0.7	1.9
PC 12	0.3	0.3	2.0	2.2	2.1	2.1	2.1	1.2	1.8	0.8	1.9	2.0	0.7	1.9	0.7	1.8
PC 13	0.3	0.3	2.0	2.1	2.0	2.0	2.0	1.1	1.8	0.7	1.9	1.8	0.7	1.8	0.7	1.8
PC 14	0.2	0.3	1.9	2.0	1.9	2.0	2.0	1.0	1.7	0.7	1.9	1.8	0.6	1.7	0.7	1.7
PC 15	0.2	0.2	1.9	2.0	1.8	1.9	1.9	1.0	1.7	0.7	1.8	1.7	0.6	1.6	0.7	1.7
PC 16	0.2	0.2	1.9	1.9	1.8	1.8	1.8	1.0	1.6	0.6	1.8	1.6	0.6	1.6	0.6	1.6
PC 17	0.2	0.2	1.8	1.8	1.7	1.7	1.8	0.9	1.5	0.6	1.6	1.5	0.6	1.5	0.6	1.5
PC 18	0.2	0.2	1.6	1.7	1.6	1.6	1.6	0.9	1.4	0.6	1.6	1.5	0.5	1.4	0.6	1.5
PC 19	0.2	0.2	1.6	1.7	1.5	1.6	1.6	0.9	1.4	0.6	1.5	1.4	0.5	1.3	0.6	1.4
PC 20	0.2	0.2	1.5	1.6	1.5	1.6	1.5	0.8	1.4	0.6	1.5	1.4	0.5	1.3	0.6	1.4
PC 21	0.2	0.2	1.5	1.6	1.5	1.5	1.5	0.8	1.3	0.5	1.5	1.3	0.5	1.3	0.5	1.3
PC 22	0.2	0.2	1.3	1.4	1.4	1.3	1.3	0.8	1.1	0.5	1.2	1.3	0.4	1.2	0.5	1.3
PC 23	0.2	0.2	1.2	1.3	1.4	1.2	1.2	0.7	1.0	0.5	1.2	1.2	0.4	1.0	0.5	1.1
PC 24	0.2	0.2	1.1	1.2	1.1	1.1	1.1	0.6	1.0	0.5	1.1	1.1	0.4	1.0	0.5	1.0
PC 25	0.2	0.2	1.1	1.1	1.1	1.1	1.1	0.6	1.0	0.5	1.1	1.0	0.4	0.9	0.4	1.0
PC 26	0.2	0.1	1.0	1.0	1.1	1.0	0.9	0.5	0.9	0.5	1.1	0.9	0.4	0.9	0.4	1.0
PC 27	0.2	0.1	1.0	0.9	1.0	0.9	0.9	0.5	0.9	0.5	0.9	0.9	0.3	0.9	0.4	0.9
PC 28	0.2	0.1	0.9	0.9	0.9	0.9	0.8	0.5	0.8	0.4	0.9	0.8	0.3	0.8	0.3	0.8
PC 29	0.1	0.1	0.9	0.9	0.9	0.9	0.8	0.5	0.8	0.4	0.9	0.8	0.3	0.8	0.3	0.8
PC 30	0.1	0.1	0.9	0.9	0.8	0.9	0.8	0.4	0.8	0.4	0.9	0.8	0.3	0.8	0.3	0.8

Table F.4 Individual contributions of first 30 PCs from residual FRFs of laboratory two-storey framed structure of different boundary conditions for measurement locations '1' to '14' and horizontal and vertical summation FRFs (SumH and SumV).

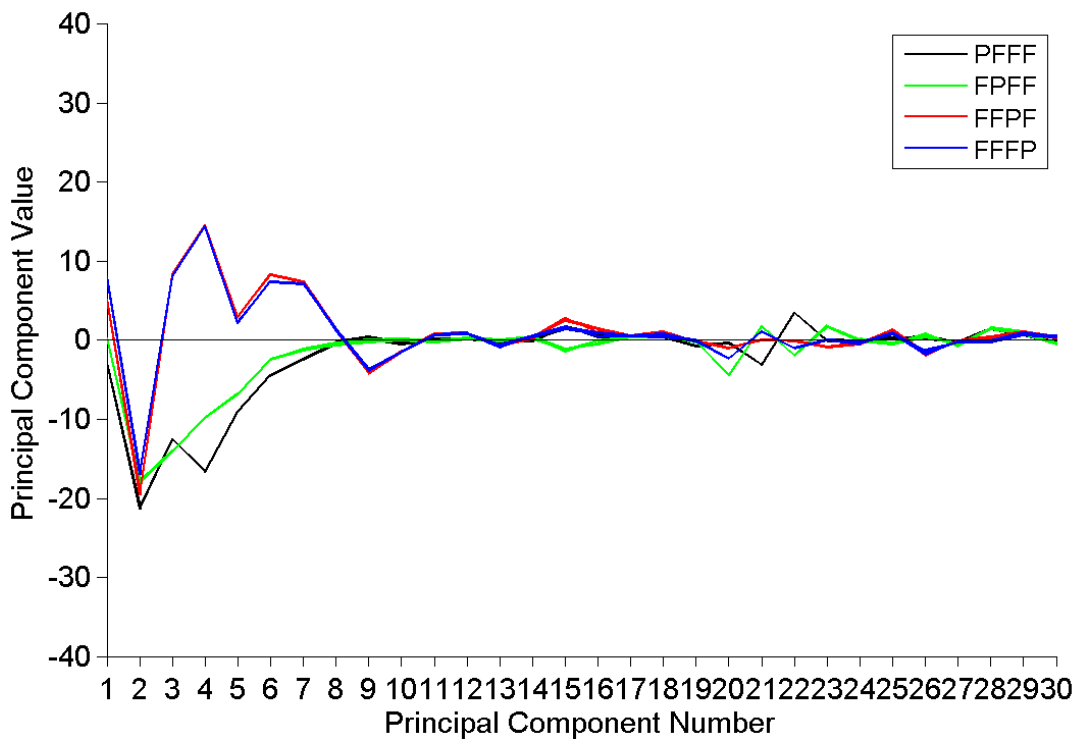
	Individual contribution of PCs derived from residual FRFs in [%]														SumH	SumV
	'1'	'2'	'3'	'4'	'5'	'6'	'7'	'8'	'9'	'10'	'11'	'12'	'13'	'14'		
PC 1	24.2	15.0	35.6	25.9	20.6	16.7	19.4	20.8	27.0	26.2	24.2	37.5	33.9	29.9	30.0	29.2
PC 2	16.8	9.5	22.8	10.6	14.8	10.0	18.0	13.3	14.1	17.2	12.1	13.8	14.2	19.1	15.7	15.1
PC 3	8.6	7.9	11.0	9.0	8.7	9.1	13.4	7.9	10.5	10.6	10.5	10.6	10.7	13.1	11.1	11.2
PC 4	6.7	7.0	6.3	7.9	7.8	8.1	6.9	6.7	7.7	7.3	7.0	7.5	10.0	9.1	7.8	10.7
PC 5	5.1	6.4	4.6	6.0	6.0	7.9	6.7	6.3	5.9	5.4	6.1	5.9	6.4	6.2	5.3	7.4
PC 6	4.3	6.1	3.5	5.6	5.6	6.9	5.8	6.1	5.5	4.8	5.5	4.1	5.6	5.5	5.2	4.7
PC 7	4.0	6.0	3.3	4.9	5.2	6.2	4.9	5.6	4.4	3.7	4.7	3.9	3.6	4.2	4.4	4.3
PC 8	3.4	5.0	2.8	4.5	5.0	4.9	3.9	5.3	3.9	3.6	4.3	2.9	2.8	2.4	3.0	3.4
PC 9	3.2	4.5	2.2	4.0	4.3	4.3	3.4	4.5	3.3	3.0	4.0	2.4	1.9	1.9	2.8	2.8
PC 10	2.7	3.6	2.0	3.3	3.8	3.0	3.1	3.0	3.3	2.2	4.0	2.2	1.8	1.7	2.6	2.4
PC 11	2.5	2.5	1.2	2.6	3.4	2.4	3.0	2.2	2.8	2.1	3.6	1.8	1.5	1.3	2.4	1.9
PC 12	2.1	2.0	0.9	1.8	2.6	1.5	2.4	2.0	2.7	1.8	2.4	1.2	0.9	0.9	2.1	1.0
PC 13	2.0	1.8	0.7	1.5	2.3	1.3	2.3	1.3	1.7	1.7	1.9	1.2	0.8	0.5	1.3	0.9
PC 14	1.1	1.5	0.2	1.0	0.7	1.1	0.4	1.1	0.6	1.0	0.6	1.0	0.8	0.4	0.6	0.8
PC 15	0.9	1.3	0.2	0.7	0.6	0.9	0.4	0.8	0.5	0.6	0.6	0.8	0.7	0.4	0.5	0.5
PC 16	0.7	1.2	0.2	0.7	0.5	0.9	0.3	0.8	0.4	0.6	0.6	0.4	0.3	0.3	0.4	0.4
PC 17	0.7	1.2	0.2	0.6	0.5	0.8	0.3	0.7	0.4	0.5	0.5	0.2	0.3	0.3	0.4	0.3
PC 18	0.6	1.1	0.1	0.5	0.4	0.7	0.3	0.7	0.3	0.5	0.4	0.2	0.3	0.2	0.3	0.2
PC 19	0.6	1.0	0.1	0.5	0.4	0.7	0.3	0.6	0.3	0.4	0.4	0.2	0.2	0.2	0.3	0.2
PC 20	0.5	0.9	0.1	0.5	0.4	0.7	0.3	0.6	0.3	0.4	0.3	0.1	0.2	0.2	0.3	0.2
PC 21	0.5	0.8	0.1	0.4	0.4	0.7	0.3	0.6	0.3	0.4	0.3	0.1	0.2	0.2	0.2	0.2
PC 22	0.5	0.8	0.1	0.4	0.3	0.7	0.3	0.6	0.2	0.3	0.3	0.1	0.2	0.2	0.2	0.1
PC 23	0.5	0.7	0.1	0.4	0.3	0.6	0.2	0.5	0.2	0.3	0.3	0.1	0.2	0.1	0.2	0.1
PC 24	0.4	0.7	0.1	0.4	0.3	0.6	0.2	0.5	0.2	0.3	0.3	0.1	0.2	0.1	0.2	0.1
PC 25	0.4	0.7	0.1	0.4	0.3	0.6	0.2	0.5	0.2	0.3	0.3	0.1	0.2	0.1	0.2	0.1
PC 26	0.4	0.6	0.1	0.4	0.3	0.6	0.2	0.5	0.2	0.3	0.2	0.1	0.1	0.1	0.2	0.1
PC 27	0.4	0.6	0.1	0.4	0.3	0.5	0.2	0.5	0.2	0.3	0.2	0.1	0.1	0.1	0.2	0.1
PC 28	0.4	0.6	0.1	0.4	0.3	0.5	0.2	0.5	0.2	0.3	0.2	0.1	0.1	0.1	0.2	0.1
PC 29	0.3	0.6	0.1	0.3	0.3	0.5	0.2	0.4	0.2	0.3	0.2	0.1	0.1	0.1	0.1	0.1
PC 30	0.3	0.6	0.1	0.3	0.2	0.5	0.2	0.4	0.2	0.2	0.2	0.1	0.1	0.1	0.1	0.1

Table F.5 Individual contributions of first 30 PCs from residual FRFs of laboratory two-storey framed structure of different added mass scenarios for measurement locations '1' to '14' and horizontal and vertical summation FRFs (SumH and SumV).

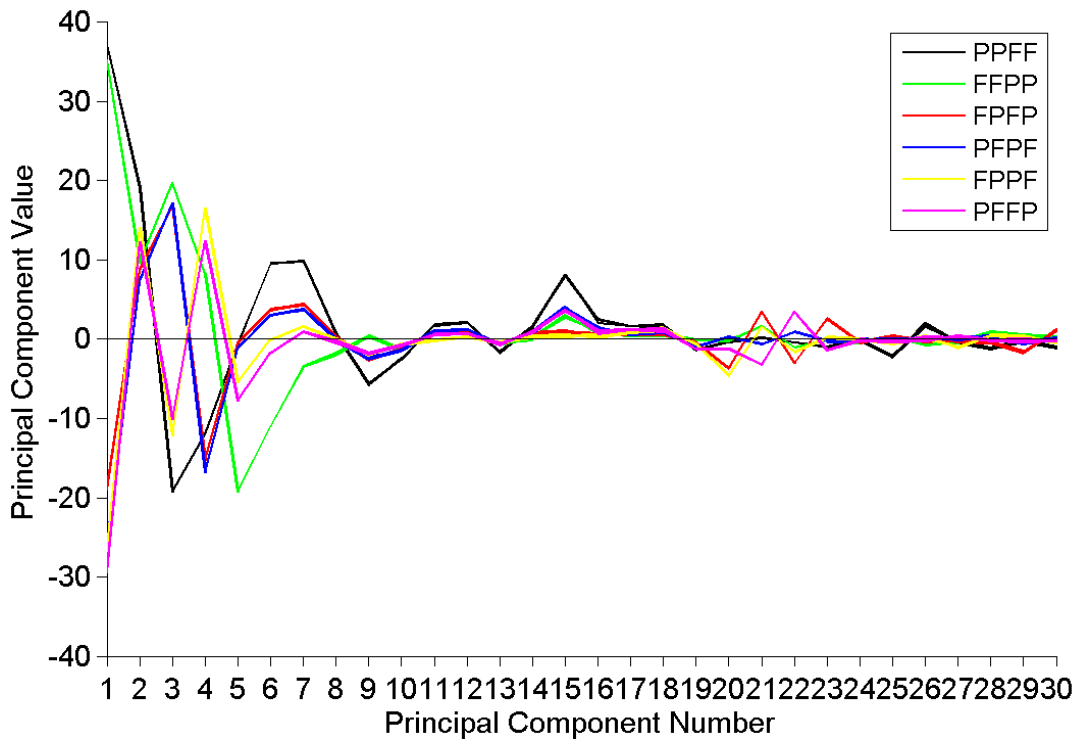
	Individual contribution of PCs derived from residual FRFs in [%]														SumH	SumV
	'1'	'2'	'3'	'4'	'5'	'6'	'7'	'8'	'9'	'10'	'11'	'12'	'13'	'14'		
PC 1	22.4	23.0	34.5	45.5	18.1	17.8	40.1	44.3	19.1	24.7	19.0	37.8	33.1	46.3	43.8	31.9
PC 2	15.0	11.6	23.8	9.6	15.3	12.0	21.1	8.9	17.7	18.2	14.4	16.8	15.6	17.7	17.1	22.5
PC 3	12.8	9.3	13.9	7.9	12.0	11.4	16.3	8.3	11.7	15.5	11.0	12.0	12.0	7.3	11.8	9.7
PC 4	7.4	7.7	11.0	7.2	10.0	10.8	6.2	7.2	9.4	7.2	7.5	6.9	5.8	6.3	6.6	8.9
PC 5	6.0	7.4	7.2	6.3	8.7	9.5	4.7	6.8	7.5	4.3	6.9	4.2	4.8	2.9	6.1	4.4
PC 6	5.4	6.4	2.2	5.4	7.7	8.4	3.0	6.4	7.3	3.8	6.5	4.0	4.3	2.7	4.3	4.2
PC 7	5.0	5.6	1.3	5.0	6.6	5.6	1.9	5.6	7.1	2.8	5.9	3.6	3.9	2.5	2.6	3.3
PC 8	4.6	4.7	1.2	2.4	5.0	4.2	1.7	2.1	6.0	2.7	5.6	3.5	3.7	2.3	2.5	3.1
PC 9	4.2	3.4	0.7	1.8	4.1	3.9	1.3	1.1	3.4	2.4	3.9	2.9	2.8	2.0	1.6	2.4
PC 10	1.6	1.8	0.7	0.7	1.3	1.3	0.6	0.8	0.9	2.3	2.0	0.8	1.7	1.1	0.4	1.5
PC 11	1.5	1.7	0.4	0.6	0.9	1.1	0.5	0.7	0.8	2.1	1.6	0.7	1.1	0.8	0.4	0.8
PC 12	1.3	1.7	0.4	0.6	0.8	1.1	0.4	0.6	0.7	1.2	1.4	0.7	0.9	0.7	0.4	0.7
PC 13	1.2	1.6	0.3	0.5	0.7	0.9	0.3	0.5	0.6	1.0	1.2	0.6	0.8	0.6	0.3	0.6
PC 14	1.1	1.4	0.2	0.5	0.7	0.9	0.2	0.5	0.6	0.9	1.0	0.6	0.7	0.5	0.2	0.5
PC 15	1.1	1.2	0.2	0.5	0.6	0.8	0.2	0.5	0.5	0.9	1.0	0.5	0.6	0.5	0.2	0.5
PC 16	0.9	1.1	0.2	0.4	0.6	0.8	0.1	0.4	0.5	0.9	0.9	0.4	0.6	0.4	0.2	0.4
PC 17	0.8	0.8	0.2	0.4	0.6	0.7	0.1	0.4	0.5	0.8	0.9	0.4	0.6	0.4	0.2	0.4
PC 18	0.7	0.8	0.2	0.4	0.6	0.7	0.1	0.4	0.5	0.7	0.9	0.3	0.5	0.4	0.1	0.4
PC 19	0.6	0.7	0.2	0.4	0.5	0.7	0.1	0.4	0.5	0.6	0.8	0.3	0.5	0.4	0.1	0.4
PC 20	0.6	0.7	0.1	0.4	0.5	0.7	0.1	0.4	0.4	0.6	0.8	0.3	0.5	0.4	0.1	0.3
PC 21	0.6	0.7	0.1	0.3	0.5	0.6	0.1	0.4	0.4	0.6	0.8	0.3	0.5	0.4	0.1	0.3
PC 22	0.5	0.6	0.1	0.3	0.5	0.6	0.1	0.4	0.4	0.6	0.7	0.3	0.5	0.3	0.1	0.3
PC 23	0.5	0.6	0.1	0.3	0.4	0.6	0.1	0.3	0.4	0.6	0.7	0.2	0.5	0.3	0.1	0.3
PC 24	0.5	0.6	0.1	0.3	0.4	0.6	0.1	0.3	0.4	0.5	0.7	0.2	0.5	0.3	0.1	0.3
PC 25	0.5	0.6	0.1	0.3	0.4	0.5	0.1	0.3	0.4	0.5	0.6	0.2	0.4	0.3	0.1	0.3
PC 26	0.5	0.6	0.1	0.3	0.4	0.5	0.1	0.3	0.4	0.5	0.5	0.2	0.4	0.3	0.1	0.3
PC 27	0.4	0.6	0.1	0.3	0.4	0.5	0.1	0.3	0.4	0.5	0.5	0.2	0.4	0.3	0.1	0.2
PC 28	0.4	0.6	0.1	0.3	0.4	0.5	0.1	0.3	0.3	0.5	0.5	0.2	0.4	0.3	0.1	0.2
PC 29	0.4	0.5	0.1	0.2	0.4	0.5	0.1	0.3	0.3	0.5	0.4	0.2	0.4	0.3	0.1	0.2
PC 30	0.4	0.5	0.1	0.2	0.4	0.5	0.1	0.3	0.3	0.4	0.4	0.2	0.4	0.3	0.1	0.2

Table F.6 Individual contributions of first 30 PCs from residual FRFs of laboratory two-storey framed structure of different section reduction cases for measurement locations '1' to '14' and horizontal and vertical summation FRFs (SumH and SumV).

	Individual contribution of PCs derived from residual FRFs in [%]														SumH	SumV
	'1'	'2'	'3'	'4'	'5'	'6'	'7'	'8'	'9'	'10'	'11'	'12'	'13'	'14'		
PC 1	33.9	19.3	47.4	23.4	37.3	24.0	52.2	17.8	30.9	29.0	28.7	25.4	22.7	33.7	43.9	37.6
PC 2	7.9	5.4	16.7	13.7	7.4	6.0	10.6	6.5	10.6	9.9	6.5	7.2	14.0	16.0	13.6	9.2
PC 3	5.1	4.9	6.4	5.5	5.0	5.3	6.7	5.7	4.9	4.2	4.8	5.2	10.1	6.7	6.5	5.7
PC 4	3.9	4.7	3.0	4.9	3.8	5.1	3.7	5.4	3.8	4.0	4.3	4.8	4.0	4.6	3.4	3.7
PC 5	3.8	4.1	2.4	4.3	3.7	4.9	2.3	5.0	3.8	3.8	4.1	4.7	3.6	3.7	3.0	3.3
PC 6	3.3	4.0	1.8	4.1	3.6	4.4	1.8	4.4	3.7	3.5	3.8	4.4	3.1	3.1	2.4	2.9
PC 7	3.0	3.9	1.6	3.6	3.3	3.9	1.7	4.1	3.6	2.9	2.7	2.5	3.0	2.6	2.2	2.5
PC 8	2.6	3.3	1.5	3.3	3.2	3.8	1.7	3.9	3.2	2.6	2.3	2.4	2.9	2.5	1.8	2.1
PC 9	2.4	3.0	1.5	3.0	2.8	3.4	1.5	3.7	2.9	2.2	2.1	2.1	2.7	2.2	1.8	1.8
PC 10	2.2	2.5	1.2	2.9	2.7	3.1	1.4	3.5	2.8	2.1	2.1	2.1	2.7	2.1	1.7	1.6
PC 11	1.9	2.4	1.2	2.2	2.2	2.6	1.4	2.2	2.5	1.9	2.0	2.1	2.5	2.0	1.6	1.6
PC 12	1.8	2.3	1.1	1.6	1.9	2.2	1.3	2.1	2.0	1.9	1.9	2.0	2.3	1.8	1.5	1.5
PC 13	1.7	2.2	1.0	1.6	1.7	2.0	1.1	2.0	1.8	1.8	1.9	2.0	2.3	1.6	1.3	1.4
PC 14	1.6	2.1	1.0	1.5	1.6	1.8	1.0	1.9	1.7	1.7	1.8	1.9	1.8	1.4	1.2	1.4
PC 15	1.5	2.1	0.8	1.4	1.4	1.7	0.9	1.8	1.5	1.7	1.8	1.9	1.7	1.3	1.1	1.4
PC 16	1.4	2.0	0.8	1.4	1.3	1.6	0.8	1.8	1.4	1.6	1.8	1.8	1.5	1.3	1.0	1.3
PC 17	1.4	2.0	0.7	1.4	1.2	1.5	0.8	1.7	1.4	1.6	1.7	1.8	1.4	1.2	0.9	1.3
PC 18	1.4	1.9	0.7	1.3	1.1	1.5	0.7	1.7	1.3	1.5	1.7	1.8	1.3	1.0	0.9	1.3
PC 19	1.3	1.8	0.7	1.3	1.1	1.5	0.6	1.6	1.2	1.5	1.6	1.7	1.2	0.9	0.8	1.3
PC 20	1.3	1.8	0.6	1.3	1.1	1.4	0.6	1.6	1.2	1.5	1.6	1.7	1.2	0.9	0.8	1.2
PC 21	1.2	1.8	0.6	1.2	1.0	1.4	0.6	1.6	1.1	1.4	1.6	1.7	1.1	0.8	0.7	1.2
PC 22	1.2	1.8	0.6	1.2	1.0	1.3	0.6	1.6	1.1	1.4	1.6	1.7	1.1	0.8	0.7	1.2
PC 23	1.2	1.7	0.6	1.2	0.9	1.3	0.6	1.5	1.1	1.4	1.5	1.6	1.0	0.7	0.7	1.2
PC 24	1.2	1.7	0.6	1.2	0.9	1.3	0.5	1.5	1.0	1.4	1.5	1.6	1.0	0.7	0.6	1.1
PC 25	1.2	1.7	0.6	1.1	0.9	1.3	0.5	1.5	1.0	1.3	1.4	1.6	1.0	0.7	0.6	1.1
PC 26	1.1	1.7	0.5	1.1	0.9	1.3	0.5	1.4	0.9	1.3	1.4	1.5	0.9	0.6	0.6	1.1
PC 27	1.1	1.6	0.5	1.1	0.8	1.2	0.5	1.4	0.9	1.3	1.4	1.5	0.9	0.6	0.6	1.0
PC 28	1.1	1.6	0.5	1.1	0.8	1.2	0.5	1.4	0.9	1.2	1.4	1.5	0.9	0.6	0.5	1.0
PC 29	1.1	1.5	0.5	1.0	0.8	1.2	0.5	1.4	0.9	1.2	1.3	1.5	0.9	0.6	0.5	1.0
PC 30	1.0	1.5	0.5	1.0	0.8	1.1	0.4	1.3	0.8	1.2	1.3	1.4	0.8	0.6	0.5	1.0

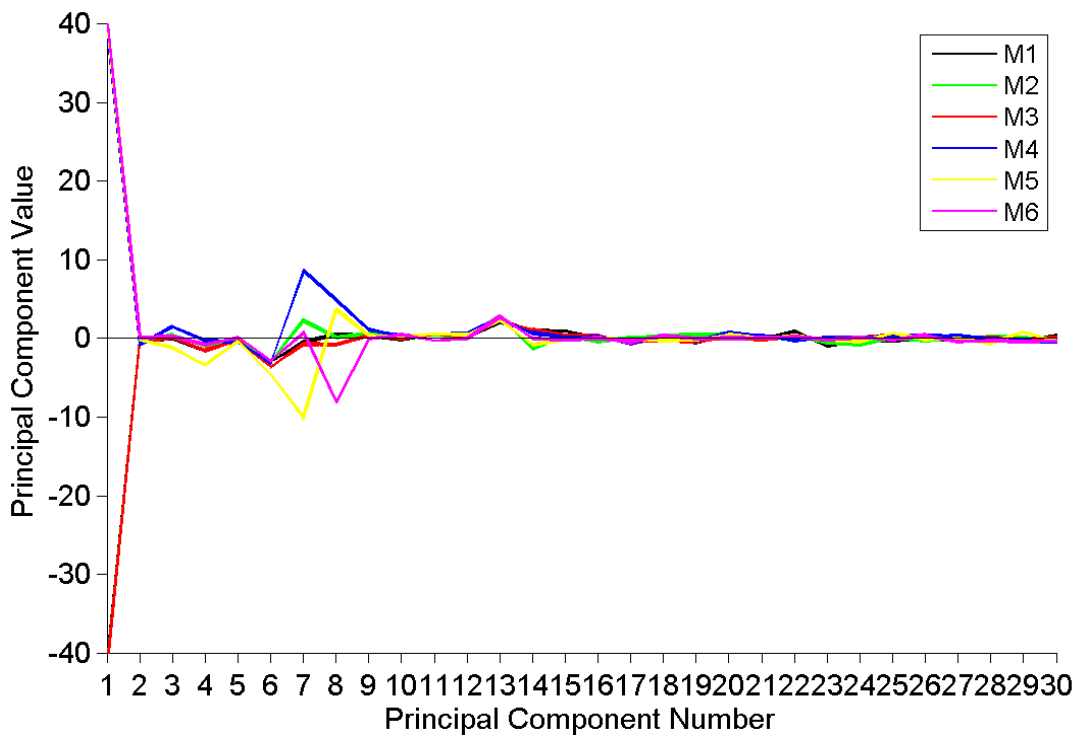


(a)

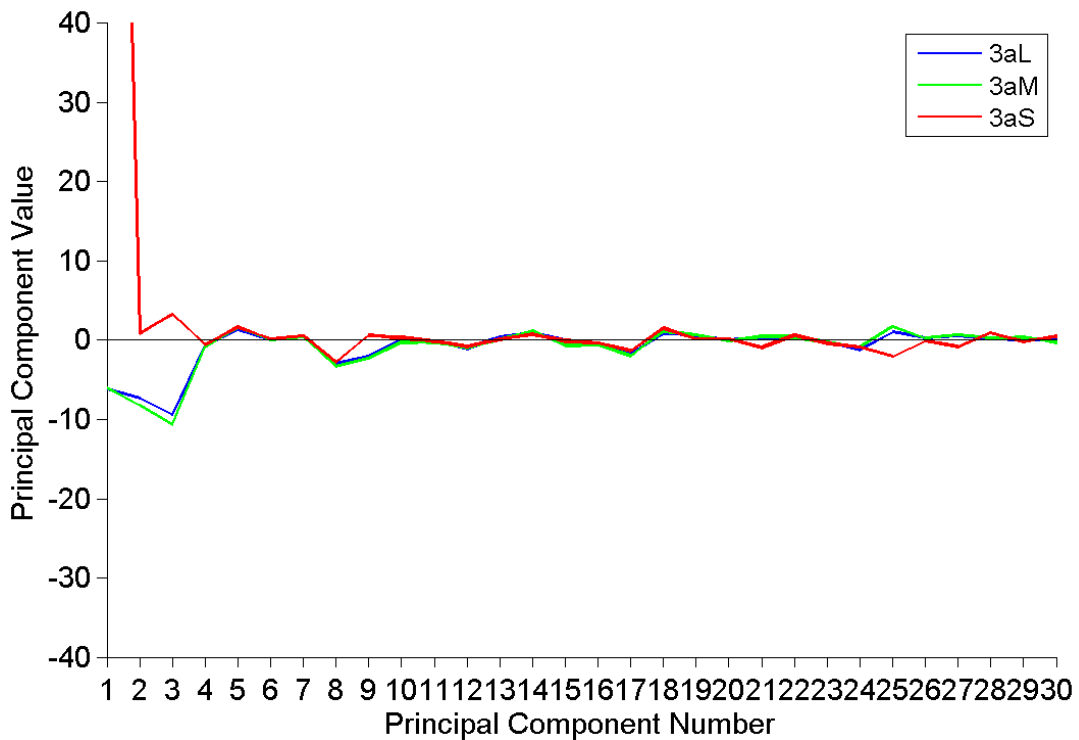


(b)

Figure F.1 The first 30 PCs of residual FRFs of numerical simulations of the two-storey framed structure polluted with 1% white Gaussian noise of (a) different boundary condition scenarios with one altered joint and (b) boundary condition scenarios with two joints altered.

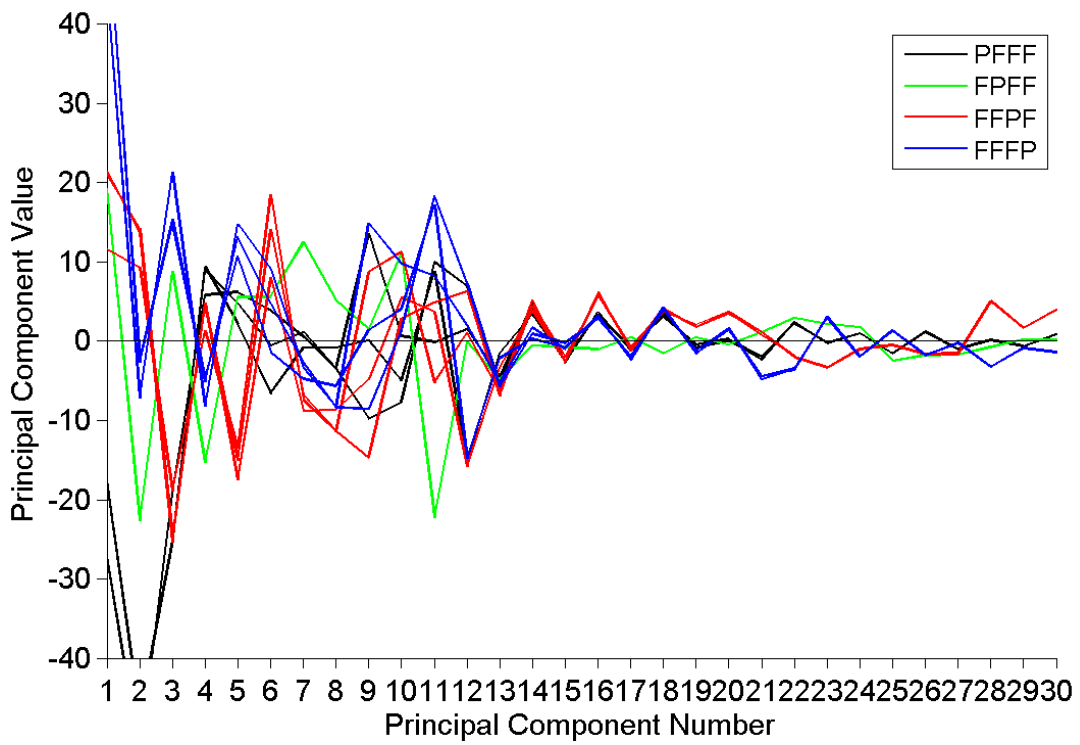


(a)

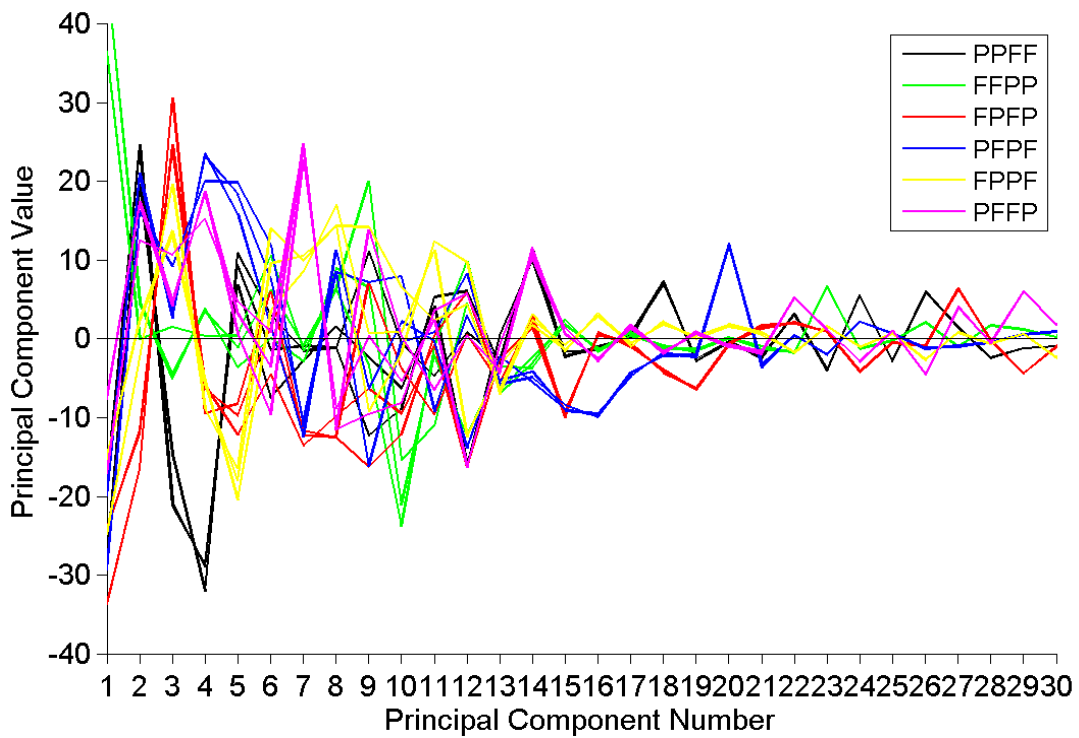


(b)

Figure F.2 The first 30 PCs of residual FRFs of numerical simulations of the two-storey framed structure polluted with 1% white Gaussian noise of (a) added mass scenarios and (b) different section reduction cases.



(a)



(b)

Figure F.3 The first 30 PCs of residual FRFs of laboratory two-storey framed structure of (a) different boundary condition scenarios with one altered joint and (b) boundary condition scenarios with two joints altered.

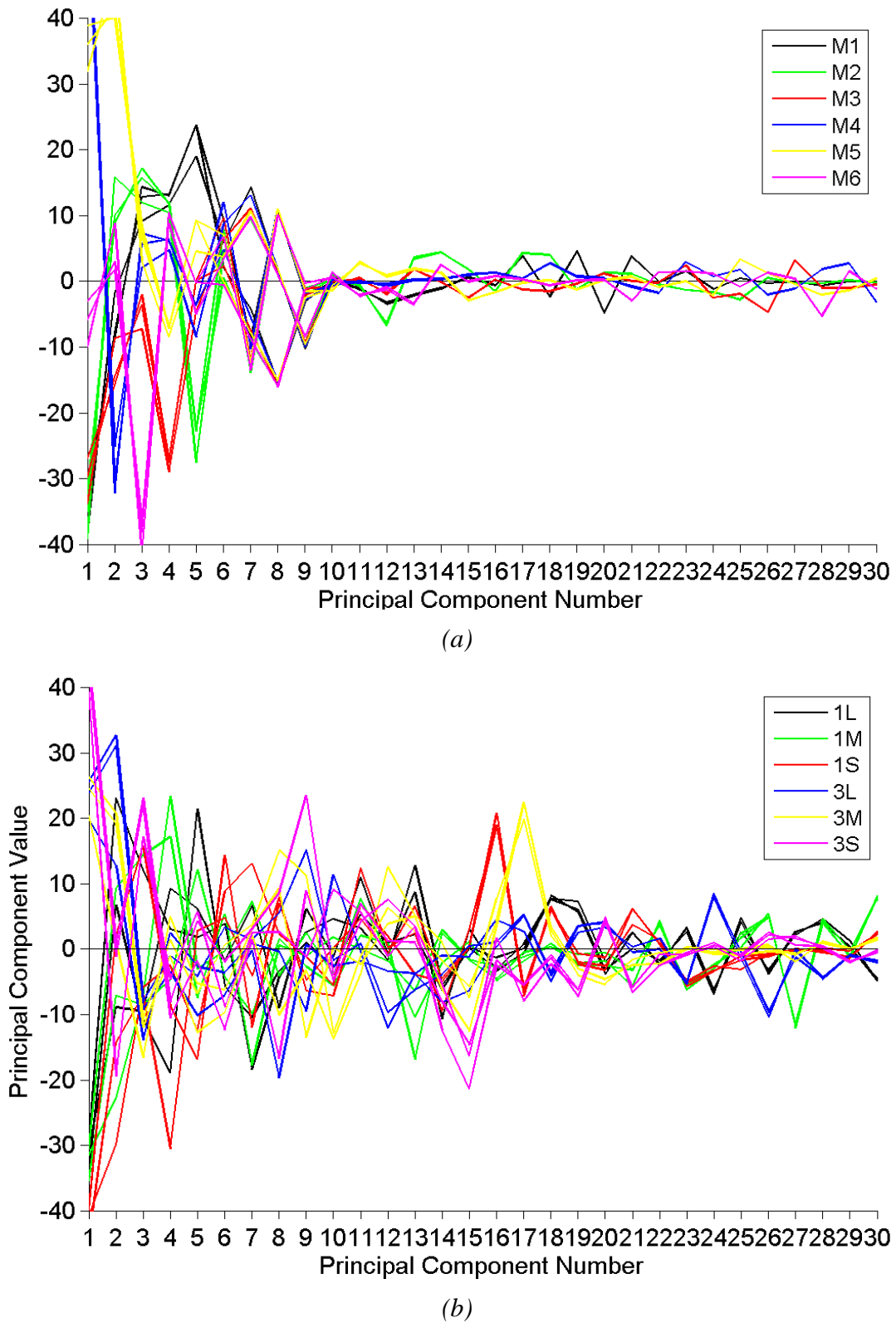


Figure F.4 The first 30 PCs of residual FRFs of laboratory two-storey framed structure of (a) added mass scenarios and (b) different section reduction cases.

APPENDIX G

DAMAGE IDENTIFICATION OUTCOMES OF BEAM STRUCTURE BASED ON DAMAGE INDEX METHOD

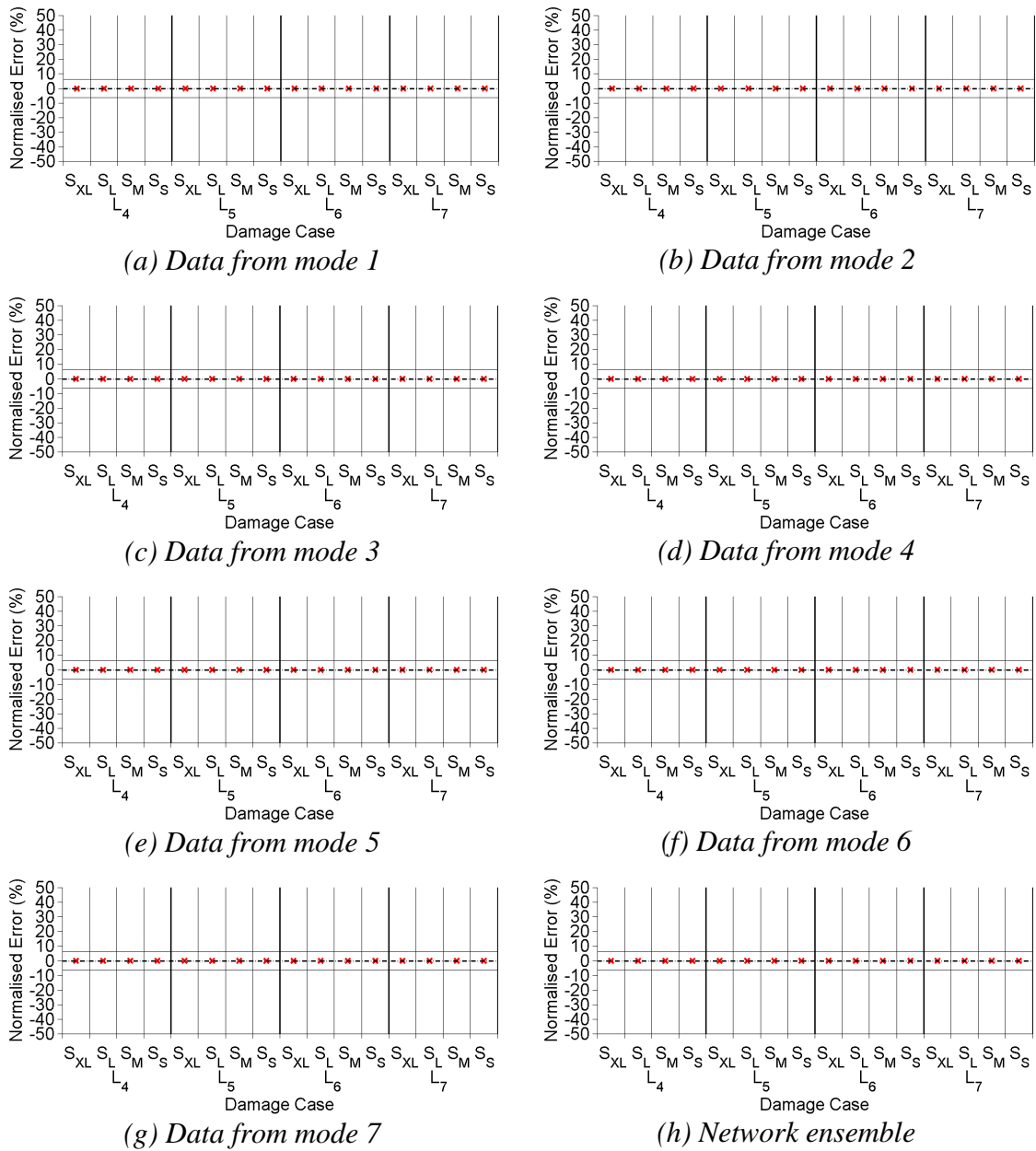


Figure G.1 Neural network testing set outcomes trained with PCA-compressed Z_j values of noise-free numerical beams to identify damage locations.

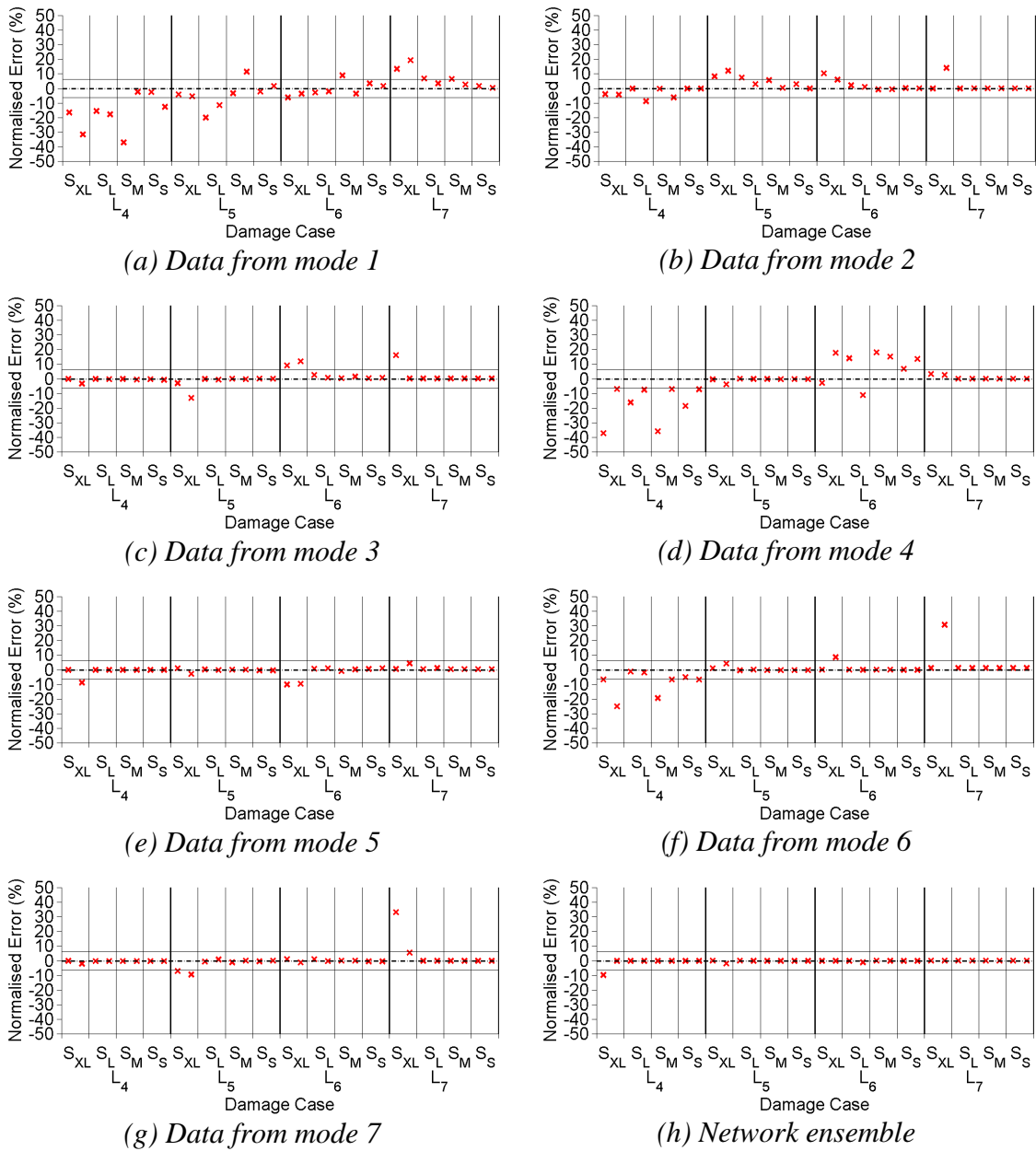


Figure G.2 Neural network testing set outcomes of networks trained with PCA-compressed Z_j values to identify damage locations of numerical beams polluted with 1% noise.

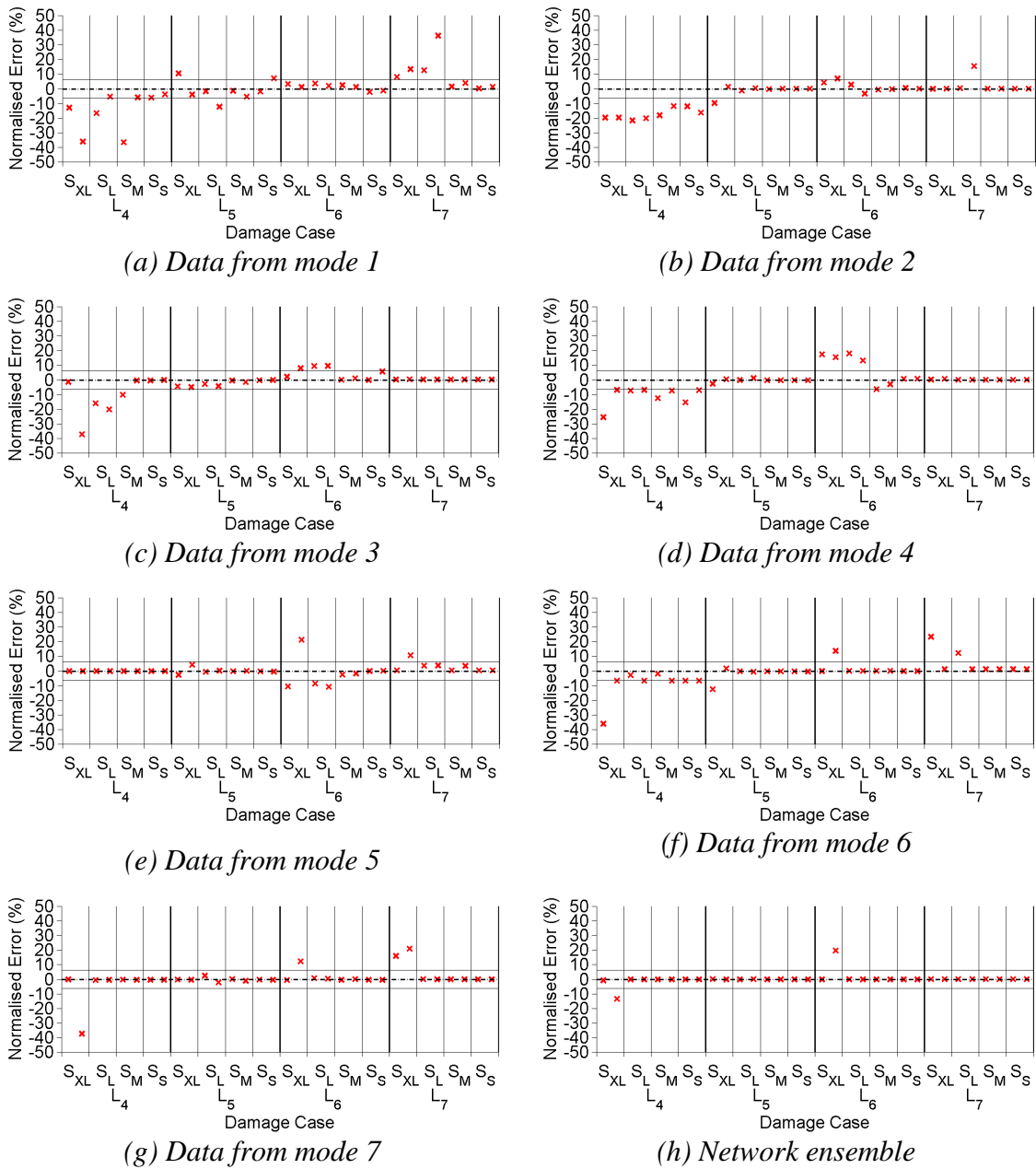


Figure G.3 Neural network testing set outcomes of networks trained with PCA-compressed Z_j values to identify damage locations of numerical beams polluted with 2% noise.

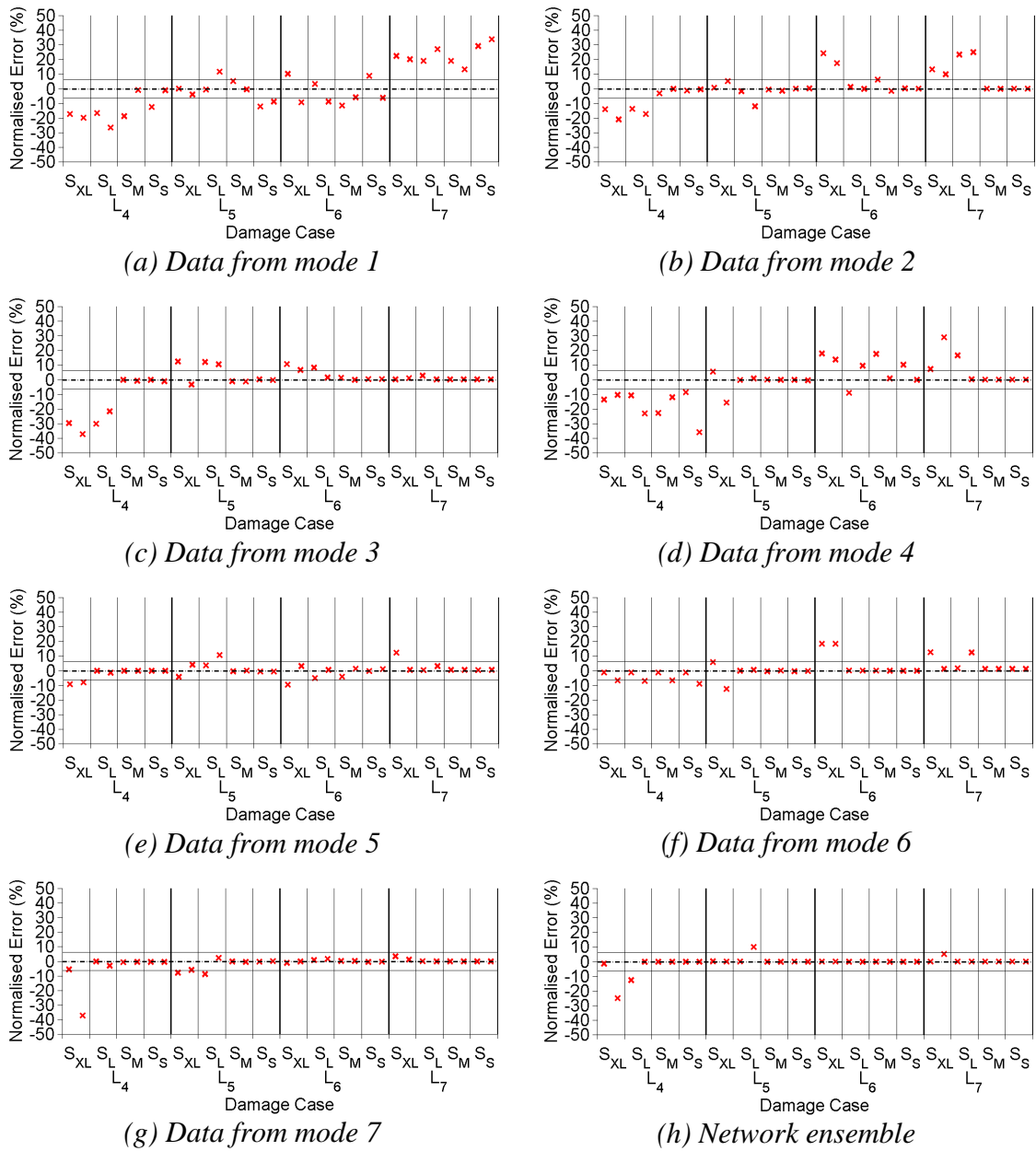


Figure G.4 Neural network testing set outcomes of networks trained with PCA-compressed Z_j values to identify damage locations of numerical beams polluted with 5% noise.

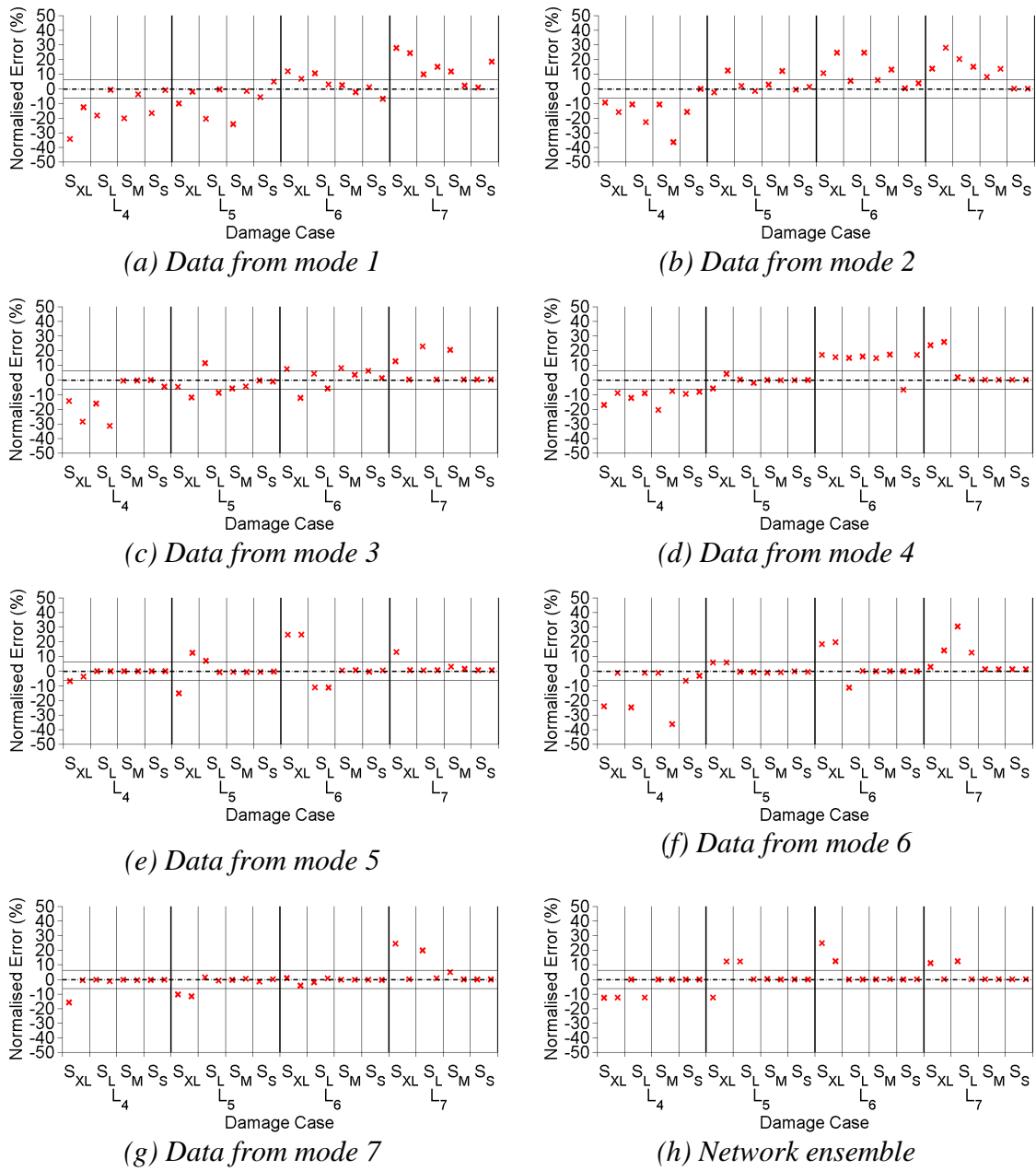
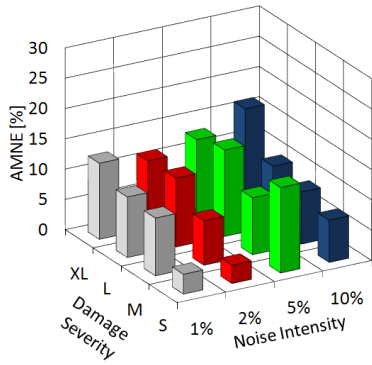
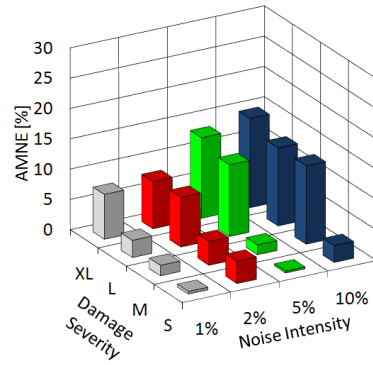


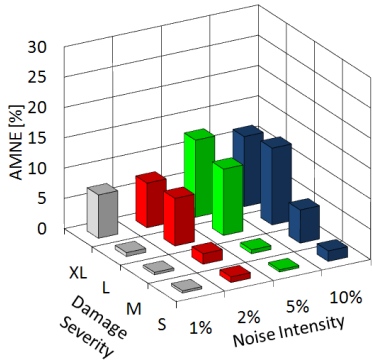
Figure G.5 Neural network testing set outcomes of networks trained with PCA-compressed Z_j values to identify damage locations of numerical beams polluted with 10% noise.



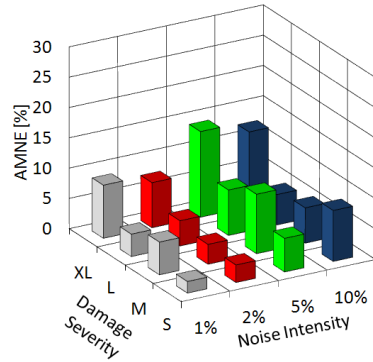
(a) Data from mode 1



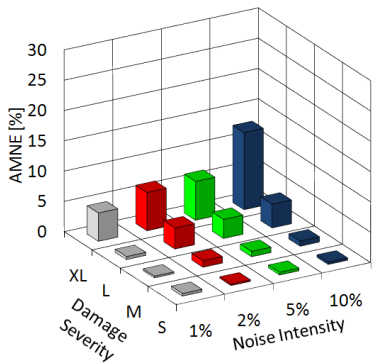
(b) Data from mode 2



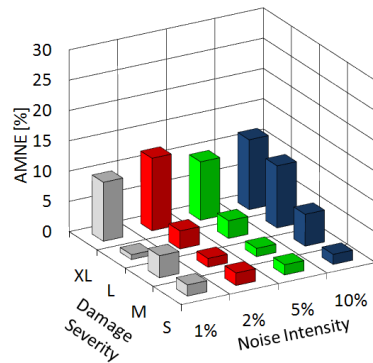
(c) Data from mode 3



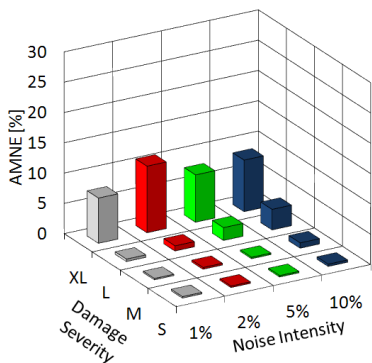
(d) Data from mode 4



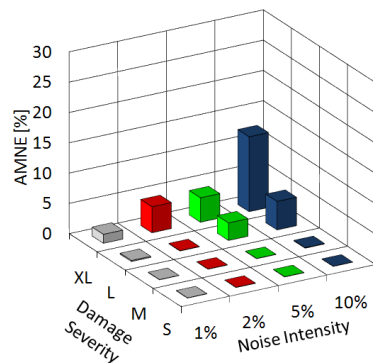
(e) Data from mode 5



(f) Data from mode 6



(g) Data from mode 7



(h) Network ensemble

Figure G.6 Comparison of testing set outcomes of networks trained with PCA-compressed Z_j values to identify damage locations of noise-polluted numerical beams subdivided by damage severity and noise pollution level.

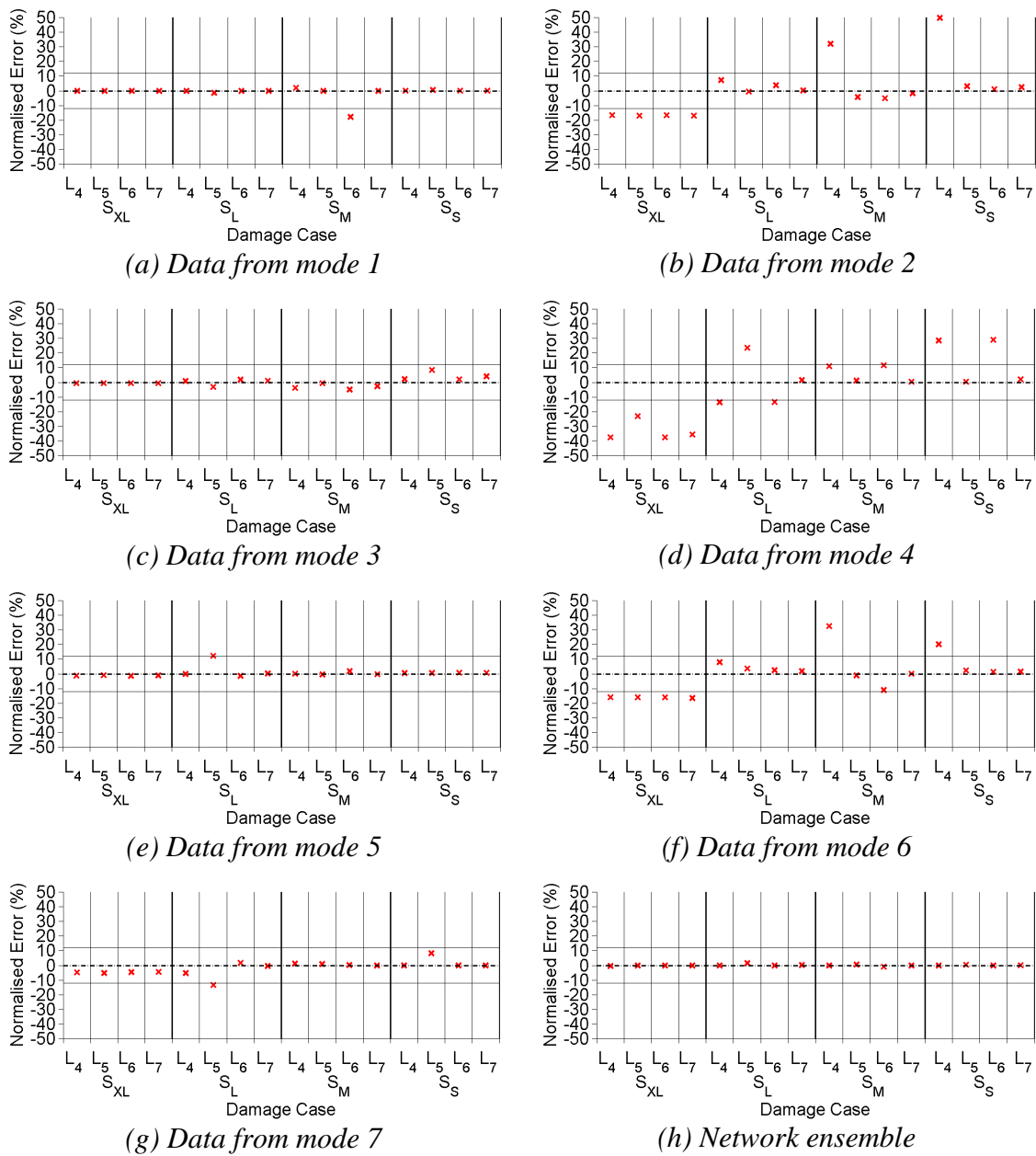


Figure G.7 Neural network testing set outcomes of networks trained with PCA-compressed a_j values of noise-free numerical beams to identify damage severities.

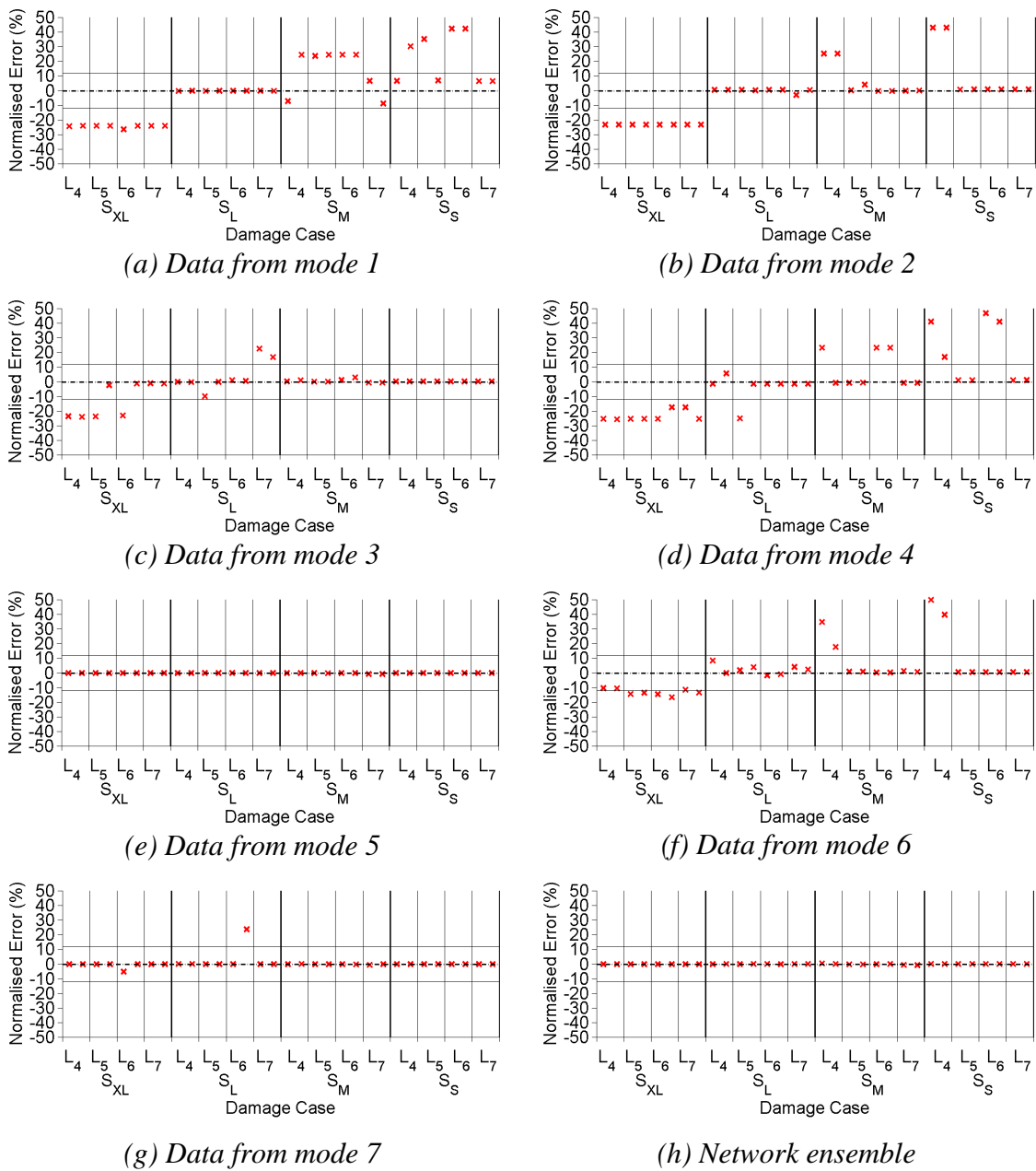


Figure G.8 Neural networks testing set outcomes of networks trained with PCA-compressed a_j values to identify damage severities of numerical beams polluted with 1% noise.

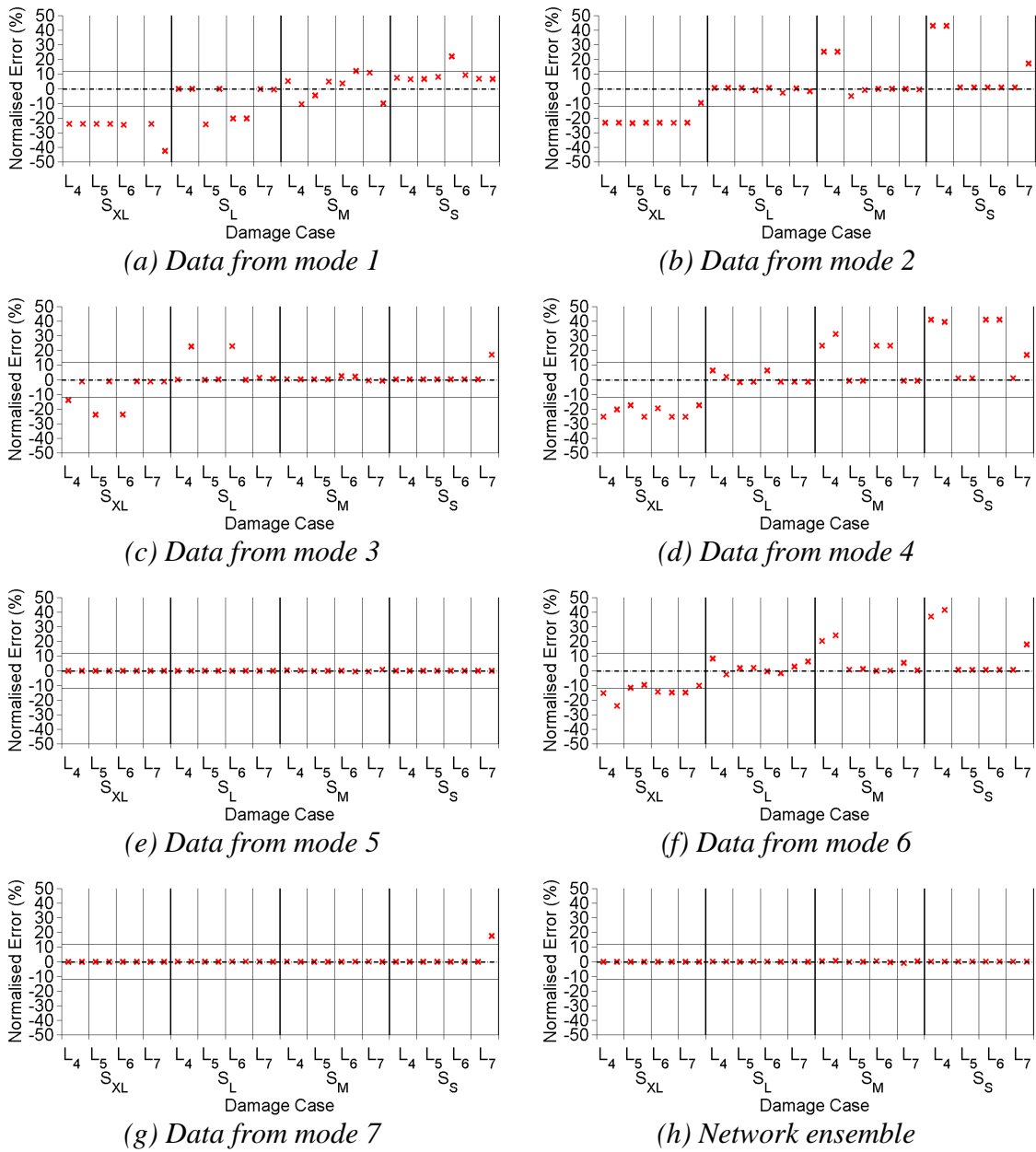


Figure G.9 Neural networks testing set outcomes of networks trained with PCA-compressed a_j values to identify damage severities of numerical beams polluted with 2% noise.

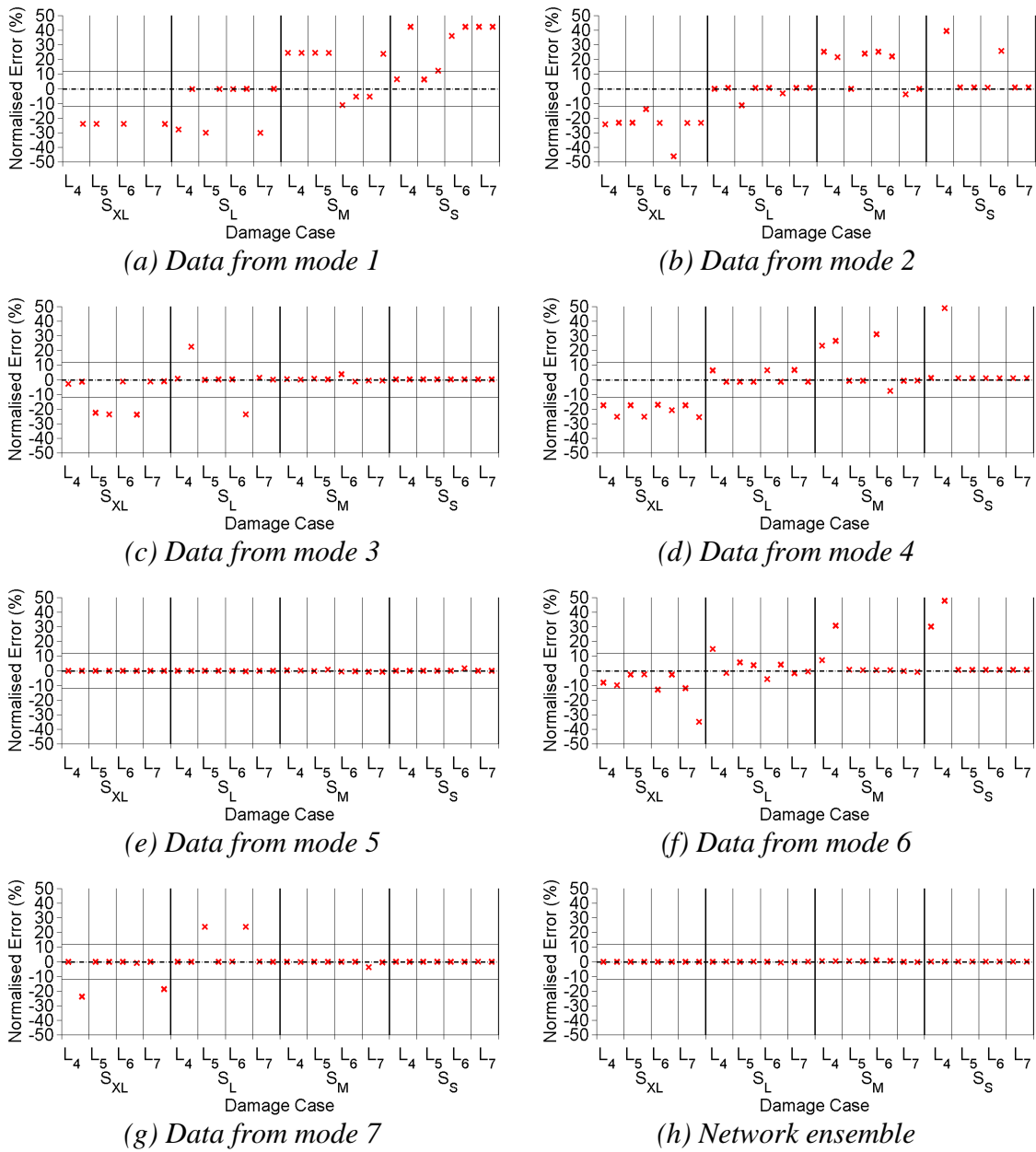


Figure G.10 Neural networks testing set outcomes of networks trained with PCA-compressed a_j values to identify damage severities of numerical beams polluted with 5% noise.

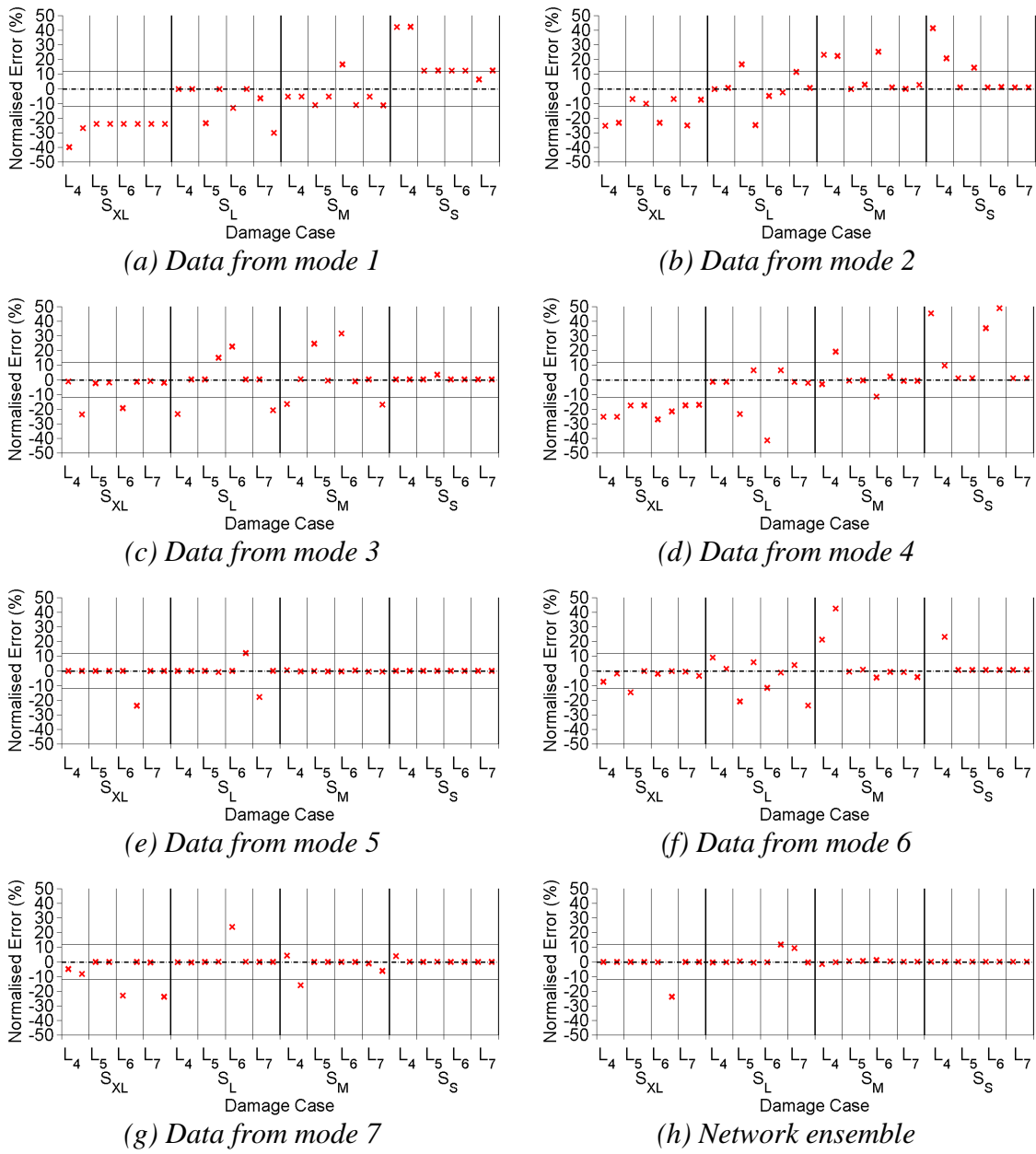
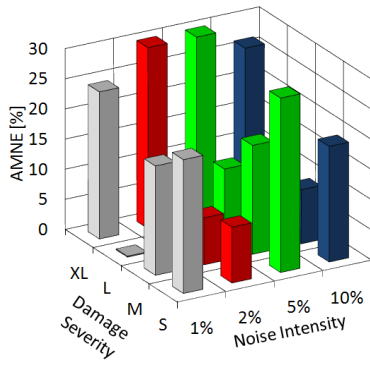
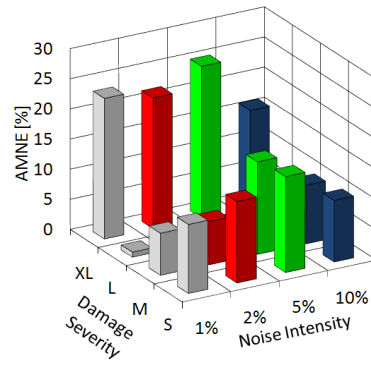


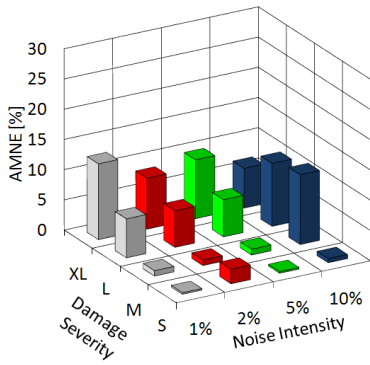
Figure G.11 Neural networks testing set outcomes of networks trained with PCA-compressed α_j values to identify damage severities of numerical beams polluted with 10% noise.



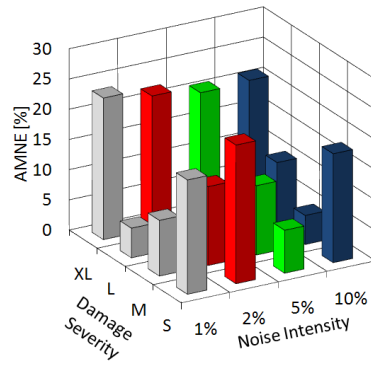
(a) Data from mode 1



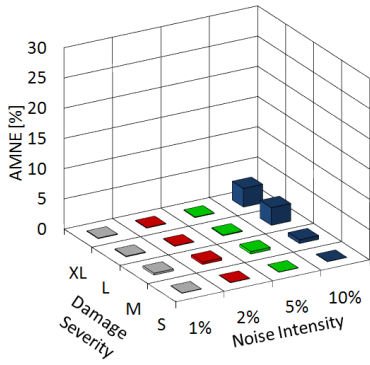
(b) Data from mode 2



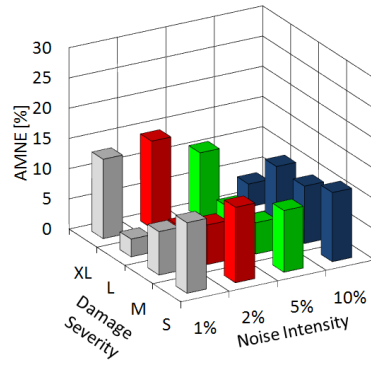
(c) Data from mode 3



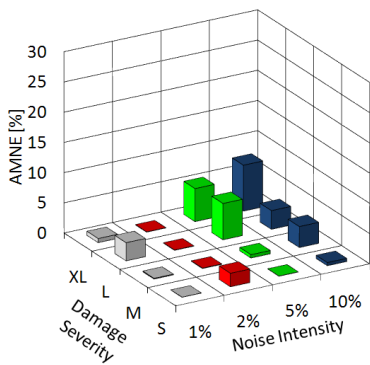
(d) Data from mode 4



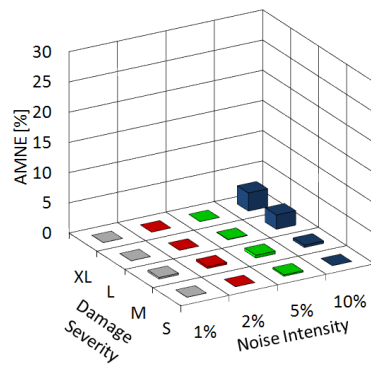
(e) Data from mode 5



(f) Data from mode 6



(g) Data from mode 7



(h) Network ensemble

Figure G.12 Comparison of testing set outcomes of networks trained with PCA-compressed α_j values to identify damage severities of noise-polluted numerical beams subdivided by damage severity and noise pollution level.

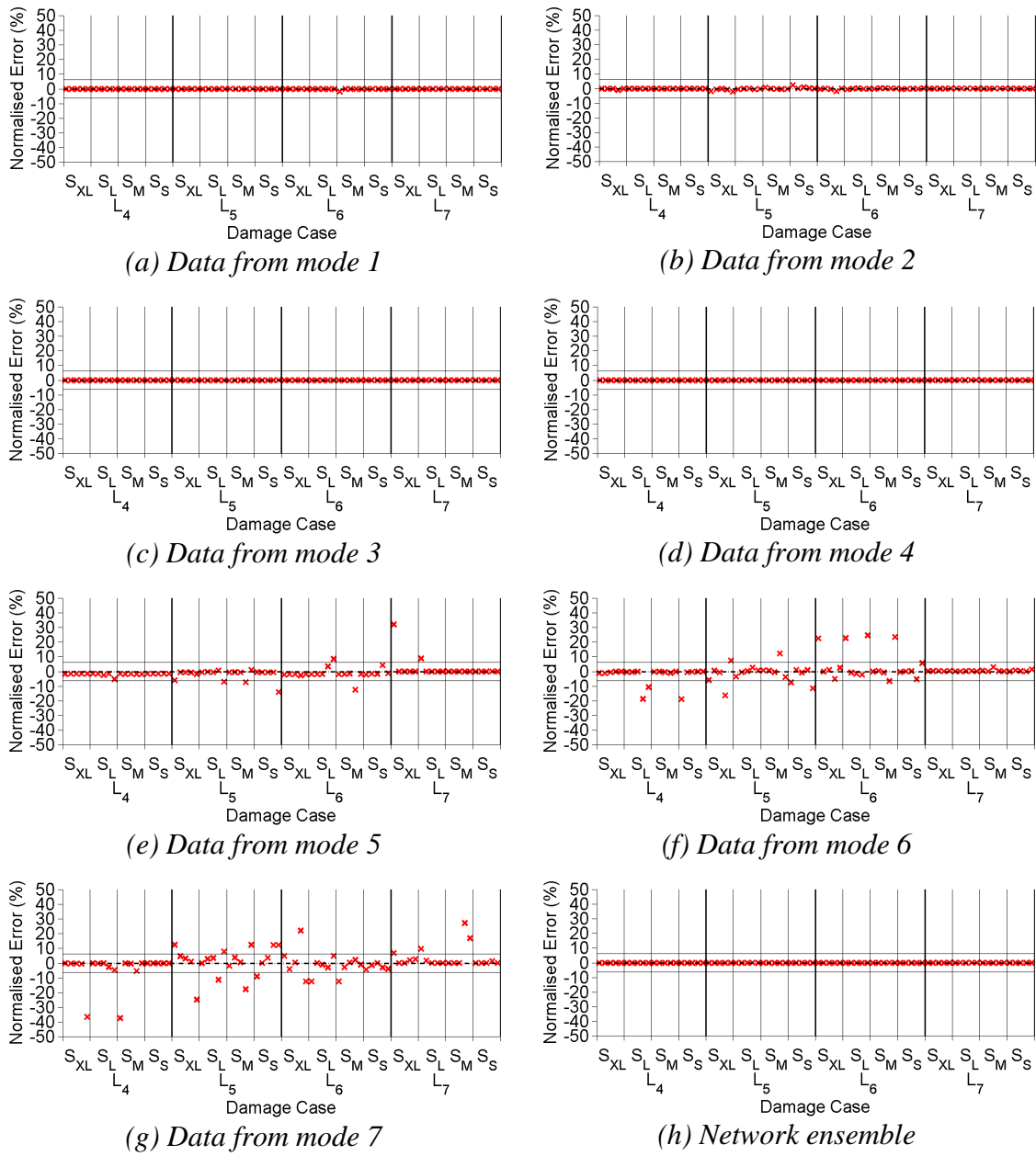


Figure G.13 Neural networks testing set outcomes of networks trained with PCA-compressed Z_j values to identify damage locations of laboratory beams.

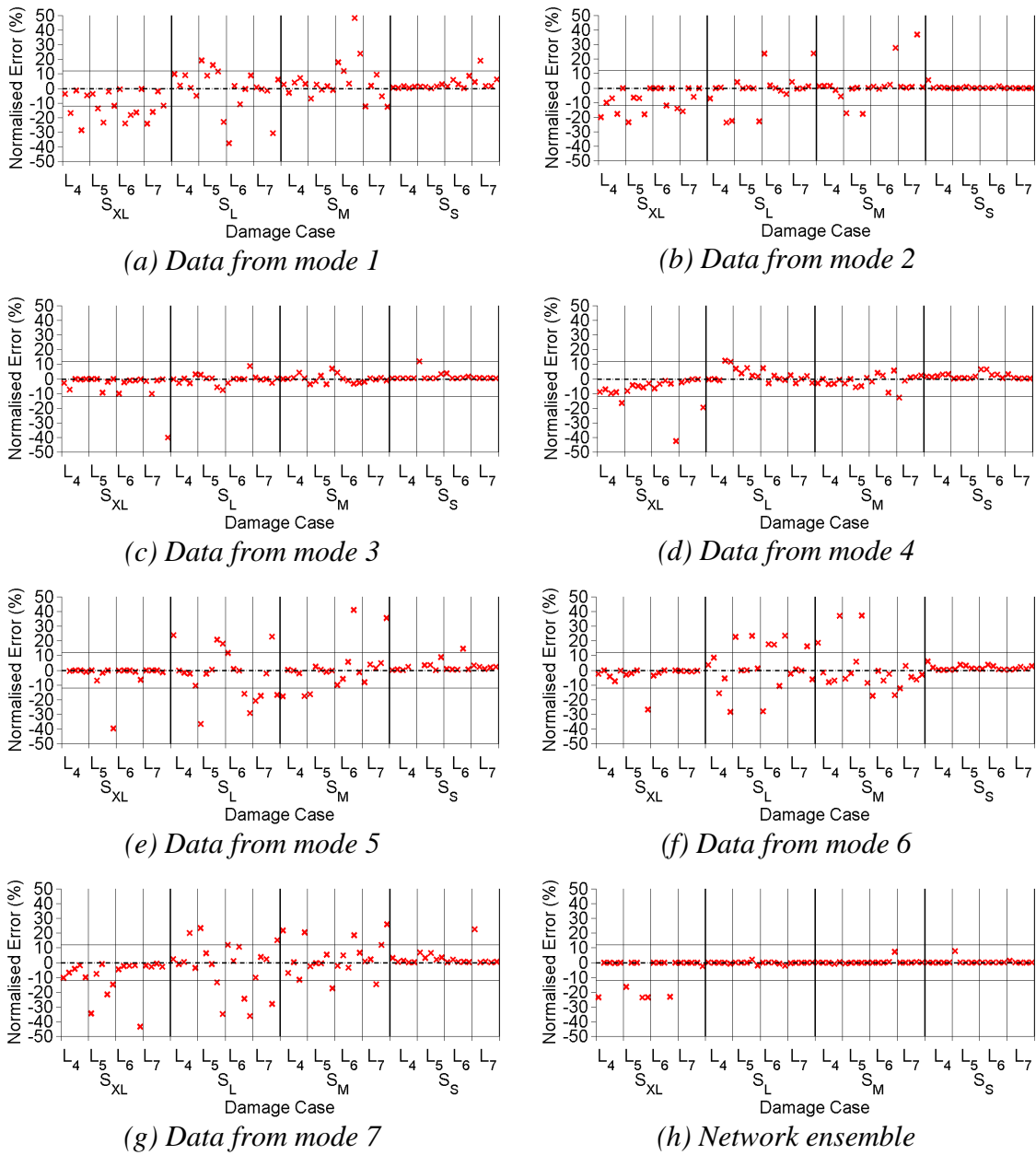


Figure G.14 Neural networks testing set outcomes of networks trained with PCA-compressed α_j values to identify damage severities of laboratory beams.

APPENDIX H

DAMAGE IDENTIFICATION OUTCOMES OF BEAM STRUCTURE BASED ON RESIDUAL FRFS

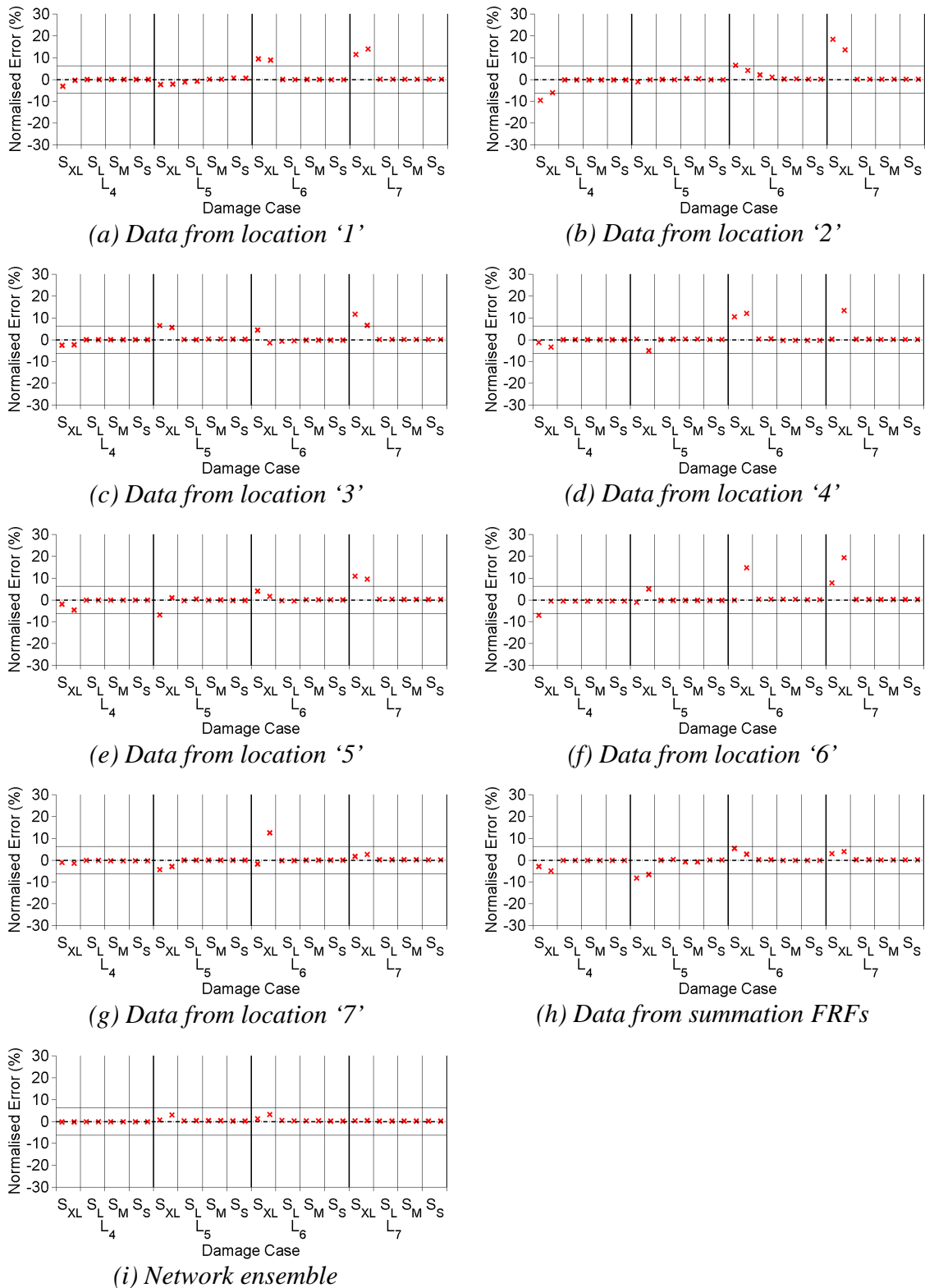


Figure H.1 Neural networks testing set outcomes of networks trained with PCA-compressed residual FRFs to identify damage locations of numerical beams polluted with 1% noise.

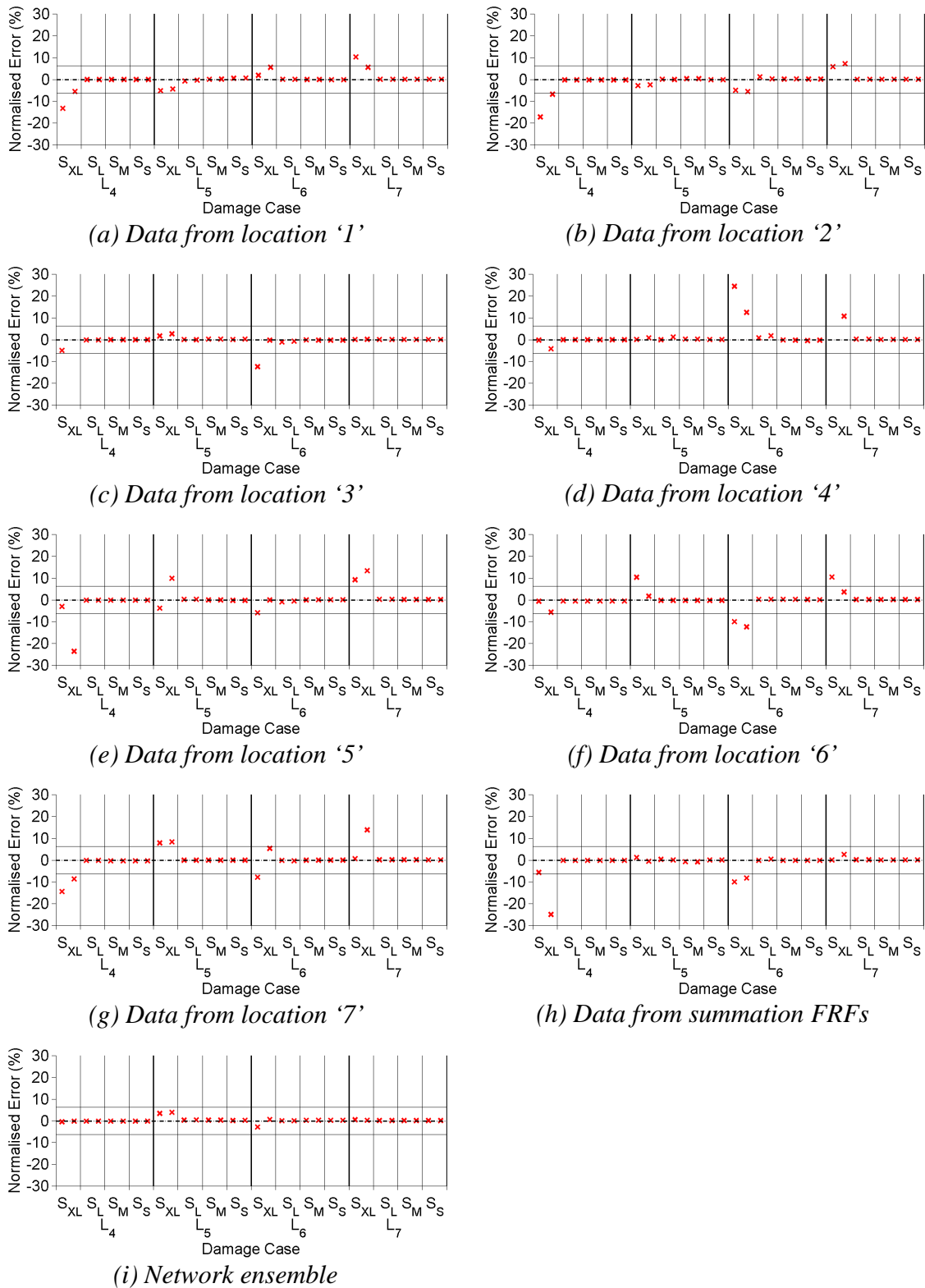


Figure H.2 Neural networks testing set outcomes of networks trained with PCA-compressed residual FRFs to identify damage locations of numerical beams polluted with 2% noise.

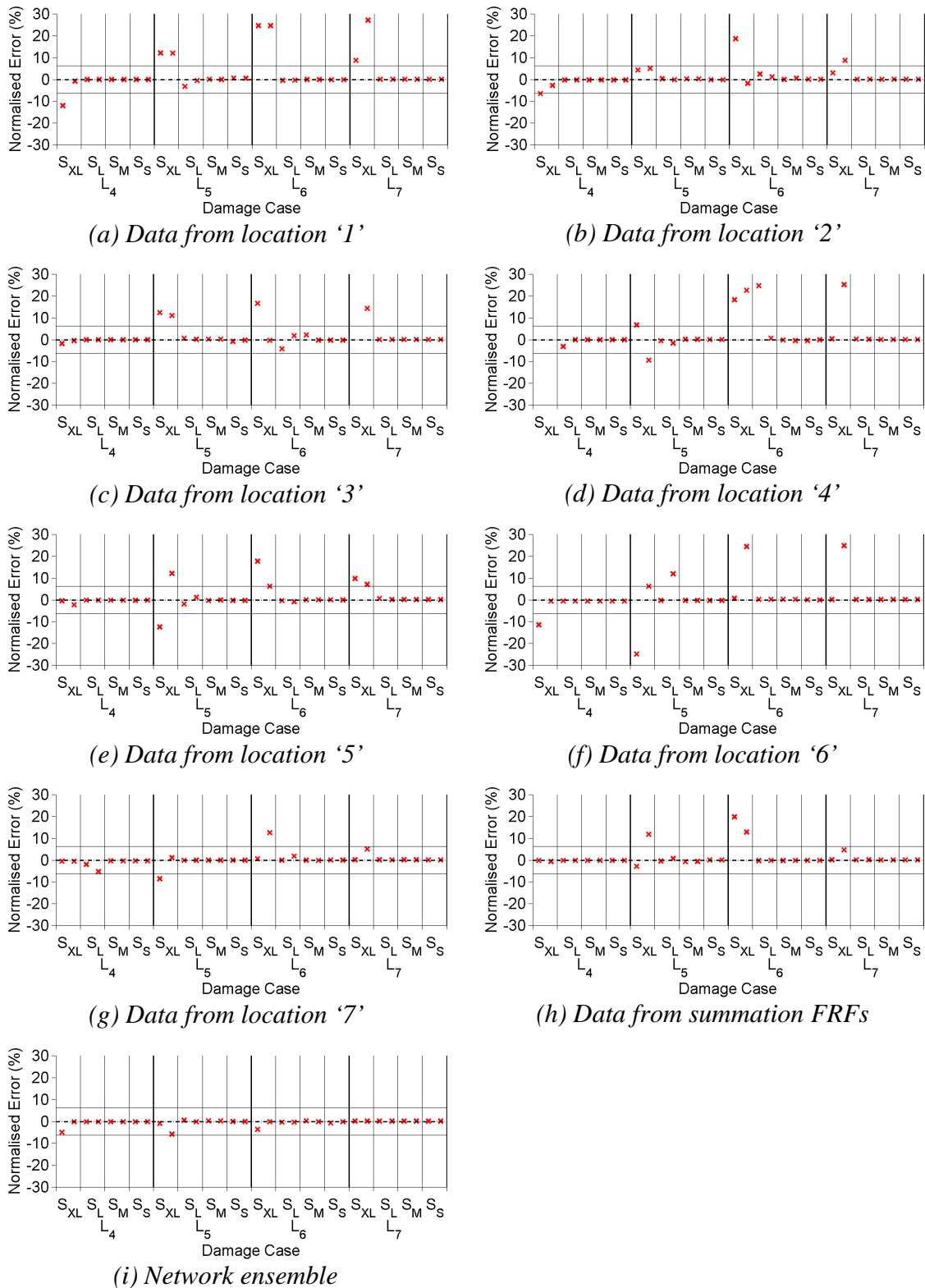


Figure H.3 Neural networks testing set outcomes of networks trained with PCA-compressed residual FRFs to identify damage locations of numerical beams polluted with 5% noise.

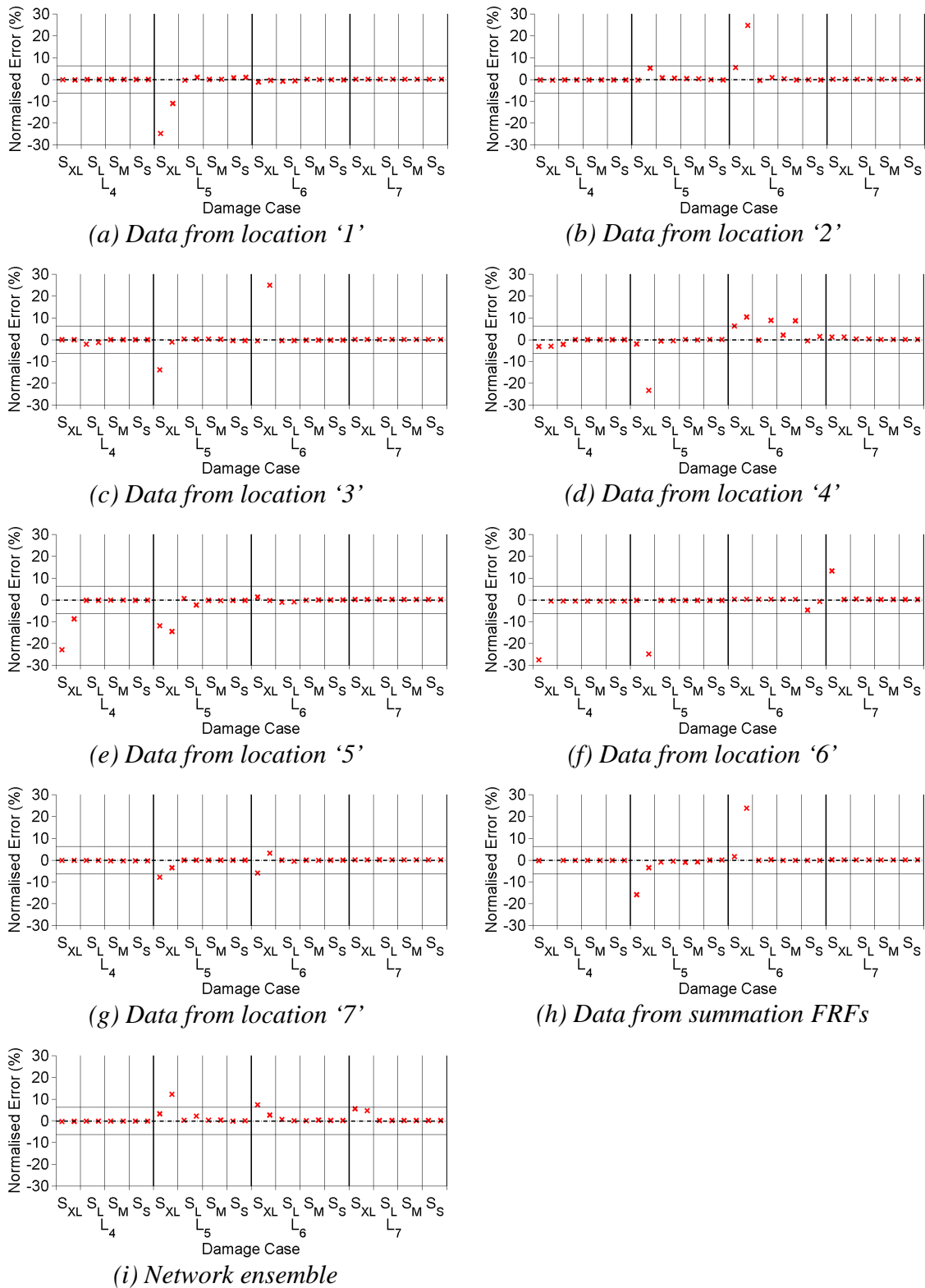


Figure H.4 Neural networks testing set outcomes of networks trained with PCA-compressed residual FRFs to identify damage locations of numerical beams polluted with 10% noise.

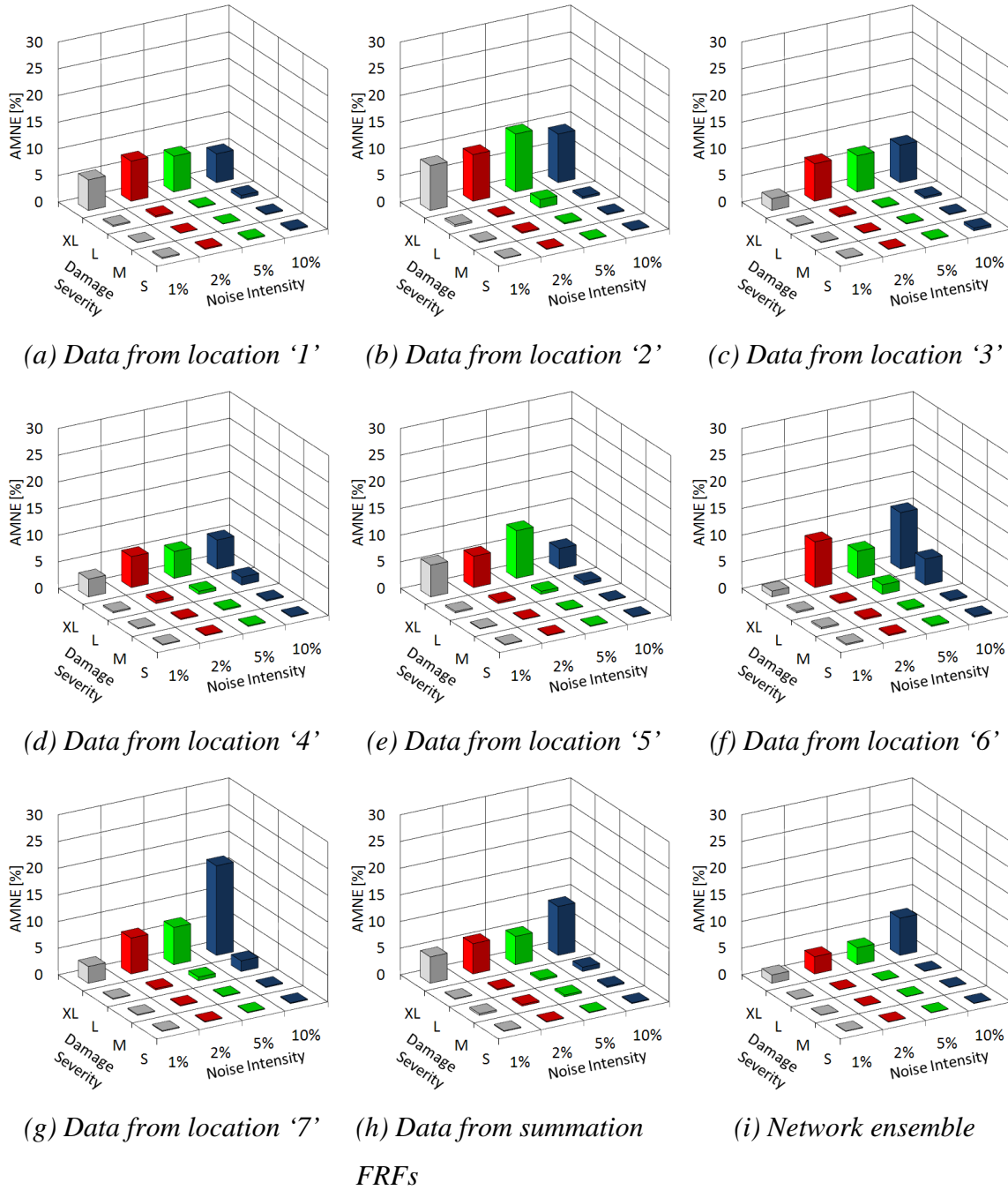


Figure H.5 Comparison of testing set outcomes of networks trained with PCA-compressed residual FRFs to identify damage locations of noise-polluted numerical beams subdivided by damage severity and noise pollution level.

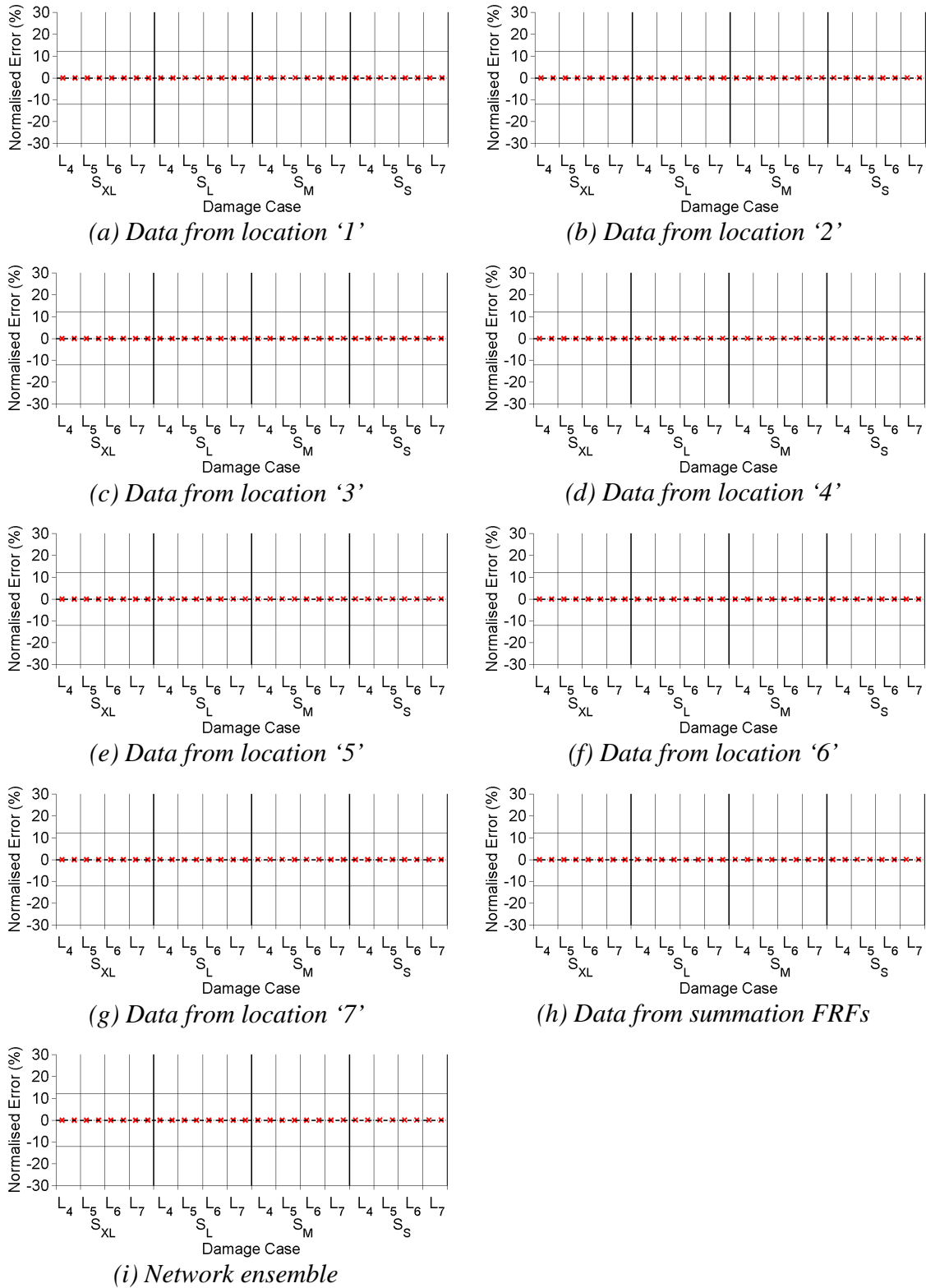


Figure H.6 Neural networks testing set outcomes of networks trained with PCA-compressed residual FRFs to identify damage severities of numerical beams polluted with 1% noise.

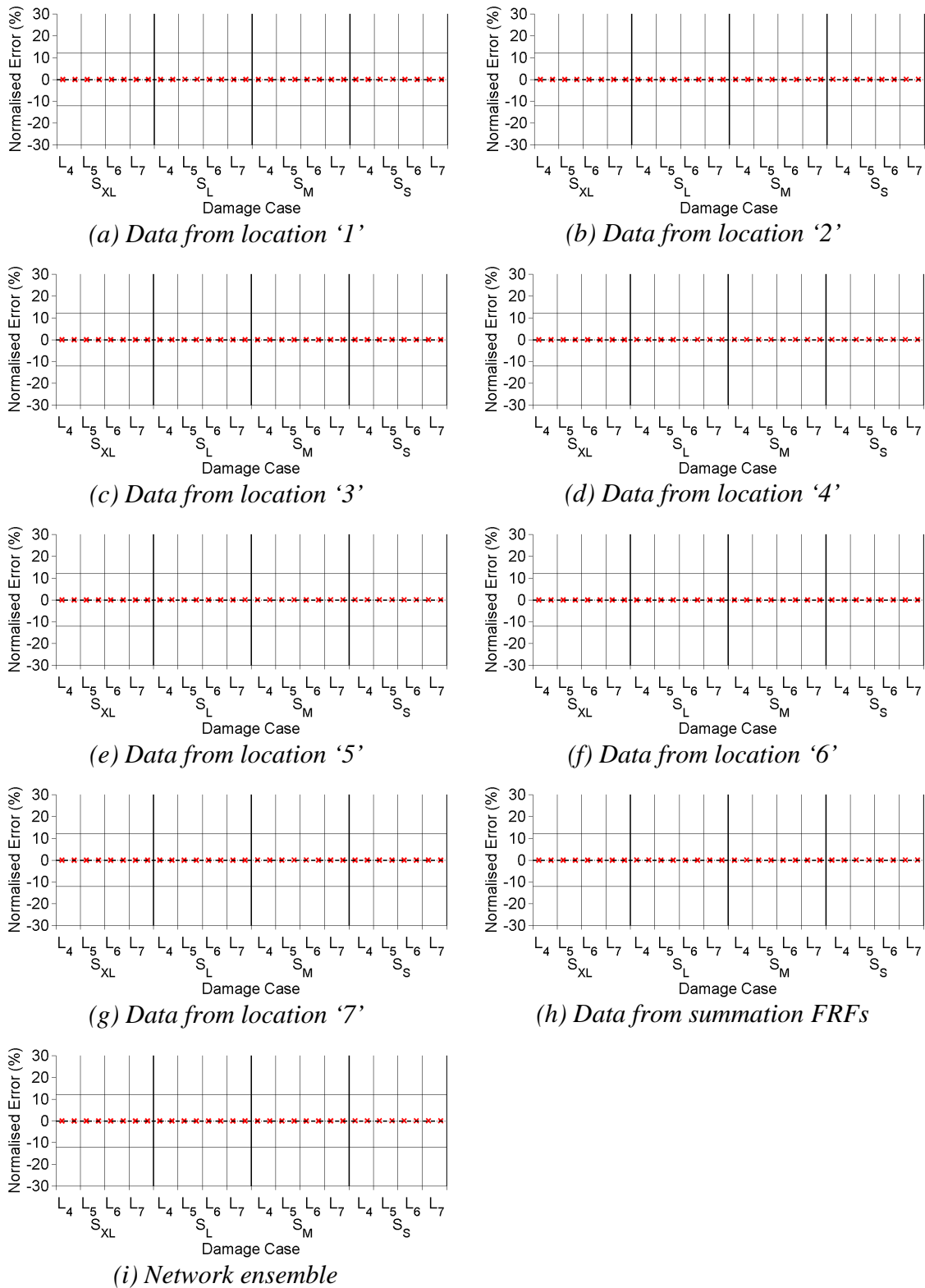


Figure H.7 Neural networks testing set outcomes of networks trained with PCA-compressed residual FRFs to identify damage severities of numerical beams polluted with 2% noise.

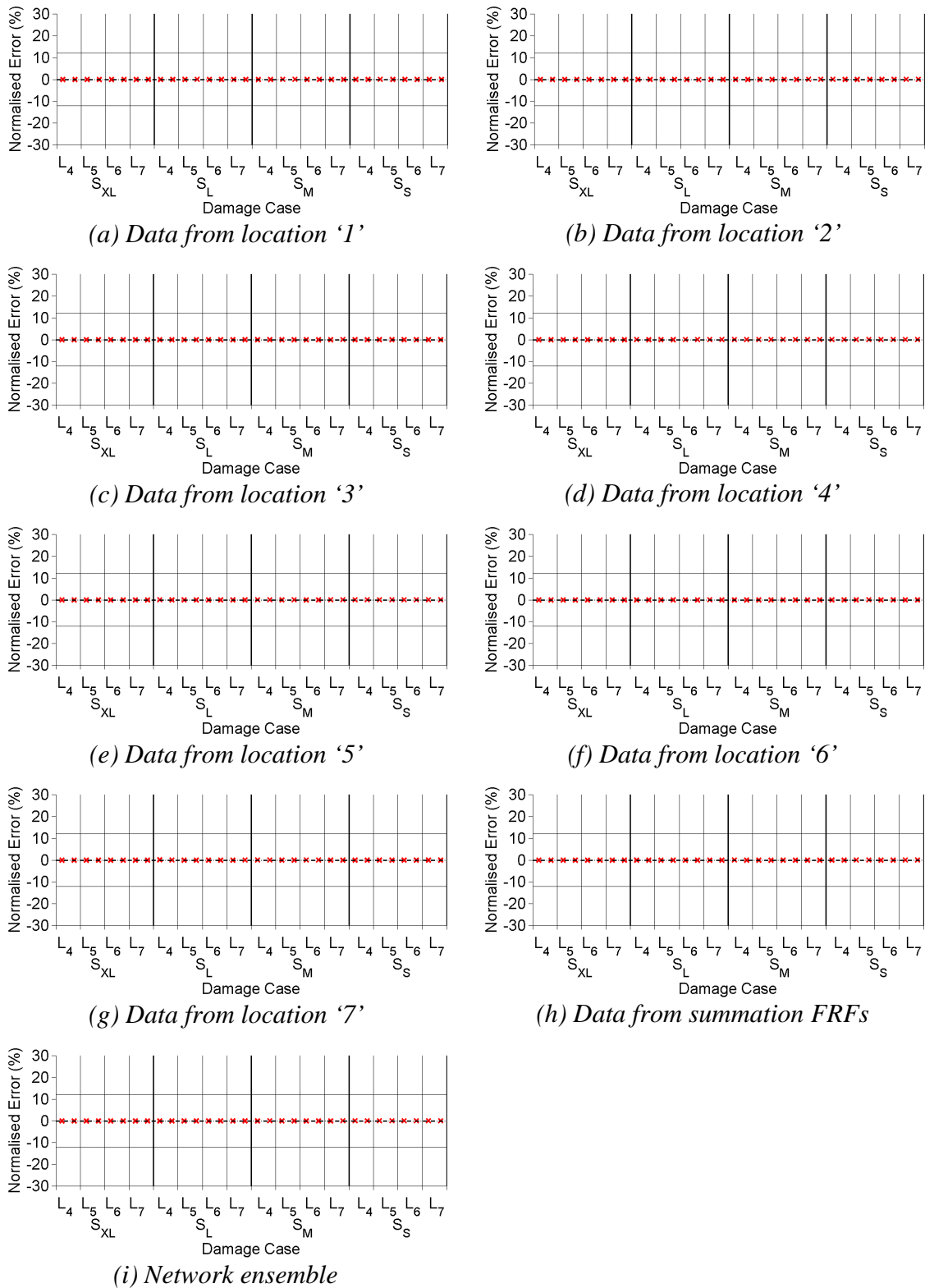


Figure H.8 Neural networks testing set outcomes of networks trained with PCA-compressed residual FRFs to identify damage severities of numerical beams polluted with 5% noise.

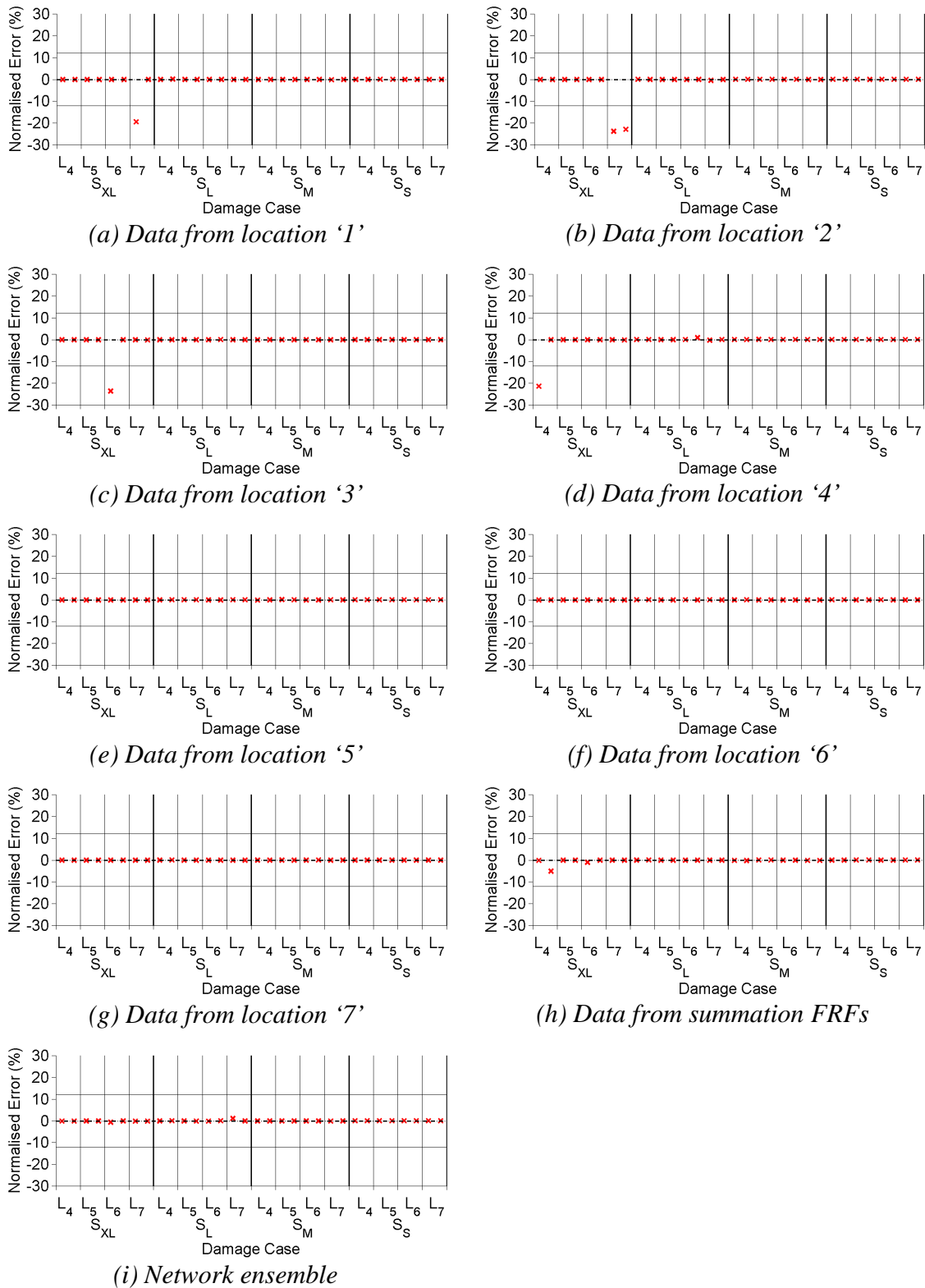


Figure H.9 Neural networks testing set outcomes of networks trained with PCA-compressed residual FRFs to identify damage severities of numerical beams polluted with 10% noise.

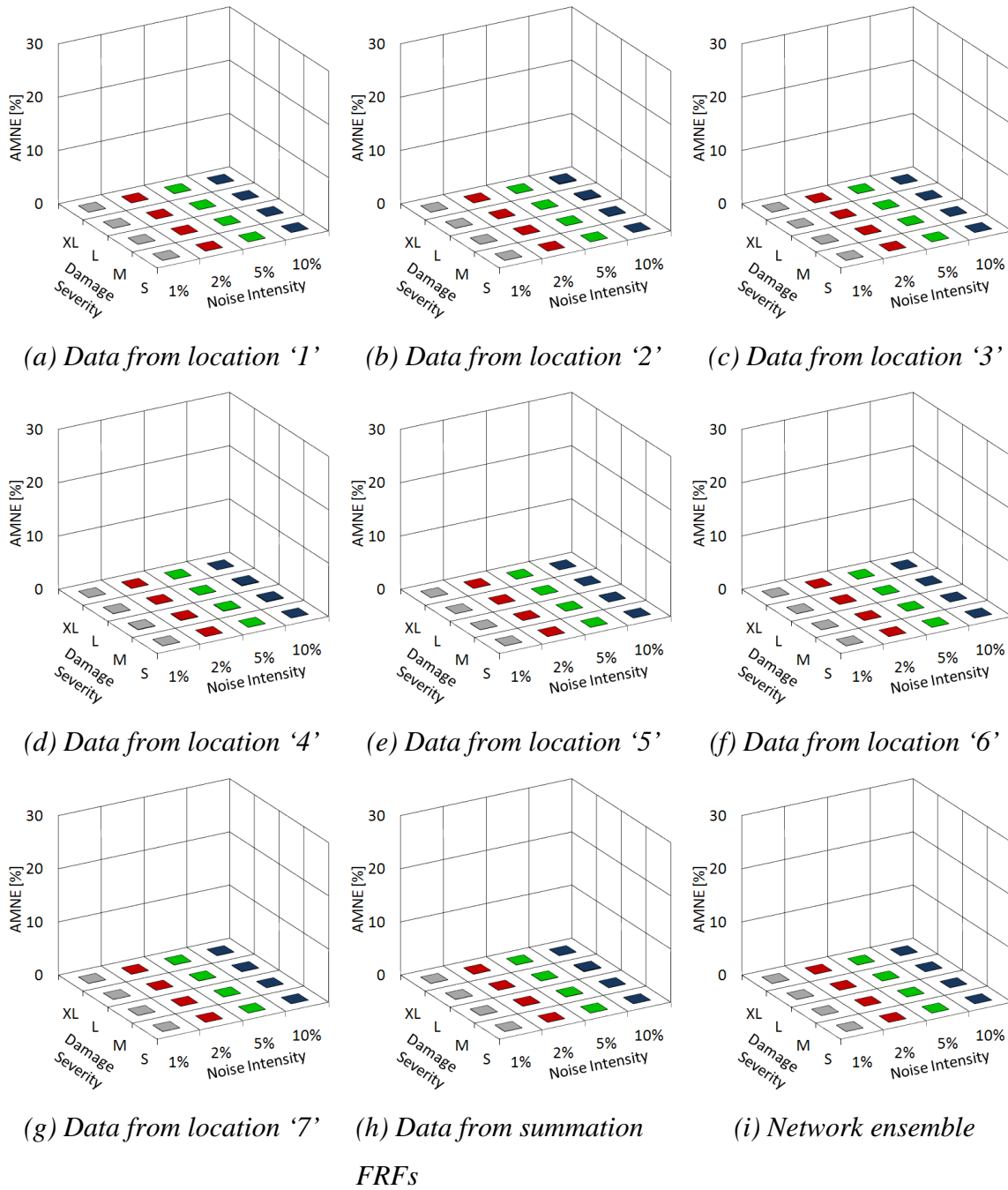


Figure H.10 Comparison of testing set outcomes of networks trained with PCA-compressed residual FRFs to identify damage severities of noise-polluted numerical beams subdivided by damage severity and noise pollution level.

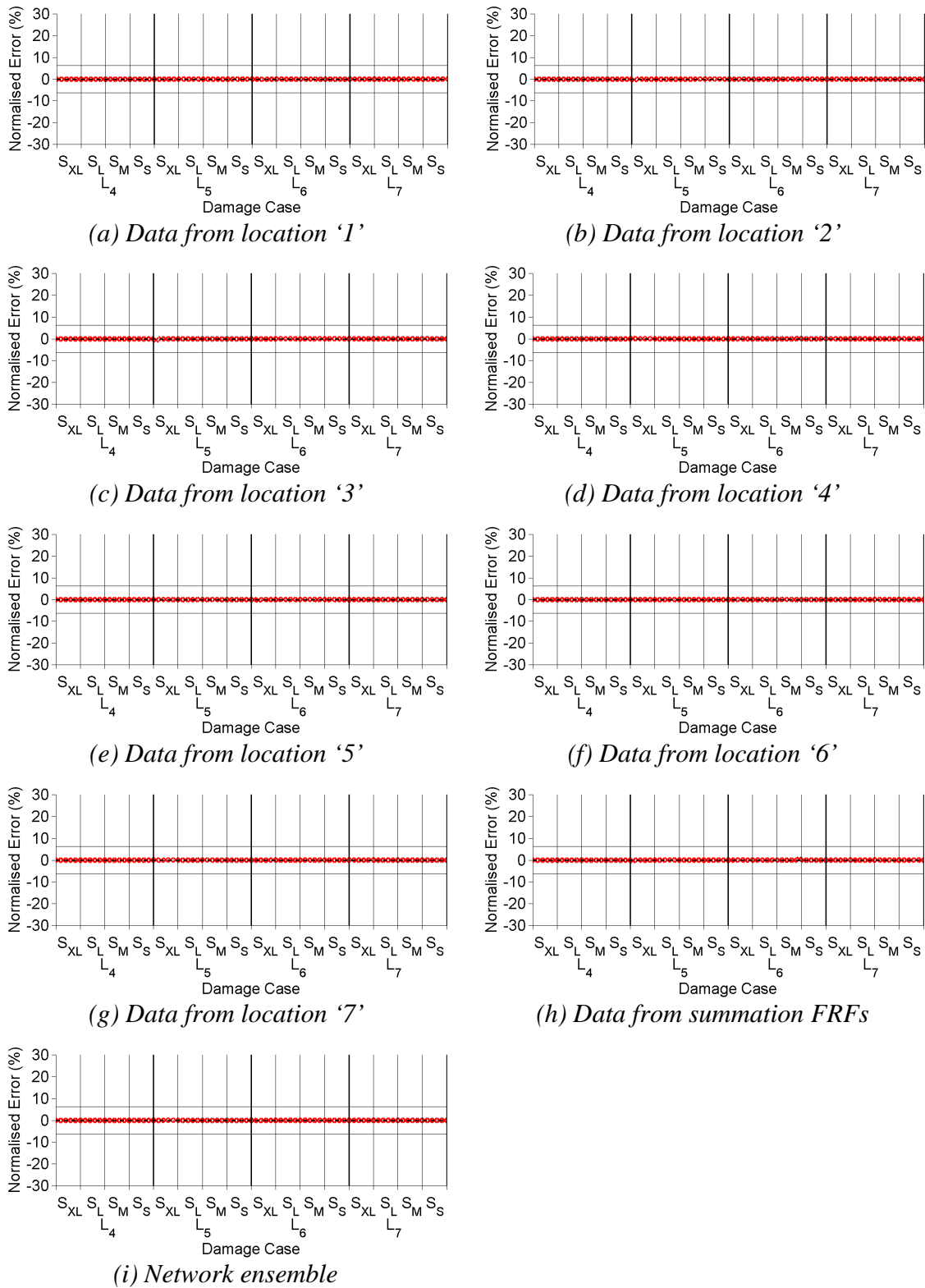


Figure H.11 Neural networks testing set outcomes of networks trained with PCA-compressed residual FRFs to identify damage locations of laboratory beams.

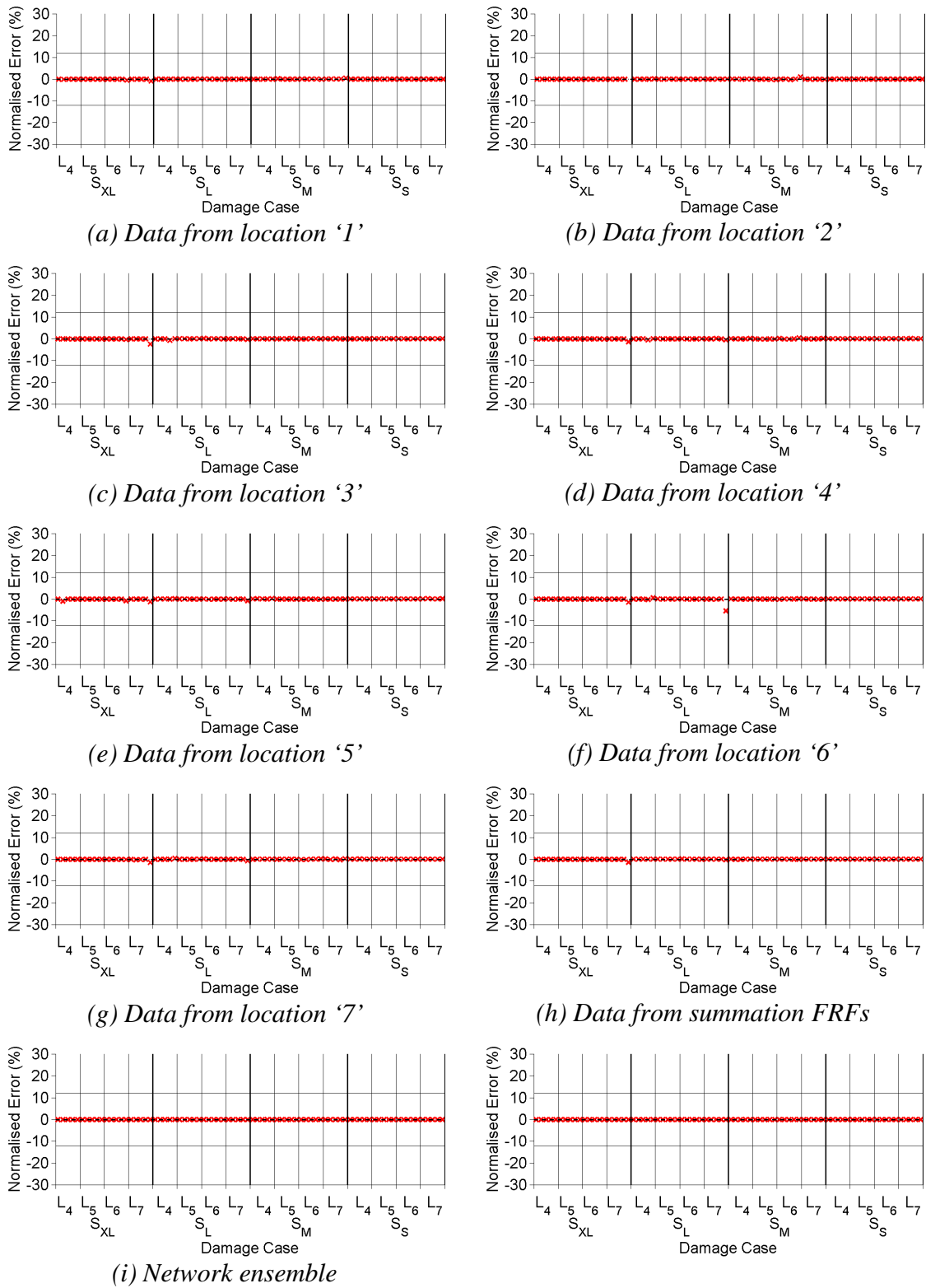


Figure H.12 Neural networks testing set outcomes of networks trained with PCA-compressed residual FRFs to identify damage severities of laboratory beams.

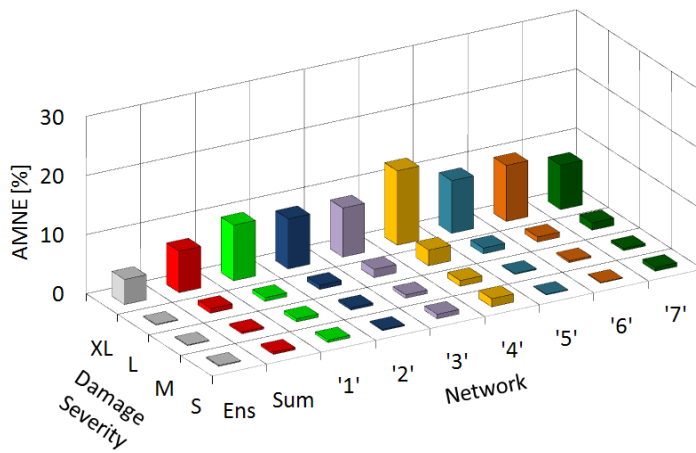
APPENDIX I

DAMAGE IDENTIFICATION OUTCOMES OF BEAM STRUCTURE BASED ON CNR-FRFS

Table I.1 Neural network specifications and performance (in AMNE) trained with PCA-compressed CNR-FRFs from noise-polluted numerical beams to identify damage locations.

Network	Network design	Convergence algorithm	Iteration	Training performance (AMNE [%])	Validation performance (AMNE [%])	Testing performance (AMNE [%])
'1'	7-6-4-2-1	Qp	5082	1.72	2.82	2.70
'2'	7-6-4-2-1	Qp	4860	1.82	2.62	2.44
'3'	7-6-4-2-1	Qp	6639	1.12	2.67	2.74
'4'	7-6-4-2-1	Qp	4392	2.93	4.19	4.39
'5'	7-6-4-2-1	Qp	7106	1.47	1.60	2.54
'6'	7-6-4-2-1	Qp	6724	1.27	1.60	2.69
'7'	7-6-4-2-1	Qp	5530	2.08	2.16	2.45
Sum	7-6-4-2-1	Qp	8711	1.29	1.97	2.12
Ens	7-6-4-2-1	Obp	13297	0.31	0.89	1.16

Note: Qp = Quick propagation function
 Obp = Online backpropagation function



Network	Network performance (AMNE [%])			
	S _{XL}	S _L	S _M	S _S
Ens	4.23	0.13	0.12	0.15
Sum	7.02	0.79	0.31	0.37
Mode 1	9.41	0.63	0.52	0.42
Mode 2	8.47	0.71	0.38	0.20
Mode 3	8.28	1.38	0.56	0.75
Mode 4	12.58	2.65	0.97	1.38
Mode 5	8.91	0.97	0.17	0.10
Mode 6	9.48	0.85	0.30	0.12
Mode 7	7.51	1.25	0.38	0.64

Figure I.1 Neural network testing set performance (in AMNE) subdivided by damage severity trained with PCA-compressed CNR-FRFs from noise-polluted numerical beams to identify damage locations.

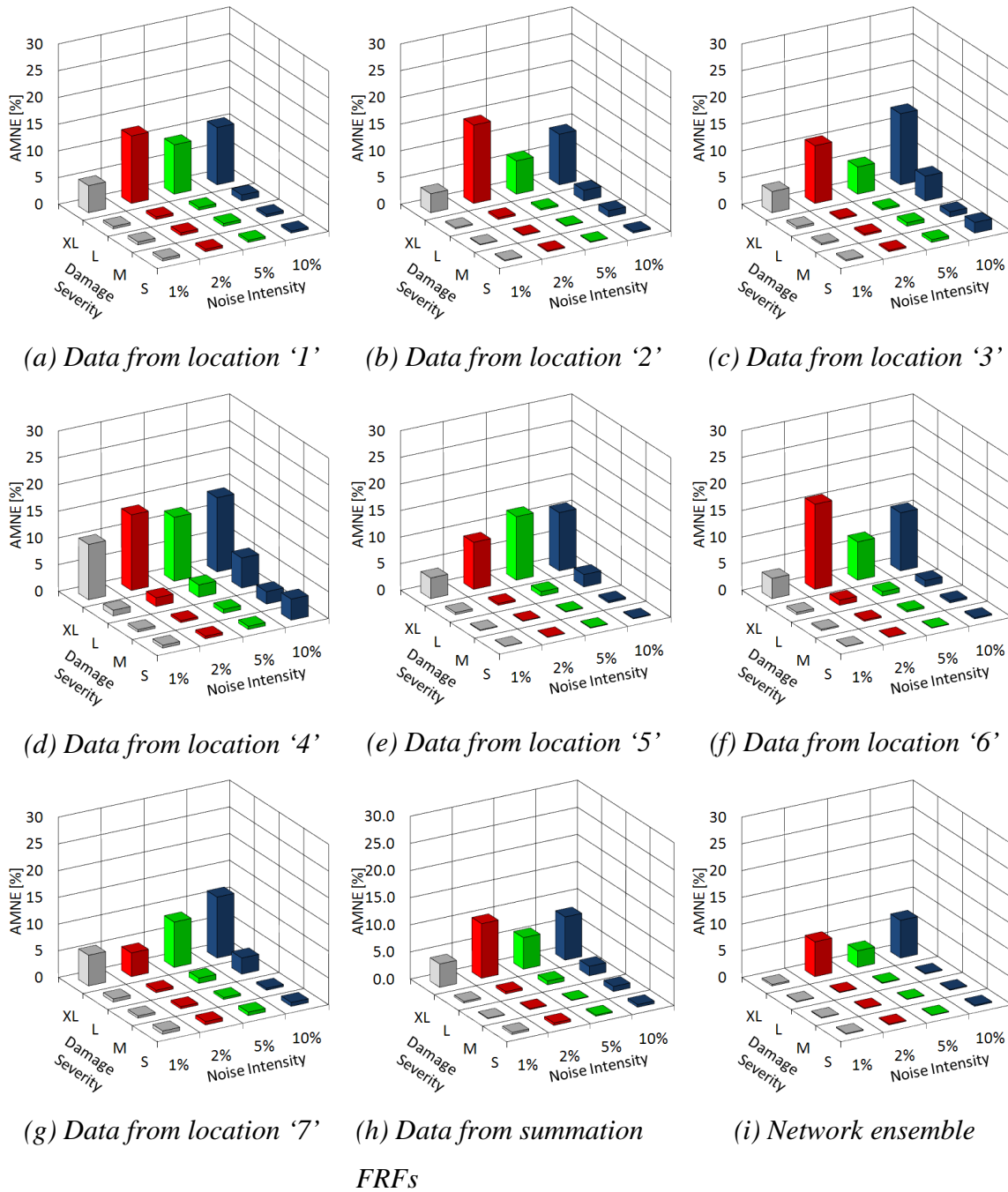


Figure I.2 Comparison of testing set outcomes of networks trained with PCA-compressed CNR-FRFs to identify damage locations of noise-polluted numerical beams subdivided by damage severity and noise pollution level.

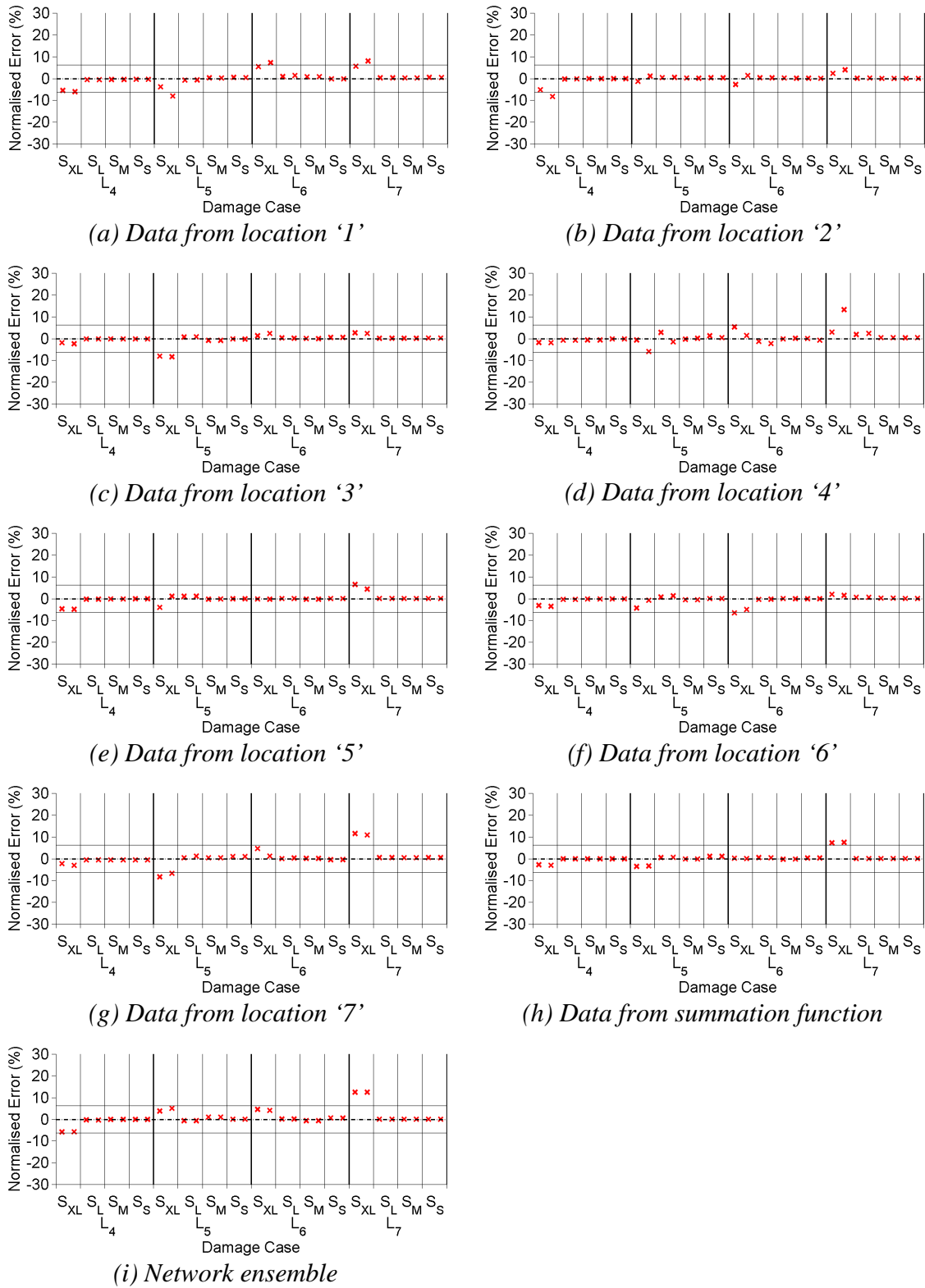


Figure I.3 Neural networks testing set outcomes of networks trained with PCA-compressed CNR-FRFs to identify damage locations of numerical beams polluted with 1% noise.

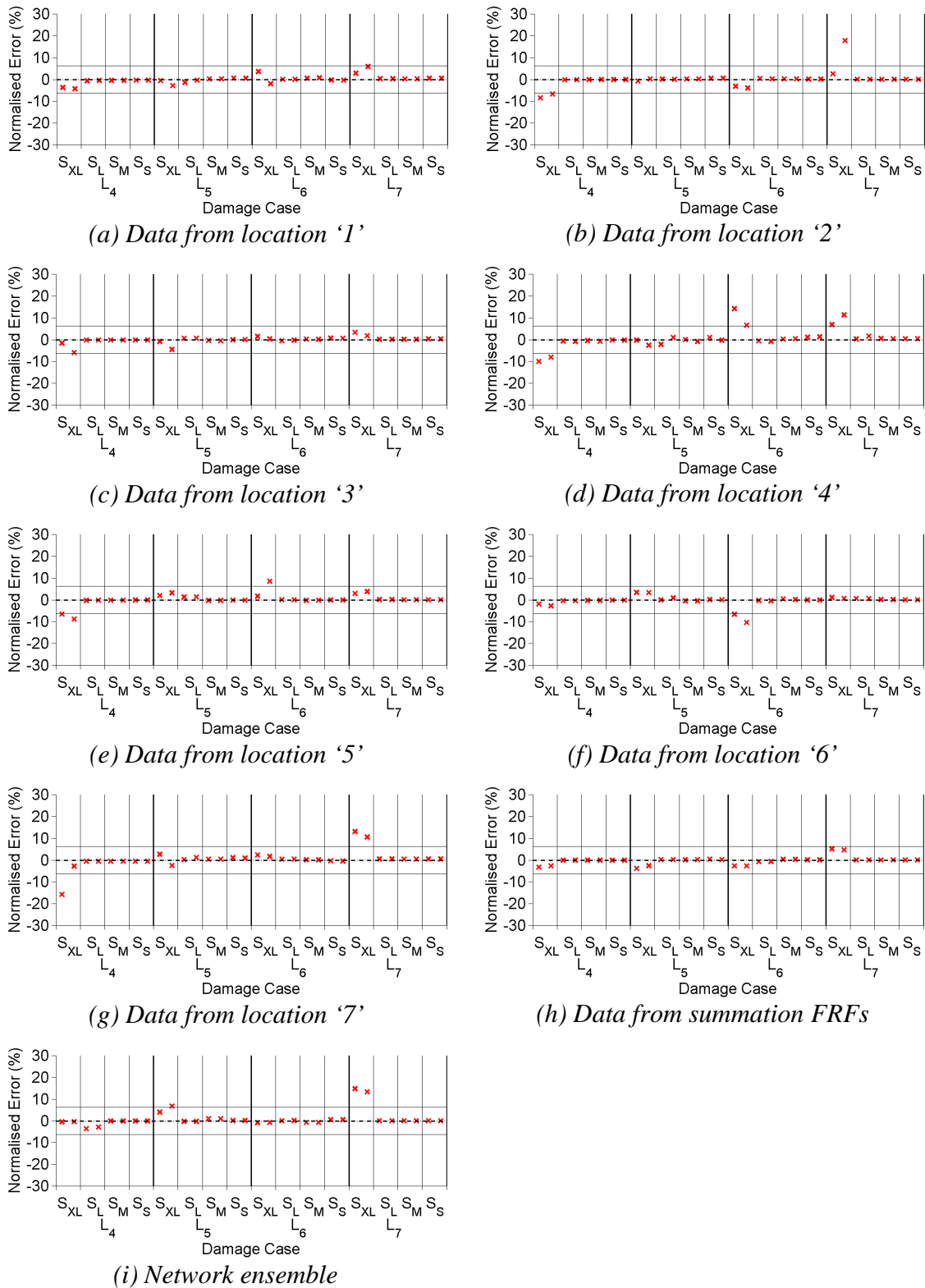


Figure I.4 Neural networks testing set outcomes of networks trained with PCA-compressed CNR-FRFs to identify damage locations of numerical beams polluted with 2% noise.

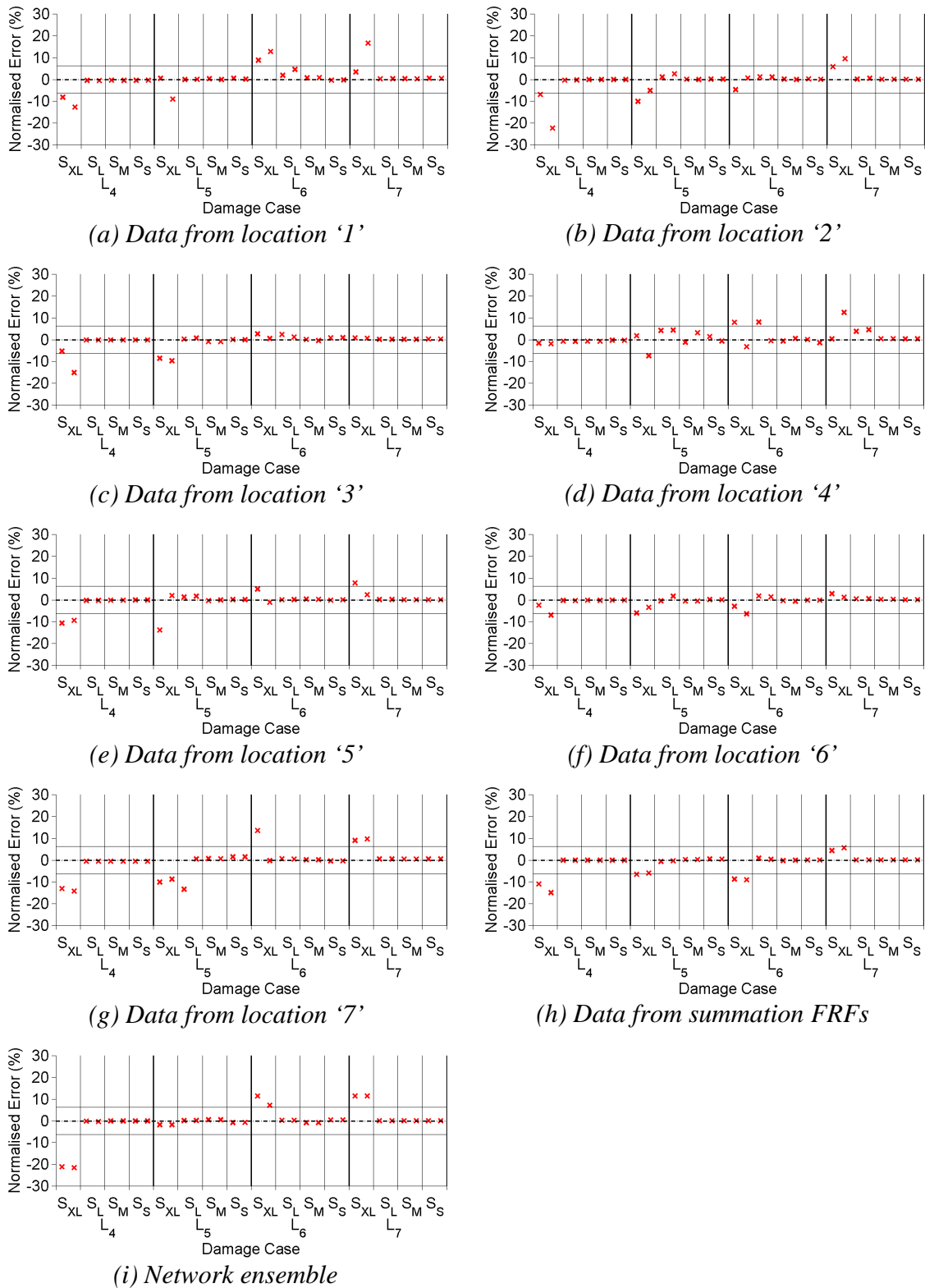


Figure I.5 Neural networks testing set outcomes of networks trained with PCA-compressed CNR-FRFs to identify damage locations of numerical beams polluted with 5% noise.

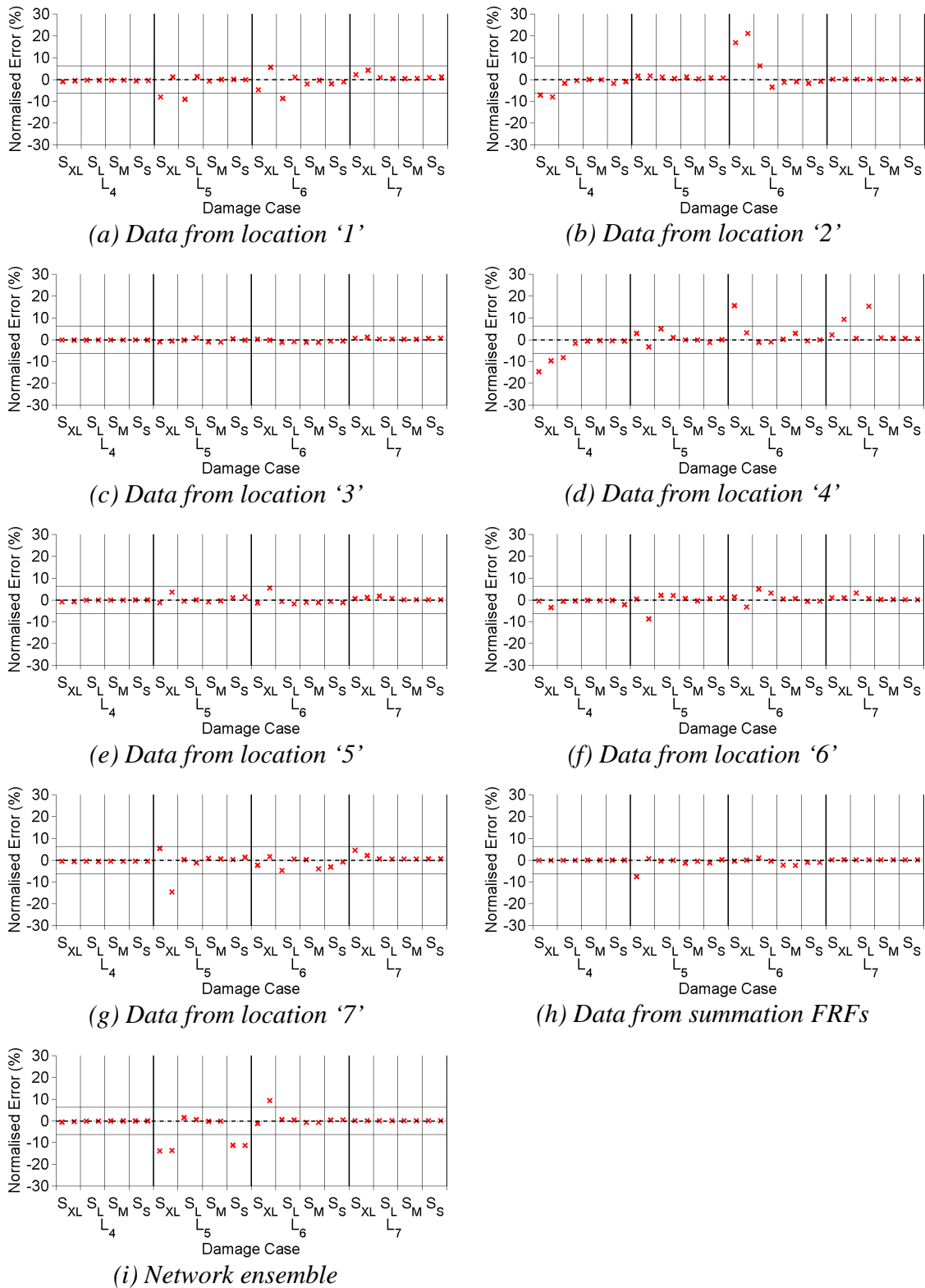
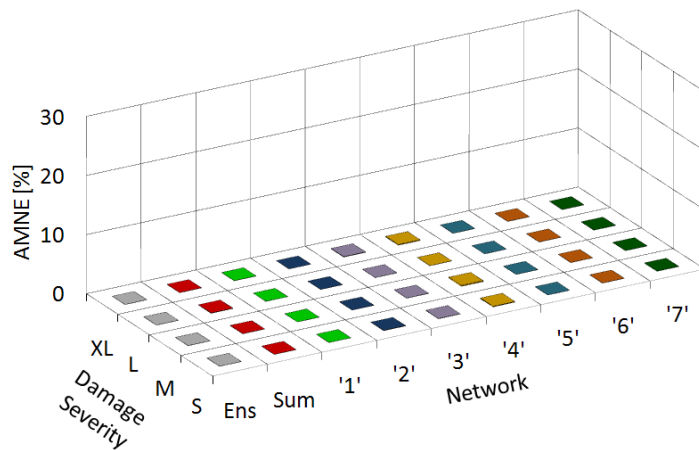


Figure I.6 Neural networks testing set outcomes of networks trained with PCA-compressed CNR-FRFs to identify damage locations of numerical beams polluted with 10% noise.

Table I.2 Neural network specifications and performance (in AMNE) trained with PCA-compressed CNR-FRFs from noise-polluted numerical beams to identify damage severities.

Network	Network design	Convergence algorithm	Iteration	Training performance (AMNE [%])	Validation performance (AMNE [%])	Testing performance (AMNE [%])
'1'	7-6-4-2-1	Obp	2436	<0.01	<0.01	<0.01
'2'	7-6-4-2-1	Obp	3424	0.01	0.01	0.02
'3'	7-6-4-2-1	Obp	1264	0.03	0.03	0.03
'4'	7-6-4-2-1	Obp	836	0.09	0.09	0.09
'5'	7-6-4-2-1	Obp	3697	0.01	0.01	0.01
'6'	7-6-4-2-1	Obp	3926	0.01	0.01	0.01
'7'	7-6-4-2-1	Obp	4378	0.01	0.01	0.01
Sum	7-6-4-2-1	Obp	2647	0.01	0.01	0.02
Ens	7-6-4-2-1	Obp	15598	0.01	0.01	0.01

Note: Cgd = Obp = Online backpropagation function



Network	Network performance (AMNE [%])			
	S _{XL}	S _L	S _M	S _S
Ens	0.01	0.01	0.01	0.01
Sum	0.01	0.04	0.02	0.01
Mode 1	0.01	<0.01	<0.01	<0.01
Mode 2	<0.01	0.01	0.01	0.04
Mode 3	0.06	0.01	0.02	0.03
Mode 4	0.11	0.01	0.15	0.10
Mode 5	0.01	<0.01	0.01	0.01
Mode 6	0.01	0.01	0.01	0.01
Mode 7	0.01	0.01	0.01	0.01

Figure I.7 Neural network testing set performance (in AMNE) subdivided by damage severity trained with PCA-compressed CNR-FRFs from noise-polluted numerical beams to identify damage severities.

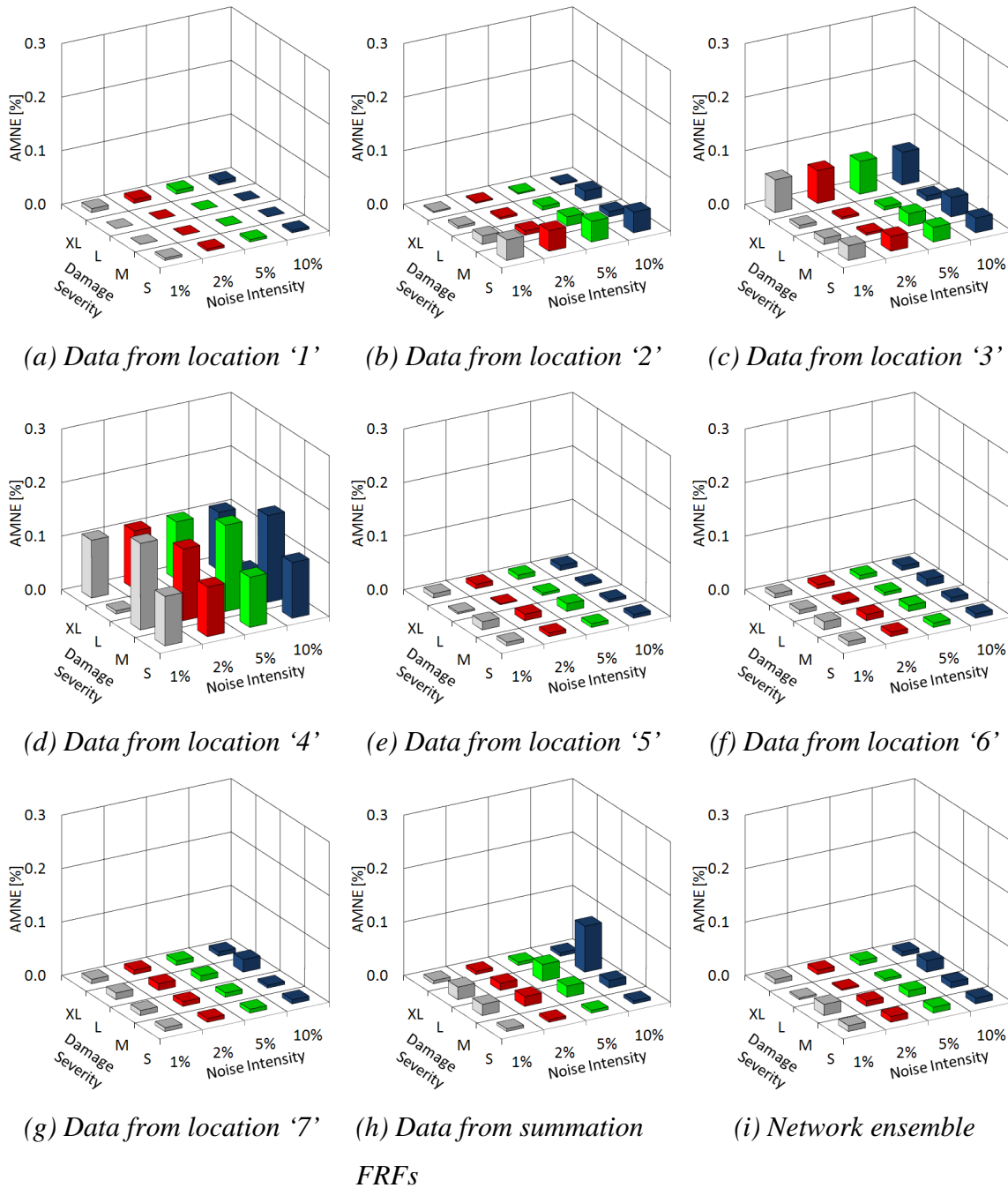


Figure I.8 Comparison of testing set outcomes of networks trained with PCA-compressed CNR-FRFs to identify damage severities of noise-polluted numerical beams subdivided by damage severity and noise pollution level.

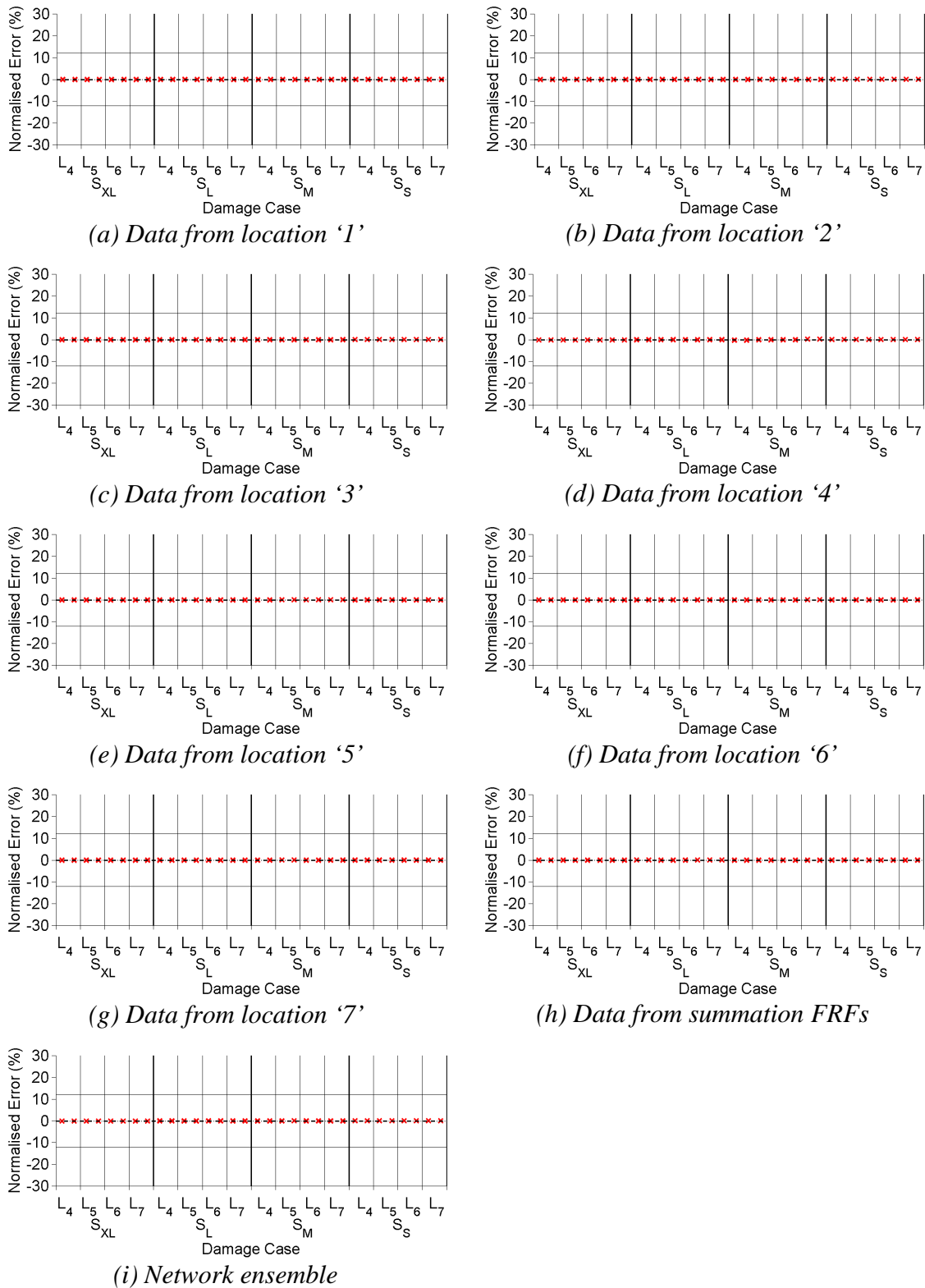


Figure I.9 Neural networks testing set outcomes of networks trained with PCA-compressed CNR-FRFs to identify damage severities of numerical beams polluted with 1% noise.

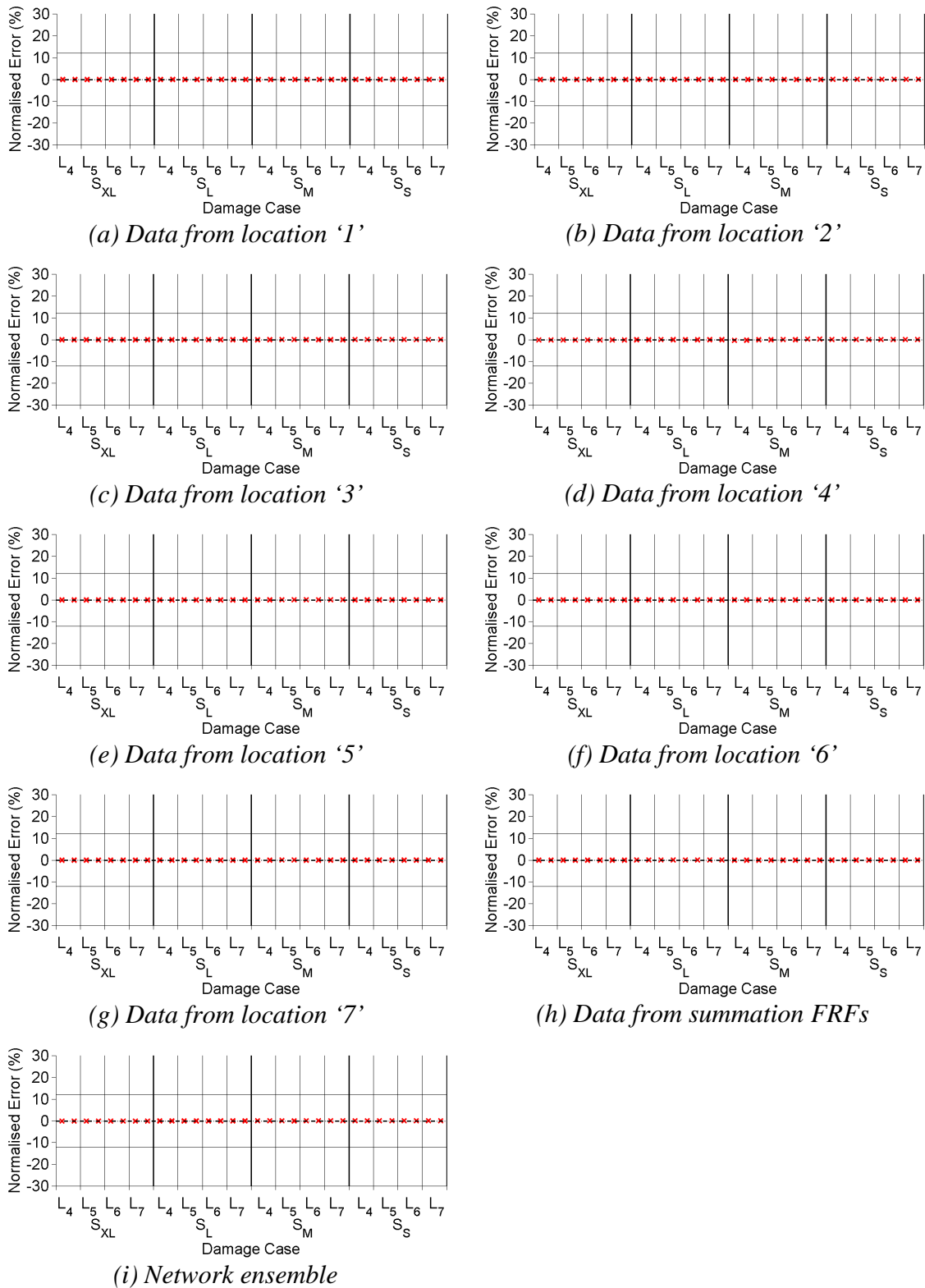


Figure I.10 Neural networks testing set outcomes of networks trained with PCA-compressed CNR-FRFs to identify damage severities of numerical beams polluted with 2% noise.

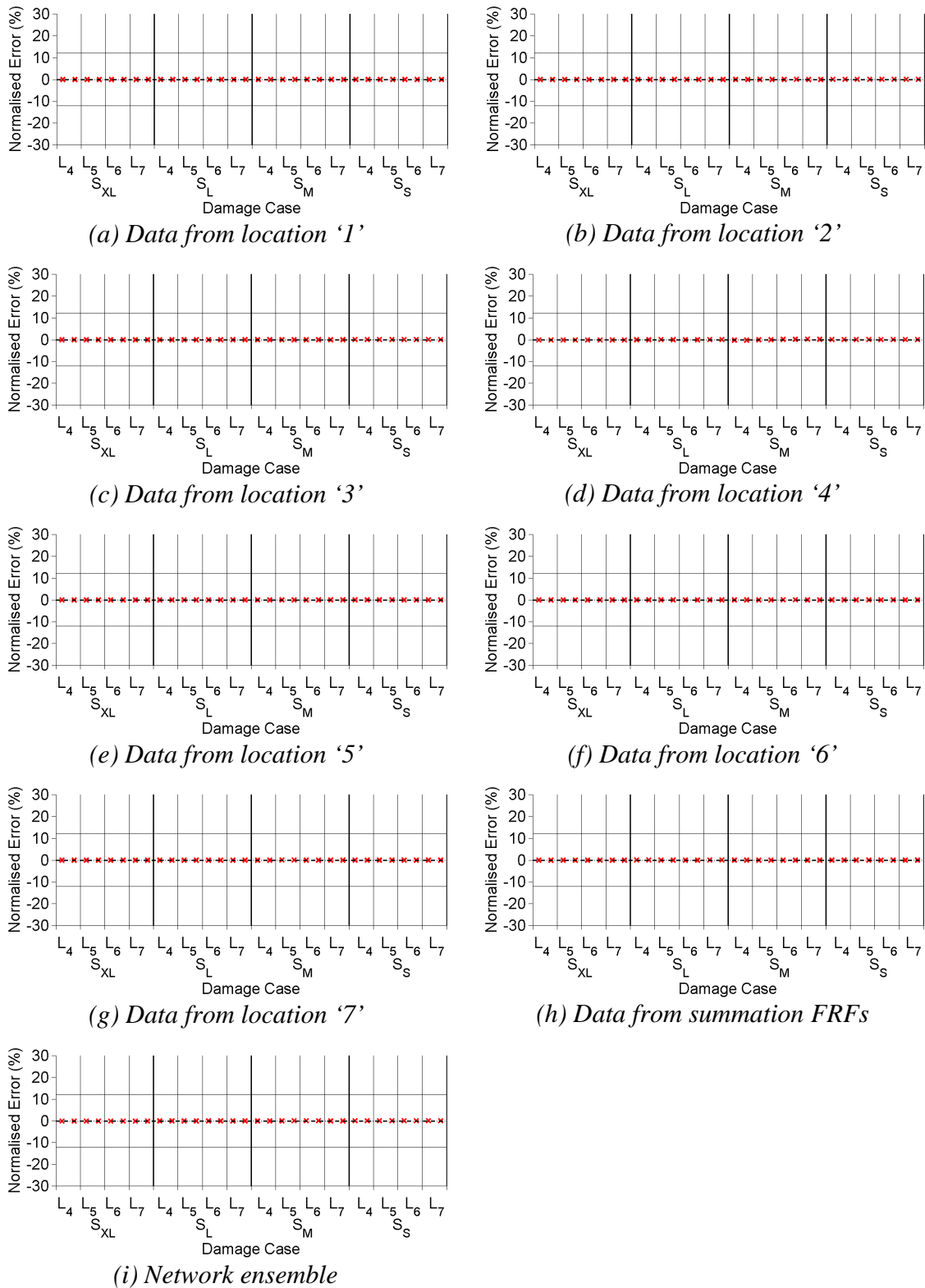


Figure I.11 Neural networks testing set outcomes of networks trained with PCA-compressed CNR-FRFs to identify damage severities of numerical beams polluted with 5% noise.

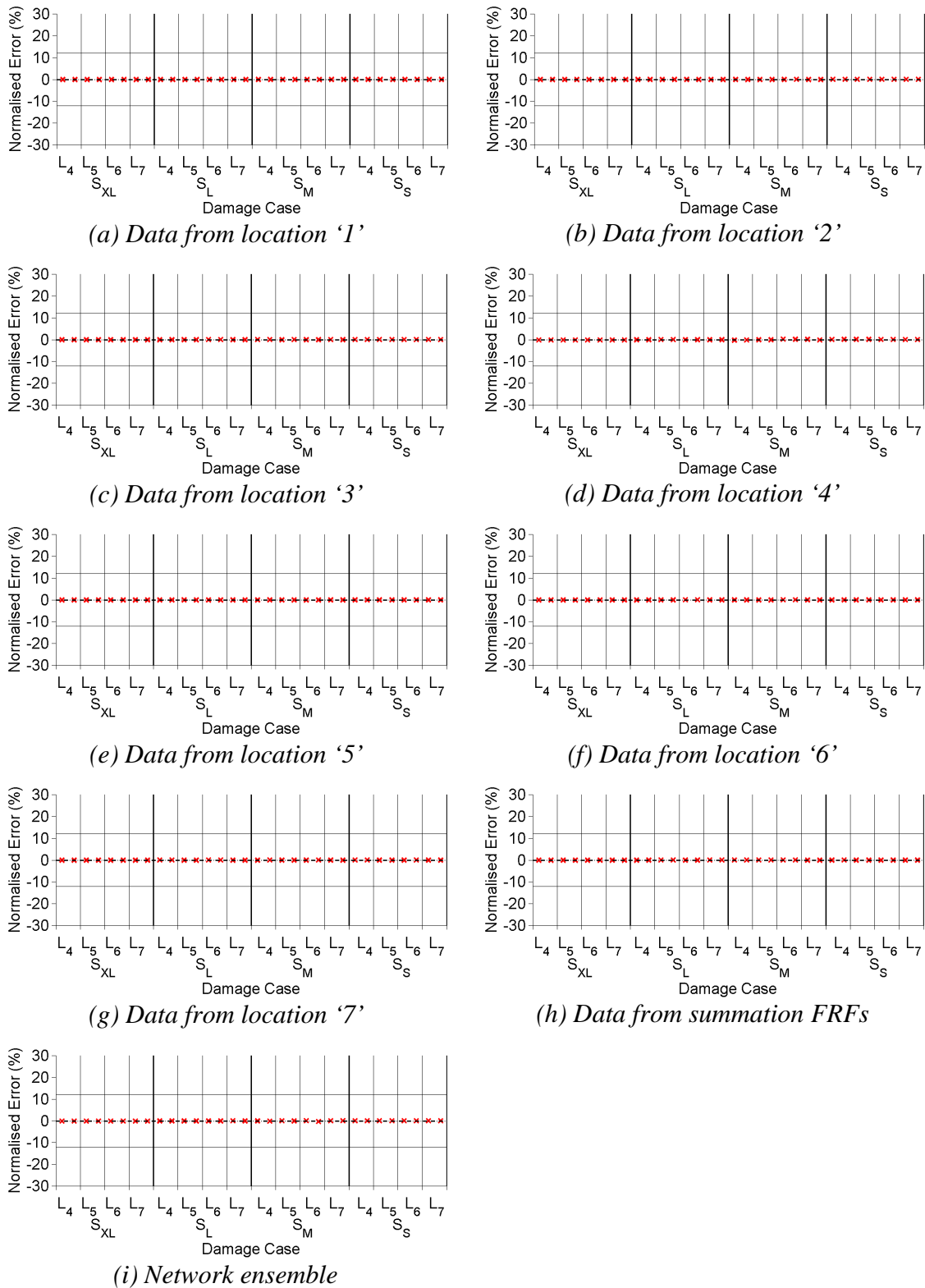
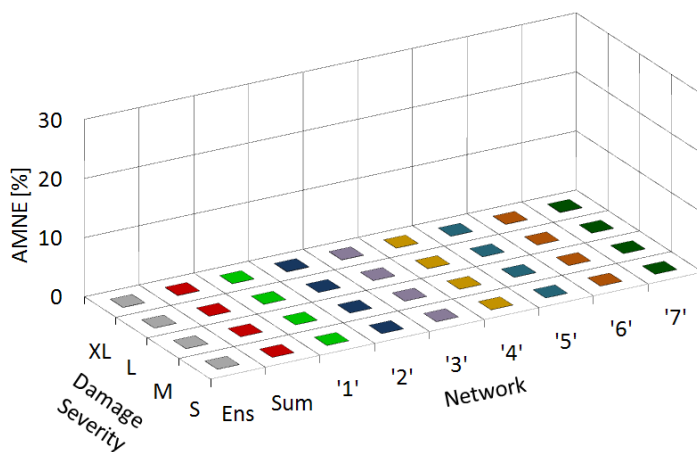


Figure I.12 Neural networks testing set outcomes of networks trained with PCA-compressed CNR-FRFs to identify damage severities of numerical beams polluted with 10% noise.

Table I.3 Neural network specifications and performance (in AMNE) trained with PCA-compressed CNR-FRFs from laboratory beams to identify damage locations.

Network	Network design	Convergence algorithm	Iteration	Training performance (AMNE [%])	Validation performance (AMNE [%])	Testing performance (AMNE [%])
'1'	7-6-4-2-1	Obp	13528	0.01	0.01	0.01
'2'	7-6-4-2-1	Obp	11572	0.01	0.03	0.02
'3'	7-6-4-2-1	Obp	15688	0.01	0.01	0.01
'4'	7-6-4-2-1	Obp	14526	0.01	0.01	0.02
'5'	7-6-4-2-1	Obp	13696	0.01	0.02	0.01
'6'	7-6-4-2-1	Obp	15086	0.01	0.01	0.01
'7'	7-6-4-2-1	Obp	11255	0.01	0.02	0.02
Sum	7-6-4-2-1	Obp	16854	0.01	0.01	0.01
Ens	7-6-4-2-1	Obp	15944	0.01	0.01	0.01

Note: Obp = Online backpropagation function



Network	Network performance (AMNE [%])			
	S _{XL}	S _L	S _M	S _S
Ens	0.02	0.01	0.01	0.01
Sum	0.03	0.01	0.01	0.01
Mode 1	0.02	0.01	0.01	0.01
Mode 2	0.05	0.01	0.01	0.01
Mode 3	0.03	0.01	0.01	0.01
Mode 4	0.02	0.02	0.01	0.01
Mode 5	0.02	0.01	0.02	0.01
Mode 6	0.02	0.01	0.01	0.01
Mode 7	0.05	0.01	0.01	0.01

Figure I.13 Neural network testing set performance (in AMNE) subdivided by damage severity trained with PCA-compressed CNR-FRFs from laboratory beams to identify damage locations.

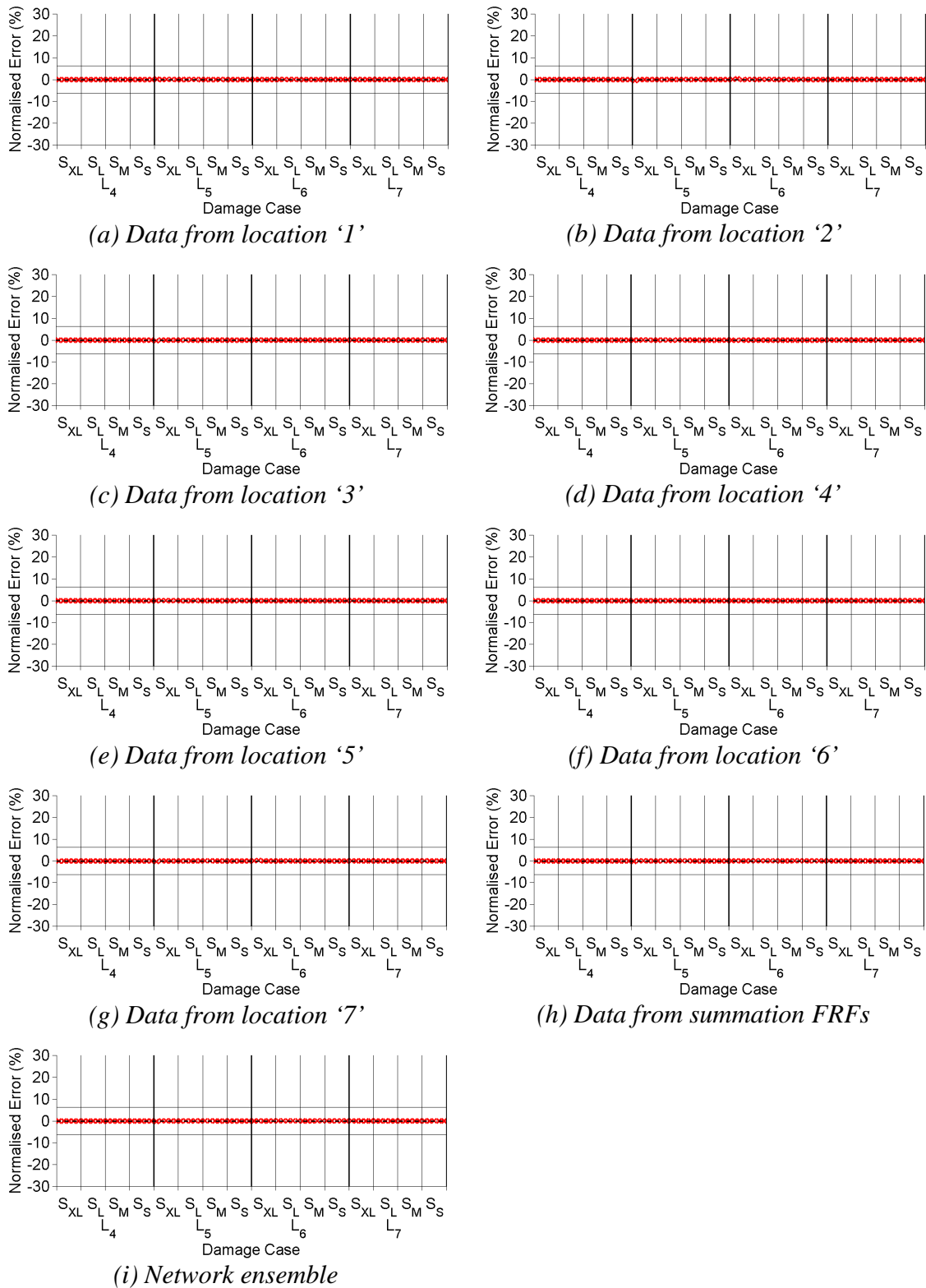
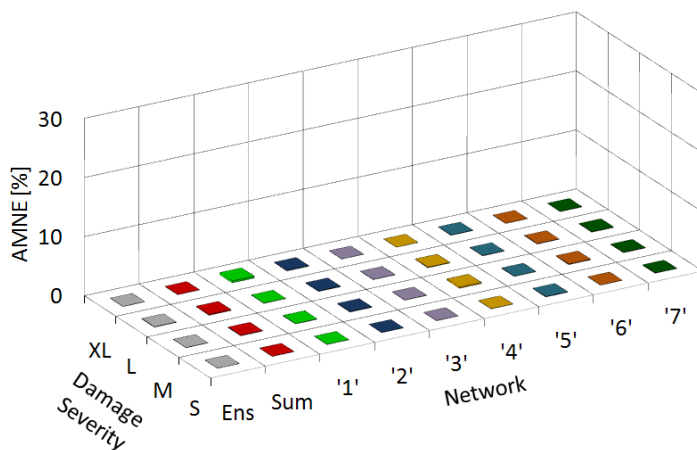


Figure I.14 Neural networks testing set outcomes of networks trained with PCA-compressed CNR-FRFs to identify damage locations of laboratory beams.

Table I.4 Neural network specifications and performance (in AMNE) trained with PCA-compressed CNR-FRFs from laboratory beams to identify damage severities.

Network	Network design	Convergence algorithm	Iteration	Training performance (AMNE [%])	Validation performance (AMNE [%])	Testing performance (AMNE [%])
'1'	7-6-4-2-1	Obp	12458	0.02	0.04	0.10
'2'	7-6-4-2-1	Obp	13258	0.02	0.03	0.07
'3'	7-6-4-2-1	Obp	11522	0.02	0.06	0.02
'4'	7-6-4-2-1	Obp	14773	0.02	0.05	0.07
'5'	7-6-4-2-1	Obp	9254	0.02	0.04	0.06
'6'	7-6-4-2-1	Obp	8511	0.02	0.06	0.05
'7'	7-6-4-2-1	Obp	7365	0.02	0.07	0.05
Sum	7-6-4-2-1	Obp	8821	0.03	0.08	0.07
Ens	7-6-4-2-1	Obp	14853	0.02	0.02	0.02

Note: Obp = Online backpropagation function



Network	Network performance (AMNE [%])			
	S _{XL}	S _L	S _M	S _S
Ens	0.02	0.06	0.03	0.01
Sum	0.02	0.15	0.08	0.02
Mode 1	0.33	0.03	0.04	0.02
Mode 2	0.08	0.10	0.07	0.02
Mode 3	0.01	0.03	0.03	0.02
Mode 4	0.01	0.10	0.20	0.02
Mode 5	0.05	0.05	0.04	0.09
Mode 6	0.02	0.06	0.10	0.02
Mode 7	0.03	0.07	0.06	0.03

Figure I.15 Neural network testing set performance (in AMNE) subdivided by damage severity trained with PCA-compressed CNR-FRFs from laboratory beams to identify damage severities.

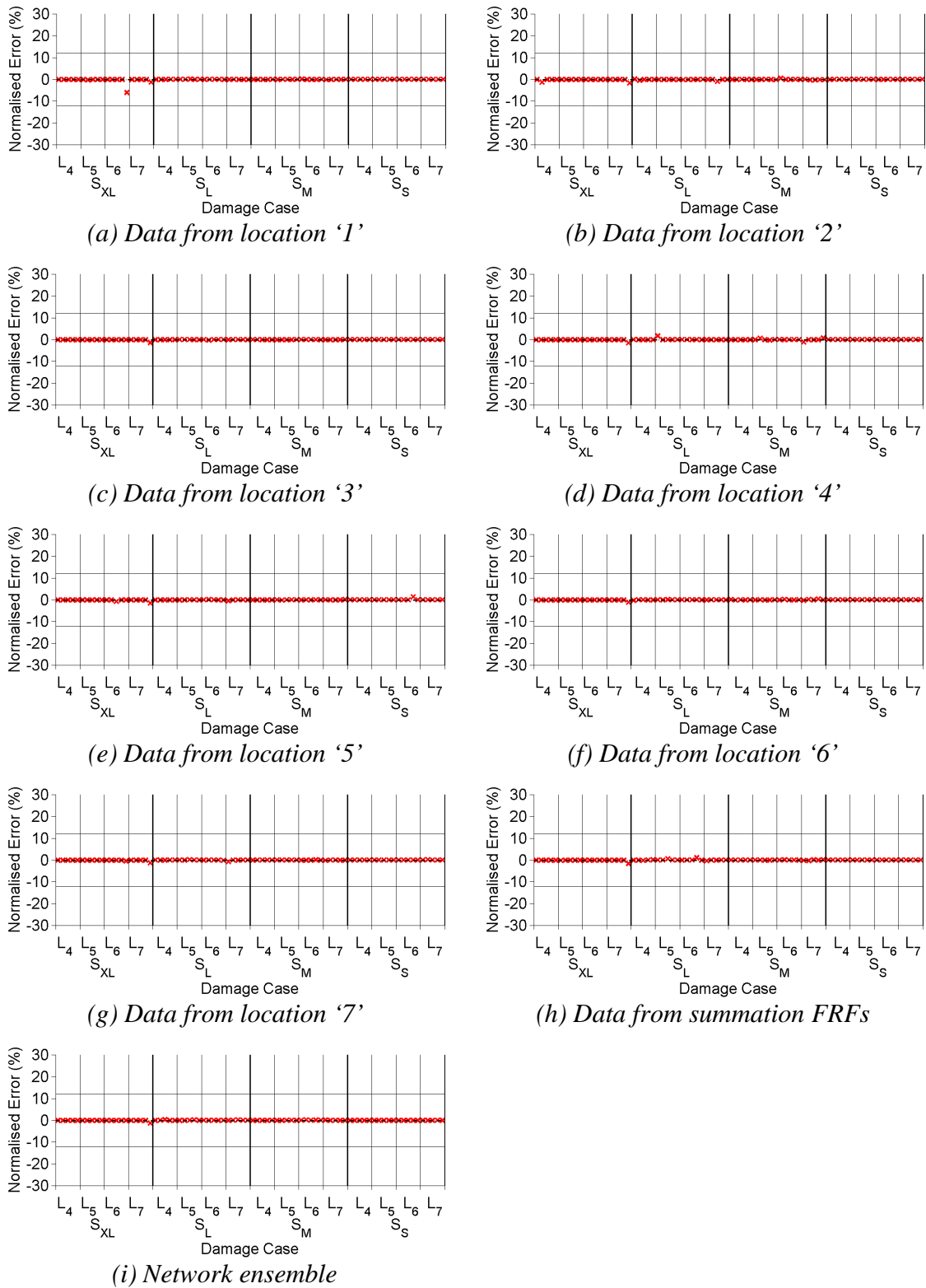
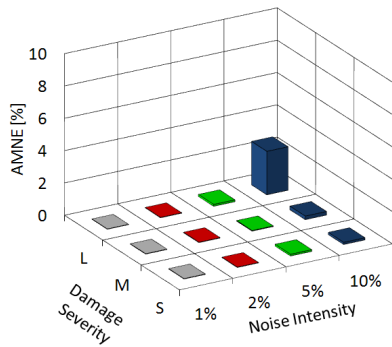


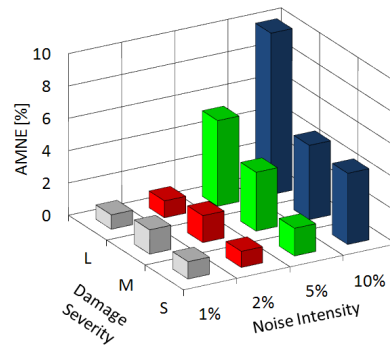
Figure I.16 Neural networks testing set outcomes of networks trained with PCA-compressed CNR-FRFs to identify damage severities of laboratory beams.

APPENDIX J

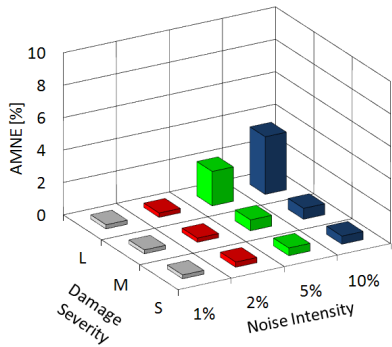
DAMAGE IDENTIFICATION OUTCOMES OF TWO-STOREY FRAMED STRUCTURE



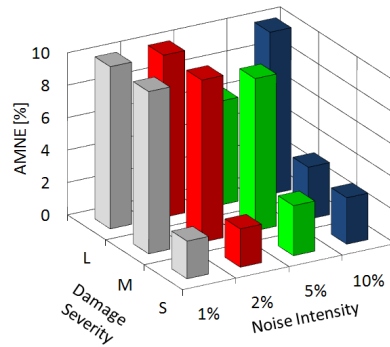
(a) Data from location '1'



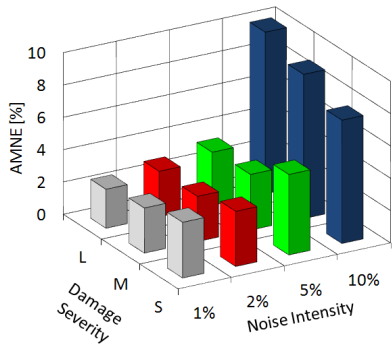
(b) Data from location '2'



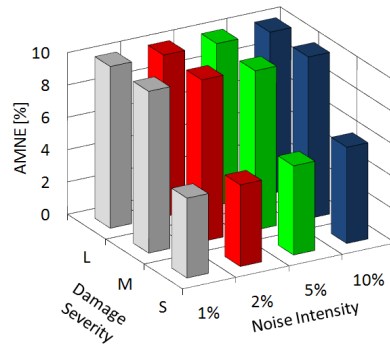
(c) Data from location '3'



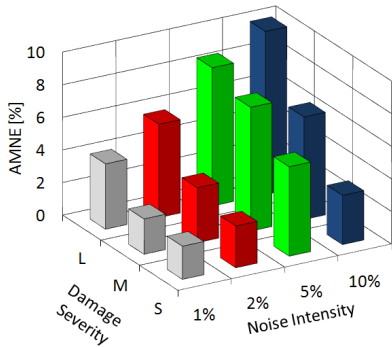
(d) Data from location '4'



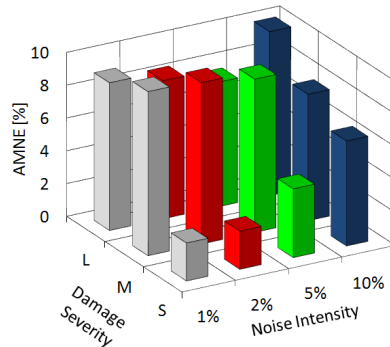
(e) Data from location '5'



(f) Data from location '6'



(g) Data from location '7'



(h) Data from location '8'

Figure J.1 Comparison of testing set outcomes of networks trained with PCA-compressed residual FRFs to identify damage locations of noise-polluted numerical two-storey framed structures subdivided by damage severity and noise pollution levels. Outcomes of networks trained with data from locations '1' to '8' are shown.

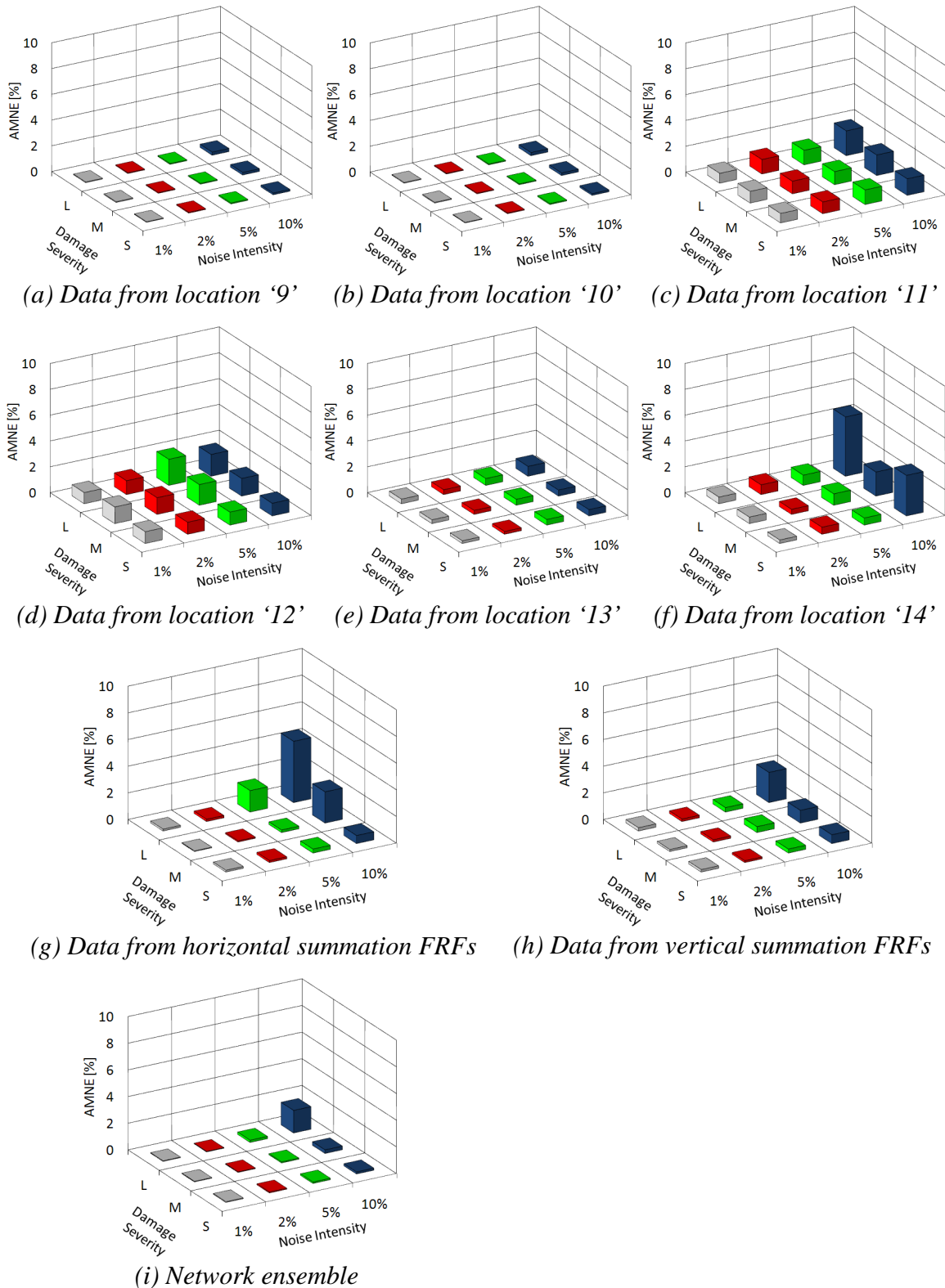


Figure J.2 Comparison of testing set outcomes of networks trained with noise-polluted numerical data to locate damage subdivided by damage severity and noise pollution level. Outcomes of networks trained with data from locations '9' to '14' and data from horizontal/vertical summation FRFs, and of the network ensemble are shown.

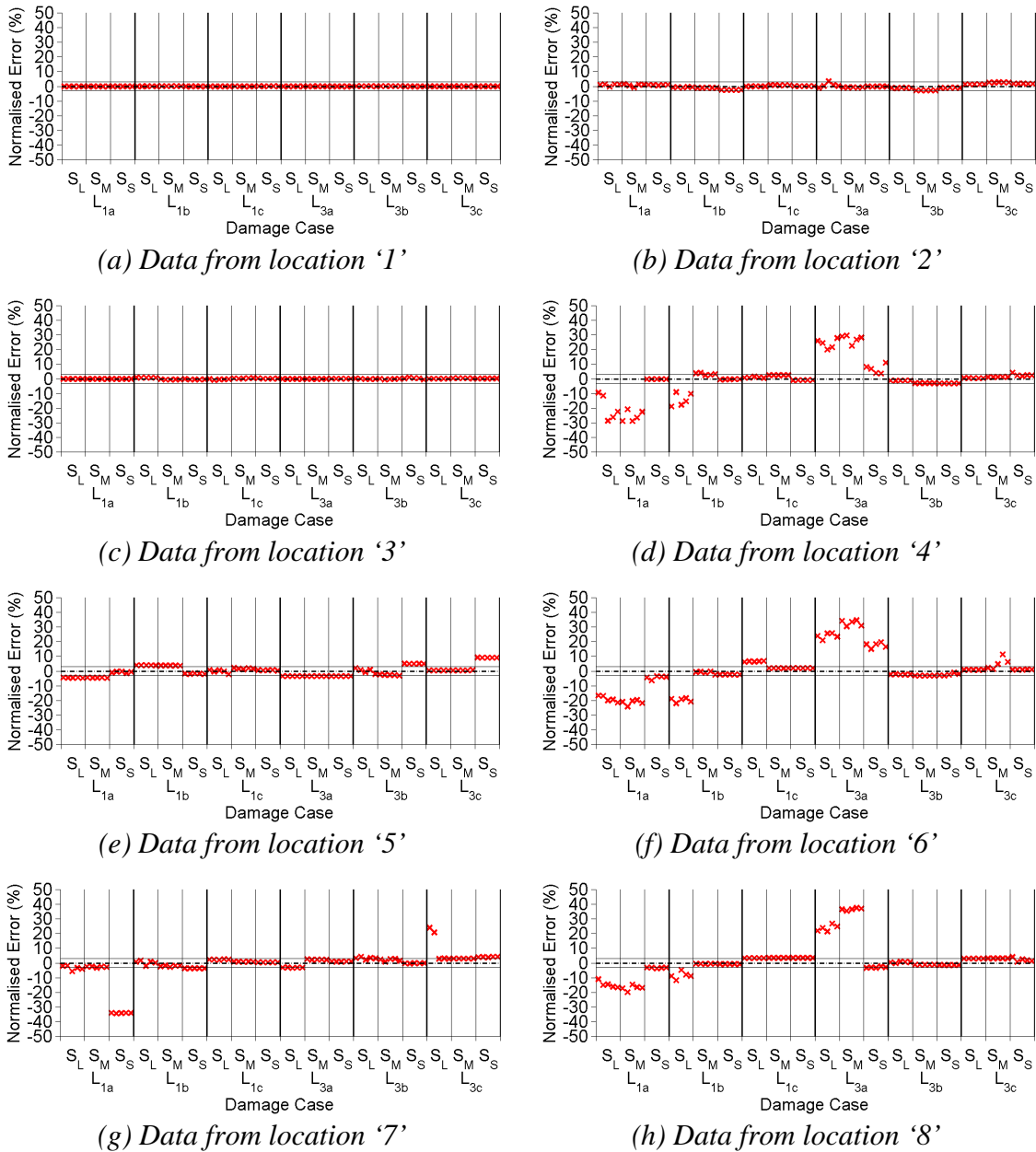


Figure J.3 Neural network testing set outcomes of networks trained with data of 1% noise pollution to locate damage of numerical two-storey framed structure. Outcomes of networks trained with data from locations '1' to '8' are shown.

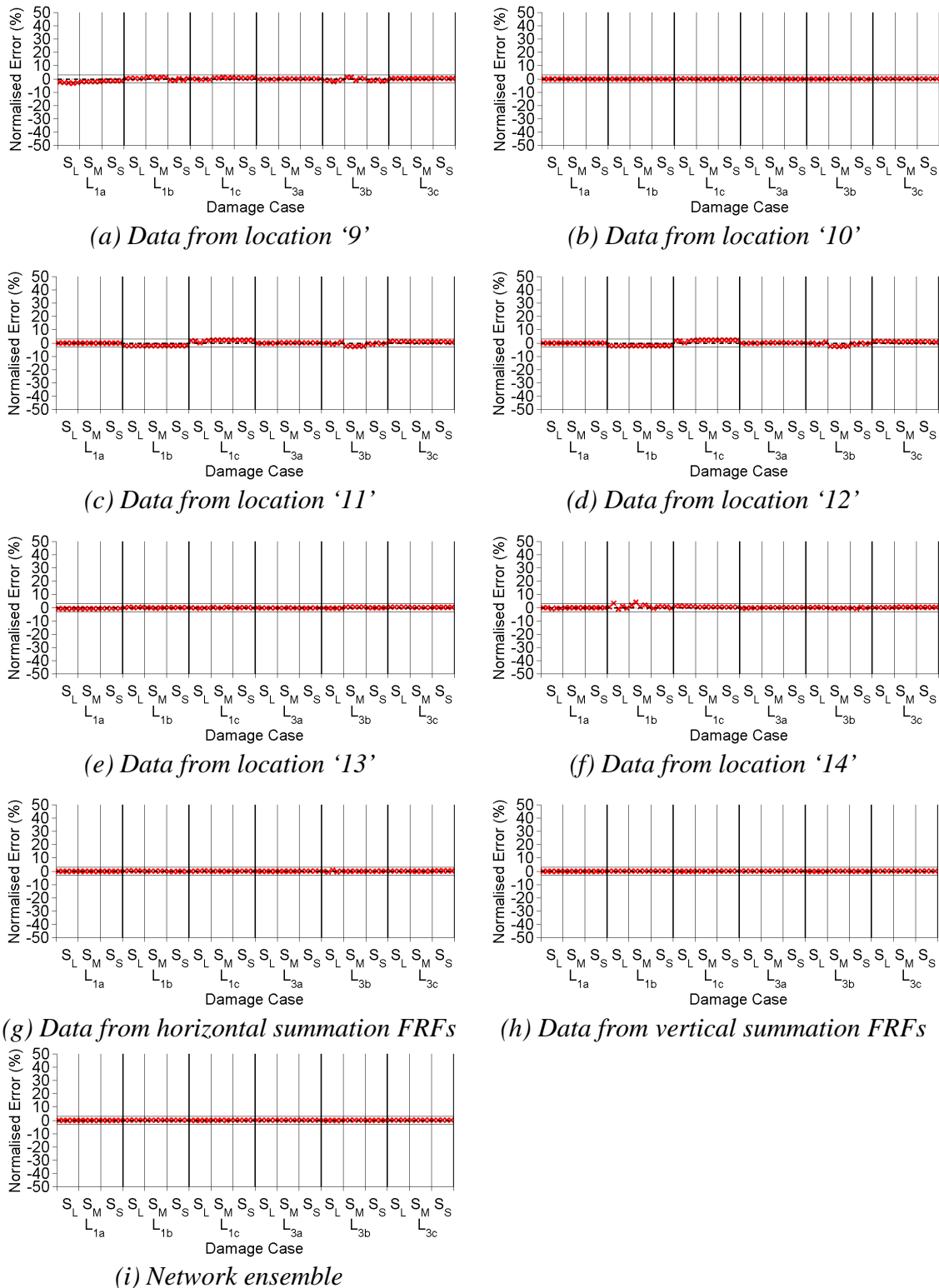


Figure J.4 Neural network testing set outcomes of networks trained with data of 1% noise pollution to locate damage of numerical two-storey framed structure. Outcomes of individual networks trained with data from locations '9' to '14' and data from horizontal/vertical summation FRFs, and of the network ensemble are shown.

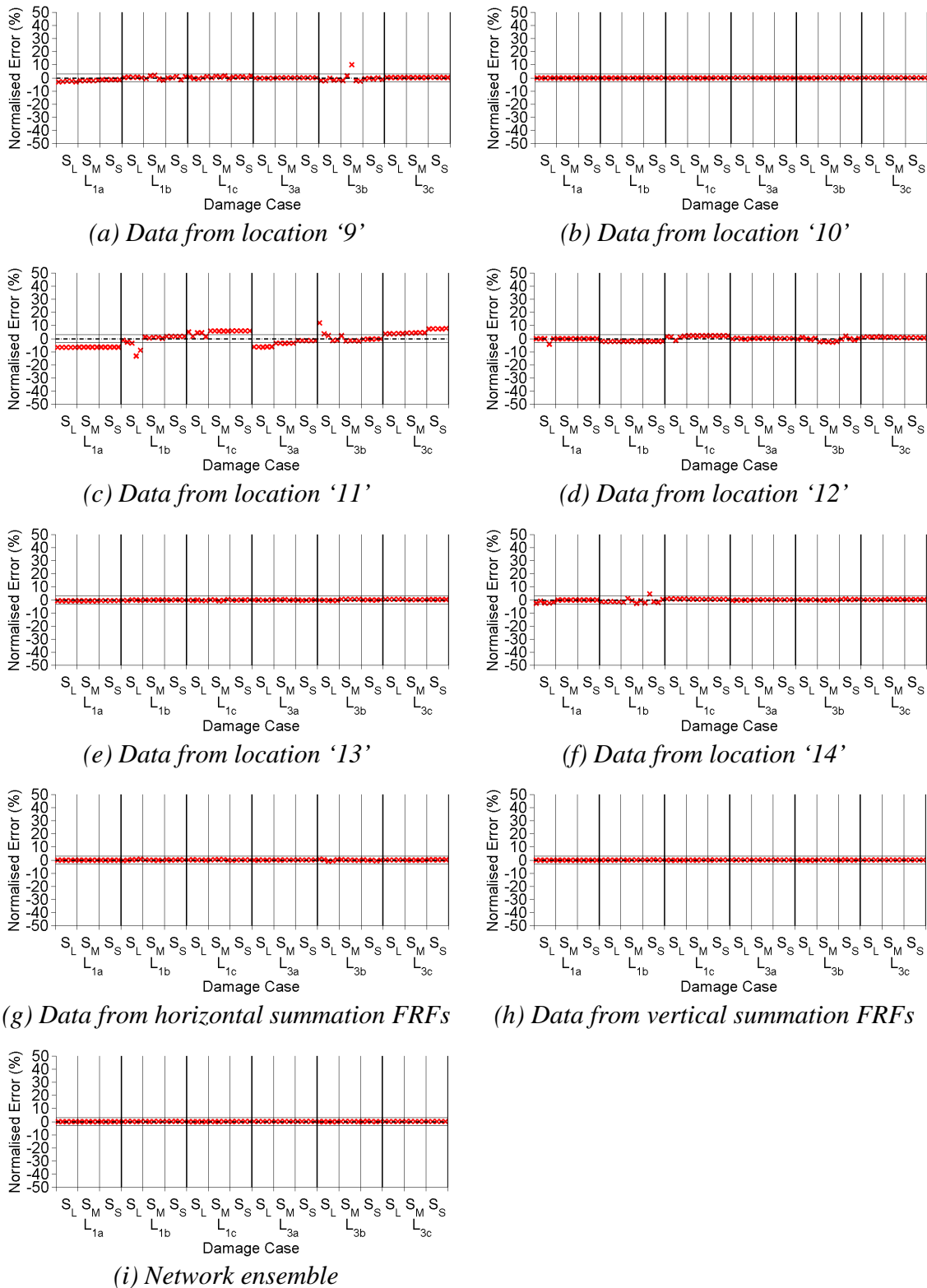


Figure J.6 Neural network testing set outcomes of networks trained with data of 2% noise pollution to locate damage of numerical two-storey framed structure. Outcomes of individual networks trained with data from locations '9' to '14' and data from horizontal/vertical summation FRFs, and of the network ensemble are shown.

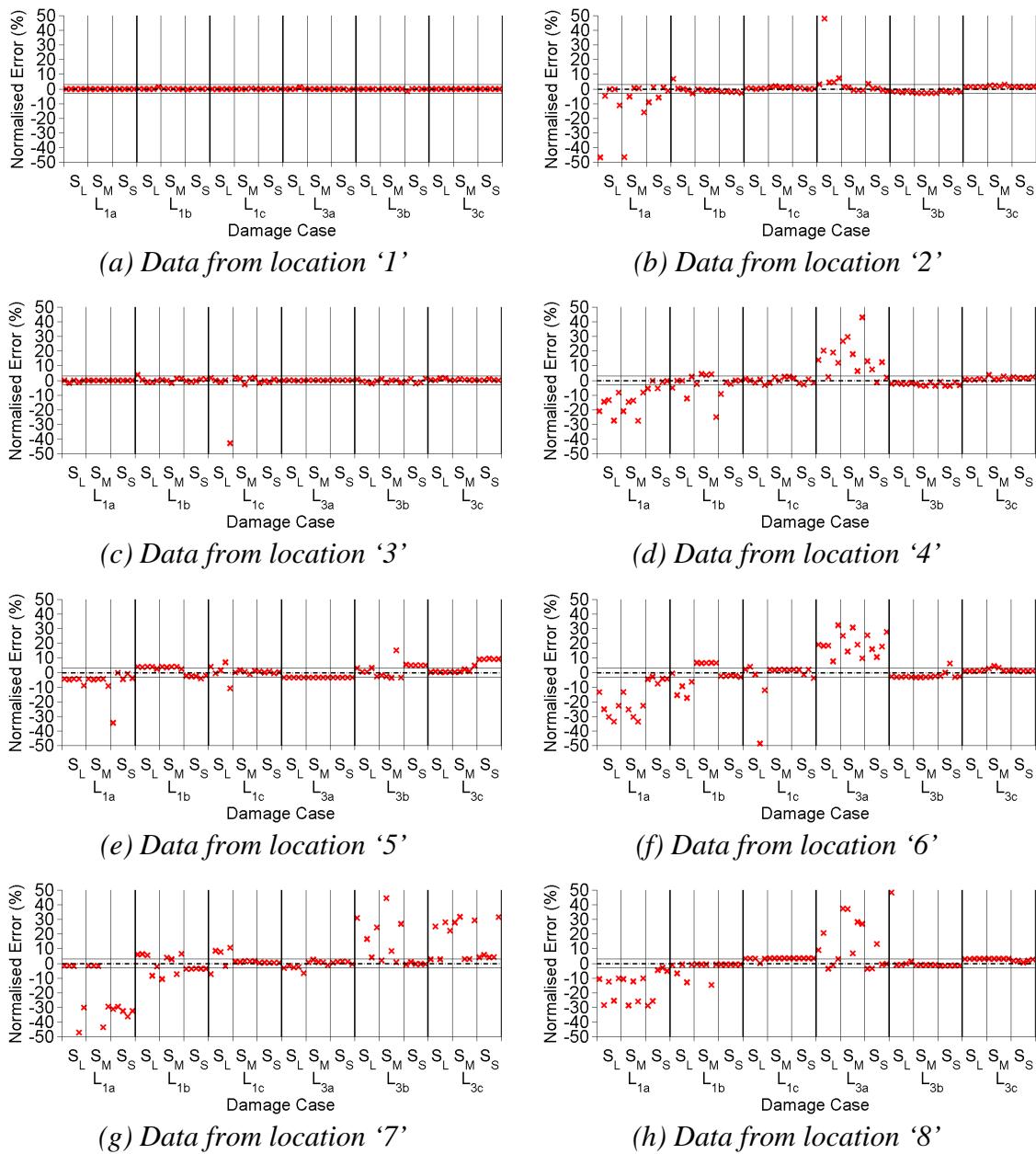


Figure J.7 Neural network testing set outcomes of networks trained with data of 5% noise pollution to locate damage of numerical two-storey framed structure. Outcomes of networks trained with data from locations '1' to '8' are shown.

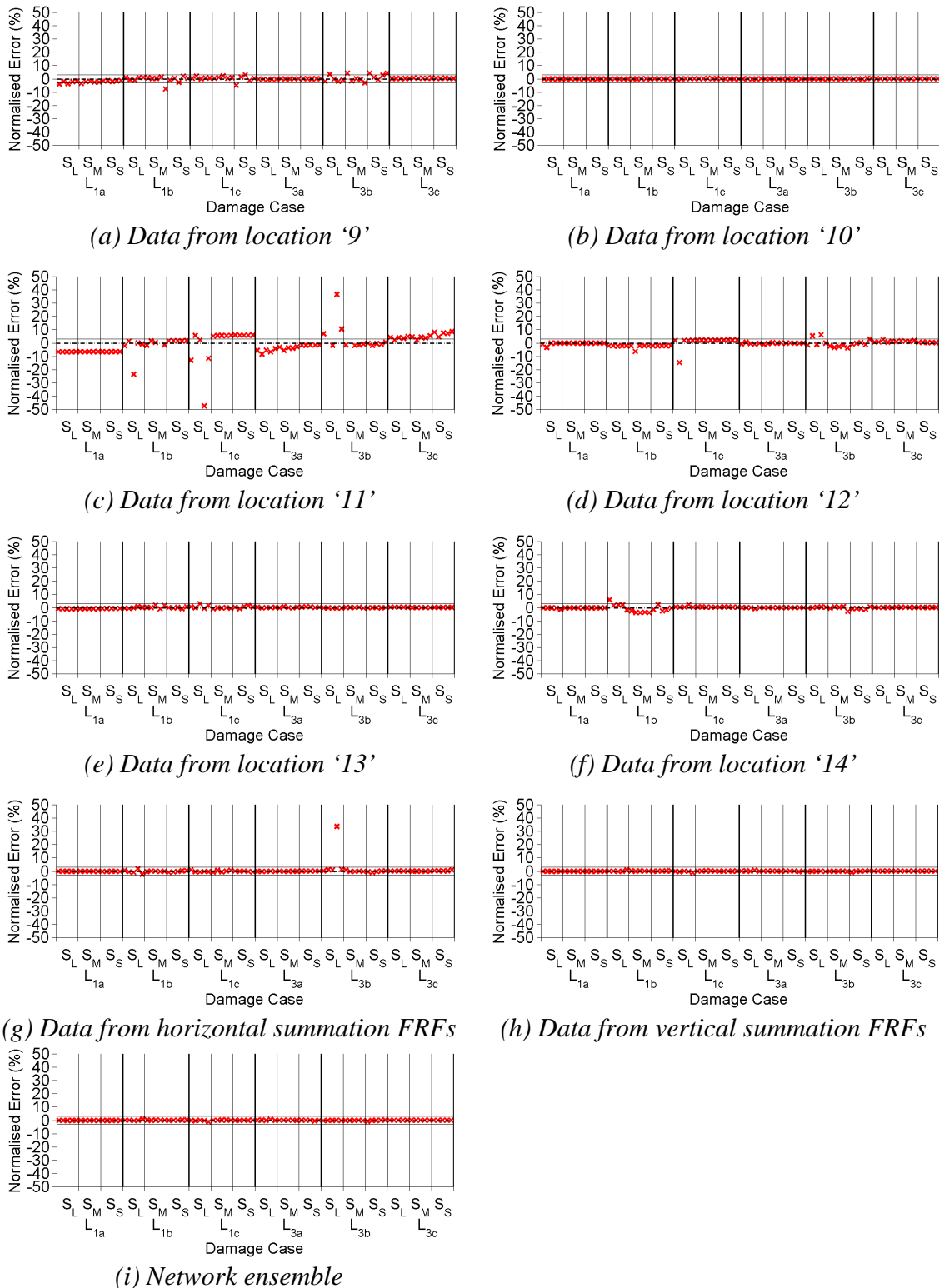


Figure J.8 Neural network testing set outcomes of networks trained with data of 5% noise pollution to locate damage of numerical two-storey framed structure. Outcomes of individual networks trained with data from locations '9' to '14' and data from horizontal/vertical summation FRFs, and of the network ensemble are shown.

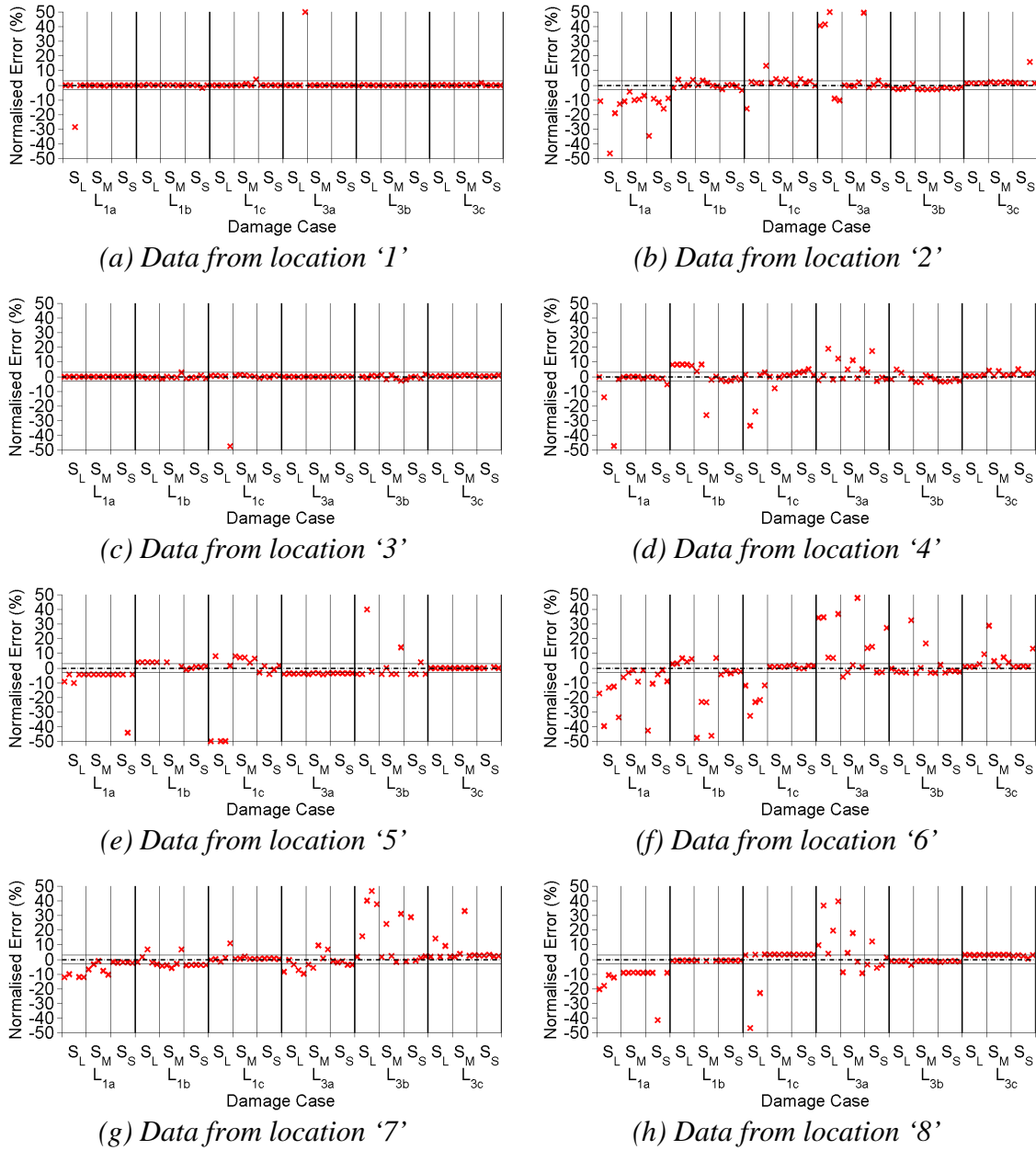


Figure J.9 Neural network testing set outcomes of networks trained with data of 10% noise pollution to locate damage of numerical two-storey framed structure. Outcomes of networks trained with data from locations '1' to '8' are shown.

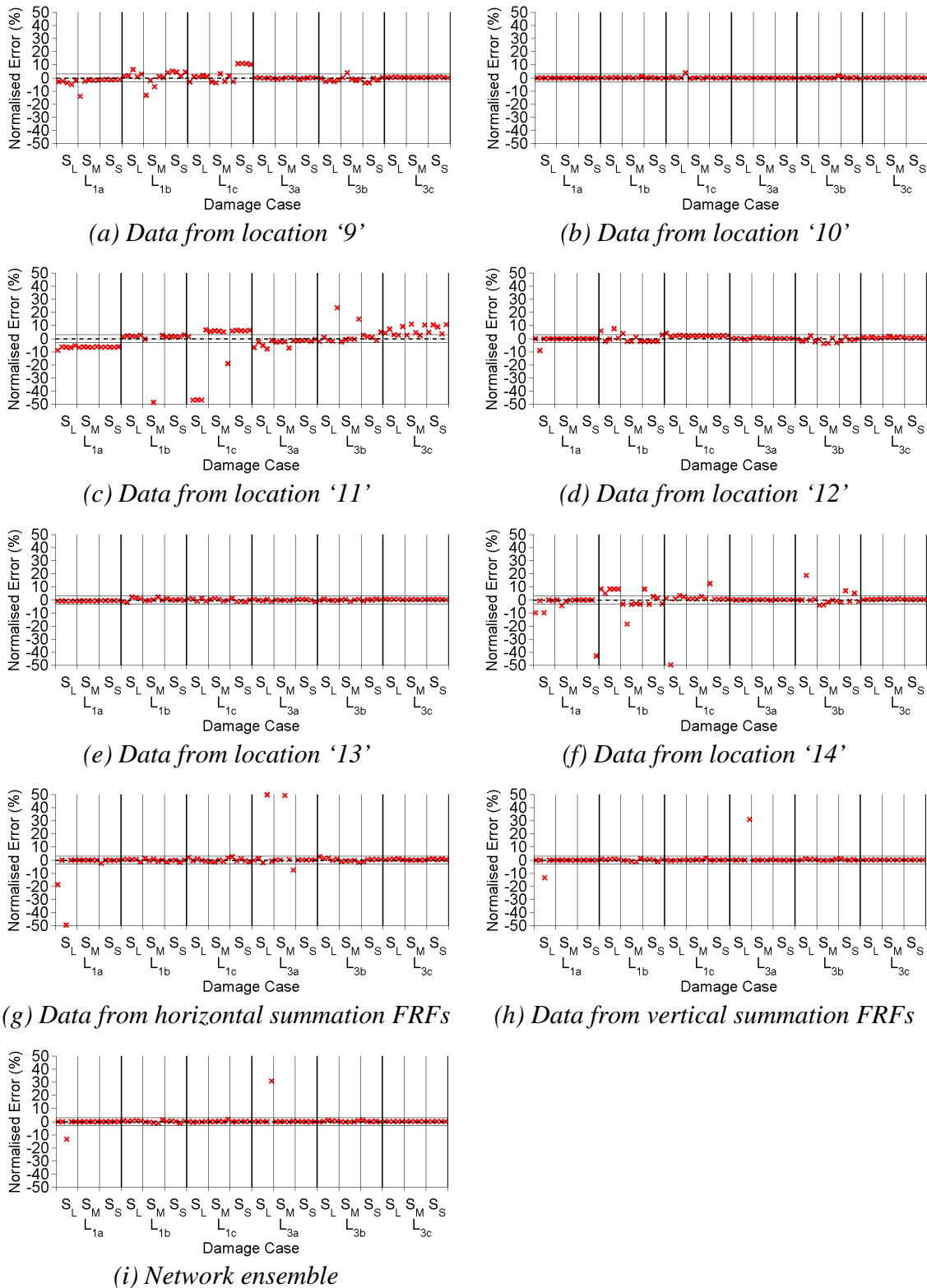
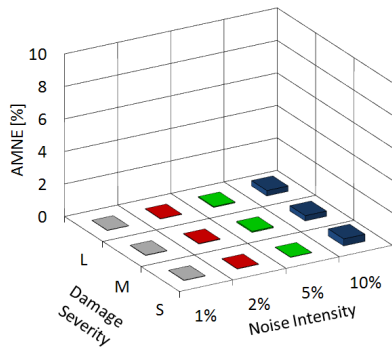
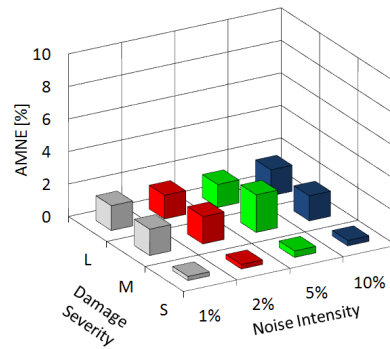


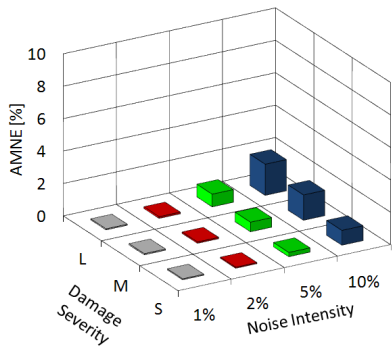
Figure J.10 Neural network testing set outcomes of networks trained with data of 10% noise pollution to locate damage of numerical two-storey framed structure. Outcomes of individual networks trained with data from locations '9' to '14' and data from horizontal/vertical summation FRFs, and of the network ensemble are shown.



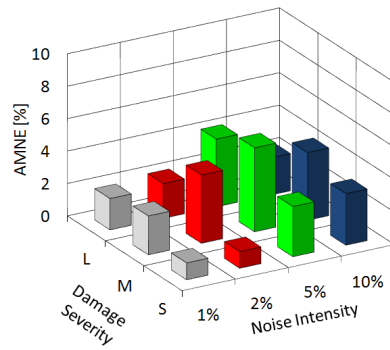
(a) Data from location '1'



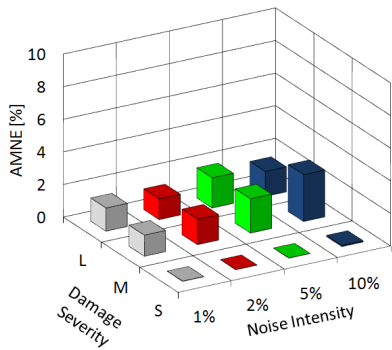
(b) Data from location '2'



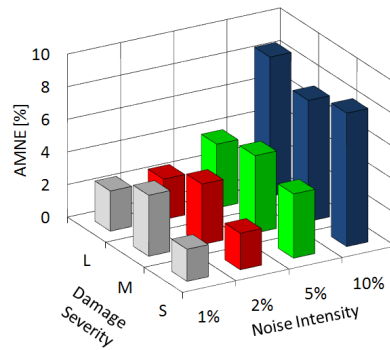
(c) Data from location '3'



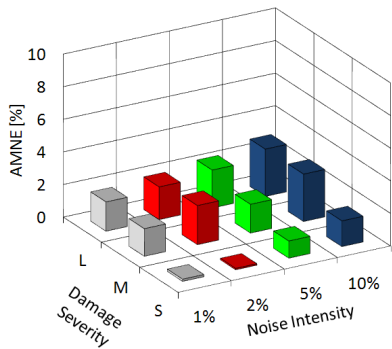
(d) Data from location '4'



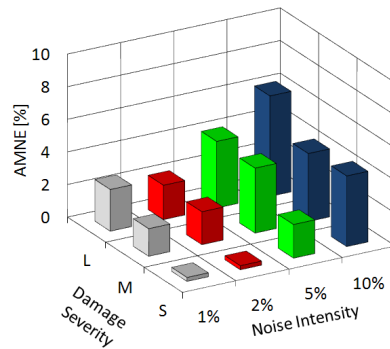
(e) Data from location '5'



(f) Data from location '6'



(g) Data from location '7'



(h) Data from location '8'

Figure J.11 Comparison of testing set outcomes of networks trained with PCA-compressed residual FRFs to identify damage severities of noise-polluted numerical two-storey framed structures subdivided by damage severity and noise pollution level. Outcomes of networks trained with data from locations '1' to '8' are shown.

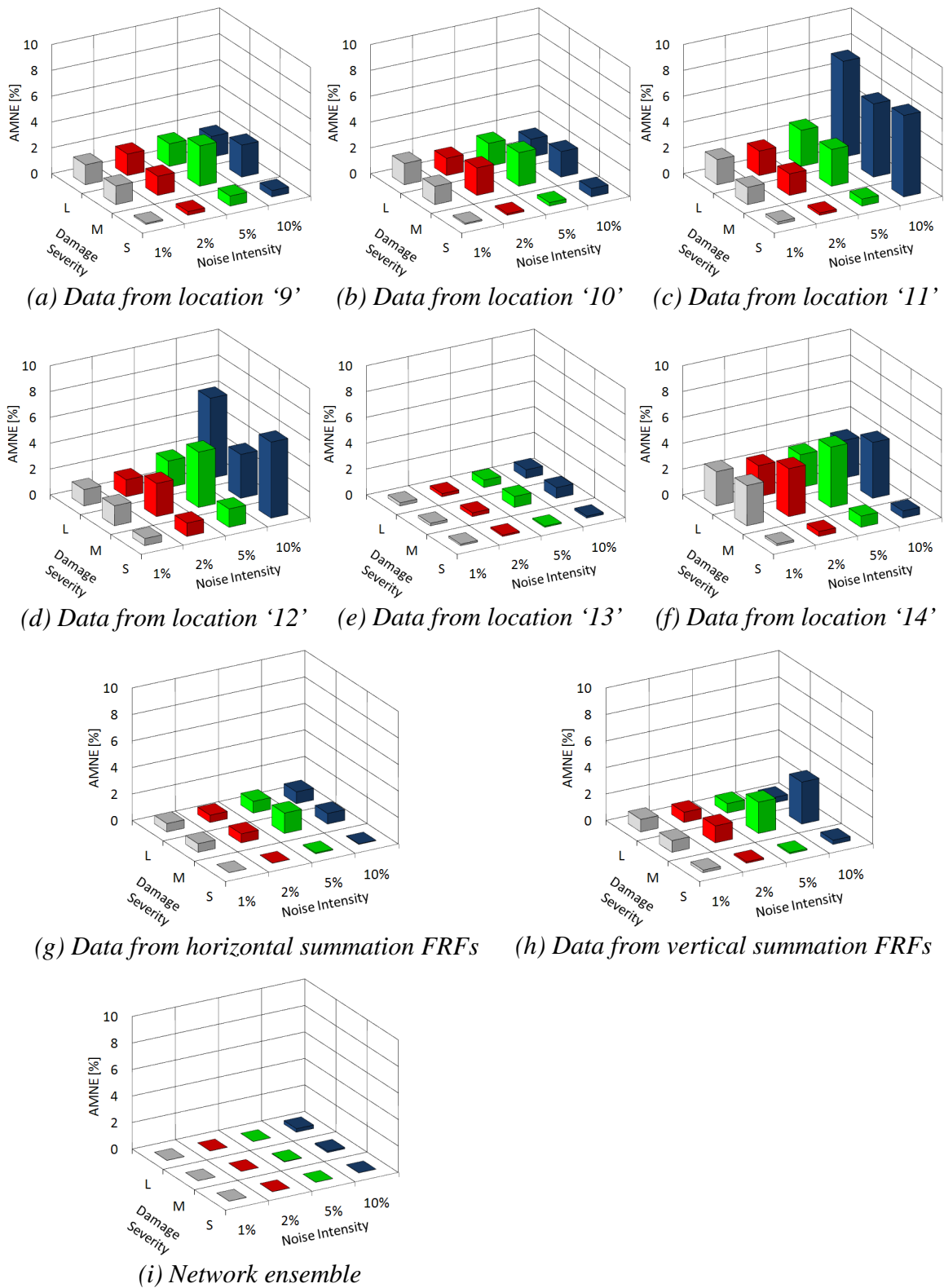


Figure J.12 Comparison of testing set outcomes of networks trained with noise-polluted numerical data to identify severities subdivided by damage severity and noise pollution level. Outcomes of networks trained with data from locations '9' to '14', data from horizontal/vertical summation FRFs and of the network ensemble are shown.

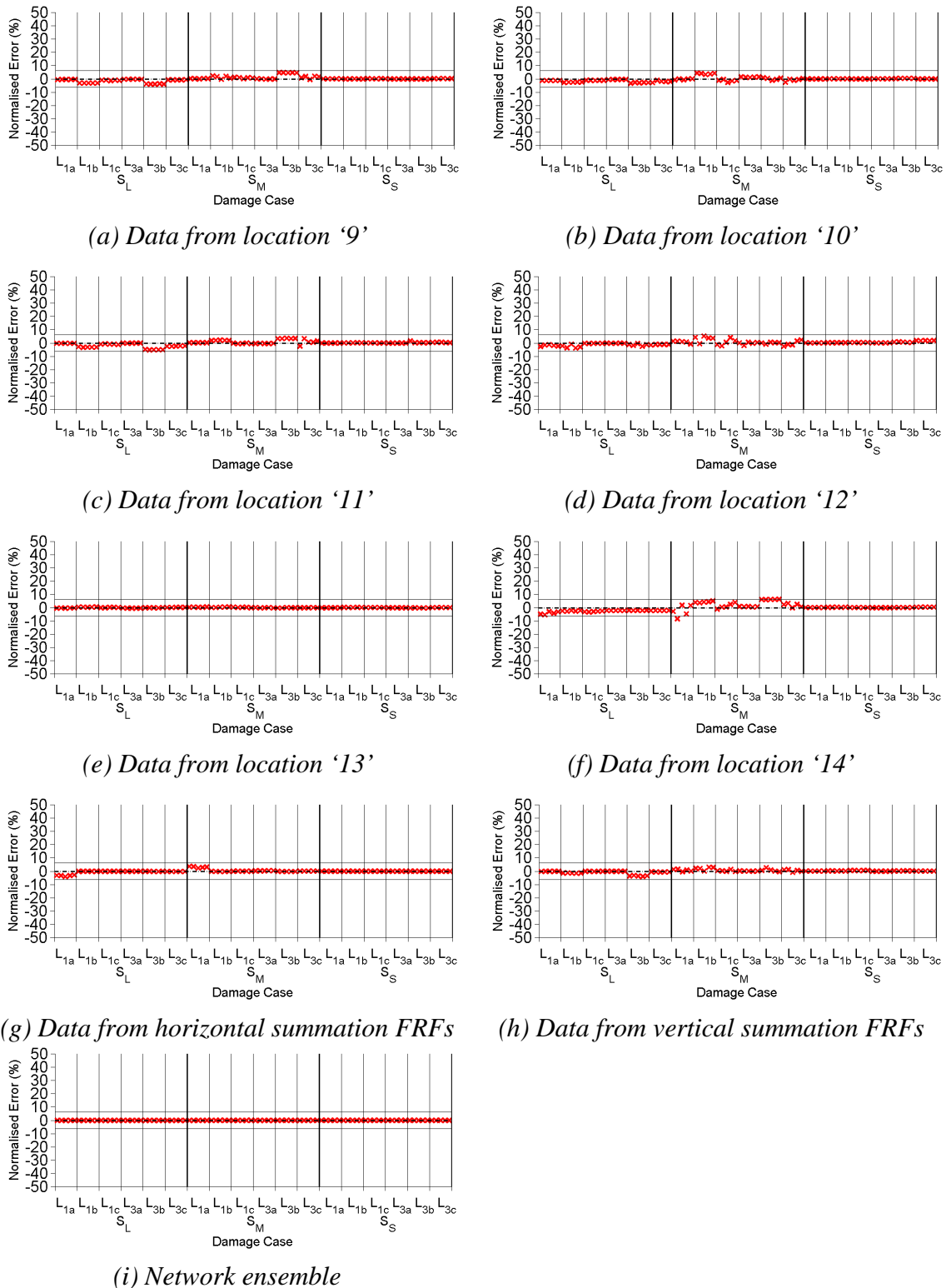


Figure J.14 Neural network testing set outcomes of networks trained with data of 1% noise pollution to estimate damage severity of numerical two-storey framed structure. Outcomes of individual networks trained with data from locations '9' to '14' and data from horizontal/vertical summation FRFs, and of the network ensemble are shown.

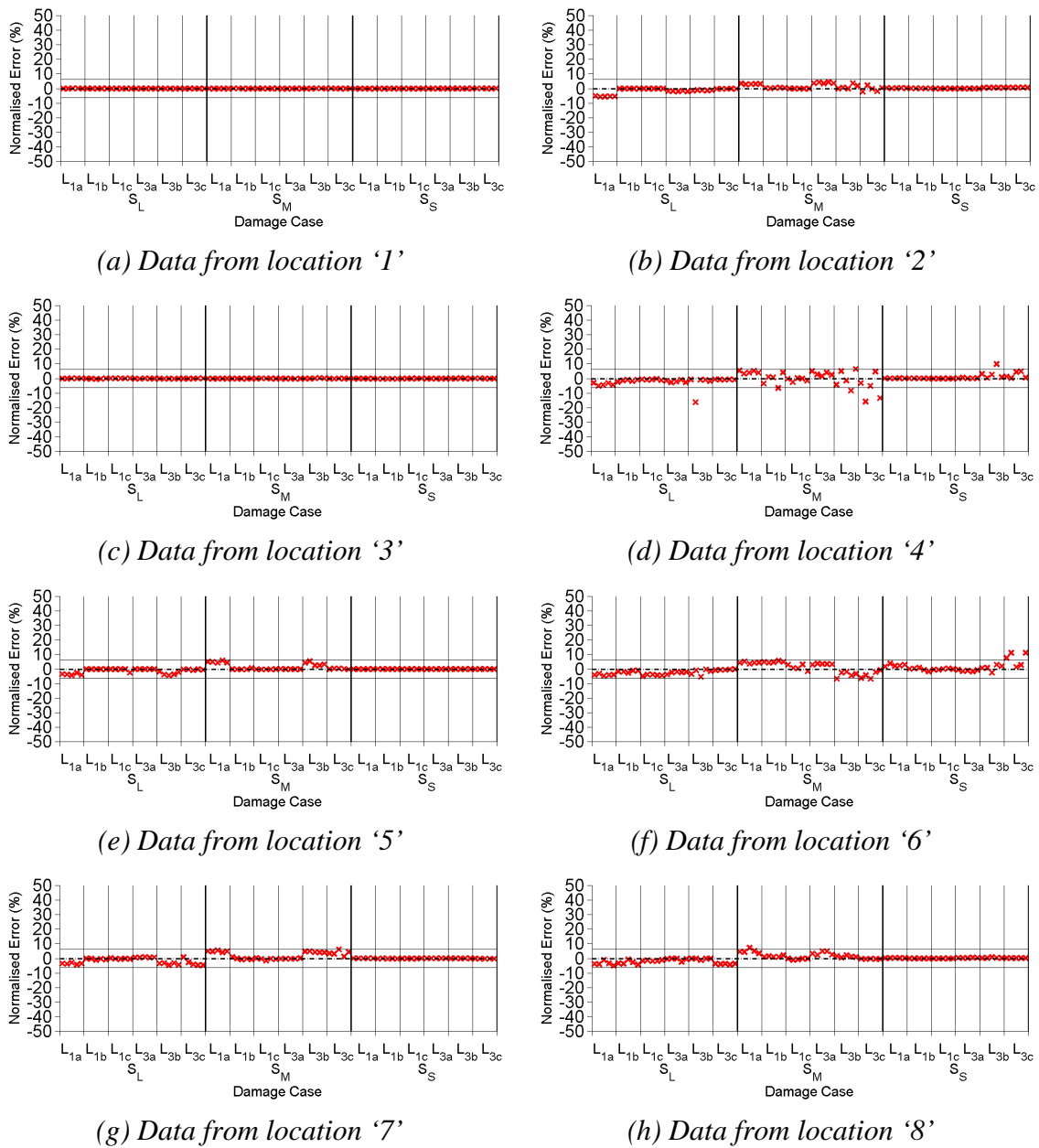


Figure J.15 Neural network testing set outcomes of networks trained with data of 2% noise pollution to estimate the severity of damage of numerical two-storey framed structure. Outcomes of networks trained with data from locations '1' to '8' are shown.

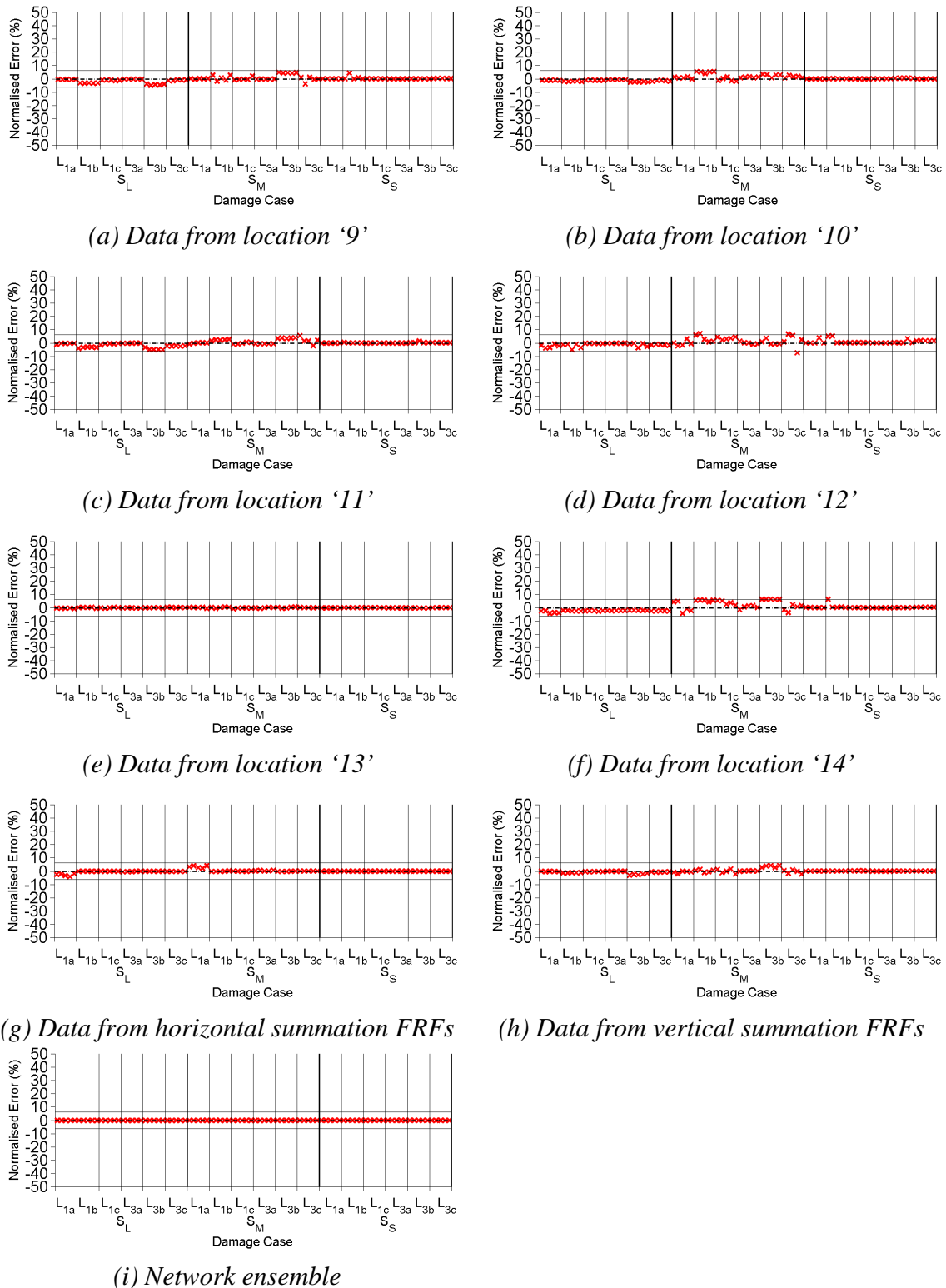


Figure J.16 Neural network testing set outcomes of networks trained with data of 2% noise pollution to estimate damage severity of numerical two-storey framed structure. Outcomes of individual networks trained with data from locations '9' to '14' and data from horizontal/vertical summation FRFs, and of the network ensemble are shown.

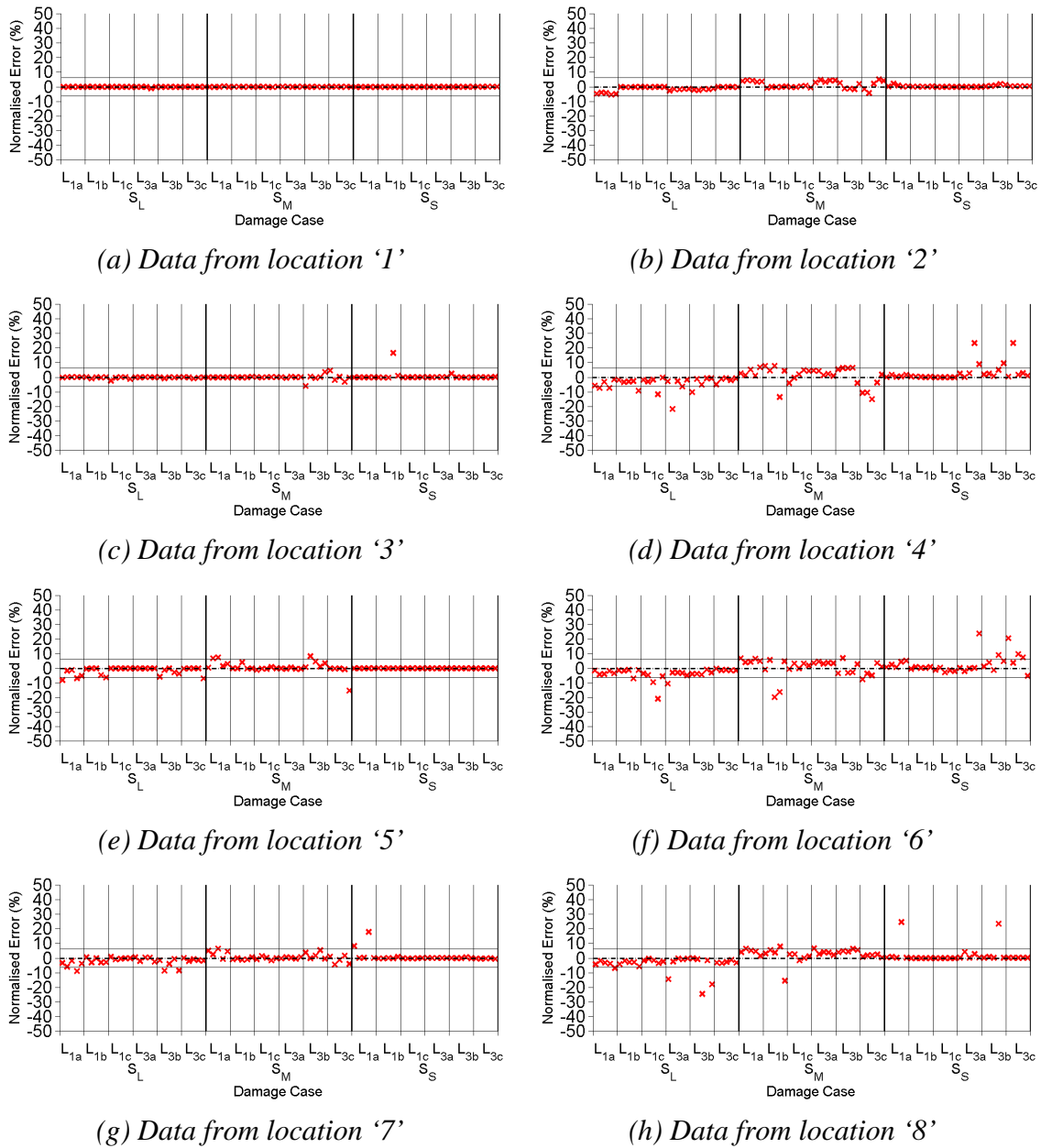


Figure J.17 Neural network testing set outcomes of networks trained with data of 5% noise pollution to estimate the severity of damage of numerical two-storey framed structure. Outcomes of networks trained with data from locations '1' to '8' are shown.

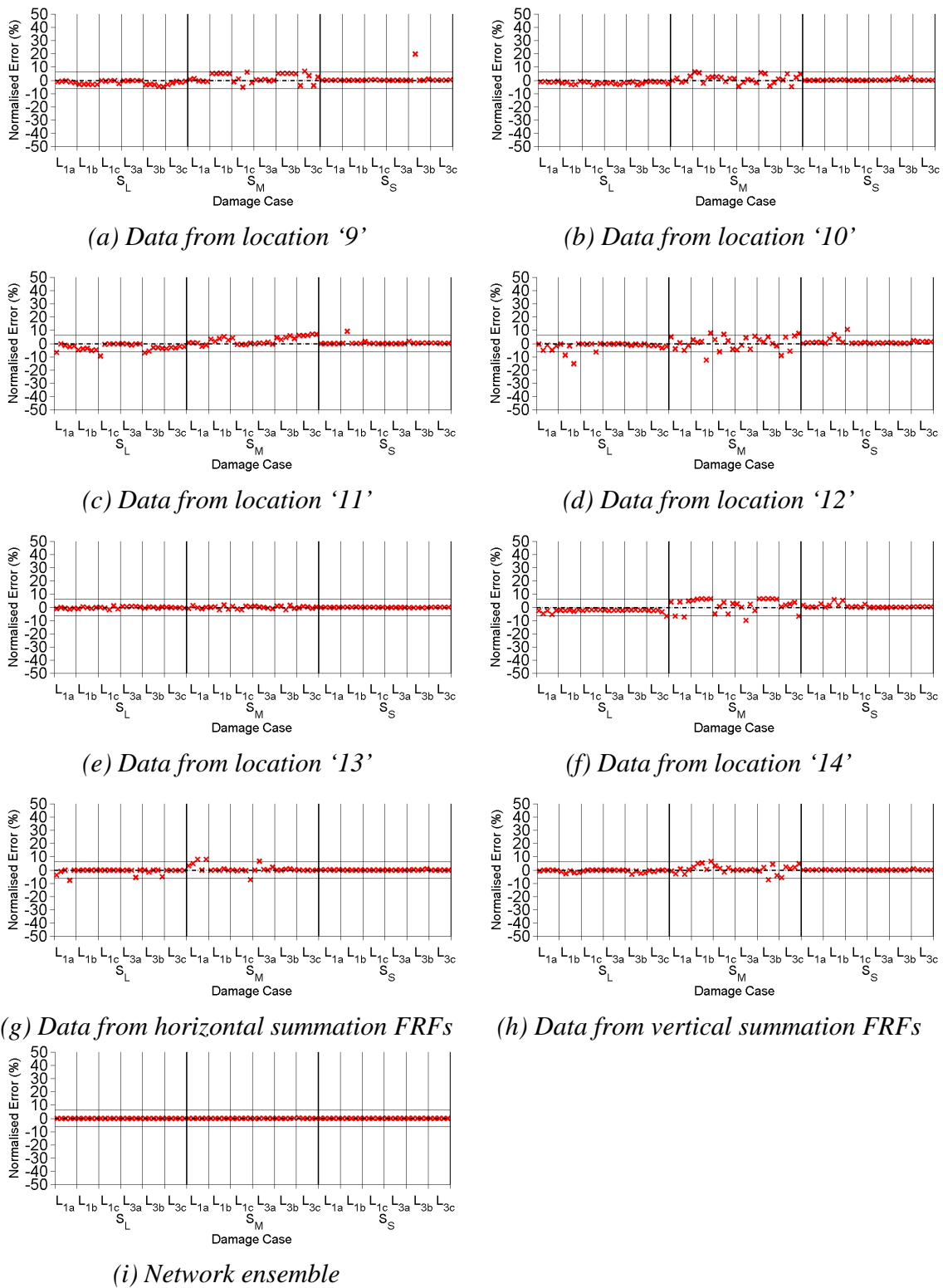


Figure J.18 Neural network testing set outcomes of networks trained with data of 5% noise pollution to estimate damage severity of numerical two-storey framed structure. Outcomes of individual networks trained with data from locations '9' to '14' and data from horizontal/vertical summation FRFs, and of the network ensemble are shown.

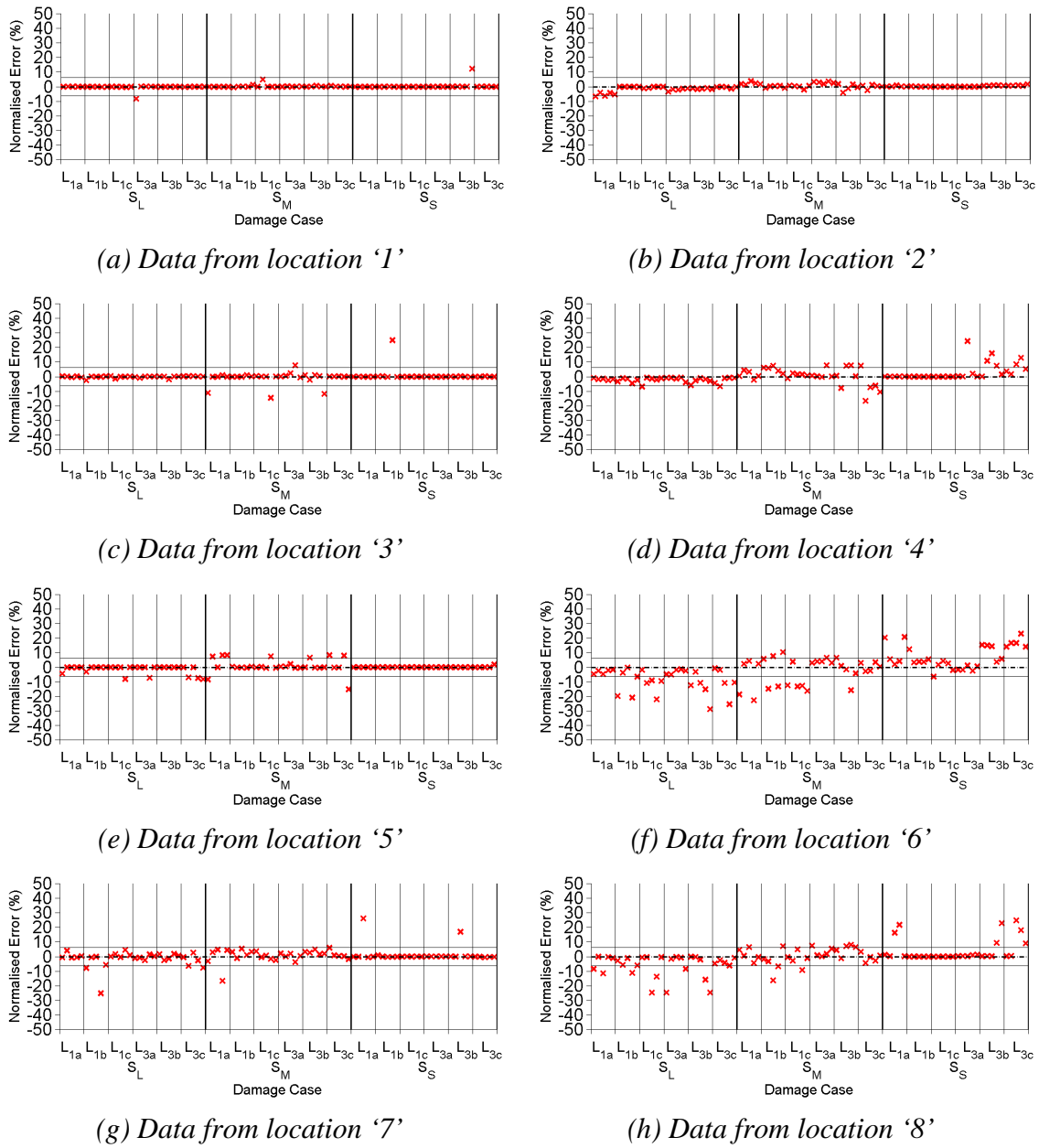


Figure J.19 Neural network testing set outcomes of networks trained with data of 10% noise pollution to estimate the severity of damage of numerical two-storey framed structure. Outcomes of networks trained with data from locations '1' to '8' are shown.

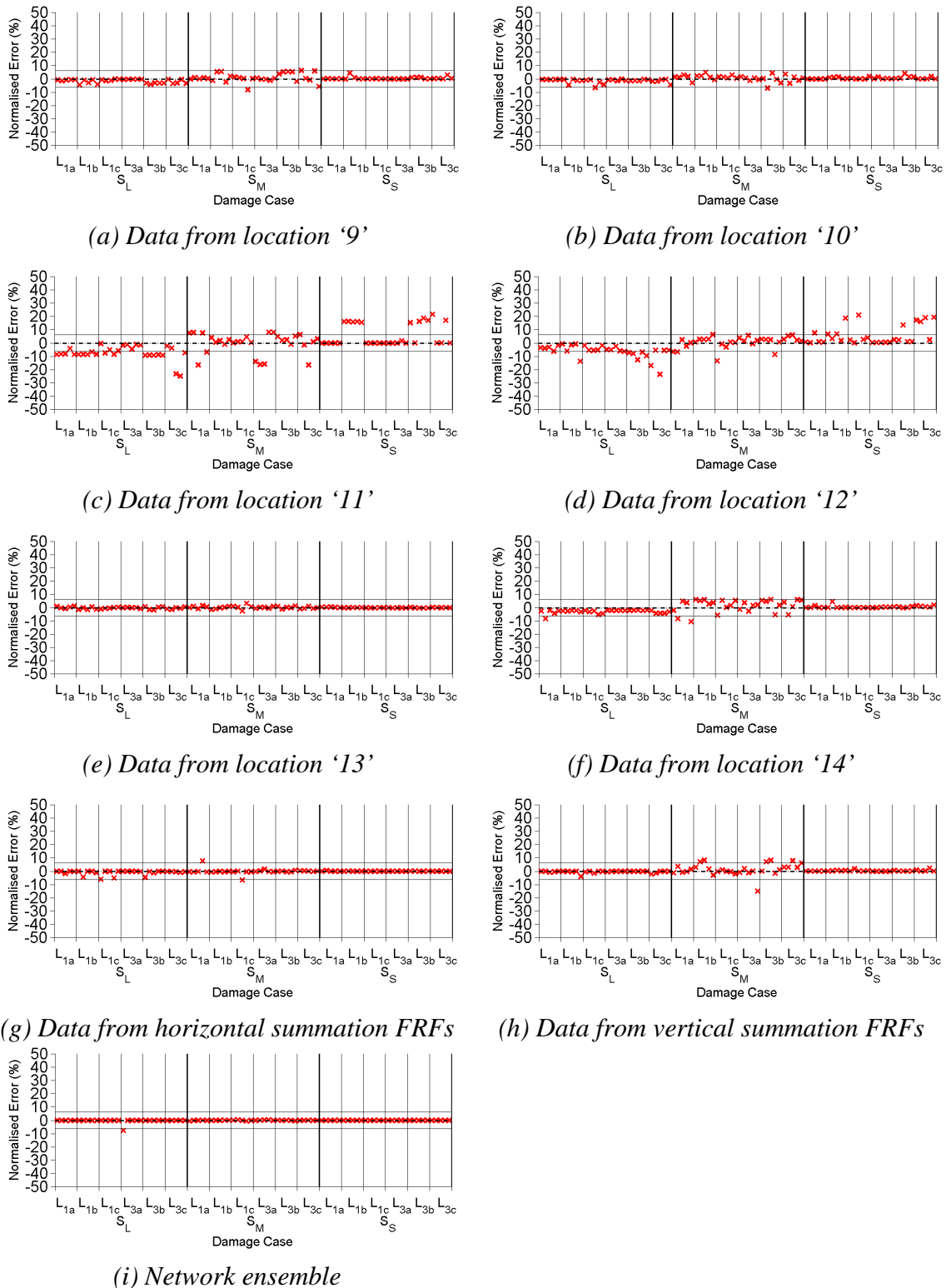


Figure J.20 Neural network testing set outcomes of networks trained with data of 10% noise pollution to estimate damage severity of numerical two-storey framed structure. Outcomes of individual networks trained with data from locations '9' to '14' and data from horizontal/vertical summation FRFs, and of the network ensemble are shown.

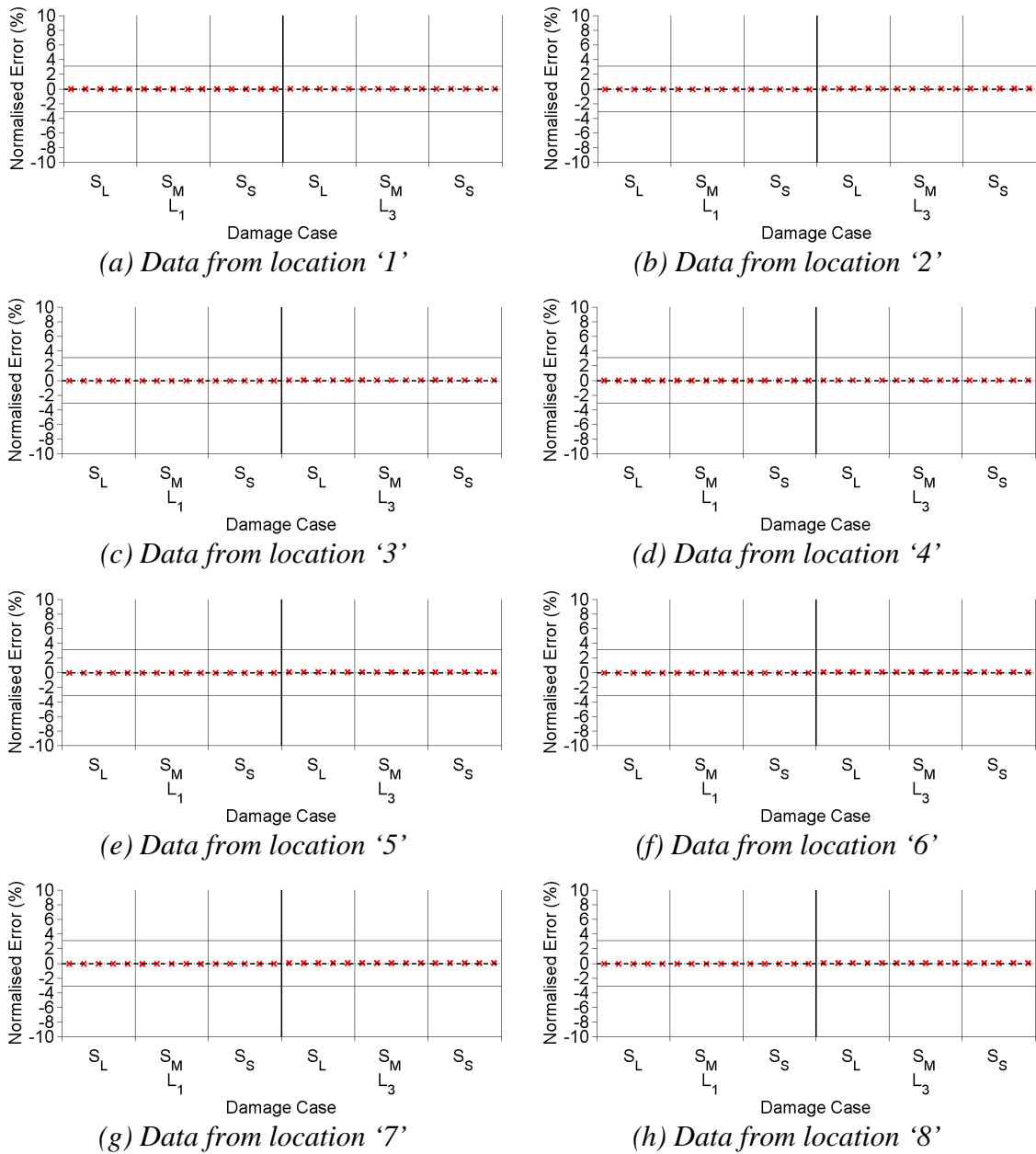


Figure J.21 Neural network testing set outcomes of networks trained to locate damage of laboratory two-storey framed structure. Outcomes of networks trained with data from locations '1' to '8' are shown.

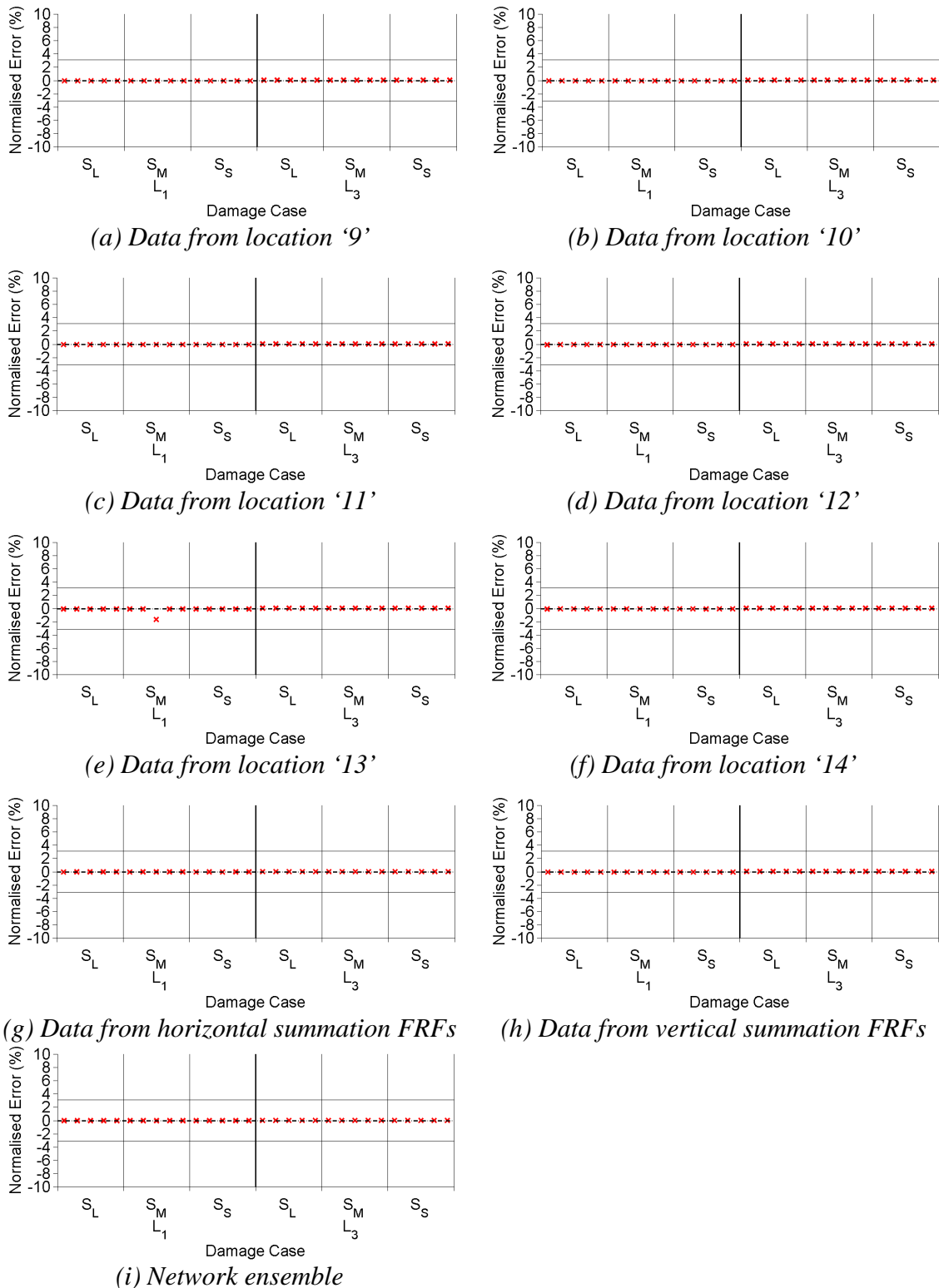


Figure J.22 Neural network testing set outcomes of networks trained to locate damage of laboratory two-storey framed structure. Outcomes of networks trained with data from locations '9' to '14', and data from horizontal/vertical summation FRFs, and of the network ensemble are shown.

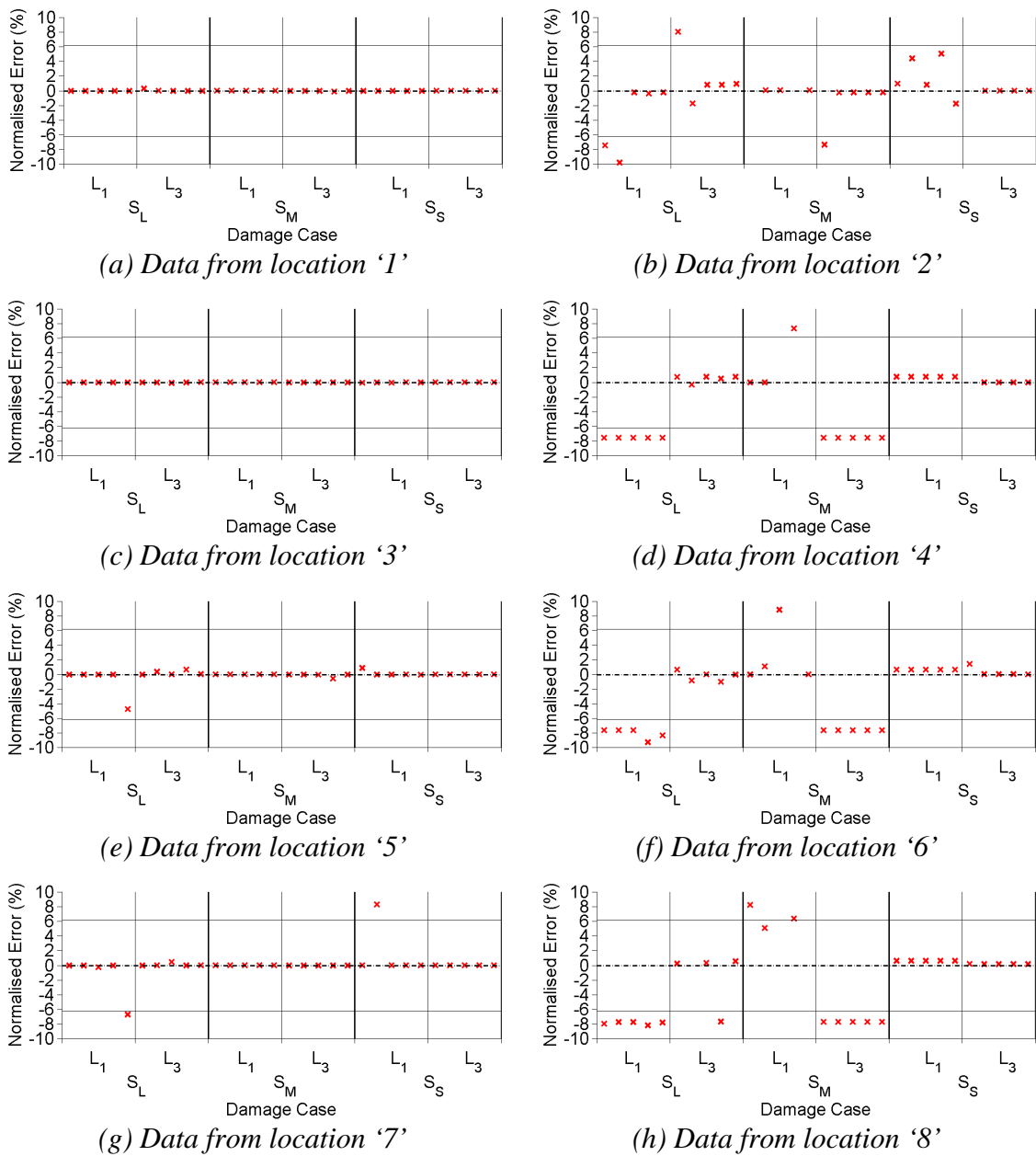


Figure J.23 Neural network testing set outcomes of networks trained to quantify damage of laboratory two-storey framed structure. Outcomes of networks trained with data from locations '1' to '8' are shown.

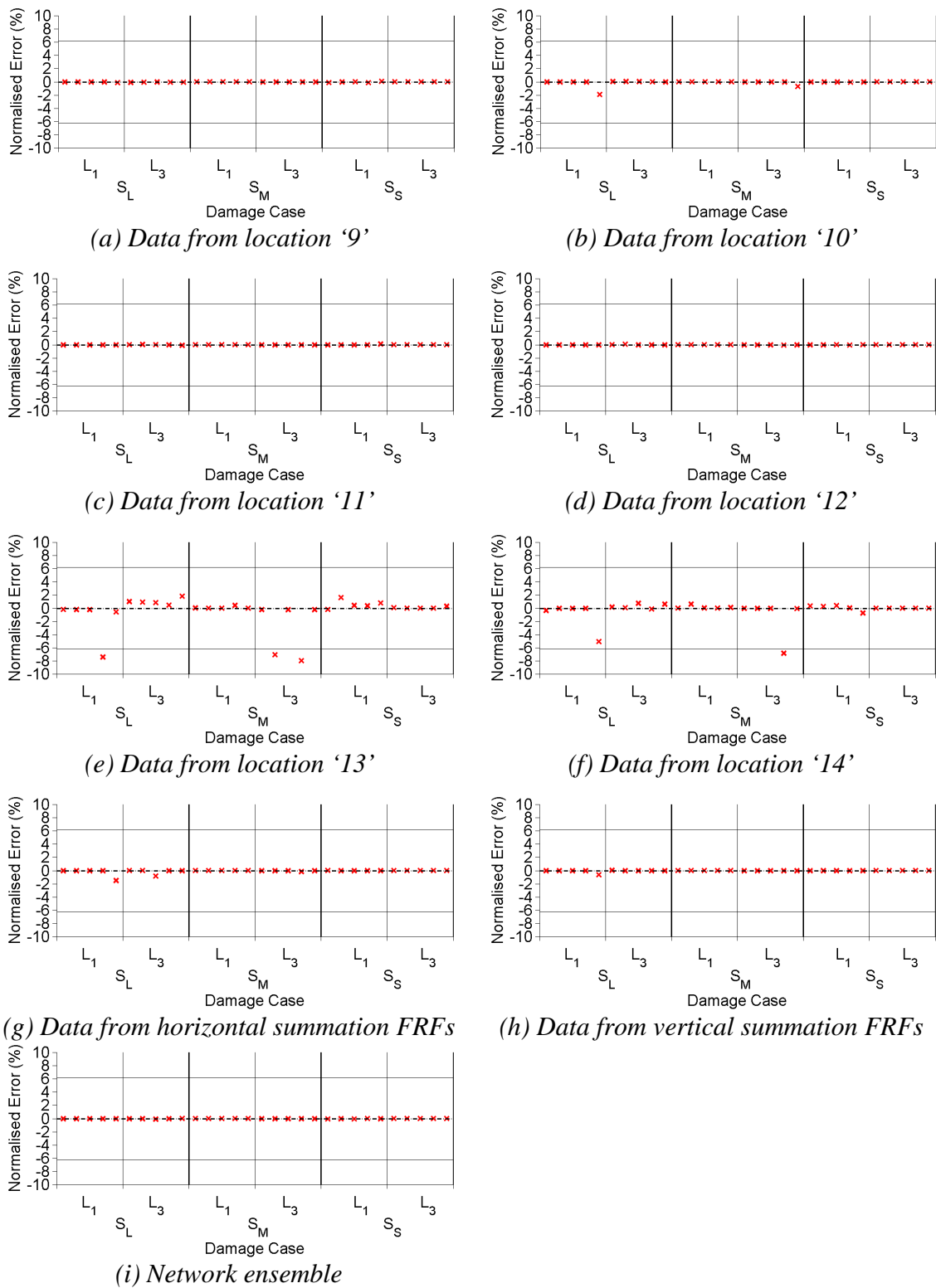


Figure J.24 Neural network testing set outcomes of networks trained to quantify damage of laboratory two-storey framed structure. Outcomes of networks trained with data from locations '9' to '14' and data from horizontal/vertical summation FRFs, and of the network ensemble are shown.